AJNR

AMERICAN JOURNAL OF NEURORADIOLOGY

APRIL 2014
VOLUME 35
NUMBER 4
WWW.AJNR.ORG

THE JOURNAL OF DIAGNOSTIC AND INTERVENTIONAL NEURORADIOLOGY

Ethical use of neuroimaging in medical testimony

Stent retrievers in stroke

Stent-assisted coiling vs. coiling alone for aneurysms

Official Journal ASNR • ASFNR • ASHNR • ASPNR • ASSR

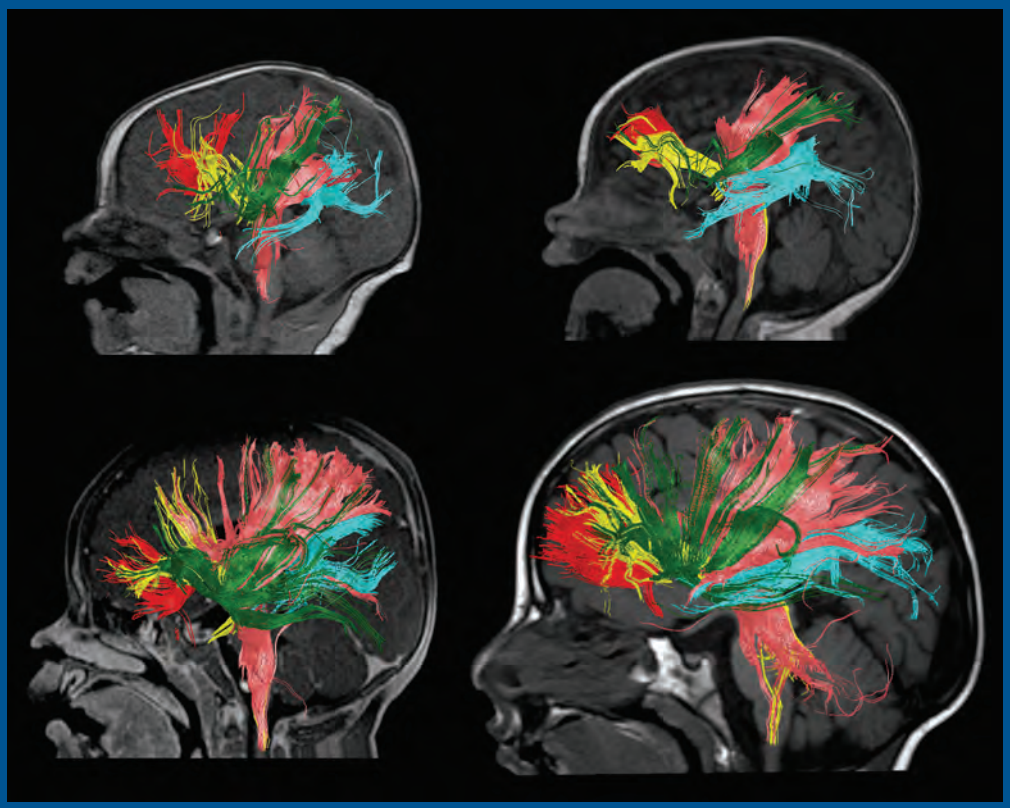

MicroVention® TERUMO

Dedicated to the development

The MicroVention family of neuroendovascular products:

DELIVERY & DETACHMENT SYSTEMS

V-Trak®

V-Trak® Soft

V-Grip®

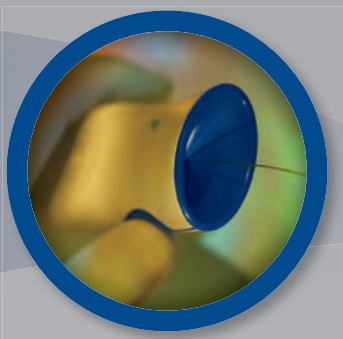

ACCESS PRODUCTS

Traxcess® Guidewire

Chaperon® Guiding Catheter

Headway® Microcatheter

Headway Duo microcatheter

Scepter Occlusion Balloon Catheter

microvention.com

CE 0297

# of innovative endovascular technologies

HYDROGEL COIL PRODUCTS

HydroFrame® HydroCoil® Embolic System

HydroSoft® HydroCoil® Embolic System

HydroFill® HydroCoil® Embolic System

PLATINUM COIL PRODUCTS

MICROPLEX® coil system

COSMOS® complex coil

VFC® Versatile Range Fill Coil

HYPERSOFT® finishing coil

Introducing…

HyperSoft® 3D complex coil

The softness of the HyperSoft® Coil available in Complex Form!

Now you can Frame, Fill and Finish with the softness
you need to match almost any aneurysm morphology.

MicroVention, Inc.
Worldwide Headquarters PH +1.714.247.8000
1311 Valencia Avenue
Tustin, CA 92780 USA
MicroVention UK Limited PH +44 (0) 191 258 6777
MicroVention Europe, S.A.R.L. PH +33 (1) 39 21 77 46
MicroVention Deutschland GmbH PH +49 211 210 798-0

Target®
DETACHABLE COILS

Smooth and Stable

Whether you are framing, filling or finishing, Target Detachable Coils deliver consistently smooth deployment and exceptional microcatheter stability. Focused on design, Target Coils feature a host of advantages to ensure the high-powered performance you demand.

For more information, please visit www.strykerneurovascular.com/Target or contact your local Stryker Neurovascular sales representative.

stryker® Neurovascular

Stroke: *Our Only Focus. Our Ongoing Promise.*

AJNR

AMERICAN JOURNAL OF NEURORADIOLOGY

APRIL 2014
VOLUME 35
NUMBER 4
WWW.AJNR.ORG

Publication Preview at www.ajnr.org features articles released in advance of print. Visit www.ajnrblog.org to comment on AJNR content and chat with colleagues and AJNR's News Digest at http://ajnrdigest.org to read the stories behind the latest research in neuroimaging.

EDITORIALS

PERSPECTIVES

615 **Thinking in Different Directions** *M. Castillo*

EDITORIAL

616 **Acute Stroke Intervention Results: The "Denominator" Fallacy** *M. Goyal*

REVIEW ARTICLES

619 **Raise the Bar and Lower the Dose: Current and Future Strategies for Radiation Dose Reduction in Head and Neck Imaging** *M. Ibrahim, H. Parmar, E. Christodoulou, and S. Mukherji*

625 **The Role of MR Imaging in Assessment of Brain Damage from Carbon Monoxide Poisoning: A Review of the Literature** *T. Beppu*

METHODOLOGIC PERSPECTIVES

632 **Guidelines for the Ethical Use of Neuroimages in Medical Testimony: Report of a Multidisciplinary Consensus Conference** *C.C. Meltzer, G. Sze, K.S. Rommelfanger, K. Kinlaw, J.D. Banja, and P.R. Wolpe*

PRACTICE PERSPECTIVES

638 **Attitudes about Medical Malpractice: An American Society of Neuroradiology Survey** *N.P. Pereira, J.S. Lewin, K.P. Yousem, and D.M. Yousem*

PATIENT SAFETY

644 **Radiation Dose Reduction in Paranasal Sinus CT Using Model-Based Iterative Reconstruction** *J.M. Hoxworth, D. Lal, G.P. Fletcher, A.C. Patel, M. He, R.G. Paden, and A.K. Hara*

650 **Neurointerventions in Children: Radiation Exposure and Its Import** *D.B. Orbach, C. Stamoulis, K.J. Strauss, J. Manchester, E.R. Smith, R.M. Scott, and N. Lin*

HEALTH CARE REFORM VIGNETTE

657 **Budget Sequester: Potential Impact on Health Care Providers** *M.J. Ferrara*

BRAIN

660 **DWI Reversal Is Associated with Small Infarct Volume in Patients with TIA and Minor Stroke** *N. Asdaghi, B.C.V. Campbell, K.S. Butcher, J.I. Coulter, J. Modi, A. Qazi, M. Goyal, A.M. Demchuk, and S.B. Coutts*

667 **The Impact of Arterial Collateralization on Outcome after Intra-Arterial Therapy for Acute Ischemic Stroke** *S. Seeta Ramaiah, L. Churilov, P. Mitchell, R. Dowling, and B. Yan*

Indicates Editor's Choices selection

Indicates Fellows' Journal Club selection

Indicates open access to non-subscribers at www.ajnr.org

Indicates article with supplemental on-line table

Indicates article with supplemental on-line photo

Indicates article with supplemental on-line video

EBM 1 Indicates Evidence-Based Medicine Level 1

EBM 2 Indicates Evidence-Based Medicine Level 2

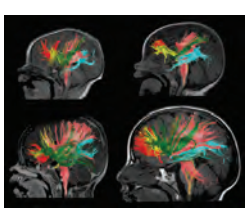

DKI tractography at various stages of brain development.

BARRICADE™ COIL SYSTEM

PERFORMANCE AND VALUE DELIVERED

BLOCKADE MEDICAL

18 TECHNOLOGY DRIVE #169, IRVINE CA 92618 | **P** 949.788.1443
WWW.BLOCKADEMEDICAL.COM

MADE IN AMERICA

CE 0297

MKTG-020 REV. B

673 **Pretreatment ADC Histogram Analysis Is a Predictive Imaging Biomarker for Bevacizumab Treatment but Not Chemotherapy in Recurrent Glioblastoma** *B.M. Ellingson, S. Sahebjam, H.J. Kim, W.B. Pope, R.J. Harris, D.C. Woodworth, A. Lai, P.L. Nghiemphu, W.P. Mason, and T.F. Cloughesy*

680 **White Matter Water Diffusion Changes in Primary Sjögren Syndrome** *L.C. Tzarouchi, A.K. Zikou, N. Tsifetaki, L.G. Astrakas, S. Konitsiotis, P. Voulgari, A. Drosos, and M.I. Argyropoulou*

686 **Imaging Features of a Gelatin-Thrombin Matrix Hemostatic Agent in the Intracranial Surgical Bed: A Unique Space-Occupying Pseudomass** *K.O. Learned, S. Mohan, I.Z. Hyder, L.J. Bagley, S. Wang, and J.Y. Lee*

FUNCTIONAL

691 **Shoulder Apprehension Impacts Large-Scale Functional Brain Networks** *S. Haller, G. Cunningham, A. Laedermann, J. Hofmeister, D. Van De Ville, K.-O. Lovblad, and P. Hoffmeyer*

INTERVENTIONAL *Published in collaboration with Interventional Neuroradiology*

698 **Stent-Assisted Coiling versus Coiling Alone in Unruptured Intracranial Aneurysms in the Matrix and Platinum Science Trial: Safety, Efficacy, and Mid-Term Outcomes** *S.W. Hetts, A. Turk, J.D. English, C.F. Dowd, J. Mocco, C. Prestigiacomo, G. Nesbit, S.G. Ge, J.N. Jin, K. Carroll, Y. Murayama, A. Gholkar, S. Barnwell, D. Lopes, S.C. Johnston, and C. McDougall, on behalf of the Matrix and Platinum Science Trial Investigators*

706 **Endovascular Treatment of 300 Consecutive Middle Cerebral Artery Aneurysms: Clinical and Radiologic Outcomes** *A.M. Mortimer, M.D. Bradley, P. Mews, A.J. Molyneux, and S.A. Renowden*

715 **Endovascular Treatment of Middle Cerebral Artery Aneurysms for 120 Nonselected Patients: A Prospective Cohort Study** *B. Gory, A. Rouchaud, S. Saleme, F. Dalmay, R. Riva, F. Caire, and C. Mounayer*

721 **Validation and Initial Application of a Semiautomatic Aneurysm Measurement Software: A Tool for Assessing Volumetric Packing Attenuation** *H. Takao, T. Ishibashi, T. Saguchi, H. Arakawa, M. Ebara, K. Irie, and Y. Murayama*

727 **Variable Porosity of the Pipeline Embolization Device in Straight and Curved Vessels: A Guide for Optimal Deployment Strategy** *M. Shapiro, E. Raz, T. Becske, and P.K. Nelson*

734 **Stent Retrievers in Acute Ischemic Stroke: Complications and Failures during the Perioperative Period** *G. Gascou, K. Lobotesis, P. Machi, I. Maldonado, J.F. Vendrell, C. Riquelme, O. Eker, G. Mercier, I. Mourand, C. Arquizan, A. Bonafé, and V. Costalat*

741 **Emergency Cervical Internal Carotid Artery Stenting in Combination with Intracranial Thrombectomy in Acute Stroke** *S. Stampfl, P.A. Ringleb, M. Möhlenbruch, C. Hametner, C. Herweh, M. Pham, J. Bösel, S. Haehnel, M. Bendszus, and S. Rohde*

747 **The Outcome and Efficacy of Recanalization in Patients with Acute Internal Carotid Artery Occlusion** *J.H. Kwak, L. Zhao, J.K. Kim, S. Park, D.-g. Lee, J.H. Shim, D.H. Lee, J.S. Kim, and D.C. Suh*

EXTRACRANIAL VASCULAR

754 **Correlation between Fissured Fibrous Cap and Contrast Enhancement: Preliminary Results with the Use of CTA and Histologic Validation** *L. Saba, E. Tamponi, E. Raz, L. Lai, R. Montisci, M. Piga, and G. Faa*

AJNR
AMERICAN JOURNAL OF NEURORADIOLOGY

2013 LUCIEN LEVY BEST RESEARCH ARTICLE

AWARD WINNER AND NOMINEES

The Editors of *AJNR* are pleased to announce the first annual Lucien Levy Best Research Article Award has been presented to

"Potential Role of Preoperative Conventional MRI Including Diffusion Measurements in Assessing Epidermal Growth Factor Receptor Gene Amplification Status in Patients with Glioblastoma"

by R.J. Young, A. Gupta, A.D. Shah, J.J. Graber, A.D. Schweitzer, A. Prager, W. Shi, Z. Zhang, J. Huse, and A.M.P. Omuro.

This award is named for the late *AJNR* Senior Editor who championed its establishment and recognizes the best original research paper accepted in 2013. The winning paper, submitted by authors from Memorial Sloan-Kettering Cancer Center and Weill Cornell Medical College/New York Presbyterian Hospital in New York City, was published electronically on June 27, 2013 and appeared in the December print issue. It was selected by a vote of the Journal's Editor-in-Chief and Senior Editors.


Potential Role of Preoperative Conventional MRI Including Diffusion Measurements in Assessing Epidermal Growth Factor Receptor Gene Amplification Status in Patients with Glioblastoma

Other nominated papers were:

"When Is Carotid Angioplasty and Stenting the Cost-Effective Alternative for Revascularization of Symptomatic Carotid Stenosis? A Canadian Health System Perspective" by M.A. Almekhlafi, M.D. Hill, S. Wiebe, M. Goyal, D. Yavin, J.H. Wong, and F.M. Clement

"Differences in Imaging Characteristics of HPV-Positive and HPV-Negative Oropharyngeal Cancers: A Blinded Matched-Pair Analysis" by S.C. Cantrell, B.W. Peck, G. Li, Q. Wei, E.M. Sturgis, and L.E. Ginsberg

"Higher Rates of Decline for Women and *Apolipoprotein E* ε4 Carriers" by D. Holland, R.S. Desikan, A.M. Dale, and L.K. McEvoy, for the Alzheimer's Disease Neuroimaging Initiative

"Role of Diffusion Tensor Imaging as an Independent Predictor of Cognitive and Language Development in Extremely Low-Birth-Weight Infants" by U. Pogribna, K. Burson, R.E. Lasky, P.A. Narayana, P.W. Evans, and N.A. Parikh

"Phlebographic Study Does Not Show Differences between Patients with MS and Control Subjects" by M. Stefanini, S. Fabiano, F.G. Garaci, S. Marziali, A. Meschini, V. Cama, M. Fornari, S. Rossi, D. Centonze, R. Floris, R. Gandini, and G. Simonetti

"Mind the Gap: Impact of Computational Fluid Dynamics Solution Strategy on Prediction of Intracranial Aneurysm Hemodynamics and Rupture Status Indicators" by K. Valen-Sendstad and D.A. Steinman

760 **Can Doppler Flow Parameters of Carotid Stenosis Predict the Occurrence of New Ischemic Brain Lesions Detected by Diffusion-Weighted MR Imaging after Filter-Protected Internal Carotid Artery Stenting?**
Y. Gunduz, R. Akdemir, L.T. Ayhan, and N. Keser

766 **Predicting Carotid Plaque Characteristics Using Quantitative Color-Coded T1-Weighted MR Plaque Imaging: Correlation with Carotid Endarterectomy Specimens** *S. Narumi, M. Sasaki, H. Ohba, K. Ogasawara, M. Kobayashi, T. Natori, J. Hitomi, H. Itagaki, T. Takahashi, and Y. Terayama*

HEAD & NECK

772 **Craniopharyngeal Canal and Its Spectrum of Pathology** *T.A. Abele, K.L. Salzman, H.R. Harnsberger, and C.M. Glastonbury*

778 **An Exponential Growth in Incidence of Thyroid Cancer: Trends and Impact of CT Imaging** *J.K. Hoang, K.R. Choudhury, J.D. Eastwood, R.M. Esclamado, G.H. Lyman, T.M. Shattuck, and X.V. Nguyen*

784 **Spontaneous Lateral Sphenoid Cephaloceles: Anatomic Factors Contributing to Pathogenesis and Proposed Classification** *F. Settecase, H.R. Harnsberger, M.A. Michel, P. Chapman, and C.M. Glastonbury*

PEDIATRICS

790 **Role of Diffusion Tensor Imaging as an Independent Predictor of Cognitive and Language Development in Extremely Low-Birth-Weight Infants**
U. Pogribna, K. Burson, R.E. Lasky, P.A. Narayana, P.W. Evans, and N.A. Parikh

797 **MR Imaging Evaluation of Inferior Olivary Nuclei: Comparison of Postoperative Subjects with and without Posterior Fossa Syndrome**
Z. Patay, J. Enterkin, J.H. Harreld, Y. Yuan, U. Löbel, Z. Rumboldt, R. Khan, and F. Boop

803 **Time-Dependent Structural Changes of the Dentatothalamic Pathway in Children Treated for Posterior Fossa Tumor** *S. Perreault, R.M. Lober, S. Cheshier, S. Partap, M.S. Edwards, and K.W. Yeom*

808 **Diffusional Kurtosis Imaging of the Developing Brain** *A. Paydar, E. Fieremans, J.I. Nwankwo, M. Lazar, H.D. Sheth, V. Adisetiyo, J.A. Helpern, J.H. Jensen, and S.S. Milla*

815 **Diffusion Imaging for Tumor Grading of Supratentorial Brain Tumors in the First Year of Life** *S.F. Kralik, A. Taha, A.P. Kamer, J.S. Cardinal, T.A. Seltman, and C.Y. Ho*

BOOK REVIEWS *R.M. Quencer, Section Editor*
Please visit www.ajnrblog.org to read and comment on Book Reviews.

stryker® Neurovascular

Trevo® XP
PROVUE RETRIEVER

Take Control. Capture More.

48%
Less Delivery Force

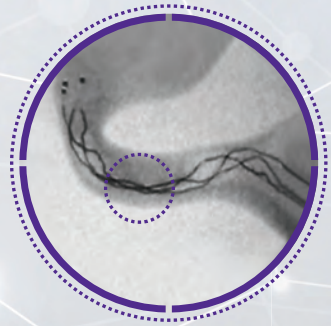

Easy to Deliver

- **48% less delivery force** required as demonstrated in bench testing*

Easy to Place

- **Distal FlexCell Design** including softer distal segment,† shorter landing zone‡ and bright radiopaque markers

Easy to See

- **Full-length radiopacity††** for precise placement, visible integration and interactive retrieval

See for Yourself: TrevoXP.com

All photographs taken by Stryker Neurovascular.
Bench test results may not necessarily be indicative of clinical performance.
Testing completed by Stryker Neurovascular. Data on file and available upon request.

* Compared to Solitaire FR, 4x20mm.
† Bench testing included Trevo XP ProVue, 4x20mm (n=57) and Solitaire FR, 4x20mm and 4x15mm (n=8).
‡ Compared to Trevo® ProVue Retriever.
†† Bench model photo.
Solitaire is a trademark of Tyco Healthcare Group LP composed of Covidien, Inc.

Stroke: *Our Only Focus. Our Ongoing Promise.*

Target® Detachable Coils

See package insert for complete indications, contraindications, warnings and instructions for use.

INTENDED USE / INDICATIONS FOR USE

Target Detachable Coils are intended to endovascularly obstruct or occlude blood flow in vascular abnormalities of the neurovascular and peripheral vessels. Target Detachable Coils are indicated for endovascular embolization of:

- Intracranial aneurysms
- Other neurovascular abnormalities such as arteriovenous malformations and arteriovenous fistulae
- Arterial and venous embolizations in the peripheral vasculature

CONTRAINDICATIONS

None known.

POTENTIAL ADVERSE EVENTS

Potential complications include, but are not limited to: allergic reaction, aneurysm perforation and rupture, arrhythmia, death, edema, embolus, headache, hemorrhage, infection, ischemia, neurological/intracranial sequelae, post-embolization syndrome (fever, increased white blood cell count, discomfort), TIA/stroke, vasospasm, vessel occlusion or closure, vessel
perforation, dissection, trauma or damage, vessel rupture, vessel thrombosis. Other procedural complications including but not limited to: anesthetic and contrast media risks, hypotension, hypertension, access site complications.

WARNINGS

- Contents supplied STERILE using an ethylene oxide (EO) process. Do not use if sterile barrier is damaged. If damage is found, call your Stryker Neurovascular representative.
- For single use only. Do not reuse, reprocess or resterilize. Reuse, reprocessing or resterilization may compromise the structural integrity of the device and/or lead to device failure which, in turn, may result in patient injury, illness or death. Reuse, reprocessing or resterilization may also create a risk of contamination of the device and/or cause patient infection or cross-infection, including, but not limited to, the transmission of infectious disease(s) from one patient to another. Contamination of the device may lead to injury, illness or death of the patient.
- After use, dispose of product and packaging in accordance with hospital, administrative and/or local government policy.
- **This device should only be used by physicians who have received appropriate training in interventional neuroradiology or interventional radiology and preclinical training on the use of this device as established by Stryker Neurovascular.**
- Patients with hypersensitivity to 316LVM stainless steel may suffer an allergic reaction to this implant.
- MR temperature testing was not conducted in peripheral vasculature, arteriovenous malformations or fistulae models.
- The safety and performance characteristics of the Target Detachable Coil System (Target Detachable Coils, InZone Detachment Systems, delivery systems and accessories) have not been demonstrated with other manufacturer's devices (whether coils, coil delivery devices, coil detachment systems, catheters, guidewires, and/or other accessories). Due to the potential incompatibility of non Stryker Neurovascular devices with the Target Detachable Coil System, the use of other manufacturer's device(s) with the Target Detachable Coil System is not recommended.
- To reduce risk of coil migration, the diameter of the first and second coil should never be less than the width of the ostium.
- In order to achieve optimal performance of the Target Detachable Coil System and to reduce the risk of thromboembolic complications, it is critical that a continuous infusion of appropriate flush solution be maintained between a) the femoral sheath and guiding catheter, b) the 2-tip microcatheter and guiding catheters, and c) the 2-tip microcatheter and Stryker Neurovascular guidewire and delivery wire. Continuous flush also reduces the potential for thrombus formation on, and crystallization of infusate around, the detachment zone of the Target Detachable Coil.
- Do not use the product after the "Use By" date specified on the package.
- Reuse of the flush port/dispenser coil or use with any coil other than the original coil may result in contamination of, or damage to, the coil.
- Utilization of damaged coils may affect coil delivery to, and stability inside, the vessel or aneurysm, possibly resulting in coil migration and/or stretching.
- The fluoro-saver marker is designed for use with a Rotating Hemostatic Valve (RHV). If used without an RHV, the distal end of the coil may be beyond the alignment marker when the fluoro-saver marker reaches the microcatheter hub.
- If the fluoro-saver marker is not visible, do not advance the coil without fluoroscopy.
- Do not rotate delivery wire during or after delivery of the coil. Rotating the Target® Detachable Coil delivery wire may result in a stretched coil or premature detachment of the coil from the delivery wire, which could result in coil migration.
- Verify there is no coil loop protrusion into the parent vessel after coil placement and prior to coil detachment. Coil loop protrusion after coil placement may result in thromboembolic events if the coil is detached.
- Verify there is no movement of the coil after coil placement and prior to coil detachment. Movement of the coil after coil placement may indicate that the coil could migrate once it is detached.
- Failure to properly close the RHV compression fitting over the delivery wire before attaching the InZone® Detachment System could result in coil movement, aneurysm rupture or vessel perforation.
- Verify repeatedly that the distal shaft of the catheter is not under stress before detaching the Target Detachable Coil. Axial compression or tension forces could be stored in the 2-tip microcatheter causing the tip to move during coil delivery. Microcatheter tip movement could cause the aneurysm or vessel to rupture.
- Advancing the delivery wire beyond the microcatheter tip once the coil has been detached involves risk of aneurysm or vessel perforation.
- The long term effect of this product on extravascular tissues has not been established so care should be taken to retain this device in the intravascular space.
- To reduce risk of coil migration, the diameter of the first and second coil should never be less than the width of the ostium.
- In order to achieve optimal performance of the Target Detachable Coil System and to reduce the risk of thromboembolic complications, it is critical that a continuous infusion of appropriate flush solution be maintained between a) the femoral sheath and guiding catheter, b) the 2-tip microcatheter and guiding catheters, and c) the 2-tip microcatheter and Stryker Neurovascular guidewire and delivery wire. Continuous flush also reduces the potential for thrombus formation on, and crystallization of infusate around, the detachment zone of the Target Detachable Coil.
- Do not use the product after the "Use By" date specified on the package.
- Reuse of the flush port/dispenser coil or use with any coil other than the original coil may result in contamination of, or damage to, the coil.

Damaged delivery wires may cause detachment failures, vessel injury or unpredictable distal tip response during coil deployment. If a delivery wire is damaged at any point during the procedure, do not attempt to straighten or otherwise repair it. Do not proceed with deployment or detachment. Remove the entire coil and replace with undamaged product.

- Verify repeatedly that the distal shaft of the catheter is not under stress before detaching the Target Detachable Coil. Axial compression or tension forces could be stored in the 2-tip microcatheter causing the tip to move during coil delivery. Microcatheter tip movement could cause the aneurysm or vessel to rupture.
- After use, dispose of product and packaging in accordance with hospital, administrative and/or local government policy.

CAUTIONS / PRECAUTIONS

- Federal Law (USA) restricts this device to sale by or on the order of a physician.
- Besides the number of InZone Detachment System units needed to complete the case, there must be an extra InZone Detachment System unit as back up.
- Removing the delivery wire without grasping the introducer sheath and delivery wire together may result in the detachable coil sliding out of the introducer sheath.
- Failure to remove the introducer sheath after inserting the delivery wire into the RHV of the microcatheter will interrupt normal infusion of flush solution and allow back flow of blood into the microcatheter.
- Some low level overhead light near or adjacent to the patient is required to visualize the fluoro-saver marker; monitor light alone will not allow sufficient visualization of the fluoro-saver marker.
- Advance and retract the Target Detachable Coil carefully and smoothly without excessive force. If unusual friction is noticed, slowly withdraw the Target Detachable Coil and examine for damage. If damage is present, remove and use a new Target Detachable Coil. If friction or resistance is still noted, carefully remove the Target Detachable Coil and microcatheter and examine the microcatheter for damage.
- If it is necessary to reposition the Target Detachable Coil, verify under fluoroscopy that the coil moves with a one-to-one motion. If the coil does not move with a one-to-one motion or movement is difficult, the coil may have stretched and could possibly migrate or break. Gently remove both the coil and microcatheter and replace with new devices.
- Increased detachment times may occur when:
  – Other embolic agents are present.
  – Delivery wire and microcatheter markers are not properly aligned.
  – Thrombus is present on the coil detachment zone.
- Do not use detachment systems other than the InZone Detachment System.
- Increased detachment times may occur when delivery wire and microcatheter markers are not properly aligned.
- Do not use detachment systems other than the InZone Detachment System.

Stryker Neurovascular
47900 Bayside Parkway
Fremont, CA 94538-6515
stryker.com/neurovascular

Date of Release: FEB/2014
EX_EN_US

Trevo® XP ProVue Retrievers

See package insert for complete indications, complications, warnings, and instructions for use.

INDICATIONS FOR USE

The Trevo Retriever is intended to restore blood flow in the neurovasculature by removing thrombus in patients experiencing ischemic stroke within 8 hours of symptom onset. Patients who are ineligible for intravenous tissue plasminogen activator (IV t-PA) or who fail IV t-PA therapy are candidates for treatment.

COMPLICATIONS

Procedures requiring percutaneous catheter introduction should not be attempted by physicians unfamiliar with possible complications which may occur during or after the procedure. Possible complications include, but are not limited to, the following: air embolism; hematoma or hemorrhage at puncture site; infection; distal embolization; pain/headache; vessel spasm, thrombosis, dissection, or perforation; emboli; acute occlusion; ischemia; intracranial hemorrhage; false aneurysm formation; neurological deficits including stroke; and death.

COMPATIBILITY

3x20 mm retrievers are compatible with Trevo® Pro 14 Microcatheters (REF 90231) and Trevo® Pro 18 Microcatheters (REF 90238). 4x20 mm retrievers are compatible with Trevo® Pro 18 Microcatheters (REF 90238). Compatibility of the Retriever with other microcatheters has not been established. Performance of the Retriever device may be impacted if a different microcatheter is used. The Merci® Balloon Guide Catheters are recommended for use during thrombus removal procedures. Retrievers are compatible with the Abbott Vascular DOC® Guide Wire Extension (REF 22260).

WARNINGS

- Contents supplied STERILE, using an ethylene oxide (EO) process. Nonpyrogenic.
- To reduce risk of vessel damage, adhere to the following recommendations:
  – Take care to appropriately size Retriever to vessel diameter at intended site of deployment.
  – Do not perform more than six (6) retrieval attempts in same vessel using Retriever devices.
  – Maintain Retriever position in vessel when removing or exchanging Microcatheter.
- To reduce risk of kinking/fracture, adhere to the following recommendations:
  – Immediately after unsheathing Retriever, position Microcatheter tip marker just proximal to shaped section. Maintain Microcatheter tip marker just proximal to shaped section of Retriever during manipulation and withdrawal.
  – Do not rotate or torque Retriever.
  – Use caution when passing Retriever through stented arteries.
- Do not resterilize and reuse. Structural integrity and/or function may be impaired by reuse or cleaning.
- The Retriever is a delicate instrument and should be handled carefully. Before use and when possible during procedure, inspect device carefully for damage. Do not use a device that shows signs of damage. Damage may prevent device from functioning and may cause complications.
- Do not advance or withdraw Retriever against resistance or significant vasospasm. Moving or torquing device against resistance or significant vasospasm may result in damage to vessel or device. Assess cause of resistance using fluoroscopy and if needed resheath the device to withdraw.
- If Retriever is difficult to withdraw from the vessel, do not torque Retriever. Advance Microcatheter distally, gently pull Retriever back into Microcatheter, and remove Retriever and Microcatheter as a unit. If undue resistance is met when withdrawing the Retriever into the Microcatheter, consider extending the Retriever using the Abbott Vascular DOC guidewire extension (REF 22260) so that the Microcatheter can be exchanged for a larger diameter catheter such as a DAC® catheter. Gently withdraw the Retriever into the larger diameter catheter.
- Administer anti-coagulation and anti-platelet medications per standard institutional guidelines.

PRECAUTIONS

- Prescription only – device restricted to use by or on order of a physician.
- Store in cool, dry, dark place.
- Do not use open or damaged packages.
- Use by "Use By" date.
- Exposure to temperatures above 54°C (130°F) may damage device and accessories. Do not autoclave.
- Do not expose Retriever to solvents.
- Use Retriever in conjunction with fluoroscopic visualization and proper anti-coagulation agents.
- To prevent thrombus formation and contrast media crystal formation, maintain a constant infusion of appropriate flush solution between guide catheter and Microcatheter and between Microcatheter and Retriever or guidewire.
- Do not attach a torque device to the shaped proximal end of DOC® Compatible Retriever. Damage may occur, preventing ability to attach DOC® Guide Wire Extension.

Concentric Medical
301 East Evelyn
Mountain View, CA 94041

Stryker Neurovascular
47900 Bayside Parkway
Fremont, CA 94538-6515
stryker.com/neurovascular

Date of Release: FEB/2014
EX_EN_US

AJNR

AMERICAN JOURNAL OF NEURORADIOLOGY

Publication Preview at www.ajnr.org features articles released in advance of print. Visit www.ajnrblog.org to comment on AJNR content and chat with colleagues and AJNR's News Digest at http://ajnrdigest.org to read the stories behind the latest research in neuroimaging.

APRIL 2014 • VOLUME 35 • NUMBER 4 • WWW.AJNR.ORG

AJNR (Am J Neuroradiol ISSN 0195–6108) is a journal published monthly, owned and published by the American Society of Neuroradiology (ASNR), 800 Enterprise Drive, Suite 205, Oak Brook, IL 60523. Annual dues for the ASNR include $170.00 for journal subscription. The journal is printed by Cadmus Journal Services, 5457 Twin Knolls Road, Suite 200, Columbia, MD 21045; Periodicals postage paid at Oak Brook, IL and additional mailing offices. Printed in the U.S.A. POSTMASTER: Please send address changes to American Journal of Neuroradiology, P.O. Box 3000, Denville, NJ 07834, U.S.A. Subscription rates: nonmember $370 ($440 foreign) print and online, $300 online only; institutions $430 ($495 foreign) print and basic online, $850 ($915 foreign) print and extended online, $355 online only (basic), extended online $770; single copies are $35 each ($40 foreign). Indexed by PubMed/Medline, BIOSIS Previews, Current Contents (Clinical Medicine and Life Sciences), EMBASE, Google Scholar, HighWire Press, Q-Sensei, RefSeek, Science Citation Index, and SCI Expanded.

Thinking in Different Directions

M. Castillo, *Editor-in-Chief*

A few days ago, we were having our weekly case conference and we saw a patient with an interesting intracranial lesion. I asked a resident to look at the clinical record and find out what the discharge diagnosis was. He then proceeded to inform me that it was a meningioma. "How do they know if they have not biopsied it?" I asked. After much searching, our trainee found out that the neurosurgeons had used our initial impression as the final diagnosis, and slowly we had all begun to assume that this was indeed the confirmed diagnosis and kept quoting it on our own reports. This is an example of thinking that begins and ends with an assumption (often wrong), also known as circular or paradoxical thinking and in logic called a "logical fallacy."[1] It is my impression that in imaging and in medicine in general, we spend a considerable amount of time engaged in this type of reasoning and that this process is more common now than in the past, perhaps because of the repetition ("cutting and pasting") that is found in patient medical records. In circular thinking, a conclusion cannot be proved false or true if it arose from a false premise. Because repeating a statement in circular fashion seems to make it stronger, circular thinking ends by creating statements that sound true and gain wide support (thus, the above-mentioned patient now carries a diagnosis of "meningioma"). There is no doubt that circular thinking is dangerous and that we must do our best to avoid it.

The opposite of circular thinking is linear (vertical) thinking. In this type of reasoning, progress is made in a step-by-step fashion and a response to each step must exist before advancing to the next one. Although linear thinking advances by logic, it is by its own nature highly focused on single pathways and as such tends to ignore other possibilities and alternatives. Linear thinking is basically a binary process in which answers are "Yes" or "No" (correct or incorrect), excluding all considerations beyond these 2 responses. These features make it fast, organized, and sequential and therefore it is the most common type of thought process used.[2] People generally regard linear thinking as an honest, mature, and intelligent process when in reality it lacks ingenuity, innovation, and originality. Similar to circular thinking, linear thinking is characterized by repetition and is, in the long term, detrimental to intellectual advancement.

Where linear thinking is a "safe" process, a third type of reasoning called lateral (horizontal) thinking is risky, uneven, adventurous, more difficult, and not widely accepted. Lateral thinking views a problem from multiple perspectives, many of them random. Because lateral thinking is based on discovery and exploration of spontaneous events, it is the opposite of linear thinking: slow, disorganized, and nonsequential. Lateral thinking teeters close to the edge of disaster because it is greatly affected by luck and chance and may easily turn into chaos. Most individuals are not organized enough to use it and rapidly become overwhelmed by the choices it offers. The brightest individuals know when to use vertical and lateral thinking and avoid circular reasoning. In popular culture, linear thinking is linked to men while lateral thinking is linked to women.

Howard E. Gardner, a world-famous professor of cognition and education at Harvard University, formulated the concept of multiple intelligences.[3] We humans have different ways of learning and processing information and thus we are different and independent from each other. Although those who favor this concept oppose the idea of a "general intelligence factor," it is likely that all individuals share both, that is, they are smart as individuals but also share a collective intelligence that makes them similar to all other human beings. Dr. Gardner has separated intelligence into the following categories: linguistic, logical-mathematical, musical, spatial, bodily/kinesthesic, interpersonal, intrapersonal, naturalistic, and possibly existential (after much thinking I have come to the conclusion that there must be others because I believe I do not possess any of these!). However, I agree with him when he states that education (not only in America but worldwide) is based mostly on logical (mathematics) and linguistic (language arts) intelligence and that current methods for assessing intelligence (such as IQ tests) measure only these 2 features. This brings up the inadequacy of the current schooling systems that disregard other types of intelligence. Most current education (and research) depends on mainly linear thinking.

A fascinating endeavor that encourages folks to express their different intelligences and to think laterally is TED.com (TED stands for: technology, entertainment, design). This nonprofit organization that was started in 1984 contains more than 1400 (as of this writing) varied and exciting conferences by some of the world's smartest and most diverse and laterally thinking individuals. For a fantastic account of how it works, I suggest reading Nathan Heller's article in *The New Yorker* titled "List and Learn."[4] The most viewed TED conference (more than 15 million times) is one given by British education specialist Sir Ken Robinson in 2006 (a newer one was posted in May 2010 and has been viewed nearly 4 million times).[5] Robinson argues that university professors educate students to become, well… university professors in a process so linear that it kills all creativity and discourages many students from exploring alternative avenues. He also calls attention to the ever-diminishing value of education degrees (and those of us who live in university towns know that sometimes all that a PhD gets you is a better waitressing job). The rigidity of school systems that are based on mathematics and linguistics results in linear thinking stifling the creativity associated with lateral thinking and is thus harmful to society.

In an article in *The New York Times*,[6] Andrew Hacker explains why more than one-third of high school students fail algebra and states that difficulty with mathematics may be responsible for up to 45% of high school dropouts in the United States. Aptitude

http://dx.doi.org/10.3174/ajnr.A3647

tests such as the American SAT (Scholastic Aptitude Test) and the ACT (American College Testing) concentrate in measuring 2 subjects: mathematics and linguistics (the pillars of linear thinking, as stated previously). Mr. Hacker proposes that perhaps just basic algebra and what he astutely calls "citizen statistics" may be enough for most us, whereas more advanced courses such as calculus should be reserved for fewer, gifted individuals who seek careers that depend on the understanding of higher mathematics. As Sir Ken Robinson states, "We are educating people out of their creative capacities."

Does studying liberal arts and the humanities make us better physicians? I believe it does. I have been unable to notice any differences with respect to knowledge of biologic sciences in our daily work between residents who come from a "hard" science background and those with a liberal arts education, and I find that personally I like the latter better. Medical schools are aware of this, and some such as Boston University and Brown University encourage this type of liberal arts curriculum and reserve a number of places in their medical schools for these individuals. More than 40% of medical students at the University of Pennsylvania come from non-premed backgrounds.[7] The liberal arts may also be useful to medical students, and the Mount Sinai School of Medicine in New York has a specific humanities and medicine program. The separation of liberal arts from sciences is, in my opinion, damaging and ends up suppressing the human qualities of many excellent and caring young individuals. Because liberal arts are characterized by lateral thinking, bringing these individuals into our world of linear thinking will prove to be beneficial for all.

I am not aware of imaging methods having been used to study these different types of thinking. There are, however, several principles that control all human thought processes.[8] A basic principle of thinking is that it is the product of concurrent brain activity in multiple regions that together form a large-scale cortical network. This is a type of functional connectivity that has been documented in thousands of fMRI reports. Also, each cortical region can perform multiple functions, and these same functions can also be performed by different regions, an observation that may explain thought (and function) plasticity. Rather than a strict linear or vertical organization, the brain prefers a lateral or horizontal organization that serves as its own backup and redundant system. Unfortunately, each cortical region can only do so much and thus has a limited capacity. Conversely, these constraints force other parts of the brain to collaborate, and this helps it adapt to many situations. The topologies of large-scale networks are in constant flux, adapting themselves to the demands of tasks. The brain is not dumb: it uses the minimum amount of resources needed for each activity, but, if one network becomes insufficient, additional ones are immediately recruited. The brain's topology has 2 components: membership and connectivity, and both are in constant flux. Just as the Internet does, the brain also has a limited bandwidth, resulting in a finite amount of resources that it can use. This bandwidth, up to a certain extent, varies from individual to individual and thus some are more successful in multitasking than others. Increased brain bandwidth seems to be connected to lateral thinking.

Lateral thinking is important and is not used sufficiently in the sciences, but this is beginning to change. Of course, we radiologists can take it to a silly extreme, as seen in a recent advertisement that intended to recruit a lateral-thinking technologist for a vertical MR imaging (upright) scanner![9] Radiologists actually think dimensionally, and 2D and 3D processes play an important role in the interpretation of images in which it all begins as the former and ends as the latter. I like to think of this as a process that also begins vertically and then branches horizontally. Some of our trainees have more trouble making this transition and thus take longer to learn the specialty. It is possible that some may survive and graduate not being able to think 3-dimensionally, but they will never survive if they think circularly.

REFERENCES

1. **Circular reasoning.** http://en.wikipedia.org/wiki/Circular_reasoning. Accessed on May 2, 2013
2. **Is linear thinking bad?** http://www.andyeklund.com/creativestreak/2012/06/is-linear-thinking-bad.html. Accessed on May 2, 2013
3. http://www.howardgardner.com. Accessed on May 2, 2013
4. Heller N. **List and Learn.** *The New Yorker,* July 9, 2012
5. http://www.ted.com/talks/ken_robinson_says_schools_kill_creativity.html. Accessed on May 2, 2013
6. Hacker A. **Is algebra necessary?** *The New York Times,* July 28, 2012. http://www.nytimes.com/2012/07/29/opinion/sunday/is-algebra-necessary.html. Accessed on May 2, 2013
7. Kliff S. **Why medical schools like to accept STS majors.** *Newsweek,* September 10, 2007
8. Just MA, Varma S. **The organization of thinking: what functional brain imaging reveals about the neuroarchitecture of complex cognition.** *Cogn Affect Behav Neurosci* 2007;7:153–91
9. http://www.radmagazine.co.uk/JobPDFs/441115.pdf. Accessed on May 2, 2013

EDITORIAL

Acute Stroke Intervention Results: The "Denominator" Fallacy

M. Goyal

It is common these days to have conversations at meetings related to outcome of endovascular procedures for acute stroke. Very often, interventionalists can be seen stating proudly how their good outcome rate (mRS <2) is $>60\%$, or much higher than the other center in their city, or higher than the various trials in the literature. Of course, their basis of calculation for their good outcome rate uses the total number of stroke cases that underwent intra-arterial (IA) therapy at their center. Very often, the numerator and the denominator are limited to anterior circulation strokes. This process takes a further leap forward when devices or imaging paradigms (for acute stroke treatment) are being compared. Various recent studies such as IMS III,[1] SYNTHESIS,[2] MR-RESCUE,[3] TREVO 2,[4] SWIFT,[5] and STAR[6] have different good outcome rates. Speakers at meetings, discussions in hallways, and vendor sales pitches have a tendency to use these good outcome rates without necessarily paying enough attention to the denominator. What kind of patients received IA therapy? What were the precise selection criteria? Did every patient who fulfilled those

http://dx.doi.org/10.3174/ajnr.A3770

criteria receive IA therapy, or was there a selection bias? I recently reviewed a paper for a pre-eminent journal. In the article, the authors claimed that perfusion imaging improves patient outcome. This is not the first time that I read this sentence. I have heard it said multiple times at meetings as well. Why is this wrong?

The "Denominator" Fallacy

Here is an illustrative example. Let us take two towns: City A and City B. Both towns have the same population and similar demographics. Both cities have 200 patients in the year 2012 with acute ischemic strokes caused by large-vessel occlusion, specifically the M1 segment of the middle cerebral artery. In City A, of these 200 patients, 120 patients receive IA therapy (on the basis of certain selection criteria), and, by use of device Extractor A, clots are removed. Sixty patients (50%) have a good outcome. In City B, of the 200 patients, 20 patients receive IA therapy (on the basis of slightly different selection criteria by use of complex, sophisticated imaging), and, by use of the device Decimator B, clots are removed. Eighteen patients (90%) have a good outcome. What can one conclude from the data? With the use of selective information, one could try and conclude that Decimator B is a superior device compared with Extractor A or that the interventionalists in City B are better than in City A or that complex imaging selection improves patient outcome. However, from a societal perspective, clearly, the treatment paradigm at City A (with a 30% good outcome; 60 of 200) is better than that at City B (9% good outcome rate; 18 of 200). However, even that is not a totally correct statement. The correct way from a societal perspective would be, how many patients of the 200 had good outcome irrespective of whether they got endovascular treatment. On the basis of current literature and imaging-based patient selection paradigms, it seems likely that the "best" patients would get chosen for endovascular treatment (those with small core, large penumbra, good premorbid status, and those presenting early). Hence, it is quite likely that the patients who do not undergo endovascular treatment would have a very high likelihood of having a poor outcome. Of course, it is quite likely that some of the patients who underwent IA therapy could have had a good outcome without endovascular treatment, especially if they received intravenous thrombolytic agents[1] (potentially further reducing the effectiveness of City B's approach).

Cost and Resource Implications

Is City A spending much more money and resources compared with City B with many more futile recanalizations? This question is complex and must be considered in the overall perspective of the cost of stroke care. Recent data from Canada suggest that the first-year cost of disabling strokes (mRS 3–5) was approximately $108,000 as compared with approximately $48,000 for nondisabling strokes (mRS 0–2).[7] Given these figures, it would be easy to justify the costs associated with the "futile recanalizations." Although there is not much literature on the cost of endovascular stroke intervention, it is clearly going to be significantly less than the $60,000 difference from this study.

Natural History of the Untreated Patients and Complication Rate of Procedure

Unfortunately, we do not have very good data to answer the question: What is the natural history of a patient with M1 occlusion who may or may not be eligible for treatment with intravenous tPA and could be treated with endovascular devices within 8 hours of symptom onset (on the basis of the labeling on some of the recently approved stent retrievers)? The main factors that would determine patient outcome for the conservative arm probably would be: patient's premorbid status and comorbidities, quality of collaterals, brain eloquence, size of final infarct, and receiving intravenous thrombolytics. Of note, selective use of data from recent trials such as IMS III suffers from the same "denominator fallacy." The good outcome rate in IMS III of patients with M1 occlusion in the medical arm was 51%. The total number of patients in this category was 47, and we do not know the true denominator of the total number of patients with M1 occlusion who were treated at the centers participating in IMS III and those who were treated outside of the trial. Also, all patients in the medical arm of IMS III were treated within 3 hours of symptom onset with intravenous tPA. Thus, in my opinion, the natural history of these 200 patients at either City A or City B is essentially unknown. Recent multi-center studies with the use of newer devices such as the STAR registry[6] demonstrate very low rates of symptomatic intracranial hemorrhage (1.5%), and, as such, intracranial hemorrhage is not likely to play a significant role in the overall picture. Overall, imaging-based patient selection cannot improve patient outcome. It can reduce the number of futile recanalizations. On the other hand, there is a definite possibility of reducing the likelihood of a good outcome by use of complex imaging-based patient selection, especially if centers spend large amounts of valuable time in complex imaging and decision-making.

Ceiling Effect

This brings up the question: Why bother with patient selection? Why not take all the patients to the interventional suite? Ultimately, it ends up being a balance between likelihood of benefit, potential complications, resource availability, existent data, and practice of evidence-based medicine. Also, it is very likely that there is going to be a ceiling effect wherein taking more and more patients to the interventional suite will not increase the number of patients with good clinical outcome. Where is the correct balance between, on the one hand, having very loose selection criteria and taking nearly all patients to the interventional suite versus, on the other hand, having very sophisticated, complex imaging-based criteria and taking very few patients to the interventional suite? When do we know that we have reached the "ceiling"? I suspect that the answer to the question of patient selection will be a somewhat middle ground and will need to be backed by good data. The ceiling probably is not fixed. It will be dependent on multiple factors, with the main modifiable one being efficiency, which can be improved with more societal education regarding recognizing stroke, and having patients reach the appropriate hospital faster and receive treatment faster. Over a period of time, anything that compromises efficiency of treatment is, in my opinion, probably not going to survive. Recent articles have talked about various

parameters such as picture to puncture (P2P), and catheter to capture (C2C) and about focusing on efficiency.[8] We have previously reported our experience of ultrafast recanalization with "CT to recanalization" of <60 minutes.[9] However, ultimately, the only time that matters is "onset to recanalization" time. Of course, the other major factor would be the presence of collaterals that would keep the brain alive while vessel recanalization is achieved. At the current moment, however, we have no technology to increase collaterals before the stroke has taken place. The dream of neuroprotection also remains unfulfilled.

Conclusions

The only denominator that makes sense is the total magnitude of disease in the society—in this case, the total number of patients with acute ischemic stroke caused by proximal vessel occlusion. Stated this way, the results incorporate all the various aspects of stroke care including systems of transportation, patient selection, procedural efficacy, and complication. Also, when presented this way, one can determine the total impact on society across different locations and over different periods of time. It is quite understandable that in many situations at the current moment, this denominator is difficult to calculate. In any big city, there may be many different centers providing acute stroke care and hence it may not be possible to determine the total number of patients in the population with endovascular-amenable acute ischemic stroke. In the meantime, however, it may be prudent to refrain from making inaccurate comparisons across different trials with different centers, different imaging paradigms, and various devices unless these are tested in a head-to-head fashion, use the same denominator, and/or have the same selection criteria.

REFERENCES

1. Broderick JP, Palesh YY, Demchuk AM, et al. **Endovascular therapy after intravenous tPA versus tPA alone for stroke.** *N Engl J Med* 2013;368:893–903
2. Ciccone A, Valvassori L, Nichelatti M, et al. **Endovascular treatment for acute ischemic stroke.** *N Engl J Med* 2013;368:904–13
3. Kidwell CS, Jahan R, Gornbein J, et al. **A trial of imaging selection and endovascular treatment for ischemic stroke.** *N Engl J Med* 2013;368:914–23
4. Nogueira RG, Lutsep HL, Gupta R, et al, for the TREVO 2 Investigators. **Trevo vs MERCI retrievers for thrombectomy revascularisation of large vessel occlusions in acute ischemic stroke: a randomized trial.** *Lancet* 2012;380:1231–40
5. Saver JL, Jahan R, Levy EI, et al, for the SWIFT Trialists. **Solitaire flow restoration device versus the Merci retriever in patients with acute ischaemic stroke (SWIFT): a randomized, parallel-group, non-inferiority trial.** *Lancet* 2012;380:1241–49
6. Gralla J, Pereira VM, Davalos A, et al. **Prospective, multi-center, single-arm study of mechanical thrombectomy using Solitaire FR in acute ischemic stroke: STAR.** *Stroke* 2013;44:2802–07
7. Mittmann N, Seung SJ, Hill MD, et al. **Impact of disability status on ischemic stroke costs in Canada in the first year.** *Can J Neurol Sci* 2012;39:793–800
8. Zaidat OO, Lazzaro MA, Gupta R, et al. **'Time' for success.** *J Neurointerv Surg* 2013 [Epub ahead of print]
9. Almekhlafi MA, Eesa M, Menon BK, et al. **Ultrashort imaging to reperfusion time interval arrests core expansion in endovascular therapy for acute ischemic stroke.** *J Neurointerv Surg* 2013;5(Suppl 1):i58–56

Raise the Bar and Lower the Dose: Current and Future Strategies for Radiation Dose Reduction in Head and Neck Imaging

M. Ibrahim, H. Parmar, E. Christodoulou, and S. Mukherji

ABSTRACT

SUMMARY: Technologic advances in CT have generated a dramatic increase in the number of CT studies, with a resultant increase in the radiation dose related to CT scanning. Such increase in radiation dose is becoming a concern for the radiology community, especially with increasing public awareness of the dose burden related to examinations. To cope with the increase in CT-related radiation exposure, it is becoming necessary to optimize CT imaging protocols and apply radiation dose reduction techniques to ensure the best imaging with the lowest radiation dose.

ABBREVIATIONS: ASIR = adaptive statistical iterative reconstruction algorithm; ATCM = automated tube current modulation; CTDI = CT dose index; DLP = dose-length product; FBP = filtered back-projection

Despite the introduction of MR imaging, the overall frequency of CT studies in neuroimaging has failed to decrease. Indeed, the advent of helical and multidetector row CT with rapid acquisitions times and new diagnostic fields (eg, CT angiography, perfusion CT) has led to a further increase in CT examinations. As application of CT is becoming more widespread, there is an emergent need for radiation dose reduction to avoid a reversal of the risk-benefit ratio associated with this imaging technique. Individual patient doses are increasing with newer faster scanners because of volume scanning, thinner sections, overlapping scans, and increasing scan coverage. The as low as reasonably achievable principle (ALARA) emphasizes optimizing CT imaging protocols to achieve the lowest radiation dose possible while maintaining an optimal image quality.

Radiation dose is proportional to the amount of energy delivered by the photons within the x-ray beam. This is generally dependent on the total number of the photons and the individual photon energy within the x-ray beam, which is dictated by the image-acquisition parameters such as kilovolt(peak), milliampere, and x-ray tube rotation time, along with other factors such as section thickness, scan coverage, and pitch. Additionally, body habitus and size of the patient are important factors of the radiation dose delivered, which is especially relevant in pediatric patients and small adults. As a response to the increased concern of the higher radiation dose, there have been several advances in dose-reduction techniques with the introduction of tube current modulation, peak voltage optimization, noise-reduction reconstruction algorithms, adaptive dose collimation, and improved detection-system efficiency. Such techniques not only address the increased concern about radiation dose but also are becoming a marketing tool. The radiology community, including radiologists, technicians, and physicists, should be familiar with such dose-reduction techniques and should optimize the imaging protocols to achieve the best images with a lower radiation dose.

CT Radiation Dose Measurement

CT is a unique imaging technique with continuous exposure around the patient as the gantry rotates to cover the region to be examined. Consequently, energy deposition is fairly uniform at fixed radial positions across the scanned plane with a relatively symmetric gradient from the surface toward the center of the patient because the patient is equally irradiated from all directions. CT is unlike plain radiography, in which exposure is highest at the skin entrance with continuous reduction of the dose toward the skin exit. Due to x-ray scattering, deposition of the radiation beam energy will extend beyond the directly scanned volume into the adjacent tissues. Furthermore, the divergence of the beam and limited efficiency of the collimator contribute to energy deposition in tissues that are not imaged in the specific section. The radiation dose in the scanned section is the summation of the dose due to the direct beam in the scanned plane and dose contributions from radiation scattering from all the sections scanned before and after the specific section (Table 1).

The conventional metric representing the integrated dose of

From the University of Michigan Health System, Ann Arbor, Michigan.

Please address correspondence to Mohannad Ibrahim, MD, University of Michigan Health System, 1500 East Medical Center Dr, Ann Arbor, MI 48109; e-mail: mibrahim@med.umich.edu

http://dx.doi.org/10.3174/ajnr.A3473

Table 1: Descriptions for MSAD and CTDI variants

Dose Index	Description
MSAD	Average dose over 1 scan interval in the center region of multiple scans
CTDI	Integrated dose profile for a single section, normalized to the beam width; equivalent to MSAD and measured by using multiple TLDs or 1 ionization chamber
$CTDI_{100}$	Radiation dose index for 100 mm along the length of an entire pencil ionization chamber
$CTDI_w$	Weighted average of the $CTDI_{100}$ measured at the periphery and at the center of phantoms
$CTDI_{vol}$	$CTDI_w$ divided by pitch
DLP	$CTDI_{vol}$ multiplied by the length of the scan

Note:—TLD indicates thermoluminescent dosimeter; MSAD, multiple scan average dose.

the direct irradiation of the scanned volume and the scattered radiation from the adjacent scanned volumes is the CT dose index measured in milligrays (10^- Gy).[1] "CTDI" is defined as the dose profile of a single x-ray tube rotation integrated over a scan length in the z-direction and normalized to the table travel per tube rotation in a scan with a pitch of 1. The CTDI is equivalent to the multiple scan average dose, which is the average dose in the center region of the scan range over which CT is performed.[2] It can be measured either in air or in a phantom by using either a pencil ion chamber or a row of thermoluminescent dosimeters. A 16-cm-diameter phantom is used to represent a patient's head, and a 32-cm-diameter phantom is used to represent a patient's body. $CTDI_{100}$, is a radiation dose index with integration-dose limits of −50–50 mm, where 100 mm is the length of the active volume of the pencil ionization chamber used for the measurement (integration of the dose profile). The use of this chamber assumes that its length is sufficient for a complete integration of the exposure due to the scatter radiation from a single tube rotation in the middle of the chamber length. The $CTDI_w$ is the weighted average of the $CTDI_{100}$ measured at the periphery and at the center of cylindric acrylic phantoms ($2/3 \times CTDI_{100,periphery} + 1/3 \times CTDI_{100,center}$). The $CTDI_{vol}$ is defined as $CTDI_w$ / pitch. The value of $CTDI_{vol}$ multiplied by the length of the scan (in centimeters) is known as the dose-length product and is measured in units of milligray-centimeters. The DLP is commonly reported on the CT scanner for each CT study and is included in the patient dose report. When thinking about the potential dose due to the CT scan, the metric to take into consideration is the DLP because it contains both the CTDI, which is a measure of scanner output for a particular scanning technique, and the total scanning length along the patient's body. The CTDI descriptors are not accurate estimates of the radiation dose received by the patient. The CTDI descriptors represent the scanner radiation output when measured in a standardized phantom.

CT Acquisition Parameters and Basics of Dose Reduction

Recommendations for reducing radiation dose have mainly focused on limiting the radiation exposure. The US Food and Drug Administration has established guidelines to address the growing concern over CT-associated radiation dose.[3] These guidelines give recommendations on how to optimize CT protocols and encourage the elimination of inappropriate referrals for CT with reduction of the number of unnecessary repeat examinations. The basic pillars of dose reduction include justification of the study and eliminating inappropriate CT referrals, limiting scan range to the region of interest, limiting the number of contrast phases, and use of a relatively large pitch. The goal is an ALARA radiation dose.

There are several acquisition parameters and factors that have a direct effect on radiation dose, such as the photon energy (determined by the tube potential [kilovolt (peak)]); photon fluence, determined by the tube milliamperes; rotation or exposure time; reconstructed section thickness; object thickness or attenuation; pitch and/or spacing of the consecutive sections; and distance from the x-ray tube to the isocenter.[4] The basic strategies in minimizing radiation dose involve changes in the acquisition parameters (kilovolt(peak), milliampere, x-ray tube rotation time, pitch) to achieve a lower radiation dose with an acceptable quantum mottle. Typically, if one of these parameters is decreased, another needs to be increased to maintain image quality. The effect of CT acquisition parameters on image quality and noise is interlinked and complex. The noise in a CT image is determined by several factors, with the number of the photons reaching the detectors (quantum mottle) having the most dominant role.

Beam Energy. The energy of the incident x-ray beam is determined by the tube voltage or kilovolt(peak). Any variation in tube potential causes substantial change in the CT radiation dose. When all other parameters are held constant and the kilovolt(peak) is decreased, the radiation dose will also decrease. The relationship between the change in effective dose and tube potential is exponential.[5]

The effect of peak voltage on image quality is complex because it affects both image noise and tissue contrast. Image contrast is affected by the mean photon energy of the x-ray beam and the imaged material.[6] In general, lower kilovolt(peak) yields better contrast, especially for bone and iodine, with the effect being much smaller for soft tissues like fat and muscle.[6] The effect of improved image contrast at the lower kilovolt(peak) (while maintaining a constant milliampere-second) is reduced by the increased noise, especially with thick objects and near-dense bone, where the beam-hardening effect can, in fact, result in loss of the improved contrast achieved with a lower kilovolt(peak). The increase in image noise when lowering the kilovolt(peak) is most significant in individuals with larger body habitus, with the benefit of lowering the kilovolt(peak) best seen in pediatric patients and small adults. Lowering the kilovolt(peak) settings and increasing the milliampere-second, either by using automatic tube current modulation or by using a technique chart, is considered an effective strategy in lowering radiation dose while maintaining image quality.[7-9]

Moreover, lowering the kilovolt(peak) increases vascular enhancement because the attenuation of iodine-based contrast agents increases with reduced photon energy distribution due to the high atomic number of iodine and the effect of the iodine k-edge in the x-ray attenuation at such energy levels. By reducing the kilovolt(peak), the mean photon energy in the x-ray beam approaches the energy of the k-edge of the iodinated contrast media, which increases the x-ray attenuation coefficient and yields an improved contrast enhancement without a decrease in image quality.[10] This will particularly improve the conspicuity of hypervascular pathologies (Fig 1).

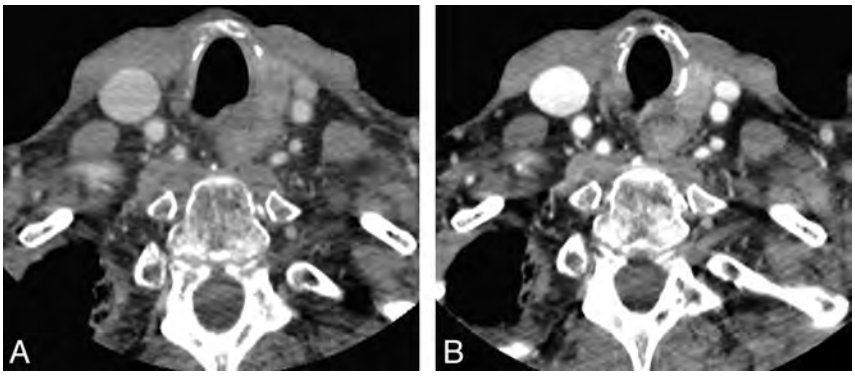

FIG 1. Patient scanned with a protocol at 140 kV(p) ($CTDI_{vol}$, 14.26; W450, L75) (*A*) and 100 kV(p) ($CTDI_{vol}$, 8.26; W450, L75) (*B*). Note the improved contrast and increased attenuation of the vessels (carotid arteries and jugular veins) and vertebral bodies and increased contrast of the metastatic node in the left tracheoesophageal groove with the lower kilovolt(peak) technique.

Photon Fluence. The photon fluence, determined by the tube current (milliampere) and x-ray tube rotation time (second), has a direct effect on patient radiation dose. The radiation dose is directly proportional to the milliampere-second value; with the radiation dose increasing linearly with increasing milliampere-second. Generally, decreasing (or increasing) the tube current by 50% will decrease (or increase) the radiation dose by half. Any decrease in tube current should be considered carefully because such reduction causes an increase in image noise, which may affect the diagnostic outcome of the examination.[11] Image noise in CT is dominated by quantum mottle, which is determined by the number of photons incident, and is collected by the detector. The number of the photons is proportional to the milliampere-second. The electronic noise also affects the image noise and is the result of fluctuation of the electronic components of the data-acquisition system. Increasing the milliampere-second will increase the number of photons emitted from the x-ray tube but will not change the energy spectrum of the photons.

Collimation, Table Speed, and Pitch. The helical or spiral acquisition involves continuous gantry rotation while simultaneously translating the table through the gantry during data acquisition. New acquisition parameters are being introduced in helical imaging such as table speed and pitch, which is defined as the ratio of table feed per gantry rotation to the nominal beam width. The pitch value has a direct influence and is inversely proportional to the radiation dose of the patient (Dose $\sim$ 1/Pitch).[12,13] This is because any increase in the pitch decreases the duration of the exposure to any particular section of the patient per gantry rotation and increases the gaps between successive gantry rotations.

Beam collimation, table speed, and pitch are interlinked parameters that affect the diagnostic quality and radiation dose of an imaging study. Faster table speed for a given collimation, resulting in higher pitch, is associated with a lower radiation dose because of a shorter exposure time. Although smaller beam collimation will result in a higher degree of overlap between the adjacent scans, this yields only minimal change in the radiation dose in comparison with a larger collimation for a given collimation and table speed.[12] The effect of pitch on radiation dose and image quality is negated in scanners that use an "effective milliampere-second setting" (defined as milliampere-second divided by pitch).[14] In such scanners, a constant effective milliampere-second value is held, irrespective of pitch value, by adjusting the tube current and increasing the tube current–time product approximately proportional to the increased pitch (or decreasing the tube current–time product proportional to the decreased pitch). This will keep the radiation dose relatively constant despite a variation of pitch. Additionally, an increase in the pitch value in modern scanners equipped with automatic milliampere modulation (see below) will not necessarily lead to dose reduction because the milliampere will be automatically adjusted to account for the increase in pitch.

Although scanning at a higher pitch value is dose-efficient, a higher pitch value causes helical artifacts and degradation of the section sensitivity profile with increased volume averaging and a potential decrease in spatial resolution. Furthermore, noise is dependent on pitch in multidetector row CT because the spiral interpolation algorithm will make use of the redundant data acquired by different detector rows and will decrease the noise for pitch values of <1 (and increase it for a pitch value of >1).[12]

Current Strategies in Dose Reduction

Automated Tube Current Modulation. The most widely available technical innovation for significant radiation dose reduction is automated tube current modulation, also known as automatic exposure control. This technique allows constant image quality in the CT examination at a lower radiation dose, regardless of the patient size or the attenuation characteristics of the body part being scanned. Tube current modulation may be preprogrammed by determining the attenuation values obtained by refined analysis of the projection scouts obtained at the start of the examination (Fig 2*A*) or may be adjusted by using a feedback circuit with near real-time adjustment of the tube current based on the attenuation values of the preceding image or may incorporate a combination of preprogramming and feedback circuit.

ATCM enables automatic adjustment of the tube current in the xy plane (angular modulation), along the z-axis (longitudinal modulation), or both (combined modulation) to maintain a user-selected noise level in the image (Fig 2*B*, -*C*).[15] Longitudinal modulation adjusts the tube current along the z-axis, which results in a lower tube current in the neck region with a higher tube current at the skull base and thoracic inlet, rendering images of similar noise, independent of patient size or anatomy. In angular modulation, the tube current is adjusted in each angular projection within the same section, with increased tube current in the lateral projection compared with the anteroposterior projection. Depending on the manufacturer, ATCM systems operate on the basis of several methods: noise index (GE Healthcare, Milwaukee, Wisconsin), standard deviation (Toshiba Medical Systems, Tokyo, Japan), reference image (Philips Healthcare, Best, the Netherlands), and quality reference milliampere-second (Siemens, Erlangen, Germany) (Table 2).[15] There have been several studies

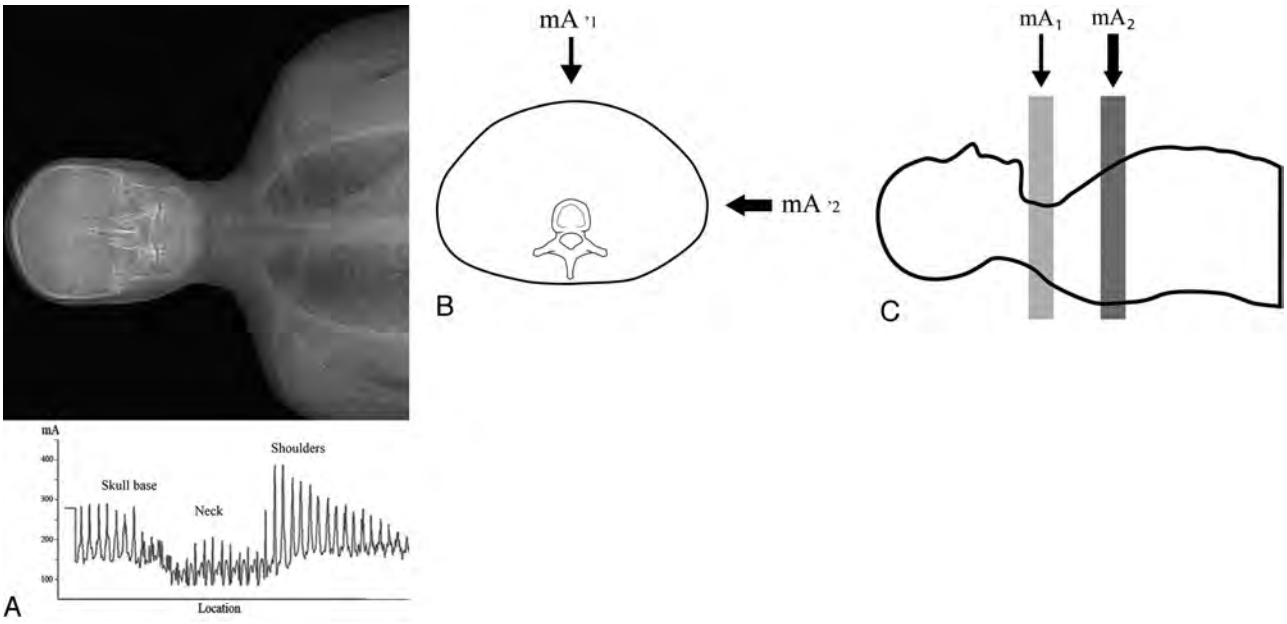

FIG 2. Schematic illustration demonstrating the modulation of the tube current for neck CT with variable milliampere values in each location based on the automatic analysis of attenuation values from the scout image (*A*). Schematic illustration of the angular tube current modulation at 2 different angles in the xy plane (*B*) and modulation of the milliampere along the z-axis (*C*).

Table 2: Automated tube current modulation: manufacturer and principle

Manufacturer	Trade Name	Image Quality Reference	Principle
GE Healthcare	AutomA, SmartmA	Noise index	Maintain a constant noise level (defined as noise index), using tube current within prescribed minimum and maximum values
Toshiba	Sure Exposure	SD	Maintain a constant noise level (defined in standard deviation), using tube currents and preset minimum and maximum values
Siemens	CARE Dose4D	Quality reference milliampere-second	Maintain the same image quality with reference to target effective milliampere-second levels for standard-size patients
Philips	DoseRight	Reference image	Keep the same image quality as in the reference image

that showed variable and sometimes significant levels of dose reduction with use of ATCM, depending on body region and patient size.[16-18] It is important to be familiar with the different parameters of the ATCM technique to achieve appropriate image quality for each specific diagnostic task, to not generate images with lower noise than necessary. An appropriate minimum and maximum milliampere value with a designated noise index or SD (depending on the manufacturer) based on the observer preference is prudent to prevent an inappropriate increase in the image noise related to lower photon fluence.

Adaptive Dose Shielding. Helical CT imaging acquires additional data with a number of extra gantry rotations before the beginning and after the end of the scanned volume, a process called "over-ranging" (or "z overscanning"). The extra data are needed for the interpolation required in the image reconstruction of a helical acquisition of the scanned volume. Consequently, tissue that will never be part of the reconstructed images will be exposed to radiation. This factor is especially significant with the trend toward developing scanners with greater detector collimation because the dose increase from over-ranging is proportional to pitch and collimation.[19] To reduce the impact of over-ranging, it is better to use an axial protocol rather than a helical protocol, or by reducing the pitch or using narrower detector collimation. The adaptive dose shield is a technology based on precise and independent movement of collimator blades that limits this over-ranging (Fig 3). The collimator will asymmetrically open at the beginning and close at the end of each spiral scan, blocking the parts of the x-ray beam that are not used for image reconstruction. The proportion of radiation dose reduction depends on the scan range, detector collimation, and pitch and has been shown to range from 7% to 38%.[19,20]

Image Reconstruction Algorithms. CT image reconstruction from raw data was first performed by using an iterative reconstruction algorithm, which was computationally demanding and resulted in a relatively long reconstruction time. Iterative reconstruction accurately models the data-collection process in CT by generating a set of synthesized projections. The model incorporates details of the geometric information of the scanner (including dimensions of the focal spot, the size of each detector cell, and the shape and size of each image voxel) and system statistical information (including photon statistics and electronic noise in the data-acquisition system).[21] Iterative reconstruction starts with an initial estimate of the object, which is iteratively improved in a stepwise fashion by comparing the synthesized projection with the acquired projection data and making an incremental change to the previous guess.[21] Iterative reconstruction was

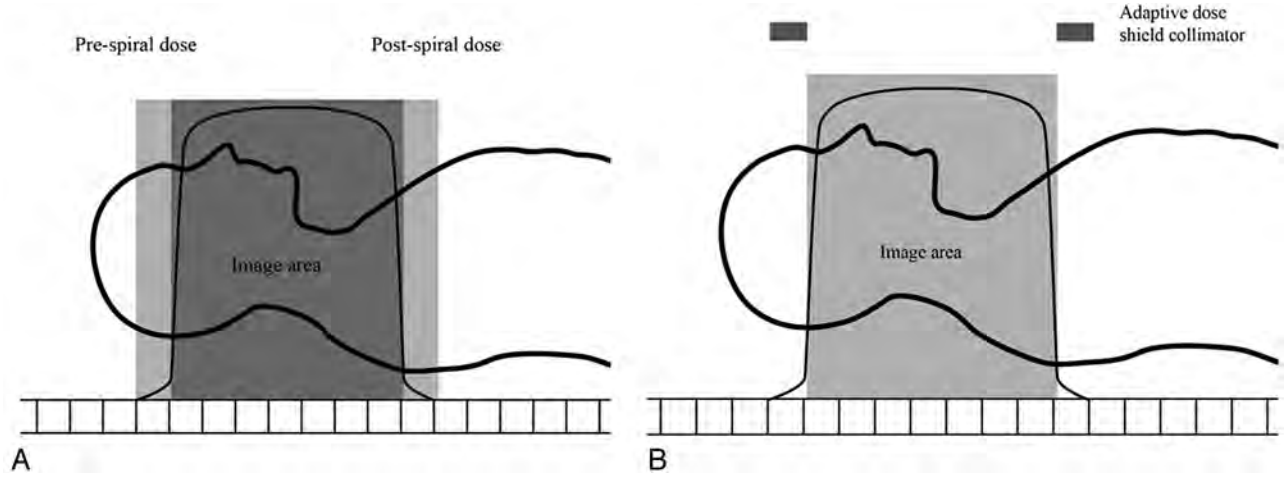

FIG 3. Schematic illustration of over-ranging (*A*) and the effect of the adaptive dose shield technique (*B*). The area marked in light gray in *A* represents the range along the z-axis that is exposed by the extra gantry rotation, before and after the imaged volume, which is needed for image reconstruction during a helical scan. With adaptive dose shield (*B*), a collimator closes asymmetrically at the beginning and the end of the examination, while opening fully in the center of the scan range.

quickly replaced by a filtered back-projection technique, which is an analytic reconstruction technique that operates on several fundamental assumptions about the scanner geometry and offers a compromise between reconstruction speed and image noise. A major drawback for the FBP algorithm is increased image noise that stems from the fact that FBP assumes noiseless projection data, which then must be overpowered by increasing the radiation dose. Iterative reconstruction reduces image noise without compromising spatial resolution, while in FBP, higher spatial resolution is achieved with higher image noise. With the increasing computational power in the recent decade, iterative reconstruction has come to focus on noise suppression and artifacts reduction associated with lowering the radiation dose. Major CT manufacturers are implementing their own iterative image-reconstruction methods to achieve dose reduction without image-quality degradation. These include the adaptive statistical iterative reconstruction algorithm and, more recently, a model-based iterative reconstruction technique (VEO) from GE Healthcare; Iterative Reconstruction in Image Space, and Sinogram-Affirmed Iterative Reconstruction from Siemens; Adaptive Iterative Dose Reduction from Toshiba[22]; and iDose from Philips Healthcare.

ASIR (GE Healthcare) is a modified iterative-reconstruction technique that starts iterative reconstruction after a first-pass FBP reconstruction.[23] It models the photon statistics in x-ray attenuation but does not model the system geometrics. Thus, it is more computationally complex than FBP but considerably less computationally complex than more comprehensive iterative reconstruction methods. ASIR can help shorten the longer reconstruction time of iterative reconstruction while maintaining much lower image noise when constructing the same raw data by using the FBP algorithm, allowing radiation dose reduction with no change in spatial or temporal resolution of the CT image.[24] ASIR images may appear to have an unusual "texture," particularly when the radiation dose used is not sufficiently low. In clinical practice, using variable blending levels of image reconstruction with FBP and ASIR techniques can be performed to generate clinically acceptable images.

Future Advancement in Dose Reduction

Automated Organ-Based Current Modulation. This technique reduces the tube current for certain projections to avoid direct exposure of radiosensitive organs, for example the thyroid gland and ocular lens.[25] It modulates the current along the z-axis according to the body habitus and along the x and y planes by reducing the tube current over a 120° radial arc prescribed over the anterior, lateral, or posterior aspect of the body (based on the operator preference). The overall radiation dose in the cross-sectional plane will remain constant, while decreasing the dose over the 120° radial arc and increasing the dose in the remaining 240° arc. Lowering the dose in the anterior projection by using organ-based current modulation will limit direct exposure to the thyroid gland and the ocular lens while preserving image quality.[25] The dose in the prescribed projection can be near zero, which will take advantage of the fact that only 180° of data and the fan angle are necessary to reconstruct a CT image.[26] The radio-sensitive organs, for example the thyroid gland, will be indirectly exposed to the beam coming from the posterior projection; however, this beam has been attenuated and filtered by the soft tissues of the patient.

Automated (Optimized) Tube-Voltage Modulation. Conventional dose-modulation techniques will modulate the tube current, while the tube voltage, the kilovolt(peak), setting is left unchanged. However, there is a large potential for dose reduction by optimizing the tube kilovolt(peak) setting. Such optimization of the kilovolt(peak) setting can be performed automatically for each individual patient and specific examination, by analyzing the information gathered by the topogram (scout view) to optimize kilovolt(peak) and milliampere-second to maintain a certain contrast-to-noise ratio. This will improve the selection of kilovolt(peak) for a particular examination beyond manual kilovolt(peak) selection.

Noise-Reduction Algorithm with Image Reconstruction and Data Processing. Improving the overall image quality with lower noise levels can be achieved by using optimally designed data processing

and image reconstruction methods without sacrificing other image properties. Several noise-control techniques have been developed, operating on the raw projection data, the log-transformed sinogram, or the images after reconstruction, to achieve a lower noise in CT images. Computational advancement is allowing sophisticated reconstruction methods to be used to control noise and streak artifacts in the projection data domain before the image reconstruction. Because CT manufacturers are presenting different iterative image reconstruction methods to achieve lower noise, newer versions of such methods are being introduced, allowing further reduction of CT image noise and hence radiation dose. For example, a model-based iterative reconstruction algorithm (VEO; GE Healthcare) has been introduced following ASIR to achieve further noise reduction and a lower radiation dose.[27] Additionally, several image-based filtering techniques usually perform quite well with regard to reducing image noise while maintaining high contrast resolution.[28,29]

CONCLUSIONS

There are significant variations between sites and scanners in imaging protocols with a wide range of radiation doses for the same scan indication. Furthermore, adult scan protocols sometimes have been directly applied to pediatrics without making proper adjustments. Consequently, there is true demand to optimize protocols and to become familiar with the factors affecting the CT radiation dose and available dose-reduction options. Several dose-reduction techniques have been successfully implemented and have been shown to reduce radiation exposure, including tube-current modulation, reducing tube voltage, adaptive dose shielding, and noise reduction filters. The increased noise and degraded image quality related to using a lower radiation dose have been successfully improved by using advanced image reconstruction techniques.

Disclosures: Suresh Mukherji—*UNRELATED*: *Consultancy*: Philips Medical Systems.

REFERENCES

1. Shope TB, Gagne RM, Johnson GC. **A method for describing the doses delivered by transmission x-ray computed tomography**. *Med Phys* 1981;8:488–95
2. Bauhs JA, Vrieze TJ, Primak AN, et al. **CT dosimetry: comparison of measurement techniques and devices.** *Radiographics* 2008;28:245–53
3. Feigal DW Jr. **FDA public health notification: reducing radiation risk from computed tomography for pediatric and small adult patients.** *Int J Trauma Nurs* 2002;8:1–2
4. McNitt-Gray MF. **AAPM/RSNA physics tutorial for residents: topics in CT—radiation dose in CT.** *Radiographics* 2002;22:1541–53
5. Schindera ST, Nelson RC, Yoshizumi T, et al., **Effect of automatic tube current modulation on radiation dose and image quality for low tube voltage multidetector row CT angiography: phantom study.** *Acad Radiol* 2009;16:997–1002
6. Huda W, Scalzetti EM, Levin G. **Technique factors and image quality as functions of patient weight at abdominal CT.** *Radiology* 2000;217:430–35
7. Mulkens TH, Marchal P, Daineffe S, et al. **Comparison of low-dose with standard-dose multidetector CT in cervical spine trauma.** *AJNR Am J Neuroradiol* 2007;28:1444–50
8. Sigal-Cinqualbre AB, Hennequin R, Abada HT, et al., **Low-kilovoltage multi-detector row chest CT in adults: feasibility and effect on image quality and iodine dose.** *Radiology* 2004;231:169–74
9. Waaijer A, Prokop M, Velthuis BK, et al. **Circle of Willis at CT angiography: dose reduction and image quality—reducing tube voltage and increasing tube current settings.** *Radiology* 2007;242:832–39
10. Matsuoka S, Hunsaker AR, Gill RR, et al. **Vascular enhancement and image quality of MDCT pulmonary angiography in 400 cases: comparison of standard and low kilovoltage settings.** *AJR Am J Roentgenol* 2009;192:1651–56
11. Kalra MK, Maher MM, Toth TL, et al. **Strategies for CT radiation dose optimization.** *Radiology* 2004;230:619–28
12. Primak AN, McCollough CH, Bruesewitz MR, et al. **Relationship between noise, dose, and pitch in cardiac multi-detector row CT.** *Radiographics* 2006;26:1785–94
13. McNitt-Gray MF, Cagnon CH, Solberg TD, et al. **Radiation dose in spiral CT: the relative effects of collimation and pitch.** *Med Phys* 1999;26:409–14
14. Mahesh M, Scatarige JC, Cooper J, et al. **Dose and pitch relationship for a particular multislice CT scanner.** *AJR Am J Roentgenol* 2001;177:1273–75
15. Lee CH, Goo JM, Ye HJ, et al. **Radiation dose modulation techniques in the multidetector CT era: from basics to practice.** *Radiographics* 2008;28:1451–59
16. Russell MT, Fink JR, Rebeles F, et al. **Balancing radiation dose and image quality: clinical applications of neck volume CT.** *AJNR Am J Neuroradiol* 2008;29:727–31
17. Lee EJ, Lee SK, Agid R, et al. **Comparison of image quality and radiation dose between fixed tube current and combined automatic tube current modulation in craniocervical CT angiography.** *AJNR Am J Neuroradiol* 2009;30:1754–59
18. Mulkens TH, Bellinck P, Baeyaert M, et al. **Use of an automatic exposure control mechanism for dose optimization in multi-detector row CT examinations: clinical evaluation.** *Radiology* 2005;237:213–23
19. Tzedakis A, Damilakis J, Perisinakis K, et al. **The effect of z overscanning on patient effective dose from multidetector helical computed tomography examinations.** *Med Phys* 2005;32:1621–29
20. Christner JA, Zavaletta VA, Eusemann CD, et al. **Dose reduction in helical CT: dynamically adjustable z-axis x-ray beam collimation.** *AJR Am J Roentgenol* 2010;194:W49–55
21. Xu J, Mahesh M, Tsui BM. **Is iterative reconstruction ready for MDCT?** *J Am Coll Radiol* 2009;6:274–76
22. Yoo RE, Park EA, Lee W, et al. **Image quality of Adaptive Iterative Dose Reduction 3D of coronary CT angiography of 640-slice CT: comparison with filtered back-projection.** *Int J Cardiovasc Imaging* 2012 Aug 26. [Epub ahead of print]
23. Silva AC, Lawder HJ, Hara A, et al. **Innovations in CT dose reduction strategy: application of the adaptive statistical iterative reconstruction algorithm.** *AJR Am J Roentgenol* 2010;194:191–99
24. Kilic K, Erbas G, Guryildirim M, et al. **Lowering the dose in head CT using adaptive statistical iterative reconstruction.** *AJNR Am J Neuroradiol* 2011;32:1578–82
25. Hoang JK, Yoshizumi TT, Choudhury KR, et al. **Organ-based dose current modulation and thyroid shields: techniques of radiation dose reduction for neck CT.** *AJR Am J Roentgenol* 2012;198;1132–38
26. Vollmar SV, Kalender WA. **Reduction of dose to the female breast in thoracic CT: a comparison of standard-protocol, bismuth-shielded, partial and tube-current-modulated CT examinations.** *Eur Radiol* 2008;18:1674–82
27. Katsura M, Matsuda I, Akahane M, et al. **Model-based iterative reconstruction technique for radiation dose reduction in chest CT: comparison with the adaptive statistical iterative reconstruction technique.** *Eur Radiol* 2012;22:1613–23
28. Yu L, Liu X, Leng S, et al. **Radiation dose reduction in computed tomography: techniques and future perspective.** *Imaging Med* 2009;1:65–84
29. Szucs-Farkas Z, Bensler S, Torrente JC, et al. **Nonlinear three-dimensional noise filter with low-dose CT angiography: effect on the detection of small high-contrast objects in a phantom model.** *Radiology* 2011;258:261–69

The Role of MR Imaging in Assessment of Brain Damage from Carbon Monoxide Poisoning: A Review of the Literature

T. Beppu

ABSTRACT

SUMMARY: The aim of this article is to review how MR imaging and associated imaging modalities provide clinicopathologic information on brain damage after carbon monoxide poisoning. Initially, many authors documented typical findings of conventional MR imaging in the gray matter structures such as the globus pallidus and in various regions of cerebral white matter. The focus of investigation has since shifted to observation of cerebral white matter areas that are more frequently detected on MR imaging and are more responsible for chronic symptoms than the gray matter. DWI has dramatically contributed to the ability to quantitatively assess cerebral white matter damage. Subsequently, DTI has enabled more sensitive evaluation than DWI and can demonstrate progressive pathologic changes in the early stage, allowing prediction of chronic conditions. In addition, MR spectroscopy reveals changes in metabolite levels, offering quantitative clinicopathologic information on brain damage after carbon monoxide poisoning.

ABBREVIATIONS: CO = carbon monoxide; CWM = cerebral white matter; DNS = delayed neuropsychiatric sequelae; FA = fractional anisotropy; GP = globus pallidus; MBP = myelin basic protein

CO poisoning causes serious damage to the brain and cardiac muscles. Damage to the brain directly affects the prognosis for patients who survive CO poisoning. Some clinical obstacles exist to the assessment of brain damage among such patients. First, predicting clinical behaviors such as specific types of chronic neuropsychiatric symptoms is difficult. Surviving patients will display 1 of 3 clinical behavioral types in the chronic phase after CO poisoning: approximately 70% of survivors present with various transient symptoms only in the acute phase; 20% of patients present with symptoms persisting from the acute to the chronic phase; and the remaining 10% exhibit DNS, representing recurrent neuropsychiatric symptoms occurring after an interval of apparent normality (the so-called lucid interval; mean duration, 22 days) after the apparent resolution of acute symptoms.[1-5] Acute conditions including level of consciousness and carboxyhemoglobin concentration have been considered and found to be unhelpful in the prediction of chronic clinical behaviors.[6,7] In particular, predicting whether patients who exhibit resolved acute symptoms have escaped or will experience DNS represents a very important clinical issue.[8] A second problem is the difficulty of assessing the severity of brain damage. Chronic symptoms include parkinsonism, dystonia or other motor impairments, cognitive or executive dysfunction, akinetic mutism, mood disorder, and personality change. The severity of brain damage cannot be directly compared among patients with different symptoms. One of the strategies to resolve these clinical problems is to apply objective assessments of brain damage by using MR imaging, a readily available and minimally invasive procedure. Here, I review the literature on assessment of brain damage secondary to CO poisoning by use of conventional MR imaging in addition to other sequences, such as DWI, DTI, and MR spectroscopy, and summarize what MR imaging can currently accomplish in the assessment of brain damage after CO poisoning.

MECHANISMS CAUSING BRAIN DAMAGE AFTER CO EXPOSURE

Comprehension of the mechanisms causing brain damage after CO exposure is crucial to understanding the findings of MR imaging in the assessment of brain damage. Brain damage has been considered to result from complicated mechanisms, as follows.[4] The uptake of CO by hemoglobin with an affinity 200 times that of oxygen leads to hypoxia in tissues, and a shift in the oxyhemoglobin dissociation curve to the left inhibits release of oxygen, further exacerbating tissue hypoxia.[9] Whereas hypotension adds to hypoxia, the hypoxic-hypotension process leads to ischemic changes in the arterial border zones in the brain.[10] Brain hypoxia increases the level of excitatory amino acids including glutamine, leading to

From the Department of Neurosurgery, Department of Hyperbaric Medicine, Iwate Medical University, Morioka, Japan.

Please address correspondence to Takaaki Beppu, MD, PhD, Department of Neurosurgery, Department of Hyperbaric Medicine, Iwate Medical University, Morioka, Japan., 19-11, Uchimaru, Morioka, 020-8505 Japan; e-mail: tbeppu@iwate-med.ac.jp

Indicates open access to non-subscribers at www.ajnr.org

http://dx.doi.org/10.3174/ajnr.A3489

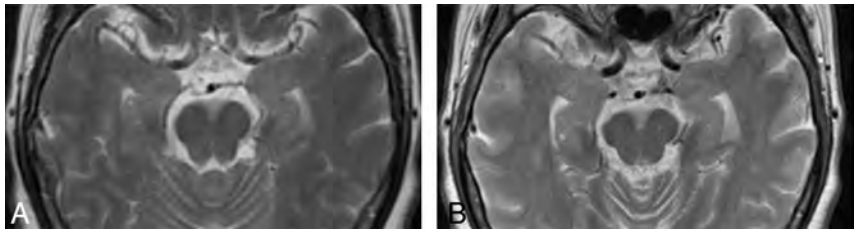

FIG 1. Atrophic change of the hippocampus and cerebral cortex in a 61-year-old woman after CO poisoning. When compared with initial T2-weighted imaging in the acute phase (*A*), imaging at 3 months after CO inhalation demonstrates enlargement of the bilateral inferior horns of the lateral ventricles and expansion of the cerebral sulci, suggesting atrophy of the hippocampus and cerebral cortex (*B*). Recent memory disturbance was recovered, but persistent chronic symptoms including slow movement and personality change remained at 3 months after CO inhalation.

elevated nitrite levels and causing subsequent injuries to the cerebral cortex.[11] Furthermore, hypoxia in the brain causes oxidative stress, cellular necrosis, apoptosis, and ongoing inflammation.[12]

Although it is important to emphasize the damage to the brain that results from hypoxia-related effects, brain damage can also be caused by mechanisms other than hypoxia. CO also combines with cytochrome A and A3 to cause direct poisoning effects, and decreases in levels of cytochrome C oxidase inhibit mitochondrial metabolism, leading to cellular respiratory dysfunction.[13] Furthermore, CO-mediated brain damage associated with free radicals has been noticed. CO binds to platelet heme proteins, causing the release of nitric oxide. Excess nitric oxide produces peroxynitrite, impairing mitochondrial function.[14] As another example, CO causes platelet-to-neutrophil aggregation, and neutrophil degranulation leads to release or production of myeloperoxidase, proteases, and reactive oxygen species, which cause oxidative stress, lipid peroxidation, and apoptosis.[14,15] Lipid peroxidation alters the structure of MBP, triggering lymphocytic immunologic responses and increasing the activation of microglia. Immunologic responses to altered MBP cause progressive demyelination accompanied with ongoing inflammation in the CWM.[4]

CONVENTIONAL MR IMAGING

As mentioned in the previous section, pathologic changes induced by complicated mechanisms progress in the brain from the time of CO inhalation to even some years later. The timing of MR imaging will thus have a major effect on the results of imaging.[16] In this review, times between CO inhalation and MR imaging were strictly defined as the ultra-acute phase within 24 hours; the acute phase between 24 hours and 7 days; the subacute phase between 8 and 21 days; and the chronic phase from 22 days and thereafter.

Since the end of the 1980s, findings of damaged brain from CO poisoning by using conventional MR imaging instead of CT have been reported. In those days, most articles were case reports that described findings in the chronic phase and documented typical findings of bilateral hyperintensities in the GP and CWM on T2-weighted images.[17,18] In these reports, the authors speculated that the main pathologic changes depicted on MR imaging were necrosis in the GP and demyelination in the CWM. These suppositions were based on a report of autopsy findings by Lapresle and Fardeau,[19] which identified 1) necrosis in the GP, 2) demyelination in the CWM, 3) spondylotic changes in the cerebral cortex, and 4) necrosis in the hippocampus. Damage in the GP is frequently seen in patients poisoned with CO.[20] In contrast, damage in other basal ganglia such as the caudate nucleus, putamen, and thalamus has not been reported as frequently as that in the GP.[21,22] Authors have generally adopted 1 of 2 reasons for selective damage to the GP: that this region is easily affected by the hypoxic-hypotension process because of a poor anastomotic blood supply[18,21,23] or that CO binds directly to heme iron in the GP, which happens to be a brain region with the highest iron content.[24-26] Furthermore, some reports have described a "pallidoreticular pattern" of damage to the substantia nigra in addition to the GP, another region with high iron content.[26,27] The GP often demonstrates different findings of hemorrhagic infarction, which match the phase in which MR imaging is performed.[23,28-30] Because the main pathologic features are edema in the acute phase and necrosis in the chronic phase, the size of the GP lesion may shrink on consecutive evaluations.[31] Parkinsonism is the most commonly seen symptom in patients with CO exposure.[1,32] The possibility that damage to the GP relating to the extrapyramidal tract causes parkinsonism is readily apparent, but parkinsonism can also occur in patients without damage to the GP. Pavese et al[32] hypothesized that lesions in the CWM containing tracts outputting and/or inputting to the basal ganglia might cause parkinsonism in patients without GP damage.

Regarding gray matter structures other than the GP, many previous reports have described damage to the hippocampus (Fig 1*A*, -*B*). Almost all of these reports documented findings of hippocampal atrophy in the chronic phase (2 months to 21 years) and patients experiencing severe persistent symptoms.[22,33-35] On the contrary, a few reports have mentioned damage to the cerebral cortex.[30,32,36] These studies documented cortical atrophy in patients with persistent symptoms in the chronic phase. Such damage to both the hippocampus and the cerebral cortex might create lesions responsible for persistent symptoms in the chronic phase. In a report regarding hippocampal lesions in the acute phase, 2 of 4 patients had died within a short period.[28] Hippocampal lesions in the acute phase may be predictive of a very poor prognosis.

Gray matter could be predicted to be more vulnerable to hypoxia from poisoning than WM, as neurons in gray matter show high activity and a high blood demand. However, neurons may be able to tolerate pure hypoxia for longer than they can tolerate ischemia.[37] Damage to gray matter should be caused by ischemic changes through the hypoxic-hypotension process. Some authors have pointed out that CWM damage is more frequently detected on MR imaging than damage in the gray matter. A prospective study in which 73 patients with CO poisoning were consecutively enrolled without any selection reported that 12% of these patients showed CWM damage, whereas damage to the basal ganglia was found in only 1 patient.[5] CWM has been recognized to be more responsible for chronic symptoms than gray matter. The most common regions of CWM to be affected are the centrum semiovale and periventricular WM.[21,28,31,38] On T2-weighted images, both lesions are depicted as hyperintense in the bilateral CWM either symmetrically[21,39] or asymmetrically.[36,40] The finding of

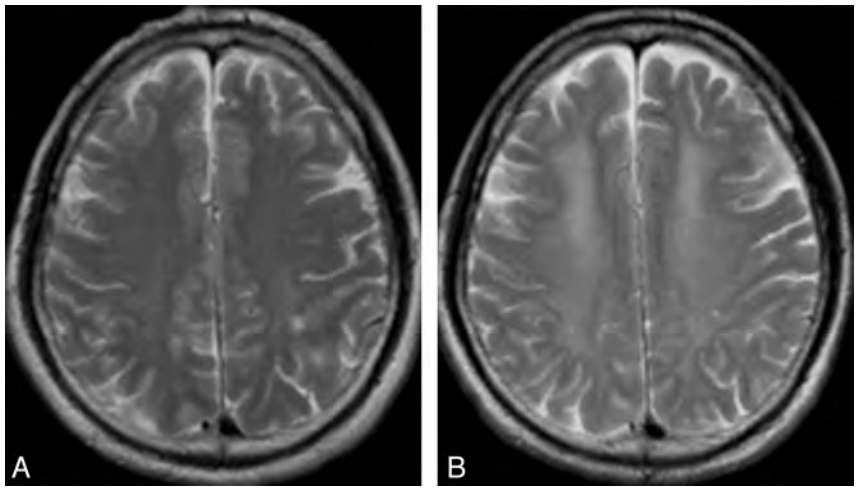

FIG 2. Hyperintensities in the deep WM involving the centrum semiovale in a 53-year-old man with DNS after CO poisoning. *A*, T2-weighted imaging within 24 hours after CO inhalation reveals slight hyperintensity in the bilateral deep WM and shows a necrotic focus in the left parietal lobe. *B*, At 2 days after the occurrence of DNS, hyperintense areas appear widespread in the bilateral deep WM. Brain atrophy is also apparent in the bilateral frontal lobes.

asymmetric hyperintensity has been speculated to be caused by differences in presumably original arterial blood supply among patients.[36] Damaged CWM may occasionally show hemosiderin-deposit foci suggesting hemorrhagic infarctions or iron extravasation after CO poisoning.[41,42] CWM damage can be observed in various regions other than the centrum semiovale and periventricular WM, such as the temporal lobe,[17,22] occipital lobe,[17,22] parietal lobe,[17,43] and corpus callosum.[38,44] However, few reports have provided detailed information regarding damage to the cerebellum and brain stem. This may result from a high tolerance of the posterior structures for hypoxia, and such damage would thus appear under severely hypotensive conditions in addition to hypoxia.[28] Indeed, patients demonstrating cerebellar damage in the acute or subacute phase uniformly show a poor prognosis.[37,39,45] Prognosis parallels the amount of damage to WM such as lesions involving the cerebellum.[28] Consequently, many reports have indicated that the amount of WM damage closely relates to prognosis.[6,18,36,46] Specific regions in the CWM corresponding to each symptom have also been investigated. Damage to the frontal lobe has been considered to be associated with apathy, loss of motivation, and mutism.[32] Some prospective studies have examined the relationship between MR imaging findings and results of neurocognitive tests in the chronic phase after CO poisoning. Kesler et al[47] performed consecutive MR imaging in 69 patients and reported that atrophy of the fornix was already apparent at 2 weeks after poisoning, and was associated with reduced verbal memory at 6 months. Parkinson et al[48] performed serial MR imaging and cognitive tests on the day of onset, and 2 weeks and 6 months after poisoning in 72 patients, revealing that damage to the centrum semiovale was closely associated with cognitive dysfunction in all phases. Porter et al[44] observed atrophy of the corpus callosum at 6 months after poisoning in 62 patients, but cognitive dysfunction in that study appeared independently of corpus callosum atrophy. As mentioned above, however, the brain is damaged more widely in patients with CO poisoning who have more severe and varied symptoms. Elucidating the specific regions responsible for each symptom may thus be difficult in patients with severe CO poisoning.

Pathologic findings associated with CWM lesions after CO poisoning have been mainly recognized as demyelination.[19] CWM lesions can be categorized into 3 groups, albeit with a great deal of overlap among groups: 1) the first is small necrotic foci, 2) the second is widespread necrosis accompanying extensive axon destruction and numerous lipid-laden macrophages, and 3) the third is demyelination with relative preservation of the axon in the deep WM. This third group is most often seen in patients with delayed encephalopathy and so-called biphasic myelinopathy of Grinker.[21] Differences in the extent of demyelination among patients must have major effects on clinical behaviors. Progressive demyelination has been recognized as a cause of DNS and is considered reversible. Many reports have documented that hyperintense areas in the periventricular area and centrum semiovale on T2-weighted imaging are more widespread after the appearance of DNS than before DNS (Fig 2*A*, *-B*).[31,46,49] These findings indicate a process of progressive demyelination while DNS develops. DNS can improve within 1–2 years in approximately 60%–70% of patients.[50] Some investigators have observed areas of decreased hyperintensity on T2-weighted imaging when DNS improved during the chronic phase.[21,43,51] These findings suggest that MR imaging can depict real-time changes in remyelination of damaged tract fibers with the relative preservation of axons. The extent of damage to WM fibers exerts a large influence on individual prognosis. However, speculation on the histologic changes associated with WM damage by use of conventional MR imaging has limitations because damaged white mater can be caused by various conditions such as cytotoxic edema, necrosis, vasogenic edema, hemorrhagic infarction, iron deposition,[41] or even previous ischemic lesions before CO poisoning,[48] in addition to demyelination.

DWI AND DTI

Since the early 2000s, brain damage from CO poisoning has been evaluated by DWI, which objectively and quantitatively indicates the magnitude of water molecule diffusion in tissues. Cytotoxic edema in acute ischemic lesions was demonstrated as areas of signal hyperintensity on DWI, leading to a decreased ADC. In such situations, DWI has also been performed for patients with CO poisoning in the acute or subacute phase (Fig 3*A*–*D*). Two reports have provided findings of DWI in the ultra-acute or acute phase, showing hyperintense areas in WM of bilateral frontal and parietal lobes, and reduced ADC values at 12 hours[52] and 48 hours[43] after CO poisoning. In these reports, the authors concluded that DWI could depict cytotoxic edema in the damaged WM more sensitively and earlier than conventional MR imaging. Some reports regarding findings of DWI in the subacute and

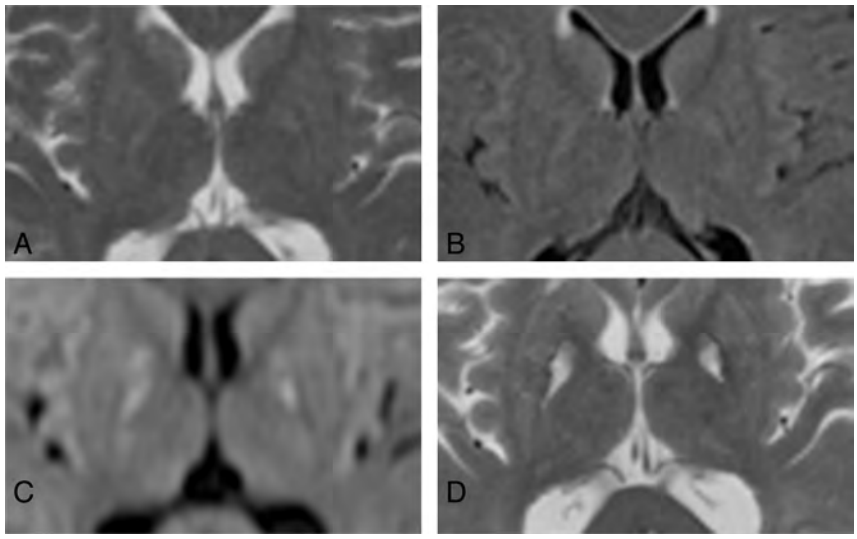

FIG 3. High-sensitivity DWI in the acute phase after CO poisoning in a 64-year-old woman. *A*, T2-weighted imaging; *B*, FLAIR; and *C*, DWI, all taken within 24 hours after CO inhalation. *D*, T2-weighted imaging at 3 months after CO poisoning. T2-weighted imaging (*A*) and FLAIR (*B*) did not demonstrate clear abnormalities in the basal ganglia within 24 hours after CO poisoning, but markedly high signals were depicted in the bilateral GP on DWI (*C*) at the same time. Clear hyperintense areas in the bilateral GP were found on T2-weighted imaging after 3 months (*D*).

chronic phases have been found.[25,26,40,53] All of these reports documented that areas of signal hyperintensity and low ADC in the CWM remained in the subacute and chronic phases, as in the acute phase. In cases of DNS, ADC after the occurrence of sequelae was lower than before that, and low ADC remained for another 1–2 months.[26,40] From a pathologic perspective, these findings suggest progressive demyelination with cytotoxic edema. Because these findings of DWI in CO poisoning differ from those in cerebral infarction (ie, low ADC remains for 3–5 days and normalizes within 1–4 weeks after stroke), CWM damage in CO poisoning cannot be explained simply by ischemic change.[25,40] In a comparison between DWI of the GP and CWM in the subacute phase, the GP appeared hypointense in areas with high ADC, whereas CWM was hyperintense in areas with low ADC.[25] In that report, the authors concluded that the GP probably undergoes necrosis earlier than CWM; therefore, WM damage would be attributed not only to ischemic changes from the hypoxic-hypotension process as in GP damage, but also to progressive demyelination. Many reports have found that increases in ADC parallel improvements in symptoms after the appearance of DNS.[40,43,53] These phenomena might indicate demyelination of myelinated CWM.

Because CWM after CO poisoning shows various histologic changes as mentioned in the previous section, a definite quantitative parameter to specifically indicate demyelination of WM fibers has been desired. DTI, which can show the directionality of water molecule diffusion, and FA as its quantitative value have been recognized to be more suitable than DWI for quantitative evaluation in demyelinating diseases such as multiple sclerosis. DTI has been applied to evaluate CO poisoning since approximately 2005. Most such evaluations have reported low FA values, suggesting a reduction in the directionality of water molecule diffusion because of demyelination, when DTI was performed in the subacute or chronic phases after the appearance of DNS.[49,54-56] Low FA values might continue until 3 months after poisoning,[55] and improvement in FA has correlated with improvement in DNS.[49,56] These changes in FA values should sensitively demonstrate progressive demyelination causing DNS and gradual remyelination while DNS improves. As DNS have been recognized to occur when the extent of demyelination progresses beyond a certain threshold, use of DTI to predict the occurrence of DNS has been suggested. At our institute, FA at the centrum semiovale has been measured at 2 weeks after poisoning in consecutive patients. As a result, we observed that FA in the centrum semiovale had already decreased before the appearance of DNS, and reported the possibility that FA in the subacute phase could offer a predictor for the occurrence of DNS.[8] The concentration of MBP in CSF, as a marker of demyelinating disease activity, has been proposed as a predictor of DNS.[57] Another of our previous studies demonstrated that FA in the centrum semiovale roughly correlates with MBP concentration in the subacute phase (approximately 2 weeks) in patients with CO poisoning who present with chronic persistent symptoms or DNS.[58] These reports suggest that FA in DTI must be able to sensitively and quantitatively indicate the extent of demyelination after CO poisoning and, in particular, could demonstrate progressive damage leading to DNS.

Different areas where the region of interest is placed on the CWM might influence the FA values. Lo et al[55] reported FA values measured by using regions of interest placed on the centrum semiovale and explained why they placed regions of interest on these areas as follows. All patients in their study showed abnormalities in the deep WM involving the centrum semiovale on T2-weighted imaging, and areas involving the centrum semiovale were relatively homogeneous WM zones related to worse cognitive performance. Selection of these areas was sensible because some reports have shown a relationship between damage in the centrum semiovale and cognitive disorder after CO poisoning.[48,59] Our previous study in which we used DTI with voxel-based analysis also showed that deep WM areas including the centrum semiovale were the most widely damaged regions in those patients presenting with chronic symptoms (Fig 4).[60] When the CO-damaged brain is assessed by DWI or DTI, it is important to emphasize that evaluations of deep WM, including the centrum semiovale, are indispensable.

MR SPECTROSCOPY

MR spectroscopy enables noninvasive monitoring of changes in metabolism from brain damage in a specified region. Although most previous studies regarding findings of MR spectroscopy in patients with CO poisoning were only case reports and differences existed in the regions used for placement of the voxel of interest in the brain, these reports have consistently shown increased levels

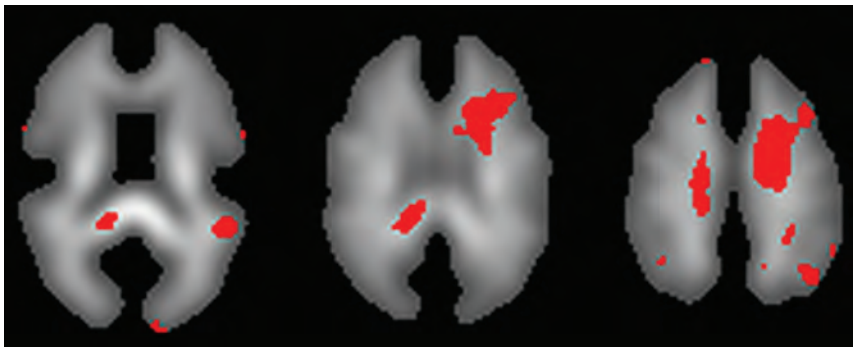

FIG 4. Detection of damaged regions of the CWM by use of voxel-based analysis with DTI. When FA values in all voxels on the FA map were compared voxel by voxel between 2 patient groups (patients with and without chronic neuropsychiatric symptoms), voxels showing a significant difference in FA ($P < .03$) between groups were identified as reddish voxels on the FA template. The number of reddish voxels was greater in the region corresponding to the deep CWM, including the centrum semiovale, than in other regions.

of Cho indicating active membrane metabolism associated with pathologic conditions such as degeneration and gliosis, decreased NAA reflecting loss or degeneration of axons and/or neurons, and the presence of lactate representing anaerobic glycolysis under ischemic and/or hypoxic conditions.[56,61-67] These metabolites are usually evaluated by using the relative ratio to Cr as an indication of stored energy, which reportedly remains relatively stable even in the presence of rapid fluctuations in energy metabolism. When attention is focused on the period in which each metabolite appears, these studies reported that the Cho/Cr ratio increased earliest in metabolites and decreased in the late period of the chronic phase, the NAA/Cr ratio began to decrease at the earliest from 3 to 4 weeks, and lactate began to appear at the earliest from 1 to 2 months after CO poisoning in patients with chronic symptoms.[56,61-67] It is noteworthy that declines in NAA levels have been proposed as a good prognostic factor, as the NAA/Cr ratio correlates with symptom development, and the presence of lactate acts as a marker of irreversible brain damage because it has been observed in patients with severe chronic symptoms such as akinetic mutism and apallic state. MR spectroscopy findings by 3T MR imaging in the subacute phase in 29 patients with CO poisoning found that the Cho/Cr ratio in the centrum semiovale was slightly but significantly higher in patients with subsequent chronic-phase symptoms than in patients with transient symptoms in the acute phase.[68] Increased Cho level in the subacute phase demonstrates inflammation accompanied with progressive demyelination in CWM and may enable prediction of the patient's condition in the chronic phase.

CURRENT AND FUTURE

So far, most investigations by use of MR imaging and its optional sequences have been rigorously focused on either the GP or CWM as the sites of typical lesions in the chronic phase after CO poisoning. In particular, findings of MR imaging and other sequences on CWM correlating with chronic symptoms allow us to monitor the condition of the patient in the chronic phase. However, brain damage after CO poisoning should be attributed not only to injury of the CWM, but also to injury of gray matter structures such as the hippocampus or cerebral cortex. In the chronic phase, investigations are needed regarding relationships between damage to both gray and WM and the severity of symptoms. On the contrary, few reports have described investigations of MR imaging in gray matter structures and CWM in the acute or subacute phase. DTI and MR spectroscopy in the subacute phase have already revealed slight pathologic changes from progressive demyelination starting immediately after CO inhalation. Interest will eventually migrate to whether findings of MR imaging in the acute phase offer a predictor of the occurrence, severity, and type of chronic symptoms, because DNS can occur as early as within days after CO inhalation. In our experience of using 3T MR imaging, however, progressively pathologic changes in the acute phase must be too small to observe on conventional MR imaging and even on DWI, DTI, or MR spectroscopy in most patients. In the future, new approaches to the use of MR imaging, such as new sequences or more sensitive imaging such as 7T MR imaging, may reveal and resolve these issues.

Disclosure: Takaaki Beppu—*UNRELATED: Grants/Grants Pending:* Ministry of Science, Education, Sports and Culture, Japan.* (**Money paid to institution.*)

REFERENCES

1. Choi IS, Cheon HY. **Delayed movement disorders after carbon monoxide poisoning.** *Eur Neurol* 1999;42:141–44
2. Weaver LK, Hopkins RO, Elliott G. **Carbon monoxide poisoning.** *N Engl J Med* 1999;340:1290; author reply 1292.
3. Weaver LK, Hopkins RO, Chan KJ, et al. **Hyperbaric oxygen for acute carbon monoxide poisoning.** *N Engl J Med* 2002;347:1057–67
4. Weaver LK. **Clinical practice. Carbon monoxide poisoning.** *N Engl J Med* 2009;360:1217–25
5. Hopkins RO, Fearing MA, Weaver LK, et al. **Basal ganglia lesions following carbon monoxide poisoning.** *Brain Inj* 2006;20:273–81
6. Prockop LD, Naidu KA. **Brain CT and MRI findings after carbon monoxide toxicity.** *J Neuroimaging* 1999;9:175–81
7. Hurley RA, Hopkins RO, Bigler ED, et al. **Applications of functional imaging to carbon monoxide poisoning.** *J Neuropsychiatry Clin Neurosci* 2001;13:157–60
8. Beppu T, Nishimoto H, Ishigaki D, et al. **Assessment of damage to cerebral white matter fiber in the subacute phase after carbon monoxide poisoning using fractional anisotropy in diffusion tensor imaging.** *Neuroradiology* 2010;52:735–43
9. Ernst A, Zibrak JD. **Carbon monoxide poisoning.** *N Engl J Med* 1998;339:1603–08
10. Okeda R, Funata N, Takano T, et al. **The pathogenesis of carbon monoxide encephalopathy in the acute phase–physiological and morphological correlation.** *Acta Neuropathol* 1981;54:1–10
11. Piantadosi CA. **Toxicity of carbon monoxide: hemoglobin vs. histotoxic mechanisms**. In: Penney DG, ed. *Carbon monoxide.* Boca Raton, Florida: CRC Press;1996:163–86
12. Piantadosi CA, Zhang J, Levin ED, et al. **Apoptosis and delayed neuronal damage after carbon monoxide poisoning in the rat.** *Exp Neurol* 1997;147:103–14
13. Alonso JR, Cardellach F, López S, et al. **Carbon monoxide specifically inhibits cytochrome C oxidase of human mitochondrial respiratory chain.** *Pharmacol Toxicol* 2003;93:142–46
14. Thom SR, Bhopale VM, Han ST, et al. **Intravascular neutrophil ac-**

tivation due to carbon monoxide poisoning. *Am J Respir Crit Care Med* 2006;174:1239–48
15. Thom SR, Bhopale VM, Fisher D, et al. **Delayed neuropathology after carbon monoxide poisoning is immune-mediated.** *Proc Natl Acad Sci U S A* 2004;101:13660–65
16. Hantson P, Duprez T. **The value of morphological neuroimaging after acute exposure to toxic substances.** *Toxicol Rev* 2006;25:87–98
17. Horowitz AL, Kaplan R, Sarpel G. **Carbon monoxide toxicity: MR imaging in the brain.** *Radiology* 1987;162:787–88
18. Vieregge P, Klostermann W, Blümm RG, et al. **Carbon monoxide poisoning: clinical, neurophysiological, and brain imaging observations in acute disease and follow-up.** *J Neurol* 1989;236:478–81
19. Lapresle J, Fardeau M. **The central nervous system and carbon monoxide poisoning. II. Anatomical study of brain lesions following intoxication with carbon monoxide (22 cases).** *Prog Brain Res* 1967;24:31–74
20. Sharma P, Eesa M, Scott JN. **Toxic and acquired metabolic encephalopathies: MRI appearance.** *AJR Am J Roentgenol* 2009;193:879–86
21. Chang KH, Han MH, Kim HS, et al. **Delayed encephalopathy after acute carbon monoxide intoxication: MR imaging features and distribution of cerebral white matter lesions.** *Radiology* 1992;184:117–22
22. Bruno A, Wagner W, Orrison WW. **Clinical outcome and brain MRI four years after carbon monoxide intoxication.** *Acta Neurol Scand* 1993;87:205–09
23. Bianco F, Floris R. **MRI appearances consistent with haemorrhagic infarction as an early manifestation of carbon monoxide poisoning.** *Neuroradiology* 1996;38 Suppl 1:S70–72
24. Gandini C, Prockop LD, Butera R, et al. **Pallidoreticular-rubral brain damage on magnetic resonance imaging after carbon monoxide poisoning.** *J Neuroimaging* 2002;12:102–03
25. Chu K, Jung KH, Kim HJ, et al. **Diffusion-weighted MRI and 99mTc-HMPAO SPECT in delayed relapsing type of carbon monoxide poisoning: evidence of delayed cytotoxic edema.** *Eur Neurol* 2004;51:98–103
26. Kinoshita T, Sugihara S, Matsusue E, et al. **Pallidoreticular damage in acute carbon monoxide poisoning: diffusion-weighted MR imaging findings.** *AJNR Am J Neuroradiol* 2005;26:1845–48
27. Kawanami T, Kato T, Kurita K, et al. **The pallidoreticular pattern of brain damage on MRI in a patient with carbon monoxide poisoning.** *J Neurol Neurosurg Psychiatry* 1998;64:282
28. O'Donnell P, Buxton PJ, Pitkin A, et al. **The magnetic resonance imaging appearances of the brain in acute carbon monoxide poisoning.** *Clin Radiol* 2000;55:273–80
29. Yoshii F, Kozuma R, Takahashi W, et al. **Magnetic resonance imaging and 11C-N-methylspiperone/positron emission tomography studies in a patient with the interval form of carbon monoxide poisoning.** *J Neurol Sci* 1998;160:87–91
30. Silverman CS, Brenner J, Murtagh FR. **Hemorrhagic necrosis and vascular injury in carbon monoxide poisoning: MR demonstration.** *AJNR Am J Neuroradiol* 1993;14:168–70
31. Inagaki T, Ishino H, Seno H, et al. **A long-term follow-up study of serial magnetic resonance images in patients with delayed encephalopathy after acute carbon monoxide poisoning.** *Psychiatry Clin Neurosci* 1997;51:421–23
32. Pavese N, Napolitano A, De Iaco G, et al. **Clinical outcome and magnetic resonance imaging of carbon monoxide intoxication. A long-term follow-up study.** *Ital J Neurol Sci* 1999;20:171–78
33. Carlesimo GA, Fadda L, Turriziani P, et al. **Selective sparing of face learning in a global amnesic patient.** *J Neurol Neurosurg Psychiatry* 2001;71:340–46
34. Gale SD, Hopkins RO, Weaver LK, et al. **MRI, quantitative MRI, SPECT, and neuropsychological findings following carbon monoxide poisoning.** *Brain Inj* 1999;13:229–43
35. Henke K, Kroll NE, Behniea H, et al. **Memory lost and regained following bilateral hippocampal damage.** *J Cogn Neurosci* 1999;11:682–97
36. Uchino A, Hasuo K, Shida K, et al. **MRI of the brain in chronic carbon monoxide poisoning.** *Neuroradiology* 1994;36:399–401
37. Singhal AB, Topcuoglu MA, Koroshetz WJ. **Diffusion MRI in three types of anoxic encephalopathy.** *J Neurol Sci* 2002;196:37–40
38. Chalela JA, Wolf RL, Maldjian JA, et al. **MRI identification of early white matter injury in anoxic-ischemic encephalopathy.** *Neurology* 2001;56:481–85
39. Durak AC, Coskun A, Yikilmaz A, et al. **Magnetic resonance imaging findings in chronic carbon monoxide intoxication.** *Acta Radiol* 2005;46:322–27
40. Kim JH, Chang KH, Song IC, et al. **Delayed encephalopathy of acute carbon monoxide intoxication: diffusivity of cerebral white matter lesions.** *AJNR Am J Neuroradiol* 2003;24:1592–97
41. Finelli PF, DiMario FJ Jr. **Hemorrhagic infarction in white matter following acute carbon monoxide poisoning.** *Neurology* 2004;63:1102–04
42. Weaver LK, Hopkins RO. **Hemorrhagic infarction in white matter following acute carbon monoxide poisoning.** *Neurology* 2005;64:1101; author reply 1101
43. Teksam M, Casey SO, Michel E, et al. **Diffusion-weighted MR imaging findings in carbon monoxide poisoning.** *Neuroradiology* 2002;44:109–13
44. Porter SS, Hopkins RO, Weaver LK, et al. **Corpus callosum atrophy and neuropsychological outcome following carbon monoxide poisoning.** *Arch Clin Neuropsychol* 2002;17:195–204
45. Antón M, Alcaraz A, Rey C, et al. **Acute hydrocephalus in carbon monoxide poisoning.** *Acta Paediatr* 2000;89:361–64
46. Gotoh M, Kuyama H, Asari S, et al. **Sequential changes in MR images of the brain in acute carbon monoxide poisoning.** *Comput Med Imaging Graph* 1993;17:55–59
47. Kesler SR, Hopkins RO, Blatter DD, et al. **Verbal memory deficits associated with fornix atrophy in carbon monoxide poisoning.** *J Int Neuropsychol Soc* 2001;7:640–46
48. Parkinson RB, Hopkins RO, Cleavinger HB, et al. **White matter hyperintensities and neuropsychological outcome following carbon monoxide poisoning.** *Neurology* 2002;58:1525–32
49. Vila JF, Meli FJ, Serqueira OE, et al. **Diffusion tensor magnetic resonance imaging: a promising technique to characterize and track delayed encephalopathy after acute carbon monoxide poisoning.** *Undersea Hyperb Med* 2005;32:151–56
50. Choi IS. **Delayed neurologic sequelae in carbon monoxide intoxication.** *Arch Neurol* 1983;40:433–35
51. Yamazaki Y, Yamada A. **Delayed encephalopathy after carbon monoxide intoxication.** *Intern Med* 2008;47:1071–72
52. Sener RN. **Acute carbon monoxide poisoning: diffusion MR imaging findings.** *AJNR Am J Neuroradiol* 2003;24:1475–77
53. Kim HY, Kim BJ, Moon SY, et al. **Serial diffusion-weighted MR imaging in delayed postanoxic encephalopathy. A case study.** *J Neuroradiol* 2002;29:211–15
54. Lin WC, Lu CH, Lee YC, et al. **White matter damage in carbon monoxide intoxication assessed in vivo using diffusion tensor MR imaging.** *AJNR Am J Neuroradiol* 2009;30:1248–55
55. Lo CP, Chen SY, Chou MC, et al. **Diffusion-tensor MR imaging for evaluation of the efficacy of hyperbaric oxygen therapy in patients with delayed neuropsychiatric syndrome caused by carbon monoxide inhalation.** *Eur J Neurol* 2007;14:777–82
56. Terajima K, Igarashi H, Hirose M, et al. **Serial assessments of delayed encephalopathy after carbon monoxide poisoning using magnetic resonance spectroscopy and diffusion tensor imaging on 3.0T system.** *Eur Neurol* 2008;59:55–61
57. Kamijo Y, Soma K, Ide T. **Recurrent myelin basic protein elevation in cerebrospinal fluid as a predictive marker of delayed encephalopathy after carbon monoxide poisoning.** *Am J Emerg Med* 2007;25:483–85
58. Beppu T, Fujiwara S, Nishimoto H, et al. **Fractional anisotropy in the centrum semiovale as a quantitative indicator of cerebral white matter damage in the subacute phase in patients with carbon monoxide poisoning: correlation with the concentration of myelin basic protein in cerebrospinal fluid.** *J Neurol* 2012;259:1698–705

59. Chang CC, Chang WN, Lui CC, et al. **Longitudinal study of carbon monoxide intoxication by diffusion tensor imaging with neuropsychiatric correlation.** *J Psychiatry Neurosci* 2010;35:115–25
60. Fujiwara S, Beppu T, Nishimoto H, et al. **Detecting damaged regions of cerebral white matter in the subacute phase after carbon monoxide poisoning using voxel-based analysis with diffusion tensor imaging.** *Neuroradiology* 2012;54:681–89
61. Kado H, Kimura H, Murata T, et al. **Carbon monoxide poisoning: two cases of assessment by magnetization transfer ratios and 1H-MRS for brain damage.** *Radiat Med* 2004;22:190–94
62. Prockop LD. **Carbon monoxide brain toxicity: clinical, magnetic resonance imaging, magnetic resonance spectroscopy, and neuropsychological effects in 9 people.** *J Neuroimaging* 2005;15:144–49
63. Kondziella D, Danielsen ER, Hansen K, et al. **1H MR spectroscopy of gray and white matter in carbon monoxide poisoning.** *J Neurol* 2009;256:970–79
64. Murata T, Kimura H, Kado H, et al. **Neuronal damage in the interval form of CO poisoning determined by serial diffusion weighted magnetic resonance imaging plus 1H-magnetic resonance spectroscopy.** *J Neurol Neurosurg Psychiatry* 2001;71:250–53
65. Murata T, Itoh S, Koshino Y, et al. **Serial proton magnetic resonance spectroscopy in a patient with the interval form of carbon monoxide poisoning.** *J Neurol Neurosurg Psychiatry* 1995;58:100–03
66. Sakamoto K, Murata T, Omori M, et al. **Clinical studies on three cases of the interval form of carbon monoxide poisoning: serial proton magnetic resonance spectroscopy as a prognostic predictor.** *Psychiatry Res* 1998;83:179–92
67. Kamada K, Houkin K, Aoki T, et al. **Cerebral metabolic changes in delayed carbon monoxide sequelae studied by proton MR spectroscopy.** *Neuroradiology* 1994;36:104–06
68. Beppu T, Nishimoto H, Fujiwara S, et al. **1H-magnetic resonance spectroscopy indicates damage to cerebral white matter in the subacute phase after CO poisoning.** *J Neurol Neurosurg Psychiatry* 2011; 82:869–75

Guidelines for the Ethical Use of Neuroimages in Medical Testimony: Report of a Multidisciplinary Consensus Conference

C.C. Meltzer, G. Sze, K.S. Rommelfanger, K. Kinlaw, J.D. Banja, and P.R. Wolpe

ABSTRACT

SUMMARY: With rapid advances in neuroimaging technology, there is growing concern over potential misuse of neuroradiologic imaging data in legal matters. On December 7 and 8, 2012, a multidisciplinary consensus conference, Use and Abuse of Neuroimaging in the Courtroom, was held at Emory University in Atlanta, Georgia. Through this interactive forum, a highly select group of experts—including neuroradiologists, neurologists, forensic psychiatrists, neuropsychologists, neuroscientists, legal scholars, imaging statisticians, judges, practicing attorneys, and neuroethicists—discussed the complex issues involved in the use of neuroimaging data entered into legal evidence and for associated expert testimony. The specific contexts of criminal cases, child abuse, and head trauma were especially considered. The purpose of the conference was to inform the development of guidelines on expert testimony for the American Society of Neuroradiology and to provide principles for courts on the ethical use of neuroimaging data as evidence. This report summarizes the conference and resulting recommendations.

ABBREVIATIONS: AMA = American Medical Association; ASNR = American Society of Neuroradiology

Neuroradiologic imaging techniques have rapidly evolved during the past 3 decades to offer exquisite anatomic detail and, increasingly, a variety of functional insights. While excellent for diagnosing neurologic disease, current neuroimaging technologies have a limited role in the clinical setting of behavioral disorders or psychiatric disease. Research using brain imaging spans a wide range of ongoing investigations into the neurobiologic mechanisms underlying normal human behavior and psychiatric disorders. Promising approaches for diagnostic and/or prognostic imaging for cognitive impairment (including following mild traumatic brain injury),[1] lie detection,[2,3] psychoses,[4,5] mood disorders,[6] and other behavioral paradigms[7] are evolving. Much of this research is performed with study designs that compare groups of well-characterized subjects, but validation in single-subject analyses is often lacking.[8] With advancements in brain imaging and postprocessing techniques, both acquisition methods and data interpretation can vary greatly by site and scanner.[9] This variation makes the standardization of image generation highly challenging.

While medical images are commonly included in courtroom evidence, neuroimaging presents special complexity, and both structural and functional neuroimaging remains controversial in several common forensic settings. The specific use of functional imaging for making inferences about human behavior or motivation is particularly problematic.[10] Technologies that promise "images of" or "windows to" the mind are especially compelling and enticing to general audiences. Indeed studies have suggested that nonsensical science texts are more convincing when accompanied by brain-based data and especially a brain image.[11,12] Despite these concerns, however, there is no comprehensive set of guidelines to inform imaging experts or the courts. In 1996, the Brain Imaging Council of the Society of Nuclear Medicine published a cautionary note warning of the potential for over-reach with positron-emission tomography and single-photon emission tomography of the brain in expert testimony.[13] Yet, although general guidelines for physicians engaged in medical testimony for radiology[14,15] and other medical specialties[16,17] do exist, there is

Received May 2, 2013; accepted after revision May 13.

From the Departments of Radiology and Imaging Sciences (C.C.M.), Neurology (C.C.M., K.S.R.), Psychiatry and Behavioral Sciences (C.C.M., P.R.W.), Rehabilitation Medicine (J.D.B.), Pediatrics (K.K., P.R.W.), Medicine (P.R.W.), and Sociology (P.R.W.), Emory University, Atlanta, Georgia; and Department of Diagnostic Radiology (G.S.), Yale University School of Medicine, New Haven, Connecticut.

This work was supported by the American Society of Neuroradiology, the Atlanta Clinical and Translational Science Institute (NIH U54 UL1RR02500), and the Emory University Neuroscience Initiative.

American Society for Functional Neuroradiology DTI Guidelines Disclaimer: Please note that DTI and tractography are based on certain biophysical assumptions and mathematical approximations; their results should be interpreted in conjunction with conventional anatomical imaging as well as other clinical data including physical examination and, if clinically indicated, intraoperative subcortical stimulation.[46]

Please address correspondence to Carolyn C. Meltzer, MD, FACR, Emory University School of Medicine, Emory University Hospital, D-112, 1364 Clifton Rd NE, Atlanta, GA; e-mail: cmeltze@emory.edu

http://dx.doi.org/10.3174/ajnr.A3711

an unmet need to address specific guidelines on expert testimony concerning the unique challenges of brain imaging.

A consensus conference, supported by the American Society of Neuroradiology (ASNR), the Atlanta Clinical and Translational Science Institute, and the Emory University Neuroscience Initiative, brought together experts from multiple disciplines—including neuroradiology, ethics, law, biostatistics, forensic psychiatry, neuroscience, neurology, and neuropsychology—to inform the development of guidelines on the ethical use of neuroimaging in the courtroom. We considered 5 framing questions:

1) What standards or guidelines should be used in testimony about brain-behavior relationships to determine when generalized research findings are applicable to individuals?

2) What kinds of testimony are outside an expert's expertise/qualifications?

3) How can bias in medical testimony be diminished?

4) How do judicial standards of legal evidence apply to medical expert opinions on causality and associations in court?

5) When is medical testimony outside what is generally accepted in the field and is such testimony ever justifiable?

On the basis of several case examples considered within the framework of the 5 framing questions, we discussed the need for guidelines and considered the following key issues.

Need for Guidelines

The obligation to protect the public trust by ensuring that expert testimony is accurate and reliable is well recognized.[18] Yet, despite concern over insufficient regulation of the use of neuroimaging in forensic evidence,[19] some professional societies have been reluctant to sanction members for medical testimony, deemed to be inappropriate due to concerns about impugning the individual's reputation.[15] In *Austin v American Association of Neurologic Surgeons*,[20] the courts upheld the right of professional societies to sanction members for irresponsible expert testimony. The position of the American Medical Association (AMA) is that expert witness testimony can be considered the practice of medicine and thus is subject to peer review (http://www.ama-assn.org/resources/doc/code-medical-ethics/907a.pdf) (AMA H-265–993). In fact, the Ethics Committee of the American College of Radiology has reviewed medical testimony and sanctioned members.[21] Because expert witnesses are secured to assist triers of fact in achieving truth, a need for guidelines that qualify the admissibility and reliability of proffered neuroimaging evidence is self-evident. The material that follows highlights themes and topical areas that were especially prominent as the guideline discussion proceeded at the consensus conference.

Key Considerations

Qualifications of Experts and Scope of Testimony. If expert medical testimony is to be valued, it must be balanced, accurate, and aligned with the qualifications of the witness. If indeed expert medical testimony represents the practice of medicine, as postulated by the AMA (AMA H-265–993), then it should be subject to peer review.

While it is generally agreed that expert testimony should be provided only by those who have considerable experience in the relevant subject matter,[22] most professional society guidelines do not clearly address testimony that is outside of subspecialty expertise. Is a specialist's testimony superior to that of a generalist? One would assume that expert testimony should be given by an expert, yet the AMA report states that an expert witness should have education, training, and occupational experience comparable with those of the defendant in medical malpractice cases. This approach applies primarily to experts who are reviewing cases for adherence to the standard of care, in which physicians of comparable knowledge and experience may be optimal choices. In cases in which causation is an issue or advanced techniques are involved, then greater expertise may be desirable to more accurately delineate the findings and relevant differential diagnosis. For example, in birth injury cases, a wide range of diagnoses (eg, hypoxic-ischemic injury, congenital malformation, in utero infection, complex inborn error of metabolism, and so forth) may be consistent with the imaging presentation.

Several society guidelines require that the expert providing medical testimony be board-certified in the relevant field.[16,23] However, nonphysician, nonradiologist professionals who are expert in advanced brain imaging techniques in research settings have been called to testify on the diagnostic and prognostic value of imaging studies. In such cases, jurors may assume causality from testimony on brain imaging even though clinical context is absent. The distinction between medical and scientific testimony is not always clear to the lay person.

Bias in Expert Testimony. There are several sources of bias that may account for substantial variability in expert testimony, even for the most well-meaning professionals.[24] Hindsight bias is a widely recognized phenomenon: Faced with the knowledge of an abnormality, radiologists are more likely to detect a lesion on imaging.[25] Outcome bias also comes into play in the retrospective nature of reviewing imaging studies for medical testimony, when the reader is already aware of an adverse event.[25] Financial incentives may be a particularly concerning source of bias.[26] Given the adversarial nature of legal proceedings, innate tendencies toward reciprocity may introduce subconscious bias,[27,28] and attorneys seek experts who are inclined to support their position. Kesselheim and Studdert[29] observed that physicians who testified frequently tended to act consistently for one side (ie, plaintiff or defendant). Alternatively, in cases that use functional neuroimaging methods typically performed in the research setting, the expert may be influenced by a professional investment in promoting his or her research area or specific research findings.[30] In some situations, such as death row cases, the expert may also be biased by a political or ethical position, such as opposition to the death penalty.

Scientific Validity

Advanced brain imaging techniques, such as functional MR imaging, diffusion tensor imaging, perfusion imaging, PET, and SPECT, are used in care in only a few clinical settings in which sufficient literature and/or clinical evidence has demonstrated sensitivity and specificity. Such techniques are most often applied in the research setting, typically by using group comparisons, and statistical validity is a well-recognized challenge for fMRI. The translation of fMRI and other experimental neuroimaging methods to single-subject uses is highly challenging and, thus far, is

applied only in clinical situations in which a relatively strong activation signal may be obtained, such as in presurgical mapping of the motor cortex. The validity of using single-subject fMRI data to uncover evidence of behavioral aberration, pain, or deception is more problematic.[19,31] Furthermore, the applicability of normative imaging databases (typically comprising young, healthy subjects) in courtroom testimony is questionable. We also note that the use of normative imaging databases for comparisons with individual subjects for the purpose of expert witness testimony may constitute an inappropriate use of materials collected from research subjects.

The reliability of scientific evidence is judged according to 1 of 2 alternative rules, depending on the jurisdiction. The dominant standard originating from the 1993 case *Daubert v Merrell Dow Pharmaceuticals* (509 U.S. 579, 1993) assigns a duty to the trial judge to serve as a gatekeeper for scientific evidence. This case considers 5 factors: whether the expert's theory can and has been tested, whether the theory has been subject to peer review, the known or expected error rate, the existence and maintenance of standards controlling the operation of the technique, and acceptability in the relevant scientific community. The expert's opinion must be based on scientific knowledge. The broader and older ruling known as the Frye standard[32] remains in effect in states that have not elected to follow the *Daubert* approach. Frye requires that the party introducing the evidence show that the theory or methodology used by the expert is generally accepted within the relevant scientific community; it does not consider the reliability of the proposed evidence.[10]

The growth of technology development in neuroimaging is staggering, making it difficult to develop standards for its acquisition and postacquisition processing. For example, MR imaging by using DTI is a highly promising technique for evaluating the integrity of brain white matter, yet results may vary by scanner field strength, scanner type, pulse sequence, and postprocessing. The representational nature of color-coded DTI fiber-tracking maps may not be evident to the lay public, such as a jury, who may assume they are pictures of actual brain connections.[33] Similarly, it may not be obvious that areas of activation generated from fMRI are a statistical representation of data, while raw data are rarely peer-reviewed for acceptability of methods. Because of the strong presence and appearance of objectivity of the visual images that are the products of neuroimaging technology, some have argued that their value may be outweighed by their potential prejudicial influence.[19,34]

Use and Abuse Cases

We used breakout groups to explore cases that were exemplary of use and abuse of neuroradiologic data in the courtroom. Consensus conference participants considered 4 cases regarding the use of imaging in the courtroom: 1) conventional (structural) imaging, 2) criminal/forensics, 3) brain trauma, and 4) child abuse. The use of neuroimaging in criminal trials and brain trauma may be most controversial and thus was emphasized.

Conventional (Structural) Imaging

Because much of clinical imaging interpretation is nonquantitative, there is an imperative for experts to use standardized, accepted medical terminology in describing findings. Relevant definitions of what constitutes normal variation are highly desirable yet often lacking.[35] Issues bearing on the credentials and experience of the expert witness are also important to consider. Particularly in malpractice cases, peer-review panels could add validity, because the standard of care can be difficult to establish. Furthermore, the context of the imaging data should be evaluated in light of other relevant records.

Neuroimaging in Criminal Cases

Brain imaging findings have limited application to the primary question of the court of determining criminal intent.[36] The practice of performing imaging studies on a defendant in order to shed light on brain function or state of mind at the time of a prior criminal act is problematic. The retrospective nature of this evaluation makes it particularly difficult to attribute causality to specific imaging findings. Currently brain imaging methods cannot readily determine whether a defendant knew right from wrong or maintained criminal intent or *mens rea* at the time of the criminal act. Also, there is an inherent difficulty in translating mechanistic (neural) system data into human behavior. While functional imaging research has correlated numerous behaviors and moods with regions of the brain, issues of individual variation, plasticity, and the challenge of assuming knowledge of past motivational states limits the utility of brain images to infer causality of behaviors. Morse[37] argued that the detection of structural or functional brain findings that correlate with behavioral syndromes does not convincingly imply causation or criminal responsibility, or predict future behaviors.

Neuroimaging evidence is most often introduced in criminal cases in the sentencing or punishment phase, to address the consideration of mitigating circumstances.[32] Criminal defense attorneys are increasingly using brain imaging data and neuroimaging experts in capital sentencing. Attorneys may argue that while the defendant may be legally guilty, evidence of abnormal brain function diminishes his or her culpability.[38] From a compassionate perspective, the argument that a defendant's brain may be shown to be "hard-wired" to predispose the individual to criminal behaviors is appealing. Yet this approach may be used not only to mitigate sentences (by implying a lack of criminal intent) but also to support more severe sentencing (ie, hard-wired individuals may pose a continued threat to society). Also, neuroimaging evidence for the lack of complete myelination of the adolescent brain has been used to conclude that adolescents' culpability should be inherently mitigated.[39] Still, there is substantial debate as to whether brain imaging can contribute value to the behavioral approach that courts have traditionally used to comprehend these issues.

Brain Trauma

Public attention to the sequelae of brain trauma has grown.[40] In particular, DTI is under intense investigation for its potential application for predicting persistent cognitive deficits in individuals who have experienced trauma. Some investigations have demonstrated relationships between DTI findings and clinical symptoms and/or outcome,[1,41,42] though others have not.[43,44] This technique promises to offer unique insights into the natural history of

brain injury and potentially inform therapeutic approaches. Yet the manner in which DTI data are acquired produces findings that not only lack specificity but also continue to be highly variable across institutions and among researchers.[45] The American Society for Functional Neuroradiology has developed general guidelines for the acquisition and postprocessing of DTI data.[46] However, the rapid evolution of this technique has contributed to the challenge of achieving true standardization. At present, the American Society for Functional Neuroradiology guidelines include a suggested disclaimer in clinical reports of DTI and note that "it is critical that physicians basing clinical decisions on DTI be familiar with the limitations and potential pitfalls inherent to the technique."[43]

Furthermore, the neuroradiology community has not arrived at a consensus view of the value of DTI in (particularly mild) head trauma. Nonspecific patterns or findings obtained with DTI prohibit the confirmation or diagnosis of mild TBI with reliability. If DTI or other nonspecific imaging findings are introduced into legal evidence, the expert should offer alternative explanations for the findings, including technical factors and normal variations.[47]

Child Abuse

Shaken Baby Syndrome, with its traditional trilogy of subdural hematoma, retinal hemorrhages, and diffuse axonal injury, can cause devastating brain injury in young children and infants.[48] Neuroradiologic imaging coupled with a consistent clinical examination may detect a pattern of lesions consistent with Shaken Baby Syndrome and thus provide diagnostic evidence of nonaccidental trauma.[49] Yet the specificity of these findings is not as robust as was previously thought.[50] New questions and speculations in this area have been prompted by other potential medical explanations including stroke, infection, sinus thrombosis, and previous bleeding due to an undiagnosed clotting disorder.[49,51] Therefore, it is vital that the expert witness articulate what other diagnoses may present similarly.

Conference participants emphasized the need for balanced objectivity in presenting testimony and in including the identification of other possibilities in the differential diagnosis. Due to the special expertise required to diagnose nonaccidental trauma in children, experts should be trained in neuroradiology and include pediatric neuroradiology in their clinical practice.

Proposed Standards

On the basis of the above, the following guidelines for neuroradiology imaging testimony are put forth. These may both serve to guide subspecialty societies like the ASNR and inform the legal community.

1) Experts should present all relevant facts available in their testimony, ensure truthfulness and balance, and consider opposing points of view.

2) Experts should specify known deviations from standard practice.

3) Experts should have substantive knowledge and experience in the area in which they are testifying.

4) Experts should use standard terminology and describe standardization methods and the cohort characteristic from which claims are determined, when applicable.

5) Nonvalidated findings that are used to inform clinical pathology should be approached with great caution.

6) Recognized appropriateness guidelines should be used to assess whether the imaging technique used is appropriate for the particular question.

7) Experts should avoid drawing conclusions about specific behaviors based on the imaging data alone.

8) Experts should be willing to submit their testimony for peer review.

9) Experts should be prepared to provide a description of the nature of the neuroimages (eg, representational/statistical maps when derived from computational postprocessing of several images) and how they were acquired.

10) Raw images and raw data should be made available for replication if requested.

11) Experts should be able to explain the reasoning behind their conclusions.

12) False-positive rates should be known and considered if the expert's testimony includes quantitative imaging.

13) Experts should be prepared to discuss limitations of the technology and provide both confirming research and disconfirming studies.

Sanction

Leaders of professional societies may be reluctant to sanction members who act outside of established guidelines and/or offer inappropriate testimony because this may put the professional society at risk of legal action from a disgruntled member. Yet, if medical expert testimony is indeed a part of the practice of medicine, as observed by the AMA, then developing procedures for peer review of testimony and potential sanction is warranted.[21] In addition, while fear of sanctions might prevent experts from testifying, the AMA guidelines also suggest that serving as an expert witness when called upon is also a professional, medical responsibility.

CONCLUSIONS

While neuroimaging involves powerful and robust technologies, its premature or inappropriate use in the courtroom may cause more harm than good. Premature use may not only have detrimental effects in the legal setting but may also breed societal distrust in innovative technologies that could hinder their future development and research. On the basis of a multidisciplinary consensus conference, we have developed a set of guidelines that may be used by neuroradiologists and the courts to ensure that images and expert testimony introduced into evidence are reliable. It is our intent that both appropriate medical and legal professional societies consider adoption of these guidelines to provide a standardized ethical foundation for the medical testimony involving neuroimaging.

ACKNOWLEDGMENTS

We are appreciative of the kind support from the American College of Radiology. We would also like to thank the Emory University Center for Ethics and its staff for hosting the conference. We are deeply grateful to the consensus conference participants for sharing their expertise and exchanging ideas: Vikas Agarwal, MD;

Peter Ash, MD; Randall R. Benson, MD; Leonard G. Berlin, MD; F. DuBois Bowman, PhD; William S. Duffey, Jr, JD; David Emerson, JD; Christopher G. Filippi, MD; Alisa D. Gean, MD; Ruben C. Gur, PhD; William G. Jungbauer, JD; Ivo Dinov, PhD; Peter Kalina, MD; Marcel Just, PhD; Helen S. Mayberg, MD; Stephen J. Morse, JD, PhD; Jane Campbell Moriarty, JD; Thomas Nichols, PhD; James Provenzale, MD; Bruce Rosen, MD, PhD; David Seidenwurm, MD; O. Carter Snead, JD; A. John Tsiouris, MD; and Hal Wortzel, MD. We also thank the following individuals for logistic and documentation support: Linda Burr, Kate Bush, Cyd Cipolla, Cynthia Drake, Lidia Hanevold, Ross Gordon, Jonah Queen, Vivek Bansal, MD, and Marc Benayoun, MD.

Disclosures: Carolyn C. Meltzer—*RELATED*: *Grant*: American Society of Neuroradiology,* *UNRELATED*: *Board Membership*: Image Matrix of the American College of Radiology,* General Electric-Association of University Radiologists Award Board,* Association of University Radiologists,* ASNR executive committee,* *Comments*: travel reimbursement only; *Consultancy*: Thomas Jefferson University, University of Arizona, *Comments*: review of radiology department. Gordon Sze—*RELATED*: *Support for Travel to Meetings for the Study or Other Purposes*: ASNR, American College of Radiology, Emory Neuroscience Initiative, Emory Center for Ethics, Atlanta Clinical and Translational Institute, *Comments*: Plane flights and ground transportation were provided to all participants outside of Atlanta to attend the symposium, *UNRELATED*: *Board Membership*: Guerbet Advisory Board, *Expert Testimony*: scattered law firms, *Grants/Grants Pending*: National Institutes of Health,* Remedy Pharmaceuticals,* *Travel/Accommodations/Meeting Expenses Unrelated to Activities Listed*: ASNR. Kathy Kinlaw—*RELATED*: *Grant*: Support for the conference was provided by the ASNR, the Atlanta Clinical and Translational Science Institute (NIH U54 UL1RR02500), and the Emory University Neuroscience Initiative. This support was for the consensus conference overall, not to support my direct participation in the project or writing. John D. Banja—*RELATED*: *Grant*: ASNR,* Atlanta Clinical and Translational Science Institute,* American College of Radiology,* *Comments*: These entities supported a consensus conference from which the article was derived; *UNRELATED*: *Board Membership*: American Society of Cataract and Refractive Surgery, *Comments*: I am the public member of the governing board. That affiliation has nothing to do, however, with issues in forensic neuroradiology, *Other*: Atlanta Clinical and Translational Science Institute,* *Comments*: I direct the ethics program of the Atlanta Clinical and Translational Science Institute, which is made possible by a grant from the National Center for Advancing Translational Science (of the National Institutes of Health). This speaks to the (dual) use of translational technologies. However, I do not see how that role would suggest a "conflict" bearing on this article. Paul R. Wolpe—*RELATED*: *GRANT*: ASNR,* *Comments*: They helped fund the consensus conference on which the article was based. *Money paid to the institution.

REFERENCES

1. Kraus M, Susmaras T, Caughlin B, et al. **White matter integrity and cognition in chronic traumatic brain injury: a diffusion tensor imaging study.** *Brain* 2007;130:2508–19
2. Mohamed F, Faro S, Gordon N, et al. **Mapping of deception and truth telling about an ecologically valid situation: functional MR imaging and polygraph investigation—initial experience.** *Radiology* 2006;238:679–88
3. Karim A, Schneider M, Lotze M, et al. **The truth about lying: inhibition of the anterior prefrontal cortex improves deceptive behavior.** *Cerebral Cortex* 2010;20:205–13
4. Jukuri T, Kiviniemi V, Nikkinen J, et al. **Default mode network in young people with familial risk for psychosis: the Oulu Brain and Mind Study.** *Schizophr Res* 2013;143:239–45
5. Woodward N, Karbasforoushan H, Heckers S. **Thalamocortical dysconnectivity in schizophrenia.** *Am J Psychiatry* 2012;169:1092–99
6. Korgaonkar M, Grieve S, Etkin A, et al. **Using standardized fMRI protocols to identify patterns of prefrontal circuit dysregulation that are common and specific to cognitive and emotional tasks in major depressive disorder: first wave results from the iSPOT-D Study.** *Neuropsychopharmacology* 2013;38:863–71
7. Sato J, de Araujo Filho G, de Araujo T, et al. **Can neuroimaging be used as a support to diagnosis of borderline personality disorder? An approach based on computational neuroanatomy and machine learning.** *J Psychiatr Res* 2012;46:1126–32
8. Anderson JS, Ferguson M, Lopez-Larson M, et al. **Reproducibility of single-subject functional connectivity measurements.** *AJNR Am J Neuroradiol* 2011;32:548–55
9. Jovicicha J, Czannera S, Grevea D, et al. **Reliability in multi-site structural MRI studies: effects of gradient non-linearity correction on phantom and human data.** *Neuroimage* 2006;30:436–43
10. Moriarty J. **Flickering admissibility: neuroimaging evidence in the U.S. courts.** *Behav Sci Law* 2008;26:29–49
11. McCabe D, Castel A. **Seeing is believing: the effect of brain images on judgments of scientific reasoning.** *Cognition* 2008;107:343–52
12. Weisberg DS, Keil FC, Goodstein J, et al. **The seductive allure of neuroscience explanations.** *J Cogn Neurosci* 2008;20:470–77
13. **Ethical clinical practice of functional brain imaging: Society of Nuclear Medicine Brain Imaging Council.** *J Nucl Med* 1996;37:1256–59
14. ACR Practice Guideline on the Physician Expert Witness in Radiology and Radiation Oncology. Revised 2012. http://www.acr.org/~/media/ACR/Documents/PGTS/guidelines/Expert_Witness.pdf. Accessed November 26, 2012
15. Janower M, Hoffman T. **An overview of the ACR Committee on Ethics: from hospital contracts to expert witness testimony.** *J Am Coll Radiol* 2005;2:424–27
16. **Guidelines for expert witness testimony in medical malpractice litigation: Committee on Medical Liability—American Academy of Pediatrics.** *Pediatrics* 2002;109:974–79
17. Maggiore W, Kupas D, Glushak C. **Expert witness qualifications and ethical guidelines for emergency medical services litigation: resource document for the National Association of EMS Physicians position statement.** *Prehosp Emerg Care* 2011;15:426–31
18. Feld A, Carey W. **Expert witness malfeasance: how should societies respond?** *Am J Gastronenterol* 2005;100:991–95
19. Kulich R, Maciewicz R, Scrivani S. **Functional magnetic resonance imaging (fMRI) and expert testimony.** *Pain Med* 2009;10:373–80
20. *Austin v American Association of Neurologic Surgeons*, Lexis 12143 (US App 7th Cir 2001)
21. Berlin L, Hoffman T, Shields W, et al. **When does expert witness testimony constitute a violation of the ACR Code of Ethics? The role of the ACR Committee on Ethics.** *J Am Coll Radiol* 2006;3:252–58
22. Berlin L, Williams D. **When an expert witness is not an expert.** *AJR Am J Roentgenol* 2000;174:1215–19
23. Williams M, Mackin G, Beresford H, et al. **American Academy of Neurology qualifications and guidelines for the physician expert witness.** *Neurology* 2006;66:13–14
24. Lindberg DM, Lindsell CJ, Shapiro RA. **Variability in expert assessments of child physical abuse likelihood.** *Pediatrics* 2008;121:e945–53
25. Hugh T, Dekker S. **Hindsight bias and outcome bias in the social construction of medical negligence: a review.** *J Law Med* 2009;16:846–57
26. Vohs K, Mead N, Goode M. **The psychological consequences of money.** *Science* 2006;314:1154
27. Konrad KA, Morath F. **Evolutionarily stable in-group favoritism and out-group spite in intergroup conflict.** *J Theor Biol* 2012;306:61–67
28. Nakamura M, Masuda N. **Groupwise information sharing promotes ingroup favoritism in indirect reciprocity.** *BMC Evol Biol* 2012;12:213
29. Kesselheim A, Studdert D. **Characteristics of physicians who frequently act as expert witnesses in neurologic birth injury litigation.** *Obstet Gynecol* 2006;108:273–79
30. Shore S. **Is the medical witness a legal advocate?** *Med Trial Tech Q* 1971;18:121–23
31. Ganis G, Rosenfeld J, Meixner J, et al. **Lying in the scanner: covert countermeasures disrupt deception detection by functional magnetic resonance imaging.** *Neuroimage* 2011;55:312–19
32. fMRI Evidence Used in Murder Sentencing. 2009. ScienceInsider.

http://news.sciencemag.org/scienceinsider/2009/11/fmri-evidence-u.html. Accessed November 26, 2012
33. Feigl GC, Hiergeist W, Fellner C, et al. **Magnetic resonance imaging diffusion tensor tractography: evaluation of anatomical accuracy of different fiber tracking software packages.** *World Neurosurg* 2013;pii:S1878–8750(13)00011–19
34. Brown T, Murphy E. **Through a scanner darkly: functional neuroimaging as evidence of a criminal defendant's past mental states.** *Stanford Law Rev* 2010;62:1119–208
35. Vernooij M, Ikram M, Tanghe H, et al. **Incidental findings on brain MRI in the general population.** *N Engl J Med* 2007;357:1821–28
36. Morse S. **The future of neuroscientific evidence.** In: Henderson C, Epstein J, eds. *The Future of Evidence How Science and Technology will Change the Practice of Law.* Chicago: American Bar Association; 2011:137–63
37. Morse S. **Brain overclaim syndrome and criminal responsibility: a diagnostic note.** *Ohio State Journal of Criminal Law* 2006;3:397–412
38. Carter Snead O. **Neuroimaging and the "complexity" of capital punishment.** *New York University Law Review* 2007;82:1265–339
39. Johnson S, Blum R, Giedd J. **Adolescent maturity and the brain: the promise and pitfalls of neuroscience research in adolescent health policy.** *J Adolesc Health* 2009;45:216–21
40. DeKosky S, Ikonomovic M, Gandy S. **Traumatic brain injury: football, warfare, and long-term effects.** *N Engl J Med* 2010;363:1293–96
41. Arfanakis K, Haughton V, Carew J, et al. **Diffusion tensor MR imaging in diffuse axonal injury.** *AJNR Am J Neuroradiol* 2002; 23:794–802
42. Bazarian J, Zhong J, Blyth B, et al. **Diffusion tensor imaging detects clinically important axonal damage after mild traumatic brain injury: a pilot study.** *J Neurotrauma* 2007;24:1447–59
43. Lange R, Iverson G, Brubacher J, et al. **Diffusion tensor imaging findings are not strongly associated with postconcussional disorder 2 months following mild traumatic brain injury.** *J Head Trauma Rehabil* 2012;27:188–98
44. Levin H, Wilde E, Troyanskaya M, et al. **Diffusion tensor imaging of mild to moderate blast-related traumatic brain injury and its sequelae.** *J Neurotrauma* 2010;27:683–94
45. White T, Nelson M, Lim K. **Diffusion tensor imaging in psychiatric disorders.** *Top Magn Reson Imaging* 2008;19:97–109
46. Field A, Filippi C, Kalnin A, et al. ASFNR Guidelines for Clinical Application of Diffusion Tensor Imaging. American Society of Functional Neuroradiology. 2012:5. http://www.asfnr.org/docs/ASFNR_Guidelines-for-DTI.pdf. Accessed November 26, 2012
47. Katzman G, Dagher A, Patronas N. **Incidental findings on brain magnetic resonance imaging from 1000 asymptomatic volunteers.** *JAMA* 1999;281:36–39
48. Bruce D, Zimmerman R. **Shaken impact syndrome.** *Pediatr Ann* 1989;18:482–84, 486
49. Findley KA, Barnes PD, Moran DA, et al. **Shaken baby syndrome, abusive head trauma, and actual innocence: getting it right.** *Houston Journal of Health and Policy* 2012;Univ. of Wisconsin Legal Studies Research Paper No. 1195
50. Barnes P. **Ethical issues in imaging nonaccidental injury: child abuse.** In: Barnes P, ed. *Topics in Magnetic Resonance Imaging: Nonaccidental Central Nervous System Injury*. Vol. 13. Philadelphia: Lippincott Williams & Wilkins; 2002:85–94
51. Sieswerda-Hoogendoorn T, Boos S, Spivack B, et al. **Abusive head trauma. Part II. Radiological aspects.** *Eur J Pediatr* 2012;171: 617–23

Attitudes about Medical Malpractice: An American Society of Neuroradiology Survey

N.P. Pereira, J.S. Lewin, K.P. Yousem, and D.M. Yousem

ABSTRACT

SUMMARY: The concern over medicolegal liability is pervasive among physicians. We sought, through an email survey to the members of the ASNR, to assess the experience with and attitudes about the medicolegal environment among neuroradiologists. Of 4357 physicians surveyed, 904 answered at least 1 of the questions in the survey; 449 of 904 (49.7%) had been sued: 180 (44.9%) had been sued once, 114 (28.4%) twice, 60 (15.0%) 3 times, and 47 (11.7%) more than 3 times. The payouts for suits were most commonly in the $50,000 to $150,000 range, except for interventional neuroradiologists, in whom the most common value was $600,000 to $1,200,000. Only 9 of 481 (1.9%) of suits returned a plaintiff verdict. Despite reported outcomes that favored physicians with respect to cases being dropped (270/481 = 56.1%), settled without a payment (11/481 = 2.3%), or a defense verdict (46/481 = 9.6), most respondents (81.1%, 647/798) believed that the medicolegal system was weighted toward plaintiffs. More than half of the neuroradiologists (55.2%, 435/787) reported being mildly to moderately concerned, and 19.1% (150/787) were very or extremely concerned about being sued.

ABBREVIATIONS: ASNR = American Society of Neuroradiology; PIAA = Physician Insurers Association of America

Malpractice lawsuits are a significant source of concern for physicians.[1] In one report of physicians covered by a large professional liability insurer, 7.4% of physicians had a claim made against them every year.[2] There is a high variation of probability for facing a claim within medical specialties. Obstetricians/gynecologists, internists, family physicians, general surgeons, and orthopedists are more likely to be sued than radiologists.[3] Of the top 10 specialties sued, plastic surgeons, anesthesiologists, cardiologists, and gastroenterologists are named less frequently than are radiologists as defendants in malpractice suits.[4,5] Radiology also occupies the 6th position in terms of dollars paid per claim.[5] Overall, approximately 30% of radiologists will be the subjects of at least 1 malpractice claim during their careers.[6] The highest rates of claims of malpractice suits that include radiologists classified by organ system category are breast, followed by vertebral/musculoskeletal, pulmonary, and gastrointestinal systems.[6] CNS-related claims ranked sixth among organ systems.[4]

Once a claim is made, the mean time between an injury claim being served and its resolution is 5 years, which means that the time taken to resolve the case can seem interminable to the parties involved.[7] However, accordingly to the Physician Insurers Association of America (PIAA), 65% of claims are dropped, dismissed, or withdrawn; 25.7% are settled; and 5% are resolved by trial.[4] Sixty percent of all radiologists' claims that are resolved out of court result in a payment to a plaintiff. On the contrary, when a case goes to trial, 80% of verdicts are in favor of physicians.[7] The mean legal costs associated with cases that go to trial, are settled, or are dropped/dismissed/withdrawn are $375,000, $200,000, and $40,000, respectively.[3]

Although there have been many studies published on medical malpractice in the United States, the experience and attitudes of neuroradiologists specifically have not been addressed. This study was designed to evaluate the opinions of neuroradiologists toward malpractice suits and the judicial system. On the basis of the experience in our own institution, in which less than 20% of the faculty have been named in a suit, we hypothesized that a minority of American Society of Neuroradiology (ASNR) members would have been named in malpractice suits. On the basis of the level of anxiety experienced within our own division, despite the low rate of suits, we hypothesized that the fear of being sued would outweigh the actual experience of ASNR members.

MATERIALS AND METHODS

Our data were based on an e-mail survey of 4357 ASNR members conducted in February 2013. The survey questions from which this report is based can be found in On-line Table 1.

Received July 22, 2013; accepted July 24.

From The Russell H. Morgan Department of Radiology and Radiological Science, The Johns Hopkins Medical Institution, Baltimore, Maryland.

Please address correspondence to David M. Yousem, MD, MBA, Johns Hopkins Medical Institution, 600 N Wolfe St, Phipps B100F, Baltimore, MD 21287; e-mail: dyousem1@jhu.edu

Indicates article with supplemental on-line table.

http://dx.doi.org/10.3174/ajnr.A3730

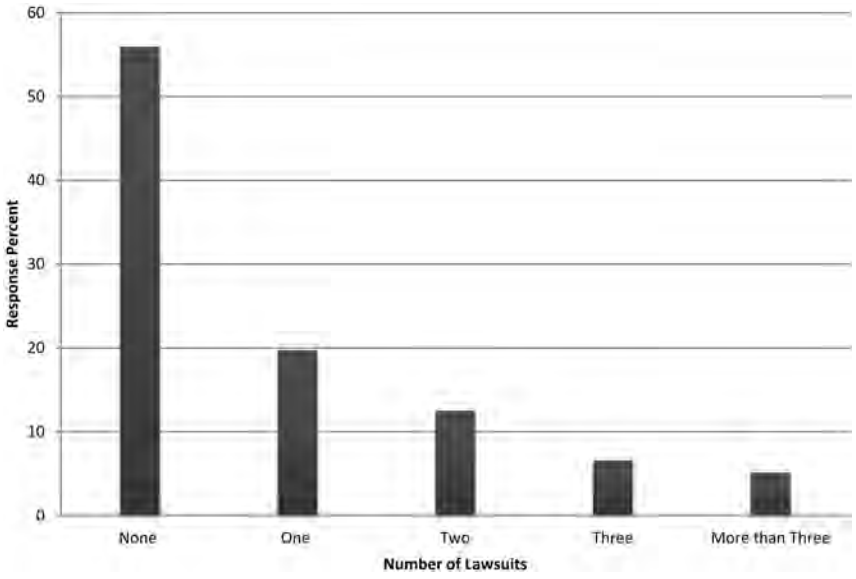

FIG 1. Distribution, in percentage, of lawsuits a radiologist has been named in (total of 776 lawsuits from 401 respondents who had been sued).

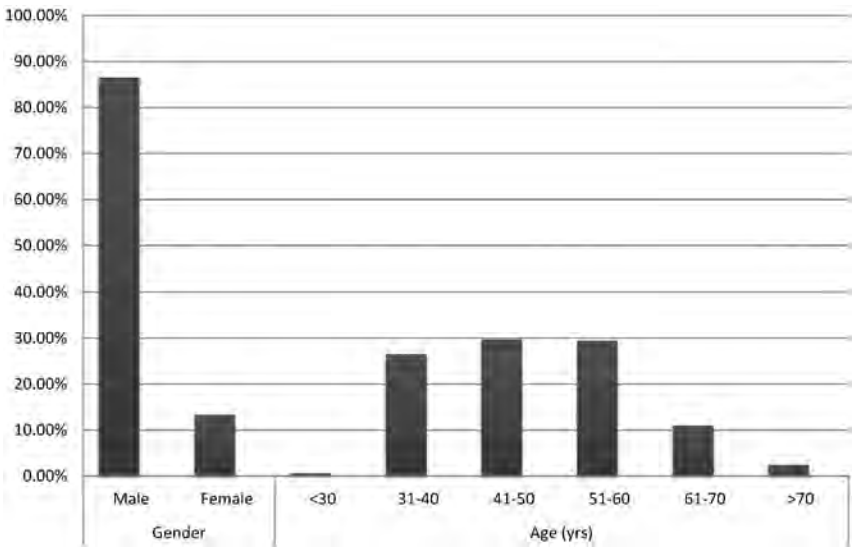

FIG 2. Demographic information of radiologists enrolled in the survey who answered the question about sex ($n = 806$) and age ($n = 808$).

The full results of the survey can be viewed at the following Web address:

http://www.surveymonkey.com/sr.aspx?sm=4y1SduJ73pusEREHU34PyiMKMhry2RDb9LzA3P06UCM_3d.

The survey was sent by means of a Web link. Through repeated e-mailing (2 reminders), a response rate of 20.7% (904/4357) was reached.

The survey was conducted by an outside vendor (SurveyMonkey, http://www.surveymonkey.com) and administered by the ASNR. Data were sent to the ASNR SurveyMonkey Web site. The data were anonymized without individual respondent identification. Confidentiality was ensured to respondents. Open-question answers were grouped for trends in responses by the 2 reviewers in concert, for example, lawsuits were still pending judgment, people were named in suits for no apparent reason, the medicolegal system must be reconstructed, and so forth. These open-ended comments were analyzed by 2 radiologists independently, and, if disagreements arose in the categorization of the comments, they met to achieve consensus.

RESULTS

Nine hundred four of 4357 ASNR members (20.7%) answered at least 1 survey question, but as many as 117 (2.7%) skipped various mandatory questions. Of these, 455 of 904 (50.3%) said that they had never been sued during their career life and 449 of 904 (49.7%) had been sued. One hundred eighty (44.9%) of the 401 radiologists who answered the question said they had been sued once, 114 (28.4%) had been sued twice, 60 (15.0%) had been sued 3 times, and 47 (11.7%) had been sued more than 3 times. If one uses 4 suits for the value of "more than 3 suits," these 401 respondents represent at least 776 claims in total (Fig 1). More than half of the 401 sued respondents had been sued 2 or more times.

Of these 904 respondents, 806–808 answered demographic questions. Of those providing sex data, 86.6% (698/806) were men and 13.4% (108/806) were women. Of the 808 who responded to the question about their age, most were between 41–60 years old (479/806; 59.4%). Use of the midpoint of the age ranges for the categories yielded a mean age of 48.1 years, a median age of 50 years, and a mode of 45 years (Fig 2). Whereas just 13.7% (30/219) of respondents less than 40 years old had been sued, the percentage of those aged 41–50 years who had been sued was 46.1% (111/241), and, for age group 51–60 years, it rose to 72.9% (172/236). Above this age, the percentage remained relatively steady at 72.5% (79/109) (Fig 3). Thirty-eight and nine-tenths percent (42/108) of female neuroradiologists had been sued compared with 50.1% (348/695) of male neuroradiologists; 35.7% (15/42) of women had been sued more than once compared with 57.4% (198/345) of men.

Among all radiologists answering survey questions, most practiced predominantly in diagnostic neuroradiology (657/771; 85.2%), with a small portion representing interventional neuroradiology (61/771; 7.9%) and "in training" (44/771; 5.7%); 49.7% (325/657) of diagnostic and 57.4% (35/61) of interventional neuroradiologists had been sued.

The outcome for each lawsuit was available for 481 claims. Many lawsuits were noted to be still pending an outcome or no information was provided. Most of the lawsuits were dropped (270/481 cases; 56.1%). Many suits were settled with a payout to the plaintiff (145/481 cases, 30.1%). Although a minority of cases

went to a trial, the verdict was mostly in favor of the defendant (46/55 cases with a verdict; 83.6%). Thus, between being dropped (270/481), settled without a payment (11/481), and a defense verdict in favor of the physician (46/481), a favorable outcome for physicians was noted in 68.0% (327/481) (Table 1).

For diagnostic neuroradiologists, the rates of dropped, settled with a payment, settled without a payment, defense verdict, and plaintiff verdict were 57.4% (221/385), 29.4% (113/385), 2.1% (8/385), 1.3% (5/385), and 9.9% (38/385), respectively. For interventionalists, these same rates were 49.0% (25/51), 37.3% (19/51), 0%, 5.9% (3/51), and 7.8% (4/51).

In terms of dollars paid to the plaintiff in settled or litigated cases, the most frequent amount paid for all the suits was less than $50,000. The percentage of suits that had a mean payout of less than $50,000 increased with increasing age [from 26% (6/23) of suits in the 41–50-year-old group to 75% (3/4) in those older than 70 years]. Regarding the most expensive payment for each lawsuit, the most frequently cited value was between $50,000 and $150,000 paid to the plaintiff (Fig 4). However, the most common average value of the suits cited was higher for interventional neuroradiologists ($600,000 to $1.2 million) than diagnostic neuroradiologists (less than $50,000).

Among causes of the alleged negligence, nondetection of a lesion was the most common (31.0% = 165/532), followed by complication of a procedure [17.3% (92/532) overall but 60% (24/40) for interventional neuroradiologists] and misinterpretation of a finding (16.0%, 85/532); 19.9% (106/532) of the respondents provided a comment regarding other reasons for being sued that were not mentioned as a survey choice. Of the comments provided, most said they were sued merely because they had their names on the radiology report (30 cases), there was a delay in treatment and/or diagnosis (20 cases), or there was a complication after a procedure (18 cases) (Table 2).

Table 3 depicts the respondents' fears and the main concerns about being sued. It shows that most neuroradiologists have mild (199/784, 25.4%) to moderately high (235/784, 30.0%) fear of being sued. Interestingly, with increasing age, the fear of being sued becomes progressively less, with 29.4% (5/17) of those older than 70 years, 22.5% (18/80) ages 61–70 years, 14.9% (34/228) ages 51–60, 10.5% (24/231) ages 41–50, and 2.8% (6/210) of physicians younger than 40 years old never or rarely thinking about being sued. Women and men had similar ratings of their fears of being sued. The percentage of individuals expressing moderate to extreme fear of being sued was higher in those in training (60.4%, 26/43) and doing neurointerventional procedures (62.5%, 35/56) than for diagnostic neuroradiologists (48.0%, 302/629).

Physicians were mainly concerned about the risk to their personal assets if they are sued (164/813, 20.2%). This was true for all age groups and either sex, except for the 41–50-year-old group, who were more concerned about losing their confidence leading to practicing defensive medicine. Women were also more concerned (25%, 22/88) than were men (15.4%, 91/592) about the impact of the malpractice on the injured plaintiff.

Respondents (81.1%, 647/798) opined that the US judicial system is somewhat to heavily weighted in favor of the plaintiff (Table 4). As the age of the respondent increased, the degree to which they thought that the system favored the plaintiff decreased; 83% (87/105) of women and 80.7% (551/683) of men thought that the judicial system favored the plaintiff. A higher percentage of diagnostic (81.3%, 522/642) than neurointerventionalists (73.3%, 44/60) think the judicial system is biased against them.

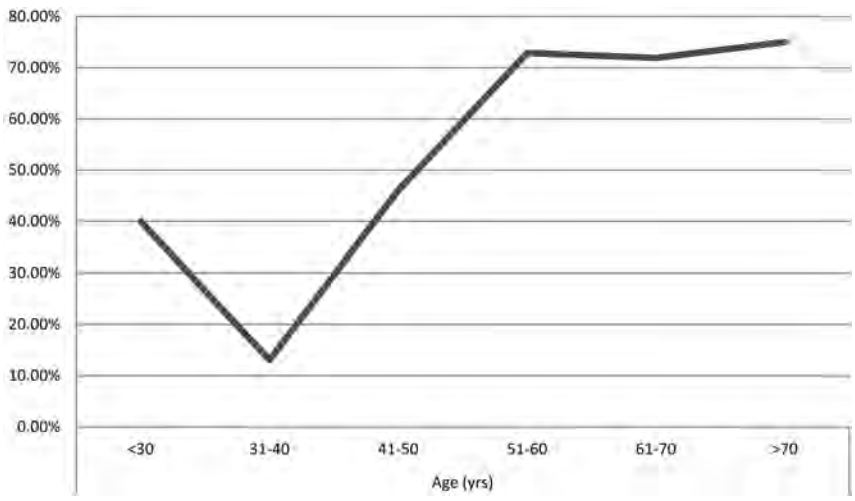

FIG 3. Percentage of the radiologists who answered, who were named in a malpractice lawsuit by age (<30 years, $n = 5$; 31–40 years, $n = 214$; 41–50 years, $n = 241$; 61–70 years, $n = 89$; >70 years, $n = 20$).

DISCUSSION

Despite the large number of studies published about malpractice in the area of radiology, the rate at which neuroradiologists have been sued in the United States has not been specifically addressed. According to a recent study that provided the rate of radiologists sued with regard to organ system,[4] neuroradiology's related organs ranked third (spinal, mus-

Table 1: Outcome for each lawsuit ($n = 481$ cases)

Lawsuit Outcome	Suit 1 *n* (%)	Suit 2 *n* (%)	Suit 3 *n* (%)	Total Count *n* (%)
It was dropped	174 (61.1)	61 (47.3)	35 (13.0)	270 (56.1)
The case was settled with a payout to the plaintiff	74 (26.0)	50 (38.8)	21 (14.5)	145 (30.1)
The case was settled without a payout to the plaintiff	4 (1.4)	3 (2.3)	4 (36.4)	11 (2.3)
The case went to trial with a plaintiff verdict	4 (1.4)	4 (3.1)	1 (11.1)	9 (1.9)
The case went to trial with a defendant verdict	29 (10.2)	11 (8.5)	6 (13.3)	46 (9.6)
Totals	285	129	67	481

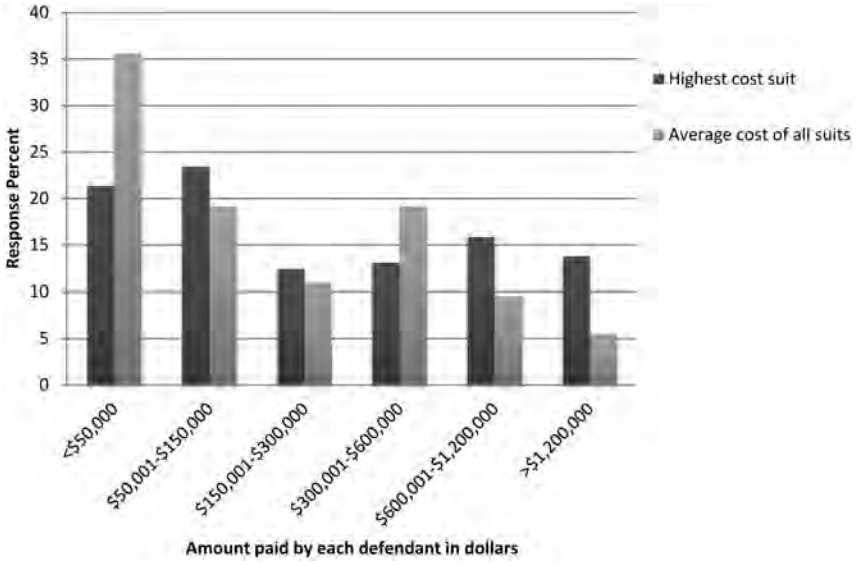

FIG 4. Highest cost and average amount paid (in dollars) by each defendant in the cases settled with a payout to the plaintiff, in percentage ($n = 149$).

Table 2: Nature of alleged negligence (number of total claims = 532)

Nature of Alleged Negligence	*n* (%)
Non-detection of a lesion	165 (31.0)
Misinterpretation of a finding (saw abnormality but called it the wrong thing)	85 (16.0)
Lack of communication of a finding	54 (10.2)
Technical error with machinery	6 (1.1)
Complication during performance of a procedure	92 (17.3)
Issue unrelated to a patient's study (fall, trip, HIPAA violation)	16 (3.0)
Informed consent issue	8 (1.5)
Other	106 (19.9)

culoskeletal) and sixth (brain) in position within the 15 organs cited.

To assess the rate of malpractice lawsuits in neuroradiology, we designed the present study through the use of the ASNR members as the study population. We hypothesized that a minority of ASNR members would be named in malpractice suits. Surprisingly, a large number of the respondents answered that they had been sued, with almost half saying that they had been named in at least 1 claim in their career (49.7%). Of those who had been sued, most (221/401 = 55.1%) answered that they had been sued twice or more.

A similar survey about malpractice stress syndrome in radiologists, performed in Italy, showed that the frequency of radiologists and radiotherapists who were named in a malpractice suit was one-third, which is less than our findings.[8] That can be explained by the cultural difference between the incidence of lawsuits in both countries, which is higher in the United States than in Italy. Because we did not perform our study on a randomized population, that information may show a bias of who answered the poll and could also explain the high prevalence of ASNR members sued at least once in their professional career.

Concerning the rates of age and sex, our data agreed with a previous study that included demographic characteristics of malpractice claims against radiologists in the United States.[6] Both studies found that the probability of being sued increased with years in practice, and men were sued more often than were women. Interventionalists had a higher rate of suits than did diagnostic neuroradiologists. This statement is in accord with previous study findings that found that procedural complications are one of the main causes of medical malpractice suits against radiologists in the United States.[4]

The study conducted in Italy showed that the relationship between age and the probability of being sued is contradictory because most of their respondents thought that older radiologists were more proficient than younger ones, though the youthful may be more up to date with advanced technology.[8] By contrast, their respondents believed that newer radiologists are inclined to make more mistakes than are their more experienced coworkers.[8] Meanwhile, it was theorized in the same study that advanced age and deteriorating cognitive skills might affect the capacity to identify radiologic findings.[8] Certainly as years in practice extend, the prospect of being sued at least once increases with increasing age as more cases are read.

Comparing our data with a recent study that determined the most frequent causes of suits in US radiologists,[4] there were similarities in the sources of suits between all of radiology and those related to the neuroradiology. We found that the main cause reported in our study was the nondetection of a finding, which is in agreement with what the previous authors described as "failure to diagnose" as the most common cause of malpractice suits in general radiology. We also found that our next most common causes of suits, complications during performance of a procedure and the lack of communication of a finding, were near the top of their results as well.[4] It is important to highlight that the previously mentioned study reviewed cases mainly related to breast imaging because mammography suits lead to most claims in the United States (followed by malpractice suits related to fractures).[4] Notwithstanding, our findings were compatible with the general radiology results.

In addition to the assessment regarding the frequency information about the malpractice lawsuits in neuroradiology, we sought to evaluate the opinions of neuroradiologists concerning malpractice litigation and the judicial system. It was assumed that the fear of being sued was unfounded. That hypothesis was discredited, and only 25.4% of the respondents had mild fear of being sued and 30.0% were occasionally concerned, whereas only 6.5% were always concerned with being sued in their career life.

It has been suggested that physicians who are most concerned with the probability of being sued are often the ones who had already been through malpractice litigation. The literature shows that some physicians who responded to a lawsuit would have had a malpractice syndrome, which includes tension, anxiety, low self-esteem, depression, frustration, and insomnia, among other

Table 3: Extent of fear and concerns about being sued

Fear of Being Sued	*n* (%)	Main Concern About Being Sued	*n* (%)
Extremely low: Never think about it	29 (3.7)	Reputation among peers	57 (7.0)
Very low: Rarely crosses my mind	60 (7.6)	The cost of malpractice insurance	38 (4.7)
Relatively low: Not very concerned	113 (14.4)	Personal assets at risk	165 (20.2)
Mild	199 (25.3)	The impact on the patient who is "injured"	117 (14.4)
Moderately high: occasionally concerned	235 (29.9)	Lose his/her own confidence and practice defensive medicine	156 (19.1)
Very high: frequently concerned	99 (12.6)	The impact on the overall health care system	43 (5.3)
Extremely high: always concerned	51 (6.5)	Being named in the national practitioners data bank	87 (10.7)
		Unfavorable publicity in the media	12 (1.5)
		Ego	20 (2.5)
		Other	120 (14.7)
Totals	786		815

Table 4: Fairness of malpractice legal process in the United States

Assessment of the Malpractice Legal Process in the United States (*n* = 798)	*n* (%)	General Comments About Malpractice Litigation in United States (*n* = 94)	*n* (%)
Heavily weighted to plaintiff	275 (34.5)	It is unfair	27 (23.7)
Somewhat weighted to the plaintiff	372 (46.6)	Negative about lawyers in general/uniformly	23 (20)
Fair	93 (11.7)	We all make mistakes	15 (13)
Somewhat weighted to the defendant	46 (5.8)	We should punish bad experts	8 (7)
Heavily weighted to the defendant	12 (1.5)	We need another system/arbitration panels	12 (11)
		The system is good	1 (1)
		Tort reform is needed	8 (7)

Note:—*n* indicates total of respondents for each question.

symptoms.[8] Thus, it would lead the physician to be more concerned about being named in another lawsuit in the future and to adopt a defensive practice. Unfortunately, we were not able to make that correlation with the use of our data base.

Our study demonstrated that most of the lawsuits in the area of neuroradiology were dropped or settled with payment to the plaintiff, but that payment was most commonly less than $50,000. The questions were not specific to know whether this represented the individual radiologist's "share" of the payment or the payment for the all members of the case. When going to trial, the verdict was in favor of the defendant in 46 of 55 (83.6%) cases (Table 1). These data are in agreement with the PIAA[3] in regard to the malpractice lawsuits of physicians in the United States. Our survey showed that most frequently, the largest compensation paid to plaintiffs in these suits was between $50,000 and $150,000. According to PIAA, this is below the associated mean legal costs per suit, when considering cases that are either settled or litigated, which lies between $200,000 and $375,000.

One apparent contradiction identified in our survey is the high rate of favorable outcomes (dropped suits, settlements without payment, court judgments in favor of defendants) and low payouts (less than $50,000 selected most commonly) yet the perception by neuroradiologists that the medicolegal system is heavily weighted toward the plaintiffs. This may be because of the perceived ease with which a plaintiff may bring a suit against a physician.

The other paradox that we noted was the relatively low rate of suits cited with a payout more than $150,000 for diagnostic neuroradiologists yet the fear among neuroradiologists that their personal assets may be at risk. Because most physicians carry malpractice insurance coverage for $1,000,000 per case and very few cases exceed that value, the risk to one's personal assets would seem highly improbable.

These paradoxes may be explained by the Prospect Theory, proposed by Kahneman and Tversky, awarded the Nobel Prize in Economics in 2002.[9] They showed, through experimental behavior, that the decisions made by human beings follow some patterns that are not necessarily based on probabilities only. Thus, people will alter their behavior on the value of the gains or losses rather than on the probability of the occurrence. Therefore, even though the probability of being sued is low and even though the likelihood of one's personal assets being encumbered is low, because of the negative impact and high "value" of these potential outcomes, physicians alter their behavior to avoid that potentiality. On the basis of the Prospect Theory, people "overvalue" the risks. This may explain why healthy people still buy health insurance and why outstanding physicians, even if it was optional, would still buy malpractice insurance. It also explains why physicians will change practice patterns even though the risk of malpractice suits may be quite small.[9,10]

Limitations

The major limitation of our study is the potential for selection bias, with only 904 of 4357 neuroradiologists answering survey questions. We believe this was caused in part by a high rate of surveys submitted for participation by the ASNR this year on top of the customer service and patient satisfaction and job satisfaction surveys that have become standard fare in medicine. Physicians may have survey fatigue. Some questions were answered by far fewer respondents. This limits the reliability of the calculated response rates to each specific question. For example, the overall rate of malpractice suits might be overrepresented if ASNR members who had been sued were more likely to spend the time filling out the survey to share their experience, or the suit rate could be underestimated if physicians were embarrassed about having been named in a suit, justly or unjustly, and either did not answer truthfully or did not respond to the survey at all because of unhappy associations with the topic. Selection bias is a limitation of

all survey-based investigations, and the similarity between our results and previously published rates suggests that this source of bias did not play a major role in our results.

The study also did not control for the respondents' ages across sex and practice patterns (diagnostic versus interventional), nor did it assess whether the respondent was in the private, academic, or government sector. In addition, the survey did not inquire as to the home country of the respondent. The ASNR now has a significant number of non-American members among which the incidence of malpractice suits is lower than in the United States. The ASNR also has a small percentage of nonclinical research scientists, unlikely to be named in a suit, who may have diluted the malpractice sample.

We also had a plethora of open-ended comments for cases in which the respondents did not select the proffered choices in the survey. These responses could not be counted by the rates shown in the tables and graphics, but they were analyzed by the authors and added to the results and discussion, on the basis of our interpretation of the comments. The fact that so many people added comments to many of the questions may be related to 1) the emotionally charged nature of the topic, 2) many respondents' answers did not fit into the choices provided, and 3) simple options in a multiple choice format cannot tell the full story of what physicians experienced in their medicolegal environment.

We were not able to detail the major economic concerns of respondents with respect to litigation expenses. The impact of days away from work, practice expenses litigating cases, malpractice insurance limits, and increased premiums for malpractice insurance were issues not addressed in this survey.

CONCLUSIONS

Almost half of the ASNR respondents have been sued at least once, and, of those named in a suit, more than half have been named in more than 1 suit. These suits tend to be about nondetection of lesions, complications of procedures, misinterpretation of a finding, or perceived random naming of a physician whose name was in the medical record. Although the outcomes overall reported are heavily weighted toward physicians by virtue of many dropped suits, small payouts, defense verdicts, or favorable settlements, neuroradiologists have a high level of anxiety about being sued that affects many physicians on a daily basis. Many fear that their personal assets may be at risk despite the favorable outcomes listed above and the extremely low risk of personal exposure. This may be because, although the probability of such an event is low, the value placed on loss of assets is very high, as explained by the Prospect Theory. Therefore, behaviors to reduce the likelihood of that improbable event may still be used. Overall, the neuroradiologists responding believe that the medicolegal system is strongly to somewhat heavily biased in favor of plaintiffs.

ACKNOWLEDGMENTS

We would like to express our appreciation to Angelo Artemakis for his help in constructing our survey questionnaire and for collating the results of this research study.

Disclosures: Kelly Yousem—*OTHER RELATIONSHIPS:* While I do not believe this influenced the report, it should be noted I am a medical malpractice attorney. David Yousem—*UNRELATED: Expert Testimony:* Medicolegal consultations; *Payment for Lectures (including service on speakers' bureaus):* ACR Education Center, Comments: Compensation received both directly and by institution; *Royalties:* Elsevier, for 3 books; *Payment for Development of Educational Presentations:* ACR Education Center, Comments: Compensation received both directly and by institution.

REFERENCES

1. Jena AB, Chandra A, Lakdawalla D, et al. **Outcomes of medical malpractice litigation against US physicians.** *Arch Intern Med* 2012;172:892–94
2. Jena AB, Seabury S, Lakdawalla D, et al. **Malpractice risk according to physician specialty.** *N Engl J Med* 2011;365:629–36
3. *Claim Trend Analysis: A Comprehensive Analysis of Medical Malpractice Data Reported to the PIAA Data Sharing Project.* Physician Insurers Association of America, Rockville, Maryland. 2004
4. Whang JS, Baker SR, Patel R, et al. **The causes of medical malpractice suits against radiologists in the United States.** *Radiology* 2013;266:548–44
5. Thomson NB 3rd, Patel M. **Radiology liability update: review of claims, trends, high-risk conditions and practices, and tort reform alternatives.** *J Am Coll Radiol* 2012;9:729–33
6. Baker SR, Whang JS, Luk L, et al. **The demography of medical malpractice suits against radiologists.** *Radiology* 2013;266:539–47
7. Studdert DM, Mello MM, Gawande AA, et al. **Claims, errors, and compensation payments in medical malpractice litigation.** *N Engl J Med* 2006;354:2024–33
8. Fileni A, Magnavita N, Mammi F, et al. **Malpractice stress syndrome in radiologists and radiotherapists: perceived causes and consequences.** *Radiol Med (Torino)* 2007;112:1069–84
9. Kahneman D, Tversky A. **Prospect theory: an analysis of decision under risk.** *Econometrica* 1979;47:263
10. Lawthers AG, Laird NM, Lipsitz S, et al. **Physicians' perceptions of the risk of being sued.** *J Health Polit Policy Law* 1992;17:463–82

Radiation Dose Reduction in Paranasal Sinus CT Using Model-Based Iterative Reconstruction

J.M. Hoxworth, D. Lal, G.P. Fletcher, A.C. Patel, M. He, R.G. Paden, and A.K. Hara

ABSTRACT

BACKGROUND AND PURPOSE: CT performed with Veo model-based iterative reconstruction has shown the potential for radiation-dose reduction. This study sought to determine whether Veo could reduce noise and improve the image quality of low-dose sinus CT.

MATERIALS AND METHODS: Twenty patients consented to participate and underwent low- and standard-dose sinus CT on the same day. Standard-dose CT was created with filtered back-projection (120 kV[peak], 210 mA, 0.4-second rotation, and 0.531 pitch). For low-dose CT, mA was decreased to 20 (the remaining parameters were unchanged), and images were generated with filtered back-projection and Veo. Standard- and low-dose datasets were reconstructed by using bone and soft-tissue algorithms, while the low-dose Veo reconstruction only had a standard kernel. Two blinded neuroradiologists independently evaluated the image quality of multiple osseous and soft-tissue craniofacial structures. Image noise was measured by using multiple regions of interest.

RESULTS: Eight women and 12 men (mean age, 63.3 years) participated. Volume CT dose indices were 2.9 mGy (low dose) and 31.6 mGy (standard dose), and mean dose-length products were 37.4 mGy-cm (low dose) and 406.1 mGy-cm (standard dose). Of all the imaging series, low-dose Veo demonstrated the least noise ($P < .001$). Compared with filtered back-projection low-dose CT using soft-tissue and bone algorithms, Veo had the best soft-tissue image quality but the poorest bone image quality ($P < .001$).

CONCLUSIONS: Veo significantly reduces noise in low-dose sinus CT. Although this reduction improves soft-tissue evaluation, thin bone becomes less distinct.

ABBREVIATIONS: BONE FBP LD = bone algorithm, filtered back-projection, low dose; BONE FBP SD = bone algorithm, filtered back-projection, standard dose; IRIS = iterative reconstruction in image space; SAFIRE = sinogram-affirmed iterative reconstruction; SOFT FBP LD = soft-tissue algorithm, filtered back-projection, low dose; SOFT FBP SD = soft-tissue algorithm, filtered back-projection, standard dose; VEO LD = Veo model-based iterative reconstruction, low dose

A number of radiation dose-reduction strategies have been successfully used for paranasal sinus CT. Because radiation is unavoidably transmitted to the lens of the eye, orbital bismuth shielding has been used to reduce lens radiation exposure with minimal impact on image quality.[1,2] Greater attention has been directed toward adjusting CT parameters, most commonly through the reduction of milliampere-second (mAs) (tube current time product), to allow reduced radiation exposure while maintaining acceptable image quality.[3-13] Recently, high-pitch dual source multidetector CT systems have shown promise of even greater dose reduction.[14,15] Nevertheless, because of progressively decreasing signal-to-noise, a threshold for tube output is invariably reached, below which imaging becomes unacceptable.

With the large computational capacities now available on normal workstations, iterative reconstruction techniques have emerged in CT as a viable alternative to the standard algorithm of filtered back-projection. Through increased complexity with more precise modeling of the acquisition process and the incorporation of various physical models, image quality can be maintained even at progressively lower radiation doses.[16] Indeed, one such technique known as iterative reconstruction in image space (IRIS; Siemens, Erlangen, Germany) allows significant radiation-dose reduction in sinus CT without compromising the image quality.[17] More recently, sinogram-affirmed iterative reconstruction (SAFIRE; Siemens) demonstrated effective noise reduction in sinus CT at the expense of some image quality degradation.[18] Unfortunately, because of the proprietary and vendor-specific nature of the iterative reconstruction techniques, results cannot be directly extrapolated across different CT platforms. As a result,

Received July 9, 2013; accepted after revision August 11.

From the Departments of Radiology (J.M.H., G.P.F., A.C.P., R.G.P, A.K.H.) and Otolaryngology (D.L.), Mayo Clinic, Phoenix, Arizona; and School of Computing, Informatics, and Decision Systems Engineering, (M.H.), Arizona State University, Tempe, Arizona.

Please address correspondence to Joseph M. Hoxworth, MD, Department of Radiology, Mayo Clinic, 5777 E Mayo Blvd, Phoenix, AZ 85054; e-mail: hoxworth.joseph@mayo.edu

http://dx.doi.org/10.3174/ajnr.A3749

Table 1: Image-noise measurement[a]

	Pons (n = 20)	Globe (n = 20)	Masseter (n = 20)	Maxillary Sinus (n = 20)	Total (n = 80)
SOFT FBP LD	74.9 (10.60)[b]	55.6 (8.79)[b]	52.6 (8.79)[b]	45.3 (13.16)[b]	57.1 (15.06)[b]
BONE FBP LD	278.8 (36.73)[b]	173.0 (19.66)[b]	175.3 (27.03)[b]	105.5 (15.64)[b]	183.1 (67.38)[b]
VEO LD	18.9 (2.98)	12.4 (1.37)	14.3 (2.16)	12.3 (2.11)	14.5 (3.49)
SOFT FBP SD	24.7 (5.14)[b]	19.5 (3.06)[b]	19.1 (3.35)[b]	17.5 (2.48)[b]	20.2 (4.48)[b]
BONE FBP SD	97.4 (14.47)[b]	66.9 (7.78)[b]	66.3 (8.96)[b]	50.1 (6.42)[b]	70.2 (19.73)[b]

[a] Values are expressed as mean (SD) of image noise measured in Hounsfield units.
[b] Statistically significant difference ($P < .001$) in paired comparison with VEO LD.

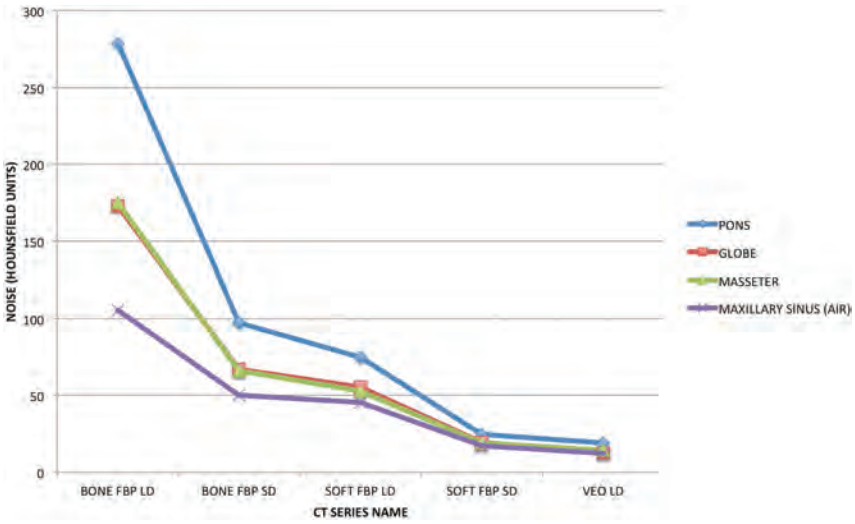

FIG 1. Graphic representation of mean image noise for the pons, globe, masseter, and air within the maxillary sinus for each of the tested CT series: soft-tissue algorithm, filtered back-projection, low dose; bone algorithm, filtered back-projection, low dose; Veo model-based iterative reconstruction, low dose; soft-tissue algorithm, filtered back-projection, standard dose; and bone algorithm, filtered back-projection, standard dose.

the objective of this study was to compare low-radiation-dose sinus CT processed with Veo model-based iterative reconstruction (GE Healthcare, Milwaukee, Wisconsin) with standard and low-dose sinus CT generated with filtered back-projection through the evaluation of image noise and diagnostic image quality in 20 patients.

MATERIALS AND METHODS

This Health Insurance Portability and Accountability Act–compliant study was approved by the Mayo Clinic Institutional Review board, and all patients provided written informed consent. Twenty patients 18 years of age or older who were previously scheduled for a clinically indicated sinus CT were invited to participate. Individuals with a history of previous sinonasal surgery or a known maxillofacial neoplasm were specifically excluded.

Noncontrast paranasal sinus CT was performed on all study participants by using a 64-detector row multidetector CT scanner (Discovery CT750 HD, GE Healthcare) with the patient in the supine position, extending from the hard palate superiorly to include the frontal sinuses. Standard-dose sinus CT was performed by using 120 kV(peak), 210 mA, 0.4-second rotation time, 0.531 pitch, and 0.625-mm section collimation; images were generated by using filtered back-projection. Next, a low-dose sinus CT was acquired by using the same parameters except that the mA were reduced to 20. Low-dose images were generated by using both filtered back-projection and Veo model-based iterative reconstruction. Low- and standard-dose datasets from filtered back-projection were reconstructed by using bone (GE kernel, bone) and soft-tissue (GE kernel, standard) algorithms, while low-dose CT was also reconstructed with Veo (note that Veo only offered a single standard kernel). As a result, 5 imaging series were created for each patient: 1) soft-tissue algorithm, filtered back-projection, low dose [SOFT FBP LD], 2) bone algorithm, filtered back-projection, low dose [BONE FBP LD], 3) Veo model-based iterative reconstruction, low dose [VEO LD], 4) soft-tissue algorithm, filtered back-projection, standard dose [SOFT FBP SD], and 5) bone algorithm, filtered back-projection, standard dose [BONE FBP SD].

Each image set was transferred to an AW Workstation (Version 4.2; GE Healthcare) in an anonymized fashion, where it was reformatted at 1-mm increments in the axial and coronal planes. Using a round region of interest with a diameter of 1 cm, a single blinded observer measured the mean attenuation and SD in Hounsfield units of the central pons, right globe (vitreous), right masseter muscle, and air within the center of the right maxillary sinus in the axial plane. The SD was used to represent image noise. For the evaluation of diagnostic image quality, 2 board-certified neuroradiologists independently reviewed the imaging series blinded to all patient identifiers and CT parameters. Specifically, they graded image quality for the nasal septum, middle turbinate, lamina papyracea, cribriform plate, optic nerve, inferior rectus muscle, globe (eye), and brain on a scale from 1 (unacceptable noise, nondiagnostic) to 5 (excellent image quality, best diagnostic value). For each of the 5 series, the reviewers were limited to 2 preset window level and width settings for emphasis on bone (window level, 800 HU; window width, 3500 HU) and soft tissue (window level, 40 HU; window width, 400 HU). Last, an experienced endoscopic sinus surgeon was asked to qualitatively assess the low-dose sinus CT scans without and with VEO LD to determine whether there was sufficient anatomic detail for preoperative planning, and this assessment was recorded in a binary fashion as yes or no.

Statistical analyses were performed by using SAS, Version 9.2 (SAS Institute, Cary, North Carolina). For descriptive analysis, the image-quality score and noise level of different imaging series by structure were presented as mean and SD; the differences among structures were assessed by the Kruskal-Wallis test. Separate mixed models were developed for image quality and image noise. For the image noise mixed model, 5 imaging series and 4 structures were included as fixed effects, and the interaction term

Table 2: Image-quality assessment[a]

	Brain (*n* = 40)	Globe (*n* = 40)	Inferior Rectus Muscle (*n* = 40)	Optic Nerve (*n* = 40)	Cribriform Plate (*n* = 40)	Lamina Papyracea (*n* = 40)	Middle Turbinate (*n* = 40)	Nasal Septum (*n* = 40)	Total (*n* = 320)
SOFT FBP LD	1.5 (0.51)[b]	1.6 (0.55)[b]	1.9 (0.43)[b]	1.8 (0.52)[b]	3.3 (0.47)	3.1 (0.38)[b]	3.3 (0.44)	3.1 (0.38)	2.4 (0.90)[b]
BONE FBP LD	1.0 (0.00)[b]	1.0 (0.16)[b]	1.0 (0.16)[b]	1.1 (0.27)[b]	3.7 (0.62)[b]	3.7 (0.56)[b]	3.4 (0.58)	3.6 (0.59)[b]	2.3 (1.35)[b]
VEO LD	2.8 (0.41)	2.9 (0.35)	3.1 (0.32)	3.1 (0.32)	3.2 (0.48)	2.7 (0.53)	3.2 (0.53)	3.0 (0.45)	3.0 (0.46)
SOFT FBP SD	3.4 (0.55)[b]	4.0 (0.42)[b]	4.0 (0.58)[b]	4.1 (0.40)[b]	4.0 (0.51)[b]	3.9 (0.47)[b]	4.0 (0.55)[b]	3.9 (0.56)[b]	3.9 (0.54)[b]
BONE FBP SD	2.0 (0.28)[b]	2.5 (0.51)[b]	3.0 (0.53)	3.1 (0.45)	4.7 (0.47)[b]	4.9 (0.33)[b]	4.7 (0.46)[b]	4.9 (0.36)[b]	3.7 (1.19)[b]

[a] Values are expressed as mean (SD). Image-quality scale ranges from 1 (unacceptable noise, nondiagnostic) to 5 (excellent image quality, best diagnostic value).
[b] Statistically significant difference ($P < .001$) in paired comparison with VEO LD.

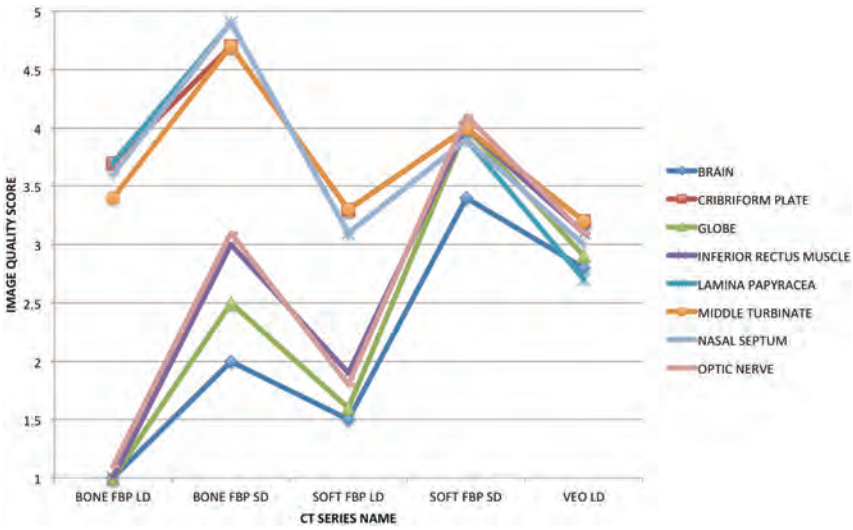

FIG 2. Graphic representation of mean image quality for the brain, cribriform plate, globe, inferior rectus muscle, lamina papyracea, middle turbinate, nasal septum, and optic nerve for each of the tested CT series: soft-tissue algorithm, filtered back-projection, low dose; bone algorithm, filtered back-projection, low dose; Veo model-based iterative reconstruction, low dose; soft-tissue algorithm, filtered back-projection, standard dose; and bone algorithm, filtered back-projection, standard dose.

for the "structure*imaging series" was significant and was included in the model. For the image quality mixed model, 5 imaging series, 2 readers, and 8 structures were included as fixed effects. The interaction term for the "structure*image" series was significant and was included in the model, while nonsignificant interaction terms such as "reader*structure" and "reader*image series" were removed from the final model. Random effects allowed covariance to vary due to subject. Post hoc paired *t* tests were conducted to compare image quality scores and noise levels between each possible imaging series pair overall and for each subgroup of structures. *P* values $< .05$ were considered statistically significant.

RESULTS

Twenty patients were recruited, and the study cohort consisted of 8 women and 12 men with an average age of 63.3 ± 14.9 years. Volume CT dose index means for LD and SD were 2.9 ± 0 mGy and 31.6 ± 0 mGy, respectively, while the corresponding mean dose-length products were 37.4 ± 2.5 mGy-cm and 406.1 ± 25.9 mGy-cm.

The results of noise quantification are summarized in Table 1 and graphically represented in Fig 1. As expected, the use of a lower radiation dose and application of a bone algorithm resulted in an increase in image noise in instances in which images were generated by using filtered back-projection. However, despite a markedly reduced radiation dose, VEO LD demonstrated significantly less image noise compared with all other imaging series ($P < .001$).

Image quality assessment is reported in Table 2 and illustrated in Fig 2. Compared with bone-containing structures (cribriform plate, lamina papyracea, middle turbinate, nasal septum), the soft-tissue structures (brain, optic nerve, globe, inferior rectus muscle) were suboptimally evaluated secondary to increased noise in the filtered back-projection series reconstructed with a bone algorithm and/or obtained with a low radiation dose (ie, BONE FBP SD, BONE FBP LD, SOFT FBP LD). The image quality for the soft-tissue and bone-containing structures converged in the SOFT FBP SD series with improved soft-tissue detail at the expense of mildly reduced image quality in the evaluation of bone-containing structures. A similar pattern of image quality convergence for bone and soft-tissue structures was observed in the VEO LD group, albeit at a significantly lower image quality compared with SOFT FBP SD, despite lower image noise. Representative examples from the 5 imaging series are presented in soft-tissue (Fig 3) and bone algorithms (Fig 4).

If patients were exclusively imaged by using the low-radiation-dose technique for sinus CT, the most relevant question is whether the noise reduction of VEO LD improves image quality. In an aggregate analysis of all structures, image quality was significantly improved in VEO LD compared with BONE FBP LD and SOFT FBP LD. However, in analyzing the results by structure, this benefit was derived from VEO LD outperforming BONE FBP LD and SOFT FBP LD in the evaluation of soft-tissue structures. In contrast, VEO LD generally had poorer image quality for the bone-containing structures (Table 2).

Irrespective of the inclusion of VEO LD, none of the low-dose sinus CT scans were graded as adequate for preoperative planning.

DISCUSSION

In contrast to reducing radiation exposure by modifying dose-related technical parameters within the confines of a filtered back-projection algorithm, new CT systems offer the potential for fur-

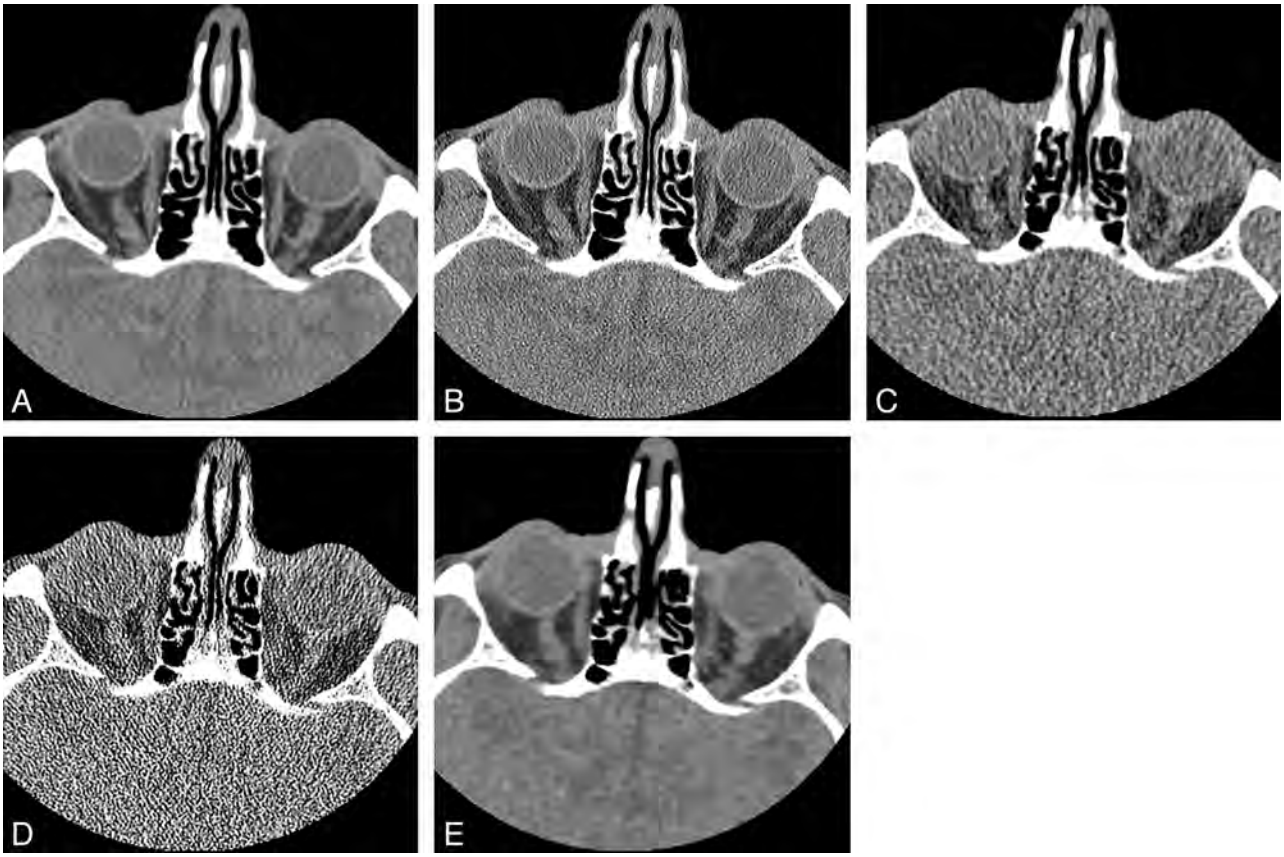

FIG 3. Axial noncontrast sinus CT (window level, 40 HU; window width, 400 HU) through the level of the orbits for the following imaging series: soft-tissue algorithm, filtered back-projection, standard dose (*A*); bone algorithm, filtered back-projection, standard dose (*B*); soft-tissue algorithm, filtered back-projection, low dose (*C*); bone algorithm, filtered back-projection, low dose (*D*); and Veo model-based iterative reconstruction, low dose (*E*). The decreased image noise secondary to Veo allows improved visualization of orbital and intracranial soft-tissue structures relative to the other low-dose protocols but not to the level of the standard-dose sinus CT.

ther dose reduction while preserving image quality through the use of iterative reconstruction.[16] Whether using statistical or model-based methods, these techniques proceed through an iterative loop in which a forward-projected image is compared with measured raw data and a correction factor is applied to the volumetric estimate, which is then back-projected. This iteration continues to converge toward a better solution until a predefined criterion for stopping is met. Unfortunately, the commercially available iterative reconstruction techniques from the major CT vendors must largely be viewed as a "black box," because radiation dose-reduction strategies allow a competitive advantage in the marketplace. Consequently, the performance of iterative reconstruction algorithms must be independently tested and validated in different body regions.

The use of Veo in low-dose sinus CT performed with a mean dose-length product of 37.4 mGy-cm significantly reduced image noise in comparison with filtered back-projection, and this reduction translated into improved image quality in the evaluation of craniofacial soft-tissue structures. Unfortunately, the smoothing effect of the Veo model-based iterative reconstruction impaired evaluation of structures containing thin bone at a low dose. Despite suboptimal performance for bone resolution, Veo may still prove to be a useful adjunct reconstruction technique for low-dose sinus CT. In evaluating the impact of radiation-dose reduction on multidetector sinus CT image quality, Brem et al[4] found that soft tissues tolerate much less dose reduction compared with bone. Effective mAs could only be decreased to 134 to maintain diagnostic image quality for soft-tissue components, but diagnostic quality was maintained to an effective mAs of 67 if only osseous structures were considered. As a result, Veo may allow greater dose reduction for sinus CT by helping to salvage soft-tissue image quality.

To date, only 2 other studies have evaluated iterative reconstruction for potential radiation-dose reduction in the performance of sinus CT, both of which were developed by Siemens. Bulla et al[17] incorporated IRIS into a low-dose sinus CT protocol that compared their standard-dose CT (60 mAs, 120 kV) with image datasets acquired at 48 mAs, 36 mAs, and 24 mAs, through the evaluation of subjective image quality. Compared with filtered back-projection at 60 mAs, IRIS was found to improve image quality at 48 mAs, with no statistically significant decrement in image quality at the lower doses of 36 and 24 mAs. Notably, the authors still could reconstruct images in a bone kernel with IRIS, which is not an option with Veo tested in the current study. Because quantitative noise measurements were not made in the study of Bulla et al, it is not possible to draw any comparison of image quality and the degree of noise reduction. Schulz et al[18] tested sinogram-affirmed iterative reconstruction by using a phantom head model at different radiation doses (100–120 kV, 25–100 mAs). They evaluated image quality and measured noise,

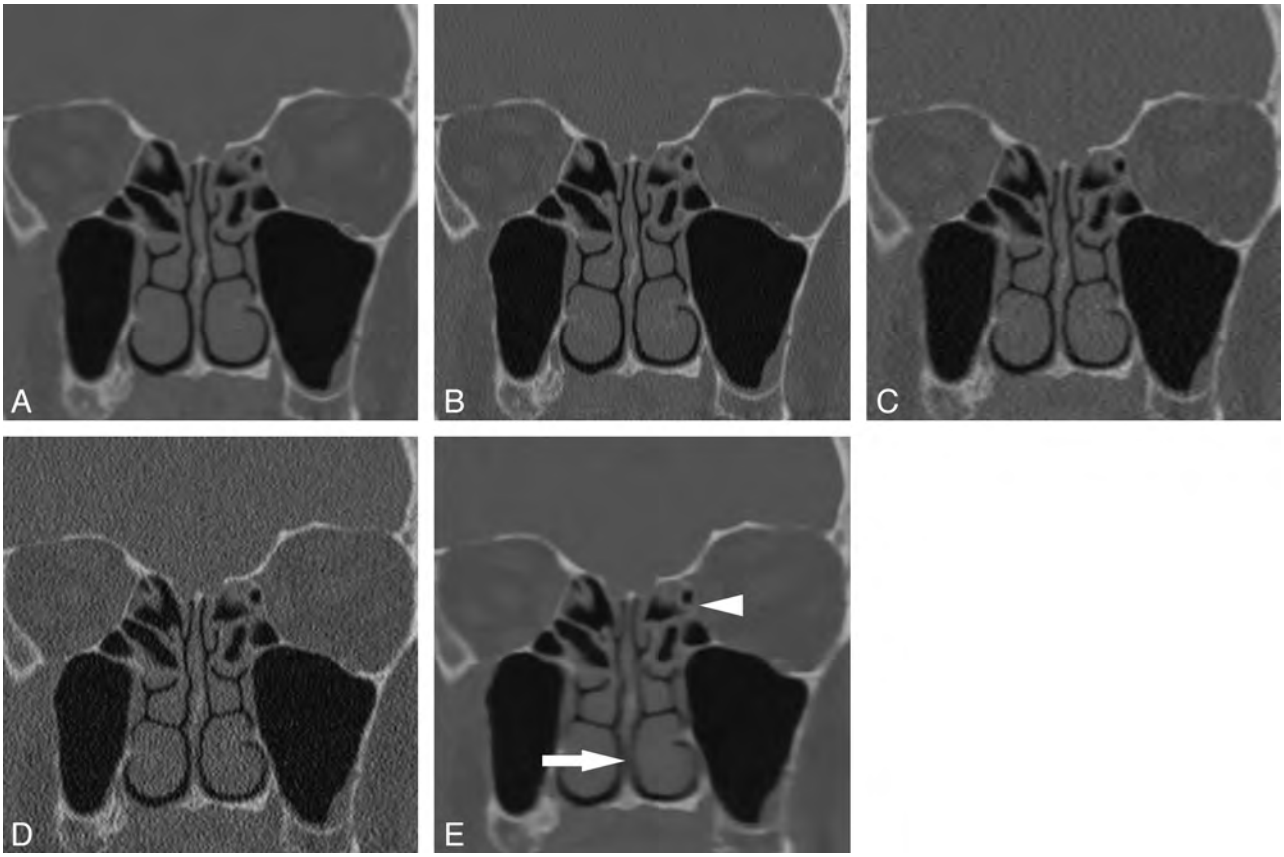

FIG 4. Coronal noncontrast sinus CT (window level, 800 HU; window width, 3500 HU) through the level of the maxillary sinuses for the following imaging series: soft-tissue algorithm, filtered back-projection, standard dose (*A*); bone algorithm, filtered back-projection, standard dose (*B*); soft-tissue algorithm, filtered back-projection, low dose (*C*); bone algorithm, filtered back-projection, low dose (*D*); and Veo model-based iterative reconstruction, low dose (*E*). The noise reduction achieved with Veo results in loss of edge enhancement, making thin bones such as the nasal septum (*white arrow*) and left lamina papyracea (*white arrowhead*) difficult to see.

and comparison was made with both filtered back-projection and IRIS. The SAFIRE software permits 5 different levels of noise suppression (I-V), and these were tested by using both hard and soft kernels. SAFIRE V behaved closest to Veo in that it achieved the greatest degree of noise reduction (up to 85%) but also received the lowest scores for image quality. The readers in that study preferred the highest tube current images rendered with filtered back-projection, even though the lowest setting of SAFIRE I also had less noise. The authors concluded that it may not be possible to compensate for insufficient photons through greater levels of iterative reconstruction because the latter may soften bone edges and cortical structures to an unacceptable level.

Wide variation exists in the radiation dose of sinus CT protocols at different institutions, largely because of the individual preferences of both radiologists and surgeons.[19-21] Because no universally accepted standard exists for image quality, Hojreh et al[6] proposed using image noise measured in a phantom as an indicator of appropriate sinus CT radiation dose. It was suggested that low-dose sinus CT be characterized by a pixel noise of 70–90 HU, normal-dose sinus CT have a pixel noise of 50–70 HU, and high-dose sinus CT produce a pixel noise of <50 HU. Although the objective and reproducible nature of this technique is appealing, the noise measurements must be referenced to an edge-enhancing reconstruction algorithm with filtered back-projection because the current study of Veo and previous work with SAFIRE reveal that lower noise cannot be equated to improved image quality for sinus CT by using iterative reconstruction.[18]

Previous studies have tested the impact of reducing the radiation dose to as low as a volume CT dose index of 1.1 mGy on computer-assisted surgical navigation and have found no technical limitation on the surface registration algorithm or navigation accuracy.[20,22] Instead, the level of dose reduction was dictated by the different needs for image quality of the individual surgeon, which are heavily driven by bone anatomic detail. In the current study, the inclusion of Veo did not convert any of the low-dose sinus CT scans from unacceptable to acceptable for preoperative planning. Compared with the bone algorithm reconstruction of a filtered back-projection low-dose CT, an iterative reconstruction technique would need to improve the bone detail of sinonasal landmarks to accomplish this conversion.

Limitations of this study include the small sample size, though the statistical power was sufficient to demonstrate key differences between Veo and filtered back-projection. Only a single low-dose sinus CT was performed in each patient, without the evaluation of additional tube current settings. The very low mAs used in this study was selected in an attempt to better elicit potential differences in image quality and noise between filtered back-projection and Veo. Although Veo improved the image quality of soft-tissue structures, the image quality was still suboptimal at this very low dose. A higher radiation dose, perhaps at 50% of the standard

dose, would provide better image quality but would still significantly reduce the dose. However, it is likely that Veo would perform similarly at an intermediate radiation dose by reducing image noise without improving bone detail. Ultimately, radiation dose reduction in sinus CT must balance noise reduction and bone resolution. Future refinement of Veo for use in low-dose sinus CT should include the option of a high-resolution bone algorithm. This is currently not available with Veo but is included with some other commercially available adaptive statistical and model-based iterative reconstruction packages. Given that the VEO LD series had significantly lower image noise than all filtered back-projection imaging series regardless of radiation dose, it may be possible to sacrifice some noise reduction at the expense of improved edge enhancement.

CONCLUSIONS

Veo model-based iterative reconstruction significantly reduces image noise in low-dose sinus CT. As tested, this reduction caused some obscuration of fine detail of thin bone, and future versions of Veo should ideally include the option of a high-resolution bone algorithm. Veo improved visualization of soft-tissue structures, though not to a diagnostic level because of the very low radiation dose used in this study. Given that low-dose sinus CT performed with standard filtered back-projection still permits visualization of high contrast bone at the expense of soft-tissue image quality, the incorporation of Veo into a low-dose sinus imaging protocol may be useful for improving soft-tissue evaluation.

Disclosures: Joseph M. Hoxworth, Devyani Lal, Geoffrey P. Fletcher, Ameet C. Patel, Amy K. Hara, and Robert G. Paden—*RELATED*: *Other*: GE Healthcare,* *Comments*: Through a research agreement with GE Healthcare, the Veo model-based iterative reconstruction system was installed on a single Discovery CT750 HD scanner and the cost was offset to $0 through the performance of multiple research studies to assist with product development. GE Healthcare did not participate in any aspect of subject recruitment, data collection, data analysis, or manuscript preparation. Amy K. Hara—*UNRELATED*: *Royalties*: GE Healthcare,* *Comments*: for CT colonography software. *Money paid to the institution.

REFERENCES

1. Perisinakis K, Raissaki M, Theocharopoulos N, et al. **Reduction of eye lens radiation dose by orbital bismuth shielding in pediatric patients undergoing CT of the head: a Monte Carlo study.** *Med Phys* 2005;32:1024–30
2. Hein E, Rogalla P, Klingebiel R, et al. **Low-dose CT of the paranasal sinuses with eye lens protection: effect on image quality and radiation dose.** *Eur Radiol* 2002;12:1693–96
3. Abul-Kasim K, Strombeck A, Sahlstrand-Johnson P. **Low-dose computed tomography of the paranasal sinuses: radiation doses and reliability analysis.** *Am J Otolaryngol* 2011;32:47–51
4. Brem MH, Zamani AA, Riva R, et al. **Multidetector CT of the paranasal sinus: potential for radiation dose reduction.** *Radiology* 2007;243:847–52
5. Hagtvedt T, Aalokken TM, Notthellen J, et al. **A new low-dose CT examination compared with standard-dose CT in the diagnosis of acute sinusitis.** *Eur Radiol* 2003;13:976–80
6. Hojreh A, Czerny C, Kainberger F. **Dose classification scheme for computed tomography of the paranasal sinuses.** *Eur J Radiol* 2005;56:31–37
7. Kearney SE, Jones P, Meakin K, et al. **CT scanning of the paranasal sinuses–the effect of reducing mAs.** *Br J Radiol* 1997;70:1071–74
8. Lam S, Bux S, Kumar G, et al. **A comparison between low-dose and standard-dose non-contrasted multidetector CT scanning of the paranasal sinuses.** *Biomed Imaging Interv J* 2009;5:e13
9. Mulkens TH, Broers C, Fieuws S, et al. **Comparison of effective doses for low-dose MDCT and radiographic examination of sinuses in children.** *AJR Am J Roentgenol* 2005;184:1611–18
10. Sohaib SA, Peppercorn PD, Horrocks JA, et al. **The effect of decreasing mAs on image quality and patient dose in sinus CT.** *Br J Radiol* 2001;74:157–61
11. Tack D, Widelec J, De Maertelaer V, et al. **Comparison between low-dose and standard-dose multidetector CT in patients with suspected chronic sinusitis.** *AJR Am J Roentgenol* 2003;181:939–44
12. Duvoisin B, Landry M, Chapuis L, et al. **Low-dose CT and inflammatory disease of the paranasal sinuses.** *Neuroradiology* 1991;33:403–06
13. Marmolya G, Wiesen EJ, Yagan R, et al. **Paranasal sinuses: low-dose CT.** *Radiology* 1991;181:689–91
14. Schulz B, Potente S, Zangos S, et al. **Ultra-low dose dual-source high-pitch computed tomography of the paranasal sinus: diagnostic sensitivity and radiation dose.** *Acta Radiol* 2012;53:435–40
15. Schell B, Bauer RW, Lehnert T, et al. **Low-dose computed tomography of the paranasal sinus and facial skull using a high-pitch dual-source system–first clinical results.** *Eur Radiol* 2011;21:107–12
16. Beister M, Kolditz D, Kalender WA. **Iterative reconstruction methods in X-ray CT.** *Phys Med* 2012;28:94–108
17. Bulla S, Blanke P, Hassepass F, et al. **Reducing the radiation dose for low-dose CT of the paranasal sinuses using iterative reconstruction: feasibility and image quality.** *Eur J Radiol* 2012;81:2246–50
18. Schulz B, Beeres M, Bodelle B, et al. **Performance of iterative image reconstruction in CT of the paranasal sinuses: a phantom study.** *AJNR Am J Neuroradiol* 2013;34:1072–76
19. Koller CJ, Eatough JP, Bettridge A. **Variations in radiation dose between the same model of multislice CT scanner at different hospitals.** *Br J Radiol* 2003;76:798–802
20. Nauer CB, Eichenberger A, Dubach P, et al. **CT radiation dose for computer-assisted endoscopic sinus surgery: dose survey and determination of dose-reduction limits.** *AJNR Am J Neuroradiol* 2009;30:617–22
21. Stewart AE, Stalp JT, Futerman C, et al. **Variability of radiation exposure with in-office sinus computed tomography examinations.** *Int Forum Allergy Rhinol* 2011;1:313–18
22. Dubach P, Eichenberger A, Caversaccio M. **Radiation dose reduction in computer assisted navigation for functional endoscopic sinus surgery: cadaver head experiments and clinical implementation.** *Rhinology* 2010;48:339–43

Neurointerventions in Children: Radiation Exposure and Its Import

D.B. Orbach, C. Stamoulis, K.J. Strauss, J. Manchester, E.R. Smith, R.M. Scott, and N. Lin

ABSTRACT

BACKGROUND AND PURPOSE: Neurointerventions in children have dramatically improved the clinical outlook for patients with previously intractable cerebrovascular conditions, such as vein of Galen malformations and complex arteriovenous fistulas. However, these complex and sometimes lengthy procedures are performed under fluoroscopic guidance and thus unavoidably expose vulnerable pediatric patients to the effects of ionizing radiation. Recent epidemiologic evidence from a national registry of children who underwent CT scans suggests a higher-than-expected incidence of secondary tumors. We sought to calculate the predicted risk of secondary tumors in a large cohort of pediatric neurointerventional patients.

MATERIALS AND METHODS: We reviewed our cohort of pediatric neurointerventions, tabulated radiation dose delivered to the skin, and calculated the range of likely brain-absorbed doses by use of previously developed mathematical models. The predicted risk of secondary tumor development as a function of brain-absorbed dose in this cohort was then generated by use of the head CT registry findings.

RESULTS: Maximal skin dose and brain-absorbed doses in our cohort were substantially lower than have been previously described. However, we found 1) a statistically significant correlation between radiation dose and age at procedure, as well as number and type of procedures, and 2) a substantial increase in lifetime predicted risk of tumor above baseline in the cohort of young children who undergo neurointerventions.

CONCLUSIONS: Although neurointerventional procedures have dramatically improved the prognosis of children facing serious cerebrovascular conditions, the predicted risk of secondary tumors, particularly in the youngest patients and those undergoing multiple procedures, is sobering.

ABBREVIATIONS: MSD = maximal skin dose; RAD-IR = Radiation Doses in Interventional Radiology Procedures

Children undergoing fluoroscopy are exposed to ionizing radiation. Commonly used measures of tumor risk from this exposure are based on decades of observations in survivors from the regions surrounding Hiroshima and Nagasaki, as summarized in BEIR-VII.[1] However, a recent study[2] analyzing a national registry in the United Kingdom of >178,000 children who underwent CT scans reported a higher incidence of brain tumors and leukemia than would be expected on the basis of the BEIR data. For children undergoing neurointerventions, these results suggest that previous predictions may underestimate the actual rate of radiation-related tumor development.

We retrospectively analyzed our data base of radiation doses delivered to a cohort of children who underwent 355 cerebral angiograms and neurointerventions at a single high-volume pediatric cerebrovascular center. We converted the reported maximal skin dose (MSD) to an estimate of the range of brain-absorbed doses by use of previously derived age-based conversion factors.[3,4] On the basis of recent data from the UK CT study, we then estimated the predicted risk of brain tumors in this cohort, related to the procedures that the children underwent.

MATERIALS AND METHODS

Approval was obtained from the Institutional Review Board at Boston Children's Hospital for retrospective review of our neuro-

Received July 16, 2013; accepted after revision August 11.

From the Division of Neurointerventional and Interventional Radiology (D.B.O., J.M.), Departments of Radiology (C.S., J.M.), Neurology (C.S.), and Neurosurgery (E.R.S., R.M.S.), Children's Hospital Boston, Boston, Massachusetts; Harvard Medical School (D.B.O., C.S., E.R.S., R.M.S.), Boston, Massachusetts; Department of Radiology (K.J.S.), Cincinnati Children's Hospital Medical Center, Cincinnati, Ohio; and Departments of Radiology and Neurosurgery (N.L.), Brigham and Women's Hospital, Boston, Massachusetts.

Please address correspondence to Darren B. Orbach, MD, PhD, Neurointerventional Radiology, Children's Hospital Boston, 300 Longwood Ave, Boston, MA 02115; e-mail: darren.orbach@childrens.harvard.edu

http://dx.doi.org/10.3174/ajnr.A3758

Table 1: Distribution of number of procedures per patient and number of procedures per age bracket

No. of Procedures per Patient	No. of Patients	Age Cohort	No. of Cases
1	125	<1 year	27
2	42	1–2 years	37
3	20	3–7 years	80
4	5	8–13 years	101
5	4	13–17 years	91
6	2	18–20 years	19
7	2		
9	1		
11	1		

Note:—Total number of procedures = 355; total number of unique patients = 202. Most patients underwent a single procedure, the vast majority underwent 3 or fewer, and a very small number underwent 5 or more. The mean age of the cohort was 9.7 years.

interventional data base of children younger than 21 years of age who underwent cerebral angiography and/or transarterial neuroembolization between September 2006 and June 2012; percutaneous procedures, such as sclerotherapy, were not included. The included procedures were performed by a single operator (D.B.O.) on 1 of 2 Axiom Artis biplane flat-panel fluoroscopic units (Siemens, Erlangen, Germany).

The radiation physicist at Boston Children's Hospital worked with a Siemens design engineer in 2005 to create examination-set protocols tailored to patient size (age) and body part, with fluoroscopy and DSA. This resulted in skin dose rate reductions up to 30% relative to standard configurations, depending on the type of examination and thickness of the patient. A dose data base was installed: Patient Exposure Management Network (PEMNET, Clinical Microsystems, Arlington, Virginia). PEMNET automatically captures the uncalibrated cumulative air kerma data at the end of each procedure and additionally captures C-arm angles of multiple projections used during a procedure, needed to estimate peak skin dose from cumulative air kerma. Before the implementation of PEMNET, radiation data were not consistently stored. During the time range, radiation dose information was available for 355 cases. Skin radiation dose can be calculated as follows:

$$\text{Skin dose} \sim AK \times CF \times ISL \times BS, \text{ where}$$

AK = displayed cumulative air kerma; CF = calibration factor for displayed air kerma ~1; ISL = inverse square law correction for entrance skin plane versus interventional reference point at which air kerma meter is calibrated, ~0.8; and BS = backscatter factor, ~1.4–1.45 for skull, depending on patient age.[5]

CF is 1 ± 5%, with appropriate annual measurement and adjustment by a medical physicist. Because the entrance plane of the patient's head positioned at isocenter is 5–9 cm from the interventional reference point, depending on patient size, ISL ranges from 0.75–0.85.

We tabulated the number of procedures undergone by each patient and the distribution of procedures by patient age (Table 1). The descriptive statistics for maximal skin radiation dose (in each plane and in total) and fluoroscopy time as a function of procedure type and as a function of the date of the study are summarized in Table 2. MSD values in the frontal and lateral imaging planes were corrected for age by multiplying by the following scaling factors: for age ≤5 years, 1.12 for frontal plane, 1.06 for lateral plane, and for age >5 years, 1.24 for frontal plane, 1.16 for lateral plane. There were 175 cases between September 2006 and June 2010 and 180 cases between July 2010 and June 2012 (Table 2). Mean MSD and fluoroscopy time stratified by patient age are summarized in Table 3. Cumulative MSD statistics, stratified by number of procedures, are summarized in Table 4.

Using the conversion factors generated by mathematical modeling and the Radiation Doses in Interventional Radiology Procedures (RAD-IR) study data (in particular, Table 6 of Thierry-Chef et al.),[3,4] we converted the maximal skin dose to estimates of absorbed brain dose. Absorbed brain dose varies widely (by a factor of 4–8), depending on whether tight collimation and varying positions for the imaging system were used. Following the lead of the RAD-IR investigators, we accordingly report the brain-absorbed doses under the 2 conditions of tight and wide collimation separately (Tables 4 and 5).

We extrapolated the increased risk of brain tumors above the expected baseline, hereafter referred to as predicted risk, attributable to the absorbed brain dose in our cohort, by use of a linear no-threshold model and the values for excess relative risk per mGy exposure reported by the UK CT study investigators.[2]

Statistical Analysis

All analyses were performed at the patient level.

Regression. To assess the correlation between type of procedure(s) and cumulative radiation dose and the effect of patient age on that correlation, we developed an ordinary regression model with (cumulative) radiation dose as the outcome and procedure type, age, and number of procedures as the explanatory (independent) variables. For patients with multiple procedures, age at the last procedure was included. Procedure type was modeled as a categoric variable. For patients with 1 procedure, type = 1 for angiogram and type = 2 otherwise (implying embolization). For patients with multiple procedures, type = 1 if all procedures were angiograms and type = 2 otherwise. All statistical analysis was performed with the use of Matlab (MathWorks, Natick, Massachusetts) and R (www.r-project.org).

Estimation of Predicted Risk. In the absence of a clinical outcome (cancer) for this cohort, we estimated predicted risk for tumors based on the data in the UK study.[2] In that study, a linear relationship between relative risk and absorbed brain dose radiation was estimated, with slope of the fitted line 0.023 and intercept 1. Note that in our study, predicted risk was estimated on the basis of cumulative radiation doses, that is, at the patient level rather than at the case level. For patients who underwent only 1 procedure, case and patient radiation levels are identical. However, for patients who underwent multiple procedures, we were interested in cancer risk after cumulative exposure.

RESULTS

The 355 procedures in our data base with available radiation data were performed in 202 unique patients. Whereas the mean number of procedures per patient was 1.8, the underlying distribution was skewed, with most patients undergoing 1 procedure, 83% undergoing 2 or fewer procedures, and <3% undergoing 6 or

Table 2: Maximal skin dose of radiation (in mGy) and fluoroscopy time per procedure (in minutes), as a function of case type and date

Case Type	Dates	Mean Radiation Dose, Frontal Plane, mGy	SD Radiation Dose Frontal Plane, mGy	Mean Radiation Dose, Lateral Plane, mGy	SD Radiation Dose, Lateral Plane, mGy	Mean Radiation Dose, Total, mGy	SD Radiation Dose, Total, mGy	Fluoroscopy Time, Frontal Plane, min	Fluoroscopy Time, Lateral Plane, min
All cases	9/06–6/10	319	289.6	201.2	279.2	520.2	498.9	26.7	22.2
	7/10–6/12	215.6	211.5	112.4	186.9	328	350.1	17.9	12.6
Diagnostic angiograms	All	164.9	161.1	74.6	69.5	239.4	217.5	11.2	6.2
	9/06–6/10	185.7	212.7	88	86.8	273.7	284.9	10.9	6.4
	7/10–6/12	150	109.1	65	52.2	215	148.6	11.4	6.1
Embolizations	All	449.4	306	298.4	345	747.7	540.6	42.4	37.4
	9/06–6/10	482.2	290.7	340.5	364.9	822.7	542.6	48.8	44.5
	7/10–6/12	430.5	303.1	267.2	343.9	697.7	531.8	34.5	28.8

Note:—SD indicates standard deviation (inter-case variability).

Table 3: Maximal skin dose of radiation and the fluoroscopy time per procedure as stratified by patient age

Age, y	Radiation Dose, Frontal Plane, mGy	SD Radiation Dose, Frontal Plane, mGy	Radiation Dose, Lateral Plane, mGy	SD Radiation Dose, Lateral Plane, mGy	Radiation Dose, Total, mGy	SD Radiation Dose, Total, mGy	Fluoroscopy Time, Frontal Plane, min	Fluoroscopy Time, Lateral Plane, min
<1	186.7	168.3	186.2	198.5	372.9	361.2	40.5	37.7
1–2	296.3	350.3	147.2	109.3	443.5	434.4	26.1	22.5
3–7	236	241.3	147.2	189.3	383.3	398.9	24.0	17.6
8–12	244.5	233.4	110.8	131	355.3	341.9	19.1	14.6
13–17	329.	292	192.2	318.7	521.3	529.7	17.8	13.1
18–21	328.5	260.2	255.1	553.6	583.5	729.3	19.5	12.6
All ages	266.6	257.9	156.2	240.7	422.7	440	21.9	17.0

Note:—SD indicates standard deviation (inter-procedure variability).

Table 4: Maximal cumulative skin radiation dose stratified by number of procedures

No. of Procedures	No. of Patients	Mean Age, y	SD Age, y	Mean Radiation Dose, Total, mGy	SD Radiation Dose, Total, mGy	Mean Radiation Dose, Embolizations, mGy	SD Radiation Dose, Embolizations, mGy	Mean Radiation Dose, Angiograms, mGy	SD Radiation Dose, Angiograms, mGy
1	125	10.2	5.97	318.2	409.9	643.4	730.8	232.8	202.4
2	42	10.1	5.5	1330.2	784.8	598.7	538.9	514.6	318.8
3	20	9.5	5.7	1131.5	862.1	2677.8	1017.9	535.6	269
4	5	8.3	4.9	1207.4	392.9	1736.1	–	–	–
5	4	11.4	5.8	2204.8	791.4	1814.1	–	–	–
6	2	10.3	12.1	582.3	168.3	–	–	–	–
7	2	5.1	1.5	4749.0	1737.6	–	–	–	–
9	1	6.3	–	8625.7	–	–	–	–	–
11	1	15.05	–	5563.3	–	–	–	–	–

Note:—For patients with multiple procedures, the age at the last procedure is reported, and embolizations or angiogram doses are reported only for those patients with all procedures of the same type.
SD indicates standard deviation (inter-patient variability).

more procedures. The age range of our cohort was 4 days to 20 years, with a mean age of 9.7 years, and standard deviation (SD) of 5.8 years. The distribution of cases among patients and the breakdown of number of cases for each age cohort are presented in Table 1. Although some pathologies such as brain AVM, pial fistulas, aneurysms, dural fistulas, and extracranial AVM or AVF were found in all age groups, particular conditions occurred exclusively in subsets of the cohort, such as vein of Galen malformation in the <1-year and 1- to 2-year age groups.

At the doses received by our cohort, deterministic effects of radiation were nearly entirely absent, with a single case of transient hair loss (possibly related to scalp positioning) and a single case of transient scalp erythema.

As expected, the radiation dose associated with diagnostic cerebral angiography was significantly lower than that associated with embolizations, with the mean dose of the former <50% the mean dose of the latter (Table 2). When we split the cohort by date of procedure, with approximately equivalent numbers of procedures from September 2006 to June 2010 and from July 2010 to June 2012, there was a statistically significant decrease in mean total dose across all cases in the later cohort as compared with the earlier ($P < .0001$). When angiography and embolization procedures were examined separately, there was a statistically significant decrease in mean total dose for angiograms after July 2010 ($P = .04$) but a statistically nonsignificant decrease in dose for embolizations ($P = .09$). A nonparametric Wilcoxon rank sum test was used to test statistical significance.

On the basis of the regression analysis, procedure type and number of procedures were statistically significant predictors of radiation dose, and the effect of age at procedure was also statistically significant. The results of this analysis and model parameters are summarized in Table 7. The model was overall statistically significant ($P < .0001$), with a coefficient of determination $R^2 = 0.67$, which suggests an adequate fit to the data.

Table 5: Large (uncollimated), uniform field condition: brain absorbed dose of radiation and relative risk of developing brain tumors as a function of patient age

Age, y	MSD, Both Planes, mGy	SD, Both Planes, mGy	Brain Dose–to–MSD Conversion Factor	Brain-Absorbed Dose, mGy	Projected Risk of Developing Brain Tumors (×Baseline)
<1	372.9	361.2	0.48	164.4	4.8
1–2	443.5	434.4	0.38	160.0	4.7
3–7	383.3	398.9	0.30	93.3	3.2
8–12	355.3	341.9	0.25	74.1	2.7
13–17	521.3	529.7	0.24	103.9	3.4
18–21	583.5	729.3	0.23	106.3	3.4
All ages	422.7	440	0.25	90.1	3.1

Note:—Projected risk is calculated as (excess relative risk = 0.023/mGy)+1.
SD indicates standard deviation (inter-patient variability).

Table 6: Small (collimated), non-uniform field condition: brain-absorbed dose of radiation and excess relative risk of developing brain tumors as a function of patient age

Age, y	MSD, Both Planes, mGy	SD, Both Planes, mGy	Brain Dose–to–MSD Conversion Factor	Brain-Absorbed Dose, mGy	Projected Risk of Developing Brain Tumors (×Baseline)
<1	372.9	361.2	0.14	47.9	2.1
1–2	443.5	434.4	0.11	46.3	2.1
3–7	383.3	398.9	0.09	28.0	1.6
8–12	355.3	341.9	0.05	14.8	1.3
13–17	521.3	529.7	0.03	13.0	1.3
18–21	583.5	729.3	0.03	13.9	1.3
All ages	422.7	440	0.08	18.0	1.4

Note:—Projected risk is calculated as (excess relative risk = 0.023/mGy)+1.
SD indicates standard deviation (inter-patient variability).

Table 7: Linear regression model parameters including regression coefficients, their confidence intervals, *P* values, and Wald statistic values

Parameter	Coefficient (*b*)	Confidence Interval	Standard Error	*P* Value	Wald Statistic
Intercept	−1081.1	[−1403.4, −0.7587]	163.5	<.0001	43.7
Age at procedure	18.6	[3.1, 34.0]	7.8	.018	5.6
Procedure type	454.9	[261.7, 648.2]	98.0	<.0001	21.5
No procedures	555.5	[487.7, 623.3]	34.4	<.0001	260.9

Because of the differences in conversion factors for MSD to brain-absorbed dose as a function of age, the brain-absorbed dose showed greater differences across age groups (varying by a factor of >2.2) than did the MSD (Table 5). The highest mean brain-absorbed dose was in the <1-year-old subgroup, followed by the 1- to 2-year-old subgroup. In the case of tight collimation (Table 5), brain-absorbed doses dropped markedly in every age group, but the differences across age groups increased further (varying by a factor of 3.7).

Estimated predicted risk, as a function of age at last exposure, is shown in Fig 1 (for small and large radiation field conditions; top and bottom, respectively), along with the fitted regression line. There was no clear correlation between projected relative risk and age at last exposure for large uniform field conditions. There was a statistically significant relationship between age at last exposure and projected relative risk under small nonuniform field conditions (on the basis of a linear regression model for risk as a function of age, $b = -0.08$, $P = .001$, Wald statistic = 10.8). There was no statistically significant relationship between projected relative risk and age under large uniform field conditions ($b = -0.087$, $P = .33$). The distribution of predicted risk for our cohort is shown in the histogram in Fig 2. Although for most patients (~80%) predicted risk was in the range of 1–2 times baseline for small field conditions and 1–5 times baseline for large field conditions, for ~20% of patients, predicted risk was substantially higher: 3–15 times baseline for small field conditions and 9–57 times baseline for large field conditions.

Finally, we also examined predicted risk as a function of age, separately, only for the subset of patients with 1 procedure, under both field conditions (Fig 3). There was a statistically significant relationship between age at exposure and predicted risk for small nonuniform field conditions ($b = 0.012$, $P = .004$, Wald statistic = 8.58). There was no statistically significant relationship between age at exposure and projected risk for large uniform field conditions ($b = 0.018$, $P = .11$).

DISCUSSION

Several recent studies have documented the overall procedural safety of cerebral angiography in children at high-volume centers.[6,7] However, both diagnostic cerebral angiography and transcatheter cerebral interventions are performed under fluoroscopic visualization, and as such, unavoidably expose patients to ionizing radiation. Children are more vulnerable to deleterious effects from radiation than are adults, with increasing vulnerability at younger ages. Neurointerventions, with their inherent risk, are complex and lengthy and are associated with prolonged periods of fluoroscopic exposure to patients. Thus, outside of patients undergoing radiation therapy procedures, children who undergo neurointerventions are potentially at greatest risk of having iatrogenic adverse effects from ionizing radiation.

Although we focus here on the stochastic effects of incident radiation, we did find an extremely low incidence of deterministic adverse events relatable to radiation, with only 2 deterministic adverse events, both transient, in the total cohort.

The most detailed and careful prior study of pediatric radiation doses from neurointerventions (in 49 children) was performed[3,4] as a subset of the larger RAD-IR study.[8-10] The investigators described the maximal skin dose delivered, calculated probable absorbed brain doses, and predicted the expected increase in incidence of brain tumors as a result of this exposure. The MSD and brain-absorbed doses that we report here are substantially lower than those reported for the 49 children who underwent neurointerventions in RAD-IR, probably a reflection both of technological improvements in the time since that earlier study, and of our fluoroscopy parameters, highly optimized for procedures in children.[3,4]

After splitting the cohort into 2 approximately equal subsets by date of procedure, we found that the radiation dose in the more recent subset was markedly lower for the set of procedures per-

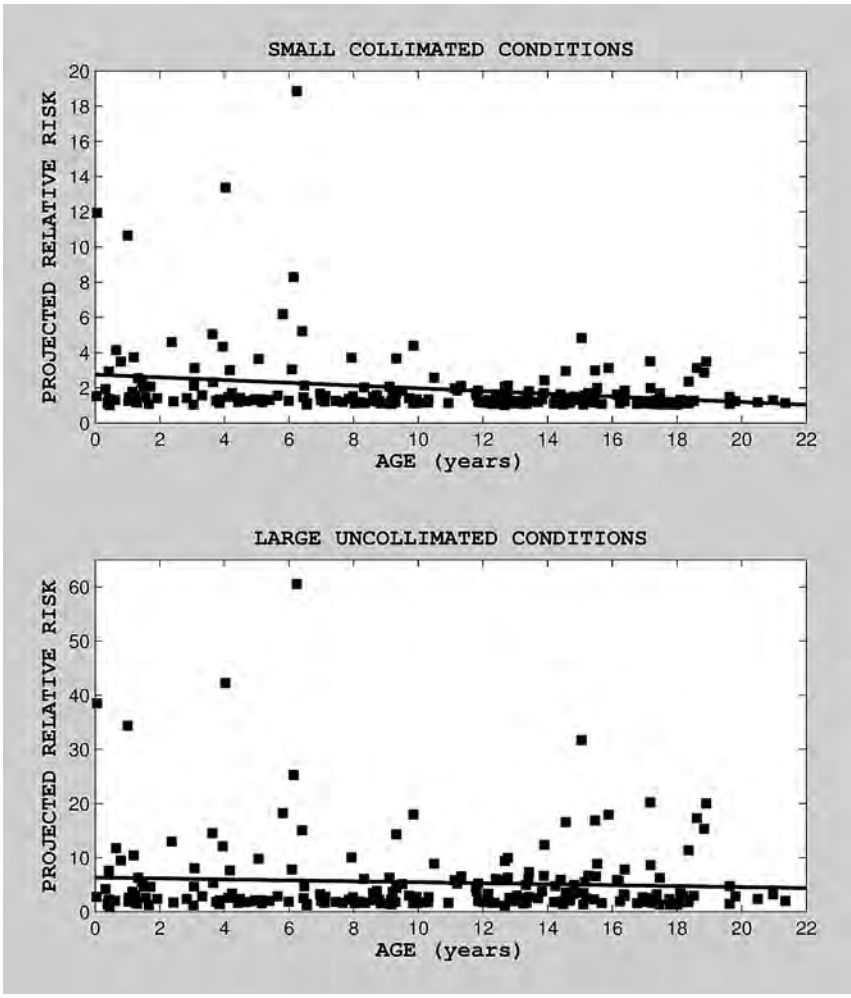

FIG 1. Projected relative risk as a function of age at (last) exposure, under nonuniform (top) and uniform (bottom) field conditions. Median predicted (projected) risk was 1.34 (mean = 1.96, SD = 2; range, 1.0–18.85) under small nonuniform field conditions and 2.72 (mean = 5.45, SD = 7.36; range, 1.02–60.5) under large uniform field conditions.

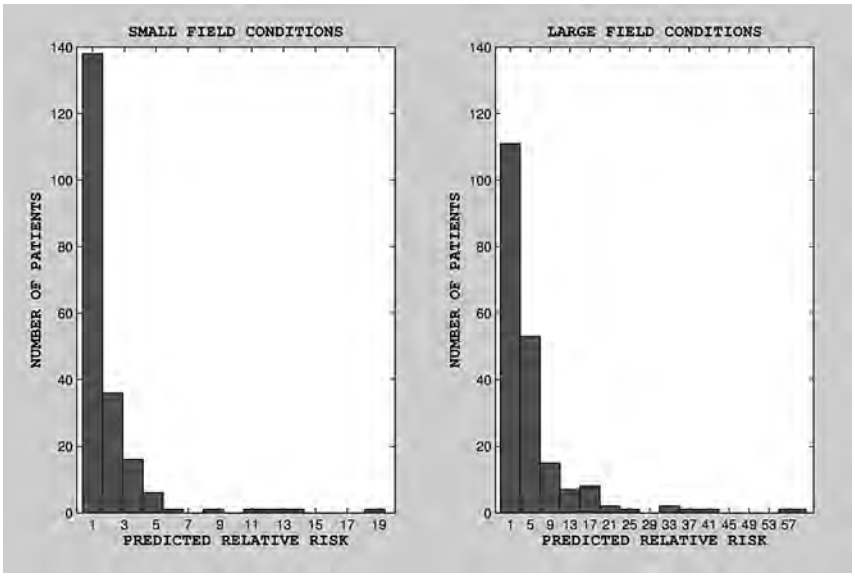

FIG 2. Distribution of projected relative risk under small (left) and large (right) field conditions.

formed in the last 2 years. There was a statistically significant decrease in total radiation dose for these procedures, as well as specifically for angiograms in the last 2 years, but no statistically significant decrease in embolization doses. Because there were no changes in hardware or software during this time range that could explain this diminution in radiation dose, this change over time may relate to progressively increased attention paid to radiation dose by the primary operator (D.B.O.), with ongoing time at a dedicated pediatric facility. Most embolization procedures are already tightly focused, with angiography performed in the target vessels before and after the embolization and with relatively little flexibility for performing fewer angiographic runs. Diagnostic angiography, on the other hand, allows the pediatric practitioner significant latitude in terms of limiting what vessels are injected, how many views are obtained, and so forth.

Comparing the <1-year cohort with the 13- to 17-year cohort in Table 3 shows that whereas fluoroscopy time was markedly higher in infants, MSD was much lower; this effect is largely caused by the small body size of the youngest patients. Additionally, fewer DSA runs tend to be performed in the infants, as road-mapping and other image-store techniques are maximally utilized.

It is likely that some of the differences in MSD with stratification by age (Table 3) result from particularities of the pathology seen at various ages. For example, the 3- to 7-year and 8- to 12-year cohorts, which had the lowest MSD, are notable for a preponderance of Moyamoya cases, in nearly all of which the procedure performed was diagnostic angiography, either before surgery or at 1-year postsynangiosis follow-up, rather than embolizations.

In shifting the focus from MSD to brain-absorbed dose (Tables 4 and 5), the highest doses were seen in the youngest patients (<1 year), followed by the next-youngest cohort (1–2 years). Thus biologic factors, such as low skull thickness and attenuation in the youngest patients, resulting in brain absorption of a very high fraction of the radiation incident on the skin, are the key operative determinants of radiation dose delivered to the brain.

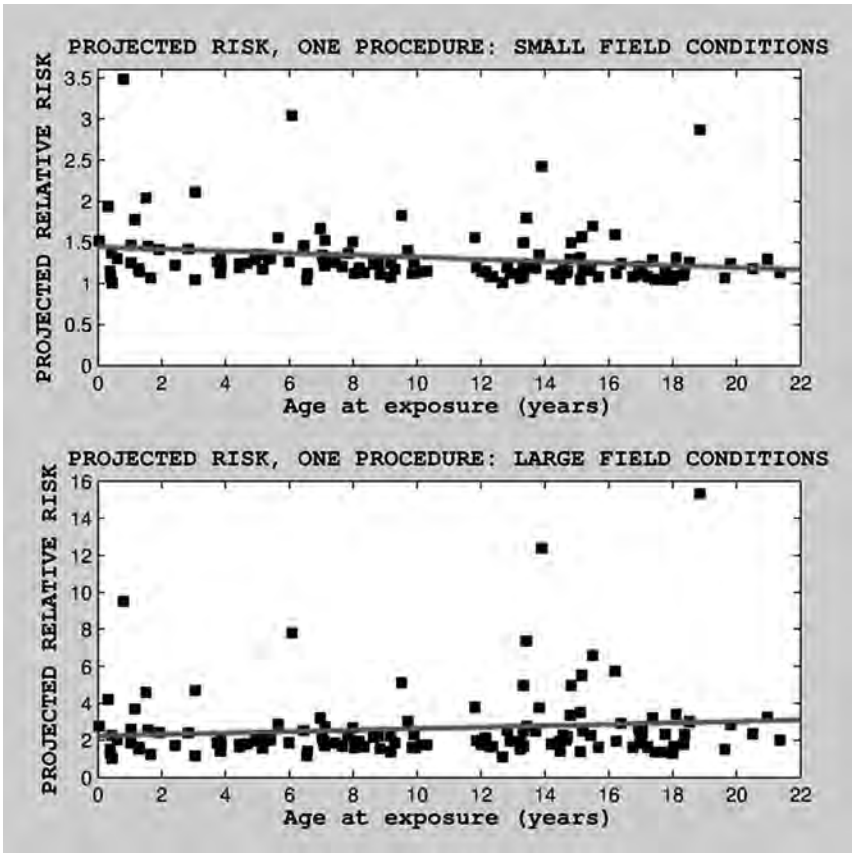

FIG 3. Projected relative risk as a function of age at (last) exposure, under nonuniform (top) and uniform (bottom) field conditions, for subjects with only 1 procedure and thus no cumulative radiation exposure caused by multiple procedures. Median projected risk was 1.2 (mean = 1.31, SD = 0.37; range, 1.0–3.48) for small nonuniform field condition and 2.03 (mean = 2.6, SD = 2; range, 1.02–15.32) for large uniform field conditions.

The degree of increase in lifetime relative risk of development of brain tumor reported here is higher than has been previously reported. Some prior reports of only minimally increased risk[11] were marred by the conversion of measured radiation dose to effective dose, a unit designed for assessing risk from whole-body radiation dose on the part of radiation workers or victims of environmental disasters. However, even methodologically sound prior reports, such as the RAD-IR study, found lower predicted risk than we report here (a median of 1.3–2.7 times baseline risk, depending on collimation), with their estimate of predicted risk, even for the large collimation condition, being 1.4 times baseline.[3] This discrepancy with our results is explained by the reliance on the part of prior investigators on the BEIR data for translation from radiation dose to tumor risk. However, the BEIR data reflect the condition of whole-body environmental exposure. In contrast, the projected risk we report here is based instead on the UK CT study[2]; in CT, patients undergo focal deposition of radiation to the target organ, as occurs as well during neurointerventions. The UK investigators reported a mean value of excess relative risk of 0.023/mGy, independent of age, in accord with a linear model of risk dependence on dose.

The BEIR investigators found increased risk of solid tumors of many types in various organs after whole-body exposure in atom bomb survivors. In focusing on the induction of brain tumors after head CT, the UK investigators found a positive (and independent) association between the scans and 2 categories of tumors: gliomas and meningiomas/schwannomas.[2] In terms of timeframe, the induction of solid tumors can span decades; the age range of patients included in the UK CT study was 6–45 years, and the maximal follow-up period was 23 years.

Several operator-dependent variables can dramatically reduce radiation dose, as seen by contrasting the wide-field uncollimated condition with the tightly collimated condition (ie, Tables 4 and 5). However, although, like the RAD-IR investigators, we do not have specific data on FOV size in our cohort, the ability to tightly collimate the FOV in neurointerventions is offset by the need to see critical surrounding vascular anatomy. Thus, most intracranial interventions probably approximate the wide-field condition. As mentioned, our system has been highly optimized to minimize radiation dose, with attention paid to technical factors, such as use of pulsed fluoroscopy, aggressive filtration, automated dose rate control, minimization of the air gap between patient and detector, maximal use of image-hold technologies (such as the overlay mode and care position for the Siemens system), and the use of age- and sex-specific lead shields, from the outset of this study.

One important limitation of our study is the relatively small sample size. In particular, the number of patients who underwent repeated neurointerventional procedures is small. Although we have projected risk values for this subset, they may not necessarily be representative of the population as a whole. Although our center is a high-volume tertiary pediatric cerebrovascular referral site, most conditions leading to neurointerventional procedures in children are rare, and a multi-institutional, national, or international data collection effort will be needed to materially increase the size of the cohort.

The predicted stochastic risk associated with neurointerventions in children undergoing multiple procedures we report here is sobering. Although most patients in our cohort underwent only 1 procedure, nearly one-third of the cohort underwent 2–3 procedures, and a smaller fraction underwent many more (Table 1). Although there may be some benefit to divided doses as compared with larger, single-procedure doses though mechanisms such as adaptive response,[12] this has yet to be explicitly demonstrated, and thus it may be assumed that the predicted risk across procedures is approximately additive.

CONCLUSIONS

All children undergoing neurointerventions face conditions that are life-threatening or that pose a risk of severe neurologic impairment, and thus the risk-benefit ratio impels treatment. However,

in cases in which there are few data to buttress multiple repeated interventions, such as staged embolization of highly complex brain AVMs with the goal of reducing flow rather than achieving definitive cure, the lifetime risks of radiation dose in children must be added to the procedural risks of vascular injury. Particularly in the youngest patients, it behooves the practitioner to weigh the risk of radiation dosage in comparing treatment alternatives and in determining the number of acceptable rounds of neurointerventional procedures. These data support the importance of developing alternative, nonfluoroscopic approaches for treating children, such as MR-based procedures.

Disclosures: Catherine Stamoulis—*UNRELATED: Consultancy:* Beth Israel Deaconess Medical Center, Comments: Entirely unrelated study on sleep.

REFERENCES

1. National Research Council (US) Committee to Assess Health Risks from Exposure to Low Levels of Ionizing Radiation. *Health Risks From Exposure to Low Levels of Ionizing Radiation: BEIR VII Phase 2.* Washington, DC: National Academies Press; 2006
2. Pearce MS, Salotti JA, Little MP, et al. **Radiation exposure from CT scans in childhood and subsequent risk of leukaemia and brain tumours: a retrospective cohort study.** *Lancet* 2012;380:499–505
3. Thierry-Chef I, Simon SL, Land CE, et al. **Radiation dose to the brain and subsequent risk of developing brain tumors in pediatric patients undergoing interventional neuroradiology procedures.** *Radiat Res* 2008;170:553–65
4. Thierry-Chef I, Simon SL, Miller DL. **Radiation dose and cancer risk among pediatric patients undergoing interventional neuroradiology procedures.** *Pediatr Radiol* 2006;36(Suppl 2):159–62
5. Petoussi-Henss N, Zankl M, Drexler G, et al. **Calculation of backscatter factors for diagnostic radiology using Monte Carlo methods.** *Phys Med Biol* 1998;43:2237–50
6. Wolfe TJ, Hussain SI, Lynch JR, et al. **Pediatric cerebral angiography: analysis of utilization and findings.** *Pediatr Neurol* 2009;40:98–101
7. Burger IM, Murphy KJ, Jordan LC, et al. **Safety of cerebral digital subtraction angiography in children: complication rate analysis in 241 consecutive diagnostic angiograms.** *Stroke* 2006;37:2535–39
8. Balter S, Schueler BA, Miller DL, et al. **Radiation doses in interventional radiology procedures: the RAD-IR study, part III: dosimetric performance of the interventional fluoroscopy units.** *J Vasc Interv Radiol* 2004;15:919–26
9. Miller DL, Balter S, Cole PE, et al. **Radiation doses in interventional radiology procedures: the RAD-IR study, part II: skin dose.** *J Vasc Interv Radiol* 2003;14:977–90
10. Miller DL, Balter S, Cole PE, et al. **Radiation doses in interventional radiology procedures: the RAD-IR study: part I: overall measures of dose.** *J Vasc Interv Radiol* 2003;14:711–27
11. Raelson CA, Kanal KM, Vavilala MS, et al. **Radiation dose and excess risk of cancer in children undergoing neuroangiography.** *AJR Am J Roentgenol* 2009;193:1621–28
12. Vares G, Wang B, Tanaka K, et al. **Mutagenic adaptive response to high-LET radiation in human lymphoblastoid cells exposed to X-rays.** *Mutat Res* 2011;706:46–52

Budget Sequester: Potential Impact on Health Care Providers

M.J. Ferrara

ABBREVIATIONS: FY = fiscal year; NIH = National Institutes of Health

I present an overview of the potential impact on health care providers due to blanket federal spending cuts (the Sequester) triggered by the Budget Control Act of 2011, highlighting specific areas of impact to both academic and private practice physicians.[1] The aim is to provide some clarity and context to the health care component of the Sequester and, consequently, defuse some of the hype and hyperbole that can accompany a discussion of such complexity, rife with so many impassioned stakeholders.

The Budget Control Act of 2011 was enacted to avert a looming debt-ceiling crisis, which could have resulted in the United States defaulting on its sovereign debt for the first time in the history of the country. The impact of this would be analogous to a private citizen defaulting on his mortgage, restricting his ability to borrow more money in the future. Among other mandates, the law requires $1.2 trillion in federal spending cuts during 9 years, for FY 2013 through 2021.[2] These cuts are split evenly between defense (military) and nondefense spending. The initial start date of January 1, 2013, was postponed through additional legislation (American Taxpayer Relief Act)[3] to March 1.

Medicare Cuts

Health care spending is impacted in 2 major ways. First, physician reimbursements through Medicare absorbed a 2% across-the-board cut, effective April 1, 2013, resulting in aggregate cuts of a projected $122 billion during the 9 years. Additionally, decreases in Medicare Part B premiums will produce an additional $31 billion in reductions.[4] For 2013, the total spending reduction is expected to be $10.84 billion.[4] Total Medicare spending in 2012 was $551 billion.[5] The dollar amount attached to the 2% cut will scale up as Medicare spending trends upward. The Congressional Budget Office projects 2015 Medicare spending to breach $600 billion ($12 billion cut) and, by 2019, to exceed $800 billion ($16 billion).[6]

Ancillary Department Cuts

Second, federal spending cuts in research dollars face even deeper reductions than Medicare. For FY 2013, the National Institutes of Health must cut 5.5% ($1.71 billion) across all Programs, Projects, and Activities.[7] This would reduce by 703 (7.8% drop) the number of competing research grants awarded.[8] The NIH budget funds the work of >300,000 research personnel.[9] The National Science Foundation faces 5% in cuts, projecting 1000 fewer grants awarded for 2013.[10]

The FDA will see $218 million (8% across the board) in cuts, including $39 million to Human Drugs, $17 million to Biologics, and $26.5 million to Devices.[11] Industries regulated by the FDA pay upward of $83 million a year in user fees, in part to fund drug approvals. Even though these dollars are not generated by tax revenue, they are nonetheless still subject to Sequestration cuts, a contentious point within the industry.[12]

The Centers for Disease Control and Prevention will see budget cuts of $285 million (5%) for FY 2013 from the Sequester. Combine these with additional, non-Sequester-related cuts and the Centers for Disease Control and Prevention for FY 2013 will have $580 million fewer dollars available than in the previous year.[13] Medicaid is on a list of programs protected from the Budget Control Act of 2011 and thus is insulated from related cuts.

Demographics

Health care professionals often see Medicare as a government liability with harrowing prospects because it is a "pay-as-you-go" program with worrisome demographic trending. Retirees today have the brunt of Medicare costs covered by the payroll taxes of active workers. As baby boomers continue to age, the ratio of active workers paying into the system (payroll taxes) to retirees pulling out (Medicare recipients) is worsening: 3.0:1 in 2009 sliding to 2.1:1 by 2035.[14] For context, the ratio of workers to Social Security beneficiaries in 1955 was 8.6:1.[15] The strength of that

Received June 15, 2013; accepted after revision July 24.

From Northwestern Mutual/The Miami Group, Miami, Florida.

Please address correspondence to Matthew J. Ferrara, Financial Advisor, Northwestern Mutual/The Miami Group, 2 S. Biscayne Blvd, Suite 220, Miami FL, 33131; e-mail: matthew.ferrara@nm.com

http://dx.doi.org/10.3174/ajnr.A3726

1955 ratio is, in part, bolstered by the fact that Social Security did not start writing checks to retirees until 1940. As of 2012, there were 50 million people covered by Medicare, 85% of whom were elderly (as opposed to disabled beneficiaries).[16] Ten thousand Americans will turn 65, every day, through 2030.[17]

Analytic Challenges

In evaluating the Sequester as it relates to private practice physicians, it is sensible to focus on Medicare reimbursements because these rates set the benchmark for both government and private insurance reimbursement rates. When it comes to how physicians are compensated for the care they provide, Medicare rates are the straw that stirs the drink.

Less than 6 months into the 2% cuts of the Budget Control Act of 2011, there are few compelling empiric data available that could lead one to any definitive diagnosis of the impact on the day-to-day lives of physicians, especially because these cuts fall close on the heels of a series of previous cuts in recent years. One cannot place the latest cuts in a vacuum to analyze the direct impact nor can 3–6 months be considered a representative sample size worthy of analysis.

In that light, it seems that the more edifying discourse lies in placing the Sequester cuts of the Budget Control Act of 2011 in the context of the broad trends in third-party reimbursement and the effects they are having on physicians. Viewed from 30,000 feet up, are the Sequester cuts a tipping point leading to the demise of the independent private practice physician?—all signs point to no. However, is it another layer of ice on the glacial expansion that erodes the independent physician's ability to maintain the status quo of his or her business model—that seems the prevailing sentiment.

Private Practice

The slow pace of the ebb may actually be part of the problem. In the same way that a lobster sitting in a pot heating a single degree per hour may be unaware of the long-term peril he finds himself in, these incremental cuts viewed in isolation can appear much ado about nothing. Dr Joshua Lenchus (President of the Jackson Health System Medical Staff, Associate Professor, Clinical Medicine and Anesthesiology at the University of Miami Miller School of Medicine) illuminates this concern (written communication; June 6, 2013): "We are not feeling any direct effects from sequestration aside from the 2% cut (but)…. My biggest fear is that, due to the lack of meaningful negative effect on a physician's daily life or the practice of medicine, we will become complacent, emboldening the Federal Government to do something like this again."

Alfred A. Caminos, Chief Operating Officer of Med Health Services (a multispecialty group, serving >200 regional, physician-based health care facilities) in Pittsburgh, Pennsylvania, feels a mounting pressure on the sustainability of the private practice testing model, akin to an assault by 1000 paper cuts (written communication; June13, 2013): "The 2% across the board Medicare Sequester cut is not a game changer in and of itself, but catastrophic for outpatient, independent physician clinics when added to the 35%–40% reimbursement cuts already experienced in Echocardiography and Cardiac Nuclear SPECT imaging, 50% cuts in electromyogram test and nerve conduction velocity testing and 25% reduction in technical component payment for additional imaging procedures (when more than one procedure is performed on the same day). Couple the reimbursement cuts with rising uncollected debt as a result of increased patient deductibles and an onerous preauthorization process for many medical imaging procedures and one finds that many practices today are experiencing significant drops in revenues while their operating costs continue [to] rise. As industry revenues continue to dip, we have seen sequential 15% and 25% annual hikes the last two years in our own health insurance premiums."

Academia

The Sequester cuts in academic settings are less pervasive but far more impactful for those directly affected. Grant dollars often comprise the entirety of a research team's salary source. Principal Investigators and their associated teams (fellows, technicians, and so forth) who experience a decrease or outright loss of funding can see dramatic reductions in their base compensation, including the elimination of positions altogether. Unlike the Medicare cut, which is 2% across the board and thus incrementally more manageable, the Sequester will manifest itself largely in the research arena through the reduction and elimination of entire grants or limiting the scope of new ones. Dr Jose Pizarro (Section Chief of Neuroradiology, Chairman of Radiology, Mount Sinai Medical Center) reflects (written communication; June 13, 2013): "We are now doing research projects that are simpler and of a smaller scale than what we did in the past."

Beyond 2013

The arithmetic is challenging because the spending reductions are tied to the moving target of Medicare spending; it will always be 2 cents of every dollar, but how many dollars? The delta between low- and high-end estimates of Medicare spending plots an expansive pendulum swing. In 2010, the Congressional Budget Office estimated cumulative Medicare spending between 2013 and 2020 at $6.6 trillion. Conversely, the 2013 estimate of the Congressional Budget Office for that same period has been revised down to $5.6 trillion, a net drop of $1.0 trillion.[18] In economies of this scale within a model so sensitive to human behavior, even slight shifts in the delivery of health care (or the calculus used to project it) can deliver dramatic swings in the cumulative numbers. Either way, a physician should be concerned less by the aggregate number and more focused on further action that trims individual rates. The shrinking margin on the cost of delivering care and what one can charge is the pivotal metric.

If the law stands in its current form, annual cuts affecting research funding and Medicare reimbursements will continue through 2021. However, what if Congress acts? Handicapping the next move of Washington is never easy, but urgency seems to be waning. The "cash flow" situation of the federal government is slightly less dire than it was this time last year: We are seeing slower growth in Medicare spending and, at the same time, increasing tax revenues coming into the Treasury. Policy battles such as immigration reform are on the front burner. Couple that with the murky political ramifications (neither party is sure if renegotiating the Sequester is to their political gain) and the pre-

vailing view of the moment is that any serious discussion will be pushed back until after the 2014 midterm elections.[19]

Disclosures: Matthew J. Ferrara—*OTHER RELATIONSHIPS:* I work as a financial advisor serving primarily physician clients. I lecture at hospitals but receive no compensation or special access of any kind.

REFERENCES

1. Public Law 112-25 S. 365 The Budget Control Act of 2011. 112th Congress. Superintendent of Documents. United States Government Printing Office. January 5th, 2011 http://www.gpo.gov/fdsys/pkg/BILLS-112s365enr/pdf/BILLS-112s365enr.pdf
2. Labonte M, Levit MR. The Budget Control Act of 2011: effects on spending levels and the budget deficit. Congressional Research Service. November 19, 2011. http://www.fas.org/sgp/crs/misc/R42013.pdf. Accessed April 16, 2013
3. President Obama signs the American Taxpayer Relief Act of 2012. Centers for Medicare & Medicaid Services. January 2, 2013. http://www.cms.gov/Outreach-and-Education/Outreach/FFSProvPartProg/Downloads/2013-01-03-Standalone.pdf. Accessed May 12, 2013
4. Estimated impact of automatic budget enforcement procedures specified in the Budget Control Act. Congressional Budget Office. September 12, 2011. http://www.cbo.gov/publication/42523. Accessed June 13, 2013
5. Gottlieb S. Medicare's temporary reprieve. *Forbes Online*. February 13, 2013. Accessed June 12, 2013
6. CBO Medicare Baseline, March 2009; CRS analysis of CBO Cost Estimates for the PPACA as amended by the Reconciliation Act, March 20, 2010. http://www.ncsl.org/documents/health/mcprov.pdf Accessed June 5, 2013
7. The National Institutes of Health current operating year, fiscal year 2013. National Institutes of Health Office of Budget. http://officeofbudget.od.nih.gov/cy.html. Accessed June 13, 2013
8. Kaiser J. NIH details impact of 2013 sequester cuts. *Science Insider* May 8, 2013. http://news.sciencemag.org/people-events/2013/05/nih-details-impact-2013-sequester-cuts. Accessed June 12, 2013
9. Fact sheet: impact of sequestration on the National Institutes of Health. National Institutes of Health. June 3, 2013. http://www.nih.gov/news/health/jun2013/nih-03.htm. Accessed June 13, 2013
10. Important Notice to Presidents of Universities and Colleges and Heads of Other National Science Foundation Awardee Organizations. Notice No. 133. National Science Foundation Office of the Director. February 27, 2013. http://www.nsf.gov/pubs/2013/in133/in133.pdf. Accessed June 12, 2013
11. Alliance for a Stronger FDA. FDA: sequesterable funding by center/user free. http://fdaalliance.files.wordpress.com/2009/11/sequesterable-fda-funding-by-center-10–17-12-doc-doc.pdf. Accessed June 13, 2013
12. Ethridge E. Sequester withholding of FDA user fees irks industry. *Roll Call*. May 17, 2013. http://www.rollcall.com/news/sequester_withholding_of_fda_user_fees_irks_industry-224910–1.html?pos=hln. Accessed June 11, 2013
13. Fact sheet: impact of sequestration and other budget changes on the Centers for Disease Control and Prevention. CDC 24/7. http://www.cdc.gov/fmo/topic/budget%20information/appropriations_budget_form_pdf/Sequester_Impacts.pdf. Accessed June 13, 2013
14. Levit MR, Labonte M. The Budget Control Act of 2011: effects on spending levels and the budget deficit. Congressional Research Service 7–5700 2011. May 4, 2012. http://www.fas.org/sgp/crs/misc/R42506.pdf. Accessed April 16, 2013
15. Table II.F19: comparison of OASDI covered workers and beneficiaries by alternative, calendar years 1945–2070. Social Security Administration. http://www.ssa.gov/history/reports/trust/1995/tbiif19. Accessed June 13, 2013
16. The 2012 long-term budget outlook. Congressional Budget Office. June 5, 2012. http://www.cbo.gov/publication/43288. Accessed June 14, 2013
17. Cohn D, Taylor P. Baby boomers approach 65–glumly. *Pew Research Social & Demographic Trends*. December 20, 2010. http://www.pewsocialtrends.org/2010/12/20/baby-boomers-approach-65-glumly/. Accessed June 14, 2013
18. Thompson D. Don't look now, but our Medicare spending projections are plummeting. *The Atlantic*. May 14, 2013. http://www.theatlantic.com/business/archive/2013/05/dont-look-now-but-our-medicare-spending-projections-are-plummeting/275849/. Accessed June 12, 2013
19. Nicholas P, Hook J, Paletta D. Deficit deal even less likely. *The Wall Street Journal*. June 2, 2013. http://online.wsj.com/article/SB10001424127887324423904578521600404730028.html. Accessed June 11, 2013

DWI Reversal Is Associated with Small Infarct Volume in Patients with TIA and Minor Stroke

N. Asdaghi, B.C.V. Campbell, K.S. Butcher, J.I. Coulter, J. Modi, A. Qazi, M. Goyal, A.M. Demchuk, and S.B. Coutts

ABSTRACT

BACKGROUND AND PURPOSE: More than half of patients with TIA/minor stroke have ischemic lesions on early DWI, which represent irreversibly damaged tissue. The presence and volume of DWI lesions predict early deterioration in this population. We aimed to study the rate and implications of DWI reversal in patients with TIA/minor stroke.

MATERIALS AND METHODS: Patients with TIA/minor stroke were prospectively enrolled and imaged within 24 hours of onset. Patients were followed for 3 months with repeat MR imaging either at day 30 or 90. Baseline DWI/PWI and follow-up FLAIR final infarct volumes were measured.

RESULTS: Of 418 patients included, 55.5% had DWI and 37% had PWI (time-to-peak of the impulse response ≥2 seconds' delay) lesions at baseline. The median time from symptom onset to baseline and follow-up imaging was 13.4 (interquartile range, 12.7) and 78.73 hours (interquartile range, 60.2), respectively. DWI reversal occurred in 5.7% of patients. The median DWI lesion volume was significantly smaller in those with reversal (0.26 mL, interquartile range = 0.58 mL) compared with those without (1.29 mL, interquartile range = 3.6 mL, P = .002); 72.7% of DWI reversal occurred in cortically based lesions. Concurrent tissue hypoperfusion (time-to-peak of the impulse response ≥2 seconds) was seen in 36.4% of those with DWI reversal versus 62.4% without (P = .08). DWI reversal occurred in 3.3% of patients with penumbral patterns (time-to-peak of the impulse response ≥6 seconds − DWI) > 0 and in 6.8% of those without penumbral patterns (P = .3). The severity of hypoperfusion, defined as greater prolongation of time-to-peak of the impulse response (≥2, ≥4, ≥6, ≥8 seconds), did not affect the likelihood of DWI reversal (linear trend, P = .147). No patient with DWI reversal had an mRS score of ≥2 at 90 days versus 18.2% of those without reversal (P = .02).

CONCLUSIONS: DWI reversal is uncommon in patients with TIA/minor stroke and is more likely to occur in those with smaller baseline lesions. DWI reversal should not have a significant effect on the accuracy of penumbra definition.

ABBREVIATIONS: CATCH = CT and MR Imaging in the Triage of TIA and Minor Cerebrovascular Events to Identify High-Risk Patients; DEFUSE = Diffusion and Perfusion Imaging Evaluation for Understanding Stroke Evolution; EPITHET = Echo-Planar Imaging Thrombolytic Evaluation Trial; IQR = interquartile range; Tmax = time-to-peak of the impulse response; VISION = Vascular Imaging of Acute Stroke for Identifying Predictors of Clinical Outcome and Recurrent Ischemic Events

Multiple studies have shown that more than half of patients with TIA/minor stroke have evidence of acute ischemic tissue injury on early DWI.[1-3] The presence and the volume of DWI lesions carry a negative prognostic value in this population.[4-6] The DWI-restricted lesions are thought to represent the irreversibly damaged ischemic core.[7] This premise was recently brought into question by studies suggesting a high rate of DWI lesion reversal in patients with stroke who had undergone thrombolytic therapy.[8,9] A recent systematic review of the published literature on DWI hyperintense tissue outcome reported variable rates of DWI reversal (0%–83%), with a mean reversal rate of 24% in patients with ischemic stroke.[10] In most patients, the size of the acute infarct correlated with both the final infarct volume on follow-up T2/FLAIR imaging and the clinical outcome.[11,12] Most previous work on DWI reversal has been undertaken in patients with moderate-to-severe strokes. Patients with TIA or minor stroke have smaller volumes of ischemia and potentially may have a higher likelihood of reversal. Previous imaging studies have reported reversal of the DWI signal in patients with TIA, but these were

Received April 5, 2014; accepted after revision July 15.

From Departments of Clinical Neurosciences (N.A., J.I.C., A.Q., M.G., A.M.D., S.B.C.) and Radiology (J.M., M.G., A.M.D., S.B.C.) and Hotchkiss Brain Institute (M.G., A.M.D., S.B.C.), University of Calgary, Calgary, Alberta, Canada; Division of Neurology (N.A., K.S.B.), University of Alberta, Edmonton, Alberta, Canada; The Royal Melbourne Hospital (B.C.V.C.), University of Melbourne, Parkville, Victoria, Australia; and British Columbia Centre for Stroke and Cerebrovascular Diseases (N.A.), University of British Columbia, Vancouver, British Columbia, Canada.

Please address correspondence to Negar Asdaghi, MD, S169-2211 Wesbrook Mall, University of British Columbia, Vancouver, BC, Canada V6T 2B9; e-mail: negar.asdaghi@ubc.ca

Indicates open access to non-subscribers at www.ajnr.org

http://dx.doi.org/10.3174/ajnr.A3733

relatively small series, without scheduled follow-up imaging and DWI reversal was not studied systematically.[13-15]

Potentially salvageable tissue known as the "ischemic penumbra" represents viable tissue at risk of infarct that has not yet infarcted.[16] Various methods are used to define the ischemic penumbra on MR imaging, including the mismatch between perfusion and diffusion[17] or clinical-diffusion mismatch.[18] All of these definitions rely on DWI lesions representing irreversibly damaged ischemic core.

DWI reversibility, therefore, has implications in both accurate assessment of ischemic core and penumbra and outcome prediction.

We, therefore, aimed to determine the rate and characteristics of DWI reversal in 2 large prospective imaging cohorts of patients with TIA/minor stroke. We studied the correlation among the DWI lesion volume, lesion location, concurrent baseline hypoperfusion on perfusion-weighted imaging, the severity of the perfusion deficit, and the reversal of DWI signal on follow-up FLAIR/T2 imaging in this population.

MATERIALS AND METHODS

Patients

Patients with high-risk TIA (focal weakness or speech disturbance lasting ≥ 5 minutes) or minor ischemic stroke (with initial NIHSS scores of ≤ 3) were prospectively enrolled. All patients presented to the Foothills Medical Centre, and informed consent was obtained before enrollment. The first cohort included patients with TIA/minor stroke who underwent perfusion MR imaging in the Vascular Imaging of Acute Stroke for Identifying Predictors of Clinical Outcome and Recurrent Ischemic Events (VISION) study.[19] To be included in this substudy, patients had to be 18 years of age or older, have a premorbid mRs score of <2, have a CT scan of the brain and be examined by a stroke neurologist within 12 hours of onset, and have a brain MR imaging, including PWI, within 24 hours of onset. Patients were excluded if they had evidence of intracerebral hemorrhage or other nonvascular pathology on CT. The second cohort included patients who underwent PWI in the CT and MR Imaging in the Triage of TIA and Minor Cerebrovascular Events to Identify High-Risk Patients (CATCH)[20] study. The inclusion criteria in CATCH were similar to those of VISION, with the exception that patients were included if they were assessed by a stroke neurologist and imaged within 24 hours of symptom onset. Standard clinical and demographic information was recorded for all patients. In both studies, secondary stroke prevention measures were implemented in accordance with current practice guidelines.[21]

MR Imaging Protocol

Patients in both studies had MR imaging brain scans completed as soon as possible and within 24 hours of symptom onset. Patients were imaged by using a 3T scanner (Signa VH/i; GE Healthcare, Milwaukee, Wisconsin) with an 8-channel head and a neck coil (Neurovascular Array Coil; Medrad, Indianola, Pennsylvania). Sequences included sagittal T1, axial T2, and axial FLAIR. Acute ischemic lesions were identified on the DWI sequence in the first cohort and on diffusion tensor imaging in the second cohort. DWI was performed with single-shot spin-echo diffusion echo-planar imaging with the following parameters: 240-mm FOV; twenty-seven 5-mm axial sections with 0.0-mm gap; a b-value of 1000 s/mm^2 along 3 orthogonal directions; TR/TE, 9000/85–90 ms; acceleration factor, $R = 2$; matrix size, 192 × 192, zero-filled to 256 × 256, after April 2004. Before this date, the DWI sequences had the same parameters except that sections were 5-mm-thick and had 2-mm gaps. Parameters identical to those of DWI (after April 2004) were used in DTI imaging with 11 diffusion directions. Dynamic susceptibility-weighted contrast PWI was acquired by using a gadopentetate dimeglumine (Magnevist, 0.1 mmol/kg; Schering, Berlin, Germany) injection delivered via a power injector at 5 mL/s through an 18-ga needle in an antecubital vein, followed by a 20-mL saline flush at the same rate; and echo-planar gradient-echo (T2*) images were acquired every 2 seconds for 80 seconds (17 axial 5 + 0.0 mm gap sections at each time point).

Follow-up MR imaging without PWI was performed at day 30 in VISION and at day 90 in CATCH, respectively. The FLAIR sequence (TR/TE/TI, 9000/140/2250 ms; NEX, 1; FOV, 24 × 24 cm^2; section thickness, 3.0 mm with no gap; acquisition time, 6 minutes 26 seconds) was used in all CATCH follow-up patients and in the VISION study after April 2004. Before April 2004, the follow-up FLAIR sequences (within VISION) had identical parameters except that the sections were 5-mm thick and there was a 2.0-mm gap between adjacent sections.

Image Analysis

MR imaging sequences (DWI/ADC, FLAIR, and T2) were reviewed for the presence of ischemic lesions at each time point. PWI source images (T2*) were imported into custom Matlab 7.4 (MathWorks, Natick, Massachusetts) software (PGUI Perfusion Analysis Software; Center of Functionally Integrative Neuroscience, Aarhus University Hospital Norrebrogade, Denmark; 2007).[22,23] A whole-brain mask was drawn to include all cerebral regions and vessels within scanning range. An arterial input function was manually selected from the middle cerebral artery contralateral to the visible DWI lesion, and a block circulant deconvolution algorithm was used to calculate voxelwise maps of time-to-peak of the impulse response (Tmax).[24] Maps of Tmax were imported into the Analyze software package (Biomedical Imaging Resource, Rochester, New York).[25] Hypoperfused brain tissue was defined as those voxels with a Tmax delay of ≥2 seconds. A penumbral pattern was defined as the presence of PWI-DWI mismatch, where DWI lesion volume subtracted from the volume of lesions with a Tmax of ≥6 seconds' delay was greater than zero. Planimetric PWI and DWI lesion volume measurement was performed by using Quantomo software (Cybertrial, Calgary, Alberta, Canada).[26]

The intensity of hypoperfusion was characterized by the hypoperfusion intensity ratio, defined as the volume of tissue with severe hypoperfusion (Tmax ≥ 8 seconds) divided by the volume of tissue with any hypoperfusion (Tmax ≥ 2 seconds) as previously described.[27] DWI hyperintense lesion borders were defined by using a semiautomated threshold intensity technique. We referenced these lesions to the corresponding areas on the apparent diffusion coefficient maps to avoid selecting regions of T2

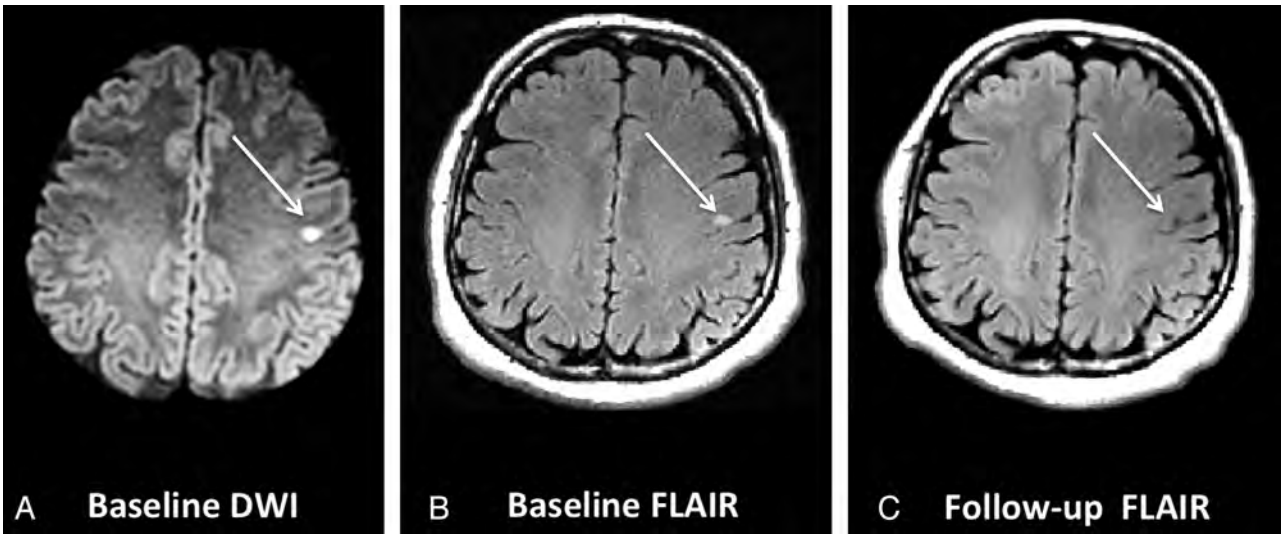

FIG 1. Example of focal atrophy on follow-up FLAIR imaging in the region of the original DWI lesion that could mimic DWI reversal. Baseline DWI lesion (*A*) and baseline FLAIR (*B*) show the acute ischemic infarct. *C*, An area of focal atrophy in the region of the baseline DWI lesion.

shinethrough. The b = 1000 image was used as the primary template because quantitative ADC thresholds tend to vary depending on the time after stroke onset and concurrent perfusion status.[28] For DWI volume measurement, a standardized display method with B0 images, was used to standardize the window width and level before volumetric measurements.[29] The final infarct volume was measured on follow-up FLAIR sequences, with reference to the baseline FLAIR and DWI sequences.

All images were reviewed by 2 investigators (N.A. and J.M.) for persistence of T2 hyperintense signal or complete reversal of DWI signal on follow-up FLAIR imaging. In those who had apparent DWI reversal (ie, complete signal resolution), automated coregistration of the follow-up FLAIR images to the acute DWI was performed by a third reviewer (B.C.V.C.) using open-source McConnell Brain Imaging Centre Tools software (Montreal Neurological Institute, Montreal, Quebec, Canada) and visually verifying them for accuracy.

Primary and Secondary Outcome

The primary outcome was the rate of DWI reversal on follow-up FLAIR imaging. This was *a priori* defined as the absence of T2/FLAIR hyperintense signal on follow-up imaging in the region of the brain with the baseline DWI restriction. The patients were not considered to have DWI reversal if there was evidence of atrophy or gliosis in the same region that had DWI restriction or if they showed partial resolution of signal on follow-up imaging (Fig 1). Secondary outcome was the rate of clinical disability as defined by an mRS score of ≥2 at 90-day clinical follow-up.

Statistical Analysis

Statistical analyses were performed by using the Statistical Package for Social Sciences, Version 20.0 (IBM, Armonk, New York). Data are reported by using standard descriptive statistics. Parametric and nonparametric testing was applied where appropriate to assess clinical and imaging predictors of DWI lesion reversal.

RESULTS

Baseline Clinical and Imaging Characteristics

A total of 418 patients in the pooled VISION (n = 137) and CATCH (n = 281) studies had DWI and PWI at baseline. The median age in the pooled cohort was 68.2 years (IQR = 21.3), and the median NIHSS score was 1 (IQR = 2); 45.5% had a history of hypertension; 13%, diabetes; 9.6%, known atrial fibrillation; and 16.3% were smokers at the time of the presenting symptoms. There were more male patients in VISION (60%) relative to CATCH (42%, P = .001); otherwise patients had comparable vascular risk factors in the 2 cohorts. The median time between symptom onset and baseline MR imaging was 13.4 hours (IQR = 12.7). At baseline, DWI positivity was seen in 55.5% (232/418; 95% CI, 50.6–60.3) of patients, and 37.3% (156/418; 95% CI, 32.8–42) had a perfusion deficit (Tmax ≥ 2 seconds delay). A total of 143/418 (34.2%; 95% CI, 29.7–39) patients had concurrent perfusion and diffusion deficits. The median volume of DWI-positive lesions was 1.15 mL (IQR = 3.36).

Follow-Up Imaging and DWI Reversal

Follow-up imaging was available in 80.6% (337/418; 95% CI, 76.5–84) of patients, of whom 57% (192/337; 95% CI, 51.5–62) had positive DWI lesions at baseline. Reasons for lack of follow-up imaging included a new contraindication to MR imaging (pacemaker insertion, mechanical heart valve insertion), death, or patient refusal.

The median time from symptom onset to follow-up imaging was 78.7 days (IQR = 60.2). In patients with positive DWI lesions at baseline, DWI reversal on follow-up imaging was seen in 5.7% (11/192; 95% CI, 3.2–9.9) of patients (Fig 2). The rate of DWI reversal was similar between the first and second cohorts (6%; 95% CI, 1.8–13.3) versus (5.6; 95% CI, 2.4–10.5), P = .91, respectively.

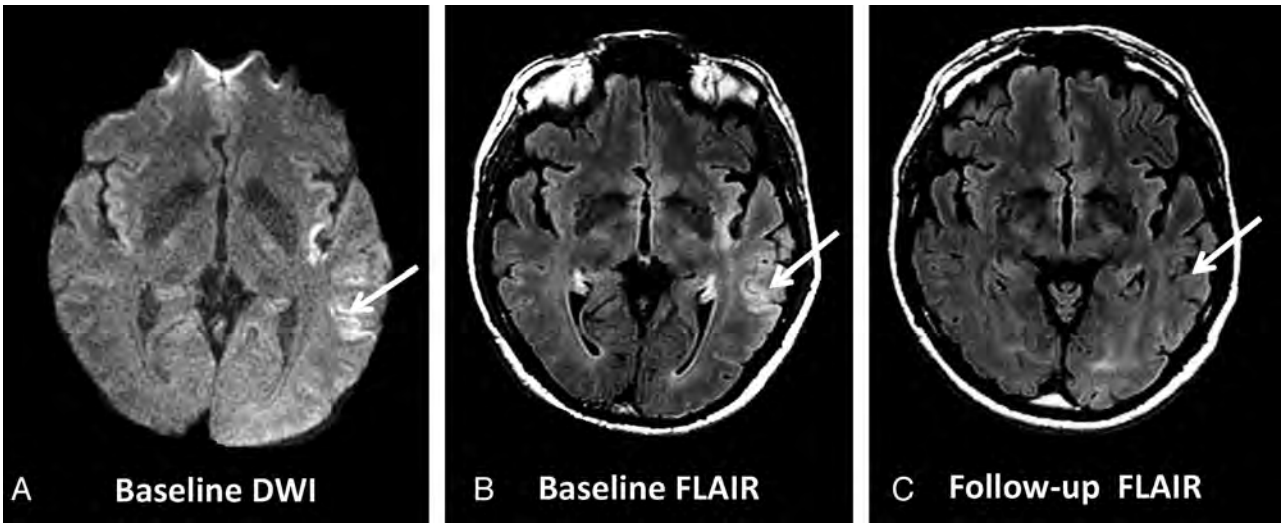

FIG 2. Example of a patient with DWI reversal. Baseline DWI (*A*) and baseline FLAIR (*B*) show the acute ischemic infarct corresponding to the patient's presenting symptoms. *C*, Complete resolution of the DWI signal on follow-up MR imaging (FLAIR).

Clinical and radiographic characteristics of the DWI-positive patients with or without reversal

Clinical and Radiographic Characteristics	DWI Reversal (*n* = 11)	No. DWI Reversals (*n* = 181)	*P* Value
Age (median) (IQR) (yr)	68.5 (20.7)	68.5 (16.3)	.95
HTN (No., %)	5 (45.5%)	101 (55.8%)	.50
Diabetes (No., %)	1 (9.1%)	24 (13.3%)	.69
Atrial fibrillation (No., %)	1 (9.1%)	18 (9.9%)	.96
Smoking (No., %)	2 (18.2%)	36 (19.9%)	.89
Time from symptom onset to baseline DWI/PWI in hours (IQR)	13.3 (11.4)	11 (8.6)	.15
Time from symptom onset to follow-up FLAIR in days (IQR)	76.5 (46)	79.6 (59.4)	.61
Median DWI lesion volume	0.26 mL (0.58)	1.29 mL (3.6)	.002[a]
Concurrent PWI deficit (Tmax +2 seconds) (No., %)	4 (36.4%)	113 (62.4%)	.08
Concurrent penumbra (Tmax +6 seconds), DWI (No., %)	2 (18%)	58 (32%)	.33
Topography			.034[a]
Cortical	72.7%	27.6%	
Subcortical WM	18.2%	12.2%	
Subcortical GM	0%	8.8%	
Cortical and subcortical	9.1%	41.4%	
Infratentorial	0%	8.3%	
Multiterritorial	0%	1.7%	
Acute FLAIR hyperintensity	18.2%	23.8%	.67

Note:—HTN indicates hypertension.
[a] Statistically significant.

The Table summarizes the clinical and radiographic characteristics of patients with DWI reversal relative to those without. More patients with persistent DWI lesions had concurrent perfusion deficits (tissue with Tmax of ≥2 seconds' delay) or concurrent ischemic penumbra ([Tmax ≥ 6 seconds]-DWI), though these differences did not reach statistical significance (Table). The likelihood of DWI reversal did not decrease with an increased severity of hypoperfusion, defined as greater prolongation of Tmax (≥2, ≥4, ≥6, ≥8 seconds' delay) (linear trend, $P = .147$). The hypoperfusion intensity ratio was not a predictor of DWI reversal in a regression analysis, adjusting for the volume of baseline DWI lesions (OR = 0.73 [95% CI, 0.01–36], $P = .87$).

A total of 22% of patients (92/418, 18%–26%) had evidence of ischemic penumbra (Tmax ≥ 6 seconds − DWI) > 0. The median volume of penumbra in these patients was 12.5 mL (IQR = 31.3, geometric mean = 9.63). When we adjusted for the cases with DWI reversal, the volume of baseline penumbra changed in only 3 patients. Moreover, 2 additional patients would have had penumbra at baseline when considering DWI reversibility. Despite this, the median baseline penumbra was not significantly changed after adjusting for the DWI reversibility (12.2, IQR = 30.3, geometric mean = 9.6).

The median DWI lesion volume was significantly smaller in those with reversal (median = 0.26 mL, geometric mean = 0.32 mL, IQR = 0.58 mL) versus those who did not reverse (1.29 mL, geometric mean = 1.47 mL, IQR = 3.6 mL, $P = .002$) (Table). Despite this, DWI reversal was not exclusively seen in patients with small baseline lesions. The largest DWI lesion with complete reversal on follow-up FLAIR measured 12 mL at baseline (Fig 2). Similarly, 22.6% (39/172; 95% CI, 16.6–29.7) of patients who did not show DWI reversal had baseline infarct volumes of <0.5 mL. The optimal volume for prediction of DWI reversal in this cohort was <0.4 mL, which correctly predicted infarct reversal with 80% sensitivity and 73% specificity (area under the curve = 0.77; 95% CI, 0.61–0.94; $P = .002$).

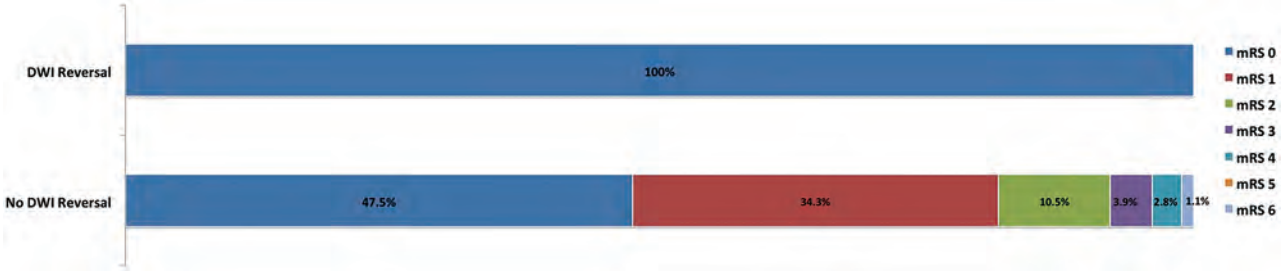

FIG 3. The distribution of the modified Rankin Scale at 90 days in patients with follow-up imaging based on DWI persistence or reversal.

Correlation between DWI Reversal, Lesion Location, and Clinical Outcome

The Table shows the distribution of baseline DWI lesions in patients with or without DWI reversal. Most patients with DWI reversal had a small cortically based lesion (72.7%, 8/11; 95% CI, 45.1–91.7).

A total of 13.4% (56/418) of patients had a 90-day mRS ≥ 2. Figure 3 shows the distribution of mRS at 90 days in patients with follow-up imaging based on DWI persistence or reversal. Patients with DWI reversal were significantly less likely to be dependent (mRS > 2; 0%, 0/11) compared with those with persistent lesions (18.2%, 33/181, $P = .028$). In a multivariate regression analysis adjusting for age, infarct size, and DWI reversal, the only independent predictor of good outcome was infarct size (OR = 1.05; 95% CI. 1.01–1.1; $P = .01$).

DISCUSSION

This is the largest prospective perfusion-diffusion MR imaging study to date that addresses the clinical and radiographic characteristics of patients with TIA/minor stroke with DWI reversal. We found that complete DWI reversal is uncommon in this population and only occurs in 5.7% of patients. Patients with DWI reversal commonly had a small cortically based lesion. More patients with DWI reversal had early reperfusion, evident by the absence of concurrent tissue hypoperfusion on PWI. In our cohort, only 2 patients with evidence of ischemic penumbra had DWI reversal on follow-up imaging. Adjusting for the DWI reversal did not have a major impact on the calculated volume of baseline ischemic penumbra.

Our findings are in keeping with previous reports in patients with moderate and severe ischemic stroke in whom DWI reversal occurred on prompt recanalization with intra-arterial thrombolysis.[8] Similarly, in a preliminary analysis of the Diffusion and Perfusion Imaging Evaluation for Understanding Stroke Evolution (DEFUSE) data, diffusion reversal rates were significantly increased among patients in whom early recanalization was achieved and specifically occurred in the regions with normal baseline perfusion.[30] In our cohort, although there was an association between tissue hypoperfusion and persistence of DWI lesion, this difference did not reach statistical significance. This discrepancy may be related to a relatively small total number of patients with reversal rather than a lack of association between reperfusion and DWI reversibility.

Our findings are in keeping with a pooled analysis of DEFUSE and Echo-Planar Imaging Thrombolytic Evaluation Trial (EPITHET) images, which reported a small median DWI reversal volume of only 1.5 mL.[31] The previously reported higher rate of apparent DWI reversal in these cohorts was subsequently thought to be secondary to coregistration inaccuracies and infarct shrinkage related to gliosis/atrophy rather than true signal reversal. A separate analysis of the EPITHET data by Chemmanam et al[32] reported a correlation between DWI reversibility and the severity of tissue hypoperfusion. Although our findings are in agreement with these results, we were unable to show a decline in the rate of DWI reversal with greater prolongation of Tmax. This discrepancy may, in part, be related to the very small median volume of infarct in our patients and complete (not partial) signal resolution used as the definition of DWI reversal in our cohort.

The pathophysiologic processes that result in the development of high signal intensity on DWI and corresponding low signal on the ADC maps are important in understanding the meaning and significance of acute DWI-restricted lesions. Putative mechanisms for development of DWI-restricted lesions include failure of adenosine triphosphatase–dependent Na^+-K^+ pumps, resulting in restriction of intracellular water motion.[33] Others have suggested a reduction in the extracellular water content[34] or alteration of pH due to anaerobic metabolism in the areas where adenosine triphosphatase levels are still maintained[35] as potentially reversible causes of signal changes detected by diffusion-weighted imaging. The latter mechanisms suggest that DWI-restricted lesions can represent both areas of ischemic core and penumbra and may provide an explanation for its reversibility.

Our study has some limitations: Neither of the 2 cohorts included consecutive patients because this analysis was restricted to patients with TIA/minor stroke in whom we were able to obtain MR imaging scans within the first 24 hours of onset. Furthermore, it is possible that some early DWI reversals occurred before the initial MR imaging study was completed. Forty patients with a baseline DWI-restricted lesion did not have follow-up imaging, which can affect our reported rate of DWI reversal. Also, the follow-up imaging of 2 patients with DWI reversal contained 2.0-mm gaps; and as such, we cannot rule out the possibility that the apparent reversal may be related to technical issues in these 2 patients. Although 3 investigators separately assessed the images, the decision for DWI reversal was made on the basis of a consensus among the 3, and we did not perform inter-rater reliability for DWI reversal. Despite these limitations, this is the largest prospective study to date to address the rate and characteristics of lesions with DWI reversal in the population of minor stroke and TIA. We think it is unlikely that these results are due to infarct atrophy or focal gliosis in those regions because we used coregistration tech-

niques combined with careful visual inspection of the baseline and follow-up images to ensure that the loss of DWI signal on follow-up T2/FLAIR imaging represented true DWI reversal.

Recanalization therapies remain a controversial area in patients with TIA or minor stroke presentation.[36] Currently, there is an ongoing clinical trial to assess the efficacy of thrombolysis in this population.[37] The volume of perfusion-diffusion mismatch has been suggested as a surrogate marker for selection of patients suitable for revascularization therapies.[38] This volume is dependent on the correct definition of infarct core. Our results show that the infarct core is well-represented by DWI imaging and reversal is uncommon, especially in those with concurrent hypoperfusion. Mismatch volume can reliably be used for selection of eligible patients in future thrombolysis trials in minor stroke.

CONCLUSIONS

In summary, the presence of DWI lesions in patients with minor or completely resolved neurologic symptoms not only confirms the diagnosis of an ischemic attack but also has prognostic implications for recurrence of stroke and the development of disability in this population. The prognostic value of DWI reversal was not previously known in this population. Our results confirm that DWI reversal is uncommon but is associated with a more favorable profile and outcome in patients with TIA/minor stroke. DWI reversal usually occurs in those without concurrent perfusion deficits and should not have a significant impact on the estimated volume of the ischemic penumbra.

Disclosures: Negar Asdaghi—*RELATED*: *Grant*: Supported by a fellowship from the Canadian Institutes for Health Research and a research allowance from the Vancouver General Hospital and University of British Columbia hospital foundation. Ken S. Butcher—*UNRELATED*: *Payment for Lectures (including service on Speakers Bureaus)*: Boehringer Ingelheim, Bayer Canada, *Comments*: Speakers fees for NOACs (unrelated to the current manuscript). Mayank Goyal—*UNRELATED*: *Consultancy*: Covidien, ev3, *Comments*: for teaching engagements, for trial design, *Grants/Grants Pending*: Covidien,* ev3*, *Comments*: partly sponsoring the ESCAPE (Endovascular treatment for Small Core and Anterior circulation Proximal occlusion with Emphasis on minimizing CT to recanalization times) trial, *Payment for Lectures (including service on Speakers Bureaus)*: Covidien, ev3, *Comments*: For teaching engagements, *Stock/Stock Options*: Calgary Scientific Inc, NoNO Inc. Shelagh B. Coutts—*RELATED*: Receives salary support from Alberta Innovates - Health Solutions and the Heart and Stroke Foundation of Canada Distinguished Clinician Scientist award, supported in partnership with the Canadian Institute of Health Research and Institute of Circulatory and Respiratory Health and AstraZeneca Canada Inc. The VISION study was supported by grant funding from the Canadian Institutes for Health Research (CIHR MOP-118096) and Heart and Stroke Foundation of Alberta, Northwest Territories and Nunavut. The CATCH study was funded by grant funding from the Canadian Institutes for Health Research (CIHR MOP - 89937) and a Pfizer Cardiovascular research award. The 3T MR Scanner in the Seaman Family MR Research Centre used in this study was partially funded by Canada Foundation for Innovation., *UNRELATED*: *Grants/Grants Pending*: Genome Canada,* Heart and Stroke Foundation of Canada,* Canadian Stroke Network,* Alberta Innovates,* *Comments*: grant funding. *Money paid to the institution.

REFERENCES

1. Merwick A, Albers GW, Amarenco P, et al. **Addition of brain and carotid imaging to the ABCD(2) score to identify patients at early risk of stroke after transient ischaemic attack: a multicentre observational study.** *Lancet Neurol* 2010;9:1060–69
2. Giles MF, Albers GW, Amarenco P, et al. **Early stroke risk and ABCD2 score performance in tissue- vs time-defined TIA: a multicenter study.** *Neurology* 2011;77:1222–28
3. Coutts SB, Hill MD, Simon JE, et al. **Silent ischemia in minor stroke and TIA patients identified on MR imaging.** *Neurology* 2005;23 65:513–17
4. Ay H, Oliveira-Filho J, Buonanno FS, et al. **'Footprints' of transient ischemic attacks: a diffusion-weighted MRI study.** *Cerebrovasc Dis* 2002;14:177–86
5. Coutts SB, Simon JE, Eliasziw M, et al. **Triaging transient ischemic attack and minor stroke patients using acute magnetic resonance imaging.** *Ann Neurol* 2005;57:848–54
6. Asdaghi N, Hameed B, Saini M, et al. **Acute perfusion and diffusion abnormalities predict early new MRI lesions 1 week after minor stroke and transient ischemic attack.** *Stroke* 2011;42:2191–95
7. Beaulieu C, de Crespigny A, Tong DC, et al. **Longitudinal magnetic resonance imaging study of perfusion and diffusion in stroke: evolution of lesion volume and correlation with clinical outcome.** *Ann Neurol* 1999; 46:568–78
8. Kidwell CS, Saver JL, Mattiello J, et al. **Thrombolytic reversal of acute human cerebral ischemic injury shown by diffusion/perfusion magnetic resonance imaging.** *Ann Neurol* 2000;47:462–69
9. Parsons MW, Barber PA, Chalk J, et al. **Diffusion- and perfusion-weighted MRI response to thrombolysis in stroke.** *Ann Neurol* 2002;51:28–37
10. Kranz PG, Eastwood JD. **Does diffusion-weighted imaging represent the ischemic core? An evidence-based systematic review.** *AJNR Am J Neuroradiol* 2009;30:1206–12
11. Sorensen AG, Buonanno FS, Gonzalez RG, et al. **Hyperacute stroke: evaluation with combined multisection diffusion-weighted and hemodynamically weighted echo-planar MR imaging.** *Radiology* 1996;199:391–401
12. Warach S, Dashe JF, Edelman RR. **Clinical outcome in ischemic stroke predicted by early diffusion-weighted and perfusion magnetic resonance imaging: a preliminary analysis.** *J Cereb Blood Flow Metab* 1996;16:53–59
13. Kidwell CS, Alger JR, Di Salle F, et al. **Diffusion MRI in patients with transient ischemic attacks.** *Stroke* 1999; 30:1174–80
14. Marks MP, de Crespigny A, Lentz D, et al. **Acute and chronic stroke: navigated spin-echo diffusion-weighted MR imaging.** *Radiology* 1996;199:403–08
15. Oppenheim C, Lamy C, Touze E, et al. **Do transient ischemic attacks with diffusion-weighted imaging abnormalities correspond to brain infarctions?** *AJNR Am J Neuroradiol* 2006;27:1782–87
16. Astrup J, Siesjo BK, Symon L. **Thresholds in cerebral ischemia: the ischemic penumbra.** *Stroke* 1981;12:723–25
17. Donnan GA, Davis SM. **Breaking the 3 H barrier for treatment of acute ischaemic stroke.** *Lancet Neurol* 2008;7:981–82
18. Dávalos A, Blanco M, Pedraza S, et al. **The clinical-DWI mismatch: a new diagnostic approach to the brain tissue at risk of infarction.** *Neurology* 2004;62:2187–92
19. Coutts SB, Hill MD, Eliasziw M, et al. **Final 2 year results of the vascular imaging of acute stroke for identifying predictors of clinical outcome and recurrent ischemic events (VISION) study.** *BMC Cardiovasc Disord* 2011;11:18
20. Coutts SB, Modi J, Patel SK, et al. **CT/CT angiography and MRI findings predict recurrent stroke after transient ischemic attack and minor stroke: results of the prospective CATCH study.** *Stroke* 2012;43:1013–17
21. Sacco RL, Adams R, Albers G, et al, for the American Heart Association/American Stroke Association Council on Stroke; Council on Cardiovascular Radiology and Intervention; American Academy of Neurology. **Guidelines for prevention of stroke in patients with ischemic stroke or transient ischemic attack: a statement for healthcare professionals from the American Heart Association/American Stroke Association Council on Stroke—co-sponsored by the Council on Cardiovascular Radiology and Intervention: the American Academy of Neurology affirms the value of this guideline.** *Circulation* 2006;113:e409–449
22. Ostergaard L, Sorensen AG, Kwong KK, et al. **High resolution measurement of cerebral blood flow using intravascular tracer bolus passages. Part II. Experimental comparison and preliminary results.** *Magn Reson Med* 1996;36:726–36
23. Ostergaard L, Weisskoff RM, Chesler DA, et al. **High resolution mea-**

surement of cerebral blood flow using intravascular tracer bolus passages. Part I. Mathematical approach and statistical analysis. *Magn Reson Med* 1996;36:715–25
24. Wu O, Ostergaard L, Weisskoff RM, et al. **Tracer arrival timing-insensitive technique for estimating flow in MR perfusion-weighted imaging using singular value decomposition with a block-circulant deconvolution matrix.** *Magn Reson Med* 2003;50:164–74
25. Robb RA. **The biomedical imaging resource at Mayo Clinic.** *IEEE Trans Med Imaging* 2001;20:854–67
26. Kosior JC, Idris S, Dowlatshahi D, et al. **Quantomo: validation of a computer-assisted methodology for the volumetric analysis of intracerebral haemorrhage.** *Int J Stroke* 2011;6:302–05
27. Bang OY, Saver JL, Alger JR, et al. **Determinants of the distribution and severity of hypoperfusion in patients with ischemic stroke.** *Neurology* 2008;71:1804–11
28. An H, Ford AL, Vo K, et al. **Signal evolution and infarction risk for apparent diffusion coefficient lesions in acute ischemic stroke are both time- and perfusion-dependent.** *Stroke* 2011; 42:1276–81
29. Sasaki M, Ida M, Yamada K, et al. **Standardizing display conditions of diffusion-weighted images using concurrent B0 images: a multi-vendor multi-institutional study.** *Magn Reson Med Sci* 2007; 6:133–37
30. Olivot JM, Mlynash M, Thijs VN, et al. **Relationships between cerebral perfusion and reversibility of acute diffusion lesions in DEFUSE: insights from RADAR.** *Stroke* 2009;40:1692–97
31. Campbell BC, Purushotham A, Christensen S, et al. **The infarct core is well represented by the acute diffusion lesion: sustained reversal is infrequent.** *J Cereb Blood Flow Metab* 2012;32:50–56
32. Chemmanam T, Campbell BC, Christensen S, et al. **Ischemic diffusion lesion reversal is uncommon and rarely alters perfusion-diffusion mismatch.** *Neurology*. 2010;75:1040–47
33. Dijkhuizen RM, de Graaf RA, Tulleken KA, et al. **Changes in the diffusion of water and intracellular metabolites after excitotoxic injury and global ischemia in neonatal rat brain.** *J Cereb Blood Flow Metab* 1999;19:341–49
34. Qiao M, Malisza KL, Del Bigio MR, et al. **Transient hypoxia-ischemia in rats: changes in diffusion-sensitive MR imaging findings, extracellular space, and Na+-K+ -adenosine triphosphatase and cytochrome oxidase activity.** *Radiology* 2002;223:65–75
35. Kohno K, Hoehn-Berlage M, Mies G, et al. **Relationship between diffusion-weighted MR images, cerebral blood flow, and energy state in experimental brain infarction.** *Magn Reson Imaging* 1995;13:73–80
36. Khatri P, Kleindorfer DO, Yeatts SD, et al. **Strokes with minor symptoms: an exploratory analysis of the National Institute of Neurological Disorders and Stroke recombinant tissue plasminogen activator trials.** *Stroke* 2010;41:2581–86
37. Hill MD. **TNK-tPA evaluation for minor ischemic stroke with proven occlusion (TEMPO-1).** http://clinicaltrials.gov/ct2/show/NCT01654445?term=TEMPO+coutts&rank=1. Accessed 2013
38. Asdaghi N, Hill MD, Coulter JI, et al. **Perfusion MR predicts outcome in high-risk transient ischemic attack/minor stroke: A derivation-validation study.** *Stroke* 2013;44:2486–92

The Impact of Arterial Collateralization on Outcome after Intra-Arterial Therapy for Acute Ischemic Stroke

S. Seeta Ramaiah, L. Churilov, P. Mitchell, R. Dowling, and B. Yan

ABSTRACT

BACKGROUND AND PURPOSE: Although intra-arterial therapy for acute ischemic stroke is associated with superior recanalization rates, improved clinical outcomes are inconsistently observed following successful recanalization. There is emerging concern that unfavorable arterial collateralization, though unproven, predetermines poor outcome. We hypothesized that poor leptomeningeal collateralization, assessed by preprocedural CTA, is associated with poor outcome in patients with acute ischemic stroke undergoing intra-arterial therapy.

MATERIALS AND METHODS: We retrospectively analyzed patients with acute ischemic stroke with intracranial ICA and/or MCA occlusions who received intra-arterial therapy. The collaterals were graded on CTA. Univariate and multivariate analyses were used to investigate the association between the dichotomized leptomeningeal collateral score and functional outcomes at 3-months mRS ≤2, mortality, and intracranial hemorrhages.

RESULTS: Eighty-seven patients were included. The median age was 66 years (interquartile range, 54–76 years) and the median NIHSS score at admission was 18 (interquartile range, 14–20). The leptomeningeal collateral score 3 was found to have significant association with the good functional outcome at 3 months: OR = 3.13; 95% CI, 1.25–7.825; $P = .016$. This association remained significant when adjusted for the use of IV tissue plasminogen activator: alone, OR = 2.998; 95% CI, 1.154–7.786; $P = .024$; and for IV tissue plasminogen activator and other confounders (age, baseline NIHSS score, and Thrombolysis in Cerebral Infarction grades), OR = 2.985; 95% CI, 1.027–8.673; $P = .045$.

CONCLUSIONS: We found that poor arterial collateralization, defined as a collateral score of <3, was associated with poor outcome, after adjustment for recanalization success. We recommend that future studies include collateral scores as one of the predictors of functional outcome.

ABBREVIATIONS: IAT = intra-arterial therapy; IQR = interquartile range

Intravenous tissue plasminogen activator is the only proved reperfusion therapy for acute ischemic stroke. However, a narrow therapeutic time window (<4.5 hours) limits its use because the clinical effectiveness is critically time-dependent.[1-3] In addition, recanalization rates with IV-tPA are low in the setting of large-artery occlusion, (eg, ICA occlusion <10%).[4-6] Intra-arterial therapy (IAT) has higher recanalization rates than intravenous thrombolysis, but this result has not been matched by concordant improvement in clinical outcomes.[7-9] Two recent randomized trials comparing IAT with IV-tPA, the Interventional Management of Stroke III trial and the Local versus Systemic Thrombolysis for Acute Ischemic Stroke trial, did not demonstrate superiority.[10,11]

Inadequate arterial collateralization is a possible mechanism to explain the mismatch between recanalization success and clinical outcome, apart from the presence of an already infarcted ischemic core and an incomplete microcirculatory reperfusion after focal cerebral ischemia.[12,13] A favorable arterial collateralization as determined by a robust leptomeningeal anastomoses profile may enhance recanalization, improve downstream reperfusion, reduce the extent of infarct core and ischemic lesion growth, decrease hemorrhagic transformation, and improve outcome postrevascularization.[14-16]

The leptomeningeal collateral scoring system based on CTA correlates with clinical outcome.[17-21] However, its role in IAT is unclear. We hypothesized that a poor leptomeningeal CTA score predicts clinical futility in patients undergoing IAT independent of recanalization status.

Received July 25, 2013; accepted August 26.

From the Melbourne Brain Centre (S.S.R., B.Y.) and Neurointervention Service (P.M., R.D., B.Y.), Department of Radiology, Royal Melbourne Hospital, Parkville, Victoria, Australia; and Department of Mathematics and Statistics (L.C.), and National Stroke Research Institute (L.C.), Florey Neuroscience Institutes, Austin Health, University of Melbourne, Parkville, Victoria, Australia.

Please address correspondence to Bernard Yan, MD, Royal Melbourne Hospital, 300 Grattan St, Parkville, Victoria 3050, Australia; e-mail: Bernard.yan@mh.org.au

http://dx.doi.org/10.3174/ajnr.A3862

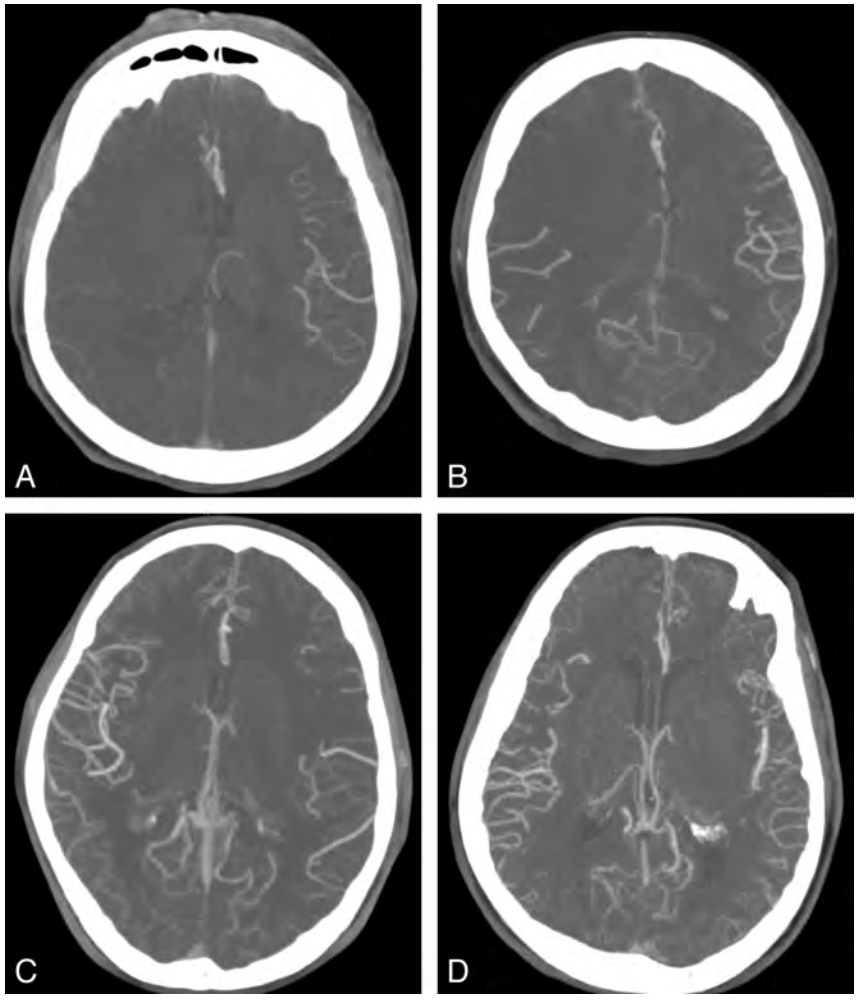

FIG 1. Leptomeningeal collateral CTA scores; *A*, score = 0; *B*, score = 1; *C*, score = 2; *D*, score = 3.

MATERIALS AND METHODS

Study Design and Patient Cohort

This was a single-center retrospective review of 104 patients with acute ischemic stroke with ICA and/or MCA occlusion who received IAT at the Royal Melbourne Hospital from January 2008 to March 2013. The local research and ethics committee granted the study approval.

Clinical parameters, identified through computerized data bases, were prospectively collected. The following parameters were recorded in a specific data bank: 1) demographics (age, sex); 2) medical history and risk factors such as hypertension (previous clinical diagnosis or regular treatment with antihypertensive medication), diabetes mellitus (previous diagnosis or current treatment with insulin or oral hypoglycemic medication), hypercholesterolemia (previous diagnosis or current treatment with lipid-lowering medication), atrial fibrillation (previous diagnosis or evident on admission), coronary artery disease, history of previous stroke or TIA; 3) "time from onset of symptoms to CTA" (defined from the time of symptom onset or from the time when the patient was last seen neurologically well, to the time of CTA), "time from onset of symptoms to recanalization" (defined from the time of symptom onset, or from the time when the patient was last seen neurologically well, to the time of intervention with any form of IAT), administration of IV-tPA before endovascular therapy, administration of intra-arterial tPA; and 4) clinical outcome variables: 3-month mRS score, intracranial hemorrhage, and 1-month mortality. The baseline severity of neurologic deficits was graded on admission according to the NIHSS.

CTA and DSA Analysis

CTAs of all patients were reviewed by 3 neurointerventionists (B.Y., P.M., and R.D.), with consensus opinion reached on collateral supply. The reviewers were blinded to all clinical information during the consensus collateral grading. The CTA source images (20-mm, axial) were edited with MPR technique for assessment of leptomeningeal collaterals based on distribution of vessels at the Sylvian fissure and the leptomeningeal convexity. The MPR images were assessed with an MIP technique at 32 mm to evaluate the leptomeningeal collaterals. Collateral statuses were divided into 4 categories (Fig 1): score 0 = absence of contrast reaching the cortical surface of the affected hemisphere; score 1 = contrast reaching the cortical surface but not the Sylvian fissure; score 2 = contrast reaching the Sylvian fissure but opacifying <50% of hemisphere; score 3 = contrast reaching the Sylvian fissure and opacifying >50% of the hemisphere.

The Thrombolysis in Cerebral Infarction system was used to grade recanalization success.[22] TICI grade 0 is no perfusion and no antegrade flow beyond the point of occlusion. TICI grade 1 is penetration with minimal perfusion. The contrast material passes beyond the area of obstruction but fails to opacify the entire cerebral bed distal to the obstruction for the duration of the angiographic run. TICI grade 2 is partial perfusion. The contrast material passes beyond the obstruction and opacifies the arterial bed distal to the obstruction. However, the rate of entry of contrast into the vessel distal to the obstruction or its rate of clearance from the distal bed or both are perceptibly slower than its entry into and/or clearance from comparable areas not perfused by the previously occluded vessel (eg, the opposite cerebral artery or the arterial bed proximal to the obstruction). In TICI grade 2a, only partial filling (less than two-thirds) of the entire vascular territory is visualized; in TICI grade 2b, complete filling of all of the expected vascular territory is visualized, but the filling is slower than normal. TICI grade 3 is complete perfusion; antegrade flow into the bed distal to the obstruction occurs as promptly as that into the obstruction and clearance.

Statistics

Statistical analysis was performed by using the STATA, Version 12 IC statistics package (StataCorp, College Station, Texas). We in-

cluded the following baseline clinical variables: age, sex, comorbidities (history of hypertension, diabetes, atrial fibrillation, coronary artery disease, TIA, or stroke), baseline NIHSS score, IV-tPA, intra-arterial tissue plasminogen activator, onset time to CTA, and onset time to recanalization. Continuous variables were reported as median ± interquartile range (IQR). Categoric variables were reported as proportions. *P* values were reported by using the Fisher exact test for categoric variables and the Wilcoxon-Mann-Whitney rank sum test for continuous variables (age, NIHSS score, and time-to-event data). Effect sizes were reported as odds ratios for categoric variables and Hodges-Lehman median differences for continuous variables (age, NIHSS score, and time-to-event data). Receiver operating characteristic analysis curves were used to determine the collateral score threshold with functional outcome (3-month mRS score). Univariate and multivariate analyses were used to investigate the association between the dichotomized leptomeningeal collateral score with functional outcomes, mortality, and intracranial hemorrhages. Given the strong clinical association with clinical outcomes, we planned a priori to include the following independent variables in the model: age, baseline NIHSS score, TICI grade, and IV-tPA. A 2-sided *P* value <.05 was considered significant.

RESULTS

Of the initial 104 patients with acute ischemic stroke with ICA and/or MCA occlusion who underwent IAT, CTA was not available for 14 patients before IAT. Three patients had poor image quality on CTA, and these patients were excluded. Eighty-seven patients with both adequate CTA and angiographic data with clinical outcome (mRS) at 90 days available were entered into the leptomeningeal collateral assessment. The baseline characteristics did not differ in a statistically significant manner between the patients with and without CTA (Table 1). In the CTA group, the median age was 66 years (IQR, 54–76 years). Fifty (57%) patients were men. The median NIHSS score at admission was 18 (IQR, 14–20). Forty (46%) subjects were treated with IV-tPA; 13 subjects (15%) received intra-arterial tPA. Sixty-five patients (75%) were treated with the Solitaire device (Covidien, Irvine, California), 10 (12%) patients were treated with the Merci retriever (Concentric Medical, Mountain View, California), and 3 (3%) were treated with the Penumbra System (Penumbra, Alameda, California).

Table 1: Baseline characteristics of the patient cohort with and without CTA

Baseline Characteristics	Patients with CTA (*n* = 87)	Patients without CTA (*n* = 17)	*P* Value[a]
Age (yr) (median) (IQR)	66 (54–76)	65 (56–73)	.954
Male sex	50 (58%)	11 (65%)	.788
Baseline NIHSS score, (median) (IQR)	18 (14–20)	21 (14–24)	.083
IV-tPA	40 (46%)	5 (29%)	.286
IA-tPA	13 (15%)	2 (12%)	<.999
Hypertension	40 (46%)	5 (29%)	.286
Diabetes	11 (13%)	3 (18%)	.697
Dyslipidemia	26 (30%)	1 (6%)	.065
Atrial fibrillation	29 (33%)	2 (12%)	.089
Coronary artery disease	11 (13%)	0 (0%)	.204
Previous stroke or TIA	13 (15%)	1 (6%)	.457
TICI grade 2b-3	60 (69%)	11 (65%)	.779
Onset to CT[b] (min) (median) (IQR)	90 (72–136)	90 (70–130)	.926
Onset to recanalization[c] (min) (median) (IQR)	329 (274–398)	360 (322–395)	.286

Note:—IA-tPA indicates intra-arterial tissue plasminogen activator.
[a] *P* values reported using the Fisher exact test for categoric variables and the Wilcoxon-Mann-Whitney rank sum test for continuous variables (age, NIHSS score, and time-to-event data).
[b] Symptom onset or from the time when the patient was last seen neurologically well to the time of CT.
[c] Time from symptom onset or from the time when the patient was last seen neurologically well to the time of intervention with any form of IAT.

Leptomeningeal Collaterals

According to the leptomeningeal score, 34 subjects (39%) were graded as three, 30 subjects (35%) were graded as two, 12 subjects (14%) were graded as 1, and 11 subjects (13%) were graded as zero. Receiver operating characteristic analysis

Table 2: Comparison of patients for the dichotomized leptomeningeal collateral score

Characteristics	Collateral Score 3 (*n* = 34)	Collateral Score 0–2 (*n* = 53)	Effect Size[a] (95% CI)	*P* Value[b]
Baseline characteristics				
Male sex	16 (47%)	34 (64%)	2.013 (0.844–4.802)	.127
NIHSS score, median (IQR)	15.5 (11–20)	18 (14–22)	2 (0–5)	.116
Hypertension	18 (53%)	22 (42%)	1.585 (0.671–3.745)	.379
Diabetes	3 (9%)	8 (15%)	0.544 (0.146–2.067)	.517
Dyslipidemia	10 (29%)	16 (30%)	0.964 (0.381–2.442)	<.999
AF	10 (30%)	19 (36%)	0.746 (0.299–1.863)	.643
CAD	6 (18%)	5 (9%)	2.057 (0.606–6.975)	.327
Previous stroke or TIA	4 (12%)	9 (17%)	0.652 (0.195–2.204)	.556
Process-of-care characteristics				
IV-tPA	22 (65%)	18 (34%)	3.565 (1.455–8.729)	.008
IA-tPA	2 (6%)	11 (21%)	0.239 (0–1.042)	.070
Onset to CTA[c] (min) (median) (IQR)	90 (63–124)	90 (75–137)	4 (−12–24)	.651
Recanalization[d] (min) (median) (IQR)	146 (86.5–274)	175 (128.68–276.5)	−32.5 (−72–14)	.169
TICI 2b-3	25 (74%)	35 (66%)	1.429 (0.552–3.696)	.488

Note:—IA-tPA indicates intra-arterial tissue plasminogen activator; AF, atrial fibrillation; CAD, coronary artery disease.
[a] Effect sizes reported as odds ratios for categoric variables and Hodges-Lehman median differences for continuous variables (age, NIHSS score, and time-to-event data).
[b] *P* values reported using the Fisher exact test for categoric variables and the Wilcoxon-Mann-Whitney rank sum test for continuous variables (age, NIHSS score, and time-to-event data).
[c] Symptom onset or from the time when the patient was last seen neurologically well to the time of CTA.
[d] Time from symptom onset or from the time when the patient was last seen neurologically well to the time of intervention with any form of intra-arterial therapy.

demonstrated the suitability of the collateral score ≥3 for determining good functional outcome of mRS ≤2 with an area under the curve of 0.6513 (sensitivity, 51.1%; specificity, 73.8%). The leptomeningeal score was dichotomized into good (score = 3) and poor (score = 0–2) on the basis of the receiver operating characteristic analysis. A higher percentage of IV-tPA was administered for a collateral score of 3 than for a collateral score of 0–2, (P = .008). The remainder of the baseline clinical variables did not differ in a statistically significant way between the 2 groups (Table 2).

Outcome

Three-month outcome was favorable (mRS 0–2) in 47 subjects (54%), and the remaining 40 subjects (46%) had mRS scores of 3–6 (Fig 2). Patients with a good collateral score of 3 had higher odds of good functional outcome than patients with a collateral score of 0–2 (OR = 3.130; 95% CI, 1.252–7.825; P = .016). This finding remained significant after adjustment for administration of IV-tPA (OR = 2.998; 95% CI, 1.154–7.786; P = .024). In the multivariate analysis, patients with a collateral score of 3 had significantly higher odds of good outcome at 3-month follow-up after adjustment for age, baseline NIHSS score, IV-tPA, and TICI grades (adjusted OR = 2.985; 95% CI, 1.027–8.673; P = .045) (Table 3).

Survival

Of the 13 deaths at 1 month, patients with poor collateral scores of 0–2 exhibited a trend toward a higher death rate than those with a collateral score of 3 (11 versus 2) (OR = 0.239; 95% CI, 0.049–1.153; P = .070), though no statistically significant differences were found.

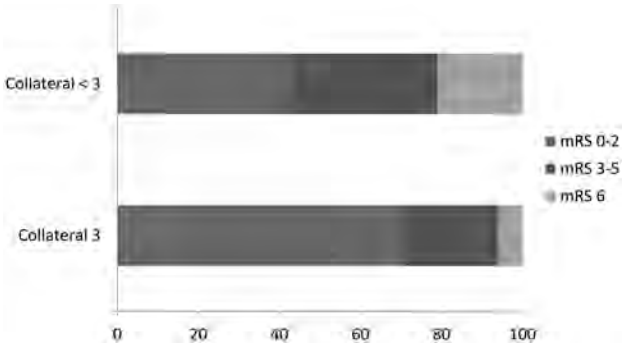

FIG 2. Distribution of mRS scores according to the leptomeningeal collateral scores.

Intracranial Hemorrhage

Although patients with a good collateral score of 3 had fewer episodes of intracranial hemorrhage than patients with a poor collateral score of 0–2 (4 versus 13), no statistically significant difference was detected (OR = 0.41; 95% CI, 0.122–1.385; P = .174).

DISCUSSION

We found that a favorable pattern of leptomeningeal collaterals, as measured by CTA on admission, was associated with improved functional outcomes at 3 months in a cohort of patients with acute ischemic stroke with ICA or proximal MCA occlusion. In a multivariate model, a good leptomeningeal collateral score remained independently associated with good clinical outcome after adjustment for age, baseline NIHSS score, IV-tPA, and recanalization status.

Various studies have used CTA to score collaterals status[14,17,19,20,23] with either CTA source images or by using MIP. Tan et al[17] demonstrated that CTA-MIP was the best technique to quantify the degree of collateral circulation. In their retrospective analysis, they reported a good correlation between the CTA-based collateral score and the final infarct volume within 6 months.[17] In another study, Miteff et al[14] assessed retrograde filling of the MCA by 3 categories of collateral scoring and concluded that a good collateral status was one of the significant univariate predictors of favorable outcome.[14] Menon et al[21] included 138 patients (MCA-M1 and/or intracranial occlusion) in a retrospective single-center study and demonstrated good regional leptomeningeal anastomoses scores in 37.6% of patients, which correlated strongly with the size of the infarct core at baseline and were a strong independent predictor of final infarct and clinical outcome.

In a recent study, Souza et al[23] found that CTA collaterals correlate with admission diffusion-weighted imaging infarct size and that a malignant collateral profile is highly specific for large admission DWI lesion size and poor functional outcome. In another study, Angermaier et al[24] demonstrated that the CTA collateral grade was an independent predictor of final infarct volume in patients with stroke treated with endovascular therapy. On the other hand, Rosenthal et al[18] reported that CTA collaterals had a positive impact on the outcomes of patients who did not achieve complete recanalization and had no impact in patients who were completely recanalized. Tan et al[25] reported that good CTA collaterals correlated with improved outcomes in uni- but not in multivariate analyses. Our study reveals that a good CTA collateral score had a positive impact on the outcomes of patients in

Table 3: Univariate analysis of associations for outcomes for the dichotomized leptomeningeal score

Outcome	Collateral Score 3 (n = 34)	Collateral Score 0–2 (n = 53)	ORs (95% CIs)					
			Unadjusted	P Value[a]	Adjusted for IV-tPA	P Value[b]	Adjusted[c]	P Value[b]
Clinical outcome mRS ≤2 at 3 months	24 (71%)	23 (43%)	3.13 (1.252–7.825)	.016	2.998 (1.154–7.786)	.024	2.985 (1.027–8.673)	.045
Intracranial hemorrhage	4 (12%)	13 (25%)	0.41 (0.122–1.385)	.174	0.5 (0.141–1.770)	.283	0.510 (0.141–1.850)	.306
Mortality at 1 month	2 (6%)	11 (21%)	0.239 (0.049–1.153)	.070	0.21 (0.041–1.073)	.061	0.215 (0.036–1.284)	.092

[a] Fisher exact test.
[b] Logistic regression.
[c] Adjusted for age, baseline NIHSS score, IV-tPA, and TICI grades.

both uni- and multivariate analyses independent of recanalization status.

The system of leptomeningeal anastomoses is anastomotic connections between distal branches of the cerebral arteries on the surface of the brain that permit blood flow from the territory of an unobstructed artery into the territory of an occluded artery and constitute the secondary network of cerebral collateral circulation apart from the circle of Willis.[26] Although the criterion standard for the assessment of leptomeningeal anastomoses is conventional DSA, the extent of leptomeningeal anastomoses formation seen on conventional DSA and with clinical outcome correlates well with collateral blood flow as assessed by CTA.[15,27,28] CTA is quicker, simpler, and noninvasive and uses IV-administered contrast to visualize the extent of leptomeningeal anastomoses with intra- and extracranial vasculature.[19,21]

There is currently no consensus on what the presence or absence of collateral circulation means with respect to treatment choices for patients with acute ischemic stroke. Some authors believe a minority of patients with robust leptomeningeal collateral circulation will have minimal damage and experience excellent recovery without recanalization.[29] On the other hand, some neurointerventionalists may want to try more aggressive IAT because there may be salvageable tissue in patients with good collateral vessel formation. Given the risks inherent in the therapeutic procedure and the clinical risk of futile recanalization,[30] practitioners need a way to consistently select patients whom IAT is likely to benefit rather than harm. Given the significance of leptomeningeal collaterals, they should be taken into account with other validated scoring systems, namely the Houston Intra-Arterial Therapy [30] and the Totaled Heath Risks in Vascular Events score,[31] in patient selection for IAT.

Our study has some limitations. First, selection bias is unavoidable in a retrospective single-center study. We sought to minimize reading bias by blinding the observers to clinical data and consensus achieved for the collateral grading. The CTA collateral scoring system was modified from Tan et al.[17] Although our collateral grading derived from a consensus by 3 experienced neurointerventionists, the utility and value of the score requires further validation in a larger study before collateral scores are used as a primary means of selecting patients for revascularization therapy. Potential biases may have influenced the selection of cases for IAT on the basis of the CTA and clinical data.

CONCLUSIONS

Evaluation of the leptomeningeal collateral blood supply before IAT for anterior circulation intracranial arterial occlusion stroke (ICA and/or MCA) with a collateral score based on CTA-MIP reconstructions is independently associated with functional outcome at 3 months. We believe that leptomeningeal collateral assessment should be included in future trials investigating the clinical efficacy of IAT.

REFERENCES

1. The National Institute of Neurological Disorders and Stroke rt-PA Stroke Study Group. **Tissue plasminogen activator for acute ischemic stroke.** *N Engl J Med* 1995;333:1581–87
2. Wahlgren N, Ahmed N, Eriksson N, et al. **Multivariable analysis of outcome predictors and adjustment of main outcome results to baseline data profile in randomized controlled trials Safe Implementation of Thrombolysis in Stroke-Monitoring Study (SITS-MOST).** *Stroke* 2008;39:3316–22
3. Lees KR, Bluhmki E, von Kummer R, et al. **Time to treatment with intravenous alteplase and outcome in stroke: an updated pooled analysis of ECASS, ATLANTIS, NINDS, and EPITHET trials.** *Lancet* 2010;375:1695–703
4. Bhatia R, Hill MD, Shobha N, et al**. Low rates of acute recanalization with intravenous recombinant tissue plasminogen activator in ischemic stroke: real-world experience and a call for action.** *Stroke* 2010;41:2254–58
5. Christou I, Felberg RA, Demchuk AM, et al. **Intravenous tissue plasminogen activator and flow improvement in acute ischemic stroke patients with internal carotid artery occlusion.** *J Neuroimaging* 2002;12:119–23
6. Zangerle A, Kiechl S, Spiegel M, et al. **Recanalization after thrombolysis in stroke patients: predictors and prognostic implications.** *Neurology* 2007;68:39–44
7. Meyers PM, Schumacher HC, Connolly ES Jr, et al. **Current status of endovascular stroke treatment.** *Circulation* 2011;123:2591–601
8. Smith WS, Sung G, Saver J, et al. **Mechanical thrombectomy for acute ischemic stroke: final results of the Multi MERCI trial.** *Stroke* 2008;39:1205–12
9. Clark W, Lutsep H, Barnwell S, et al. **The Penumbra Pivotal Stroke trial: safety and effectiveness of a new generation of mechanical devices for clot removal in intracranial large vessel occlusive disease.** *Stroke* 2009;40:2761–68
10. Broderick JP, Palesch YY, Demchuk AM, et al, for the Interventional Management of Stroke (IMS) III Investigators. **Endovascular therapy after intravenous t-PA versus t-PA alone for stroke.** *N Engl J Med* 2013;368:893–903
11. Ciccone A, Valvassori L, Nichelatti M, et al. **Endovascular treatment for acute ischemic stroke.** *N Engl J Med* 2013;368:904–13
12. Chimowitz MI. **Endovascular treatment for acute ischemic stroke: still unproven.** *N Engl J Med* 2013;368:954–55
13. Dalkara T, Arsava EM. **Can restoring incomplete microcirculatory reperfusion improve stroke outcome after thrombolysis?** *J Cereb Blood Flow Metab* 2012;32:2091–209
14. Miteff F, Levi CR, Bateman GA, et al. **The independent predictive utility of computed tomography angiographic collateral status in acute ischaemic stroke.** *Brain* 2009;132(pt 8):2231–2238
15. Bang OY, Saver JL, Buck BH, et al, for the UCLA Collateral Investigators. **Impact of collateral flow on tissue fate in acute ischaemic stroke.** *J Neurol Neurosurg Psychiatry* 2007;79:625–29
16. Bang OY, Saver JL, Kim SJ, et al. **Collateral flow predicts response to endovascular therapy for acute ischemic stroke.** *Stroke* 2011;42:693–99
17. Tan JC, Dillon WP, Liu S, et al. **Systematic comparison of perfusion-CT and CT-angiography in acute stroke patients.** *Ann Neurol* 2007;61:533–43
18. Rosenthal ES, Schwamm LH, Roccatagliata L, et al. **Role of recanalization in acute stroke outcome: rationale for a CT angiogram-based "benefit of recanalization" model.** *AJNR Am J Neuroradiol* 2008;29:1471–75
19. Maas MB, Lev MH, Ay H, et al. **Collateral vessels on CT angiography predict outcome in acute ischemic stroke.** *Stroke* 2009;40:3001–05
20. Lima FO, Furie KL, Silva GS, et al. **The pattern of leptomeningeal collaterals on CT angiography is a strong predictor of long-term functional outcome in stroke patients with large vessel intracranial occlusion.** *Stroke* 2010;41:2316–22
21. Menon BK, Smith EE, Modi J, et al. **Regional leptomeningeal score on CT angiography predicts clinical and imaging outcomes in patients with acute anterior circulation occlusions.** *AJNR Am J Neuroradiol* 2011;32:1640–45
22. Higashida RT, Anthony J Furlan, et al. **Trial design and reporting standards for intraarterial cerebral thrombolysis for acute ischemic stroke.** *J Vasc Interv Radiol* 2003;14(9 Pt 2):S493–94
23. Souza LC, Yoo AJ, Chaudhry ZA, et al. **Malignant CTA collateral profile**

is highly specific for large admission DWI infarct core and poor outcome in acute stroke. *AJNR Am J Neuroradiol* 2012;33:1331–36
24. Angermaier A, Langner S, Kirsch M, et al. **CT-angiographic collateralization predicts final infarct volume after intra-arterial thrombolysis for acute anterior circulation ischemic stroke.** *Cerebrovasc Dis* 2011;31:177–84
25. Tan IY, Demchuk AM, Hopyan J, et al. **CT angiography clot burden score and collateral score: correlation with clinical and radiologic outcomes in acute middle cerebral artery infarct.** *AJNR Am J Neuroradiol* 2009;30:525–31
26. Liebeskind DS. **Collaterals in acute stroke: beyond the clot.** *Neuroimaging Clin N Am* 2005;15:553–573, x
27. Wildermuth S, Knauth M, Brandt T, et al. **Role of CT angiography in patient selection for thrombolytic therapy in acute hemispheric stroke.** *Stroke* 1998;29:935–38
28. Liebeskind DS. **Collateral circulation.** *Stroke* 2003;34:2279–84
29. Tomsick TA, Khatri P, Jovin T, et al. **Equipoise among recanalization strategies.** *Neurology* 2010;74:1069–76
30. Hallevi Hen, Barreto AD, Liebeskind DS, et al. **Identifying patients at high risk for poor outcome after intra-arterial therapy for acute ischemic stroke.** *Stroke* 2009;40:1780–85
31. Flint AC, Kamel H, Rao VA, et al. **Validation of the Totaled Heath Risks In Vascular Events (THRIVE) score for outcome prediction in endovascular stroke treatment.** *Int J Stroke* 2014;9:32–39

Pretreatment ADC Histogram Analysis Is a Predictive Imaging Biomarker for Bevacizumab Treatment but Not Chemotherapy in Recurrent Glioblastoma

B.M. Ellingson, S. Sahebjam, H.J. Kim, W.B. Pope, R.J. Harris, D.C. Woodworth, A. Lai, P.L. Nghiemphu, W.P. Mason, and T.F. Cloughesy

ABSTRACT

BACKGROUND AND PURPOSE: Pre-treatment ADC characteristics have been shown to predict response to bevacizumab in recurrent glioblastoma multiforme. However, no studies have examined whether ADC characteristics are specific to this particular treatment. The purpose of the current study was to determine whether ADC histogram analysis is a bevacizumab-specific or treatment-independent biomarker of treatment response in recurrent glioblastoma multiforme.

MATERIALS AND METHODS: Eighty-nine bevacizumab-treated and 43 chemotherapy-treated recurrent glioblastoma multiformes never exposed to bevacizumab were included in this study. In all patients, ADC values in contrast-enhancing ROIs from MR imaging examinations performed at the time of recurrence, immediately before commencement of treatment for recurrence, were extracted and the resulting histogram was fitted to a mixed model with a double Gaussian distribution. Mean ADC in the lower Gaussian curve was used as the primary biomarker of interest. The Cox proportional hazards model and log-rank tests were used for survival analysis.

RESULTS: Cox multivariate regression analysis accounting for the interaction between bevacizumab- and non-bevacizumab-treated patients suggested that the ability of the lower Gaussian curve to predict survival is dependent on treatment (progression-free survival, $P = .045$; overall survival, $P = .003$). Patients with bevacizumab-treated recurrent glioblastoma multiforme with a pretreatment lower Gaussian curve $> 1.2\ \mu m^2/ms$ had a significantly longer progression-free survival and overall survival compared with bevacizumab-treated patients with a lower Gaussian curve $< 1.2\ \mu m^2/ms$. No differences in progression-free survival or overall survival were observed in the chemotherapy-treated cohort. Bevacizumab-treated patients with a mean lower Gaussian curve $> 1.2\ \mu m^2/ms$ had a significantly longer progression-free survival and overall survival compared with chemotherapy-treated patients.

CONCLUSIONS: The mean lower Gaussian curve from ADC histogram analysis is a predictive imaging biomarker for bevacizumab-treated, not chemotherapy-treated, recurrent glioblastoma multiforme. Patients with recurrent glioblastoma multiforme with a mean lower Gaussian curve $> 1.2\ \mu m^2/ms$ have a survival advantage when treated with bevacizumab.

ABBREVIATIONS: ADC_L = apparent diffusion coefficient in the lower Gaussian curve; GBM = glioblastoma multiforme; HR = hazard ratio; OS = overall survival; PFS = progression-free survival; UCLA = University of California, Los Angeles; VEGF = vascular endothelial growth factor

Malignant gliomas, including anaplastic astrocytomas, anaplastic oligodendrogliomas, anaplastic mixed oligoastrocytomas, and glioblastoma multiforme (GBM), account for almost 80% of malignant primary brain tumors.[1] GBM, the most aggressive and malignant type of primary brain tumor, has a mean survival of only 12–14 months under the current standard of care of radiotherapy combined with concurrent temozolomide, along with adjuvant temozolomide.[2,3] GBMs are highly vascular tumors, recruiting existing vasculature and generating neovasculature from excessive levels of circulating angiogenic growth factors, including vascular endothelial growth factor (VEGF). The

Received June 25, 2013; accepted after revision August 9.

From the Departments of Radiological Sciences (B.M.E., H.J.K., W.B.P., R.J.H., D.C.W.), Biomedical Physics (B.M.E., R.J.H., D.C.W.), Bioengineering (B.M.E.), and Neurology (A.L., P.L.N., T.F.C.), David Geffen School of Medicine, University of California Los Angeles, Los Angeles, California; and Department of Medicine (S.S., W.P.M.), Princess Margaret Hospital, University of Toronto, Toronto, Ontario, Canada.

Benjamin M. Ellingson and Solmaz Sahebjam contributed equally to this manuscript.

This work was supported by the following: National Institutes of Health/National Cancer Institute R21CA167354 (B.M.E.); UCLA Institute for Molecular Medicine Seed Grant (B.M.E.); UCLA Radiology Exploratory Research Grant (B.M.E.); University of California Cancer Research Coordinating Committee Grant (B.M.E.); American College of Radiology Imaging Network Young Investigator Initiative Grant (B.M.E.); Art of the Brain (T.F.C.); Ziering Family Foundation in memory of Sigi Ziering (T.F.C.); Singleton Family Foundation (T.F.C.); and Clarence Klein Fund for Neuro-Oncology (T.F.C.).

Paper previously presented at: Annual Meeting of the American Society of Neuroradiology; May 18–23, 2013; San Diego, California.

Please address correspondence to Benjamin M. Ellingson, PhD, Department of Radiological Sciences, David Geffen School of Medicine, University of California, Los Angeles, 924 Westwood Blvd, Suite 615, Los Angeles, CA 90024; e-mail: bellingson@mednet.ucla.edu

Indicates open access to non-subscribers at www.ajnr.org

http://dx.doi.org/10.3174/ajnr.A3748

highly vascular nature of these tumors has led to a new class of antiangogenic agents, for which there are many ongoing clinical trials in GBM.[4-6]

Standard imaging techniques are limited in their ability to evaluate the effectiveness of antiangiogenic therapy in malignant gliomas due to a reduction in contrast enhancement. These limitations have resulted in a surge of more advanced imaging biomarkers aimed at predicting response to therapy, as summarized in various review articles.[7,8] Among these new imaging biomarkers showing promise are diffusion MR imaging techniques,[9-18] including ADC histogram analysis. Previous results have shown that pretreatment ADC histogram analysis performed within the contrast-enhancing tumor regions can stratify patients with recurrent GBM into high- and low-risk groups. When using a double Gaussian mixed model to represent the ADC histogram, previous studies have shown that a lower mean value of the Gaussian curve (ADC_L) results in a significantly shorter progression-free survival (PFS) and overall survival (OS) in both single-institution[9] and multicenter clinical trial data[19] when evaluating bevacizumab in malignant gliomas. An important question remains as to whether ADC histogram analysis is a predictive biomarker specific to antiangiogenic therapy in recurrent GBM or whether it is a predictive biomarker independent of the particular treatment administered. In the current study, we performed ADC histogram analysis in patients with recurrent GBM from the University of California, Los Angeles (UCLA) treated with bevacizumab and those with recurrent GBM from the University of Toronto treated with a variety of chemotherapies and never exposed to bevacizumab, to determine whether ADC histogram analysis performed before treatment in recurrent GBM is a bevacizumab-specific or treatment-independent biomarker of treatment response.

MATERIALS AND METHODS

Patients

Eighty-nine patients with recurrent glioblastoma from UCLA treated with bevacizumab and 43 with recurrent glioblastoma from the University of Toronto treated with a variety of chemotherapies and never exposed to bevacizumab were included in this retrospective study. Data acquisition was performed in compliance with all applicable regulations of the Health Insurance Portability and Accountability Act. Bevacizumab-treated patients were retrospectively selected from the UCLA neuro-oncology data base from November 15, 2005, to August 31, 2010. All UCLA patients in this study signed institutional review board–approved informed consent to have their data included in our research data base. Bevacizumab-treated patients met the following criteria: 1) had pathologically confirmed GBM with recurrence based on MR imaging, clinical data, and/or histology; 2) were regularly treated every 2 weeks per cycle with bevacizumab (5 or 10 mg/kg body weight) alone or in combination with chemotherapy (carboplatin, irinotecan, etoposide, lomustine) at either the first (63 of 89 patients), second (22 of 89 patients), or third tumor recurrence (4 of 89 patients); 3) had baseline (pre-bevacizumab treatment) standard and diffusion MR images available for analysis; and 4) had treatment with bevacizumab at least 3 months after completion of radiation therapy to reduce the probability of pseudoprogression and treatment-induced necrosis. At the last evaluation, 72 of 89 bevacizumab-treated patients with recurrent GBM were deceased.

University of Toronto, chemotherapy-treated patients (n = 43) met the following criteria: 1) had pathologically confirmed GBM with recurrence based on MR imaging, clinical data, and/or histology; 2) were never treated with bevacizumab but instead were treated with continuous temozolomide (n = 17), were rechallenged with 5 days of temozolomide per 28-day cycle (n = 5), and were treated with etoposide (n = 4) or with lomustine (n = 17) at either the first (40 of 43 patients) or second tumor recurrence (3 of 43 patients); 3) had baseline (postrecurrence, pretreatment) standard and diffusion MR images available for analysis; and 4) had treatment at least 3 months after completion of radiation therapy to reduce the probability of pseudoprogression and treatment-induced necrosis. At the time of last evaluation, 41 of 43 chemotherapy-treated patients with recurrent GBM were deceased. The local ethics committee at the University of Toronto approved this retrospective study.

Standard and Diffusion MR Imaging

Standard and diffusion MR imaging data were acquired by using either a 1.5T or 3T MR imaging scanner (Sonata/Avanto/Trio/Verio; Siemens, Erlangen, Germany) using pulse sequences supplied by the manufacturer. Standard anatomic images included axial T1-weighted fast spin-echo or MPRAGE sequences, T2-weighted fast spin-echo, and T2-weighted FLAIR images. Diffusion MR images were acquired before injection of exogenous contrast agents. DWI was obtained with TE/TR = 80–110 ms/4–10 seconds, 1 average, section thickness = 5 mm with 1-mm intersection gap, matrix size = 128 × 128, and FOV = 22–25 cm by using a monopolar spin-echo echo-planar preparation. ADC images were calculated from acquired DWI with b=1000 s/mm^2 and b=0 s/mm^2 images. Additionally, gadopentetate dimeglumine–enhanced (Magnevist; Bayer HealthCare, Wayne, New Jersey; 0.1 mmol/kg) axial T1-weighted images were acquired shortly after contrast injection.

ADC Histogram Analysis

Contrast-enhancing tumor regions observed on pretreatment, postcontrast T1-weighted images were segmented by using standard techniques. Briefly, tumor ROIs were isolated by manually defining the relative region of tumor occurrence, thresholding postcontrast T1-weighted images within these regions by using an empiric threshold, and then manually editing the resulting masks to exclude any nontumor tissue. ADC values were then extracted from contrast-enhancing image voxels (Fig 1). A double Gaussian mixed model was then fit to the histogram data by using nonlinear regression in GraphPad Prism, Version 4.0c (GraphPad Software, San Diego, California). The double Gaussian model was defined as

$$p(ADC) = f \cdot N(\mu_{ADCL}, \sigma_{ADCL}) + (1 - f)\, N(\mu_{ADCH}, \sigma_{ADCH}),$$

where $p(ADC)$ is the probability of obtaining a particular value of ADC in the histogram, f is the relative proportion of voxels represented by the lower histogram, $N(\mu,\sigma)$ represents a normal (Gaussian) distribution with mean μ and SD σ, ADC_L represents the lower and ADC_H represents the larger of the 2 Gaussian distributions (Fig 1). The accuracy of model fits were manually examined to exclude erroneous results. In some cases, nonlinear

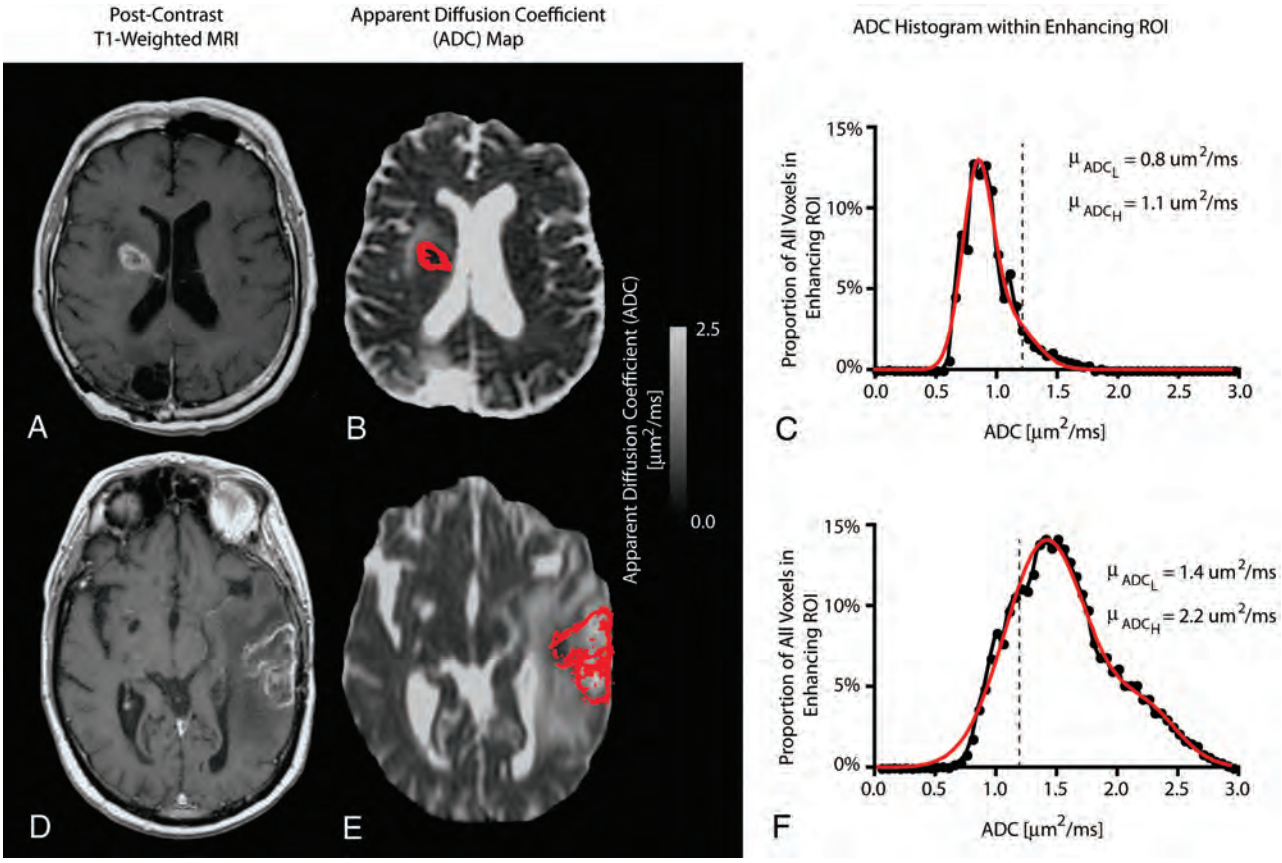

FIG 1. ADC histogram analysis in 2 representative patients with recurrent GBM. *A*, Postcontrast T1-weighted MR imaging. *B*, Apparent diffusion coefficient map. *C*, ADC histogram analysis of a 63-year-old patient with recurrent GBM treated with bevacizumab at first recurrence. This patient had $\mu_{ADCL} = 0.8\ \mu m^2/ms$, PFS = 17 days, and OS = 68 days from the first scanning date. *D*, Postcontrast T1-weighted MR imaging. *E*, ADC map. *F*, ADC histogram analysis of a 71-year-old patient with recurrent GBM treated with bevacizumab at first recurrence. This patient had $\mu_{ADCL} = 1.4\ \mu m^2/ms$ and did not progress or die >1238 days after the baseline MR imaging.

regression was rerun with different initial conditions until convergence was obtained. The mean of the lower Gaussian curve, μ_{ADCL}, was used as the primary biomarker for patient risk stratification. High-risk patients were identified by $\mu_{ADCL} \leq 1.2\ \mu m^2/ms$, whereas low-risk patients were identified by $\mu_{ADCL} > 1.2\ \mu m^2/ms$, based on empiric thresholds identified in previous studies.[9,10,19,20]

Definition of Tumor Progression

For UCLA patients, tumor recurrence was confirmed by using either direct pathologic confirmation, ^{18}F-FDOPA (3,4-dihydroxy-6-[^{18}F]-fluoro-L-phenylalanine) PET, or unequivocal evidence on MR imaging as indicated by a board-certified neuroradiologist. For University of Toronto data, tumor recurrence was confirmed by using either direct pathologic confirmation, unequivocal evidence on MR imaging as indicated by a board-certified neuroradiologist, or neurologic deterioration consistent with growing tumor. Unequivocal evidence on MR imaging was determined by >2 sequential months of increasing contrast enhancement on postcontrast T1-weighted images, along with evidence of increasing mass effect.

Statistical Analysis

Baseline characteristics of the 2 cohorts (those treated with bevacizumab on recurrence and those never treated with bevacizumab) were compared by using a *t* test and log-rank test for progression-free survival and overall survival. Kaplan-Meier curves were graphed by treatment type or by ADC_L group with the prespecified threshold of 1.2 $\mu m^2/ms$. Log-rank analysis and Cox hazard models were used to examine the hazard ratio of the ADC characteristics in the progression-free survival or overall survival within the cohort or within the ADC_L threshold. Multivariate Cox hazard models with covariates of age, treatment cohort, dichotomized ADC_L threshold, and the interaction between mean ADC_L and the 2 treatment cohorts were used to test the predictive classifier effect of ADC_L in the bevacizumab-treated group. For all analyses, $P < .05$ was considered statistically significant. Statistical analyses were performed with STATA, 12 (StataCorp, College Station, Texas).

RESULTS

No difference in age was found between the bevacizumab- and chemotherapy-treated cohorts (University of Toronto: mean, 55.3 ± 9.9 years of age; UCLA, mean = 58.0 ± 12 years of age; Student *t* test, $P = .17$). Similarly, no difference in PFS (University of Toronto: median = 76 days; UCLA: median = 127 days; log-rank, $P = .20$) or OS (University of Toronto: median = 250 days; UCLA: median = 304 days; log-rank, $P = .62$) was found between patients treated with bevacizumab at recurrence and those treated

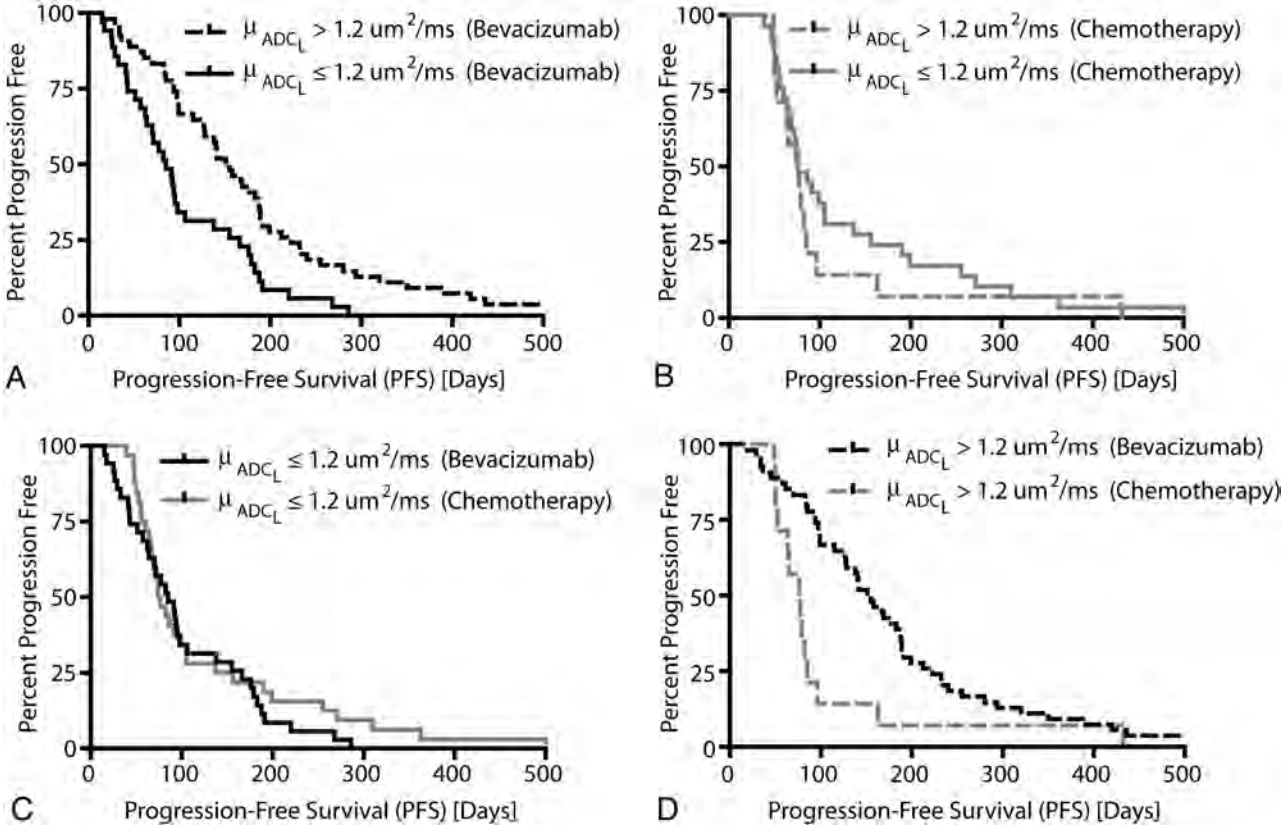

FIG 2. Progression-free survival comparisons between treatments (bevacizumab or chemotherapy) and ADC_L thresholds ($\mu_{ADCL} > 1.2$ μm^2/ms or $\mu_{ADCL} \leq 1.2$ μm^2/ms) in recurrent GBM. *A*, Comparison of PFS between $\mu_{ADCL} > 1.2$ μm^2/ms and $\mu_{ADCL} \leq 1.2$ μm^2/ms in bevacizumab-treated patients (log-rank, $P = .0006$). *B*, Comparison of PFS between $\mu_{ADCL} > 1.2$ μm^2/ms and $\mu_{ADCL} \leq 1.2$ μm^2/ms in chemotherapy-treated patients (log-rank, $P = .3737$). *C*, Comparison of PFS between bevacizumab- and chemotherapy-treated patients with recurrent GBM exhibiting $\mu_{ADCL} \leq 1.2$ μm^2/ms (log-rank, $P = .3675$). *D*, Comparison of PFS between bevacizumab and chemotherapy-treated patients exhibiting $\mu_{ADCL} > 1.2$ μm^2/ms (log-rank, $P = .0038$).

with chemotherapy and never receiving bevacizumab during their clinical history.

Consistent with previous reports,[9,19] univariate log-rank analysis applied to individual Kaplan-Meier curves indicated that bevacizumab-treated patients with $\mu_{ADCL} > 1.2$ μm^2/ms had a significantly longer PFS compared with bevacizumab-treated patients with $\mu_{ADCL} \leq 1.2$ μm^2/ms (Fig 2*A*; log-rank, median PFS = 153 days versus 85 days, HR = 0.4938, $P = .0006$). No difference in PFS was observed in the chemotherapy-treated group when stratified by mean ADC_L (Fig 2*B*; log-rank, HR = 1.324, $P = .3737$). For patients with pretreatment tumor $\mu_{ADCL} \leq 1.2$ μm^2/ms, no difference in PFS was observed between chemotherapy or bevacizumab treatment (Fig 2*C*; log-rank, HR = 0.8088, $P = .3675$). Patients with $\mu_{ADCL} > 1.2$ μm^2/ms, however, showed a significant PFS advantage when treated with bevacizumab compared with standard chemotherapies (Fig 2*D*; log-rank, HR = 0.4396, $P = .0038$). Using the lowest risk patients (bevacizumab-treated patients with $\mu_{ADCL} > 1.2$ μm^2/ms) as the baseline for comparison, multivariate Cox regression suggested that both age at diagnosis and the interaction between specific treatments and mean ADC_L were significant predictors of PFS (Cox model: overall $P = .0094$; age covariate: HR = 0.9823, $P = .036$; chemotherapy-treated $\times$ $\mu_{ADCL} > 1.2$ μm^2/ms: HR = 2.230, $P = .045$), where older patients and patients with $\mu_{ADCL} > 1.2$ μm^2/ms demonstrated a more favorable PFS.

Trends in overall survival were similar to those observed with progression-free survival. Consistent with previous studies, univariate log-rank analysis of Kaplan-Meier data suggested that patients with $\mu_{ADCL} > 1.2$ μm^2/ms had a significantly longer OS compared with bevacizumab-treated patients with $\mu_{ADCL} \leq 1.2$ μm^2/ms (Fig 3*A*; log-rank, median OS = 376 days versus 255 days, HR = 0.4883, $P = .0016$). No difference in OS was observed in the chemotherapy-treated group when stratified by mean ADC_L (Fig 3*B*; log-rank, HR = 1.691, $P = .0942$). Unlike bevacizumab-treated patients, patients with higher mean ADC_L treated with standard chemotherapy tended to have a shorter OS compared with patients exhibiting lower mean ADC_L in contrast-enhancing regions before treatment. No difference in OS was observed between chemotherapy- and bevacizumab-treated patients exhibiting $\mu_{ADCL} \leq 1.2$ μm^2/ms (Fig 3*C*; log-rank, HR = 0.6245, $P = .0516$), though chemotherapy-treated patients with $\mu_{ADCL} \leq 1.2$ μm^2/ms trended toward a longer OS compared with bevacizumab-treated patients (median OS = 309 days versus 255 days). Patients with $\mu_{ADCL} > 1.2$ μm^2/ms demonstrated a significantly longer OS when treated with bevacizumab compared with standard chemotherapy (Fig 3*D*; log-rank, HR = 1.960, $P = .0254$), showing almost double the median survival (median OS = 376 days versus 194 days). Again by using the lowest risk patients (bevacizumab-treated patients with $\mu_{ADCL} > 1.2$ μm^2/ms) as the baseline for comparison, multivariate Cox regression

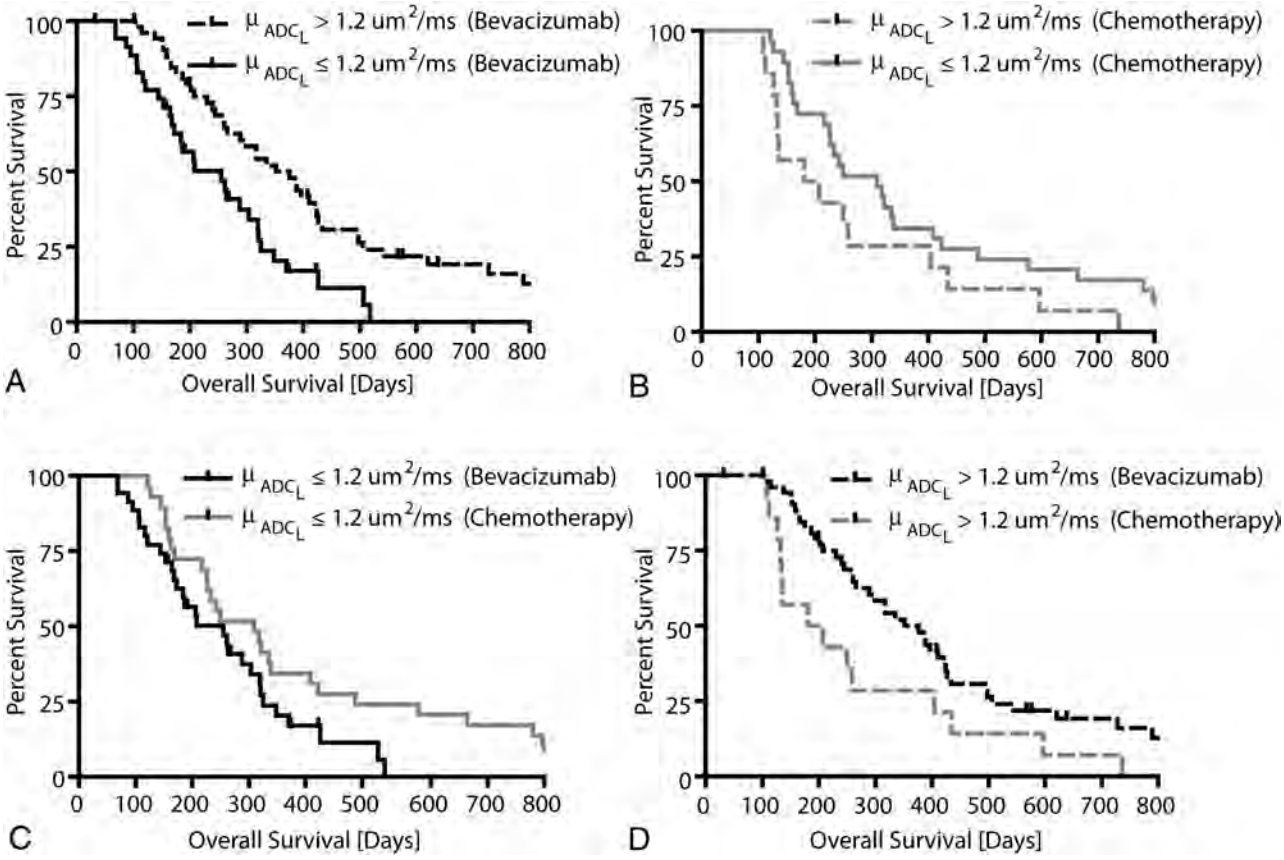

FIG 3. Overall survival comparisons between treatments (bevacizumab or chemotherapy) and ADC_L thresholds ($\mu_{ADCL} > 1.2\ \mu m^2/ms$ or $\mu_{ADCL} \leq 1.2\ \mu m^2/ms$) in recurrent GBM. *A*, Comparison of OS between $\mu_{ADCL} > 1.2\ \mu m^2/ms$ and $\mu_{ADCL} \leq 1.2\ \mu m^2/ms$ in bevacizumab-treated patients (log-rank, $P = .0016$). *B*, Comparison of OS between $\mu_{ADCL} > 1.2\ \mu m^2/ms$ and $\mu_{ADCL} \leq 1.2\ \mu m^2/ms$ in chemotherapy-treated patients (log-rank, $P = .0942$). *C*, Comparison of OS between bevacizumab- and chemotherapy-treated patients with recurrent GBM exhibiting $\mu_{ADCL} \leq 1.2\ \mu m^2/ms$ (log-rank, $P = .0516$). *D*, Comparison of OS between bevacizumab and chemotherapy-treated patients exhibiting $\mu_{ADCL} > 1.2\ \mu m^2/ms$ (log-rank, $P = .0254$).

suggested that mean ADC_L, treatment and the interaction between specific treatments and mean ADC_L were significant predictors of OS (Cox model: overall $P = .047$; $\mu_{ADCL} \leq 1.2\ \mu m^2/ms$, HR = 1.976, $P = .009$; chemotherapy: HR = 1.714, $P = .050$; chemotherapy × $\mu_{ADCL} > 1.2\ \mu m^2/ms$, HR = 0.2790, $P = .003$).

DISCUSSION

Although previous studies have demonstrated the ability of pretreatment ADC histogram analysis to predict recurrent GBM response to bevacizumab in both single-[9] and multicenter clinical trials,[19] a significant question remained as to whether this type of analysis is a predictive biomarker, specific to bevacizumab therapy, or whether it is a prognostic biomarker independent of the type of treatment. A previous study[9] did suggest that pretreatment ADC histogram analysis could predict response to recurrent GBM treated with bevacizumab, but not in matched patients with recurrent GBM treated with a non-VEGF-targeted investigative antiangiogenic agent. The patients treated with this non-VEGF-targeted investigative agent, however, were likely eventually treated with bevacizumab after tumor progression as per the standard of care for recurrent GBM in the United States. Unlike this previous investigation, the current study involved an international collaboration with a site where bevacizumab is not used routinely for recurrent GBM, allowing direct comparison of patients with recurrent GBM treated with bevacizumab with patients never exposed to bevacizumab during their clinical history. Results from the current study clearly indicate pretreatment ADC histogram analysis is a predictive imaging biomarker for bevacizumab (anti-VEGF) therapy, but not chemotherapy, within the context of recurrent glioblastoma.

Although perfusion MR imaging and MR spectroscopy have shown promise as early response biomarkers for bevacizumab once therapy has been initiated, there are currently no acceptable pretreatment clinical biomarkers for judicious preselection of patients with GBM who may maximally benefit from bevacizumab at recurrence. Results from the current study suggest that patients with recurrent GBM with a $\mu_{ADCL} > 1.2\ \mu m^2/ms$ within contrast-enhancing regions have a significant survival advantage when treated with bevacizumab compared with a standard chemotherapeutic agent, demonstrating nearly double the median PFS (153 days versus 76.5 days) and OS (376 days versus 194 days). Conversely, patients with $\mu_{ADCL} \leq 1.2\ \mu m^2/ms$ do not appear to benefit from bevacizumab therapy at recurrence, and it may, in fact, perform slightly worse than standard therapies (Fig 3*C*). These current results, along with results from previous studies,[9,19] support the use of ADC histogram analysis in recurrent GBM to guide the use of bevacizumab in second-line therapy.

The precise mechanism and biologic correlates for survival differences based on ADC histogram analysis remain controversial. In the current study, we demonstrated a decreased PFS and OS with a decrease in ADC for bevacizumab-treated patients with GBM; however, these trends may be specific to bevacizumab treatment at tumor recurrence. In a study involving newly diagnosed patients with GBM treated with bevacizumab, an ADC histogram analysis suggested that patients with $\mu_{ADCL} > 1.2\ \mu m^2/ms$ had a worse PFS and OS compared with patients demonstrating a tumor $\mu_{ADCL} \leq 1.2\ \mu m^2/ms$.[10] Differential gene expression analysis uncovered overexpression of various extracellular matrix genes in patients with upfront GBM with $\mu_{ADCL} > 1.2\ \mu m^2/ms$,[20] suggesting that an elevated ADC_L within newly diagnosed tumor may be influenced by extracellular matrix reorganization due to invading tumor. The biologic basis for the clear survival advantage of high ADC_L tumors treated with bevacizumab in the recurrent setting has not been validated with histology or gene-expression data and, therefore, remains speculative. The lack of response from low ADC_L tumors treated with bevacizumab in the recurrent setting may suggest either a more hypoxic or hypercellular tumor, because both of these factors may influence ADC measurement. Because bevacizumab-treatment-acquired resistance may result in transformation to a more aggressive, infiltrating tumor phenotype through prolonged hypoxia,[21,22] it is conceivable that a more hypoxic recurrent tumor presenting with a lower ADC_L before bevacizumab therapy may represent tumors with de novo resistance to bevacizumab. Future studies aimed at eliciting the precise biologic mechanism for observed differences in survival between ADC histogram-stratified recurrent GBMs are necessary to further guide therapy and treatment recommendations.

Study Limitations

An important advantage of the proposed ADC histogram analysis techniques used in the current study is the use of standard, clinically acquired diffusion MR imaging data for subsequent analysis, allowing retrospective comparison with other techniques at different institutions and use in controlled, multicenter clinical trials. Despite this advantage, the use of standard, clinical diffusion MR imaging parameters did not allow an ideal choice of b-values used to accurately estimate ADC. Per the recommendations of the National Cancer Institute Diffusion MR Imaging Consensus Conference,[23] ≥3 b-values (0 s/mm^2, >100 s/mm^2, and >500 s/mm^2) should be used for estimation of perfusion-insensitive ADC. Additionally, the use of standard, clinical diffusion MR images in ADC histogram analysis can be confounded by other pathologies; therefore, the possibility of confounding factors should also be considered.

Another limitation to the current study was its retrospective nature and the inability to control the timing of pretreatment MR imaging acquisitions. Studies have shown that in antiangiogenic therapies, the timing of MR imaging acquisitions is particularly important for the prediction of response.[24] Despite the retrospective nature of the current study, our results demonstrate that ADC maps obtained 1.5 weeks before initial treatment with bevacizumab allowed strong prediction of patient survival.

Last, patients treated with bevacizuamb were from one institution, and patients treated with chemotherapy were from a different institution; therefore, we were not able to account for potential site-specific differences in survival independent of therapy. In addition, despite similar criteria being used for determining tumor progression after therapy, tumor progression was determined at each site independently. Although the difference in progression-free and overall survival between institutions is likely to be small, this is a potential limitation to the current study.

CONCLUSIONS

Results suggest that mean ADC_L extracted from ADC histogram analysis is a predictive imaging biomarker for stratifying PFS and OS in bevacizumab-treated, but not chemotherapy-treated, recurrent glioblastoma. Results suggest that patients with recurrent GBM with a mean $ADC_L > 1.2\ \mu m^2/ms$ in pretreatment contrast-enhancing tumor regions have a survival advantage when treated with bevacizumab, whereas patients with mean $ADC_L \leq 1.2\ \mu m^2/ms$ may not benefit from bevacizumab.

Disclosures: Whitney B. Pope—*RELATED*: *Consulting Fee or Honorarium*: Genentech/Roche, *UNRELATED*: *Consultancy*: Amgen, Exelixis, Tocagen. Albert Lai—*UNRELATED*: *Consultancy*: Genentech/Roche,* *Comments*: Scientific Advisory Board. Warren P. Mason—*UNRELATED*: *Consultancy*: Roche, *Comments*: paid consultant for Hoffmann-La Roche, *Payment for Lectures (including service on Speakers Bureaus)*: Roche. Timothy F. Cloughesy—*RELATED*: *Grant*: Roche,* Genentech,* *Consulting Fee or Honorarium*: Roche, Genentech, *UNRELATED*: *Consultancy*: Merck Serono, Merck, Appogenix, NewGen, Tocagen. Benjamin M. Ellingson—Paid consultant for MedQIA, LLC, and nonpaid consultant for Genentech, Inc. *Money paid to the institution.

REFERENCES

1. Central Brain Tumor Registry of the United States. CBTRUS Statistical Report Primary Brain and Central Nervous System Tumors Diagnosed in the United States in 2004–2006. http://www.cbtrus.org/2010-NPCR-SEER/CBTRUS-WEBREPORT-Final-3-2-10.pdf. Accessed January 2013
2. Stupp R, Mason WP, van den Bent MJ, et al. **Radiotherapy plus concomitant and adjuvant temozolomide for glioblastoma.** *N Engl J Med* 2005;352:987–96
3. Wong ET, Hess KR, Gleason MJ, et al. **Outcomes and prognostic factors in recurrent glioma patients enrolled onto phase II clinical trials.** *J Clin Oncol* 1999;17:2572–78
4. Plate KH, Breier G, Risau W. **Molecular mechanisms of developmental and tumor angiogenesis.** *Brain Pathol* 1994;4:207–18
5. Millauer B, Shawver LK, Plate KH, et al. **Glioblastoma growth inhibited in vivo by a dominant-negative Flk-1 mutant.** *Nature* 1994;367:576–79
6. Holash J, Maisonpierre PC, Compton D, et al. **Vessel cooption, regression, and growth in tumors mediated by angiopoietins and VEGF.** *Science* 1999;284:1994–98
7. Pope WB, Young JR, Ellingson BM. **Advances in MRI assessment of gliomas and response to anti-VEGF therapy.** *Curr Neurol Neurosci Rep* 2011;11:336–44
8. Leu K, Pope WB, Cloughesy TF, et al. **Imaging biomarkers for anti-angiogenic therapy in malignant gliomas.** *CNS Oncology* 2013;2:33–47
9. Pope WB, Kim HJ, Huo J, et al. **Recurrent glioblastoma multiforme: ADC histogram analysis predicts response to bevacizumab treatment.** *Radiology* 2009;252:182–89
10. Pope WB, Lai A, Mehta R, et al. **Apparent diffusion coefficient histogram analysis stratifies progression-free survival in newly diagnosed bevacizumab-treated glioblastoma.** *AJNR Am J Neuroradiol* 2011;32:882–89
11. Ellingson BM, Bedekar DP, Malkin MG, et al. **Hybrid functional diffusion and perfusion maps for evaluation of gliomas.** In: *Proceedings of the 17th Scientific Meeting and Exhibition of the International*

Society for Magnetic Resonance in Medicine, Honolulu, Hawaii. April 18–24, 2009;17:1000
12. Ellingson BM, Cloughesy TF, Lai A, et al. **Graded functional diffusion map-defined characteristics of apparent diffusion coefficients predict overall survival in recurrent glioblastoma treated with bevacizumab.** *Neuro Oncol* 2011;13:1151–61
13. Ellingson BM, Cloughesy TF, Lai A, et al. **Cell invasion, motility, and proliferation level estimate (CIMPLE) maps derived from serial diffusion MR images in recurrent glioblastoma treated with bevacizumab.** *J Neurooncol* 2011;105:91–101
14. Ellingson BM, Cloughesy TF, Lai A, et al. **Nonlinear registration of diffusion-weighted images improves clinical sensitivity of functional diffusion maps in recurrent glioblastoma treated with bevacizumab.** *Magn Reson Med* 2012;67:237–45
15. Kothari PD, White NS, Farid N, et al. **Longitudinal restriction spectrum imaging is resistant to pseudoresponse in patients with high-grade gliomas treated with bevacizumab.** *AJNR Am J Neuroradiol* 2013;34:1752–57
16. White NS, McDonald CR, Farid N, et al. **Improved conspicuity and delineation of high-grade primary and metastatic brain tumors using "restriction spectrum imaging": quantitative comparison with high B-value DWI and ADC.** *AJNR Am J Neuroradiol* 2013;34:958–64, S1
17. Andre JB, Lu S, Spearman K, et al. **Peritumoral apparent diffusion coefficient as a metric of response in patients with recurrent glioblastoma multiforme treated with bevacizumab and irinotecan.** *NRJ* 2008;21:350–61
18. Gerstner ER, Frosch MP, Batchelor TT. **Diffusion magnetic resonance imaging detects pathologically confirmed, nonenhancing tumor progression in a patient with recurrent glioblastoma receiving bevacizumab.** *J Clin Oncol* 2010;28:e91–93
19. Pope WB, Qiao XJ, Kim HJ, et al. **Apparent diffusion coefficient histogram analysis stratifies progression-free and overall survival in patients with recurrent GBM treated with bevacizumab: a multicenter study.** *J Neurooncol* 2012;108:491–98
20. Pope WB, Mirsadraei L, Lai A, et al. **Differential gene expression in glioblastoma defined by ADC histogram analysis: relationship to extracellular matrix molecules and survival.** *AJNR Am J Neuroradiol* 2012;33:1059–64
21. Lucio-Eterovic AK, Piao Y, de Groot JF. **Mediators of glioblastoma resistance and invasion during antivascular endothelial growth factor therapy.** *Clin Cancer Res* 2009;15:4589–99
22. Keunen O, Johansson M, Oudin A, et al. **Anti-VEGF treatment reduces blood supply and increases tumor cell invasion in glioblastoma.** *Proc Natl Acad Sci U S A* 2011;108:3749–54
23. Padhani AR, Liu G, Mu-Koh D, et al. **Diffusion-weighted magnetic resonance imaging as a cancer biomarker: consensus and recommendations.** *Neoplasia* 2009;11:102–25
24. Gerstner ER, Chen PJ, Wen PY, et al. **Infiltrative patterns of glioblastoma spread detected via diffusion MRI after treatment with cediranib.** *Neuro Oncol* 2010;12:466–72

White Matter Water Diffusion Changes in Primary Sjögren Syndrome

L.C. Tzarouchi, A.K. Zikou, N. Tsifetaki, L.G. Astrakas, S. Konitsiotis, P. Voulgari, A. Drosos, and M.I. Argyropoulou

ABSTRACT

BACKGROUND AND PURPOSE: Histopathologic studies have demonstrated WM damage in primary Sjögren syndrome. The purpose of this study was to evaluate WM microstructural changes by use of DTI-derived parameters in patients with primary Sjögren syndrome.

MATERIALS AND METHODS: DTI was performed in 19 patients with primary Sjögren syndrome (age, 64.73 ± 9.1 years; disease duration, 11.5 ± 7.56 years) and 16 age-matched control subjects. Exclusion criteria were a history of major metabolic, neurologic, or psychiatric disorder and high risk for cardiovascular disease. Data were analyzed by use of tract-based spatial statistics, for which the WM skeleton was created, and a permutation-based inference with 5000 permutations was used with a threshold of $P < .01$, corrected for multiple comparisons to enable identification of abnormalities in fractional anisotropy, mean diffusivity, radial diffusivity, and axial diffusivity.

RESULTS: Tract-based spatial statistics showed decreased fractional anisotropy in multiple areas in patients with primary Sjögren syndrome compared with control subjects, located mainly in the corticospinal tract, superior longitudinal fasciculus, anterior thalamic radiation, inferior fronto-occipital fasciculus, uncinate fasciculus, and inferior longitudinal fasciculus. Increased mean diffusivity and radial diffusivity and decreased axial diffusivity were observed in most of the fiber tracts of the brain in patients with primary Sjögren syndrome, compared with control subjects.

CONCLUSIONS: Patients with primary Sjögren syndrome show loss of WM microstructural integrity, probably related to both Wallerian degeneration and demyelination.

ABBREVIATIONS: AD = axial diffusivity; FA = fractional anisotropy; MD = mean diffusivity; pSS = primary Sjögren syndrome; RD = radial diffusivity; TBSS = tract-based spatial statistics

Sjögren syndrome is a chronic systemic autoimmune disease that can be classified as primary Sjögren syndrome (pSS) when presenting in isolation or secondary when related to another connective tissue disease.[1] The prevalence of pSS reported in different studies ranges from 0.1–4.8%.[2] pSS is characterized by mononuclear infiltration and destruction of the exocrine glands, mainly the lachrymal and salivary glands, but extraglandular manifestations are also reported (eg, arthralgia, pulmonary involvement, renal tubular acidosis, etc).[1,3] Involvement of both the peripheral and the CNS has also been reported in pSS.[4-6] Although involvement of the peripheral nervous system is a well-documented feature of the disease, the prevalence, the type, and the underlying mechanism of CNS involvement remain unclear.[4,5,7] The estimated frequency of CNS involvement ranges from 10–60% in different reports, depending on the parameters studied (eg, patient selection, diagnostic criteria, etc).[4-6] Patients with pSS can present with a wide range of focal or diffuse neurologic or psychiatric manifestations, including motor/sensory deficits, transverse myelitis, and cognitive impairment.[4-6] The current data from MRI studies support an increased frequency of high signal intensity lesions in the periventricular and/or subcortical WM on FLAIR and T2-weighted imaging, observed mainly in patients with pSS and evidence of CNS disease.[8-11] The volumetric analysis of GM and WM by use of the voxel-based morphometry method demonstrated diffuse atrophy in patients with pSS.[8] SPECT and PET studies have demonstrated reduced CBF and lowered glucose metabolism in patients with pSS.[12,13]

DTI is a technique that allows assessment of the preferential direction of the Brownian motion of protons, which in the brain reflects the microscopic architecture of the WM.[14,15] Four quantitative diffusion parameters can be derived from DTI data: 1) fractional anisotropy (FA), reflecting the directionality of water diffusion and coherence of WM fiber tracts; 2) mean diffusivity

Received June 13, 2013; accepted after revision August 10.

From the Departments of Radiology (L.C.T., A.K.Z., M.I.A.), Rheumatology (N.T., P.V., A.D.), Medical Physics (L.G.A.), and Neurology (S.K.), Medical School, University of Ioannina, Greece.

Please address correspondence to Maria I. Argyropoulou, MD, Medical School University of Ioannina, 45110 Ioannina, Greece; e-mail: margyrop@cc.uoi.gr

http://dx.doi.org/10.3174/ajnr.A3756

Table 1: Demographic and clinical characteristics of 19 patients with pSS

	Patients With pSS
Age, mean ± SD	64.73 ± 9.1 years
Sex, female:male	19:0
Disease duration, mean ± SD	11.5 ± 7.56 years
Dry mouth	94.7%
Dry eyes	94.7%
Positive salivary gland biopsy	100%
Arthritis/arthralgia	63.2%
Raynaud phenomenon	47.4%

(MD), quantifying the overall magnitude of water diffusion; 3) axial diffusivity (AD), measuring the magnitude of diffusivity along the principal diffusion direction; and 4) radial diffusivity (RD), reflecting the magnitude of diffusivity perpendicular to the principal diffusion direction.[14,15] These metrics have been correlated with the microstructural organization of WM and are used to infer structural characteristics of the local tissue.[14,15] The DTI-derived parameters have been used to investigate WM microstructure in various disorders by use of an ROI approach, in which structures of interest are manually defined on MR images, but information about changes in brain diffusivity in pSS is scarce.[16] Using the ROI method, a decrease in FA and an increase in MD values have been reported in patients with pSS.[16] Similar analytic methods that are based on manually selected ROIs have limitations, mainly because they do not examine the whole brain and they are laborious and time-consuming and therefore prone to human error.[17] To eliminate the limitations of the ROI-based methods, the so-called voxelwise analysis methods have been developed, which examine the whole brain automatically at a voxel level.[17] The technique of tract-based spatial statistics (TBSS) allows voxelwise statistical analysis of DTI-derived data.[18] TBSS has been widely used for DTI analysis because of its advanced registration capabilities and its robust nonparametric assessment of local differences in WM integrity between groups.[18]

The purpose of the present study was to assess the presence and location of WM damage and to elucidate the basis of WM microstructural changes in patients with pSS by analyzing DTI-derived parameters with the automated TBSS method.

MATERIALS AND METHODS

Study Patients

The study population consisted of 19 consecutively registered, unselected patients with pSS being followed up in the outpatient rheumatology clinic of our hospital, ages 47–78 years (mean ± SD; 64.73 ± 9.1 years), with a disease duration of 5–28 years (mean ± SD; 11.5 ± 7.56 years). The diagnosis of pSS was established according to the American-European Consensus Criteria. Association with other connective tissue diseases was ruled out, and only patients with pSS were included. The demographic and clinical characteristics of the patients are shown in Table 1. The control group consisted of 16 age-matched healthy volunteers, ages 45–76 years (mean ± SD; 62.57 ± 8.3 years). The protocol and the procedure were explained in detail to all patients and control subjects who had the same educational background. The study was performed with the approval of the institutional review board, and all the participants signed a written informed consent agreement.

Exclusion criteria were a history or clinical signs of cardiovascular disease, peripheral arterial disease, hepatic dysfunction (serum transaminase levels >1.5 times the upper limit of normal), renal insufficiency (serum creatinine concentration >1.6 mg/dL), proteinuria (> 0.5 g/d), diabetes mellitus (fasting plasma glucose concentration ≥126 mg/dL or use of antidiabetic medication), hypertension (arterial blood pressure >140/90 mm Hg or use of antihypertensive medication), serum level of thyroid-stimulating hormone >5 mU/mL, and treatment with corticosteroids during the previous 6 months. None of the study patients or control subjects had findings suggestive of CNS or psychiatric disorder. A total of 30 patients with pSS were initially evaluated. However, 11 were excluded. More specifically, 3 had hypertension for many years, 2 had atrial fibrillation, 4 had diabetes mellitus and dyslipidemia, and 2 had claustrophobia. Thus, 19 patients were finally included. Routine neurologic examination was performed on all subjects and did not reveal deficits indicative of central or peripheral nervous system involvement. Similarly, patients and caregivers did not report any symptoms indicative of cognitive decline, depression, or fatigue.

Data Acquisition

DTI was performed by use of a 1.5T scanner (Gyroscan ACS NT; Philips Healthcare, Best, The Netherlands). We used a single-shot EPI sequence. Parameters for DTI acquisition were as follows: FOV = 230 × 230 mm, 112 × 128 matrix, section thickness of 3 mm, TE = 131 ms, TR = 9825 ms, number of sections = 42, section gap = 0 mm. We used 16 noncollinear gradient directions, with maximum b = 700 seconds/mm^2 and scanning time 4 minutes, 34 seconds. The imaging protocol also included 1) a FLAIR sequence (TR = 6300 ms, TE = 120 ms, FOV = 250 mm, matrix = 256 × 256, section thickness of 6 mm, intersection gap = 0.6, scanning time = 2 minutes, 50 seconds), 2) a T1-weighted, high-resolution (1 × 1 × 1 mm), 3D spoiled gradient-echo sequence (TR = 25 ms, TE = 4.6 ms, acquisition matrix = 256 × 228, FOV = 220 mm, scanning time = 5 minutes, 43 seconds).

The presence of areas of high signal intensity in the WM was assessed for each subject on FLAIR images by 2 neuroradiologists who were blinded to the patient/control status.

Data Preprocessing

Images were processed by use of the FSL (FMRIB Software Library; http://www.fmrib.ox.ac.uk/fsl) software package.[19] For each subject, all images including diffusion-weighted and B0 images were corrected for eddy current–induced distortion and subject motion effect by use of the FSL Diffusion Toolbox. Brain mask was created from the first B0 image by use of the FSL Brain Extraction Tool, and Diffusion Toolbox was used to fit the tensor model and to compute the FA, MD, AD, and RD maps.

Tract-Based Spatial Statistics Analysis

Voxelwise analysis was performed by use of TBSS.[18] First, every FA image was aligned to every other one; by use of all these comparisons, the software then identified the "most representative" one and used it as the target image. This target image was then affine-aligned into Montreal Neurological Institute 152 standard space. The FA data of all subjects were aligned to this target image

by use of the nonlinear registration tool FNIRT, which uses a b-spline representation of the registration warp field. Next, the mean FA image was created and thinned to create a mean FA skeleton, which represents the centers of all tracts common to the group. A threshold of FA >0.2 was applied to the skeleton to include only major fiber bundles. The aligned FA data of each subject were then projected onto this skeleton. By applying the original nonlinear registration of each subject's FA to standard space, the MD, RD, and AD maps were also projected onto the mean FA skeleton. The projected maps were separated into 2 groups (control subjects and patients with pSS) and were used to calculate voxelwise cross-subject diffusion statistics. The localization of all the anatomic information described was based on the Johns Hopkins University WM tractography atlas and the International Consortium for Brain Mapping DTI-81 WM labels (part of the FSL package).

Statistical Analysis

To determine FA, MD, RD, and AD differences between groups, the voxelwise analysis was performed by a permutation-based inference method as implemented in the Randomize FSL tool.[20] We used a *t* test, 5000 permutations, and threshold-free cluster enhancement with a threshold of $P < .01$, corrected for multiple comparisons by use of family-wise error correction to assess differences in the FA, MD, RD, and AD between the patients with pSS and the healthy control subjects.[21] In addition, for the patients with pSS, voxelwise associations between each diffusion metric (FA, MD, AD, and RD) and disease duration were performed by use of a nonparametric, linear regression model. The significance threshold for correlations was set at $P < .05$, corrected for multiple comparisons by use of family-wise error correction (threshold-free cluster enhancement option in the Randomize permutation-testing tool).

RESULTS

There was no significant difference in age between patients and control subjects. Areas of high signal intensity in WM were observed in 13 of the 19 patients (68.4%) and in 6 of the 16 control subjects (37.5%).

Tract-Based Spatial Statistics

In the voxelwise-based group comparison, multiple WM areas with significant FA decrease ($P < .01$, family-wise error corrections for multiple comparison) were found bilaterally in patients with pSS compared with control subjects, as shown in Fig 1*A*, in the corticospinal tract, the superior longitudinal fasciculus, the anterior thalamic radiation, the inferior fronto-occipital fasciculus, the uncinate fasciculus, and the inferior longitudinal fasciculus (Table 2).

Voxelwise-based group comparison of MD, AD, and RD between patients with pSS and control subjects showed increased MD and RD and decreased AD in the patients in a widespread, diffuse pattern involving most of the major WM tracts throughout the brain (Fig 1*B*, 1*C*, and 1*D*, respectively).

Finally, regression analysis did not show any significant association between the DTI metrics and disease duration.

DISCUSSION

The main findings in the present study were decreased FA values in patients with pSS compared with control subjects in multiple major WM tracts, including the corticospinal tract, the superior longitudinal fasciculus, the anterior thalamic radiation, the inferior fronto-occipital fasciculus, the uncinate fasciculus, and the inferior longitudinal fasciculus. These changes in FA are related to widespread decreased AD values and increased MD and RD values in patients with pSS in comparison with control subjects.

The decreased FA and the increased MD values found in the present study are in accordance with the findings of the single previous study evaluating DTI in a similar number of patients with pSS ($n = 19$), which used the ROI method to evaluate 2 areas in the frontal lobes.[16] The present study adds to these previous findings by use of the TBSS analysis, which permits voxelwise statistical analysis of all DTI data and revealed more extensive changes in patients with pSS.[18]

FA is a measure of the degree to which water diffusion is constrained in the brain, and its primary determinant is the packing attenuation of axons within a voxel.[15,22] Axonal packing attenuation encompasses a variety of microstructural level variables (eg, degree of myelination, axonal diameters, and extracellular space).[15,22] The decreased FA values demonstrated in patients with pSS thus indicate loss of WM fiber integrity. MD quantifies the amount of diffusion within a brain voxel, but it lacks directional information, and increased MD values point to an increase overall in directionally nonspecific water diffusivity and suggest tissue breakdown with an increase in brain-water content.[15]

The MD and FA indices allow for quantitative evaluation of the random translational motion of water molecules and have been shown to reflect a variety of pathologic states in the brain,[23,24] but, despite being sensitive, they are lacking in specificity. The changes in diffusion-tensor eigenvalues λ_1, λ_2, and λ_3, which are the source indexes for calculating the MD and FA, may provide further information about the underlying neuropathologic mechanisms.[25,26] The λ_1 or AD measures the diffusion coefficient along the direction of maximum diffusivity and reflects changes in restrictive barriers along the direction of a tract.[25,26] The $(\lambda_2+\lambda_3)/2$ or RD measures the diffusion coefficient perpendicular to the direction of maximum diffusivity and reflects mainly changes in the axonal membrane and the myelin sheath.[25,26] It should be noted that AD and RD, unlike FA, are not rotationally invariant metrics of the diffusion tensor, and therefore their values depend on the orientation of the diffusion tensor ellipsoid at each voxel. Consequently, their usage in multisubject studies requires precise registration that ensures alignment of the different diffusion tensor ellipsoids in every voxel; otherwise, interpretation of changes of the "axial" and "radial" diffusivities on the basis of the underlying tissue structure becomes problematic.[27] Experimental studies have demonstrated that axonal damage leads to a marked decrease in AD and modest, often insignificant, decreases in RD, whereas demyelination increases RD without changing AD when these phenomena take place in isolation.[28,29] In the present study, the decreased AD and increased RD may be suggestive of decreased organization of tracts or axonal damage, which prevents diffusion along the long (axial) axis, or alternatively, decreased myelination that allows for more room

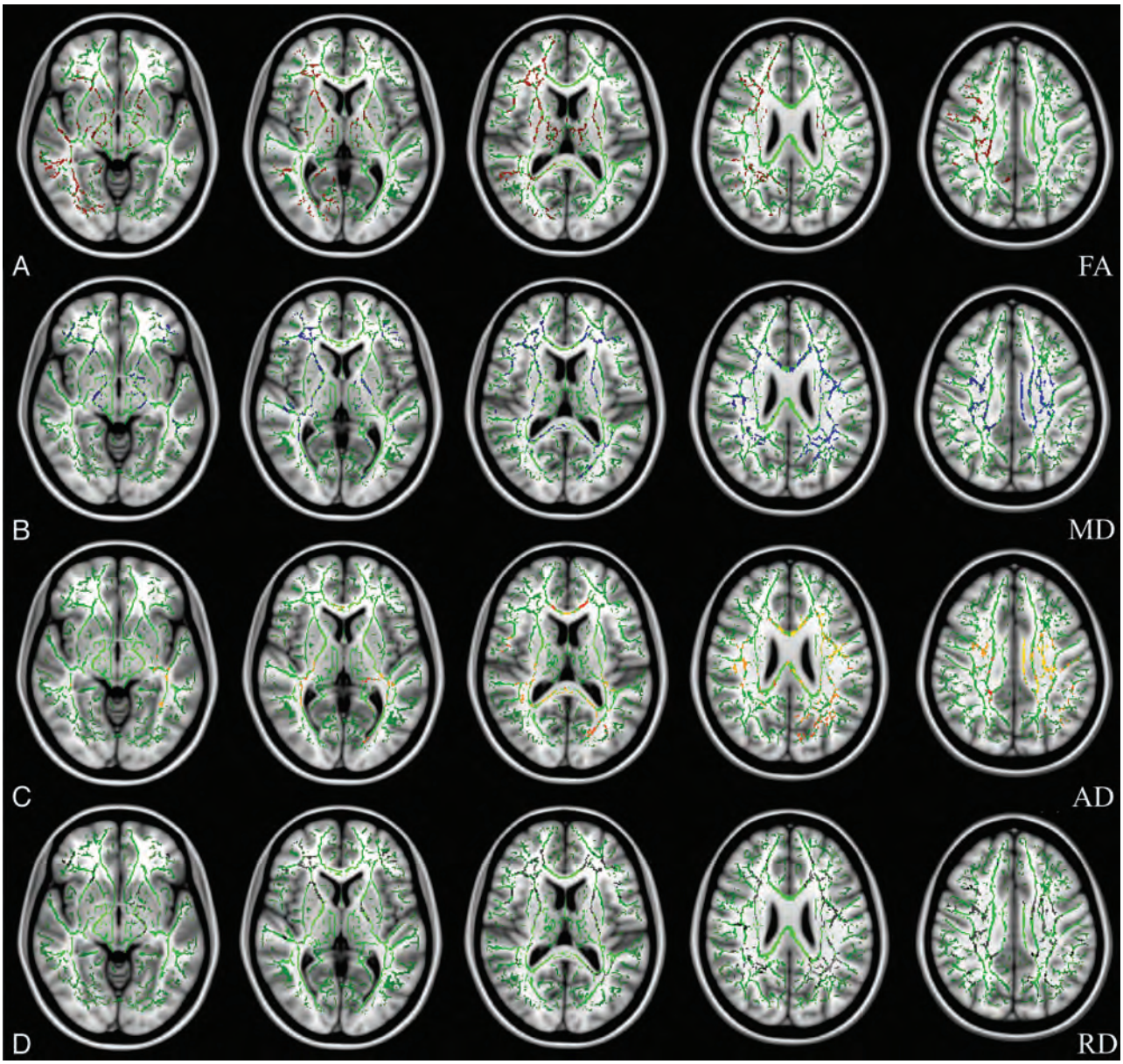

FIG 1. Tract-based spatial statistics results demonstrate voxelwise comparisons between 19 patients with pSS and 16 control subjects. Statistical maps (thresholded at threshold-free cluster enhancement, $P < .01$) are overlaid onto the mean FA skeleton and the Montreal Neurological Institute 152 template. Decreased fractional anisotropy in patients with pSS is shown in red *(A)*, increased mean diffusivity is shown in blue *(B)*, decreased axial diffusivity is shown in orange-yellow *(C)*, and increased radial diffusivity is shown in gray *(D)*. *A,* Corticospinal tract, superior longitudinal fasciculus, anterior thalamic radiation, inferior fronto-occipital fasciculus, uncinate fasciculus, and inferior longitudinal fasciculus; *B,* superior longitudinal fasciculus, thalamic radiation, inferior fronto-occipital fasciculus, uncinate fasciculus and inferior longitudinal fasciculus, corticospinal tract, cingulum, genu, and splenium of the corpus callosum; *C,* superior longitudinal fasciculus, thalamic radiation, inferior fronto-occipital fasciculus, uncinate fasciculus and inferior longitudinal fasciculus, corticospinal tract, cingulum, and genu and splenium of the corpus callosum; *D,* superior longitudinal fasciculus, thalamic radiation, inferior fronto-occipital fasciculus, uncinate fasciculus, inferior longitudinal fasciculus, corticospinal tract, and cingulum.

between axons for water molecules to move perpendicular to the tract (ie, radially).

Several pathogenetic mechanisms may account for the findings in the present study: 1) WM involvement could reflect axonal damage through anterograde or Wallerian degeneration. Cerebral small-vessel vasculitis has been reported in patients with pSS, leading to hypoperfusion of the cortex and atrophy.[12,13,30,31] With the use of voxel-based morphometry, diffuse GM atrophy has been demonstrated in patients with pSS.[8] This cortical atrophy may induce Wallerian degeneration of WM tracts.[8] Wallerian degeneration is characterized by a stereotypical course, starting with disintegration of axonal structures within days after injury, followed by fragmentation-degradation of myelin caused by infiltration of macrophages and finally, fibrosis, and atrophy of the affected fiber tracts.[32,33] Loss of axonal structure may result in less restricted diffusion perpendicular to the main direction of fibers and consequently give rise to elevated RD.[22,34] The membrane disintegration and cellular debris create new diffusion barriers that lead to a decrease in diffusivity parallel to the main fiber direction and therefore reduced AD[22,34]; 2) WM damage could be

Table 2: Neuroanatomic regions with reduced FA in patients with pSS compared with control subjects

Anatomic Region	MNI Coordinates, mm			Cluster Size
	x	*y*	*z*	
Right superior corona radiata, superior longitudinal fasciculus, anterior and posterior limb of internal capsule, inferior fronto-occipital fasciculus, uncinate fasciculus	27	8	26	4286
Left anterior thalamic radiation	−8	−18	0	284
Left inferior longitudinal fasciculus, uncinate fasciculus, inferior fronto-occipital fasciculus	−46	7	−20	202
Right anterior thalamic radiation, inferior longitudinal fasciculus	10	−17	5	103
Left anterior limb of internal capsule, anterior thalamic radiation	−23	7	14	92
Left superior corona radiata, superior longitudinal fasciculus, corticospinal tract	−28	−15	21	73
Left anterior thalamic radiation	−16	15	−6	67
Left inferior longitudinal fasciculus, uncinate fasciculus	−44	4	−36	65
Left anterior limb of internal capsule, anterior thalamic radiation	−20	0	11	46
Left inferior longitudinal fasciculus	−16	3	−5	38

Note:—$P < .01$, family-wise error–corrected. MNI indicates Montreal Neurological Institute.

caused by a direct insult from antibodies against myelin. Recently, an autoantibody targeting the water channel protein aquaporin-4 (anti–aquaporin-4) has been discovered in neuromyelitis optica, leading to death of oligodendrocytes, demyelination, and axonal loss.[35] It is well known that there is a strong association between pSS and neuromyelitis optica, and there is evidence of an increased prevalence of anti–aquaporin-4 antibodies in patients with pSS.[36-38] Loss of myelin reduces the barriers that restrict diffusion perpendicular to the WM fibers, leading to increased RD.[28] Axonal damage is an integral part of demyelination, and the concurrent axonal transactions and disruptions associated with axonal damage lead to the addition of diffusion barriers parallel to the axon and thus to reduced AD.[39] Finally, the underlying process accounting for the WM involvement might be a combination of Wallerian degeneration and demyelination, which is supported by a limited number of autopsy studies that have demonstrated both axonal degeneration and demyelination in the CNS of patients with pSS.[40,41] Similarly, decreased FA and AD and increased RD have been demonstrated in patients with neuromyelitis optica.[42,43] These changes involve multiple, major WM tracts in the normal-appearing WM, accumulate with increasing disease duration, and are probably related to both demyelination and Wallerian degeneration.[42,43]

A global decrease in WM integrity throughout the brain was observed in multiple major fiber tracts that control a wide range of brain functions. The CNS manifestations in pSS are heterogeneous, manifested as focal or diffuse involvement.[5,6] The wide spectrum of CNS manifestations in pSS includes movement disorders, motor and sensory loss, seizures, cognitive impairment, dementia, psychiatric abnormalities, encephalopathy, optic neuropathies, and others.[5,6] This wide range of CNS manifestations in patients with pSS is in accordance with the diffuse WM involvement throughout the brain detected by DTI in the present study.

The present study has some certain limitations that must be noted. First, the sample size was relatively small, which might reduce the power of the statistical significance and the generalization of the findings. Second, the cross-sectional design of the study and the reliance on a single imaging technique do not allow for assessment of the relative time that WM integrity is affected. Third, our DTI acquisition sequence had a limited number of directions that might have limited the precision of the values of the DTI parameters. Furthermore, the TBSS analysis that was used in the present study (as in any other analyses) is not without flaws or limitations. One is the lack of accuracy caused by the low-resolution DTI (partial volume effect). However, this is more an acquisition limitation rather than a postprocessing flaw, and TBSS remains one of the most reliable methods for multisubject DTI analysis available today. Finally, the lack of official cognitive or neuropsychiatric testing and reliable correlations with our imaging findings weaken their clinical interpretation/value. Notwithstanding the problematic issues raised, this study adds to the limited existing literature on CNS involvement in patients with pSS and should be considered preliminary. Therefore, future studies in larger populations, as well as prospective, longitudinal studies with the use of additional advanced MR imaging techniques with histopathologic and clinical correlations, will be useful for further probing the nature and the relationship of WM abnormalities to clinical symptoms in pSS.

CONCLUSIONS

Loss of WM microstructural integrity is demonstrated in patients with pSS as reduced FA and AD values and increased MD and RD values. Involvement of the WM might be caused by demyelination or through anterograde Wallerian degeneration. Additional histopathologic and advanced MR imaging studies evaluating larger series of patients will be necessary to better elucidate the role of CNS involvement in patients with pSS and to improve the understanding of the pathologic mechanisms behind the reduction of WM tract integrity in pSS.

REFERENCES

1. Fox RI, Howell FV, Bone RC, et al. **Primary Sjogren syndrome: clinical and immunopathologic features.** *Semin Arthritis Rheum* 1984;14:77–105
2. Mavragani CP, Moutsopoulos HM. **The geoepidemiology of Sjogren's syndrome.** *Autoimmun Rev* 2010;9:A305–10
3. Kassan SS, Moutsopoulos HM. **Clinical manifestations and early diagnosis of Sjogren syndrome.** *Arch Intern Med* 2004;164:1275–84
4. Soliotis FC, Mavragani CP, Moutsopoulos HM. **Central nervous system involvement in Sjogren's syndrome.** *Ann Rheum Dis* 2004;63:616–20
5. Fauchais AL, Magy L, Vidal E. **Central and peripheral neurological**

complications of primary Sjogren's syndrome. *Presse Med* 2012;41:e485–93
6. Tobon GJ, Pers JO, Devauchelle-Pensec V, et al. **Neurological disorders in primary Sjogren's syndrome.** *Autoimmune Dis* 2012:645967
7. Drosos AA, Andonopoulos AP, Lagos G, et al. **Neuropsychiatric abnormalities in primary Sjogren's syndrome.** *Clin Exp Rheumatol* 1989;7:207–09
8. Tzarouchi LC, Tsifetaki N, Konitsiotis S, et al. **CNS involvement in primary Sjogren syndrome: assessment of gray and white matter changes with MRI and voxel-based morphometry.** *AJR Am J Roentgenol* 2011;197:1207–12
9. Alexander EL, Beall SS, Gordon B, et al. **Magnetic resonance imaging of cerebral lesions in patients with the Sjogren syndrome.** *Ann Intern Med* 1988;108:815–23
10. Morgen K, McFarland HF, Pillemer SR. **Central nervous system disease in primary Sjogren's syndrome: the role of magnetic resonance imaging.** *Semin Arthritis Rheum* 2004;34:623–30
11. Harboe E, Beyer MK, Greve OJ, et al. **Cerebral white matter hyperintensities are not increased in patients with primary Sjogren's syndrome.** *Eur J Neurol* 2009;16:576–81
12. Kao CH, Ho YJ, Lan JL, et al. **Regional cerebral blood flow and glucose metabolism in Sjogren's syndrome.** *J Nucl Med* 1998; 39:1354–56
13. Huang WS, Chiu PY, Kao A, et al. **Detecting abnormal regional cerebral blood flow in patients with primary Sjogren's syndrome by technetium-99m ethyl cysteinate dimer single photon emission computed tomography of the brain: a preliminary report.** *Rheumatol Int* 2003;23:174–77
14. Basser PJ, Pierpaoli C. **Microstructural and physiological features of tissues elucidated by quantitative-diffusion-tensor MRI.** *J Magn Reson B* 1996;111:209–19
15. Pierpaoli C, Jezzard P, Basser PJ, et al. **Diffusion tensor MR imaging of the human brain.** *Radiology* 1996;201:637–48
16. Segal BM, Mueller BA, Zhu X, et al. **Disruption of brain white matter microstructure in primary Sjogren's syndrome: evidence from diffusion tensor imaging.** *Rheumatology* 2010;49:1530–39
17. Astrakas LG, Argyropoulou MI. **Shifting from region of interest (ROI) to voxel-based analysis in human brain mapping.** *Pediatr Radiol* 2010;40:1857–67
18. Smith SM, Jenkinson M, Johansen-Berg H, et al. **Tract-based spatial statistics: voxelwise analysis of multi-subject diffusion data.** *NeuroImage* 2006;31:1487–505
19. Smith SM, Jenkinson M, Woolrich MW, et al. **Advances in functional and structural MR image analysis and implementation as FSL.** *NeuroImage* 2004;23(Suppl 1):S208–19
20. Nichols TE, Holmes AP. **Nonparametric permutation tests for functional neuroimaging: a primer with examples.** *Hum Brain Mapping* 2002;15:1–25
21. Smith SM, Nichols TE. **Threshold-free cluster enhancement: addressing problems of smoothing, threshold dependence and localisation in cluster inference.** *NeuroImage* 2009;44:83–98
22. Pierpaoli C, Barnett A, Pajevic S, et al. **Water diffusion changes in Wallerian degeneration and their dependence on white matter architecture.** *NeuroImage* 2001;13:1174–85
23. Kanaan RA, Shergill SS, Barker GJ, et al. **Tract-specific anisotropy measurements in diffusion tensor imaging.** *Psychiatr Res* 2006; 146:73–82
24. Mukherjee P. **Diffusion tensor imaging and fiber tractography in acute stroke.** *Neuroimaging Clin North Am* 2005;15:655–65
25. Basser PJ, Pajevic S, Pierpaoli C, et al. **In vivo fiber tractography using DT-MRI data.** *Magn Reson Med* 2000;44:625–32
26. Le Bihan D. **Looking into the functional architecture of the brain with diffusion MRI.** *Nat Rev Neurosci* 2003;4:469–80
27. Wheeler-Kingshott CA, Cercignani M. **About "axial" and "radial" diffusivities.** *Magn Reson Med* 2009;61:1255–60
28. Song SK, Sun SW, Ramsbottom MJ, et al. **Dysmyelination revealed through MRI as increased radial (but unchanged axial) diffusion of water.** *NeuroImage* 2002;17:1429–36
29. Song SK, Sun SW, Ju WK, et al. **Diffusion tensor imaging detects and differentiates axon and myelin degeneration in mouse optic nerve after retinal ischemia.** *NeuroImage* 2003;20:1714–22
30. Alexander EL. **Neurologic disease in Sjogren's syndrome: mononuclear inflammatory vasculopathy affecting central/peripheral nervous system and muscle: a clinical review and update of immunopathogenesis.** *Rheum Dis Clin North Am* 1993;19:869–908
31. Belin C, Moroni C, Caillat-Vigneron N, et al. **Central nervous system involvement in Sjogren's syndrome: evidence from neuropsychological testing and HMPAO-SPECT.** *Ann Med Interne* 1999;150: 598–604
32. Johnson AC, McNabb NA, Rossiter RJ. **Chemistry of Wallerian degeneration: a review of recent studies.** *Arch Neurol Psychiatry* 1950;64:105–21
33. Lampert PW, Cressman MR. **Fine-structural changes of myelin sheaths after axonal degeneration in the spinal cord of rats.** *Am J Pathol* 1966;49:1139–55
34. Thomalla G, Glauche V, Koch MA, et al. **Diffusion tensor imaging detects early Wallerian degeneration of the pyramidal tract after ischemic stroke.** *NeuroImage* 2004;22:1767–74
35. Misu T, Fujihara K, Kakita A, et al. **Loss of aquaporin 4 in lesions of neuromyelitis optica: distinction from multiple sclerosis.** *Brain* 2007;130:1224–34
36. Estiasari R, Matsushita T, Masaki K, et al. **Comparison of clinical, immunological and neuroimaging features between anti-aquaporin-4 antibody-positive and antibody-negative Sjogren's syndrome patients with central nervous system manifestations.** *Mult Scler* 2012;18:807–16
37. Sofat N, Venables PJ. **Is Sjogren myelopathy Devic disease?** *Ann Rheum Dis* 2008;67:730–31
38. Nitescu D, Nicolau A, Caraiola S, et al. **Neuromyelitis optica: complication or comorbidity in primary Sjogren's syndrome?** *Rom J Intern Med* 2011;49:295–300
39. Bjartmar C, Yin X, Trapp BD. **Axonal pathology in myelin disorders.** *J Neurocytol* 1999;28:383–95
40. Ichikawa H, Ishihara K, Fujimoto R, et al. **An autopsied case of Sjogren's syndrome with massive necrotic and demyelinating lesions of the cerebellar white matter.** *J Neurol Sci* 2004;225:143–48
41. Yaguchi H, Houzen H, Kikuchi K, et al. **An autopsy case of Sjogren's syndrome with acute encephalomyelopathy.** *Intern Med* 2008;47: 1675–80
42. Rueda Lopes FC, Doring T, Martins C, et al. **The role of demyelination in neuromyelitis optica damage: diffusion-tensor MR imaging study.** *Radiology* 2012;263:235–42
43. Yu C, Lin F, Li K, et al. **Pathogenesis of normal-appearing white matter damage in neuromyelitis optica: diffusion-tensor MR imaging.** *Radiology* 2008;246:222–28

Imaging Features of a Gelatin-Thrombin Matrix Hemostatic Agent in the Intracranial Surgical Bed: A Unique Space-Occupying Pseudomass

K.O. Learned, S. Mohan, I.Z. Hyder, L.J. Bagley, S. Wang, and J.Y. Lee

ABSTRACT

BACKGROUND AND PURPOSE: Absorbable gelatin-thrombin matrix is increasingly being used in neurosurgical procedures; unlike other hemostats, the stable matrix is left undisturbed and fills the surgical bed after achieving hemostasis. We investigated the immediate postoperative radiographic imaging appearance of the gelatin-thrombin matrix in intracranial operative beds.

MATERIALS AND METHODS: Thirty-one consecutive patients (18 men, 13 women; mean age, 59 years) with 34 surgical cavities, had 31 brain MRIs and 9 head CTs performed ≤ 48 hours postoperatively. They were retrospectively reviewed. Images were evaluated independently by 2 neuroradiologists blinded to the surgical techniques. Surgical beds were evaluated for the presence of the gelatin-thrombin matrix, which appeared as pseudoair material (Hounsfield units ≤ −100) on CT, had characteristic T2-hypointense speckles in a T2-hyperintense background, and demonstrated complete gradient-recalled echo hypointensity on MR imaging. To determine the diagnostic performance of imaging features for the detection of the gelatin-thrombin matrix, the Fisher exact test for the association between imaging features and the presence of the gelatin-thrombin matrix and κ analysis for interobserver agreement were performed.

RESULTS: Hemostasis was achieved with standard methods in 12 surgical beds and with the gelatin-thrombin matrix in 22 beds. Interobserver agreement was substantial. The gelatin-thrombin matrix demonstrated pseudoair hypoattenuation (88% sensitivity, 100% specificity, 90% accuracy; $P = .067$, $\kappa = 0.74$) and distinctive T2-hypointense speckles in a background of T2-hyperintensity (81% sensitivity, 85% specificity, 82% accuracy; $P = <.001$, $\kappa = 0.76$). Combined characteristic T2 speckles and gradient-recalled echo hypointensity increased the specificity (81% sensitivity, 100% specificity, 88% accuracy; $P = < .001$).

CONCLUSIONS: The unique appearance (pseudoair on CT, T2 speckles with gradient-recalled echo hypointensity) of the gelatin-thrombin matrix should not be mistaken for gossypiboma, pneumocephalus, and/or hematoma.

ABBREVIATION: GRE = gradient-recalled echo

The achievement of hemostasis is of particular importance in neurosurgical procedures to ensure clear fields of vision for accurate surgical targeting and to prevent neurologic damage due to blood within the brain parenchyma. Pressure application, suture, and cautery have limited uses in brain surgery, with potential irreversible neurologic damage.[1] Bipolar coagulation at the bleeding site is effective in achieving hemostasis at the cost of longer operative times and wider surgical exposure. An armamentarium of hemostatic agents routinely used in neurosurgery includes cellulose-, gelatin-, and collagen-based agents; thrombin; and fibrin glue. They primarily stop bleeding by their contact activation of the clotting cascade and formation of an occlusive clot.[2] These agents effectively achieve hemostasis with various limitations. Fibrin glue requires a dry surface, obviating its use in an excessively oozing field. Gelatin Gelfoam (Pharmacia & Upjohn Company, Kalamazoo, Michigan) expands up to 320% with absorption of fluid and may compress the neural tissue.[3] Therefore, the necessary removal of Gelfoam from the surgical bed after achieving hemostasis risks rebleeding. Meticulous lining of the surgical bed with cellulose Surgicel (Ethicon, Somerville, New Jersey) is time-consuming and at times impossible through a narrow surgical corridor. Therefore, normal immediate postoperative surgical cavities contain extra-axial fluid and a small amount of independent air and hemostatic agents such as Surgicel along the wall.[4,5]

Gelatin-thrombin matrix (Floseal Hemostatic Matrix; Baxter

Received August 12, 2014; accepted after revision September 4.

From the Departments of Radiology (L.J.B., I.Z.H., K.O.L., S.M., S.W.) and Neurosurgery (J.Y.L.), University of Pennsylvania Health System, Perelman School of Medicine, Philadelphia, Pennsylvania; and Department of Radiology (I.Z.H.), Pennsylvania Hospital, Philadelphia, Pennsylvania.

Please address correspondence to Kim O. Learned, MD, Department of Radiology-Neuroradiology Division, University of Pennsylvania Health System, University of Pennsylvania Perelman School of Medicine, Hospital of the University of Pennsylvania, 219 Dulles Bldg, 3400 Spruce St, Philadelphia, PA 19104; e-mail: Kim.Learned@uphs.upenn.edu

http://dx.doi.org/10.3174/ajnr.A3765

Healthcare, Deerfield, Illinois) is an absorbable bovine gelatin–human thrombin composite. Following the approval of Floseal in neurosurgery in 2001 by the US Food and Drug Administration based on the safety and efficacy data from a multicenter prospective randomized clinical trial, it has been increasingly used in spine, brain, pituitary, and endoscopic sinus surgeries.[6-9] The prospective study of 214 patients undergoing cranial and spinal surgeries demonstrated the efficacy and safety of Floseal in controlling operative bleeding and minimizing damage to the surrounding healthy nervous tissue while reducing operative time.[7] Additionally, it was shown to be effective in coagulopathic disorders and refractory bleeding.[7] The advantages include fast preparation, easy delivery with a syringe applicator to various surgical beds, a hydrophilic matrix allowing effective adherence to a wet surgical field, and a granular gelatin matrix conforming to any irregular surgical cavity.[6] The granular gelatin particles swell maximally 10%–20% and are left in the surgical bed, providing a gentle tamponade effect and stable clot for effective hemostasis.[3,7,8,10] The unique postoperative radiographic imaging appearance of Floseal has been scarcely described and can be mistaken for gossypiboma, hematoma, and/or pneumocephalus. We investigated the immediate postoperative CT and MR imaging appearances of the gelatin-thrombin matrix in intracranial operative beds.

MATERIALS AND METHODS

Patients

We retrospectively reviewed our CNS tumor data base from September 2011 to June 2013 to identify patients who underwent surgical resection of intracranial neoplasms. Inclusion criteria were the following: 1) newly diagnosed neoplasms, 2) ≥95% gross total resection, 3) postoperative head CT and/or brain MR imaging performed within 48 hours after surgeries, and 4) mean size of the surgical cavities of ≥1 cm. Exclusion criteria were the following: 1) previously resected or irradiated neoplasms, pituitary or skull base neoplasms; 2) surgical biopsy; 3) mean size of surgical cavities of <1 cm; and 4) a nondiagnostic examination. Thirty-one consecutive patients (18 men, 13 women; mean age, 59 years) met the selection criteria. Thirty-four surgical cavities were evaluated with 31 brain MRIs and 10 head CTs. The resected neoplasms were glioblastoma ($n = 6$), hemangioblastoma ($n = 1$), metastasis ($n = 18$), meningioma ($n = 4$), and vestibular schwannoma ($n = 2$).

Imaging Methods and Analysis

Brain MRI was performed on 1.5T systems (Signa HD, Optima; GE Healthcare, Milwaukee, Wisconsin) with the following parameters of the sequences used for the imaging analysis: axial T2 FSE (TR/TE, 3000–4000/100–130 ms; thickness, 5 mm; skip, 1 mm), axial gradient-recalled echo (GRE) (TR/TE, 700/20 ms; thickness, 5 mm; skip, 1 mm), and axial unenhanced and enhanced T1 spin-echo (TR/TE, 500–400/9.5–12 ms; thickness, 5 mm; skip, 1 mm). Patients received 0.1 mmol/kg of gadolinium intravenously (MultiHance; Bracco Diagnostics, Princeton, New Jersey). Unenhanced head CT was performed in the helical mode (1.25-mm thickness, 120 kV, 250 mA; Somatom Definition Flash, Siemens, Erlangen, Germany) and was reconstructed in 5-mm axial images.

Two neuroradiologists blinded to the surgical technique independently reviewed the images and recorded the dominant imaging features seen in ≥75% volume of the surgical bed. Discrepancies between readers were resolved by consensus adjudication. The head CT was evaluated in brain and lung windows (approximate window widths of 150 and 1500, respectively) for the presence of pseudoair material (marked hypoattenuation ≤ −100) or other findings including air, CSF fluid, and hyperattenuated acute blood. The internal architecture and signal intensity of surgical beds were assessed with MR imaging. On the T2WI, the surgical bed was evaluated for the presence of the characteristic T2-hypointense speckles in the T2-hyperintense background of the gelatin-thrombin matrix versus other findings including T2-hyperintensity similar to that in CSF, T2-isointensity to brain, T2-hypointensity, or heterogeneous signal intensity. On the GRE sequence, the characteristic speckles on T2WI were correlated for the presence of complete hypointensity that was not secondary to susceptibility effects from pneumocephalus, calvaria, skull base, or metallic surgical hardware. Whereas hypointensity along the surgical margin and/or randomly distributed in the cavity was categorized as partial hypointensity on GRE, T1WI was assessed for the presence of T1-hyperintensity and enhancement. The imaging findings were correlated with the operative notes.

Statistical Analysis

Inter-rater agreement was measured for each imaging feature by using the κ statistic to determine consistency among the readers. Interpretation of the κ values followed the proposed standards of Landis and Koch: 0–.20 (slight), 0.21–0.40 (fair), 0.41–0.60 (moderate), 0.61–0.80 (substantial), and 0.81–1.00 (almost perfect).[11] The diagnostic performances of the imaging features, including sensitivity, specificity, positive predictive value, negative predictive value, and accuracy, were evaluated by using a 2×2 contingency table. A Fisher exact test was used to examine the association between the imaging features with the surgical use of the gelatin-thrombin matrix; a P value $< .05$ was considered significant. Statistical analysis was performed by using the Statistical Package for the Social Sciences, Version 20.0 (IBM, Armonk, New York).

RESULTS

In 12 surgical beds (mean diameter, 2.49 ± 0.63 cm), hemostasis was achieved with standard methods, including warm water irrigation; bipolar cautery; and application of Surgicel, Gelfoam, and/or collagen sponge. In 22 surgical beds (mean diameter, 2.49 ± 0.65 cm), only Floseal was used to achieve hemostasis, especially in cases of coagulopathy and/or excessive bleeding or when the standard techniques were deemed inappropriately time-consuming, thereby unfavorably prolonging the operative time, or technically difficult with potential injury to the surrounding healthy tissue (Figs 1 and 2).

The gelatin-thrombin matrix in the surgical bed appeared as a space-occupying material with pseudoair hypoattenuation on CT (−1000 ≤ Hounsfield units, ≤ −100), distinctive T2-hypointense speckles on a T2-hyperintense background, and complete hypointensity on GRE with high specificity (Figs 1 and 2). The diagnostic performances of these imaging features for the presence of the gelatin-thrombin matrix in the surgical bed are summarized in the Table. The complete hypointensity on GRE of the speckles seen on T2WI increased MR imaging diagnostic confi-

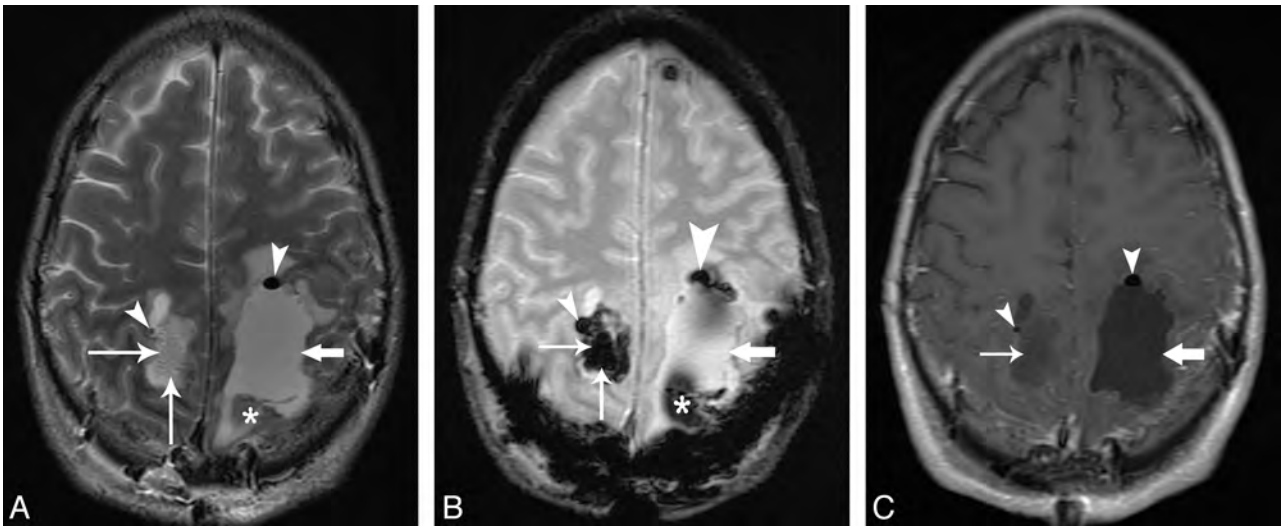

FIG 1. A 27-year-old man who has sequential resection of 2 brain metastases. Hemostasis of the first resection bed in the left parietal lobe is achieved with the standard technique. The gelatin-thrombin matrix is used in the subsequent second resection bed in the right parietal lobe to decrease operative time and effectively control bleeding from hypervascular sarcoma metastasis. *A*, Axial T2WI demonstrates the left parietal bed (*thick arrow*) filled with CSF containing a small amount of blood products posteriorly (*asterisk*) and the right parietal bed filled with a distinctive organized cluster of T2-hypointense speckles (*thin arrows*) almost in stacked layers in the T2-hyperintense background, characteristic of the gelatin-thrombin matrix. *B*, Axial GRE image demonstrates the corresponding complete hypointensity of the gelatin-thrombin matrix (*thin arrows*) filling the right cavity, different from the focal susceptibility of blood products (*asterisk*) in the left cavity. *C*, Axial T1WI shows CSF signal in the left cavity and isointensity in the right cavity without enhancement. Scattered bubbles of air (*arrowheads*) are present in the nondependent portion of the surgical beds with susceptibility on GRE.

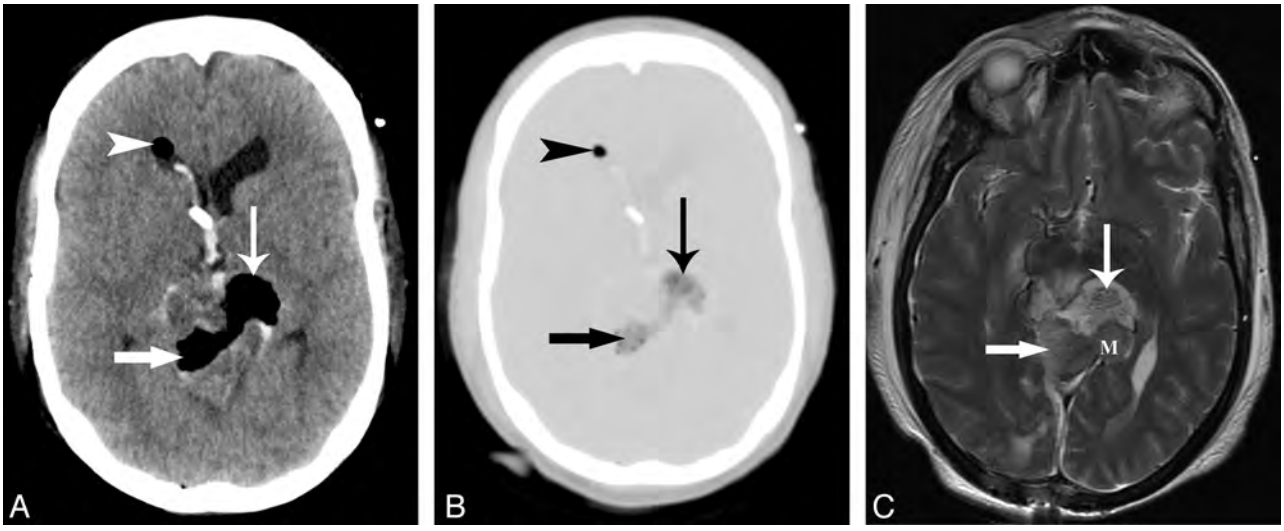

FIG 2. A 48-year-old woman who has a resection of a 5-cm pineal region meningioma. *A* and *B*, Axial CT images of the pineal resection bed in brain and lung windows, respectively, demonstrate the characteristic pseudoair hypoattenuation of the gelatin-thrombin matrix (*thin and thick arrows*), which can be easily mistaken for pneumocephalus. *C*, Axial T2WI illustrates characteristic T2-hypointense speckles of the gelatin-thrombin matrix (*thin arrow*) in the background of T2-hyperintensity. Note the less distinct speckles in the background of T2-isointensity (*thick arrow*), which may result in a falsenegative for the detection of the gelatin-thrombin matrix on MR imaging if CT is not available for correlation. Residual T2-isointense meningioma (M) shows avid enhancement on postcontrast T1WI (T1WI not shown).

dence in identifying the gelatin-thrombin matrix with a sensitivity of 81% and a specificity of 100% ($P < .001$). The presence of all 3 CT and MR imaging features had a high specificity of 100%, with an acceptable sensitivity of 75% and an accuracy of 80% for detecting the gelatin-thrombin matrix in the postoperative bed.

All the gelatin-thrombin matrix–containing cavities demonstrated a T1-isointense center. Even though 13 of 22 cavities had no T1-hyperintense rim and 9 cavities had a variable degree of peripheral T1-hyperintense rim, these findings were not statistically significant ($P = .157$). None showed enhancement.

The interobserver reliability for the raters was substantial for identifying the characteristic T2-hypointense speckles ($\kappa = 0.76$)

Diagnostic performances of different imaging features for the detection of gelatin-thrombin matrix

Imaging Sequence	Sensitivity	Specificity	Accuracy	*P* Value
T2	0.81	0.85	0.82	<.001
GRE	1	0.92	0.97	<.001
T2+GRE	0.81	1	0.88	<.001
CT	0.88	1	0.90	.067
CT+MRI	0.75	1	0.80	.133

and pseudoair hypoattenuation ($\kappa = 0.74$) and excellent for identifying the corresponding complete GRE hypointensity of gelatin-thrombin matrix ($\kappa = 1$).

DISCUSSION

Gelatin-Thrombin Matrix Application in Cranial Surgery

Floseal consists of a bovine-derived gelatin matrix component and a human-derived thrombin component.[1,2,7,10] The gelatin-thrombin matrix is readily available for delivery to the surgical bed by mixing the gelatin granules with a reconstituted thrombin solution in a syringe. Hemostasis of the deepest portion of the surgical cavity is achieved by back-filling of the gelatin-thrombin matrix by using a syringe applicator that effortlessly passes through the narrow surgical corridor (Fig 2). The unique characteristic of Floseal is the requirement for the presence of blood at its application site for activation. The hydrophilic matrix adheres well to wet tissue, and the gelatin granules conform to the irregular geometry of the bleeding site. The material swells maximally 10%–20% within 10 minutes of contact with blood or fluids, providing a gentle tamponade effect and a mechanically stable matrix for clot formation.[3,7,10] Direct application of the gelatin-thrombin matrix on an actively oozing or spurting bleeding site exposes the patient's blood to a matrix of highly concentrated thrombin, accelerating clot formation by a combination of rapid conversion of the patient's fibrinogen to fibrin and contact activation of platelets. After achieving hemostasis, only the excess matrix not incorporated into the clot is gently irrigated out of the surgical bed; thus, the stable matrix-clot integration is left undisturbed.[10] The median times to cessation of bleeding were shorter than those achieved with other hemostatic agents with a higher hemostasis success rate of 96%.[6] Therefore, Floseal has been increasingly used, and its safety and efficacy for achieving hemostasis in spine, brain, pituitary, and endoscopic sinus surgeries have been widely published in the surgical literature.[6-9]

Immediate Postoperative Head CT and Brain MR Imaging

The immediate postoperative surgical cavities normally contain extra-axial fluid and a small amount of nondependent air (Fig 1).[4] Spiller et al[5] demonstrated that Surgicel-induced clots contained methemoglobin, resulting in a T1-hyperintense rim along the cavity lined by Surgicel on early postoperative MR imaging, not to be confused with enhancing residual tumor. In our cohort, all gelatin-thrombin matrix–containing cavities had central T1-isointensity, probably reflecting the acute clot incorporated in the matrix. Even though a majority (59%) of gelatin-thrombin matrix cavities in our study lacked the T1-hyperintense rim, the finding did not reach the statistical significance needed to distinguish Floseal- from Surgicel-lined cavities.

The gelatin granules in Floseal derived from bovine dermis swell on contact with fluid and entrap microbubbles in the matrix, mimicking air and fat with Hounsfield unit ≤ -100 on postoperative CT. This finding is similar to reported marked hypoattenuation of the surgically placed gelatin sponge used in abdominal surgery (Fig 2).[12,13] The gelatin-thrombin matrix incorporates the gelatin granules into the clot, rather than providing a surface for trapping the clot as seen with the gelatin sponge. As a result, the gelatin-thrombin matrix is ball-like, which is different from the linear arrangement of the gelatin sponge or the focal linear gas collection of Surgicel.[13] These trapped microbubbles and the stable integration of the cross-linked gelatin granule platform and fibrin clot likely account for the organized cluster of T2-hypointense speckles in the surgical cavity. Most interesting, 72% of these Floseal clusters had a unique appearance on axial T2WI of particles in stacked layers. In addition, organized fluid absorbed by the granules and retained in the matrix contributes to the T2-hyperintense background (Figs 1 and 2). These microbubbles and clot formation in the matrix cause magnetic field inhomogeneity with T2* effects evident by blooming susceptibility on GRE of the gelatin-thrombin matrix in the surgical cavity.

The characteristic T2-hypointense speckles in a background of T2-hyperintensity had a moderate sensitivity of 81% and a specificity of 85% for the detection of the gelatin-thrombin matrix ($P < .001$). The proportions of absorbed fluid and blood in the gelatin-thrombin matrix and clot formation all contribute to the signal intensity and internal architecture of Floseal in the surgical bed. Consequently, the surgical beds containing Floseal may have variable T2 signal intensity, which may obscure visualization of the characteristic speckles on T2WI. In our cohort, the false-negative for the presence of Floseal in the surgical bed had T2-isointensity, which probably resulted from absorption of more blood products than fluid in the matrix. Even though these falsenegative cases demonstrated complete hypointensity on GRE, suggestive of the gelatin-thrombin matrix with the highest diagnostic accuracy in our cohort, a variety of reasons accounting for susceptibility in the postoperative bed in routine clinical practice precludes sole use of the GRE sequence hypointensity as an indicator of the presence of the gelatin-thrombin matrix. Likewise, the false-positive T2-hypointense speckles demonstrated heterogeneous hypointensity on GRE of blood products rather than the gelatin-thrombin matrix. For these reasons, these pitfalls can be avoided by combining findings of both T2-speckles and corresponding GRE complete hypointensity to identify the gelatin-thrombin matrix with a high specificity of 100% and 88% accuracy. Furthermore, the inter-rater discrepancy, false-negative, and false-positive findings occurred in irregular-geometry surgical beds and small cavities, which affected visibility and assessment of their internal architecture.

Retained surgical sponge after craniotomies has been described as a hyperattenuated serpiginous structure on CT and a hypointense serpentine foreign body with susceptibility effects on the gradient-echo sequences on MR imaging.[14] The susceptibility on the GRE sequence of the organized thrombin clot in the gelatin-thrombin matrix and its unique internal architecture create a pseudomass, which should not be mistaken for an unintended retained foreign body or a gossypiboma during immediate postoperative imaging.

Limitations

We excluded the pituitary and skull base lesions and small surgical cavities along the calvaria and skull base to eliminate the confounding factor of bone and air susceptibility effects and to optimize visual assessment of the surgical cavity. Exclusion of prior surgery and radiation, subtotal resection, and biopsy cases in our cohort minimized the complexity of the evaluated surgical beds and eliminated variables that may affect our ability to evaluate the gelatin-thrombin matrix accurately. Consequently, the findings of our cohort may not be applicable to all patient populations. A combination of excluding

small surgical cavities from our analysis and preferential use of Floseal in sizable surgical beds to decrease the operative time by our surgeons caused a selection bias with 65% of the surgical cavities containing the gelatin-thrombin matrix in our imaging analysis. The Floseal and standard-hemostasis groups were age-matched and had a similar average surgical cavity size of 2.49 cm.

Our random Hounsfield unit measurements of the pseudoair gelatin-thrombin matrix ranged from −190 to −110. Given the irregular geometry of most surgical beds and likely variable swelling and fluid absorption of the gelatin matrix, an absolute Hounsfield unit measurement cutoff as a determination for the presence of the gelatin-thrombin matrix is impractical in clinical practice. Furthermore, simple visualization of the pseudoair of the surgical bed on a wide window setting in our cohort had a high specificity of 100% and accuracy of 90% for depicting the presence of the gelatin-thrombin matrix, even though the finding did not reach statistical significance due to small sample size. Following tumor resection, postoperative brain MR imaging is necessary for baseline evaluation of the resection result and unexpected postoperative complications. Therefore, head CT is performed as adjunctive imaging in patients with a concerning postoperative course, explaining our small number of postoperative CT scans.

Standard instructions for use of Floseal in brain surgery are assumed to offset the limitation of operator-dependent results and the postoperative imaging findings thereof. However, the removal of any excess Floseal that is not incorporated into the hemostatic clot can vary among patients, surgical beds, and surgeons. Therefore, close communication with the surgeon is paramount for clinically meaningful assessment of the postoperative bed.

Future Research

Accurate assessment of the postoperative cavity after brain tumor resection is critical in neoplastic surveillance. The studies in rat brains demonstrated that Floseal is biocompatible and resorbed within 6–8 weeks, though it elicits granulomatous inflammatory reactions for up to 28 days.[3,15] There are case reports on the inflammatory reaction, granuloma, and calcification formation in response to Floseal in the body, mimicking tumor.[16,17] To the best of our knowledge, there has not been a clinical report on the length of normal resorption of surgically implanted intracranial gelatin-thrombin matrix. The blood-brain barrier effectively shields the intraparenchymal brain from the usual inflammatory processes seen outside the brain; thus, the normal degradation pathways that may resorb surgically implanted foreign bodies in the rest of the body may not accurately reflect the intracranial situation. Hemostat-associated gossypiboma can mimic recurrent intracranial neoplasm.[18] Hence, imaging can serve as the least invasive method for following the pathway of healing, and imaging study of normal gelatin-thrombin matrix resorption is imperative to avoid mistaking the matrix for neoplasm, hematoma, and/or abscess.

CONCLUSIONS

The gelatin-thrombin matrix Floseal has distinctive pseudoair hypoattenuation on CT and T2-hypointense speckles in a background of the T2-hyperintense surgical bed on MR imaging during the immediate postoperative period. Its unique space-occupying appearance should not be mistaken for retained surgical sponge, which is a serpiginous structure with CT-hyperattenuation, T2-hypointensity, and GRE-susceptibility; pneumocephalus; and/or hematoma.

Disclosures: Linda J. Bagley—*RELATED*: *Support for Travel to Meetings for the Study or Other Purposes*: University of Pennsylvania, *Comments*: reimbursement for travel expenses to the American Society of Neuroradiology meeting in San Diego, where this was a poster presentation, *UNRELATED*: Pfizer Pharmaceuticals, *Comments*: reviewer in an osteoporosis drug trial, *Payment for Lectures (including service on Speakers Bureaus)*: International Diagnostics Course Davos, Davos, Switzerland, *Comments*: honorarium for participation in neuroradiology review course. John Y.K. Lee—*RELATED*: *Other*: speaker for Baxter (maker of Floseal), *UNRELATED*: Storz,* *Comments*: research grant, endoscopy company, *Stock/Stock Options*: Visionsense,* *Comments*: 3D endoscopy company. *Money paid to the institution.

REFERENCES

1. Yao HH, Hong MK, Drummond KJ. **Haemostasis in neurosurgery: what is the evidence for gelatin-thrombin matrix sealant?** *J Clin Neurosci* 2013;20:349–56
2. Gerald AG. **Update on hemostasis: neurosurgery.** *Surgery* 2007;142:S55–60
3. Payner T, Vega F, Taw J, et al. *FloSeal Matrix Hemostatic Sealant: Safety, Biocompatibility and Biodegradation Brain Implantation Study in Rats.* Mountain View, California: Fusion Medical Technologies, Inc; 2003:Study Number P01-050
4. Sato N, Bronen RA, Sze G, et al. **Postoperative changes in the brain: MR imaging findings in patients without neoplasms.** *Radiology* 1997;204:839–46
5. Spiller M, Tenner MS, Couldwell WT. **Effect of absorbable topical hemostatic agents on the relaxation time of blood: an in vitro study with implications for postoperative magnetic resonance imaging.** *J Neurosurg* 2001;95:687–93
6. Renkens KL Jr, Payner TD, Leipzig TJ, et al. **A multicenter, prospective, randomized trial evaluating a new hemostatic agent for spinal surgery.** *Spine* 2001;26:1645–50
7. Gazzeri R, Galarza M, Neroni M, et al. **Hemostatic matrix sealant in neurosurgery: a clinical and imaging study.** *Acta Neurochir (Wien)* 2011;153:148–54
8. Ellegala DB, Maartens NF, Laws ER Jr. **Use of FloSeal hemostatic sealant in transsphenoidal pituitary surgery: technical note.** *Neurosurgery* 2002;51:513–15
9. Woodworth BA, Chandra RK, LeBenger JD, et al. **A gelatin-thrombin matrix for hemostasis after endoscopic sinus surgery.** *Am J Otolaryngol* 2009;30:49–53
10. Baxter Healthcare Corporation. Floseal Hemostatic Matrix, 10 mL. Instructions for Use. http://www.floseal.com/us/instructions-for-use.html. Accessed March 23, 2012
11. Landis JR, Koch GG. **The measurement of observer agreement for categorical data.** *Biometrics* 1977;33:159–74
12. Sandrasegaran K, Lall C, Rajesh A, et al. **Distinguishing gelatin bioabsorbable sponge and postoperative abdominal abscess on CT.** *AJR Am J Roentgenol* 2005;184:475–80
13. Young ST, Paulson EK, McCann RL, et al. **Appearance of oxidized cellulose (Surgicel) on postoperative CT scans: similarity to postoperative abscess.** *AJR Am J Roentgenol* 1993;160:275–77
14. Kim AK, Lee EB, Bagley LJ, et al. **Retained surgical sponges after craniotomies: imaging appearances and complications.** *AJNR Am J Neuroradiol* 2009;30:1270–72
15. Ereth MH, Schaff M, Ericson EF, et al. **Comparative safety and efficacy of topical hemostatic agents in a rat neurosurgical model.** *Neurosurgery* 2008;63:369–72
16. Henkel A, Cooper RA, Ward KA, et al. **Malignant-appearing microcalcifications at the lumpectomy site with the use of FloSeal hemostatic sealant.** *AJR Am J Roentgenol* 2008;191:1371–73
17. Wood SJ, Kelsey A, Brennan B, et al. **Granular hemostat deposits mimicking disseminated malignancy.** *J Pediatr Surg* 2013;48:e25–27
18. Ribalta T, McCutcheon IE, Neto AG, et al. **Textiloma (gossypiboma) mimicking recurrent intracranial tumor.** *Arch Pathol Lab Med* 2004;128:749–58

Shoulder Apprehension Impacts Large-Scale Functional Brain Networks

S. Haller, G. Cunningham, A. Laedermann, J. Hofmeister, D. Van De Ville, K.-O. Lovblad, and P. Hoffmeyer

ABSTRACT

BACKROUND AND PURPOSE: Shoulder apprehension is defined as anxiety and resistance in patients with a history of anterior glenohumeral instability. It remains unclear whether shoulder apprehension is the result of true recurrent instability or a memorized subjective sensation. We tested whether visual presentation of apprehension videos modifies functional brain networks associated with motor resistance and anxiety.

MATERIALS AND METHODS: This prospective study includes 15 consecutive right-handed male patients with shoulder apprehension (9 with right shoulder apprehension, 6 with left shoulder apprehension; 27.5 ± 6.4 years) and 10 healthy male right-handed age-matched control participants (29.0 ± 4.7 years). Multimodal MR imaging included 1) functional connectivity tensorial independent component analysis, 2) task-related general linear model analysis during visual stimulation of movies showing typical apprehension movements vs control videos, 3) voxel-based morphometry analysis of GM, and 4) tract-based spatial statistics analysis of WM.

RESULTS: Patients with shoulder apprehension had significant ($P < .05$ corrected) increase in task-correlated functional connectivity, notably in the bilateral primary sensory-motor area and dorsolateral prefrontal cortex and, to a lesser degree, the bilateral dorsomedial prefrontal cortex, anterior insula, and dorsal anterior cingulate cortex (+148% right, +144% left). Anticorrelated functional connectivity decreased in the higher-level visual and parietal areas (−185%). There were no potentially confounding structural changes in GM or WM.

CONCLUSIONS: Shoulder apprehension induces specific reorganization in apprehension-related functional connectivity of the primary sensory-motor areas (motor resistance), dorsolateral prefrontal cortex (cognitive control of motor behavior), and the dorsal anterior cingulate cortex/dorsomedial prefrontal cortex and anterior insula (anxiety and emotional regulation).

ABBREVIATIONS: dACC = dorsal anterior cingulate cortex; dlPFC = dorsolateral prefrontal cortex; dmPFC = dorsomedial prefrontal cortex; GLM = general linear model; IC = independent component; TBSS = tract-based spatial statistics; TICA = tensorial independent component analysis; VBM = voxel-based morphometry

Shoulder apprehension is defined as anxiety and resistance in patients with a history of anterior glenohumeral instability. The apprehension sign is a physical finding in which placement of the humerus in the position of abduction to 90° and maximal external rotation produces anxiety and resistance in patients with a history of anterior glenohumeral instability.[1,2]

Despite the clearly established clinical findings of shoulder apprehension, the neuronal mechanisms associated with this subjective perception of anxiety and resistance remain unexplored. In patients with recurrent complaints of persisting apprehension after surgical stabilization, it is often difficult to diagnose and appropriately address the underlying problem. Although a bony defect has been recognized as a major cause of residual instability,[3] some patients experience apprehension without any proven recurrent dislocation. It is not clear whether the origin of the complaint is true recurrent instability or whether it stems from a cerebral pattern linking a certain movement or position to a subjective sensation of apprehension. This type of apprehension could, in some cases, arise from a previously memorized unpleasant sensation associated with a particular movement or position leading to a protective reflex action, rather than being the result of true persisting instability. Failure to recognize and adequately address this issue of persisting apprehension because of cerebral patterning may result in poor outcomes and even lead to unnecessary revision surgery.

To specifically probe the neuronal activations associated with shoulder apprehension, we developed animation videos illustrat-

Received June 15, 2013; accepted after revision July 10.

From the Departments of Imaging and Medical Informatics (S.H., J.H., K.-O.L.), Orthopaedic Surgery (G.C., A.L., P.H.), and Radiology (D.V.D.V.), University Hospitals of Geneva, Geneva, Switzerland; and Institute of Bioengineering (D.V.D.V.), Ecole Polytechnique Fédérale de Lausanne, Switzerland.

Please send correspondence to PD Dr. M.Sc. Sven Haller, Service neuro-diagnostique et neuro-interventionnel DISIM, University Hospitals of Geneva, Rue Gabrielle Perret-Gentil 4, 1211 Geneva 14, Switzerland; e-mail: sven.haller@hcuge.ch

http://dx.doi.org/10.3174/ajnr.A3738

ing typical movements of shoulder apprehension and matched control videos without apprehension movements. These videos were shown during fMRI to a carefully selected group of patients with shoulder apprehension and matched healthy volunteers. Functional connectivity as well as structural changes in gray and white matter was assessed. Specifically, we addressed the hypothesis that the visual presentation of apprehension-related videos induces patterns of functional connectivity in brain networks associated with motor resistance and anxiety.

MATERIALS AND METHODS

Participants

The local institutional ethical committee approved this prospective study, and all participants gave written informed consent before inclusion. We included 15 consecutive right-handed male patients with right-sided ($n=9$) or left-sided ($n=6$) glenohumeral instability and positive shoulder apprehension test (27.5 ± 6.4 years), who were recruited during consultation by the same shoulder surgeon (A.L., 13 years of experience). They all underwent an fMRI examination before surgical shoulder stabilization by this same surgeon. Ten healthy male right-handed control-matched participants were randomly selected from the general population (29.0 ± 4.7 years, no significant difference in mean age between groups). The exclusion criteria for control patients was any history of shoulder injury or instability as well as hyperlaxity, defined as more than 85° of elbow-to-waist external rotation. All participants had normal or corrected-to-normal visual acuity, and none reported a history of major medical disorders (cancer, cardiac illness), sustained head injury, psychiatric or neurologic disorders, or alcohol or drug abuse. Participants who used psychotropics, stimulants, and β-blockers on a regular basis were excluded.

fMRI Task

The fMRI task consisted of a block-design of 2 active conditions and 1 rest condition. In the active APPREHENSION condition, self-made animation movies (10 seconds) were visually presented, including daily activities such as putting the right shoulder at risk for anteroinferior dislocation and hence triggering apprehension, for example, arming the shoulder with a javelin, quickly reaching backwards for a seatbelt, and so forth (created by C.G., 3 years of experience). The videos for the CONTROL condition presented an identical situation except for the lack of suggestive movement, which induces apprehension. After each movie, a visual analog scale was presented for 2.5 seconds, and participants rated the degree of apprehension by using a MR-compatible response box, followed by a rest period consisting of the visual presentation of a fixation cross for 17.5 seconds. The 9-point visual rating scale ranged from very unpleasant (−1) to neutral (0) to pleasant (+1). Each run consisted of 6 active and 6 control videos presented in a pseudorandomized fashion. With inclusion of the additional fixation cross-phase, each run lasted 370 seconds with each participant performing 2 runs. Before fMRI scanning, participants were familiarized with the task by using a training program outside of the fMRI scanner.

MR Imaging

MR imaging was performed on a clinical routine whole-body 3T MR scanner (Trio; Siemens, Erlangen, Germany). Functional imaging implemented a standard EPI sequence with the following fundamental parameters: 1) whole-brain coverage, 96 × 96 matrix, 39 sections, voxel size 2.3 × 2.3 × 3.3 mm^3, TE of 30 ms, TR of 2500 ms, 148 repetitions; 2) a 3D T1 sequence with the following fundamental parameters: 256 × 256 matrix, 176 sections, 1 × 1 × 1 mm^3, TE of 2.3 ms, TR of 2300 ms; and 3) a DTI sequence with the following fundamental parameters: 30 diffusion directions $b=1000$ s/mm^2 isotropically distributed on a sphere, 1 reference $b=0$ s/mm^2 image with no diffusion weighting, 128 × 128 × 64 matrix, 2 × 2 × 2 mm voxel size, TE of 92 ms, TR of 9000 ms, and 1 average.

Statistical Analysis

Statistical analysis was performed in GraphPad Prism Version 5.0 (GraphPad Software, San Diego, California; behavioral data), FSL Version 5.0.2.1 (http://fsl.fmrib.ox.ac.uk; tensorial independent component analysis [TICA], voxel-based morphometry [VBM], and tract-based spatial statistics [TBSS]), and Matlab Version R2012b (MathWorks, Natick, Massachusetts; correlation analyses) by S.H. (12 years of experience) and D.v.d.V. (14 years of experience).

Analysis of Behavioral Data

After normality testing (D'Agostino-Pearson omnibus test), the participant's age was analyzed by use of a 2-sample t test. The behavioral responses for APPREHENSION vs CONTROL for patients and control participants were analyzed by use of group-level ANOVA followed by pair-wise Bonferroni multiple comparison tests.

TICA Analysis of Functional Connectivity

Analysis was carried out by TICA[4] as implemented in MELODIC (Multivariate Exploratory Linear Decomposition into Independent Components) Version 3.10, part of FSL. The following preprocessing was applied: 1) masking of nonbrain voxels, 2) voxelwise de-meaning of the data, and 3) normalization of the voxelwise variance. Preprocessed data were whitened and projected into a 30-dimensional subspace by use of the principal component analysis (30 components by use of automatic component estimation in FSL). The whitened observations were decomposed into sets of vectors, which describe signal variation across the temporal domain (time courses), the session/participant domain, and across the spatial domain (maps) by optimization for non-Gaussian spatial source distributions by a fixed-point iteration technique.[5] Estimated component maps were divided by the standard deviation of the residual noise and thresholded by fitting a mixture model to the histogram of intensity values.[6] Three non-neurologic noise components (visual inspection, and pseudoactivation of the brain surface or vascular system) were excluded from further processing. For each of the 27 remaining independent components (ICs), the associated Smodes (which are measures of the activation strength of the component) were post hoc compared between APPREHENSION vs CONTROL by implementation of 2-sample t tests and Bonferroni correction for multiple

comparisons. The analysis was preformed 3 times: 1) right shoulder patients vs control participants, 2) left shoulder patients vs control participants, and 3) all shoulder patients vs control participants. From the 3 remaining ICs, we also post hoc identified 2 of these ICs as task positive (ICs 12 and 17), and 1 as task negative (IC 30), and correlated the combined Smodes (ie, average of Smodes of ICs 12 and 17 − Smode of IC 30) with the average behavioral responses by use of Spearman rho. The correlation coefficient was statistically evaluated by use of 2-tailed nonparametric permutation testing. It should be noted that the spatial maps of ICs 12 and 17 also contain "negative" regions (ie, dorsal anterior cingulate cortex [dACC]) that contribute as task negative.

General Linear Model Analysis of Task-Related Activation

Task-related general linear model (GLM) data processing was carried out by use of FEAT (fMRI Expert Analysis Tool) Version 5.98, part of FSL. At the first level, the contrast of APPREHENSION vs CONTROL (and the inverse comparison) was calculated separately for each run of each participant. At the second level, the intraparticipant difference in the 2 runs of APPREHENSION vs CONTROL (and the inverse comparison) was assessed individually. At the third level, the group difference between all 15 patients and 10 control participants was calculated. We carried out higher-level analysis by using a fixed-effects model, forcing the random-effects variance to zero in FLAME (FMRIB Local Analysis of Mixed Effects).[7-9] Z (Gaussianized T/F)-statistic images were thresholded by use of clusters determined by $Z > 2.3$ and a corrected cluster significance threshold of $P = .05$.

Gray Matter VBM Analysis of T1 Data

The VBM analysis was analyzed by use of the FSL software package (Version 5.0.2.1). Standard processing steps were used, as described previously.[10,11] The essential processing steps included brain extraction in BET (Brain Extraction Tool, part of FSL), tissue-type segmentation by FAST4 (part of FSL), nonlinear transformation into Montreal Neurological Institute reference space, and creation of a study-specific GM template. The native GM images were then nonlinearly re-registered to this template. The modulated segmented images were then smoothed with an isotropic Gaussian kernel with a sigma of 2 mm. Finally, we applied voxelwise GLM by using permutation-based nonparametric testing (Randomise, part of FSL), correcting for multiple comparisons implementing threshold-free cluster enhancement.[12] Fully corrected P values $< .05$ are considered as significant. Similar to the TICA analysis above, this analysis was repeated for right shoulder patients vs control participants, left shoulder patients vs control participants, and all shoulder patients vs control participants.

White Matter TBSS Analysis of DTI Data

The TBSS analysis of the DTI data was again done implementing the FSL software package (Version 5.0.2.1), according to the standard procedure described in detail.[13] In principle, TBSS projects all participants' fractional anisotropy data onto a mean fractional anisotropy tract skeleton by using nonlinear registration. The tract skeleton is the basis for voxelwise cross-participant statistics and reduces potential misregistrations as the source for false-positive or false-negative results. Equivalent to the VBM analysis discussed above, we performed voxelwise statistical analysis with threshold-free cluster enhancement[12] correction for multiple comparisons, considering fully corrected P values $< .05$ as significant. Again, analysis was repeated for right shoulder patients vs control participants, left shoulder patients vs control participants, and all shoulder patients vs control participants.

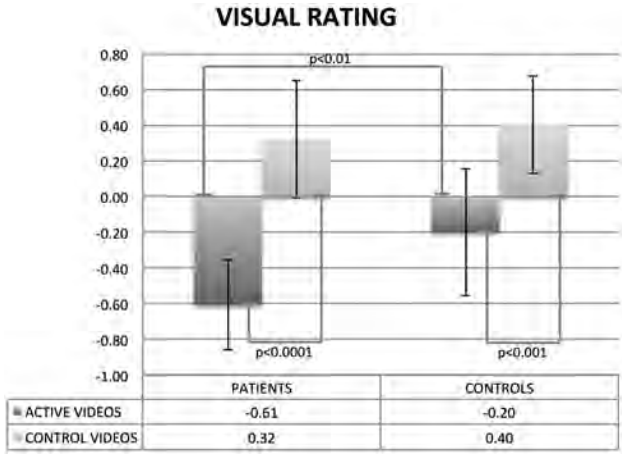

FIG 1. Visual rating ranging from unpleasant (−1) to pleasant (+1) associated with the presentation of APPREHENSION and CONTROL videos for patients and healthy volunteers. APPREHENSION vs CONTROL videos were associated with reduced rating values for both groups ($P < .0001$ corrected patients; $P < .001$ corrected control volunteers). APPREHENSION videos were associated with lower rating scores when comparing patients vs healthy volunteers ($P < .01$ corrected), whereas there was no significant effect for CONTROL videos.

RESULTS

Behavioral Data

In both patients and healthy volunteers, the APPREHENSION videos induced significantly increased ($P < .001$ corrected patients; $P < .01$ corrected control volunteers) unpleasant ratings compared with CONTROL videos. Moreover, when we compared patients vs healthy control participants, only the APPREHENSION videos ($P < .01$ corrected), but not the CONTROL videos, yielded more unpleasant ratings in patients vs control volunteers (Fig 1). These results confirm that our experimental setup induces subjective perception of unpleasantness associated with the visual perception of our shoulder apprehension movies in both patients and control participants. It also demonstrates that patients had significantly more unpleasant ratings for APPREHENSION videos vs CONTROL videos compared with matched-control participants.

Functional Connectivity fMRI Activations

The independent component analysis yielded 3 task-related ICs with a significant ($P < .05$ corrected) difference in Smode (a measure of the activation strength of the ICs) for patients compared with control participants. All 3 ICs were significant for all patients vs control participants and right shoulder patients vs control participants. In addition, IC 17 was significant for left shoulder patients vs control participants, whereas the other 2 components showed a clear equivalent but just a nonsignificant trend. It is noteworthy that there was a higher number of right vs left shoul-

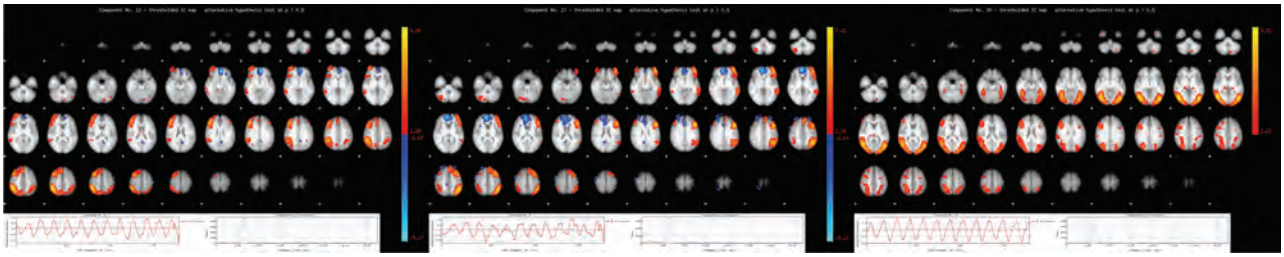

FIG 2. Patients vs control participants had a significantly ($P < .05$ corrected) higher task-correlated functional connectivity in 2 almost mirror symmetric components (IC 12 + 148% Smode in the right hemisphere; IC 17 + 144% Smode in left hemisphere). These networks include the primary sensory-motor areas compatible with motor resistance, dlPFC associated with cognitive control of motor behavior and dACC/dmPFC associated with emotional regulation. In contrast, patients had significantly reduced functional connectivity in a bilateral higher-level visual and parietal network (IC 30 −185% Smode). Moreover, this component is anticorrelated with the video presentation, in contrast to the components IC 12 and IC 17. Axial sections of the spatial representation of the ICs 12, 17, and 30 are illustrated at the top. The inserts at the bottom represent the average time courses of these ICs (left) and the corresponding Fourier spectra (right).

der patients, which explains this higher level of significance. There was no significant difference between right vs left shoulder patients. Therefore, we report the following results for all patients vs control participants.

Patients vs control participants had a significantly ($P < .05$ corrected) higher functional connectivity in 2 almost-mirror symmetric components, notably in the bilateral primary sensory-motor area and dorsolateral prefrontal cortex (dlPFC), bilateral dorsomedial prefrontal cortex (dmPFC), anterior insula, and dACC (+148% SMode in right hemisphere IC 12, and +144% Smode in left hemisphere IC 17). In contrast, patients had significantly reduced functional connectivity in a bilateral higher-level visual network including the parietal region (−185% Smode IC 30) (Fig 2).

The additionally performed correlation between task-positive minus task-negative Smodes and behavioral ratings revealed a significant negative correlation (rho = −0.47, $P = .02$) for all participants, and trends within the populations (rho = −0.63, $P = .05$ in control participants and rho = −0.31, $P = .27$ in patients).

These correlations indicate increasing functional connectivity activation strength in task-positive networks with increasing unpleasantness (Fig 3).

GLM Analysis of Task-Related Activation

The task-related GLM analysis revealed activation in the left primary sensory-motor area and dlPFC, which overlaps with IC 17, yet at a lower degree of significance. The corresponding contralateral regions showed a clear trend, which remained just below the multiple comparisons corrected threshold (Fig 4).

VBM Analysis of Gray Matter and TBSS Analysis of White Matter

The VBM analysis of GM as well as the TBSS analysis of WM revealed no differences between groups.

DISCUSSION

Patients with shoulder apprehension have increased functional connectivity in the primary sensory-motor areas compatible with motor resistance, dlPFC associated with cognitive control of motor behavior, and the dACC/dmPFC and anterior insula associated with anxiety and emotional regulation, despite the absence of potentially confounding structural alterations.

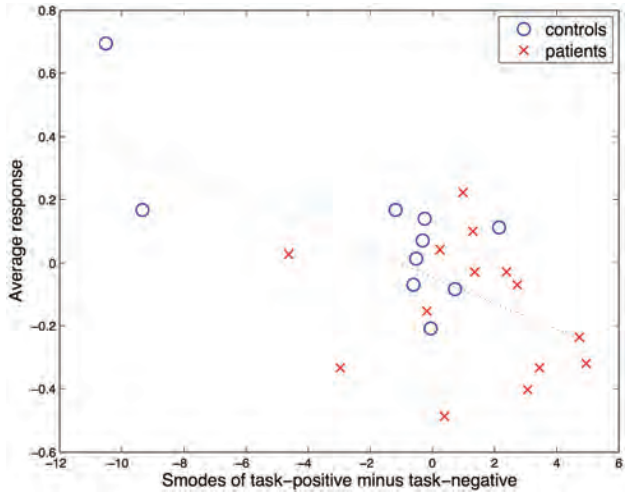

FIG 3. Correlation analysis between the Smodes (measure of activation strength) of task-positive (ICs 12 and 17) minus task-negative (IC 30) networks, and the participant average behavioral rating of unpleasantness. The negative correlation (rho = −0.4687) was significant ($P = .022$). Red "x" indicates individual patients; blue "o" indicates individual healthy volunteer data.

The current investigation is based on the observation that functional connectivity is not stationary but is variable with time. Functional connectivity may change spontaneously,[14] by exogenous stimulation,[15] or by learning.[16-18] Therefore, we exposed participants to videos of situations, which typically induce apprehension, to modulate functional connectivity related to the perception of apprehension. Our approach thus differs from "classic" resting-state fMRI studies without any specific task.[19,20] It is noteworthy that this change in paradigm is essential for the current investigation, as we only expect subtle changes at baseline in "classic" resting-state fMRI of apprehension patients who have no cognitive impairments. The presentation of apprehension videos is thus necessary to induce functional connectivity associated with the perception and, more generally, the processing of shoulder apprehension.

The functional connectivity was increased in patients vs volunteers by approximately 145% in the bilateral primary motor and sensory areas, as well as the bilateral dlPFC. It is interesting to note that during the shoulder apprehension test,[1,2] patients had an increased muscle tone and resistance in response to external rotation of the shoulder. Our findings of increased functional

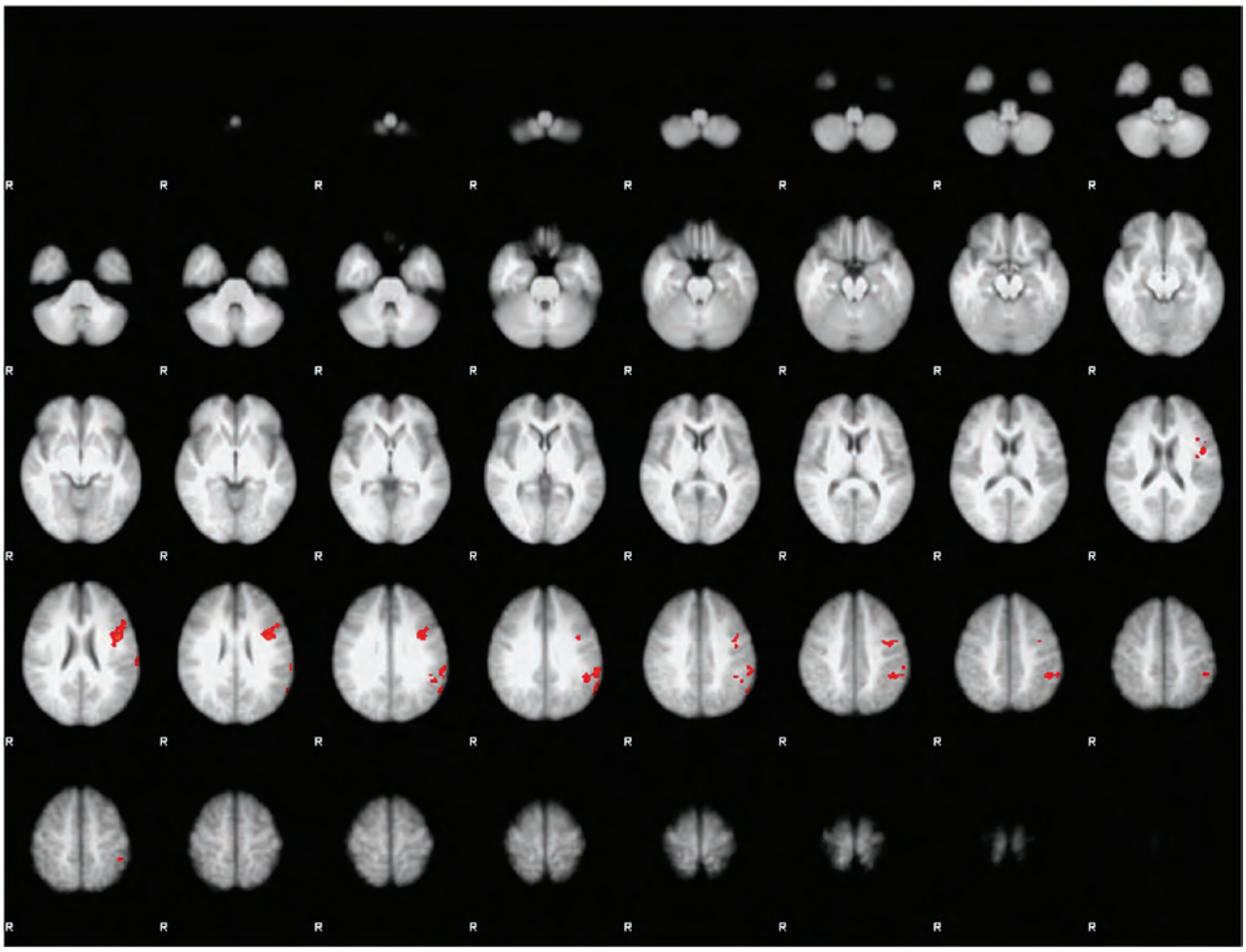

FIG 4. Hypothesis-driven GLM analysis for contrast of APPREHENSION videos vs CONTROL videos. Patients vs healthy volunteers had increased activation in the left primary sensory-motor area and dlPFC overlapping with IC 17, yet at a lower degree of significance. The corresponding contralateral regions showed a clear trend, which remained just below multiple comparisons corrected threshold (not shown). The inverse comparison of healthy volunteers vs patients yielded no significant differences.

connectivity in the primary sensory-motor area as well as in the dlPFC, which is consistently involved in the cognitive control of motor behavior,[21] are consistent with a preparation or readiness activation of the motor system in muscular resistance. Moreover, Hamilton et al[22] and Korgaonkar et al[23] propose the dlPFC is involved in the appraisal of negative emotional inputs (appraisal being deregulated in major depressive disorder). In the context of our shoulder apprehension videos, the increase in dlPFC might indicate an increased reappraisal of negative information related to the negative valence of the videos, in addition to its role in modulating pre/motor regions.

In addition, we observed an increase in functional connectivity in the dmPFC, dACC, and anterior insula. These regions are consistently involved in emotional regulation (http://neurosynth.org/terms/emotion, http://neurosynth.org/terms/regulation) and anxiety (http://neurosynth.org/terms/anxiety). Although no previous imaging study specifically addressed apprehension, we consider anxiety and fear as key cognitive processes associated with shoulder apprehension. A recent meta-analysis of instructed fear studies concludes that the dACC/dmPFC is a part of a "core" fear network, which is activated irrespective of how fear was learned.[24] One study assessed anticipatory anxiety in participants with spider phobia[25] and identified increased activation notably in the dACC/dmPFC and insula in spider phobics compared with volunteers while anticipating phobic stimulation. Another study assessed anticipation of interoceptive threat in 15 participants reporting high vs 14 participants reporting low fear.[26] Participants were trained that 1 of 2 cues predicted the occurrence of a hyperventilation task, which reliably produced body symptoms in all participants. The comparison of high-fear vs low-fear groups during the anticipation period, again, activated the dACC/dmPFC and bilateral anterior insula. Moreover, anticipatory anxiety was assessed in 14 healthy volunteers.[27] The paradigm consisted of a visual presentation of blue circles associated with a certain likelihood of aversive transcutaneous electrical nerve stimulations vs visual presentation of red circles without painful stimuli. Again, anticipatory anxiety was associated with activations in the bilateral anterior insula and midline frontal cortex (overlapping with the dACC/dmPFC). Spider phobia, hyperventilation, and transcutaneous electrical nerve stimulations as aversive stimuli evidently differ from shoulder apprehension in our current investigation. Nevertheless, the anticipatory anxiety in the discussed studies is an essential cognitive process involved in shoulder apprehension. In a consistent fashion, the reported activations of

these above-mentioned studies remarkably overlap with parts of the observed upregulated networks of our current investigation. This finding is remarkable, as the above-mentioned fMRI studies used hypothesis-driven data analyses, whereas our current investigation implemented a hypothesis-free independent component analysis. Only 1 previous study assessed functional connectivity in anticipatory anxiety; however, it implemented a fundamentally different region-of-interest approach.[28] This study included 14 anxiety-positive and 14 anxiety-normative participants performing an affective picture anticipation task. In a first step, activation in the bilateral anterior insula was identified in a task-related analysis, replicating the results of the task-related anticipatory anxiety studies discussed above. In a second step, functional connectivity was calculated with the left and right anterior insula as a seed region—in contrast to the exploratory independent component analysis of our current study, which assessed the entire brain without predefined seed regions. Nevertheless, the bilateral anterior insula in the anxiety-positive group overlap considerably with the networks identified in our study.

It is worthwhile emphasizing that the alterations in functional connectivity in the current investigation were identified by use of data-driven IC analysis without prior assumptions. Nevertheless, the observed changes in functional connectivity are by no means random yet very meaningful in the context of shoulder apprehension, as discussed above. The relevance of these task-correlated networks is further supported by the additionally performed hypothesis-driven GLM analysis, which demonstrated overlapping activations in the left sensory-motor areas and dlPFC as well as a clear and almost significant trend in the contralateral areas. That the functional-connectivity TICA analysis is more sensitive compared with the task-related GLM analysis can be explained by the fact that GLM requires strict multiple-comparisons correction of approximately 100,000 voxels instead of only 30 ICs. In addition, TICA averages signal across multiple voxels, thereby increasing the signal-to-noise ratio compared with the single-voxel GLM analysis.

Moreover, the significant correlation between ratings and functional activation strengths revealed that task-positive networks, including the sensory-motor area, dlPFC, and dACC/dmPFC, are activated more strongly during the processing of unpleasant experiences. In contrast, the task-negative higher-level visual networks are less activated in subsequent resting blocks. Therefore, shoulder apprehension progressively disturbs the balance between task-positive and task-negative networks as unpleasantness increases. Correspondingly, delayed recovery of resting-state activity in regions of the default mode network has also been reported after exposure to unpleasant visual movie fragments[29] or after a demanding cognitive task such as regulation by use of real-time fMRI neurofeedback.[30] These findings not only show the direct implication of shoulder apprehension and the motor networks but also show brain processes likely to be related to interoceptive awareness, anxiety, and emotional regulation.

Strengths and Limitations

Strengths of our current investigation are the strict patient selection, the complementary analyses of functional connectivity and task-related fMRI, and the exclusion of potentially confounding morphometric changes in both GM and WM. However, several limitations should be considered. First, the study group was small and was limited to men. Second, to increase the number of patients, we grouped together those with left and right shoulder instability, as we assumed that the cognitive processes related to apprehension were global and did not depend on the side of shoulder instability. Accordingly, we could not observe differences between patients with left shoulder instability vs control participants or those patients with right shoulder instability vs control participants, nor in the direct comparison between patients with left vs right shoulder apprehension. Third, we investigated only shoulder apprehension. We assumed that the neuronal activations associated with apprehension and anxiety were not limited to shoulder apprehension, but a general effect of apprehension including, for example, knee instability; this remains to be elucidated in future studies. Finally, we assumed that apprehension is a dynamic process, which may change with time (eg, after shoulder stabilization). In this investigation, we only assessed the phase of apprehension in patients with acute shoulder instability. Longitudinal assessment of patients with shoulder apprehension would be most interesting because the dynamic installation of apprehension-related changes in brain activations could be assessed, as well as modifications in brain activations with time associated with different treatment strategies in the sense of a surrogate marker.

CONCLUSIONS

Although shoulder apprehension is a well-known problem in sports medicine, the underlying mechanisms remain poorly understood. We demonstrate changes in neuronal processing associated with shoulder apprehension, indicating that apprehension is more complex than a pure mechanical problem of the shoulder. This also explains why mechanical stabilization alone oftentimes provides unsatisfactory results.

Disclosures: Sven Haller—*UNRELATED: Grants/Grants Pending:* Swiss National Science Foundation,* Comments: Principal investigator (SNF project 320030_147126/1), not related to this work; Dimitri Van De Ville—*UNRELATED: Grant:* Swiss National Science Foundation,* Comments: under grant PP00P2–123438 (salary DVDV). Pierre Hoffmeyer—*UNRELATED: Travel/Accommodations/Meeting Expenses Unrelated to Activities Listed:* Academic meetings (American Academy of Orthopaedic Surgeons [AAOS], European Federation of National Associations of Orthopaedics and Traumatology [EFORT], Swiss Society of Orthopaedic Surgery and Traumatology [SSOT]),* Comments: Institution funds travel and accommodations for scientific meetings. **Money paid to institution.*

REFERENCES

1. Rowe CR, Zarins B. **Recurrent transient subluxation of the shoulder.** *J Bone Joint Surg Am* 1981;63:863–72
2. Jobe FW, Kvitne RS, Giangarra CE. **Shoulder pain in the overhand or throwing athlete. The relationship of anterior instability and rotator cuff impingement.** *Orthop Rev* 1989;18:963–75
3. Burkhart SS, De Beer JF. **Traumatic glenohumeral bone defects and their relationship to failure of arthroscopic Bankart repairs: significance of the inverted-pear glenoid and the humeral engaging Hill-Sachs lesion.** *Arthroscopy* 2000;16:677–94
4. Beckmann CF, Smith SM. **Tensorial extensions of independent component analysis for multisubject fMRI analysis.** *Neuroimage* 2005;25:294–311
5. Hyvärinen A. **Fast and robust fixed-point algorithms for independent component analysis.** *IEEE Trans Neural Netw* 1999;10:626–34
6. Beckmann CF, Smith SM. **Probabilistic independent component**

analysis for functional magnetic resonance imaging. *IEEE Trans Med Imaging* 2004;23:137–52
7. Beckmann CF, Jenkinson M, Smith SM. **General multilevel linear modeling for group analysis in fMRI.** *Neuroimage* 2003;20:1052–63
8. Woolrich MW, Behrens TE, Beckmann CF, et al. **Multilevel linear modelling for fMRI group analysis using Bayesian inference.** *Neuroimage* 2004;21:1732–47
9. Woolrich M. **Robust group analysis using outlier inference.** *Neuroimage* 2008;41:286–301
10. Smith SM, Jenkinson M, Johansen-Berg H, et al. **Tract-based spatial statistics: voxelwise analysis of multi-subject diffusion data.** *Neuroimage* 2006;31:1487–505
11. Smith SM, Johansen-Berg H, Jenkinson M, et al. **Acquisition and voxelwise analysis of multi-subject diffusion data with tract-based spatial statistics.** *Nat Protoc* 2007;2:499–503
12. Smith SM, Nichols TE. **Threshold-free cluster enhancement: addressing problems of smoothing, threshold dependence and localisation in cluster inference.** *Neuroimage* 2009;44:83–98
13. Smith SM, Jenkinson M, Woolrich MW, et al. **Advances in functional and structural MR image analysis and implementation as FSL.** *Neuroimage* 2004;23 Suppl 1:S208–19
14. Raichle ME. **Two views of brain function.** *Trends Cogn Sci* 2010;14:180–90
15. Büchel C, Coull JT, Friston KJ. **The predictive value of changes in effective connectivity for human learning.** *Science* 1999;283:1538–41
16. Bassett DS, Wymbs NF, Porter MA, et al. **Dynamic reconfiguration of human brain networks during learning.** *Proc Natl Acad Sci U S A* 2011;108:7641–46
17. Lewis CM, Baldassarre A, Committeri G, et al. **Learning sculpts the spontaneous activity of the resting human brain.** *Proc Natl Acad Sci U S A* 2009;106:17558–63
18. Haller S, Kopel R, Jhooti P, et al. **Dynamic reconfiguration of human brain functional networks through neurofeedback.** *Neuroimage* 2013;81C:243–52
19. Greicius MD, Krasnow B, Reiss AL, et al. **Functional connectivity in the resting brain: a network analysis of the default mode hypothesis.** *Proc Natl Acad Sci U S A* 2003;100:253–58
20. Damoiseaux JS, Rombouts SA, Barkhof F, et al. **Consistent resting-state networks across healthy subjects.** *Proc Natl Acad Sci U S A* 2006;103:13848–53
21. Cieslik EC, Zilles K, Caspers S, et al. **Is there "one" DLPFC in cognitive action control? Evidence for heterogeneity from co-activation-based parcellation.** *Cereb Cortex* 2012 Aug 23. [Epub ahead of print]
22. Hamilton JP, Etkin A, Furman DJ, et al. **Functional neuroimaging of major depressive disorder: a meta-analysis and new integration of base line activation and neural response data.** *Am J Psychiatry* 2012;169:693–703
23. Korgaonkar MS, Grieve SM, Etkin A, et al. **Using standardized fMRI protocols to identify patterns of prefrontal circuit dysregulation that are common and specific to cognitive and emotional tasks in major depressive disorder: first wave results from the iSPOT-D study.** *Neuropsychopharmacology* 2013;38:863–71
24. Mechias ML, Etkin A, Kalisch R. **A meta-analysis of instructed fear studies: implications for conscious appraisal of threat.** *Neuroimage* 2010;49:1760–68
25. Straube T, Mentzel HJ, Miltner WH. **Waiting for spiders: brain activation during anticipatory anxiety in spider phobics.** *Neuroimage* 2007;37:1427–36
26. Holtz K, Pané-Farré CA, Wendt J, et al. **Brain activation during anticipation of interoceptive threat.** *Neuroimage* 2012;61:857–65
27. Schunck T, Erb G, Mathis A, et al. **Test-retest reliability of a functional MRI anticipatory anxiety paradigm in healthy volunteers.** *J Magn Reson Imaging* 2008;27:459–68
28. Simmons AN, Stein MB, Strigo IA, et al. **Anxiety positive subjects show altered processing in the anterior insula during anticipation of negative stimuli.** *Hum Brain Mapp* 2011;32:1836–46
29. Eryilmaz H, Van De Ville D, Schwartz S, et al. **Impact of transient emotions on functional connectivity during subsequent resting state: a wavelet correlation approach.** *Neuroimage* 2011;54:2481–91
30. Van De Ville D, Jhooti P, Haas T, et al. **Recovery of the default mode network after demanding neurofeedback training occurs in spatio-temporally segregated subnetworks.** *Neuroimage* 2012;63:1775–81

Stent-Assisted Coiling versus Coiling Alone in Unruptured Intracranial Aneurysms in the Matrix and Platinum Science Trial: Safety, Efficacy, and Mid-Term Outcomes

S.W. Hetts, A. Turk, J.D. English, C.F. Dowd, J. Mocco, C. Prestigiacomo, G. Nesbit, S.G. Ge, J.N. Jin, K. Carroll, Y. Murayama, A. Gholkar, S. Barnwell, D. Lopes, S.C. Johnston, and C. McDougall, on behalf of the Matrix and Platinum Science Trial Investigators

ABSTRACT

BACKGROUND AND PURPOSE: Stent-assisted coiling may result in less aneurysm recanalization but more complications than coiling alone. We evaluated outcomes of coiling with and without stents in the multicenter Matrix and Platinum Science Trial.

MATERIALS AND METHODS: All patients in the Matrix and Platinum Science Trial with unruptured intracranial aneurysms treated per protocol were included. Baseline patient and aneurysm characteristics, procedural details, neurologic outcomes, angiographic outcomes, and safety data were analyzed.

RESULTS: Overall, 137 of 361 (38%) patients were treated with a stent. Stent-coiled aneurysms had wider necks (≥4 mm in 62% with stents versus 33% without, $P < .0001$) and lower dome-to-neck ratios (1.3 versus 1.8, $P < .0001$). Periprocedural serious adverse events occurred infrequently in those treated with and without stents (6.6% versus 4.5%, $P = .39$). At 1 year, total significant adverse events, mortality, and worsening of mRS were similar in treatment groups, but ischemic strokes were more common in stent-coiled patients than in coiled patients (8.8% versus 2.2%, $P = .005$). However, multivariate analysis confirmed that at 2 years after treatment, prior cerebrovascular accident (OR, 4.7; $P = .0089$) and aneurysm neck width ≥4 mm (OR, 4.5; $P = .02$) were the only independent predictors of ischemic stroke. Stent use was not an independent predictor of ischemic stroke at 2 years (OR, 1.1; $P = .94$). Stent use did not predict target aneurysm recurrence at 2 years, but aneurysm dome size ≥10 mm (OR, 9.94; $P < .0001$) did predict target aneurysm recurrence.

CONCLUSIONS: Stent-coiling had similar outcomes as coiling despite stented aneurysms having more difficult morphology than coiled aneurysms. Increased ischemic events in stent-coiled aneurysms were attributable to baseline risk factors and aneurysm morphology.

ABBREVIATIONS: MAPS = Matrix and Platinum Science Trial; TAR = target aneurysm recurrence

As intracranial aneurysm treatment has shifted in the past 30 years from exclusively surgical to predominantly endovascular, aneurysm morphologies once considered untreatable endovascularly are now treatable with coils, stents, and flow diverters.[1-3] Particularly for saccular aneurysms with broad necks and short domes, stent-assisted coiling has become a common technique.[4-8] Prior studies have reported that stent-coiling may result in less aneurysm recanalization over time but more complications—both intraprocedurally and in a delayed fashion—than coiling alone.[9-13] A recent large, single-institution, retrospective series described higher morbidity and mortality rates associated with the stent-coiling technique as compared with coiling either with or without balloon assistance.[14]

Given that prospective data on stent-coiling are limited, we analyzed data from the prospective, randomized, multicenter Matrix and Platinum Science (MAPS) Trial (NCT00396981, www.clinicaltrials.gov). The MAPS Trial was primarily designed to determine whether polymer-modified coils or platinum bare metal coils result in lower aneurysm recanalization, lower aneurysm rupture or rerupture, or lower aneurysm retreatment. Although patients were

Received May 23, 2013; accepted after revision August 5.

From the Departments of Radiology and Biomedical Imaging (S.W.H., C.F.D.) and Neurology (S.C.J.), University of California, San Francisco, San Francisco, California; Department of Radiology (A.T.), Medical University of South Carolina, Charleston, South Carolina; Departments of Neurology and Radiology (J.D.E.), California Pacific Medical Center, San Francisco, California; Department of Neurosurgery (J.M.), Vanderbilt University Medical Center, Nashville, Tennessee; Department of Neurosurgery (C.P.), University of Medicine and Dentistry of New Jersey, Newark, New Jersey; Department of Radiology (G.N., S.B.), Oregon Health and Science University, Portland, Oregon; Department of Biostatistics (S.G.G., J.N.J.), Stryker Neurovascular (K.C.), Fremont, California; Department of Neurosurgery (Y.M.), Jikei University, Tokyo, Japan; Department of Neuroradiology (A.G.), Newcastle Upon Tyne Hospital, Newcastle Upon Tyne, United Kingdom; Department of Neurosurgery (D.L.), Rush University Medical Center, Chicago, Illinois; and Department of Neurosurgery (C.M.), Barrow Neurological Institute, Phoenix, Arizona.

Please address correspondence to Steven W. Hetts, MD, Interventional Neuroradiology, 505 Parnassus Ave, L-352, San Francisco, CA 94143–0628; e-mail: steven.hetts@radiology.ucsf.edu

Indicates open access to non-subscribers at www.ajnr.org

Indicates article with supplemental on-line table.

http://dx.doi.org/10.3174/ajnr.A3755

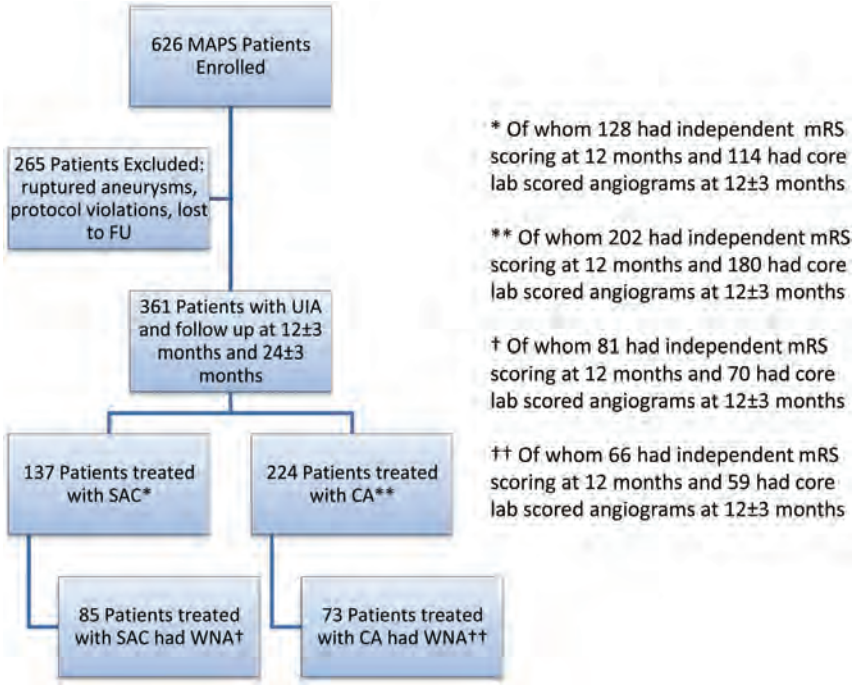

FIG 1. Patient flow for MAPS stent substudy. FU indicates follow-up; UIA, unruptured intracranial aneurysm; SAC, stent-assisted coiling; CA, coiling alone; WNA, wide-neck aneurysm.

randomly assigned to platinum bare metal coil or polymer-modified coil implantation, adjunctive devices (including balloons and stents) could be used in any case at the discretion of the operating physician.

We compared baseline patient and aneurysm characteristics, procedural details, safety data, neurologic outcomes, and angiographic outcomes in MAPS patients with unruptured intracranial aneurysms who were treated with stent-coiling or coiling without stent placement. Additionally, we analyzed results for the subset of patients with wide-neck aneurysms.

MATERIALS AND METHODS

The MAPS Trial was conceived and designed by the investigators, with advice provided by the sponsor, and was approved by all local institutional review boards. The study was conducted in accordance with the *International Conference on Harmonization (ICH) Good Clinical Practice (GCP): Consolidated Guideline*, the Declaration of Helsinki, EN ISO14155 Clinical Investigations of Medical Devices for Human Subjects, and the applicable regulations from the US Food and Drug Administration. The primary end point of the MAPS Trial was target aneurysm recurrence (TAR), designed to be a clinically relevant composite end point that comprised aneurysm rupture after treatment, retreatment, or death from an unknown cause. The trial was designed to study the TAR rate for the study device and to investigate how TAR correlated with the angiographic surrogates that are widely used in endovascular aneurysm treatment studies to evaluate outcomes. Clinical and angiographic evaluations were completed at the time of initial aneurysm treatment and within 12 ± 3 months after initial aneurysm treatment. Further clinical follow-up of subjects by telephone interview will continue annually until 5 years after initial aneurysm treatment.

Study Subjects

The study population for the current analysis included subjects 18–80 years of age with a baseline mRS score of 0–3 who had a single documented, untreated, unruptured intracranial aneurysm (4–20 mm in maximum dimension on DSA) for which both polymer modified coils (Matrix2, Stryker Neurovascular, Fremont, California) and platinum bare metal coils (GDC, Stryker Neurovascular) were treatment options and for which primary coiling treatment was planned to be completed during a single procedure. Stent placement (Neuroform stent, Stryker Neurovascular), as a separate preliminary procedure antecedent to the primary coiling, was allowed, as was stent placement in conjunction with the primary coiling procedure. Although the overall MAPS Trial prospectively enrolled patients with ruptured and unruptured aneurysms, only patients with unruptured aneurysms were included in the present post hoc data analysis.

We chose to analyze the unruptured aneurysm cohort because the stent-coiling technique is primarily applied in clinical practice to patients with unruptured aneurysms. The administration of dual antiplatelet medications typically indicated in stent-coiling is relatively contraindicated in patients with ruptured aneurysm who might need additional interventions such as ventricular drain placement. On this basis, all patients with ruptured aneurysms in the MAPS trial were excluded from our current analysis, consisting of 6 patients treated with stent-coiling and 201 patients treated with coiling (Fig 1).

A total of 361 patients in the MAPS Trial with unruptured intracranial aneurysms were treated per protocol. Data were analyzed post hoc for all unruptured intracranial aneurysms and for the wide-neck (≥4 mm) aneurysm subgroup of unruptured intracranial aneurysms. Note that because this is a post hoc analysis of the MAPS Trial, patients were not randomly assigned to stent-coiling or coiling and may be dissimilar, especially within the cohort including all unruptured intracranial aneurysms.

As defined above, the primary outcome measure was TAR. Secondary outcome measures, all defined a priori, included angiographic assessment as assessed by enrolling sites and core imaging laboratory; neurologic assessments (mRS at 12 ± 3 months and as change from baseline performed in-person by an independent certified practitioner at a scheduled clinic visit); and technical procedural success, defined as the successful placement of coils in the target aneurysm. Target aneurysm reintervention was defined as any further treatment of the aneurysm, with the retreatment decision being at the discretion of the operator.

All sites graded their own angiographic outcomes on the basis of the modified 3-point Raymond Scale after the procedure and at follow-up.[15-17] All sites also recorded an assessment of perceived change from baseline (same, better, worse) at follow-up. Digitized

copies of the angiograms were created for all cases and stored at an independent angiographic core laboratory located at the University of California, San Francisco. The core laboratory assessed all treatment and 1-year follow-up angiograms blinded to the treatment technique. Core laboratory evaluations used the same angiographic scales as did the enrolling sites. All angiographic data presented in this analysis are from core laboratory evaluations performed by 2 neurointerventionalists, with adjudication of differences in angiographic scoring by a third neurointerventionalist.[17] The core laboratory also evaluated angiograms of patients with wide-neck aneurysms receiving stent-coiling specifically for any stent migration between immediate postprocedure DSA and follow-up DSA.

An independent steering committee was responsible for overall oversight of the science and execution of the trial. Patient safety data were reviewed at regular intervals by an independent Data Monitoring Committee. An independent Clinical Events Committee was responsible for reviewing and adjudicating all deaths and neurologic events. On-site monitoring and source document verification of case report forms against original patient records were completed for more than 40% of patients at the completion of the 1-year follow-up, including all patients who had been treated with stent-coiling.

Statistical Methods

The primary end point (TAR) rate was calculated by use of Kaplan-Meier estimates in each group at the end of a 12 ± 3–month window (455 days) and a 24 ± 3–month window (820 days). Time to event was based on the real time to rupture/rerupture, retreatment, or unknown cause of death, whichever happened first for each subject. Subjects who had not had an event were censored at their last clinical visit or at 820 days, whichever came earlier.

The protocol prespecified additional univariate and multivariate regression models to analyze the time to TAR, changes in mRS from baseline to the 12-month assessment, and subgroup analyses. Additional post hoc multivariate regression analysis was performed to evaluate the contribution of baseline risk factors, aneurysm characteristics, and use of stents to stroke rates and target aneurysm recurrence. Complete data on ischemic stroke and TAR rates were included in predictor analyses, including data from all enrolling centers.

A Student *t* test was used to test distributions of continuous variables between the groups. Either χ^2 or the Fisher exact test was used to analyze binary variables according to standard statistical practice. For ordinal variables, such as the mRS, recanalization, and mRS scores, the Wilcoxon rank sum test was used to test the distribution between the groups. The differences between the groups were presented with the 95% CI estimated by the normal approximation. For the binary outcomes, the relative risks as well as its 95% CIs were also presented. All statistical analyses were performed with the use of SAS, version 9.2 (SAS Institute, Cary, North Carolina).

RESULTS

Of 626 patients in the MAPS Trial, overall, 361 with unruptured intracranial aneurysms were treated per protocol (Fig 1). Of these 361 patients with unruptured intracranial aneurysms, 137 were treated with a Neuroform stent and either platinum bare metal coils or polymer modified coils (stent-coiling group) and 224 were treated with platinum bare metal coils or polymer modified coils without a stent (coiling group). Within the unruptured intracranial aneurysm cohort, 158 patients had wide-neck aneurysms with necks ≥4 mm in diameter (wide-neck aneurysm subset). Within this wide-neck aneurysm subset, 85 patients received stent-coiling and 73 received coiling. Because stent use was at the operating physician's discretion on a case-by-case basis, some enrolling sites used many stents and some used none (Fig 2). Stent use was particularly inhomogeneous geographically: 88.3% of stent-coiling cases were performed in North American centers versus 65.6% of coiling cases without stent use ($P = .0001$, Table 1).

Baseline Demographics

Patients with stent-coiling trended toward being sicker at baseline than did coiling patients in the entire unruptured intracranial aneurysm cohort (Table 1), with coronary artery disease in 19% of stent-coiling versus 13.1% of coiling ($P = .14$). Coronary artery disease was significantly more frequent among the patients with stent-coiling with wide-neck aneurysms (22.4%) as compared with patients with wide-neck aneurysms treated with coiling (5.6%, $P = .003$). Prior stroke was also marginally more frequent in the patients with stents and coils (17.9%) versus the patients with coils alone in the wide-neck aneurysms (8.3%, $P = .08$). Otherwise, both groups were similar at baseline.

Aneurysm Characteristics

Aneurysms in the stent-coiling group had more technically challenging morphologies than those in the coiling group (Table 2). Among unruptured intracranial aneurysms, 62% of stent-coiling versus 33% of coiling were wide-neck aneurysms ($P < .0001$), and the dome-to-neck ratio was lower for stent-coiling than for coiling (1.3 versus 1.8, $P < .0001$). Among wide-neck aneurysms, patients receiving stent-coiling had smaller aneurysms (maximum dimension >10 mm in 30.6% versus 47.9%, $P = .03$), with larger necks (mean, 5.6 versus 5.0 mm; $P = .004$), and lower dome-to-neck ratios (1.2 versus 1.6, $P < .0001$). In both the overall unruptured intracranial aneurysm cohort as well as the wide-neck aneurysm subset, aneurysms treated with stent-coiling were less likely to be located on the circle of Willis than those treated with coiling.

Procedural Characteristics

Among patients with unruptured intracranial aneurysms, the stent-coiling procedure took slightly longer than did the coiling procedure (mean, 134.2 versus 117.8 minutes; $P = .02$). This time difference was not significant in the more technically challenging wide-neck aneurysm subset (mean, 147.5 versus 135.2 minutes; $P = .30$) (Table 3).

For unruptured intracranial aneurysms, coil packing attenuation trended higher with stent-coiling (26.2% versus 24.2%, $P = .07$). Among wide-neck aneurysms, packing attenuation for stent-coiling was higher than packing attenuation for coiling without stent placement (26.4% versus 21.1%, $P = .002$) despite a trend

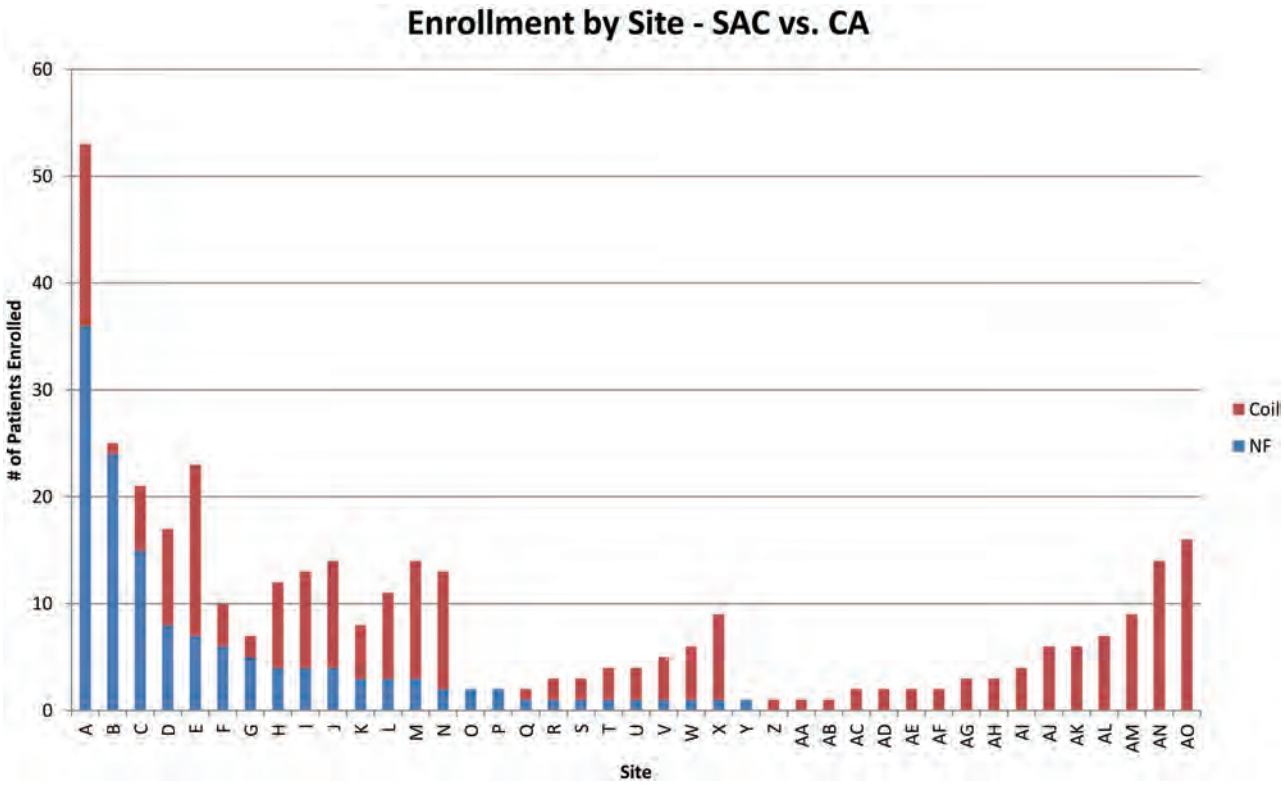

FIG 2. Stent use by enrolling site. SAC indicates stent-assisted coiling, CA, coiling alone, NF, Neuroform stent.

Table 1: Baseline patient demographics

	All Unruptured Aneurysms			Wide-Neck Aneurysms		
	Stent-Coil (*n* = 137)	Coil Alone (*n* = 224)	*P* Value	Stent-Coil (*n* = 85)	Coil Alone (*n* = 73)	*P* Value
North American	88.3%	65.6%	.0001	89.4%	61.6%	<.0001
Age, y	56.5	56.7	.90	58.4	57.7	.68
Female	76.6	76.8	.98	72.9	79.5	.34
Coronary artery disease	19.0%	13.1%	.14	22.4%	5.6%	.003
≥2 Cerebrovascular risk factors[a]	32.1%	25.9%	.20	34.1%	26.0%	.27
Prior CVA	16.9%	14.5%	.54	17.9%	8.3%	.08
Preprocedure mRS						
0	80.3%	84.4%	>.99	80.0%	90.4%	NA
1	15.3%	11.6%		14.1%	9.6%	
2	4.4%	3.6%		5.9%	0.0%	
3	0.0%	0.4%	>.99	0.0%	0.0%	NA

Note:—CVA indicates cerebrovascular accident; NA, not applicable.

[a] Cerebrovascular risk factors include hypertension, hyperlipidemia, coronary artery disease, and diabetes mellitus.

Table 2: Aneurysm characteristics

	All Unruptured Aneurysms			Wide-Neck Aneurysms		
	Stent-Coil (*n* = 137)	Coil Alone (*n* = 224)	*P* Value	Stent-Coil (*n* = 85)	Coil Alone (*n* = 73)	*P* Value
Maximum dimension	7.6	7.8	.46	8.9	10.1	.007
Height is max	43.8%	54.9%	.04	42.4%	50.7%	.30
Width is max	29.9%	21.4%	.07	30.6%	23.3%	.30
Depth is max	26.3%	23.7%	.58	27.1%	26.0%	.88
Max dimension >10 mm	19.7%	21.0%	.77	30.6%	47.9%	.03
Neck ≥4 mm	62.0%	32.6%	<.0001	100%	100%	NA
Average neck	4.7	3.5	<.0001	5.6	5.0	.004
Dome/neck radio	1.3	1.8	<.0001	1.2	1.6	<.0001
Dome/parent artery ratio	2.0	2.1	.33	2.2	2.6	.01
Circle of Willis location	44.5%	64.7%	.0002	48.2%	72.6%	.002

Note:—Max indicates maximum.

toward use of fewer coils (8.5 mean versus 10.1 mean, $P = .07$). Overall technical success was high for all groups but marginally lower for stent-coiling in the unruptured intracranial aneurysm cohort (97.8%) as compared with coiling in the unruptured intracranial aneurysm cohort (100%, $P = .054$). Among unruptured intracranial aneurysms, complete angiographic obliteration

Table 3: Procedural Characteristics

	All Unruptured Aneurysms			Wide-Neck Aneurysms		
	Stent-Coil (*n* = 137)	Coil Alone (*n* = 224)	*P* Value	Stent-Coil (*n* = 85)	Coil Alone (*n* = 73)	*P* Value
Aspirin alone	8.0%	23.2%	.0002	4.7%	28.8%	<.0001
Clopidogrel alone	5.1%	4.5%	.78	3.5%	1.4%	0.62
Aspirin + clopidogrel	78.1%	37.1%	<.0001	82.4%	37.0%	<.0001
Antiplatelet use not recorded[a]	8.8%	35.3%	<.0001	9.4%	32.9%	.0003
Procedure time, min	134.2	117.8	.02	147.5	135.2	.30
No. of coils	6.9	7.1	.70	8.5	10.1	.07
Bare metal coils	49.6%	50.9%	.82	48.2%	53.4%	.52
Matrix coils	50.4%	49.1%	.82	51.8%	46.6%	.52
Packing density	26.2%	24.0%	.07	26.4%	21.1%	.002
Technical success	97.8%	100%	.054	97.6%	100%	.50
Occlusion assessment						
Raymond 1	21.1%	33.9%	.02[b]	18.6%	27.1%	.25[c]
Raymond 2	25.4%	25.6%	.98[b]	27.1%	30.5%	.67[c]
Raymond 3	53.5%	40.6%	.03[b]	54.3%	42.4%	.18[c]

[a] No antiplatelet use recorded in these subjects: for an individual subject, this could mean no aspirin or clopidogrel was used or that data are missing.
[b] Core lab occlusion assessment for the 81% of patients who had assessable angiograms after the procedure.
[c] Core lab occlusion assessment for the 82% of patients who had assessable angiograms after the procedure.

Table 4: Safety: Stroke and Other Significant Adverse Events

	All Unruptured Aneurysms			Wide-Neck Aneurysms		
	Stent-Coil (*n* = 137)	Coil Alone (*n* = 224)	*P* Value	Stent-Coil (*n* = 85)	Coil Alone (*n* = 73)	*P* Value
Periprocedural significant adverse event rate	6.6%	4.5%	.39	3.7%	0.89%	.11
1-Year hemorrhagic stroke rate	2.9%	0.4%	.07	2.4%	0.0%	.50
1-Year ischemic stroke rate	8.8%	2.2%	.005	11.8%	4.1%	.08
if problem site is excluded[a]						
1-Year ischemic stroke rate	6.2%	2.2%	.11	8.8%	4.1%	.31

[a] One enrolling site accounted for 5 of 12 subjects with ischemic stroke in the unruptured aneurysm group. All ischemic strokes at that site occurred ≥7 days after the procedure.

Table 5: Safety: mRS at baseline and 1 year after the procedure

	All Unruptured Aneurysms					Wide-Neck Aneurysms				
	Stent-Coil		Coil Alone			Stent-Coil		Coil Alone		
12-Month mRS[a]	Base (*n* = 137)	1 Year (*n* = 128)	Base (*n* = 224)	1 Year (*n* = 202)	*P* Value	Base (*n* = 85)	1 Year (*n* = 81)	Base (*n* = 73)	1 Year (*n* = 66)	*P* Value
0	80.3%	80.5%	84.4%	87.6%		80.0%	80.2%	90.4%	92.4%	
1	15.3%	14.1%	11.6%	6.9%		14.1%	12.3%	9.6%	6.1%	
2	4.4%	1.6%	3.6%	1.0%		5.9%	2.5%	0.0%	0.0%	
3	0.0%	1.6%	0.4%	2.5%		0.0%	2.5%	0.0%	1.5%	
6	0.0%	2.3%	0.0%	2.0%		0.0%	2.5%	0.0%	0.0%	
mRS worse than base		12.5%		8.4%	.23		13.6%		4.5%	.06

[a] Twelve-month mRS scores were available for 128, 202, 81, and 66 patients, respectively, across all subsets.

of aneurysm filling at the conclusion of treatment was lower for stent-coiling than for coiling (21.1% versus 33.9%, $P = .02$). Although a similar trend was present in the wide-neck aneurysm subset, it did not reach statistical significance. Dual-antiplatelet use at the time of treatment was higher for stent-coiling than for coiling because it is the practice of most centers to use both aspirin and clopidogrel at the time of stent-coiling and for a variable period thereafter.

Safety: Stroke, Other Significant Adverse Events, and Neurologic Disability

Although total periprocedural significant adverse events did not differ between stent-coiling and coiling (6.6% versus 4.5%, $P = .39$), the rate of stroke within 1 year of treatment did differ between these groups (8.8% versus 2.2%, respectively; $P = .005$, Table 4). Of note, 42% of stent-coiling ischemic strokes occurred at one enrolling site, the exclusion of which brings the comparative ischemic stroke rates to 6.2% versus 2.2%, respectively ($P = .11$). Within the wide-neck aneurysm subgroup, there was no significant difference in ischemic stroke rates between stent-coiling and coiling, though there was a trend toward more ischemia in the stented patients ($P = .08$). Among all patients with unruptured intracranial aneurysms, 1-year hemorrhagic strokes also trended toward a higher rate in the stent-coiling group (2.9%) compared with the coiling group (0.4%, $P = .07$). At 1 year, total significant adverse events, mortality, and worsening of mRS scores were not different between stent-coiling and coiling (Table 5) in the entire unruptured intracranial aneurysm cohort, though there was a trend toward worsening mRS scores in the wide-neck aneurysm subset ($P = .06$).

Five stent-coiled patients had periprocedural strokes (<7 days after the procedure) and 7 stent-coiled patients had delayed strokes (On-line Table). Of the periprocedural strokes, one was thought related to preprocedure angioplasty or intraprocedure parent artery coil prolapse. A patient with extensive cardiovascular risk factors had both a periprocedural

Table 6: Clinical outcomes 1 year after the procedure

	All Unruptured Aneurysms			Wide-Neck Aneurysms		
	Stent-Coil (*n* = 137)	Coil Alone (*n* = 224)	*P* Value	Stent-Coil (*n* = 85)	Coil Alone (*n* = 73)	*P* Value
TAR	8.8%	8.5%	.93	14.1%	13.7%	.94
Delayed bleed	0.0%	0.4%	<.99	0.0%	1.4%	.46
Retreatment	8.8%	8.5%	.93	14.1%	13.7%	.94

Table 7: Angiographic outcomes 1 year after the procedure

	All Unruptured Aneurysms			Wide-Neck Aneurysms		
	Stent-Coil (*n* = 114)	Coil Alone (*n* = 180)	*P* Value	Stent-Coil (*n* = 70)	Coil Alone (*n* = 59)	*P* Value
Occlusion assessment						
Raymond 1	51.8%	44.4%	.22	45.7%	27.1%	.03
Raymond 2	21.1%	23.9%	.57	17.1%	30.5%	.07
Raymond 3	27.2%	31.7%	.41	37.1%	42.4%	.55
Change assessment						
Better	51.8%	31.1%	.0004	45.7%	20.3%	.003
Same	31.6%	35.6%	.48	32.9%	28.8%	.62
Worse	16.7%	33.3%	.002	21.4%	50.8%	.0005

Note:—81% of subjects in the "all unruptured aneurysms" group and 82% of subjects in the "wide-neck aneurysms" subgroup had angiograms assessable by the core lab at 1-year follow-up.

Table 8: Multivariate predictors of ischemic stroke at 1 year and 2 years

Parameter	1-Year OR (95% CI)	1-Year *P* Value	2-Year OR (95% CI)	2-Year *P* Value
Prior cerebrovascular accident	3.84 (1.29–11.4)	.0159	4.71 (1.47–15.0)	.0089
Aneurysm neck size ≥4 mm	3.70 (1.09–12.5)	.0359	4.51 (1.27–16.0)	.0196
Stent used	1.85 (0.61–5.59)	.2732	1.05 (0.34–3.27)	.9351

Note:—Complete data on ischemic stroke rates were included in predictor analysis, including data from all enrolling centers.

Table 9: Multivariate predictors of target aneurysm recurrence at 1 year and 2 years

Parameter	1-Year OR (95% CI)	1-Year *P* Value	2-Year OR (95% CI)	2-Year *P* Value
Aneurysm dome size ≥10 mm	10.1 (4.06–24.9)	<.0001	9.94 (4.12–24.0)	<.0001
Aneurysm neck size ≥4 mm	2.34 (0.94–5.81)	.0664	2.17 (0.93–5.06)	.0729
Stent used	0.89 (0.38–2.10)	.7855	0.83 (0.36–1.88)	.6505

Note:—Complete data on target aneurysm recurrence rates were included in predictor analysis, including data from all enrolling centers.

stroke and a myocardial infarction and died. Three patients had delayed strokes after documented or suspected antiplatelet medication noncompliance. One patient each had a delayed stroke after hernia surgery, after aneurysm retreatment, and after surveillance angiography. One patient with a basilar tip aneurysm had a pontine infarct thought to be related to small-vessel ischemic disease.

Outcomes at 1 Year and 2 Years

Clinical outcomes at 1 year and 2 years, on the basis of the primary MAPS composite end point of TAR, were similarly excellent in stent-coiling and coiling patients in the unruptured intracranial aneurysm cohort as well as in the wide-neck aneurysm subset (Table 6). Only a single patient from the coiling group had aneurysm rupture; all remaining TAR events were aneurysm retreatments at the discretion of the operating physician.

Complete angiographic obliteration rates for stent-coiling were significantly higher than for coiling in the wide-neck aneurysm subset at 1 year (Raymond 1 occlusion, 45.7% versus 27.1%, $P = .03$) (Table 7). Angiographic worsening (on the better-same-worse scale comparing 12 ± 3–month follow-up angiograms with immediate posttreatment angiograms) was lower for stent-coiling than for coiling in both the unruptured intracranial aneurysm (16.7% versus 33.3%, $P = .002$) and wide-neck aneurysm groups (21.4% versus 50.8%, $P = .0005$). Concomitantly, angiographic improvement at 1 year in treated aneurysms was more common for stent-coiling versus coiling in the unruptured intracranial aneurysm cohort (51.8% versus 31.1%, $P = .0004$) as well as in the wide-neck aneurysm subset (45.7% versus 20.3%, $P = .003$). Core lab analysis revealed no significant stent migration at 1 year. Because angiographic follow-up was not mandated as part of the trial beyond 12 ± 3 months, 2-year angiographic data were not collected.

Multivariate Analysis of Stroke and TAR

The higher ischemic stroke rate in patients receiving stents was attributable to a higher proportion of stent-coiling patients having a baseline history of cerebrovascular accident and a higher proportion of stent-coiling patients having aneurysms with wide necks (Table 8) both at 1 year and 2 years after treatment. TAR, which consisted almost entirely of aneurysm retreatments, was predicted by baseline aneurysm morphologic characteristics, including dome ≥10 mm and neck ≥4 mm, at both 1 year and 2 years of follow-up (Table 9). Stent use was not an independent predictor of TAR.

DISCUSSION

Self-expanding stents have greatly broadened the range of aneurysm morphologies amenable to endovascular treatment. Although the MAPS Trial was designed to evaluate polymer modified coils versus platinum bare metal coils, it allows us to analyze high-quality prospective data on patient outcomes after stent-coiling.

There was a high technical success rate for both stent-coiling and coiling. Stent-coiling was used more frequently in aneurysms with morphologies that typically limit the use of coils because of the risk of parent artery coil prolapse, including low dome-to-neck ratios and wide aneurysm necks. Aneurysm neck ≥4 mm has been associated with a higher risk of aneurysm recanalization[18,19]; in the MAPS Trial, all 12 stent-coiled aneurysms and 10 of 19 coiled aneurysms retreated within 1 year had necks ≥4 mm (Table 6). Conversely, no stent-coiled aneurysms with a <4-mm neck (and only 4% of coiled aneurysms with <4-mm neck) were retreated within 1 year. Wide-neck stent-coiled aneurysms also had higher packing densities, perhaps because the stent lessens concern for parent artery coil prolapse.[20] This higher packing attenuation may explain why wide-neck stent-coiled aneurysms had superior aneurysm occlusion (Raymond Scale scores) at 1 year as compared with wide-neck coiled aneurysms.

Although stent-coiled aneurysms had worse Raymond occlusion scores immediately after treatment than did coiled aneurysms in both the total unruptured intracranial aneurysm cohort and the wide-neck aneurysm subset, they also had more improvement in angiographic appearance at follow-up. There are 4 possible explanations. First, starting with worse initial angiograms will bias follow-up readings on the better-same-worse scale toward more improvement. Second, procedural dual-antiplatelet use is significantly more frequent in stent-coiled patients; therefore it is possible that more interstitial filling is present immediately after treatment in stent-coiled patients as compared with coiled patients. Third, stents were used in more morphologically challenging aneurysms than in the coiled group, and it may not have been possible to treat these aneurysms without a stent. For example, in a very broad-neck, low-domed, shallow aneurysm, it might be difficult to herniate coils into the proximal and distal corners of the aneurysm neck even with a stent in place; such aneurysms could not have been treated with coils alone. Fourth, stents may help to prevent coil compaction within an adjacent aneurysm, perhaps directly by acting as partial parent artery flow diverters, or indirectly by allowing practitioners to confidently pack more coils into stented aneurysms (especially at the neck), or by providing a scaffold for endothelialization across the neck. Because angiographic appearance on follow-up significantly influences aneurysm retreatment decisions and initial core laboratory angiographic score predicts retreatment at 1 year (McDougall et al, *AJNR* in press), it will be important to determine how well immediate posttreatment aneurysm occlusion ultimately predicts aneurysm retreatment over the course of the entire MAPS Trial.

Although periprocedural total significant adverse events were low and similar in stent-coiled and coiled patients, the higher delayed ischemic stroke rate observed in stent-coiled patients is concerning. It is reassuring, however, that multivariate analysis including patients from all enrolling centers confirms that this increased stroke risk is attributable to the presence of more patients in the stent-coiled group having a history of cerebrovascular accident and the presence of more wide-neck aneurysms in the stent-coiled group, as opposed to being caused by stent use per se. Other investigators have reported increased thromboembolic events with the use of intracranial stents in the treatment of aneurysms.[14] Whenever metal is placed in the parent artery, use of antiplatelet agents such as aspirin and/or clopidogrel is prudent to reduce platelet aggregation before the stent becomes endothelialized. Many centers use dual-antiplatelet medications (eg, aspirin and clopidogrel) for either a specified period of time after intracranial stent deployment (eg, 6 weeks or 6 months), until a follow-up angiogram, or indefinitely. Practitioner variability in postprocedure antiplatelet medication may significantly influence delayed ischemic risk to stent patients. This is suggested by poor patient antiplatelet compliance accounting for at least 3 of 12 ischemic strokes in the stent-coiled group and 3 additional ischemic strokes taking place immediately around the time of surgery, aneurysm retreatment, and follow-up angiography, during which antiplatelet medication regimens were uncertain (On-line Table). In addition to medication compliance and lack of consensus on antiplatelet regimen after intracranial stent placement, studies also suggest that inherent biologic resistance to the effects of aspirin and/or clopidogrel may also play a role in delayed ischemic events.[21]

The primary goal of aneurysm treatment is to prevent subarachnoid hemorrhage. Given the very low hemorrhage rate (1 of 361 patients within 2 years), it is too soon to speculate on the overall utility of stent-coiling compared with coiling in protecting patients with unruptured intracranial aneurysms from aneurysm rupture. Not surprisingly, aneurysm dome size ≥10 mm predicted TAR, possibly as the result of the greater opportunity for coil compaction in large aneurysms.

There are several limitations to our study. First, this is a post hoc data analysis from a prospective trial designed to evaluate polymer modified coils versus platinum bare metal coils, not stent-coiling versus coiling. Therefore, stent use was at the operating physician's discretion. Some centers used many stents and some used none. Stent use was significantly higher in North America as opposed to outside North America, suggesting that other geography-specific confounders may be present. Second, some aneurysm morphologies probably could not be treated with coiling alone and could only be treated with stent-coiling, thus biasing stent-coiling cases toward aneurysms with particularly wide necks and low dome-to-neck ratios, known predictors of aneurysm recanalization and procedural complications. Third, postprocedure antiplatelet medication management was not uniform. Because the delayed ischemic stroke rate for stent-coiling may be associated with antiplatelet management, this is a significant limitation. Fourth, the core angiographic laboratory could not score almost 20% of angiograms, most frequently because of image quality, nonmatched comparison views between immediate posttreatment and follow-up, and lack of digital subtraction. Fifth, because the core angiographic laboratory evaluated primarily DSA images, although stent proximal and distal markers could usually be visualized, stent struts could not be directly visualized. Given recent reports of increased delayed thromboembolic complications arising in cases in which stents do not fully appose the wall of the parent artery,[22,23] this also limits our ability to evaluate delayed ischemic risk in stent-coiled patients.

CONCLUSIONS

Stent-coiling had outcomes similar to coiling, despite stented aneurysms having more difficult morphology than did coiled aneurysms. Increased ischemic events in stent-coiled aneurysms were attributable to baseline risk factors and aneurysm morphology, underscoring the overall safety of the stent-coiling technique.

ACKNOWLEDGMENTS

The authors would like to thank Mary Farrant, Dean Menegaz, and Olivia Lam of University of California, San Francisco for their assistance in the MAPS angiographic core laboratory. The MAPS Trial was funded by Stryker Neurovascular and its predecessor Boston Scientific Neurovascular.

Disclosures: Steven Hetts—*RELATED: Grant:* Stryker Neurovascular and its predecessor Boston Scientific Neurovascular paid for the MAPS Trial, including the Core Angiographic Laboratory at UCSF*; *UNRELATED: Board membership:* ChemoFilter Inc, Comments: Scientific advisory board compensated through equity; *Consultancy:* Stryker Neurovascular, Penumbra, Silk Road Medical, Consultancy paid in cash; *Grants/grants pending:* NIH-NIBIB,* ASNR Foundation,* Comments: R01 grant to develop magnetic catheter system; ASNR Scholar grant to develop magnetic catheter system; *Patents (planned, pending, or issued):* UCSF,* Comments: Patents pending through UCSF on chemotherapy filtration system; *Stock/stock options:* Medina Medical, Comments: Scientific advisory board compensated through equity. Aquilla Turk—*RELATED: Grant:* MUSC from Stryker, Comments: Clinical trial; *Consulting fee or honorarium:* Stryker; *UNRELATED: Board membership:* Stryker; *Consultancy:* Stryker; *Grants/grants pending:* MUSC from Stryker.* Joey English—*UNRELATED: Consultancy:* Silk Road Medical, Stryker Neurovascular, Comments: I have done consultant work for a small start-up biotech company called Silk Road Medical and also for Stryker Neurovascular (the latter regarding their stent retriever device, Trevo). I have not done any consulting regarding aneurysm stents or coils; *Expert testimony:* I have previously served as an expert witness on medical-legal issues, but none currently and none regarding endovascular treatment of aneurysms. Christopher Dowd—*RELATED: Fees for participation in review activities, such as data monitoring boards, statistical analysis, endpoint committees, and the like:* Stryker, Comments: I served as Chief Adjudicator (blinded) for MAPS Trial. Charles Prestigiacomo—*RELATED: Fees for participation in review activities, such as data monitoring boards, statistical analysis, endpoint committees, and the like:* Stryker Clinical Events Committee; *UNRELATED: Consultancy:* Aesculap, Thermopeutix; *Other:* Edge Therapeutics, IBRF, Comments: Edge Therapeutics Scientific Advisory Board, no pay; IBRF board member, no pay. Sijian (Grace) Ge—*RELATED: Fees for participation in review activities, such as data monitoring boards, statistical analysis, endpoint committees, and the like/payment for writing or reviewing the manuscript/other:* I am a full-time employee as a statistician of Stryker. I am providing the professional biostatistical support to the analysis and result interpretations in this submission; *UNRELATED: Employment:* Senior Manager of Biostat & CDM, Comments: see "Related" section for details regarding Stryker employment. Yuichi Murayama—*UNRELATED: Consultancy:* Stryker, Asahi Intecc; *grants/grants pending:* Siemens,* FujiFilm*; *payment for lectures (including service on speakers bureaus):* Stryker, Covidien; *Patents (planned, pending, or issued):* UCSF; *royalties:* Stryker. Anil Gholkar—*RELATED: Grant:* Stryker Neurovascular,* Comments: Small grant for each patient recruited in the MAPS study, for the purpose of collecting and entering patient data into the study; *Support for travel to meetings for the study or other purposes:* Stryker Neurovascular, Comments: Support for travel to MAPS investigator meetings; *UNRELATED: Consultancy:* Codman Neurovascular, J&J, Comments: Act as a consultant to deliver educational meetings; courses for interventional trainees; *Travel/accommodations/meeting expenses unrelated to activities listed:* Stryker Neurovascular (to SNIS), MicroVention (to WFITN), Comments: Have received support for attending above meetings from various device manufacturing companies; *Other:* Part funding for trainee, Comments: In the past, Stryker Neurovascular (Boston Scientific) provided part funding for interventional trainee at our institute. As far as I am aware, this was stopped several years ago. Demetrius Lopes—*UNRELATED: Consultancy:* Stryker; *Payment for lectures (including service on speakers bureaus):* Stryker; *Payment for development of educational presentations:* Stryker; *Other:* Stryker, Comments: Training program for new hires. S. Claiborne Johnston—*RELATED: Grant:* Stryker,* Comments: Underlying support for the trial. Cameron McDougall—*UNRELATED: Consultancy:* Covidien (ev3), Terumo (MicroVention), Comments: Scientific advisory panel for Covidien and proctor for eV3, consultant for MicroVention. Kristen Carroll—*UNRELATED: Employment:* I am a salaried employee of Stryker Corporation; *stock/stock options:* I have received stock options and grants as an employee of Stryker Corporation (**money paid to institution*).

REFERENCES

1. Molyneux AJ, Kerr RS, Yu LM, et al. **International Subarachnoid Aneurysm Trial (ISAT) of neurosurgical clipping versus endovascular coiling in 2143 patients with ruptured intracranial aneurysms: a randomised comparison of effects on survival, dependency, seizures, rebleeding, subgroups, and aneurysm occlusion.** *Lancet* 2005;366:809–17
2. Wiebers DO, Whisnant JP, Huston J 3rd, et al. **Unruptured intracranial aneurysms: natural history, clinical outcome, and risks of surgical and endovascular treatment.** *Lancet* 2003;362:103–10
3. Raymond J, Guilbert F, Weill A, et al. **Long-term angiographic recurrences after selective endovascular treatment of aneurysms with detachable coils.** *Stroke* 2003;34:1398–403
4. Fiorella D, Albuquerque FC, Han P, et al. **Preliminary experience using the Neuroform stent for the treatment of cerebral aneurysms.** *Neurosurgery* 2004;54: 6–16
5. Higashida RT, Halbach VV, Dowd CF, et al. **Initial clinical experience with a new self-expanding nitinol stent for the treatment of intracranial cerebral aneurysms: the Cordis Enterprise stent.** *AJNR Am J Neuroradiol* 2005;26:1751–56
6. Sedat J, Chau Y, Mondot L, et al. **Endovascular occlusion of intracranial wide-necked aneurysms with stenting (Neuroform) and coiling: mid-term and long-term results.** *Neuroradiology* 2009;51:401–09
7. Raslan AM, Oztaskin M, Thompson EM, et al. **Neuroform stent-assisted embolization of incidental anterior communicating artery aneurysms: long-term clinical and angiographic follow-up.** *Neurosurgery* 2011;69: 27–37
8. Benitez RP, Silva MT, Klem J, et al. **Endovascular occlusion of wide-necked aneurysms with a new intracranial microstent (Neuroform) and detachable coils.** *Neurosurgery* 2004;54:1359–67
9. Fiorella D, Albuquerque FC, Woo H, et al. **Neuroform stent assisted aneurysm treatment: evolving treatment strategies, complications and results of long term follow-up.** *J Neurointerv Surg* 2010;2:16–22
10. Fargen KM, Hoh BL, Welch BG, et al. **Long-term results of Enterprise stent-assisted coiling of cerebral aneurysms.** *Neurosurgery* 2012;71:239–44
11. Santillan A, Greenberg E, Patsalides A, et al. **Long-term clinical and angiographic results of Neuroform stent-assisted coil embolization in wide-necked intracranial aneurysms.** *Neurosurgery* 2012;70:1232–37
12. Lawson MF, Newman WC, Chi YY, et al. **Stent-associated flow remodeling causes further occlusion of incompletely coiled aneurysms.** *Neurosurgery* 2011;69:598–603
13. Brooks NP, Turk AS, Niemann DB, et al. **Frequency of thromboembolic events associated with endovascular aneurysm treatment: retrospective case series.** *J Neurosurg* 2008;108:1095–100
14. Piotin M, Blanc R, Spelle L, et al. **Stent-assisted coiling of intracranial aneurysms: clinical and angiographic results in 216 consecutive aneurysms.** *Stroke* 2010;41:110–15
15. Raymond JPM, White PM, Molyneux AJ. **Scales, agreement, outcome measures, and progress in aneurysm therapy.** *AJNR Am J Neuroradiol* 2007;28:501–02
16. Tollard E, Darsaut TE, Bing F, et al. **Outcomes of endovascular treatments of aneurysms: observer variability and implications for interpreting case series and planning randomized trials.** *AJNR Am J Neuroradiol* 2012;33:626–31
17. Cloft HJ, Kaufmann T, Kallmes DF. **Observer agreement in the assessment of endovascular aneurysm therapy and aneurysm recurrence.** *AJNR Am J Neuroradiol* 2007;28:497–500
18. Raymond J, Salazkin I, Georganos S, et al. **Endovascular treatment of experimental wide-neck aneurysms: comparison of results using coils or cyanoacrylate with the assistance of an aneurysm neck bridge device.** *AJNR Am J Neuroradiol* 2002;23:1710–16
19. Crobeddu E, Lanzino G, Kallmes DF, et al. **Review of 2 decades of aneurysm-recurrence literature, part 1. Reducing recurrence after endovascular coiling.** *AJNR Am J Neuroradiol* 2013;34:266–70
20. Bendok BR, Hanel RA, Hopkins LN. **Coil embolization of intracranial aneurysms.** *Neurosurgery* 2003;52:1125–30
21. Fiorella D, Thiabolt L, Albuquerque FC, et al. **Antiplatelet therapy in neuroendovascular therapeutics.** *Neurosurg Clin N Am* 2005;16:517–40
22. Heller RS, Miele WR, Do-Dai DD, et al. **Crescent sign on magnetic resonance angiography revealing incomplete stent apposition: correlation with diffusion-weighted changes in stent-mediated coil embolization of aneurysms.** *J Neurosurg* 2011;115:624–32
23. Heller R, Calnan DR, Lanfranchi M, et al. **Incomplete stent apposition in Enterprise stent-mediated coiling of aneurysms: persistence over time and risk of delayed ischemic events.** *J Neurosurg* 2013;118:1014–22

Endovascular Treatment of 300 Consecutive Middle Cerebral Artery Aneurysms: Clinical and Radiologic Outcomes

A.M. Mortimer, M.D. Bradley, P. Mews, A.J. Molyneux, and S.A. Renowden

ABSTRACT

BACKGROUND AND PURPOSE: There is controversy as to the best mode of treating MCA aneurysms. We report the results of a large endovascular series of patients treated at our center.

MATERIALS AND METHODS: This study was a retrospective analysis of a prospectively acquired data base. All patients with saccular MCA aneurysms treated between November 1996 and June 2012 were included. World Federation of Neurosurgical Societies grade, aneurysm site, size, and aneurysm neck size were recorded, along with clinical outcome assessed with the Glasgow Outcome Scale and radiographic occlusion assessed with the Raymond classification at 6 months and 2.5 years.

RESULTS: A total of 295 patients with 300 MCA aneurysms were treated including 244 ruptured aneurysms (80.7%). The technical failure rate was 4.3% (13 patients). Complete occlusion or neck remnant was achieved in 264 (91.4%). Complications included rupture in 15 patients (5%), thromboembolism in 17 patients (5.7%), and early rebleeding in 3 patients (1%). Overall permanent procedural-related morbidity and mortality were seen in 12 patients (7.8%). Of the ruptured aneurysms, 189 (79.4%) had a favorable clinical outcome (Glasgow Outcome Scale score, 4–5). A total of 33 patients (13.6%) died. On initial angiographic follow-up, aneurysm remnant was seen in 18 aneurysms (8.1%). A total of 13 patients (4.3%) were re-treated.

CONCLUSIONS: Our experience demonstrates that endovascular treatment of MCA aneurysms has an acceptable safety profile with low rates of technical failure and re-treatment. Therefore, coiling is acceptable as the primary treatment of MCA aneurysms.

ABBREVIATIONS: EVC = endovascular coiling; GOS = Glasgow Outcome Scale; ISAT = International Subarachnoid Aneurysm Trial; WFNS = World Federation of Neurosurgical Societies

The International Subarachnoid Aneurysm Trial (ISAT) demonstrated an absolute 6.9% reduction in the rate of death or dependency at 1 year for patients treated with endovascular coiling (EVC).[1] ISAT did not, however, address the specific issue of patients with MCA aneurysms, who represented only 303 (14.1%) of the 2143 enrolled patients. This has resulted in controversy as to the best mode of treatment of aneurysms at this location. Surgical clipping remains the standard treatment in many institutions. The anatomic location aids surgical access, and in some cases, surgery facilitates hematoma evacuation. There is also a perceived increased risk for EVC at this site because these aneurysms are often wide-neck and have branches arising from the neck.[2,3] Recently, several surgical series have been published that demonstrate excellent clinical results with low rates of morbidity and mortality.[4-7] Therefore, we analyzed the strategy at our institution where EVC is the first-line therapy for aneurysm treatment at any location and focused on the more controversial MCA aneurysms.

MATERIALS AND METHODS

Patient Population

This was an observational, prospectively collated study of 295 consecutive patients referred to our institution for endovascular treatment of ruptured and unruptured MCA aneurysms. All patients underwent primary EVC during a 15.5-year period (between November 1996 and June 2012). All patients with SAH were considered for EVC as the primary treatment technique when a consultant interventional neuroradiologist was available. Elective cases were discussed at our institutional neurovascular multidisciplinary meeting. Patients with fusiform or dissecting aneurysms and those treated with primary parent vessel occlusion were excluded from this study. Patient information, aneurysm characteristics, details of treatment,

Received March 14, 2013; accepted after revision August 16.

From the Department of Neuroradiology, Frenchay Hospital, Bristol, United Kingdom.

Please send correspondence to Alex Mortimer, Department of Neuroradiology, Frenchay Hospital, Frenchay Park Rd, Bristol, UK, BS161LE; e-mail: alex_mortimer@hotmail.com

http://dx.doi.org/10.3174/ajnr.A3776

and clinical course were entered prospectively into a data base and subsequently analyzed.

SAH was confirmed by cranial CT or lumbar puncture and CSF analysis. Of those with unruptured aneurysms, 21 patients with 23 aneurysms had previous SAH and delayed treatment of additional MCA aneurysms or SAH that was clearly the result of another aneurysm, with the additional MCA aneurysm treated in the same procedure. Thirty-two patients with 33 MCA aneurysms diagnosed incidentally were also treated.

Endovascular Procedure

All procedures were performed by consultant interventional neuroradiologists (S.A.R., M.D.B., and A.J.M. with 5, 3, and 20 years of endovascular experience when they started coiling patients within the study period, respectively). EVC was performed by use of conventional techniques with the patients under general anesthesia and systemic heparinization. A bolus of 3000–5000 IU of heparin was followed by continuous infusion via the catheter-flushing system at a concentration of 5 IU/mL. The aim was to place coils sequentially into the aneurysmal sac to the point of angiographic occlusion. Most coils deployed were bare platinum (Boston Scientific, now Stryker, Kalamazoo, Michigan; Micrus, now Codman Neurovascular, Raynham, Massachusetts; ev3, now Covidien, Dublin, Ireland). After diagnostic angiography, the aneurysm was selectively catheterized with a microcatheter by use of standard techniques, through a guide catheter positioned in the internal carotid artery.

Where necessary, balloon remodeling (12 cases primary treatment, 4 cases re-treatment) and stent-assisted coil embolization (1 case primary treatment, 1 case re-treatment) were used for the treatment of wide-neck aneurysms. Intravenous aspirin (500 mg) was used as a prophylaxis to prevent thromboembolic complications in both ruptured and unruptured aneurysms, administered after initial coil deployment when a degree of protection had been attained. Intravenous aspirin was also administered if a stent was deployed. Technical failure was defined as an attempted embolization procedure during which coils could not be deployed safely. Any procedural or other subsequent complication was recorded in addition to any deterioration in the patient's neurologic status after the procedure. Craniotomy and hematoma evacuation or decompressive hemicraniectomy were performed to manage hematoma/herniation, after coil embolization.

Aneurysms Treated

The aneurysm responsible for hemorrhage was identified by blood distribution on CT, aneurysm appearance, and vasospasm distribution. This aneurysm was treated first. Additional aneurysms were treated during the same procedure or after recovery from hemorrhage. If it was not possible to clearly identify the ruptured aneurysm, all possible candidates were treated initially, and aneurysms were classified as ruptured. If contralateral aneurysms were treated at a later date, these were classified as unruptured.

Clinical and Radiologic Follow-Up

Clinical outcome was independently obtained for all at a 3- to 6-month clinic visit with a specialist neurovascular nurse practitioner and was assessed by use of the Glasgow Outcome Scale (GOS). Each patient was scheduled to undergo either cerebral angiography (before 2004: 48 patients) or MRA (since 2004: 174 patients) at 6 months after treatment and then at approximately 30 months after initial treatment. If early recurrence was anticipated, initial follow-up was obtained earlier. If recurrence was demonstrated on MRA, formal conventional angiography was performed.

The degree of aneurysm occlusion was assessed on immediate postembolization angiography and on follow-up angiography. Angiographic and MRA outcomes were determined by the treating physician and were classified according to the Raymond classification. An aneurysm was considered stable on follow-up if there was no increase in contrast filling on angiography or flow on MRA. Re-treatment was considered in persistent or evolving aneurysmal remnants.

Table 1: Descriptive data for the study population

Patient Characteristics	Type of Aneurysm	
	Unruptured	Ruptured
Number of patients (n = 295)	53	242
Number of aneurysms (n = 300)	56	244
Mean (SD) age (y)	52.7 (9.6)	53.9 (12.4)
Median (IQR) age (y)	55.0 (13.5)	53.0 (17)
Age range (y)	29–72	21–84
No. of women (%)	38 (73.1)	158 (65.3)
WFNS scale, *n* (%)		
1	–	136 (56.2)
2	–	38 (15.6)
3	–	25 (10)
4	–	21 (8.6)
5	–	22 (9.1)
Fisher grade, *n* (%)		
I	–	11 (4.5)
II	–	20 (8.3)
III	–	103 (42.6)
IV	–	108 (44.6)

RESULTS

Patient Population and Aneurysm Characteristics

Of the 295 patients, 196 (66.7%) were women and 98 (33.3%) were men. A total of 244 ruptured aneurysms in 242 patients and 56 unruptured aneurysms in 53 patients comprised the study cohort. The mean age of the patients in the ruptured cohort was 53.9 years; for the patients in the unruptured cohort, it was 52.7 years (Table 1). For the 242 patients with SAH, World Federation of Neurosurgical Societies (WFNS) and Fisher grading is shown in Table 1.

A total of 264 aneurysms (88%) were located at the main MCA branching point; 23 (7.7%) were positioned proximal to this location, and 13 (4.3%) were positioned more distally. There were 232 aneurysms (77%) that were small (≤10 mm) and 64 (21%) that were large (11–24 mm). Giant aneurysms constituted 1.3% of the cohort (4 cases), and 93 aneurysms (31%) were wide-neck (>4 mm). Twenty patients (8.3%) with SAH (other than those subsequently referred for clipping after a failed attempt at coiling) went on to have a craniotomy and hematoma evacuation or hemicraniectomy.

Surgical data were available from 2000–2012; 51 patients with

Table 2: Initial coiling results

Initial Angiographic Result	Unruptured Aneurysms (*n* = 56)	Ruptured Aneurysms (*n* = 244)	Total (*n* = 300)
Complete occlusion	29	186	215 (71.7%)
Neck remnant	17	42	59 (19.7%)
Aneurysm remnant	3	6	9 (3.0%)
Technical failure	5	8	13 (4.3%)
Complication precluding coiling	1	1	2 (0.7%)
Missing data	1	1	2 (0.7%)

Table 3: Complications and subsequent clinical outcomes

Complication	Aneurysm Rupture	Thromboembolic	Early Rebleed	Other	Total
Total number (%)	15 (5.0)	18 (6)	3 (1.2)	2 (0.7)	38 (12.9)
Clinically silent (%)	6	6		2	14 (4.7)
GOS 5	7	10		2	19
GOS 4	5	2			7
GOS 1 (%)	3	6	3		12 (4)

Table 4: Clinical outcomes for patients with ruptured MCA aneurysms

Clinical Outcome	Patients
GOS 5 (%)	170 (70.3)
GOS 4 (%)	23 (9.5)
GOS 3 (%)	15 (6.2)
GOS 2	0
GOS 1 (%)	33 (13.6)
Missing data (%)	1 (0.4)

ruptured aneurysms underwent primary surgical clipping. A total of 36 patients were treated with primary clipping because of either lack of availability of an interventional neuroradiologist or if the patient was being treated by a vascular neurosurgeon (most aneurysms were clipped before 2003). Eight aneurysms were clipped because of anatomic considerations after angiography. In 13 cases, the patients were treated with clipping after attempted coiling. In the same period, 16 patients with unruptured MCA aneurysms were treated with elective primary clipping. The indications were patient choice or difficult aneurysmal morphologic features.

Procedural Success

Initial coiling results are summarized in Table 2. Technical failure was seen in 13 aneurysms (5 unruptured and 8 ruptured), equating to 4.3% of treated aneurysms. These patients went on to have microsurgical clipping.

A total of 215 aneurysms were completely occluded on initial conventional angiography (71.7%), and neck remnant was seen in 59 patients (19.7%), resulting in a rate of satisfactory occlusion of 91.4%. An aneurysmal remnant was seen in 9 patients (3%). In 2 patients, a complication precluded EVC.

Complications

Complications and clinical outcome are summarized in Table 3. The technical complication rate was 12.9%, including aneurysmal perforations and thromboembolic events with either silent or transient symptoms. The overall permanent procedural-related morbidity rate was 3.8% (11 patients) and mortality rate was 4% (12 patients), equating to a permanent morbidity and mortality rate of 7.8% (23 patients). Of those patients who experienced a technical complication, 26 (68.4%) of 38 had a favorable outcome (GOS, 4 or 5). When unruptured aneurysms were considered separately, 1 patient had transient arm weakness that fully resolved and 1 patient (1.8%) died as a result of aneurysmal perforation, but no other permanent complications were encountered.

Aneurysmal Perforation. Fifteen patients (5% of procedures) had intraprocedural aneurysmal perforations. In 10 patients, the perforation occurred during coil insertion. In 1 patient, the perforation was secondary to remodeling balloon inflation; in another patient, perforation was secondary to contrast injection before intervention. When rupture occurred, heparin was reversed immediately with protamine; coiling continued to limit the extent of hemorrhage and occlude the aneurysm; and measures were used, if necessary, to reduce intracranial pressure via ventricular drainage of CSF. Six ruptures were clinically silent. Three patients died after rupture; 12 had an independent outcome (GOS, 4–5).

Thromboembolic Events. Eighteen patients (6% of procedures) experienced thromboembolic complications. These were managed by intravenous aspirin and abciximab and induced hypertension. Of these thromboembolic complications, 6 were clinically silent and 3 were transient. Twelve patients were independent (GOS, 4–5), and 6 patients died.

Rebleeds. Three patients (1.2%) experienced early rebleeds. All occurred within 24 hours of the procedure, and 3 patients died.

Other Complications. Coil protrusion was noted in 2 patients with no clinical sequelae.

Clinical Outcome

Of the patients with ruptured aneurysms, 79.8% had a favorable clinical outcome (GOS, 4–5). A total of 33 patients (13.6%) died (Table 4). One of 53 patients with an unruptured aneurysm died as a result of procedural rupture and was the only patient who experienced a permanent change in neurologic status as a result of the procedure. Of the patients who underwent a craniotomy or craniectomy for management of hematoma or mass effect, 8 (40%) of 20 achieved a clinical outcome of GOS 4. The mortality rate was 45% in this subgroup.

Anatomic Outcome

Initial follow-up (mean, 7 months; range, 3–17 months) was available in 219 patients. Allowing for those patients who died, follow-up was available in 84%. Reasons for no follow-up included a dead or severe outcome in 38 patients, advanced age in 12 patients, microsurgical clipping as a definitive treatment in 13 patients, patient choice in 7 patients, and unknown reasons in 6 patients.

Medium- to long-term follow-up (mean, 35 months; range, 18–108 months) was available in 158 patients. Twenty-two patients were ineligible because they were due this follow-up beyond the study period. Therefore, medium- to long-term follow-up was available in 80% of patients who had undergone initial follow-up

Table 5: Angiographic outcomes at initial follow-up

Characteristic	Complete Occlusion	Neck Remnant	Aneurysm Remnant	Re-treatment
All aneurysms ($n = 219$)	148 (67.6%)	53 (23.3%)	18 (8.1%)	13 (5.9%)
Ruptured aneurysms ($n = 175$)	117	42	16	13
Unruptured aneurysms ($n = 44$)	31	11	2	0
Small (≤10 mm)	137	26	11	6
Large (11–24 mm)	9	26	6	6
Giant (≥25 mm)	2	1	1	1
Wide-neck (>4 mm)	29	24	10	7

and in 66% of the patients who were eligible for late follow-up and had survived the acute episode. Reasons for halting anatomic follow-up after initial follow-up were advanced age in 17 patients, out-of-region follow-up in 5 patients, patient choice in 12 patients, death from unrelated cause in 3 patients, and unknown reasons in 2 patients.

Initial angiographic follow-up is summarized in Table 5. Complete occlusion was seen in 148 aneurysms (67.6%), a neck remnant was seen in 53 (23.3%), and an aneurysmal remnant was seen in 18 aneurysms (8.1%). Stable or improved appearances were seen in 178 (81.3%) of 219 aneurysms. Twenty-three (10.5%) showed minor anatomic deterioration to the neck remnant but remained satisfactorily occluded. Of those aneurysms with complete occlusion at postcoiling angiography undergoing initial follow-up (n=164), the probability of complete occlusion was 84.1% (138 aneurysms), of a neck remnant was 12.2% (20 aneurysms), and of aneurysmal remnant was 3.6% (6 aneurysms). Of those aneurysms with a neck remnant at postcoiling angiography undergoing initial follow-up (n=47), the probability of complete occlusion was 19.2% (9 aneurysms), of a neck remnant was 70.2% (33 aneurysms), and of an aneurysmal remnant was 10.6% (5 patients).

A total of 18 aneurysms (8.1%) showed an aneurysmal remnant at initial follow-up, 6 had shown a similar aneurysmal remnant on immediate postcoiling angiography, and 12 aneurysms demonstrated deterioration from complete occlusion or a neck remnant to an aneurysmal remnant. Aneurysmal remnants were more common in patients with large and giant aneurysms compared with small aneurysms at follow-up (15.6% vs 6.3%; $P = .04$). Wide-neck aneurysms were also significantly more common in patients who showed an aneurysmal remnant at follow-up compared with those with complete occlusion (19.6% vs 55.6%; $P < .001$). There were 13 (4.3%) of these patients who were re-treated (12 with further coiling and 1 with microsurgery). The remaining 5 patients showed a stable aneurysmal remnant and were treated conservatively.

A total of 158 patients underwent long-term follow-up: 110 patients (69.4%) showed complete occlusion, 43 (27.4%) showed a neck remnant, and 5 (3.1%) showed an aneurysmal remnant. A total of 150 (95%) patients, including the re-treated patients, showed stable appearances. A new neck remnant that did not warrant re-treatment was seen in 7 patients, and new aneurysmal remnant was seen in only 1 patient.

Re-Treatment

Twelve of 13 recurrent aneurysms were re-treated (4.3% of all aneurysms) with coil embolization and 1 with microsurgical clipping. One of 12 endovascular patients required 4 additional treatments for a recurrent, large, wide-neck aneurysm; she refused surgery. Subsequent angiographic follow-up was available in these patients, and 5 achieved complete occlusion (including 1 patient who underwent microsurgery), 4 showed a neck remnant, and 4 showed a residual aneurysm. Stent or balloon-assisted coiling was used in 5 recurrent aneurysms. No morbidity or mortality was related to EVC.

DISCUSSION

Controversy has existed as to the best mode of therapy for MCA aneurysms. The anatomy of MCA aneurysms is often considered more favorable for surgical treatment because of the frequency of a wide-neck configuration with incorporation of MCA branches that are technically more challenging to treat by EVC. ISAT demonstrated that 116 (71.6%) of 162 endovascular patients and 100 (71.9%) of 139 surgical patients attained independence (mRS, 0–2)[8]; however, MCA aneurysms were relatively underrepresented in ISAT, owing to the absence of clinical equipoise at the time of recruitment. This has led to criticism of the practice of applying ISAT to MCA aneurysms and the generalized adoption of EVC for aneurysms at this location. We therefore review the clinical and radiologic outcomes of this series in the context of the endovascular and surgical literature.

Clinical Outcome in Patients with Ruptured Aneurysms

Favorable clinical outcomes (mRS, 0–2) for ruptured aneurysms at all locations in ISAT[1] and CLARITY[9] (Clinical and Anatomical Results in the Treatment of Ruptured Intracranial Aneurysms, a multicenter prospective study of consecutively coiled patients) were 76.3% and 72.3%, respectively, with the proportion of favorable presenting clinical grade patients (WFNS, 1–2) being 88% and 65.7%, respectively. Favorable clinical outcomes (mRS, 0–2 and GOS, 5) in other large series of ruptured MCA aneurysms comprising at least 50 patients treated with EVC, are within the 67%–85% range.[10-14]

In the present study, the largest published single-center experience to date, patients with consecutive ruptured MCA aneurysms achieved good outcome (GOS, 5) in 70.3% and favorable outcome (GOS, 4 and 5) in nearly 80%, with the proportion of favorable presenting clinical grade patients (WFNS, 1–2) being 72%. We were able to directly compare the results of our present study to a large audit of ruptured aneurysms at all locations treated through EVC at our institution with similar distribution of clinical grade.[15] In this study, 711 patients with 717 ruptured aneurysms were reviewed. In the 605 patients with aneurysms at all locations other than the MCA, favorable outcome (GOS, 4 and 5) was seen in 490 (80.9%). Mortality occurred in 89 patients (14.7%). Statistical comparison of clinical outcomes for patients with ruptured MCA aneurysms in the present study showed no significant difference in the favorable outcome ($P = .58$) or mortality ($P = .69$).

Other than the ISAT[8] results, prospective data on outcomes for clipping of ruptured MCA aneurysms are lacking. In 1990, The International Cooperative Study on the Timing of Aneurysm Surgery,[16] a multicenter prospective observational study, included 786 patients with ruptured MCA aneurysms. A total of 480 pa-

tients (61%) achieved good outcome (GOS, 5) at 6 months. Following this, Rinne et al[17] published one of the largest series of 561 patients with 690 MCA aneurysms, 91% presenting with SAH and 80% with Hunt and Hess grades I–III. Overall favorable outcome (GOS, 5) was 60%. Poor outcomes (GOS, 1–3) were seen in 32%, and this rate was higher in large or giant aneurysms. It is surprising to note that there were significantly more poor outcomes among patients with ruptured MCAs than among those with any other anterior circulation aneurysms (32% and 25%, respectively).

After ISAT, several single-center studies have been published. Güresir et al[18] treated 168 patients with ruptured MCA aneurysms. Favorable outcome (mRS, 0–2) was 55% at 6 months. At the other end of the scale, among 80 patients treated by Van Dijk et al,[7] including 67% with WFNS grades I–II, 80% achieved an mRS of 0–2 at longer-term clinical follow-up (mean, 4.7 years). In one of the largest and most complete recent series, Rodríguez-Hernández et al[4] treated 282 ruptured MCA aneurysms with 78% of patients presenting with Hunt and Hess grades I–III; favorable outcomes (mRS, 0–2) were achieved in 70.2%.

These results are similar to those achieved in the present study by using EVC. Therefore, although the conservative view is that surgery should remain the treatment of choice of ruptured MCA aneurysms, except when there are extenuating comorbidities or overriding patient preferences, we believe that for the range of ruptured MCA aneurysms, at least equivalent clinical outcomes to the best surgical series can be obtained by use of conventional endovascular techniques.

Coiling in the Presence of Intracerebral Hematoma

One of the traditional advantages of a clipping strategy is that it allows hematoma evacuation. An alternative approach is to protect the aneurysm before evacuation through coiling. It is possible that this approach is more advantageous because hematoma evacuation in the presence of an unprotected aneurysm may initiate intraprocedural rupture.[19] Furthermore, clipping may require a more extensive surgical exposure to access the aneurysm, perhaps involving retraction of contused parenchyma, which can result in edema or ischemia[20]; this would no longer be required. By use of this approach in the present series, of 20 patients with WFNS grades III or higher (14/20 were grades IV and V), 40% of patients achieved an outcome of GOS 4. Other small series have also achieved more impressive outcomes in poor-grade patients by using this approach.[21]

Technical Success

The coiling procedure was successfully performed in 94.4% of aneurysms with posttreatment imaging, demonstrating that 71.7% were completely occluded and 19.7% exhibited a neck remnant, equating to a satisfactory occlusion rate of 91.4%. The technical failure rate was 4.3%. These results are very similar to the results of a systematic review of 12 series comprising a total of 1030 patients with 1076 MCA aneurysms (500 patients had ruptured aneurysms, and 541 had unruptured aneurysms).[22] In that study, the EVC failure rate was 4.8% (95% CI, 3.7%–6.3%). Overall, 82.4% (95% CI, 80.0%–84.6%) of MCA aneurysms were completely or nearly completely occluded at immediate postoperative angiographic follow-up, and 12.7% (95% CI, 10.9%–14.9%) were incompletely occluded. Prospective data specifically for MCA aneurysms are available from the results of the ATENA (Analysis of Treatment by Endovascular Approach of Nonruptured Aneurysms) study, which included 86 unruptured MCA aneurysms.[23] Complete occlusion was achieved in 69.4%, neck remnant in 19.4% (adequate occlusion in 88.8%), and aneurysmal remnant in 11.3%. In the CLARITY study, 105 MCA aneurysms were included. Complete occlusion was achieved in 45.7%, neck remnant in 39% (adequate occlusion in 84.7%), and aneurysmal remnant in 15.2%.[24] It is important to note that though occlusion rates were lower in this study, the results did not differ significantly from other anterior circulation locations.

We hope that this case series dispels the contradictory conclusions of previous publications,[2,3] suggesting that EVC is appropriate only in a minority of MCA aneurysms. Our experience, and the experience of others, concludes that EVC is feasible in most aneurysms.

Short-Term Follow-Up

Initial angiographic follow-up demonstrated satisfactory occlusion in 92% of aneurysms, with 8.1% showing residual aneurysm. A total of 81% of MCA aneurysms, most treated as part of a coil-first policy, were stable or showed improved appearances at initial angiographic follow-up. A systematic review of 748 MCA aneurysms treated by endovascular means also showed angiographic stability or progression to better obliteration in 81% of patients undergoing follow-up angiography.[22] In the CLARITY study,[25] of 53 patients undergoing midterm follow-up, 57.4% (95% CI, 44.8–69.3) showed stability or improved appearances and 42.6% (95% CI, 30.7–55.2) had shown some degree of anatomic worsening, but presumably, this was not significant in most because 77.9% (95% CI, 66.2–87.1) were classified as having adequate occlusion. Although the rate of anatomic worsening was higher in other studies, the rate was very similar to that at other anatomic locations and was not specific for MCA aneurysms.

Adjunctive Therapies

In this series, bare platinum coils were the mainstay of treatment during a long enrollment period, with many aneurysms treated by use of old-generation technology. The use of adjunctive devices such as stent placement or balloon remodeling was very infrequent, and intra-aneurysmal flow diverters were not used. This trend may explain the relatively low thromboembolic complication rate, but also lower rates of complete occlusion compared with some recently published series on use of adjunctive devices.[26,27] Adjunctive devices have been used in 20.4% of other published MCA series,[22] with the aim of obtaining complete occlusion to minimize the risk for subsequent hemorrhage.[28]

A critical appraisal of the available literature has suggested that balloon assistance has a very similar safety profile to coiling without remodeling.[29] In the CLARITY[30] and ATENA[31] studies, the use of a balloon was not associated with significantly increased rates of thromboembolic events or aneurysmal perforation but was associated with an increased rate of adequate postoperative occlusion. Vendrell et al[32] treated 63 MCA aneurysms with a balloon remodeling technique. It is interesting to note that they

found that though this technique allowed treatment of aneurysms with more complex morphologic features, it was associated with more recurrences in the long term than were treatments without balloon remodeling.

Stent assistance may lower recurrence and allow more complete treatment of more complex lesions. However, there are reservations regarding procedural safety. Procedural morbidity and mortality risks have been shown to be significantly greater in those patients who have undergone stent-assisted coiling compared with those who have not undergone stent-assisted coiling.[33] Procedural morbidity and mortality risks are significantly increased when treating ruptured aneurysms as opposed to unruptured aneurysms with a stent.[34] Several series have recently been published that focus specifically on complex MCA aneurysms.[26,27,35] In the largest series, Johnson et al[26] treated 100 MCA aneurysms with stent assistance. Follow-up imaging showed complete occlusion in 90.6% of aneurysms, residual neck in 3.5%, and residual filling in 5.9%. Four aneurysms (4.7%) required re-treatment. Long-term MRA follow-up revealed stability or progressive thrombosis in 97.9%. Permanent morbidity was seen in 1% and mortality in 1%. These authors suggested that this treatment method represented a safe and acceptable alternative to craniotomy.

Intra-aneurysmal flow diverters now represent an additional treatment option for wide-neck bifurcation aneurysms. Pierot et al[36] treated 34 ruptured and unruptured MCA aneurysms with the WEB device. Adequate occlusion (total occlusion or neck remnant) was observed in 83.3% of aneurysms with an acceptable safety profile; mortality rate of the treatment was 0.0% and morbidity rate was 3.1% (intraoperative rupture with an mRS of 3 at 1-month follow-up).

Long-Term Follow-Up, Re-Treatment, and Surgical Occlusion Rates: Do They Confer a Long-Term Advantage?

In the present series, 4.3% were re-treated. In other endovascular series of at least 50 patients, re-treatment rates varied from 2.4%–13.9%.[10-14,32] It is well recognized that the decision to re-treat is highly variable.[37] Our cohort had no additional morbidity or mortality relating to the additional procedures, and in line with previous findings,[38,39] the risk for further coil embolization did not negate the advantage of the initial embolization. At late follow-up, including re-treated aneurysms, 157 of 158 aneurysms showed complete occlusion, neck remnant, or stable aneurysmal remnant. One case showed significant delayed anatomic deterioration.

Surgical series have shown high rates of complete occlusion. Each of the series published since ISAT have claimed excellent rates of initial complete aneurysm obliteration ranging from 89%–98.3%.[4,7,18] Long-term angiographic follow-up was available in only 22%[4] and 29%[18] in 2 of these series but reported excellent rates of complete occlusion ranging from 96%–98%. This is perhaps one of the principal arguments for clipping aneurysms at any location; many of the reservations in the neurosurgical literature regarding the use of coiling stem from the lower rate of complete occlusion. A major limitation of this study was the lack of long-term morbidity data, and therefore, based on our data, long-term efficacy was unclear. However, the risk for rerupture occurs mostly within the first year.[28,40] Beyond this, the risk lies between 0.11%[28] and 0.21%[40] per year. Both ISAT,[40] CARAT (Cerebral Aneurysm Rerupture After Treatment),[28] and BRAT (Barrow Ruptured Aneurysm Trial)[41] studies have suggested that the benefits of coiling are unlikely to be superseded by the risk of delayed hemorrhage. The predicted risk has been calculated from the CARAT study, in which 57% showed a neck remnant, and ISAT, in which 27% showed a neck remnant. Prospectively acquired, independently assessed anatomic data have suggested that the neck remnant rate is not significantly different for MCA aneurysms vs other locations,[25] and re-treatment rates, both in our own series and on systematic review of the literature,[22] are not in excess of re-treatment rates at all anatomic locations.[42] Therefore, the argument that endovascular MCA occlusion rates are low and result in a greater risk of rebleeding is unlikely to be true. The data from both CARAT and ISAT also raise the question of how aggressively to manage stable neck remnants. Most of these remnants are likely to be benign. We have noted a trend to manage neck remnants conservatively. This trend may be reflected in the proportion of re-treated patients in the more recent Cerecyte[43] and HELPS (HydroCoil Endovascular Aneurysm Occlusion and Packing Study)[44] trials compared with ISAT (5.5% and 3%, respectively, vs 17%).

Morbidity and Mortality Outcomes

Aneurysmal perforation was seen in 5% of patients, with permanent morbidity and mortality relating to this at 3%. The perforation rate lies within the range of previously published studies that have demonstrated procedural perforation complicating 1%–8.5% of MCA aneurysm treatments.[10-14,32] In 2 large prospective series of unruptured aneurysms (ATENA)[45] and ruptured aneurysms (CLARITY) treated by endovascular means, the perforation rate for MCA aneurysms was 4.1% and 8.5%, respectively. We have previously suggested that the rate of aneurysmal perforation may be higher at the MCA location[15]; we demonstrated that MCA aneurysms accounted for 13% of cases but 24% of all intraprocedural ruptures. In the CLARITY study, the frequency of procedural perforation was significantly higher in the MCA group compared with aneurysms at other locations, though the cumulative morbidity and mortality rates of procedural perforation were not significantly increased.[46]

The thromboembolic rate was 6%, with permanent morbidity and mortality rate relating to this at 3%. This rate is lower than in many large endovascular series[10-14] and in prospective series[45,46] that demonstrate thromboembolism complicating 7%–19.6%. We attributed this finding, at least in part, to the routine use of intravenous aspirin and low use of adjunctive devices, particularly stents. In other series, aspirin administration was not routine with ruptured aneurysms that comprised most aneurysms in this series. In the CLARITY study,[46] although the rate of thromboembolic complications was not significantly higher in MCA aneurysms compared with those at other locations, the cumulative morbidity and mortality rate related to thromboembolic events was significantly higher in the MCA group than in the non-MCA group (7.5% vs 3.3%, respectively; $P = .038$). Therefore, it was

suggested that the clinical consequences of thromboembolism are important because of the size and function of the MCA territory.

In this study, 3 patients (1.2%) experienced rebleeds and all died. All aneurysms appeared completely occluded on postprocedure angiography, and all occurred within the first 24 hours of the procedure. The CARAT study[28] demonstrated a risk of rebleeding at all anatomic locations after complete occlusion by use of coiling to be 1.8% and clipping to be 0.9%. It appears, therefore, that the results for MCA aneurysm coiling are not dissimilar to those for all locations.

Surgical Morbidity and Mortality

Published single-center surgical series specifically focusing on ruptured MCA aneurysms have variably reported procedural complication rates. Two recent series have described complication rates. Güresir et al[18] described infarction complicating 5.5% of cases and periprocedural hemorrhage complicating 5.5% of cases in their series of 168 cases. Rodríguez-Hernández et al[4] reported the procedural-related combined morbidity and mortality to be 1.1% in a series of 282 ruptured MCA aneurysms. Intraprocedural rupture occurred in 7.5%, but there was no permanent morbidity or mortality relating to this. These results are very impressive and reflect a highly specialized service, but we do question whether they can be generalized to the neurosurgical community as a whole, particularly to centers with modest volume. Indeed, data base analysis of a large US population (2454 patients) with ruptured aneurysms from 2006–2011 at multiple centers demonstrated that patients treated with clipping demonstrated an increased likelihood of morbidity, as defined by hospital discharge to long-term care facilities, ischemic complications, and other postoperative complications, compared with patients treated with coiling.[47] Prospective data on procedural morbidity and mortality relating to ruptured MCA aneurysm clipping are lacking, but data from the PRESAT (Prospective Registry of Subarachnoid Aneurysms Treatment) trial[48] (40.5% of surgical cases were MCA aneurysms) show an overall clipping-related complication rate of 17.2%. This rate included intraoperative rupture in 6.7%, ischemic complications in 6%, and hemorrhagic complications in 5.4% (the latter included parenchymal contusions, extradural and subdural hematomas, and primary hematoma extension).

An additional potential drawback of the use of open neurosurgery is the risk for epilepsy. This finding was not assessed in the present series, but in late follow-up of ISAT,[49] it has been demonstrated that MCA location is associated with an increased epilepsy risk for both coiling and clipping but that this risk is significantly greater in patients who had undergone clipping. In the coiling group, the risk for epilepsy at 1 year was 2.6% for non-MCA locations compared with 6.5% for MCA aneurysms. At 5 years, the cumulative risk was 10.3% for the MCA location. For clipping, the risk at 1 year for non-MCA locations was 4.3%, but for MCA aneurysms, this risk was 11.5% and at 5 years, the cumulative risk was 21.7%.

Surgical and Endovascular Treatment of Unruptured MCA Aneurysms

A safety profile is key to an effective treatment in the elective setting. In the endovascular cohort of ISUIA (International Study of Unruptured Intracranial Aneurysms),[50] mortality rate was 1.7% and morbidity rate (mRS, 3–5) was 2.2% in 451 patients. In our cohort of patients with unruptured aneurysms, the mortality rate was 1.8%. There was no permanent morbidity. The prospective ATENA[45] study was not powered to compare outcomes by anatomic location, but the rate of thromboembolism and aneurysm perforation was 9.6% and 4.1%, respectively, for the MCA location and overall morbidity and mortality rate was 1.7% and 1.4%, respectively. A systematic review[22] of 500 patients with 541 unruptured MCA aneurysms treated at 12 centers by EVC demonstrated a permanent procedural morbidity rate of 5.1% and a mortality rate of 0.3%. ATENA also demonstrated no difference in anatomic occlusion between the MCA and other anterior circulation aneurysms.

For unruptured aneurysms, several large surgical series from high-volume centers have demonstrated an excellent procedural safety profile, with morbidity rates ranging from 2%–6% and mortality rates from 0%–2%.[4-6,51] In 2 studies,[5,51] approximately half of all aneurysms treated were < 5 mm and most were < 10 mm in size. This characteristic may well have contributed to the good outcomes, as it is evident that increasing age and aneurysm size are associated with increasing surgical morbidity rates. In the largest series of 263 patients with 339 aneurysms who underwent surgical clipping in 280 operations, Morgan et al[6] assessed risk based on age and aneurysm size. Patients < 60 years old with an aneurysm ≤ 12 mm constituted a low-risk group with a procedural-related combined mortality and morbidity rate of 0.6% (95% CI, 0–3.8). Patients < 60 years old with an aneurysm > 12 mm had a procedural-related combined mortality and morbidity rate of 7.4% (95% CI, 1–24.5). Patients ≥ 60 years old with an aneurysm size of ≤ 12 mm had a procedural-related combined mortality and morbidity rate of 9.3% (95% CI, 4.3–18.3). Patients ≥ 60 years old with an aneurysm size of > 12 mm had a procedural-related combined mortality and morbidity rate of 22.2% (95% CI, 8.5–45.8).

These data suggest a good safety profile for small aneurysms but do raise the specific question of whether EVC would be more appropriate for older patients with larger aneurysms. Furthermore, whether the results of these surgical series can be extrapolated to general neurosurgical practice is questionable. Multicenter data are limited, but one source is the ISUIA study. MCA aneurysms comprised 29% of the prospective ISUIA cohort, and surgical-related morbidity and mortality was seen in 13.7% of patients.[50] International Classification of Diseases code data base analysis of 2535 patients with unruptured aneurysms treated between 1998 and 2000 demonstrated that EVC was associated with fewer adverse outcomes (6.6% vs 13.2%), decreased mortality rates (0.9% vs 2.5%), and shorter lengths of hospital stay (4.5 vs 7.4 days).[52] Using a similar, but larger data base analysis of patients treated between 2001 and 2008, Brinjikji et al[53] showed that the percentage of patients discharged from the hospital to long-term facilities was 14.0% (4184/29,918) for patients who underwent clipping compared with 4.9% (1655/34,125) of patients who were treated with coiling ($P < .0001$). Patients who received clipping also had a higher mortality rate because 344 (1.2%) of these patients died compared with 215 (0.6%) of patients who received coiling ($P < .0001$).

CONCLUSIONS

Most MCA aneurysms can be effectively treated with EVC, achieving satisfactory rates of occlusion with acceptable safety profiles and rates of favorable outcome. For ruptured aneurysms, clinical results are similar to those for aneurysms at other locations and also to those achieved in many surgical series. The clinical and anatomic results of this series are also similar to those of a recently published systematic review, suggesting that they are repeatable. Recurrence is, not unexpectedly, more common in giant, large, and wide-neck aneurysms, but results of prospective trials suggest that anatomic results are not dissimilar to other anatomic locations. Therefore, the endovascular approach to MCA aneurysms is justifiable.

Disclosures: Marcus Bradley—*UNRELATED: Grants/Grants Pending:* Covidien,* Comments: Funding for nurses and trainees in the form of an educational grant; *Travel/Accommodations/Meeting Expenses Unrelated to Activities Listed:* Travel and accommodation expenses from ev3 for attendance at a meeting regarding the Pipeline device in 2012 (expenses paid directly) Travel and accommodation expenses for attendance at the American Society of Neuroradiology meeting in 2011 covered by ev3 (expenses paid directly); *Other:* Meals provided by Stryker during attendance at biannual morbidity and mortality meetings. Andrew Molyneux—*UNRELATED: Consultancy:* Sequent Medical, Comments: Current agreement, but postdated the case series. Shelley Renowden—*UNRELATED: Travel/Accommodations/Meeting Expenses Unrelated to Activities Listed:* Travel expenses/accommodation paid by Stryker and Covidien to overseas meetings. **Money paid to institution.*

REFERENCES

1. Molyneux A, Kerr R, Stratton I, et al. **International Subarachnoid Aneurysm Trial (ISAT) of neurosurgical clipping versus endovascular coiling in 2143 patients with ruptured intracranial aneurysms: a randomised trial.** *Lancet* 2002;360:1267–74
2. Ausman JI. **The future of neurovascular surgery. Part I: Intracranial aneurysms.** *Surg Neurol* 1997;48:98–100
3. Regli L Uske A, de Tribolet N. **Endovascular coil placement compared with surgical clipping for the treatment of unruptured middle cerebral artery aneurysms: a consecutive series.** *J Neurosurg* 1999;90:1025–30
4. Rodríguez-Hernández A, Sughrue ME, Akhavan S, et al. **Current management of middle cerebral artery aneurysms: surgical results with a "clip first" policy.** *Neurosurgery* 2013;72:415–27
5. Choi SW, Ahn JS, Park JC, et al. **Surgical treatment of unruptured intracranial middle cerebral artery aneurysms: angiographic and clinical outcomes in 143 aneurysms.** *J Cerebrovasc Endovasc Neurosurg* 2012;14:289–94
6. Morgan MK, Mahattanakul W, Davidson A, et al. **Outcome for middle cerebral artery aneurysm surgery.** *Neurosurgery* 2010;67:755–61
7. van Dijk JM, Groen RJ, Ter Laan M, et al. **Surgical clipping as the preferred treatment for aneurysms of the middle cerebral artery.** *Acta Neurochir (Wien)* 2011;153:2111–17
8. Molyneux AJ, Kerr RS, Yu LM, et al. **International Subarachnoid Aneurysm Trial (ISAT) of neurosurgical clipping versus endovascular coiling in 2143 patients with ruptured intracranial aneurysms: a randomised comparison of effects on survival, dependency, seizures, rebleeding, subgroups, and aneurysm occlusion.** *Lancet* 2005;366:809–17
9. Cognard C, Pierot L, Anxionnat R, et al. **Results of embolization used as the first treatment choice in a consecutive nonselected population of ruptured aneurysms: clinical results of the Clarity GDC Study.** *Neurosurgery* 2011;69:837–41
10. Iijima A, Piotin M, Mounayer C, et al. **Endovascular treatment with coils of 149 middle cerebral artery berry aneurysms.** *Radiology* 2005;237:611–19
11. Quadros RS, Gallas S, Noudel R, et al. **Endovascular treatment of middle cerebral artery aneurysms as first option: a single center experience of 92 aneurysms.** *AJNR Am J Neuroradiol* 2007;28:1567–72
12. Suzuki S, Tateshima S, Jahan R, et al. **Endovascular treatment of middle cerebral artery aneurysms with detachable coils: angiographic and clinical outcomes in 115 consecutive patients.** *Neurosurgery* 2009;64:876–88; discussion 888–89
13. Bracard S, Abdel-Kerim A, Thuillier L, et al. **Endovascular coil occlusion of 152 middle cerebral artery aneurysms: initial and midterm angiographic and clinical results.** *J Neurosurg* 2010;112:703–08
14. Oishi H, Yoshida K, Shimizu T, et al. **Endovascular treatment with bare platinum coils for middle cerebral artery aneurysms.** *Neurol Med Chir (Tokyo)* 2009;49:287–93
15. Renowden SA, Benes V, Bradley M, et al. **Detachable coil embolisation of ruptured intracranial aneurysms: a single center study, a decade experience.** *Clin Neurol Neurosurg* 2009;111:179–88
16. Kassell NF, Torner JC, Haley EC, et al. **The International Cooperative Study on the Timing of Aneurysm Surgery. Part 1: Overall management results.** *J Neurosurg* 1990;73:18–36
17. Rinne J, Hernesniemi J, Niskanen M, et al. **Analysis of 561 patients with 690 middle cerebral artery aneurysms: anatomic and clinical features as correlated to management outcome.** *Neurosurgery* 1996;38:2–11
18. Güresir E, Schuss P, Berkefeld J, et al. **Treatment results for complex middle cerebral artery aneurysms. A prospective single-center series.** *Acta Neurochir (Wien)* 2011;153:1247–52
19. Houkin K, Kuroda S, Takahashi A, et al. **Intra-operative premature rupture of the cerebral aneurysms. Analysis of the causes and management.** *Acta Neurochir (Wien)* 1999;141:1255–63
20. Yundt KD, Grubb RL Jr, Diringer MN, et al. **Cerebral hemodynamic and metabolic changes caused by brain retraction after aneurysmal subarachnoid hemorrhage.** *Neurosurgery* 1997;40:442–50
21. Tawk RG, Pandey A, Levy E, et al. **Coiling of ruptured aneurysms followed by evacuation of hematoma.** *World Neurosurg* 2010;74:626–31
22. Brinjikji W, Lanzino G, Cloft HJ, et al. **Endovascular treatment of middle cerebral artery aneurysms: a systematic review and single-center series.** *Neurosurgery* 2011;68:397–402; discussion 402
23. Pierot L, Spelle L, Vitry F, et al. **Immediate anatomic results after the endovascular treatment of unruptured intracranial aneurysms: analysis of the ATENA series.** *AJNR Am J Neuroradiol* 2010;31:140–44
24. Pierot L, Cognard C, Ricolfi F, et al. **Immediate anatomic results after the endovascular treatment of ruptured intracranial aneurysms: analysis in the CLARITY series.** *AJNR Am J Neuroradiol* 2010;31:907–11
25. Pierot L, Cognard C, Anxionnat R, et al. **Endovascular treatment of ruptured intracranial aneurysms: factors affecting midterm quality anatomic results: analysis in a prospective, multicenter series of patients (CLARITY).** *AJNR Am J Neuroradiol* 2012;33:1475–80
26. Johnson AK, Heiferman DM, Lopes DK. **Stent-assisted embolization of 100 middle cerebral artery aneurysms.** *J Neurosurg* 2013;118:950–55
27. Vendrell JF, Costalat V, Brunel H, et al. **Stent-assisted coiling of complex middle cerebral artery aneurysms: initial and midterm results.** *AJNR Am J Neuroradiol* 2011;32:259–63
28. Johnston SC, Dowd CF, Higashida RT, et al. **Predictors of rehemorrhage after treatment of ruptured intracranial aneurysms: the Cerebral Aneurysm Rerupture After Treatment (CARAT) study.** *Stroke* 2008;39:120–25
29. Pierot L, Cognard C, Spelle L, et al. **Safety and efficacy of balloon remodeling technique during endovascular treatment of intracranial aneurysms: critical review of the literature.** *AJNR Am J Neuroradiol* 2012;33:12–15
30. Pierot L, Cognard C, Anxionnat R, et al. **Remodelling technique for endovascular treatment of ruptured intracranial aneurysms had a higher rate of adequate postoperative occlusion than did conventional coil embolization with comparable safety.** *Radiology* 2011;258:546–53

31. Pierot L, Spelle L, Leclerc X, et al. **Endovascular treatment of unruptured intracranial aneurysms: comparison of safety of remodeling technique and standard treatment with coils.** *Radiology* 2009;251:846–55
32. Vendrell JF, Menjot N, Costalat V, et al. **Endovascular treatment of 174 middle cerebral artery aneurysms: clinical outcome and radiologic results at long-term follow-up.** *Radiology* 2009;253:191–98
33. Piotin M, Blanc R, Spelle L, et al. **Stent-assisted coiling of intracranial aneurysms: clinical and angiographic results in 216 consecutive aneurysms.** *Stroke* 2010;41:110–15
34. Chalouhi N, Jabbour P, Singhal S, et al. **Stent-assisted coiling of intracranial aneurysms: predictors of complications, recanalization, and outcome in 508 cases.** *Stroke* 2013;44:1348–53
35. Fields JD, Brambrink L, Dogan A, et al. **Stent assisted coil embolization of unruptured middle cerebral artery aneurysms.** *J Neurointerv Surg* 2013;5:15–19
36. Pierot L, Klisch J, Cognard C, et al. **Endovascular WEB flow disruption in middle cerebral artery aneurysms: preliminary feasibility, clinical, and anatomical results in a multicenter study.** *Neurosurgery* 2013;73:27–34; discussion 34–35
37. McDonald JS, Carter RE, Layton KF, et al. **Interobserver variability in retreatment decisions of recurrent and residual aneurysms.** *AJNR Am J Neuroradiol* 2013;34:1035–39
38. Renowden SA, Koumellis P, Benes V, et al. **Retreatment of previously embolized cerebral aneurysms: the risk of further coil embolization does not negate the advantage of the initial embolization.** *AJNR Am J Neuroradiol* 2008;29:1401–04
39. Campi A, Ramzi N, Molyneux AJ, et al. **Retreatment of ruptured cerebral aneurysms in patients randomized by coiling or clipping in the International Subarachnoid Aneurysm Trial (ISAT).** *Stroke* 2007;38:1538–44
40. Molyneux AJ, Kerr RS, Birks J, et al. **Risk of recurrent subarachnoid haemorrhage, death, or dependence and standardised mortality ratios after clipping or coiling of an intracranial aneurysm in the International Subarachnoid Aneurysm Trial (ISAT): long-term follow-up.** *Lancet Neurol* 2009;8:427–33
41. McDougall CG, Spetzler RF, Zabramski JM, et al. **The Barrow Ruptured Aneurysm Trial.** *J Neurosurg* 2012;116:135–44
42. Ferns SP, Sprengers ME, van Rooij WJ, et al. **Coiling of intracranial aneurysms: a systematic review on initial occlusion and reopening and retreatment rates.** *Stroke* 2009;40:e523–29
43. Molyneux AJ, Clarke A, Sneade M, et al. **Cerecyte Coil Trial: angiographic outcomes of a prospective randomized trial comparing endovascular coiling of cerebral aneurysms with either Cerecyte or bare platinum coils.** *Stroke* 2012;43:2544–50
44. White PM, Lewis SC, Gholkar A, et al. **Hydrogel-coated coils versus bare platinum coils for the endovascular treatment of intracranial aneurysms (HELPS): a randomised controlled trial.** *Lancet* 2011;14:377:1655–62
45. Pierot L, Spelle L, Vitry F, et al. **Immediate clinical outcome of patients harboring unruptured intracranial aneurysms treated by endovascular approach: results of the ATENA study.** *Stroke* 2008;39:2497–504
46. Pierot L, Cognard C, Anxionnat R, et al. **Ruptured intracranial aneurysms: factors affecting the rate and outcome of endovascular treatment complications in a series of 782 patients (CLARITY study).** *Radiology* 2010;256:916–23
47. McDonald JS, McDonald RJ, Fan J, et al. **Comparative effectiveness of ruptured cerebral aneurysm therapies: propensity score analysis of clipping versus coiling.** *AJNR Am J Neuroradiol* 2013 Jul 18 [Epub ahead of print]
48. Taki W, Sakai N, Suzuki H, et al. **Determinants of poor outcome after aneurysmal subarachnoid hemorrhage when both clipping and coiling are available: Prospective Registry of Subarachnoid Aneurysms Treatment (PRESAT) in Japan.** *World Neurosurg* 2011;76:437–45
49. Hart Y, Sneade M, Birks J, et al. **Epilepsy after subarachnoid hemorrhage: the frequency of seizures after clip occlusion or coil embolization of a ruptured cerebral aneurysm: results from the International Subarachnoid Aneurysm Trial.** *Neurosurg* 2011;115:1159–68
50. Wiebers DO, Whisnant, JP, Huston J 3rd, et al. **Unruptured intracranial aneurysms: natural history, clinical outcome, and risks of surgical and endovascular treatment.** *Lancet* 2003;362:103–10
51. Moroi J, Hadeishi H, Suzuki A, et al. **Morbidity and mortality from surgical treatment of unruptured cerebral aneurysms at Research Institute for Brain and Blood Vessels-Akita.** *Neurosurgery* 2005;56:224–31
52. Higashida RT, Lahue BJ, Torbey MT, et al. **Treatment of unruptured intracranial aneurysms: a nationwide assessment of effectiveness.** *AJNR Am J Neuroradiol* 2007;28:146–51
53. Brinjikji W, Rabinstein AA, Lanzino G, et al. **Effect of age on outcomes of treatment of unruptured cerebral aneurysms: a study of the National Inpatient Sample 2001–2008.** *Stroke* 2011;42:1320–24

Endovascular Treatment of Middle Cerebral Artery Aneurysms for 120 Nonselected Patients: A Prospective Cohort Study

B. Gory, A. Rouchaud, S. Saleme, F. Dalmay, R. Riva, F. Caire, and C. Mounayer

ABSTRACT

BACKGROUND AND PURPOSE: Multiple technologies have developed the endovascular approach to MCA aneurysms. We assess the safety and the efficacy of a systematic endovascular approach in nonselected patients with MCA aneurysms and determine predictors of treatment outcomes.

MATERIALS AND METHODS: We analyzed data collected between January 2007 and January 2012 in a prospective clinical registry. All patients with MCA aneurysms treated by means of the endovascular approach were included. A multivariate analysis was conducted to identify predictors of complications, recanalization, and outcome.

RESULTS: A total of 120 patients with 131 MCA aneurysms were included. Seventy-nine patients (65.8%) were treated electively and 41 (34.2%) in the setting of subarachnoid hemorrhage. Thirty-three of 131 aneurysms (25.2%) were treated with simple coiling, 79 aneurysms (60.3%) with balloon-assisted coiling, and 19 aneurysms (14.5%) with stent-assisted coiling. Complications occurred in 13.7% of patients. Stent-assisted coiling was significantly associated with more complications ($P = .002$; OR: 4.86; 95% CI, 1.60–14.72). At 1 month after treatment, both the permanent morbidity (mRS ≤2) and mortality rates were 3.3%, without any significant difference according to the endovascular techniques. Mean angiographic follow-up was 16.3 months. The rate of recanalization was 15.6% without a statistical difference, according to the technique. Larger aneurysms were a predictor of recanalization ($P = .016$; OR: 1.183; 95% CI, 1.02–1.36). Retreatment was performed in 10 of 131 aneurysms (7.6%).

CONCLUSIONS: Even though stent-assisted coiling significantly increases the risk of procedural complications, endovascular treatment of MCA aneurysms is safe, effective, and provides durable aneurysm closure in nonselected patients.

ABBREVIATIONS: EVT = endovascular treatment; HH = Hunt and Hess

Endovascular treatment (EVT) of intracranial aneurysms is an established technique for both ruptured and unruptured aneurysms.[1,2] Nevertheless, many institutions still use surgical clipping (rather than coiling) as the first treatment for MCA aneurysms because they are accessible, even with complex anatomic features, which is not usually considered suitable for EVT with standard coiling.[3-5] In a systematic review of endovascular series of MCA aneurysms, the rates of combined permanent morbidity and mortality were 5.1% and 6.0% for unruptured and ruptured aneurysms, respectively.[6] However, most of these series were highly focused on selected patients.[7-10] To date, with the advent of new endovascular tools such as balloons and stents designed specifically for the intracranial circulation, MCA aneurysms can be managed by means of the endovascular approach. However, the safety and efficacy of EVT for all patients are not well known yet.

We assess the safety and the efficacy of a systematic endovascular approach in nonselected patients with MCA aneurysms in a prospective cohort. Predictors of complications, recanalization, and clinical outcome were determined.

MATERIALS AND METHODS

Patients

Patients were identified by means of a prospective clinical registry of patients with intracranial aneurysms, which were treated at Dupuytren University Hospital, Limoges, France, from January 2007 to January 2012. Since January 2007, a systematic endovascular approach has been implemented in all patients with MCA aneurysms. Fusiform and dissecting aneurysms were excluded, as were aneurysms associated with brain arteriovenous malformations.

Received July 17, 2013; accepted after revision August 30.

From the Departments of Interventional Neuroradiology (B.G., A.R., S.S., R.R., C.M.) and Neurosurgery (F.C.), Dupuytren University Hospital, Limoges, France; and INSERM UMR-1094 (F.D.), University of Limoges, Limoges, France.

Please address correspondence to Charbel Mounayer, MD, PhD, Dupuytren University Hospital, Department of Interventional Neuroradiology, 2 Ave Martin Luther King, 87042 Cedex Limoges, France; e-mail cmounayer@hotmail.com

http://dx.doi.org/10.3174/ajnr.A3781

Endovascular Procedures

All procedures were performed with the use of general anesthesia and full anticoagulation (5000 IU of heparin given as an intravenous bolus injection). Anticoagulation was aimed at keeping the activated clotting time at 2 to 3 times above the normal value. We used bare platinum coils (GDC from Boston Scientific [Natick, Massachusetts]; Trufill from Codman & Shurtleff [Raynham, Massachusetts]; and MicroPlex from MicroVention [Tustin, California]).

In the setting of SAH, we used simple coiling or balloon-assisted techniques, considering the size of the neck and the need to protect MCA branches. We avoided the use of stents because of the risk of thrombosis. In the case of large hematomas requiring surgical evacuation, simple coiling was rapidly performed before surgery, without any aneurysm clipping.

In unruptured cases, simple coiling, double-catheter coiling,[11] balloon-assisted,[12,13] or stent-assisted coiling[14] were used, depending on the neck size and aneurysm anatomy. In some cases of stent use, we used the balloon-assisted technique before inserting a stent because it appeared that the balloon technique obtained denser packing because of the inherent difficulty of crossing the stent struts in the first instance or in regaining access into the aneurysm. However, we considered it a stent group. In addition, in the case of simple coiling or balloon-assisted coiling for unruptured aneurysms, 250 mg of aspirin was given intravenously during the procedure. In the case of stent-assisted coiling, patients were given dual-antiplatelet therapy before surgery, which was continued for 12 months (75–150 mg clopidogrel, 160 mg aspirin daily).

Data Collection

We analyzed clinical and procedural data, considering patient age and sex, state of aneurysms, technique of EVT, technical complications, anatomic results, and patient evolution, 1 month after the procedure (C.M., R.R., B.G.). Technical complications were classified into thromboembolic events (clots near the neck of the aneurysm and/or in the distal branches), aneurysm rupture (extravasation of contrast media at the level of the aneurysm), and artery perforation (extravasation of contrast media at the level of artery). All technical complications were noted, whatever the clinical issue.

Angiographic images were acquired in the anteroposterior and lateral working projections before and immediately after treatment. The angiographic follow-up protocol consisted of the first angiogram performed 1–6 months after endovascular treatment and the second angiogram being performed 1 year after the first follow-up. A third angiogram was performed 2 years after the second follow-up.

Data Analysis

The location of the aneurysms was classified into 3 groups: proximal, bifurcation, and distal MCA aneurysms.[15] Aneurysm dimensions were characterized by 3D images. The size of the aneurysm was defined on the basis of the greatest length of the aneurysmal sac. Angiographic occlusion assessment was classified by use of the simplified 3-point Raymond classification scale.[16] A 2-point classification scale was also used: total occlusion (complete obliteration) and partial occlusion (residual neck or residual aneurysm). At follow-up, we considered an aneurysm recurrence when a recanalization was found in the neck of aneurysms completely occluded, regardless of how large. We also considered it as a recurrence when we observed that the neck remnant was increased in partly occluded aneurysms.

Clinical status was given at 1 month after the treatment by use of the mRS. Permanent morbidity was defined as an mRS of 3–5. If the preoperative score was 3–4, we defined permanent morbidity when it increased by 1 point.

Statistical Analysis

Statistical analysis was performed by use of the INSERM UMR-1094 (F.D.), with the use of SAS version 9.3 (SAS Institute, Cary, North Carolina). Sex, side (left/right), aneurysm status (ruptured/unruptured), wide neck (neck size ≥4 mm), and initial total occlusion rates were evaluated for statistical significance among 3 groups, by use of the Fisher exact test. Patient age, aneurysm size, neck size, and term of follow-up were compared by use of the Kruskal-Wallis *U* test. A stepwise multivariate logistic regression analysis was performed to control for potential confounders in aneurysm characteristics and in the occurrence of technical complications. Univariate analysis was conducted to evaluate the effect of treatment technique used on recurrence. Finally, a stepwise logistic regression analysis was used to determine factors associated with angiographic recurrence. The significance threshold was set at $P = .05$.

RESULTS

Patients

One hundred twenty patients were included in this study (78 women and 42 men). The mean age was 53.2 years (range, 25–84 years), with no significant differences among the 3 groups ($P = .904$).

Initial Hunt and Hess (HH) grade of I was noted in 11 patients, HH grade of II in 10 patients, HH grade of III in 9 patients, HH grade of IV in 6 patients, and HH grade of V in 5 patients. Eleven patients had both ruptured and unruptured MCA aneurysms.

Aneurysms

One hundred thirty-one MCA aneurysms (41 ruptured, 90 unruptured) were involved. Mean aneurysm size was 6.4 mm (1.5–18.4 mm) and mean neck size was 4.1 mm (0.6–10.1 mm). Seventy (53.5%) of these had wide necks. Sixteen aneurysms (12.2%) were located on the main trunk of the artery (M1 segment), 112 (85.5%) were located at the first major bifurcation (M1-M2), and 3 (2.3%) were located beyond the major bifurcation (M2 segment). There was no significant difference of the mean size of sac and neck (Table 1).

Technique of Aneurysm Treatment

Coiling was performed in all patients with MCA aneurysms. Thirty-three aneurysms (25.2%) were treated with simple coiling (23 single-catheter and 10 double-catheter technique; Fig 1), 79 (60.3%) with balloon-assisted coiling (63 standard balloon, 12 round balloon, and 2 double-balloon technique) (Fig 2), and 19 (14.5%) with self-expandable stent-assisted coiling. Stents were delivered after coiling in 47.4% ($n = 9$; 5 Neuroform [Stryker Neurovascular, Kalamazoo, Michigan], 3 Enterprise [Codman & Shurtleff], 1 Wingspan [Stryker Neurovascular] stents), and before coiling in 52.6% ($n = 10$). We used the jailing technique ($n = 8$; 6 Neuroform and 2 Solitaire AB [Covidien, Irvine, California] stents), stent-jacking technique ($n = 1$; 1 Solitaire AB stent),[17]

Table 1: Characteristics of 131 aneurysms according to modality of endovascular treatment

	Aneurysms (*n* = 131)				
	Simple Coiling (*n* = 33)	Balloon-Assisted Coiling (*n* = 79)	Stent-Assisted Coiling (*n* = 19)	Fisher Exact Test, *P*	Kruskal-Wallis *U Test*, *P*
Side, left/right	14/19	37/42	8/11	.878	
	42%/58%	47%/53%	42%/58%		
Aneurysm status, unruptured/ruptured	16/17	56/23	18/1	.002	
	48%/52%	71%/29%	95%/5%		
Aneurysm size, mm	7.4 ± 3.8	5.9 ± 3.1	7.0 ± 4.1		.086
Neck size, mm	3.9 ± 1.4	4.1 ± 1.6	5.0 ± 1.8		.052
Wide neck ≥4 mm	16	41	13	.347	
	51%	66%	84%		
Initial total angiographic occlusion	26	66	17	.569	
	79%	85%	89%		
Total angiographic occlusion at follow-up	16	53	12	.180	
	48%	67%	63%		
Follow-up, mo	13.3 ± 9.7	17.2 ± 12.4	17.1 ± 13.3		.539

Note:—Numbers in parentheses are *n* (%) of case procedures. Data are mean ± standard deviation.

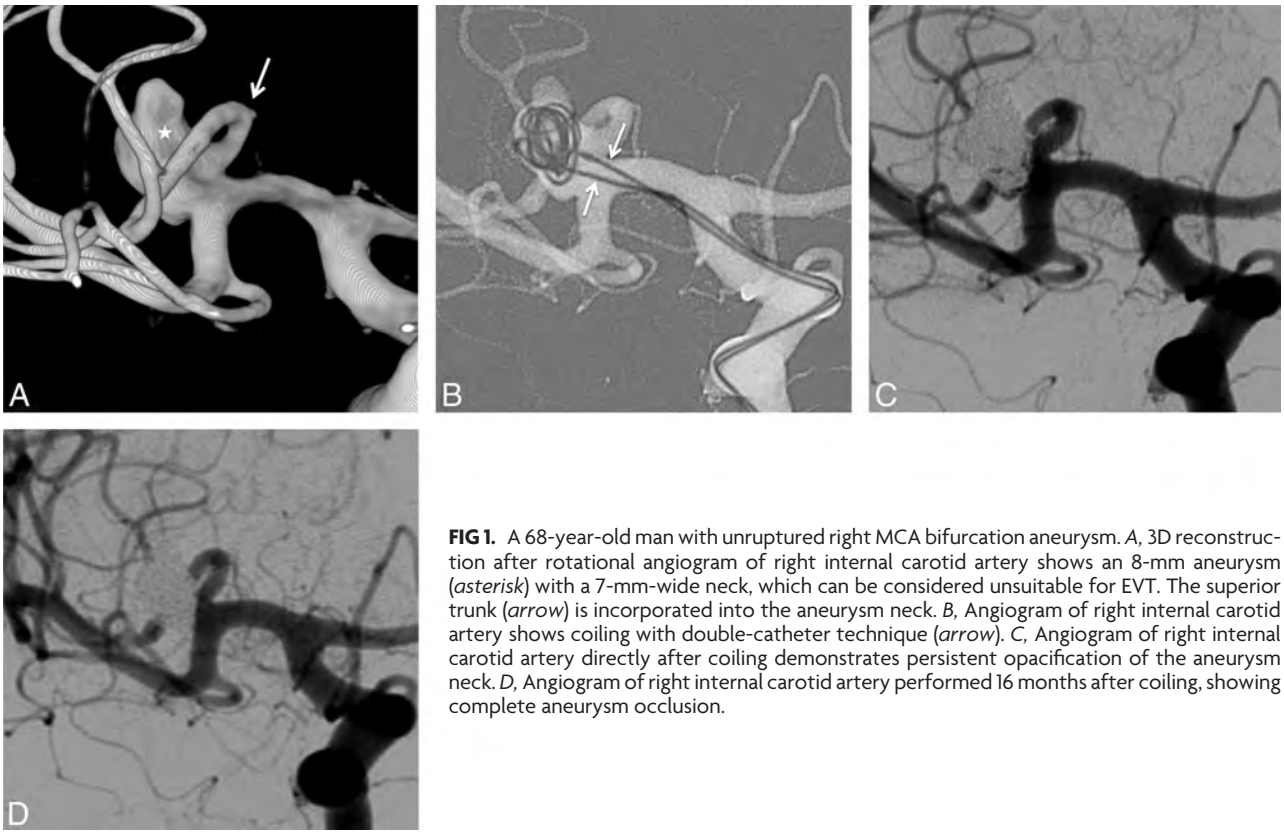

FIG 1. A 68-year-old man with unruptured right MCA bifurcation aneurysm. *A*, 3D reconstruction after rotational angiogram of right internal carotid artery shows an 8-mm aneurysm (*asterisk*) with a 7-mm-wide neck, which can be considered unsuitable for EVT. The superior trunk (*arrow*) is incorporated into the aneurysm neck. *B,* Angiogram of right internal carotid artery shows coiling with double-catheter technique (*arrow*). *C,* Angiogram of right internal carotid artery directly after coiling demonstrates persistent opacification of the aneurysm neck. *D,* Angiogram of right internal carotid artery performed 16 months after coiling, showing complete aneurysm occlusion.

and "Y" stent placement ($n = 1$; 1 Neuroform stent and 1 Enterprise stent) when stents were placed before coiling. One ruptured aneurysm (1 of 19, 5.3%) was treated with a rescue stent.

Complications

Table 2 reports complications during the procedure according to EVT technique. Eighteen complications (13.7%) occurred and included 10 aneurysm sac perforations (7.6%) (2 of 41 ruptured [4.9%] and 8 of 90 unruptured [8.9%] aneurysms), 2 distal parent artery perforations (1.5%) (1 of the 41 ruptured [2.4%] and 1 of 90 unruptured [1.1%] aneurysms), and 6 thromboembolic events (4.6%) (4 of 41 ruptured [9.7%] and 2 of 90 unruptured [2.2%] aneurysms). There were significantly more technical complications in the stent-assisted group ($P = .005$). In the multivariate analysis, stent assistance was the only statistically significant predictive risk factor for complications ($P = .002$; OR: 4.86; 95% CI, 1.60–14.72; Table 3).

Clinical Status

Clinical status of patients at 1 month after treatment according to the technique is shown in Table 2. The overall 1-month mortality rate was 3.3% ($n = 4$; 2.5% in the unruptured group and 4.9% in the ruptured group). Three deaths were directly related to the procedure (2 aneurysm perforations, 1 thromboembolic event) and the other was caused by diffuse vasospasm in an initially ruptured aneurysm. The permanent morbidity rate at 1 month after the procedure was 3.3% ($n = 4$; 3.8% in the unruptured group and 2.4% in the ruptured group). One ischemic stroke occurred secondary to focal vasospasm

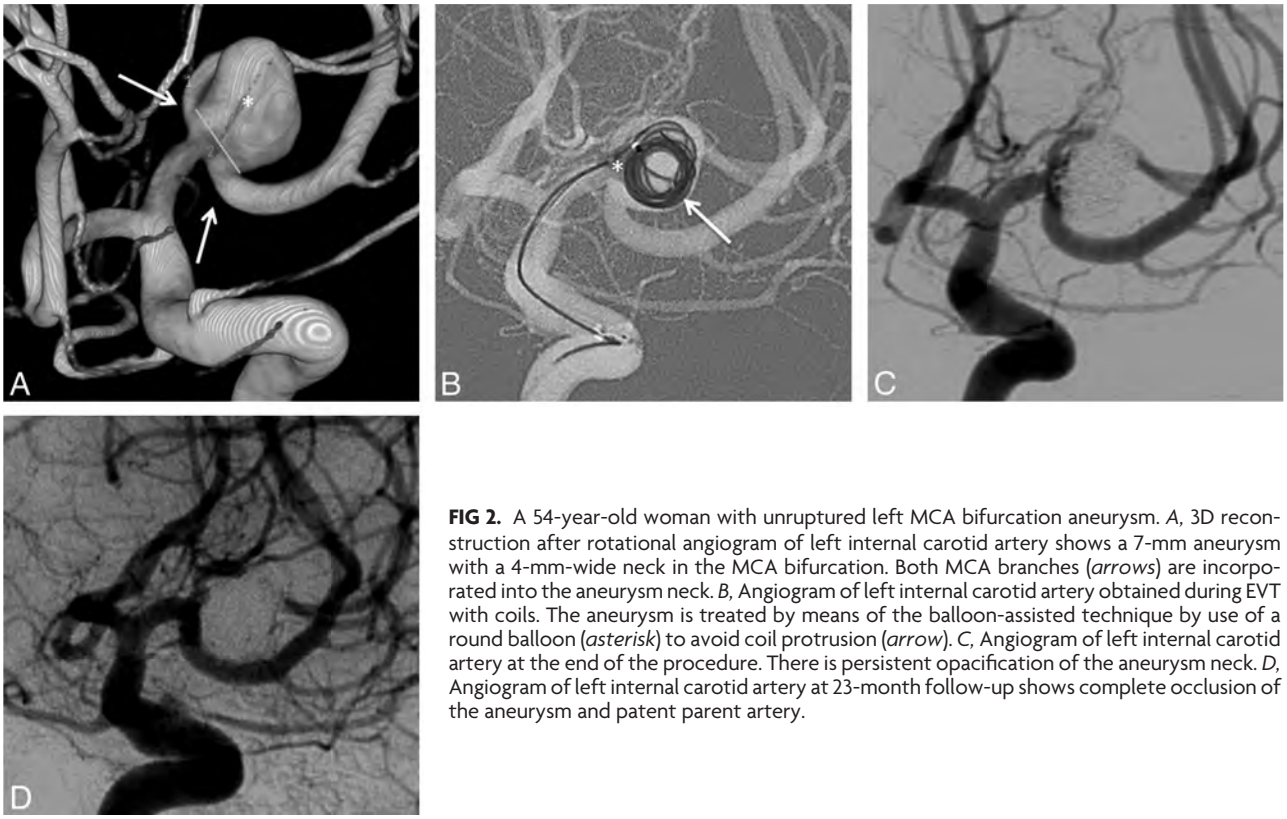

FIG 2. A 54-year-old woman with unruptured left MCA bifurcation aneurysm. *A,* 3D reconstruction after rotational angiogram of left internal carotid artery shows a 7-mm aneurysm with a 4-mm-wide neck in the MCA bifurcation. Both MCA branches (*arrows*) are incorporated into the aneurysm neck. *B,* Angiogram of left internal carotid artery obtained during EVT with coils. The aneurysm is treated by means of the balloon-assisted technique by use of a round balloon (*asterisk*) to avoid coil protrusion (*arrow*). *C,* Angiogram of left internal carotid artery at the end of the procedure. There is persistent opacification of the aneurysm neck. *D,* Angiogram of left internal carotid artery at 23-month follow-up shows complete occlusion of the aneurysm and patent parent artery.

Table 2: Complications according to modality of endovascular treatment

	Simple Coiling (*n* = 33)	Balloon-Assisted Coiling (*n* = 79)	Stent-Assisted Coiling (*n* = 19)	Fisher Exact Test, *P*
Hemorrhage	1	7	4	.642
Aneurysm perforation	1	5	4	.048
Arterial perforation	0	2	0	Not applicable
Thromboembolism	1	2	3	Not applicable
Total complications	2 (6.1%)	9 (11.4%)	7 (36.8%)	.005[a]
One-month morbidity	0 (0%)	3 (3.8%)	1 (5.3%)	Not applicable
Ruptured	0	1	0	
Unruptured	0	2	1	
One-month mortality	1 (3.0%)	3 (3.8%)	0 (0%)	Not applicable
Ruptured	1	1	0	
Unruptured	0	2	0	

Note:—Numbers in parentheses are *n* (%) of case procedures.

[a]There were significantly more technical complications among the coiling group (6.1% versus 36.8%, $P = .014$) and the balloon-assisted group (11.4% versus 36.8%, $P = .018$) than in the stent-assisted group. There was no significant difference in complication rate between coiling and balloon-assisted groups (6.1% versus 11.4%, $P = .605$).

Table 3: Logistic regression analysis for complications

Effect	Logistic Regression			Fisher Exact Test, *P*	Mann-Whitney *U Test, P*
	P	OR	95% CI		
Age	.62	0.99	0.95–1.02		.625
Male	.11	0.35	0.09–1.27	.100	
Ruptured aneurysm	.57	1.33	0.48–3.69	.573	
Side	.47	1.42	0.53–3.78	.471	
Aneurysm size	.57	1.03	0.90–1.18		.578
Neck size	.35	1.14	0.86–1.52		.362
Coiling technique	.35	0.62	0.23–1.69	.351	
Balloon-assisted coiling	.21	0.54	0.20–1.43	.212	
Stent-assisted coiling	.005	4.86	1.60–14.72	.002	
Duration of follow-up	.85	1.00	0.96–1.05		.930
Initial total angiographic occlusion	.59	0.71	0.21–2.41	.288	

in an initially ruptured aneurysm, 2 aneurysm perforations occurred, and 1 parent vessel perforation occurred. Statistically, a significant difference was not found, whatever the EVT technique. Overall permanent morbidity and mortality rates were 7.3% and 6.3% for unruptured and ruptured aneurysms, respectively.

Thirteen of 41 ruptured aneurysms (31.7%) had large hematomas; 8 needed surgical evacuation without clipping because the clinical status was serious. Four patients had a favorable outcome (mRS ≤2), 2 recorded mRS = 3, 1 had mRS = 4, and the others died. The dead patient had thromboembolic complications while being treated with 2 mg of abciximab (ReoPro). Among the other 5 patients who were treated without evacuation, 4 had a favorable outcome and the other died with severe vasospasm.

Initial Anatomic Results

Overall, we observed 83.2% with total occlusion, 16.0% with neck remnant, and 0.8% with sac remnant. In the simple coiling group, 78.8% ($n = 26$) of the aneurysms were totally occluded, 18.2% ($n = 6$) had a neck remnant, and 3.0% ($n = 1$) had a sac remnant. In the balloon group, 83.5% ($n = 66$) of the aneurysms were totally occluded and 16.5% ($n = 13$) had a neck remnant. In the stent group, 89.5% ($n = 17$) of the aneurysms were totally occluded and 10.5% ($n = 2$) had a neck remnant.

(Re)Bleeding/Retreatment

Of the 41 ruptured aneurysms treated, one (2.4%) bled again within the first 24 hours after treatment with a simple coiling technique, though the aneurysm was totally occluded.

During the follow-up period, retreatment was performed in 10 of 131 aneurysms (7.6%). Retreatment was performed ≤6 months after the initial treatment in 7 cases and >6 months after treatment in 3 cases. The size of the retreated aneurysms was ≤10

Table 4: Logistic regression analysis for factors affecting angiographic recurrence

Effect	Logistic Regression			Fisher Exact Test, *P*	Mann-Whitney *U Test, P*
	P	OR	95% CI		
Age	0.86	1.00	0.96–1.04		.867
Male	0.16	2.13	0.72–6.24	.161	
Ruptured aneurysm	0.73	1.20	0.40–3.77	.738	
Side	0.23	1.89	0.66–5.40	.228	
Aneurysm size	0.02	1.18	1.02–1.36		.016
Neck size	0.55	1.09	0.81–1.48		.556
Coiling technique	0.77	1.19	0.35–4.09	.772	
Balloon-assisted coiling	0.94	0.96	0.32–2.84	.943	
Stent-assisted coiling	0.80	0.82	0.16–4.01	.806	
Duration of follow-up	0.99	1.00	0.95–1.04		.996
Initial total angiographic occlusion	0.78	0.82	0.21–3.25	.785	

mm 6 cases and >10 mm in 4 cases. Retreated aneurysms had a neck size of <4 mm in 3 cases and ≥4 in 7 cases. Retreated aneurysms were initially treated by coiling in 3 cases, balloon-assisted coiling in 6 cases, and stent-assisted coiling in 1 case.

Anatomic Results at Follow-Up

Mean follow-up was 16.3 months (range, 4.2–28.4 months) and the overall recurrence rate was 17 (15.6%). There were 4 recurrences (17.4%) in the simple coiling group, 11 (15.5%) in the balloon-assisted group, and 2 (13.3%) in the stent-assisted group. Thirteen were observed for the first 6 months and the remainder in the second year after treatment. A larger aneurysm size was significantly associated with an increased recurrence rate ($P = .016$; OR: 1.183; 95% CI, 1.02–1.36; Table 4).

DISCUSSION

In this study, we assessed the safety and efficacy of an endovascular approach to MCA aneurysms in nonselected patients. All patients were consecutively included, not being selected by any criteria as long as they did not have fusiform or dissecting aneurysms, which minimized the effect of confounders and patient-selection bias. Even though MCA aneurysms are often considered unsuitable for endovascular therapy because of a wide neck and/or branches arising from the neck, these are now accessible because of the development of devices such as balloons and self-expanding stents. During the same time that the present study was conducted, no patients with MCA aneurysms were treated by clipping in our center. Only if the patient had symptomatic large intracerebral hematoma was a surgical evacuation conducted right after coiling. According to our results, endovascular treatment was feasible in all cases regardless of the aneurysm geometry or clinical status.

Complications occurred in 13.7% of patients in this series, causing death or permanent morbidity in 6.6%, which confirms the safety of the endovascular approach for treatment of MCA aneurysms. Of note, we used the number of patients involved as our denominator to figure out morbidity-mortality. The morbidity and mortality rates in our series are similar to those in previous EVT studies in selected cases such as the results by Suzuki et al[8] and Vendrell et al.[9] Meanwhile, morbidity-mortality of surgical clipping of MCA aneurysms is largely variable, ranging from 1.8–13.6%.[3-5,15] Recently the UCSF neurosurgical group reported a 5.3% mortality rate and a 4.6% permanent morbidity rate after managing 631 MCA aneurysms (51.9% ruptured aneurysms) in 543 patients.[3] Its combined morbidity and mortality rate was 9.9%, which seems less safe than EVT outcome. However, this UCSF study probably included high-risk aneurysms, as did our study (the size of the aneurysm was ≥10 mm in 13.7% of cases, and 53.5% of aneurysms had wide necks; illustrated in Figs 1 and 2). In our series, the percentage of complications was slightly but not significantly higher in the ruptured aneurysms group (17.1%) versus the unruptured aneurysms group (12.2%), as previously reported in a systematic review of MCA aneurysms.[6] The UCSF group also reported more complications in the case of ruptured aneurysms (8.5% versus 4.9%).

At 1 month, our global mortality and permanent morbidity rates were not negligible (7.3% and 6.3% for unruptured and ruptured aneurysms, respectively). Comparing our series of patients harboring ruptured and unruptured aneurysms who were treated by EVT with a series of patients treated by clipping, short-term mortality and morbidity are not higher. In a series by a UCSF group, at mean follow-up of 30 months, overall mortality and permanent morbidity (mRS ≤2) were 7.6% and 29.3% for unruptured and ruptured aneurysms, respectively.[6] Twenty-two percent were poor-grade patients (HH grades IV and V) in the UCSF study, whereas 27% were poor-grade in our study.

Several endovascular techniques are currently used, including double catheter,[11] balloon-assisted coiling,[12,13] and stent-assisted coiling techniques.[14,17] We used the balloon-assisted coiling technique in many cases (60.3%) without any significant increased complication rate compared with simple coiling, as reported.[18] Interestingly, our study shows that stent placement highly increases a risk of complication compared with other EVT techniques. Moreover, in logistic regression, the odds of developing complications were 4.8 times greater when stents were used. The use of antiplatelet therapy is known to increase the risk of hemorrhagic complications.[14,19] In a survey of the literature that included 1517 patients treated with stents, Shapiro et al[19] found a procedural complication in 19% of patients, which is lower compared with our series (36.8%). Our high complication rate could be related to MCA location, which is more likely to associate with procedural complications in stent-assisted coiling, as recently outlined by Chalouhi et al[20] after stent-assisted coiling of 508 intracranial aneurysms. We did not find any significant difference between ruptured and unruptured aneurysms. Improvement in stent technology is warranted to diminish complications and improve the safety of endovascular technology.

In the setting of SAH, the aim of treatment is not an optimal sac occlusion, but its rapid protection. If needed, a complementary treatment will be applied later. In our study, approximately 30% of ruptured aneurysms were related to huge hematomas, 8 needed surgery, and the other patients had favorable outcome. This result suggests that MCA ruptured aneurysms with hematomas can be safely managed without clipping. At this time, antiplatelet therapy is undesirable because of the potential need for a ventriculostomy or craniostomy. For these reasons, stent placement is generally avoided in acutely ruptured aneurysms because its safety is less favorable in ruptured aneurysms. In a systematic review that included 339 patients, Bodily et al[21] found clinically significant intracranial hemorrhagic and thromboembolic complications in 8% and 6%, respectively.

Complete aneurysm occlusion was achieved in most cases (83.2%); this suggests that EVT could be an effective treatment for all

MCA aneurysms. It also showed that EVT is a durable treatment with a low rate of angiographic recurrence at medium-term follow-up. This recurrence rate (15.6%) showed similar results to those of studies of MCA aneurysms in selected patients (13.0–38.3%).[6] This finding could be explained by the frequent use of balloon-assisted coiling, which appears to increase the long-term anatomic results compared standard coiling.[18] Our study has identified aneurysm size as the only significant risk factor for recurrence, as previously shown.[14,16] Though the rate of aneurysm recurrence appears to be low after surgical clipping, it is difficult to compare a recurrence risk of EVT with surgical clipping because only a few surgical series report long-term follow-up. There was an increased risk of recurrent bleeding from a coiled aneurysm compared with a clipped aneurysm, but the risks were very low.[22,23] In long-term follow-up of the International Subarachnoid Aneurysm Trial patients, 10 rebleedings occurred in the coiled group and 3 in the clipping group.[23] In our series, one ruptured aneurysm bled again within the first 24 hours after treatment (2.4%) on 16.3 (mean) months of follow-up. Results from the Cerebral Aneurysm Rerupture After Treatment were similar with a 1.8% risk of re-rupture in the first year.[24]

Despite widespread opinion, endovascular therapy should be the treatment of choice for MCA aneurysms, supporting the conclusion reached in the position statement of the American Association of Neurologic Surgeons and American Society of Neuroradiology.[25]

Limitations

Our study is limited by its small sample size and the absence of randomization between study groups. The results reflect a systematic and routine endovascular approach in an experienced neurovascular center. Because the duration of follow-up was short, the incidence of recurrence probably has been underestimated. However, in most intracranial aneurysms adequately occluded 6 months after coiling, prolonged imaging follow-up within the first 5–10 years after coiling does not seem beneficial in terms of detecting reopened aneurysms that need retreatment.[26]

CONCLUSIONS

Even though stent-assisted coiling significantly increases the risk of procedural complications, endovascular treatment of all MCA aneurysms is safe, effective, and provides durable aneurysm closure.

REFERENCES

1. Molyneux A, Kerr R, Stratton I, et al. **International Subarachnoid Aneurysm Trial (ISAT) Collaborative group: International Subarachnoid Aneurysm Trial (ISAT) of neurosurgical clipping versus endovascular coiling in 2143 patients with ruptured intracranial aneurysms—a randomized trial.** *Lancet* 2002;360:1267–74
2. Spetzler RF, McDougall CG, Albuquerque FC, et al. **The Barrow Ruptured Aneurysm Trial: 3-year results.** *J Neurosurg* 2013;119:146–57
3. Rodríguez-Hernández A, Sughrue ME, Akhavan S, et al. **Current management of middle cerebral artery aneurysms: surgical results with a "clip first" policy.** *Neurosurgery* 2013;72:415–27
4. Choi SW, Ahn JS, Park JC, et al. **Surgical treatment of unruptured intracranial middle cerebral artery aneurysms: angiographic and clinical outcomes in 143 aneurysms.** *J Cerebrovasc Endovasc Neurosurg* 2012;14:289–94
5. Elsharkawy A, Lehecka M, Niemelä M, et al. **A new more accurate classification of MCA aneurysms: CT angiographic study of 1009 consecutive cases with 1309 MCA aneurysms.** *Neurosurgery* 2013;73:94–102
6. Brinjikji W, Lanzino G, Cloft HJ, et al. **Endovascular treatment of middle cerebral artery aneurysms: a systematic review and single-center series.** *Neurosurgery* 2011;68:397–402
7. Bracard S, Abdel-Kerim A, Thuillier L, et al. **Endovascular coil occlusion of 152 middle cerebral artery aneurysms: initial and midterm angiographic and clinical results.** *J Neurosurg* 2010;112:703–08
8. Suzuki S, Tateshima S, Jahan R, et al. **Endovascular treatment of middle cerebral artery aneurysms with detachable coils: angiographic and clinical outcomes in 115 consecutive patients.** *Neurosurgery* 2009;64:876–89
9. Vendrell JF, Menjot N, Costalat V, et al. **Endovascular treatment of 174 middle cerebral artery aneurysms: clinical outcome and radiologic results at long-term follow-up.** *Radiology* 2009;253:191–98
10. Iijima A, Piotin M, Mounayer C, et al. **Endovascular treatment with coils of 149 middle cerebral artery berry aneurysms.** *Radiology* 2005;237:611–19
11. Kwon OK, Kim SH, Kwon BJ, et al. **Endovascular treatment of wide-necked aneurysms by using two microcatheters: techniques and outcomes in 25 patients.** *AJNR Am J Neuroradiol* 2005;26:894–90
12. Moret J, Cognard C, Weill A, et al. **The "remodeling technique" in the treatment of wide neck intracranial aneurysms.** *Intervent Neuroradiol* 1997;3:21–35
13. Gory B, Kessler I, Seizem Nekiri G, et al. **Initial experience of intracranial aneurysm embolization using the balloon remodeling technique with Scepter C, a new double-lumen balloon.** *Interv Neuroradiol* 2012;18:284–87
14. Piotin M, Blanc R, Spelle L, et al. **Stent-assisted coiling of intracranial aneurysms: clinical and angiographic results in 216 consecutive aneurysms.** *Stroke* 2010;41:110–15
15. Rinne J, Hemesniemi J, Niskanen M, et al. **Analysis of 561 patients with 690 middle cerebral artery aneurysms: anatomic and clinical features as correlated to management outcome.** *Neurosurgery* 1996;38:2–11
16. Raymond J, Guilbert F, Weill A, et al. **Long-term angiographic recurrences after selective endovascular treatment of aneurysms with detachable coils.** *Stroke* 2003;34:1398–403
17. de Paula Lucas C, Piotin M, Spelle L, et al. **Stent-jack technique in stent-assisted coiling of wide-neck aneurysms.** *Neurosurgery* 2008;62:414–17
18. Pierot L, Cognard C, Anxionnat R, Ricolfi F; CLARITY Investigators. **Remodeling technique for endovascular treatment of ruptured intracranial aneurysms had a higher rate of adequate postoperative occlusion than did conventional coil embolization with comparable safety.** *Radiology* 2011;258:546–53
19. Shapiro M, Becske T, Sahlein D, et al. **Stent-supported aneurysm coiling: a literature survey of treatment and follow-up.** *AJNR Am J Neuroradiol* 2012;33:159–63
20. Chalouhi N, Jabbour P, Singhal S, et al. **Stent-assisted coiling of intracranial aneurysms: predictors of complications, recanalization, and outcome in 508 cases.** *Stroke* 2013;44:1348–53
21. Bodily KD, Cloft HJ, Lanzino G, et al. **Stent-assisted coiling in acutely ruptured intracranial aneurysms: a qualitative, systematic review of the literature.** *AJNR Am J Neuroradiol* 2011;32:1232–36
22. Tsutsumi K, Ueki K, Morita A, et al. **Risk of aneurysm recurrence in patients with clipped cerebral aneurysms: results of long-term follow-up angiography.** *Stroke* 2001;32:1191–94
23. Molyneux AJ, Kerr RSC, Birks J, et al. **Risk of recurrent subarachnoid haemorrhage, death and the standardised mortality ratios after clipping or coiling of an intracranial aneurysm the International Subarachnoid Aneurysm Trial (ISAT): long-term follow-up.** *Lancet Neurol* 2009;8:427–33
24. Johnston SC, Dowd CF, Higashida RT, et al. **Predictors of rehemorrhage after treatment of ruptured intracranial aneurysms: the Cerebral Aneurysm Rerupture After Treatment (CARAT) study.** *Stroke* 2008;39:120–25
25. Harbaugh RE, Heros RC, Hadley MN. **AANS position statement on the International Subarachnoid Aneurysm Trial (ISAT).** *Lancet* 2003;361:783–84
26. Ferns SP, Sprengers ME, van Rooij WJ, et al. **Late reopening of adequately coiled intracranial aneurysms: frequency and risk factors in 400 patients with 440 aneurysms.** *Stroke* 2011;42:1331–37

Validation and Initial Application of a Semiautomatic Aneurysm Measurement Software: A Tool for Assessing Volumetric Packing Attenuation

H. Takao, T. Ishibashi, T. Saguchi, H. Arakawa, M. Ebara, K. Irie, and Y. Murayama

ABSTRACT

BACKGROUND AND PURPOSE: Precise aneurysm measurements and volume embolization ratios are essential for long-term durability of endovascular coil embolization. We evaluated the accuracy of newly developed semiautomatic cerebral aneurysm measurement software, NeuroVision, and explored the value of volume embolization ratio in the prediction of re-treatment.

MATERIALS AND METHODS: We compared software-derived volume measurements of 4 silicone aneurysm models with those calculated with an approximation formula and ground truth values (validation study). We used NeuroVision to retrospectively evaluate outcomes of 100 unruptured aneurysms (97 patients) treated with embolization (clinical study). Aneurysm size (height, width, and neck), volume, and volume embolization ratios were calculated for 3 groups (stable, recanalization, and re-treatment) and were compared.

RESULTS: This validation study illustrated higher accuracy of NeuroVision in computing aneurysm volume compared with an approximation formula: percentage absolute errors were 4.50% ± 3.18% and 23.07% ± 17.60%, with maximal percentage absolute errors of 8.99% and 45.63%, respectively. Of 100 unruptured aneurysms, 20 recanalized and 12 were re-treated. Average volume embolization ratios of stable and re-treated aneurysms were 24.88% ± 5.91% and 20.50% ± 4.06%, respectively ($P \leq .01$). The optimal volume embolization ratio cutoff point for re-treatment was < 19.15%, at which the Youden index was 0.50 (sensitivity, 58.33%; specificity, 87.50%; area under the receiver operating characteristic curve, 0.74).

CONCLUSIONS: The NeuroVision software provided accurate aneurysm volume measurements and may be a useful standardized tool to measure aneurysm size and volume, especially for multicenter clinical studies. Volume embolization ratio may be a valuable predictor of aneurysm occlusion changes.

ABBREVIATIONS: AF = approximation formula; GDC = Guglielmi detachable coils; NV = NeuroVision; ROC = receiver operating characteristic; VER = volume embolization ratio

Endovascular coil embolization of cerebral aneurysms is now considered a valuable method to safely and effectively prevent aneurysm rupture.[1-4] However, immediate postembolization angiographic evidence of complete aneurysm occlusion does not guarantee a good long-term outcome.[5] Volume embolization ratio (VER), the percentage of aneurysm sac volume occupied by coils, is considered a valuable predictor of aneurysm recanalization,[6-11] in addition to large size, wide neck, ruptured status, and suboptimal immediate angiographic result.

However, the accuracy of the methods used to measure aneurysm volume, and thus assess these predictors of recanalization, has not been well evaluated. A standardized aneurysm measurement methodology is necessary to enable multiple institutions to conduct collaborative investigations and compare their results.

A new analytic measurement software was developed for the measurement of cerebral aneurysms (NeuroVision [NV]; Cybernet Systems, Tokyo, Japan). We evaluated the accuracy of this software by using phantom aneurysm models. In addition, we used the software to retrospectively analyze the long-term outcome of a series of embolized aneurysms and investigate the value of VER, as semiautomatically computed by NV, in the prediction of aneurysm recurrence and re-treatment.

MATERIALS AND METHODS

Software Description and In Vitro Validation

NV Software. The NV software measurement process was initiated by a few discrete steps (Fig 1). Through a simple user interface, the image region containing the aneurysm was separated

Received April 1, 2013; accepted after revision August 26.

From the Division of Endovascular Neurosurgery and Neurosurgery (H.T., T.I., H.A., M.E., K.I., Y.M.), Jikei University School of Medicine, Tokyo, Japan; and Department of Neurosurgery (T.S.), Japanese Red Cross Medical Center, Tokyo, Japan.

Please address correspondence to Yuichi Murayama, MD, Division of Endovascular Neurosurgery, Department of Neurosurgery, Jikei University School of Medicine, 3-25-8 Nishi-Shinbashi, Minato-ku, Tokyo, Japan; e-mail: ymurayama@jikei.ac.jp

Indicates open access to non-subscribers at www.ajnr.org

http://dx.doi.org/10.3174/ajnr.A3777

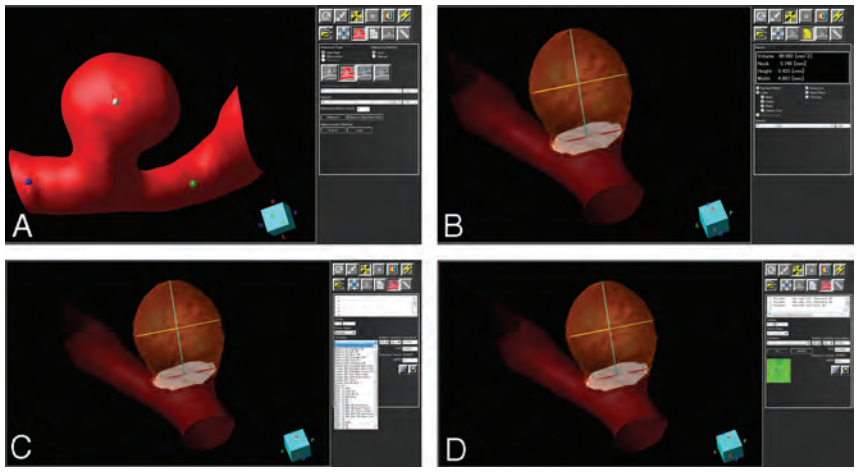

FIG 1. *A,* A white marker in the aneurysm and 2 markers (*blue and green*) in the parent artery are needed to start the measurements in NV. The markers are easily placed manually by the user. *B,* Height, width, neck length, and aneurysm volume are measured semiautomatically with NV. *C,* To measure VER, we select the type of GDC coils from the drop-down menu. *D,* Aneurysm VER is displayed on a green-colored meter on the right.

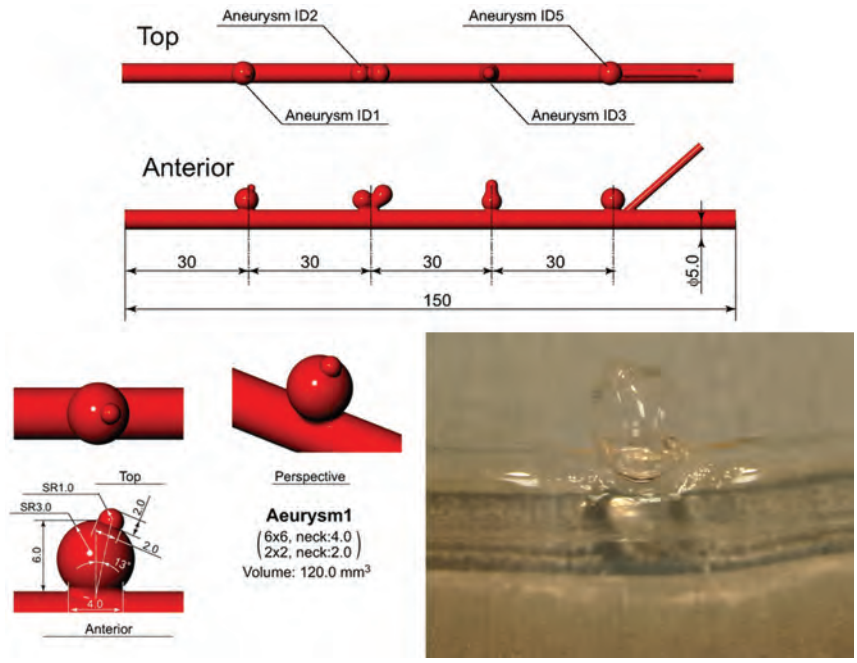

FIG 2. Silicone models.

manually, and an image threshold was subsequently applied to extract the aneurysm and blood vessels from the surrounding background image. The threshold was semiautomatically set by use of the discriminant analysis method, which guaranteed that the selected threshold optimally separated the image intensities belonging to blood vessels from those that belonged to the background.[12] The optimal threshold was that which corresponded to the maximal value of the Fisher linear discriminant, defined as the ratio of variance between the image intensities of the 2 classes (vessel and background) to the within-class variance.[13] Use of discriminant analysis to determine the image segmentation threshold avoided the problems associated with varying measurements because of the arbitrary choice of window center and with the varying image quality of different imaging systems.

Aneurysm Size Measurements. Neck length, height, and width were measured by NV. Aneurysm neck length was defined as the largest diameter at the orifice plane of the aneurysm. Aneurysm height was defined as the longest distance from the midpoint of the aneurysm neck length line to the aneurysm wall. Aneurysm width was defined as the largest aneurysm diameter perpendicular to the height line.

Aneurysm Volume Measurement. NV virtually reconstructed the parent artery after semiautomatic aneurysm removal. The aneurysm neck plane was manually adjusted for complex aneurysm neck shapes through the manipulation of 3 points on the plane. The aneurysm volume was calculated semiautomatically based on the aneurysm neck plane.

Validation Study. We prepared 4 silicone aneurysm models with known sizes and volumes. The aneurysm models had different shapes: round, with a bleb; conjoined aneurysms (heart-shaped); aneurysm with a daughter sac; and round without bleb (Fig 2).

We compared the ground truth aneurysm volumes with the NV volume measurements and the estimated volumes based on a commonly used approximation formula (AF): [aneurysm volume $= (4\pi/3) \times (d_1/2) \times (d_2/2) \times (d_3/2)$], where d_1, d_2, and d_3 are 3 orthogonal measurements denoting aneurysm height, width, and breadth.[14] We calculated the errors of each approach.

Calculation of VER with Use of NV. Coil volume was easily calculated based on the Guglielmi detachable coil (GDC) diameter and length data provided by the manufacturer (Boston Scientific, Natick, Massachusetts), which were preloaded into the NV software. VER was semiautomatically calculated based on the aneurysm volume and the volume of coils used during embolization.

Initial Testing of NV Software in a Clinical Cohort

Patient Population. To assess the value of the measurement parameters provided by the software, we used NV to retrospectively measure aneurysm volume and VER on 3D DSA images from a cohort selected from our institutional data base of patients with cerebral aneurysms who were treated with coil embolization. A total of 295 patients with 308 cerebral saccular aneurysms underwent endovascular embolization with detachable platinum coils at our institution between January 2006 and August 2008. They included 115 patients with 121 unruptured cerebral aneurysms

Table 1: Location of 100 unruptured aneurysms treated with GDC

Location	Number
ACA	
AcomA	19
Others	3
ICA	
Top	6
Anterior choroidal	5
PcomA	23
Paraclinoid	11
Ophthalmic	6
Cavernous	3
MCA	12
Vertebrobasilar system	
Tip	5
SCA	5
Trunk	1
PICA	1
Total	100

Note:—ACA indicates anterior cerebral artery; AcomA, anterior communicating artery; PcomA, posterior communicating artery; SCA, superior cerebellar artery.

treated only with GDC; only patients treated with GDC[3,11] were included in this study because only volume information for this coil was available from the manufacturer. Eighteen of the 115 patients were excluded for either refusing to undergo follow-up angiography or only undergoing MRA follow-up (follow-up rate, 84.35%). Thus, our study cohort included 97 patients with 100 aneurysms treated with GDC who underwent follow-up angiography approximately 1 year after the procedure. There were 72 women and 25 men. The mean age of the patients at the time of treatment was 58.85 ± 11.57 years (age range, 31–83 years). Seventy-eight (78.0%) aneurysms were located in the anterior circulation and 12 (12.0%) in the posterior circulation (Table 1).

Embolization of Aneurysms. Before embolization, patients underwent 3D DSA by use of a biplane flat detector C-arm angiographic system (Axiom Artis dBA; Siemens, Erlangen, Germany). 3D DSA images were reconstructed on a clinical workstation (syngo XWP VB15B; Siemens) at 256 × 256 image matrix size.

The embolization procedure was performed with the patient under general anesthesia. Systemic heparinization was administered as an initial 3000-U bolus, followed by 1000 U/hour under whole-blood activated clotting time monitoring throughout the procedure. In all patients, systemic heparinization was continued for 24 hours after embolization.

Aneurysms were embolized with GDC coils by packing as densely as possible. The percentage of occlusion at the end of the procedure was evaluated by embolized volume. VER was calculated by use of the following formula: VER = (volume of the embolization coils)/(volume of the aneurysm) × 100.

Using the classification schema reported by Raymond et al[15] and Roy et al,[16] we categorized the rate of occlusion immediately after initial treatment as measured on angiographic images as: complete occlusion, when the sac and neck were densely packed in any projection; subtotal occlusion (residual neck), when the sac was occluded but there was suspicion of a neck remnant or there was an obvious tiny neck remnant; and partial occlusion (residual aneurysm), when there was loose packing and/or persistent opacification of the sac or neck remnant.

Angiographic Follow-Up Studies. Patients were scheduled for follow-up angiography at 1 year after treatment. For the evaluation of follow-up angiographies, the Raymond et al[15,16] definition of aneurysm recanalization was modified. An aneurysm was classified as stable at follow-up if the degree of occlusion was unchanged or had improved (such as further thrombosis) compared with the end-of-treatment study. Recanalization was defined as an increase in the amount of contrast material filling the aneurysm compared with the angiographic appearance at the end of the treatment, and such an aneurysm was classified as unstable because of coil compaction and aneurysm growth.

Using these definitions, we further classified the follow-up results into 3 groups: stable group, including unchanged occlusion or further thrombosis; recanalization group, including any recanalization; and re-treatment group, including recanalization with re-treatment. Aneurysms that had contrast filling at the neck of > 15% of the aneurysm height were selected for re-treatment.

Aneurysm and VER Measurement Protocols. Radiology technologists used NV to obtain aneurysm size (millimeters), aneurysm volume (millimeters cubed), and VER (percentage) measurements for all 100 aneurysms. Two neurosurgeons who participated in the coil embolization of these aneurysms reviewed the NV measurements for accuracy.

We then compared the VERs of each group: stable group, recanalization group, and re-treatment group. We further divided the aneurysms into 2 groups according to volume and compared the VERs: The large-volume group included aneurysms with a volume of > 200 mm^3, and the small-volume group included aneurysms with a volume of < 200 mm^3.

We assessed the impact of aneurysm volume and VER on the probability of recurrence and re-treatment for all groups.

Statistical Analysis. All values were expressed as mean ± standard deviation. The statistical significance of differences in mean value between 2 populations was assessed by use of the Student *t* test if variances were equal, as determined by *F* value; otherwise, the Welch *t* test was used. If population distribution was not a "normal" distribution, we analyzed it by using the nonparametric Mann-Whitney *U* test.

A receiver operating characteristic (ROC) curve was used to analyze the effect of varying VER, as a discriminating variable, on embolization outcome (eg, re-treatment vs no re-treatment). The ROC area under the curve (and its 95% CI) was calculated to determine the discriminating level of VER.

The Youden index[17,18] (J) was defined as the difference between the true-positive rate and the false-positive rate in the outcome variable. Maximizing this index allowed us to find, from the ROC curve, an optimal cutoff point, independently from the prevalence. J was defined as the maximal vertical distance between the ROC curve and the diagonal or chance line, and it was calculated as J = maximum (sensitivity + specificity −1). With use of this measure, the cutoff point on the ROC curve was selected so that it corresponded to the maximal J.

RESULTS

Validation Study: Silicone Aneurysm Models (AF, NV)

When we compared the accuracy of an AF with that of NV at measuring volume in the 4 silicone aneurysm models, the per-

Table 2: Comparison of aneurysm volume using AF and NV to ground truth volumes for silicone aneurysm models

Model (mm^3)	Type of Model	Real Volume	Volume 1	Volume 2
1	With bleb	120.00	150.72	118.00
2	Heart	161.70	87.92	168.60
3	Two-ball	89.00	104.67	97.00
4	Ball	117.10	113.04	120.70

Note:—Volume 1 using approximation formula (AF). Volume 2 using NeuroVision (NV) software.

Table 3: Percentage absolute error for AF and NV

Percentage Absolute Error	AF (%)	NV (%)
Average	23.07	4.50
Maximum	45.63	8.99
SD	17.60	3.18

Note:—SD indicates standard deviation.

centage absolute error for an AF was 23.07% ± 17.60% and for NV 4.50% ± 3.18%, with a maximal percentage absolute error of 45.63% and 8.99%, respectively (Table 2; Table 3).

Clinical Study (NV)

Using NV, we calculated size and volume measurements for all aneurysms within 1 minute after data input. Mean aneurysm size measurements were height, 6.93 ± 3.35 mm; width, 6.07 ± 2.90 mm; and neck length, 5.48 ± 2.27 mm. Mean aneurysm volume was 280.7 ± 530.6 mm^3, and mean VER was 24.13% ± 5.75%.

The VERs by aneurysm location were ICA ($n = 54$), 24.63% ± 5.92%; MCA ($n = 12$), 22.22% ± 7.25%; anterior cerebral artery ($n = 22$), 23.80% ± 5.27%; and vertebrobasilar system ($n = 12$), 24.35% ± 4.16%. There was no statistically significant difference in VER among aneurysms at different locations.

Relationship between Immediate Angiographic Occlusion and VER

Immediate anatomic outcome on 3D angiography was complete occlusion in 17 aneurysms (17%), residual neck in 78 aneurysms (78%), and residual aneurysm in 5 aneurysms (5%). VER in completely occluded aneurysms (large-volume group, $n = 1$; small-volume group, $n = 16$.) was 26.04% ± 3.63%. VER in aneurysms with residual neck (large-volume group, $n = 25$; small-volume group, $n = 53$) was 24.08% ± 5.97%. VER in residual aneurysms (large-volume group, $n = 5$) was 18.36% ± 4.60%.

Relationship between Use of Simple or Adjunctive Technique and VER

Coiling by use of an adjunctive technique was performed in 54 aneurysms (balloon-assisted technique in 46 aneurysms, double-catheter technique in 5 aneurysms, and both combined in 3 aneurysms). VER in cases by use of an adjunctive technique was 24.79% ± 6.60%, and VER in cases by use of a simple technique was 23.34% ± 4.49%. There was no statistically significant difference in VER between cases by use of an adjunctive or a simple technique ($P = .41$, Mann-Whitney test).

Relationship between Aneurysm Volume and VER and Its Impact on Outcome

There were 31 aneurysms in the large-volume group, with a VER of 22.76% ± 4.38%. There were 69 aneurysms in the small-volume group, with a VER of 22.76% ± 4.38%. There was no statistically significant difference in VER between the large- and small-volume groups ($P = .12$, Mann-Whitney U test).

In the large-volume group, 19 aneurysms were stable and had a VER of 23.84% ± 4.28%, and 12 aneurysms with recanalization had a VER of 21.05% ± 4.13%. There was no statistically significant difference in VER between stable and recanalized aneurysms in the large-volume group ($P = .11$ at t test).

Conversely, in the small-volume group, 61 aneurysms were stable and had a VER of 25.20% ± 6.33%, and 8 aneurysms with recanalization had a VER of 21.18% ± 3.64%. There was a statistically significant difference in VER between stable and recanalized lesions in the small-volume group ($P \leq .01$, Mann-Whitney U test).

Table 4: Classification of follow-up angiography in each aneurysm group

Aneurysm Group	Average	± SD
Stable ($n = 80$)		
Height (mm)	6.06	2.14
Width (mm)	5.53	2.14
Neck (mm)	5.04	1.87
Volume (mm^3)	157.60	169.90
VER (%)	24.88	5.91
VER, large-volume ($n = 19$)	23.84	4.28
VER, small-volume ($n = 61$)	25.20	6.33
VER, adjunctive technique ($n = 41$)	26.20	6.67
VER, simple technique ($n = 39$)	23.50	4.70
Recanalization ($n = 20$)		
Height (mm)	10.40	4.88
Width (mm)	8.22	4.32
Neck (mm)	7.23	2.88
Volume (mm^3)	773.10	1014.00
VER (%)	21.10	3.85
VER, large-volume ($n = 12$)	21.05	4.13
VER, small-volume ($n = 8$)	21.18	3.64
VER, adjunctive technique ($n = 12$)	20.36	4.03
VER, simple technique ($n = 8$)	22.47	3.31
Re-treatment ($n = 12$)		
Height (mm)	11.61	5.43
Width (mm)	9.84	5.10
Neck (mm)	8.23	2.83
Volume (mm^3)	1081.00	1209.00
VER (%)	20.50	4.06
VER, large-volume ($n = 9$)	20.67	4.46
VER, small-volume ($n = 3$)	20.00	3.20
VER, adjunctive technique ($n = 9$)	19.93	4.10
VER, simple technique ($n = 3$)	22.20	4.18

Relationship between Anatomic Follow-Up Results and VER

Evaluation of anatomic outcomes at 1-year follow-up angiography showed the following: The stable group included 80 aneurysms, 55 unchanged and 25 with further thrombosis ($n = 25$); VER in the stable group was 24.88% ± 5.91%. The recanalization group (recanalization seen on follow-up angiography before re-treatment decision) included 20 aneurysms with an overall VER of 21.10% ± 3.85%. Eight aneurysms in the recanalization group were only observed, as they had minor recurrences that were considered at low risk for rupture (and with a residual space too small to re-treat), and had a VER of 22.00% ± 3.57%. The re-treatment group included 12 aneurysms with a VER of 20.50% ± 4.06% (Table 4).

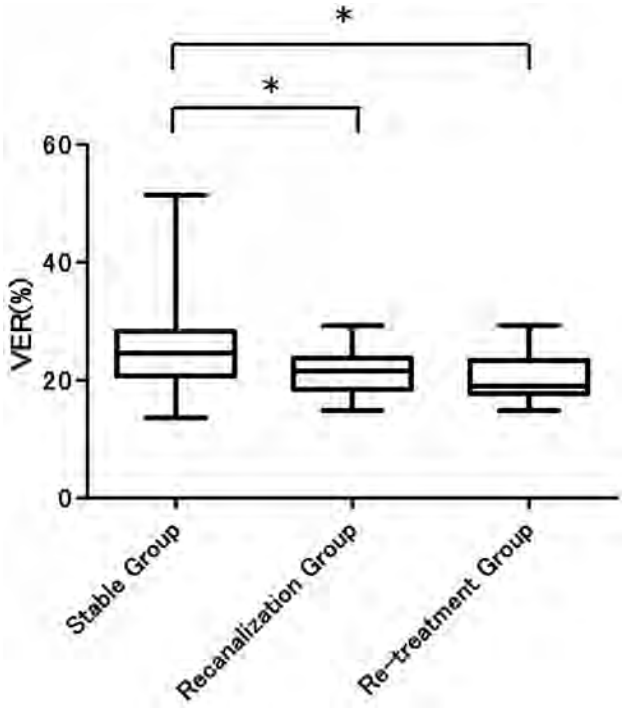

FIG 3. VER in each group (*statistically significant difference, $P < .05$).

Comparison of VER between Groups

There was a statistically significant difference in VER between the stable group and the recanalization group under the Mann-Whitney *U* test ($P \leq .01$) and between the stable group and the re-treatment group under the Mann-Whitney *U* test ($P \leq .01$) (Fig 3).

We evaluated the cutoff points in VER between the stable group and the recanalization group by using ROC curve analysis. The optimal VER cutoff point for recanalization was < 25.40%, at which the Youden index was 0.50 (sensitivity, 95.0%; specificity, 42.5%; area under the ROC curve, 0.70; 95% CI, 0.58–0.81).

We also evaluated the cutoff points in VER between the stable group and the re-treatment group by using ROC curve analysis. The optimal VER cutoff point for re-treatment was < 19.15%, at which the Youden index is 0.50 (sensitivity, 58.33%; specificity, 87.50%; area under the ROC curve, 0.74; 95% CI, 0.59–0.88).

DISCUSSION

To date, there is no universally agreed-on approach to measure cerebral aneurysm dimensions. Differences in the measured values, when comparing modalities as well as the operating personnel, are found even among major studies.[4,19-22] To address the need to standardize aneurysm measurements, Cybernet Systems developed an aneurysm measurement software, NV, for unbiased analysis. To our knowledge, there are no reports of similar software in the literature.

Recent work by Kuriyama et al[23] has confirmed the accuracy of the NV software at measuring aneurysm size (neck length, height, and width), based on studies using a phantom model as well as 74 clinical cases using the size of the first framing coil chosen for embolization. Their study, however, did not evaluate the accuracy of NV volume measurements. Our limited in vitro validation by use of 4 silicone models showed that, compared with use of an AF, NV accurately measured aneurysm volume semiautomatically: Maximal percentage absolute error in aneurysm volume measurements by use of an AF was 45.63%, which was higher than that achievable by NV (8.99%).

The study by Kuriyama et al[23] also did not evaluate the use of NV to calculate VER. VER has a strong relationship with aneurysm stability and is a useful predictor of aneurysm recanalization and re-treatment. An AF measurement may be very different from the actual aneurysm value, especially in the case of irregular aneurysm shapes, such as multilobulated aneurysms. In our study, the average AF volume was smaller than the ground truth value. Such volume measurement errors may result in a higher computed VER than the actual VER value, thereby giving the treating physician a false impression of achieving a safe treatment.

An in vitro study of VER by use of silicone sidewall aneurysms, which was published in 2000, found that adequate embolization with platinum coils required maximal and minimal VER of 30%–36% and 26%–33%, respectively.[24] Reports on the clinical application of VER and its impact on recanalization have indicated that values of ≥25% are necessary to achieve stability in aneurysms treated by endovascular embolization.[6,7,9-11] We evaluated the VER cutoff point of aneurysm stability after endovascular embolization by using the ROC curve and the Youden index,[17,18] and found a cutoff point of 25.40% in unstable aneurysms that is similar to values reported in the literature.

Recanalization alone does not imply the need for re-treatment. However, the cutoff point for re-treatment has not been previously reported in the literature. Our results showed an optimal VER cutoff point for re-treatment of < 19.15%, which suggests that it is possible to re-treat cerebral aneurysms after coiling at a VER of < 20%.

VER data have not yet been obtained for large or broad-neck aneurysms.[6,9] Considering the specifics of the management of large and small aneurysms, we evaluated the difference between those > 7 mm in size and those smaller, in view of reported[20] rupture risks. For this purpose, we chose a borderline aneurysm volume of 200 mm^3 to separate large from small lesions. There was a statistically significant difference in VER between stable small-volume aneurysms (25.20%) and recanalized small-volume aneurysms (21.18%). Three small-volume aneurysms from the re-treatment group recanalized, all having low VER.

We also found no statistically significant difference in VER when using an adjunctive or a simple technique, with 24.79% ± 6.60% (54 aneurysms) and 23.34% ± 4.49% (46 aneurysms), respectively ($P = .41$). The VER for recanalized aneurysms (recanalization group, $n = 20$) in the same 2 groups were 20.36% ± 4.03% (13 aneurysms) and 22.47% ± 3.31% (7 aneurysms), respectively. In some cases, the use of an adjunctive technique did not influence VER; in the stable group, the 41 aneurysms that were embolized by use of an adjunctive technique had a VER of 26.20% ± 6.67%, and the 39 aneurysms that were embolized with the simple technique had a VER of 23.50% ± 4.70% ($P = .08$, Mann-Whitney *U* test).

Although VER is considered a valuable predictor of aneurysm recanalization, this has yet to be verified in a controlled, prospective, multicenter study. The NV volume measurement software may be useful in such a study.

Possibility of Use of Bioactive Coils and Hydrogel-Coated Coils

The development of bioactive coils promises further improvement in the long-term outcome of patients with aneurysms.[25] With these coils, aneurysm occlusion stability may be achievable even at VER of < 25%, and even large aneurysms may become candidates for successful embolization. Watanabe et al[26] have reported the hydrogel-coated coil as being a safe and feasible device for improving the packing efficacy in endovascular coil embolization.

Study Limitations

The major limitation of our study was that it summarized data from a single center with a small number of patients treated and limited validation data from silicone phantom models. We need a multicenter, prospective cohort study with a large number of patients in which to conduct an evaluation of other detachable coils. A multicenter collaborative investigation of the NV software for the evaluation of recanalization of cerebral aneurysms after coiling is ongoing in Japan. As a next stage, we are considering the possibility of launching an international cooperative study.

CONCLUSIONS

The NV software provided accurate aneurysm volume measurements, which suggests that NV may be useful as a standardized tool to measure aneurysm size and volume, especially for conducting multicenter clinical studies. In addition to angiographic assessment, measurement of VER may be useful to predict future angiographic changes of aneurysm occlusion.

Disclosures: Toshihiaro Ishibashi—*UNRELATED: Consultancy:* Stryker; *Payment for Lectures (including service on speakers bureaus):* Stryker. Yuichi Murayama—*UNRELATED: Consultancy:* Stryker, Asahi INTECC, BrainLab; *Payment for Development of Educational Presentations:* Covidien, Comments Training course director; *Grants/Grants Pending:* Stryker,* Siemens,* FujiFilm*; *Payment for Lectures (including service on speaker bureaus):* Stryker, Terumo; *Patents (planned, pending, or issued):* Stryker*; *Royalties:* Stryker*; *Other Relationships:* Cybernet: We requested Cybernet develop NeuroVision software without payment; Cybernet decided to provide software license to our institution without any financial requirement. **Money paid to institution.*

REFERENCES

1. Gonzalez N, Murayama Y, Nien YL, et al. **Treatment of unruptured aneurysms with GDCs: clinical experience with 247 aneurysms.** *AJNR Am J Neuroradiol* 2004;25:577–83
2. Guglielmi G, Viñuela F, Sepetka I, et al. **Electrothrombosis of saccular aneurysms via endovascular approach. Part 1: electrochemical basis, technique, and experimental results.** *J Neurosurg* 1991;75:1–7
3. Murayama Y, Nien YL, Duckwiler G, et al. **Guglielmi detachable coil embolization of cerebral aneurysms: 11 years' experience.** *J Neurosurg* 2003;98:959–66
4. Wiebers DO, Whisnant JP, Huston J 3rd, et al. **Unruptured intracranial aneurysms: natural history, clinical outcome, and risks of surgical and endovascular treatment.** *Lancet* 2003;362:103–10
5. Hayakawa M, Murayama Y, Duckwiler GR, et al. **Natural history of the neck remnant of a cerebral aneurysm treated with the Guglielmi detachable coil system.** *J Neurosurg* 2000;93:561–68
6. Kawanabe Y, Sadato A, Taki W, et al. **Endovascular occlusion of intracranial aneurysms with Guglielmi detachable coils: correlation between coil packing density and coil compaction.** *Acta Neurochir (Wien)* 2001;143:451–55
7. Satoh K, Satomi J, Matsubara S, et al. **Measurement of volume ratio to predict coil compaction, on aneurysmal embolization.** *Interv Neuroradiol* 1998;4 Suppl 1:179–82
8. Szikora I, Wakhloo AK, Guterman LR, et al. **Initial experience with collagen-filled Guglielmi detachable coils for endovascular treatment of experimental aneurysms.** *AJNR Am J Neuroradiol* 1997;18:667–72
9. Tamatani S, Ito Y, Abe H, et al. **Evaluation of the stability of aneurysms after embolization using detachable coils: correlation between stability of aneurysms and embolized volume of aneurysms.** *AJNR Am J Neuroradiol* 2002;23:762–67
10. Uchiyama N, Kida S, Nomura M, et al. **Significance of volume embolization ratio as a predictor of recanalization on endovascular treatment of cerebral aneurysms with Guglielmi detachable coils.** *Interv Neuroradiol* 2000;6 Suppl 1:59–63
11. Yagi K, Satoh K, Satomi J, et al. **Evaluation of aneurysm stability after endovascular embolization with Guglielmi detachable coils: correlation between long-term stability and volume embolization ratio.** *Neurol Med Chir (Tokyo)* 2005;45:561–65; discussion 565–66
12. Takao H, Murayama Y, Ishibashi T, et al. **Comparing accuracy of cerebral aneurysm size measurements from three routine investigations: computed tomography, magnetic resonance imaging, and digital subtraction angiography.** *Neurol Med Chir (Tokyo)* 2010;50:893–99
13. Otsu N. **A threshold selection method from gray-level histograms.** *IEEE Trans Sys Man Cyber* 1979;9:62–66
14. Vallée JN, Pierot L, Mont'alverne F, et al. **Unruptured intracranial aneurysms treated by three-dimensional coil embolization: evaluation of the postoperative aneurysm occlusion volume.** *Neuroradiology* 2005;47:438–45
15. Raymond J, Guilbert F, Weill A, et al. **Long-term angiographic recurrences after selective endovascular treatment of aneurysms with detachable coils.** *Stroke* 2003;34:1398–403
16. Roy D, Milot G, Raymond J. **Endovascular treatment of unruptured aneurysms.** *Stroke* 2001;32:1998–2004
17. Fluss R, Faraggi D, Reiser B. **Estimation of the Youden Index and its associated cutoff point.** *Biom J* 2005;47:458–72
18. Perkins NJ, Schisterman EF. **The inconsistency of "optimal" cut-points obtained using two criteria based on the receiver operating characteristic curve.** *Am J Epidemiol* 2006;163:670–75
19. International Study of Unruptured Intracranial Aneurysms Investigators. **Unruptured intracranial aneurysms–risk of rupture and risks of surgical intervention.** *N Engl J Med* 1998;339:1725–33
20. UCAS Japan Investigators, Morita A, Kirino T, et al. **The natural course of unruptured cerebral aneurysms in a Japanese cohort.** *N Engl J Med* 2012;366:2474–82
21. Molyneux AJ, Kerr RS, Yu LM, et al. **International subarachnoid aneurysm trial (ISAT) of neurosurgical clipping versus endovascular coiling in 2143 patients with ruptured intracranial aneurysms: a randomised comparison of effects on survival, dependency, seizures, rebleeding, subgroups, and aneurysm occlusion.** *Lancet* 2005;366:809–17
22. Sonobe M, Yamazaki T, Yonekura M, et al. **Small unruptured intracranial aneurysm verification study: SUAVe study, Japan.** *Stroke* 2010;41:1969–77
23. Kuriyama T, Furukawa H, Shimizu K, et al. [**Importance of an automatic measurement base on the first coil diameter in regard to coil embolization of a cerebral aneurysm**]. *Nihon Hoshasen Gijutsu Gakkai Zasshi* 2012;68:95–102 [article in Japanese]
24. Piotin M, Mandai S, Murphy KJ, et al. **Dense packing of cerebral aneurysms: an in vitro study with detachable platinum coils.** *AJNR Am J Neuroradiol* 2000;21:757–60
25. Murayama Y, Tateshima S, Gonzalez NR, et al. **Matrix and bioabsorbable polymeric coils accelerate healing of intracranial aneurysms: long-term experimental study.** *Stroke* 2003;34:2031–37
26. Watanabe K, Sugiu K, Tokunaga K, et al. **Packing efficacy of HydroCoil embolic system: in vitro study using ruptured aneurysm model.** *Neurosurg Rev* 2007;30:127–30; discussion 130

Variable Porosity of the Pipeline Embolization Device in Straight and Curved Vessels: A Guide for Optimal Deployment Strategy

M. Shapiro, E. Raz, T. Becske, and P.K. Nelson

ABSTRACT

BACKGROUND AND PURPOSE: Low-porosity endoluminal devices for the treatment of intracranial aneurysms, also known as flow diverters, have been in experimental and clinical use for close to 10 years. Despite rigorous evidence of their safety and efficacy in well-controlled trials, a number of key factors concerning their use remain poorly defined. Among these, none has received more attention to date than the debate on how many devices are optimally required to achieve a safe, effective, and economical outcome. Additional, related questions concern device sizing relative to the parent artery and optimal method of deployment of the devices. While some or all of these issues may be ultimately answered on an empiric basis via subgroup analysis of growing treatment cohorts, we believe that careful in vitro examination of relevant device properties can also help guide its in vivo use.

MATERIALS AND METHODS: We conducted a number of benchtop experiments to investigate the varied porosity of Pipeline Embolization Devices deployed in a simulated range of parent vessel diameters and applied these results toward conceptualizing optimal treatment strategies of fusiform and wide-neck aneurysms.

RESULTS: The results of our studies confirm a predictable parabolic variability in device porosity based on the respective comparative sizes of the device and recipient artery, as well as device curvature. Even modest oversizing leads to a significant increase in porosity.

CONCLUSIONS: The experiments demonstrate various deleterious effects of device oversizing relative to the parent artery and provide strategies for addressing size mismatches when they are unavoidable.

ABBREVIATIONS: PED = Pipeline Embolization Device; PUFS = Pipeline for Uncoilable and Failed Aneurysms; TZ = transition zone

The clinical experience with the Pipeline Embolization Device (PED; Covidien, Irvine, California) is characterized by heterogeneity in the selection of device size, number, and deployment technique. For example, the average number of devices used in the Pipeline Embolization Device for the Intracranial Treatment of Aneurysms Trial (PITA)[1] and Pipeline for Uncoilable and Failed Aneurysms (PUFS)[2] trials is 1.52 and 3.1, respectively, a notable difference notwithstanding the larger dimensions of PUFS aneurysms. The "less is more" model remains predominant in Europe and South America, whereas a more varied mixture of strategies seems to exist in North America and Australia. Neither approach has been subjected to rigorous targeted investigation, though one might argue that the results of the best-controlled study to date—PUFS—set the metrics of efficacy based on using multiple-coverage constructs, thereby placing the burden of proof on the minimalist approach to demonstrate superiority or equipoise.

An issue that necessarily arises when considering the use of a single PED in the treatment of a complex-neck aneurysm concerns the mechanical behavior of the braided device when forced to accommodate significant mismatch in the diameters of the stented vascular segment. In a significant number of very wide-neck or fusiform aneurysms affecting the segments of the internal carotid artery for which the device is indicated, the proximal and distal landing zones tend to be of different diameters so that placement of a single device necessarily requires oversizing at one (usually the distal) end of the recipient vessel. What consequences this strategy may have on treatment efficacy may still be considered unclear, though a growing body[3] of benchtop,[4,5] flow dynamics,[6] and animal literature[7] suggests that deliberate or inadvertent oversizing of the device is likely to be detrimental to the intended flow modification.

Received April 25, 2013; accepted after revision August 3.

From the Departments of Radiology, Bernard and Irene Schwartz Neurointerventional Radiology Section, (M.S., E.R., T.B., P.K.N.), Neurosurgery (P.K.N.), and Neurology (M.S., T.B.), New York University Langone Medical Center, New York, New York.

Pipeline devices used for this research were donated by Covidien. No funds were solicited or provided for this study from any source.

Please address correspondence to Maksim Shapiro, MD, Departments of Radiology and Neurology, Bernard and Irene Schwartz Neurointerventional Radiology Section, NYU Langone Medical Center, 660 First Ave, 7th floor, New York, NY 10016; e-mail: maksim.shapiro@nyumc.org, neuroangio@neuroangio.org

 Indicates article with supplemental on-line figures.

http://dx.doi.org/10.3174/ajnr.A3742

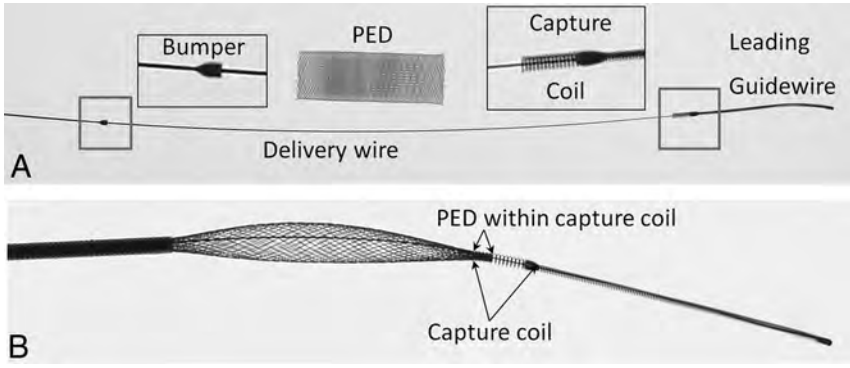

FIG 1. *A*, Pipeline device delivery system components. *B*, Partially unsheathed device demonstrating the segment inserted into the capture coil.

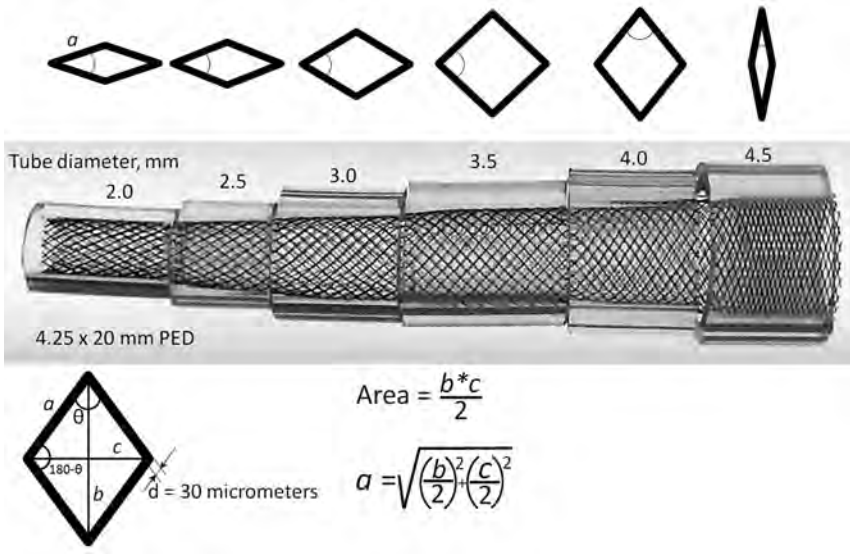

FIG 2. Representative sample of an experimental setup, with a 4.25 × 20 mm device inserted into plastic tubes of 0.5-mm incremental diameters. The corresponding parameters of cell length *a* and angle θ are shown, demonstrating that *a* remains relatively constant so that porosity is determined primarily by variance in θ.

A related issue concerns device behavior along vessel curvatures, where the degree of metal coverage is found to be inhomogeneous, predictably varying from the highest coverage (lowest porosities) along the inner curve and decreasing gradually to the minimum coverage seen on the outer curvature. The extent to which this increases porosity under different circumstances has been investigated for some devices[3,5,8] but is not established for the PED.

Device Construction

The PED is a self-expanding, cylindric, braided device consisting of 48 strands of cobalt-chromium and platinum-tungsten wire, in a 3:1 respective ratio, wound by a braiding machine to produce devices ranging from 2.5 to 5.0 mm in nominal diameter, with lengths varying from 10 to 35 mm. The device is mounted within the delivery sheath by stretching, and its leading edge is packaged beneath a capture coil to protect the strands during advancement within the microcatheter (Fig 1). During delivery, the device may expand to its maximum size, which is 0.25 mm larger than nominal diameter when unconstrained across the aneurysm neck, or it may conform to the diameter of the vessel in which it is implanted. For the subsequent discussion, the term "coverage" will be used interchangeably with "metal coverage," defined as the percentage of artery surface area covered with the metal strands of the device, reflecting the inverse of the term "porosity," which here simplistically refers to the percentage of uncovered artery area.

On close inspection, the ultrastructure of the device consists of a series of curved rhomboid cells. (Fig 2). The angle θ, or pitch, of the strands at nominal size is set during manufacture, along with the diameter of the strand (average: 30 μm per manufacturer's specifications) and number of strands, and determines the porosity and pore (cell) size of the device. However, when a device is placed into vessels of progressively smaller sizes relative to its nominal diameter, the pitch angle of the cells changes proportional to the degree of device constraint, providing lower coverage and increased surface porosity until a maximum porosity is reached at the lowest metallic coverage. This minimum coverage results when the cell angle θ, for a given cell side length, reaches 90°, corresponding to a square configuration. With higher degrees of constraint (even more oversizing), the cells again assume a diamond shape, oriented now along the long axis of the device, thereby again decreasing overall porosity (Fig 2) and increasing the surface area coverage. Thus, the theoretic curve of coverage versus vessel diameter for each device has a parabolic shape as long as the cell length, *a*, remains constant, and this turns out to be essentially true. Please note that this relationship is different from the "ideal" rhombus, whose area is independent of θ, whereas rhombi defined by braids of defined thickness (30 μm) display a more complex angle-area relationship. Under conditions of curvature, however, both the cell angle θ and the side length *a* vary so that the range of porosities throughout a cross-section of the parent artery along a curve may become quite substantial.

MATERIALS AND METHODS

A number of Pipeline Embolization Devices were deployed within clear plastic tubes of predefined diameters ranging from 2.0 to 5.0 mm, in increments of 0.5 mm. The constructs and an adjacent calibration ruler were then photographed at close range with 2 conventional cameras (Fig 2). Repeated measurements of the long, *b*, and short, *c*, cell axes were made for adjacent cells of each segment, and measurements were averaged to produce values and

Pipeline device metal coverage ± SD for each tested device diameter and recipient tube diameter

Tube Diameter (mm)	Nominal Device Diameter (mm)			
	4.75	4.25	3.75	3.25
5.0	27 ± 4%			
4.5	20 ± 3%	36 ± 5%		
4.0	18 ± 6%	21 ± 5%	28 ± 7%	
3.5	18 ± 4%	20 ± 5%	22 ± 5%	33 ± 4%
3.0	18 ± 3%	20 ± 6%	22 ± 9%	29 ± 6%
2.5	20 ± 4%	22 ± 4%	22 ± 6%	26 ± 4%
2.0	25 ± 8%	26 ± 4%	25 ± 6%	28 ± 5%

SDs for each device and recipient tube size using open-source image-processing software, ImageJ (National Institutes of Health, Bethesda, Maryland). The average diameter of the device strands was taken to be 30 μm, as specified by the manufacturer. On the basis of these parameters, the cell surface area, cell angle θ, cell side length a, and the percentage of metal coverage were calculated, with respective SD values, by using basic geometric and error-propagation formulas.

The effects of device curvature on porosity at various sections of a 180° curve were investigated by measurement of the cell area and metal coverage by using the aforementioned techniques for a 3.25 × 20 mm PED. An unconstrained device configuration (maximal opening) was chosen to reflect the clinically relevant scenario of placing the device into a fusiform aneurysm arising from a curved parent vessel.

On the basis of observations of device behavior during these experiments, additional constructs were made to investigate device properties under conditions of oversizing and to demonstrate strategies for minimizing its effects.

RESULTS

Device Sizing Relative to the Parent "Artery"

The geometric metal coverage was calculated for each device within its diameter range, as shown in the Table. The cell surface area and percentage of metal coverage were found to exhibit a parabolic relationship with respect to recipient "artery" diameter, as illustrated in On-line Figs 1 and 2. Maximum coverage was observed under conditions allowing maximal device expansion, which corresponds to 0.25 mm above the nominal diameter. As the device is placed in proportionately smaller diameter tubes, the rhomboid cells "open" until minimum coverage is achieved at the "square" configuration, following which coverage begins to increase again (Fig 2 and On-line Fig 3). Metal coverage falls rapidly with increasing device oversizing, with minimum coverage already observed when the "artery" is only 1 mm smaller than nominal device diameter (Table, On-line Fig 1). Near minimal coverage is maintained for the next ~1 mm of oversizing. For example, the coverage provided by a 4.75-mm device is already substantially diminished when placed into a 3.75-mm vessel and remains at near-minimum values down to 2.75 mm. Thus, even relatively modest degrees of oversizing translate into substantially lower metallic coverage. Although the device strands are not welded to each other, the side lengths, a, of the rhomboid cells remain relatively constant in straight vascular segments for each device throughout its range of recipient artery diameters (On-line Fig 4) so that observed changes in metal coverage result primarily from adaptations in the cell angle, θ (On-line Fig 3). Under conditions of significant vascular/device curvature, however, both parameters change substantially, as illustrated below.

Effects of Oversizing

When deployed across a fusiform aneurysmal dilation, the effects of oversizing additionally lead to the development of a funnel-shaped transitional zone (TZ) between the constrained segment of the device implanted in the recipient artery and the unconstrained segment extending across the aneurysm, particularly distally where the degree of mismatch between the device diameter and the diameter of the recipient artery is greatest (Fig 3). The dimensions of this zone of higher porosity (relative to the compressed cell structure of the fully expanded device) are determined by the magnitude of change in the device diameter while transitioning from its constrained state (implanted in the vessel beyond the aneurysm) to its unconstrained diameter (within the aneurysm)—and are fixed in that they cannot be modified (reduced) by the application of a forward load onto the freely expanded segment of the device (packing the device) (Fig 4). Therefore, oversizing will necessarily result in a segment of decreased metal coverage, which typically is located at the distal aneurysm boundary. Aside from the geometric reduction in the attenuation of metal coverage, depending on the method of deployment, this zone may contribute to the establishment of an asymmetric region of higher porosity near the aneurysm terminus, providing a zone of relatively lower resistance to inflow into the aneurysm, while the more appropriately sized proximal aneurysm segment (outflow zone) enjoys higher metal coverage, creating a mismatch in porosities across the length of the aneurysm.

A related observation was made concerning the morphology of the landing zone under conditions of device oversizing. When a device is oversized and deployed within a relatively small landing zone, the device edge tends to assume a cone-shaped morphology, a property intrinsic to all braided stent designs. This effect is exacerbated, rather than relieved, by application of forward tension (loading) onto the freely open portion of the stent (Fig 4). With progressive oversizing and increased forward load during deployment, the degree of "fishmouthing" becomes quite pronounced (Fig 4*C*, -*D*). These observations are in excellent agreement with recently published results of similar experiments by Raymond and colleagues.[4] Although these extreme in vitro scenarios are not necessarily reflective of typical in vivo deployments, the combination of oversizing and short landing zones may result in suboptimal opening of the device distally, potentially favoring progressive retraction (proximal migration, "watermelon-seeding") of the unexpanded distal end of the device into the fusiform segment where the device is fully expanded. This ultimately may lead to prolapse of the distal end of the device into the aneurysm, particularly when the distalmost segment of the device is deployed under conditions of traction (stretching) or where the exiting vessel exhibits a funnel shape.

We also observed, under conditions of longer landing zones, that the effect of oversizing manifests itself as a "lip" of decreased device apposition relative to the recipient tube, which may contribute, in vivo, to development of an endoleak as the implanted portions of the device become partially overgrown by neointima (Fig 3*A*). The same phenomenon can also be seen in vivo (Fig 5).

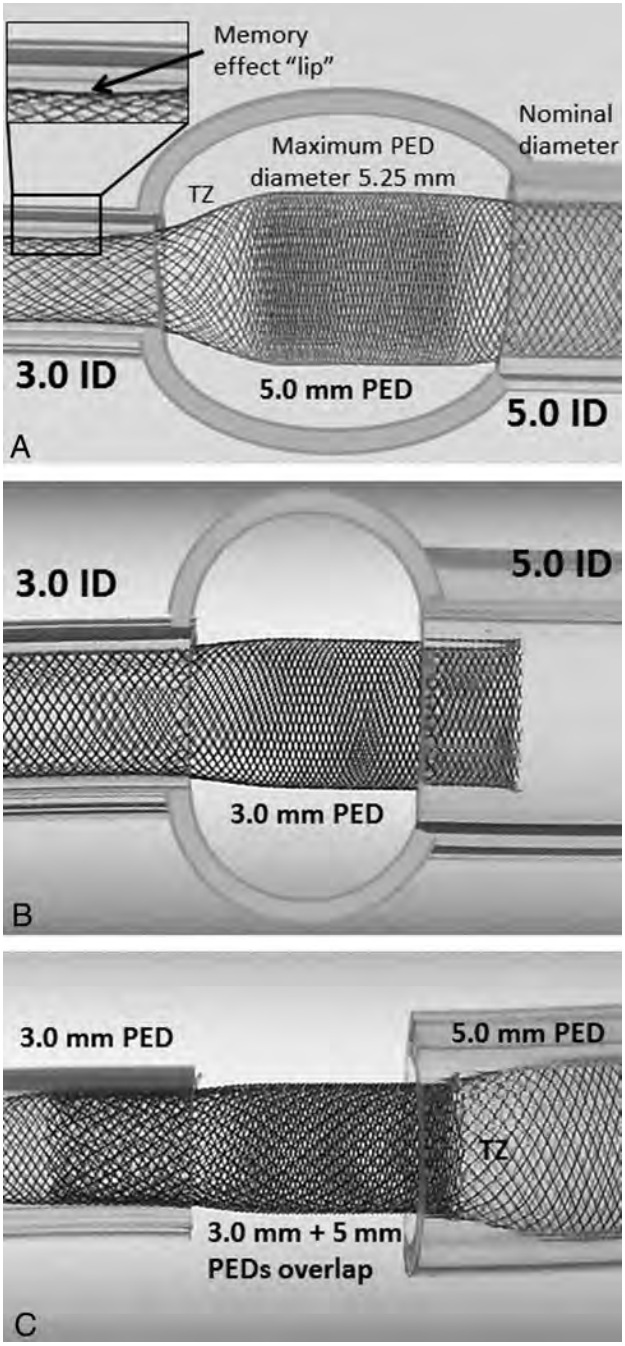

FIG 3. Morphologic effects of device oversizing and the corresponding solution. *A*, A model of a fusiform aneurysm with 3.0- and 5.0-mm landing zones, bridged by a single 5 × 20 mm device. A transition zone of minimum coverage is created as the device is constrained from its fully opened state into the 3-mm landing zone. Despite adequate length of the "landing zone" at the 3.0-mm end, the "shape memory" of the transition zone nevertheless produces a "lip" where the device remains unapposed to the inner wall of the tube. *B* and *C*, To address these issues, 2 devices are required, each of which is appropriately sized for its recipient artery. The first 3.0-mm device is deployed from the 3.0-mm-diameter vessel into the 5-mm recipient vessel (*B*), following which a second 5.0-mm-diameter device is telescoped into the first, with the 5.0-mm device anchored into its 5.0-mm vessel. Thus, the transition zone is shifted outside the aneurysm, while the aneurysmal segment receives the benefit of double coverage.

Thus, experiments of Raymond and colleagues[9] and our group suggest that oversizing results in suboptimal configurations at both the distal landing zone and within the intra-aneurysmal "transition zone," which may have anatomic and physiologic implications with respect to the effectiveness of the construct.

Metal Coverage along the Device Curvature

The geometric effects of curvature on coverage are more complex than those of simple oversizing. The PED accommodates exceptionally well to high degrees of vessel curvature, in part due to the extreme flexibility of the device, which is enabled by the unfixed property of its braided filaments. When deployed along a curved vessel, the composite metal strands slide along one another, altering the dimensions, *a*, of the individual cells. This "unfixed" characteristic leads to changes in both the angle, θ, and rhombus side length, *a*, resulting in the "opening" of cells along the outer curve and their progressive closure at the inner curve, in contrast to the more simple factors governing the behavior of the devices in straight segments of changing diameter, where only the angle, θ, changes substantially, and the side length, *a*, remains essentially constant (On-line Fig 4). All of these accommodations take place in the unconstrained state of the device, which would correspond to its in vivo morphology under a scenario in which the devices would be used in the endoluminal treatment of a fusiform aneurysm involving a curved segment of the parent vessel. If, in addition to curvature effects, the device was also constrained within the curved parent artery, the final configuration is expected to be even more complex, with myriad possible scenarios beyond the aim of the present investigation. For the unconstrained device, the representative percentage of metal coverage along different sections of a 180° curve is shown in Fig 6. From these data, it can be readily appreciated that while coverage is modestly reduced at the outer curvature, it is dramatically increased along the inner curve. While the effects of these changes on flow patterns, particularly at the outer curve, remain to be defined, there is experimental evidence to support the notion that treatment efficacy of aneurysms arising from the outer curve of a parent artery is reduced after attempted treatment with single-device placement.[8]

DISCUSSION

The above experiments serve to document certain features of the Pipeline Embolization Device and additionally illustrate potentially unanticipated effects on device porosity, final construct geometry, and implant stability arising from the use of oversized PEDs in the treatment of complex neck aneurysms. Other groups have made similar observations with similar endoluminal devices based on in vitro testing, flow modeling, and animal experiments.[6,8-10] Circumstances in which these effects are likely to be encountered include the treatment of the following: 1) complex fusiform aneurysms; 2) large dysplastic saccular aneurysms, particularly those near-circumferentially involving the parent artery; and 3) large, broad-neck aneurysms involving locations associated with significant changes in vessel diameter proximal and distal to the aneurysm neck. Under this latter condition, treatment of the target aneurysm with a single device necessitates oversizing at the smaller diameter landing zone (because no variable-diameter devices are currently on the market). This unavoidable outcome can

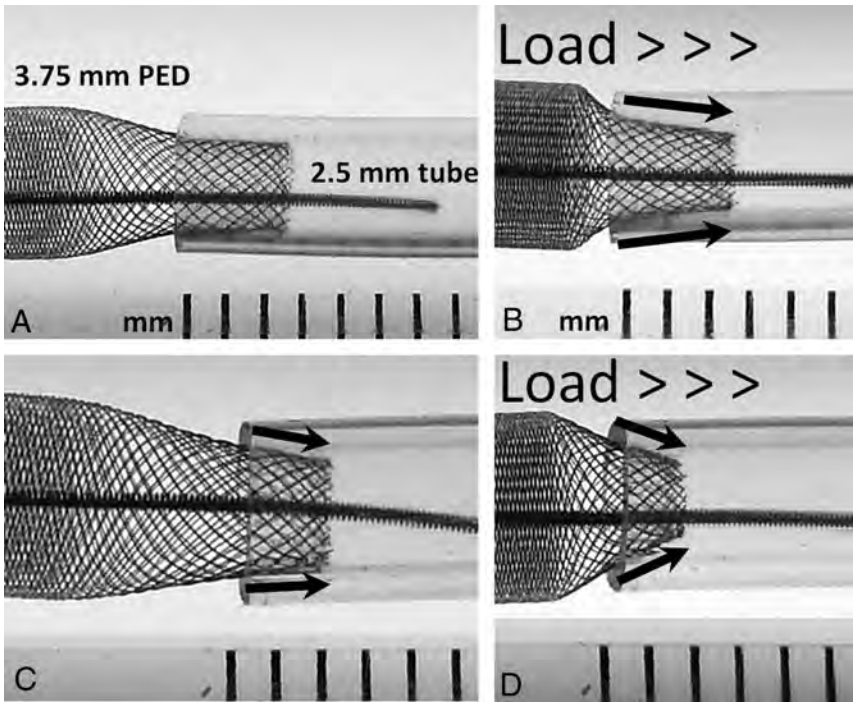

FIG 4. The "fishmouth" configuration of oversized devices in scenarios of short landing zones. A 2.5-mm landing zone (*A*) leads to no appreciable fishmouth configuration, unless the forward load is applied to the freely expanded portion of the device, as might be done in an attempt to better seat the device into the recipient artery (*B*). This, in fact, has the effect of decreasing device apposition to the wall, because the foreshortened area of decreased coverage remains unchanged, while a degree of fishmouthing is now present (*arrows*), due to an increase in the centripetal force vector along the transition zone angle. These effects are magnified when the landing zone decreases to approximately 1.5 mm in length (*C* and *D*). Altogether, these images suggest that the deleterious effects of oversizing are only likely to be exacerbated by attempts to force the device into the undersized artery.

be further exaggerated in proportion to the length of the device chosen, because the extension of longer devices proximally typically carries them into vascular segments of increasing diameters.

As evident from On-line Fig 1 and the Table, sizing mismatch invariably leads to substantial heterogeneity in metal coverage and porosity across the aneurysm neck as the device transitions from a constrained diameter to its unconstrained state (the degree of which may be mitigated by deployment technique), even under circumstances of relatively modest oversizing. Although the clinical significance of such mismatch in terms of reduced efficacy or potential deleterious changes in dynamic intra-aneurysmal flow is undefined as yet, sporadic adverse reports of worsening mass effect and delayed aneurysm rupture after treatment of large aneurysms with flow-diversion devices suggest a need for understanding the likely in situ disposition of the devices and the potential effects that suboptimal deployment may have on the hemodynamic condition of the aneurysmal environment.[11,12]

On the other hand, in different circumstances, deliberate oversizing could provide a potential advantage as a means to reduce metal coverage of eloquent perforators arising from the perianeurysmal regions of the parent artery. In this scenario, an oversized device could be selected to bridge the aneurysm neck (minimizing perforator coverage distal to the aneurysm), with additional (shorter) devices deployed across the aneurysm neck to address heterogeneities in the coverage of the aneurysm. This implicit duality with respect to therapeutic intention (maximized coverage of the aneurysm neck, minimized coverage of eloquent branch vessels) mandates a greater understanding of the device and its behavior under specific conditions, to optimize constructs to best accommodate the unique features of each aneurysm and the adjacent vascular environment.

Strategies to Address Vessel Size Mismatch

In addressing concerns related to transition zone effects, various strategies using multiple, shorter devices may minimize such effects (Fig 3). One approach exploits the partial overlapping of tandem devices, each appropriately sized for its respective landing zone, with successively larger devices sequentially telescoped to create a variable diameter construct, bridging the overall gap in size. While it is impossible to eliminate all transition effects, the transitions can be made more gradual, decreasing the abruptness of the step-off and shifting the ultimate TZ proximal to the aneurysm neck. This latter benefit can be obtained by extending a distally placed device, appropriately sized to the distal smaller diameter landing zone, fully across the aneurysm neck and, subsequently, anchoring this device within the larger parent artery proximal to the aneurysm with a second device, selected to match the larger diameter landing zone. The effective consequence of this construct is to move the TZ proximal to the aneurysm where the larger device emerges from the constraint imposed by the smaller diameter PED. This approach also provides higher metal coverage in the region of device overlap, which typically falls across the aneurysm neck (Fig 7). Alternatively, to address a perforator-rich territory (P1 segment, M1 segment) distal to an aneurysm, a construct can be built from proximal to distal, using a device sized to the vessel proximal to the aneurysm to cover the aneurysm neck, followed by a larger device, oversized to the smaller diameter vascular segment distal to the aneurysm and constrained by the proximal device across the aneurysm neck—thereby, potentially reducing the metallic coverage throughout the perforator-rich distal segment and providing double coverage of the aneurysm neck.

Although coverage initially decreases sharply with oversizing, due to the parabolic relationship between porosity and device diameter, surface coverage (in straight vascular segments) after reaching minimum values (near 20% for PED; On-line Fig 1, Table) can be expected to sharply increase at further constrained diameters. For example, the 4.75-mm device provides a minimum coverage of 18% when constrained within tubes ranging from 3 to 4 mm (Table), compared with a maximum of 27% when

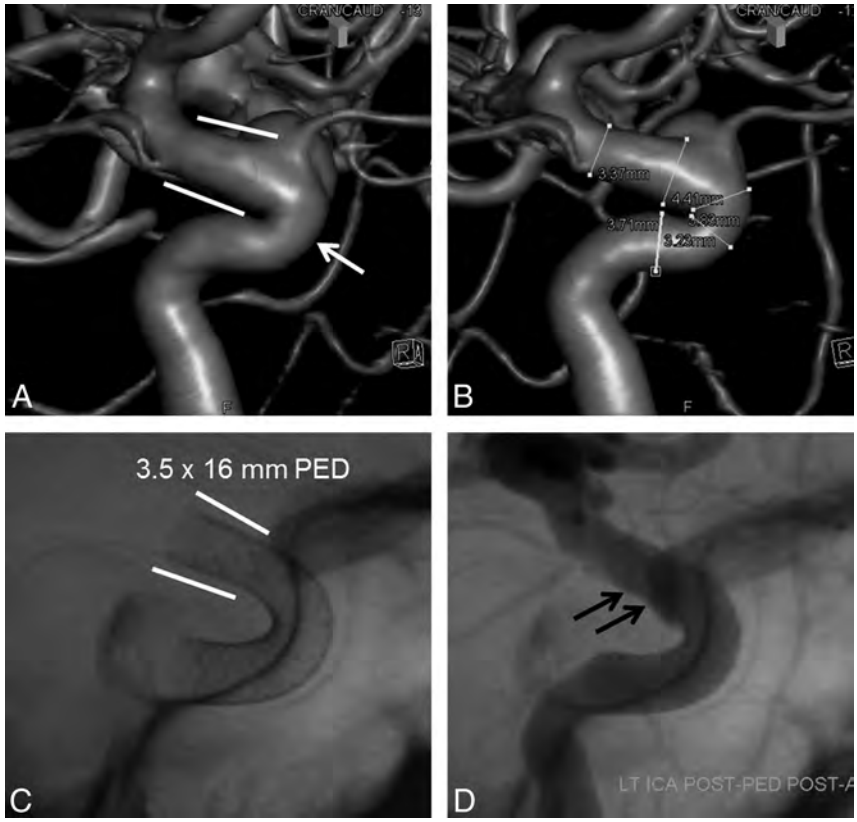

FIG 5. In vivo illustration of the memory shape effects. *A* and *B*, A wide-neck ophthalmic segment aneurysm with associated ectasia of the parent vessel, which tapers down from the ophthalmic artery to the ostium of the posterior communicating artery (*paired white lines*). The carotid artery is, however, normal in caliber at the anterior genu (*white arrow*). *C* and *D*, Native and native + contrast lateral views following Pipeline deployment. Notice the reverse morphology of the devices with the maximal diameter at the distal end (*C*, *paired white lines*). Although the device was deployed with an appropriate load, the memory effect at the anterior genu resulted in incomplete opening of the device at the level of the ophthalmic artery (*D*, *black arrows*). It is necessary to make sure that the distal end is fully in contact with the vessel to prevent an endoleak in this scenario.

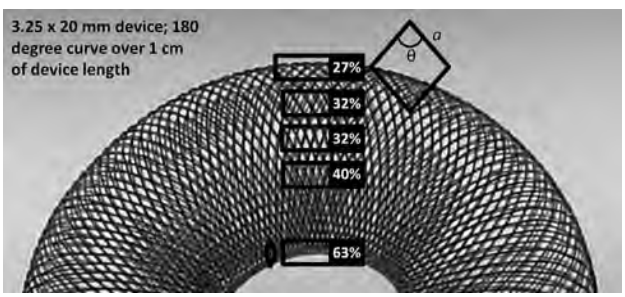

FIG 6. Photograph of a 3.25 × 20 mm device along a 180° curvature taking up ~10 mm of the device. The percentage of metal coverage at each of the stations along the curve is listed, with a corresponding illustration of cell shape, showing that both θ and cell side length a vary substantially along the curve.

deployed in a 5.0-mm tube. Below 2.75 mm, coverage again significantly increases. An implication of the observed coverage minimae measured for PEDs of differing diameters is that double-covering a segment of low coverage with a device of identical or larger diameter (to take advantage of differences in deployed pitch between overlapped devices) will increase coverage to >30%, which would be superior to the percentage coverage with a single device at its nominal opening state.

Also important is the recognition that the surface coverage of a device is fundamentally related to its deployed diameter; furthermore, in its unconstrained state, slight increases in diameter occurring with longitudinal compression of the device (loading) can drive coverage (along its parabolic curve) to very high levels. Judicious "packing" of the device is important to assure its optimal apposition to the recipient vessel. However, beyond this, for device segments optimally apposed to the vessel wall and, therefore, constrained by the parent artery, no increase in coverage within the vessel can be achieved by applying forward load onto the device. This may limit packing of the device across aneurysms with small necks. In contrast, packing (by loading the device during deployment) can substantially increase coverage in the unconstrained portion of the PED, across the aneurysm neck or within a fusiform aneurysmal segment—bearing in mind that, much like landing-zone coverage, the limited TZ coverage is not ameliorated by this strategy.

Theoretically, TZ effects could be reduced by controlling the deployed diameter of the device across the aneurysm neck by unsheathing the device under slight traction, rather than pushing it out under load. However, this must be done carefully, ensuring that the device becomes sufficiently implanted proximal to the aneurysm (possibly supported by additional anchoring devices) to avoid subsequent "migration" of the unloaded "stretched" bridging device by preventing potential gradual self-expansion to its nominal diameter in the postprocedural phase.

Curve-Related Porosity Changes

The relationships between device diameter and metal coverage in this study were calculated for devices deployed in linear models. The degree of metallic coverage observed in vivo, however, will be substantially more complex due to the effects of vessel curvature. In curved vascular segments, the constituent filaments of the device slide over one another, altering not only the angles of the rhomboids but also their side-length dimensions (Fig 6), giving rise to a variable "porosity" at each point along the vessel cross-section, from the inner to the outer curves. From a clinical standpoint, the reduced coverage (higher porosity) along the outer curve may become important in the treatment of outer curvature aneurysms, possibly requiring additional devices to achieve a therapeutic degree of coverage across the aneurysm neck, as previously observed by Darsaut and colleagues,[13] both in vitro and in animal models.[8] Conversely, there should be heightened concern

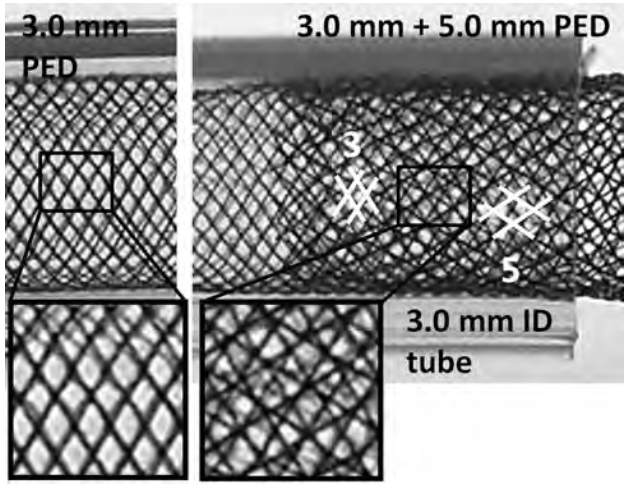

FIG 7. Illustration of double-coverage effects on the extent and morphology of metal coverage. High-magnification views of the cell structure of a single 3.0-mm device deployed in a 3.0-mm tube; a 5.0-mm device is then telescoped into the 3.0-mm device. Note the much larger cell size of the 5-mm device and different angles of overlapping pitch from each device.

for perforators originating from the inner curvature, where coverage values increase to very high numbers. There are some in vitro data to support the notion of increased neointimal overgrowth across side-branch ostia with >35%–40% metal coverage.[14,15]

The results of our experiments with the PED may be only qualitatively applicable to other braided flow-diverter devices. For example, a detailed study of the Silk device (Balt Extrusion, Montmorency, France) by Aurboonyawat et al[5] showed that this device behaves quite differently with respect to oversizing and curvature, a difference that seems to be related to the variability in nominal pitch angle θ between the 2 devices.

Given the many configurations that vascular segments (each exhibiting distinct stenoses and complex curvatures) and devices implanted within them may assume, the extent to which in vitro observations can be applied to realistic in vivo scenarios remains an open question. Nevertheless, the results presented here serve to illustrate the importance of understanding fundamental characteristics of the devices and critical anatomic features (changing vessel diameters, the nature of the aneurysm neck, the curvature of the target vascular segment, stenoses) among the number of factors that influence case selection and treatment strategy.

CONCLUSIONS

We present benchtop observations documenting important geometric properties of the Pipeline Embolization Device in various scenarios. Knowledge of these device geometries should be helpful to operators using the device, particularly under the challenging anatomic circumstances often necessitating its use. Our findings quantitatively illustrate that device metal coverage is a dynamic value with substantial variability under realistically expected deployment conditions. We hold these results as supportive of the need to consider regional metal coverage in device-treatment strategies, which may require the use of multiple devices to achieve the desired geometric configurations and maximize the overall efficacy of treatment.

Disclosures: Maksim Shapiro—*UNRELATED*: *Consultancy*: Covidien, *Comments*: Pipeline proctor consultant with Covidien, *Payment for Lectures (including service on Speakers Bureaus)*: Covidien, *Comments*: participates in Pipeline physician training courses with Covidien, *Payment for Development of Educational Presentations*: Covidien, *Comments*: developed Pipeline educational presentations for physician and staff training with Covidien. Tibor Becske—*UNRELATED*: *Consultancy*: ev3/Covidien, *Payment for Development of Educational Presentations*: ev3/Covidien, *Comments*: payment for development of Pipeline training materials, *Travel/Accommodations/Meeting Expenses Unrelated to Activities Listed*: ev3/Covidien, *Comments*: travel and accommodation support, *Other*: ev3/Covidien, *Comments*: proctoring fees. Peter K. Nelson—*UNRELATED*: *Consultancy*: Covidien, *Comments*: fees covering physician proctoring.

REFERENCES

1. Nelson PK, Lylyk P, Szikora I, et al. **The Pipeline embolization device for the Intracranial Treatment of Aneurysms trial.** *AJNR Am J Neuroradiol* 2011;32:34–40
2. Becske T, Kallmes DF, Saatci I, et al. **Pipeline for uncoilable or failed aneurysms: results from a multicenter clinical trial.** *Radiology* 2013;267:858–68
3. Wang K, Yuan S. **Actual metal coverage at the neck is critical for flow-diverting stents in treating intracranial aneurysms.** *AJNR Am J Neuroradiol* 2013;34:E31–32
4. Makoyeva A, Bing F, Darsaut TE, et al. **The varying porosity of braided self-expanding stents and flow diverters: an experimental study.** *AJNR Am J Neuroradiol* 2013;34:596–602
5. Aurboonyawat T, Blanc R, Schmidt P, et al. **An in vitro study of Silk stent morphology.** *Neuroradiology* 2011;53:659–67
6. Mut F, Cebral JR. **Effects of flow-diverting device oversizing on hemodynamics alteration in cerebral aneurysms.** *AJNR Am J Neuroradiol* 2012;33:2010–16
7. Wang K, Huang Q, Hong B, et al. **Correlation of aneurysm occlusion with actual metal coverage at neck after implantation of flow-diverting stent in rabbit models.** *Neuroradiology* 2012;54:607–13
8. Bing F, Darsaut TE, Salazkin I, et al. **Stents and flow diverters in the treatment of aneurysms: device deformation in vivo may alter porosity and impact efficacy.** *Neuroradiology* 2013;55:85–92
9. Darsaut TE, Bing F, Salazkin I, et al. **Testing flow diverters in giant fusiform aneurysms: a new experimental model can show leaks responsible for failures.** *AJNR Am J Neuroradiol* 2011;32:2175–79
10. Darsaut TE, Bing F, Salazkin I, et al. **Flow diverters can occlude aneurysms and preserve arterial branches: a new experimental model.** *AJNR Am J Neuroradiol* 2012;33:2004–09
11. Kulcsár Z, Szikora I. **The ESMINT Retrospective Analysis of Delayed Aneurysm Ruptures after flow diversion (RADAR) study.** In: *Proceedings of the Annual Meeting of the European Society of Minimally Invasive Neurological Therapy*, September 2012, Nice, France
12. Kulcsár Z, Houdart E, Bonafé A, et al. **Intra-aneurysmal thrombosis as a possible cause of delayed aneurysm rupture after flow-diversion treatment.** *AJNR Am J Neuroradiol* 2011;32:20–25
13. Darsaut TE, Bing F, Salazkin I, et al. **Flow diverters failing to occlude experimental bifurcation or curved sidewall aneurysms: an in vivo study in canines.** *J Neurosurg* 2012;117:37–44
14. Hong B, Wang K, Huang Q, et al. **Effects of metal coverage rate of flow diversion device on neointimal growth at side branch ostium and stented artery: an animal experiment in rabbit abdominal aorta.** *Neuroradiology* 2012;54:849–55
15. Lieber BB, Sadasivan C. **Endoluminal scaffolds for vascular reconstruction and exclusion of aneurysms from the cerebral circulation.** *Stroke* 2010;41:S21–25

Stent Retrievers in Acute Ischemic Stroke: Complications and Failures during the Perioperative Period

G. Gascou, K. Lobotesis, P. Machi, I. Maldonado, J.F. Vendrell, C. Riquelme, O. Eker, G. Mercier, I. Mourand, C. Arquizan, A. Bonafé, and V. Costalat

ABSTRACT

BACKGROUND AND PURPOSE: Stent retriever–assisted thrombectomy promotes high recanalization rates in acute ischemic stroke. Nevertheless, complications and failures occur in more than 10% of procedures; hence, there is a need for further investigation.

MATERIALS AND METHODS: A total of 144 patients with ischemic stroke presenting with large-vessel occlusion were prospectively included. Patients were treated with stent retriever–assisted thrombectomy ± IV fibrinolysis. Baseline clinical and imaging characteristics were incorporated in univariate and multivariate analyses. Predictors of recanalization failure (TICI 0, 1, 2a), and of embolic and hemorrhagic complications were reported. The relationship between complication occurrence and periprocedural mortality rate was studied.

RESULTS: Median age was 69.5 years, and median NIHSS score was 18 at presentation. Fifty patients (34.7%) received stand-alone thrombectomy, and 94 (65.3%) received combined therapy. The procedural failure rate was 13.9%. Embolic complications were recorded in 12.5% and symptomatic intracranial hemorrhage in 7.6%. The overall rate of failure, complications, and/or death was 39.6%. The perioperative mortality rate was 18.4% in the overall cohort but was higher in cases of failure (45%; $P = .003$), embolic complications (38.9%; $P = .0176$), symptomatic intracranial hemorrhages (45.5%; $P = .0236$), and intracranial stenosis (50%; $P = .0176$). Concomitant fibrinolytic therapy did not influence the rate of recanalization or embolic complication, or the intracranial hemorrhage rate. Age was the only significant predictive factor of intracranial hemorrhage ($P = .043$).

CONCLUSIONS: The rate of perioperative mortality was significantly increased in cases of embolic and hemorrhagic complications, as well as in cases of failure and underlying intracranial stenoses. Adjunctive fibrinolytic therapy did not improve the recanalization rate or collateral embolic complication rate. The rate of symptomatic intracranial hemorrhage was not increased in cases of combined treatment.

ABBREVIATIONS: BA = basilar artery; BGC = balloon-guided catheter; ECASS II = European Co-operative Acute Stroke Study-II; HI = hemorrhagic infarct; ICH = intracranial hemorrhage; PH = parenchymatous hemorrhage

IV fibrinolysis within 4.5 hours after stroke onset is the reference therapy for acute ischemic stroke in the Western world. Many predictors of success or failure have been reported in relationship to this treatment.[1-4] Proximal intracranial artery occlusions,[5,6] cardiovascular risk factors, and high NIHSS score have all been reported to be associated with failed recanalization after IV fibrinolysis.[3,6-8] Symptomatic risk for intracranial hemorrhage (ICH) increases gradually with increasing infarct size and patient age.[9,10] Mechanical thrombectomy is an adjuvant or alternative therapy for acute ischemic stroke when IV fibrinolysis is contraindicated or has failed. Recent studies[11-17] have shown that mechanical thrombectomy by use of a stent retriever is successful in achieving a high rate of arterial recanalization, with a low complication rate. This technique is promising; however, adverse embolic and hemorrhagic events have been reported in roughly 5%–10%[12,14] of procedures, with a failure rate ranging from 9%–33%.[11,17,18] With this in mind, we reviewed our prospective data base of 144 consecutive patients to identify predictive factors of failure, complications, and periprocedural mortality.

Received March 9, 2013; accepted after revision July 24.

From CHU Montpellier, Neuroradiology (G.G., P.M., I.M., J.F.V., C.R., O.E., A.B., V.C.) and Neurology (C.A., I.M.), Montpellier, France; Imaging Department (K.L.), Imperial College Healthcare NHS Trust, Charing Cross Hospital, London, United Kingdom; CHU Montpellier, Department of Medical Statistics (G.M.), Arnaud de Villeneuve Hospital, University of Montpellier, Montpellier, France.

All authors have made substantial contributions to all of the following: the conception and design of the study (G.G., V.C., A.B., P.M.), acquisition of data (G.G., V.C., P.M., C.R., O.E., A.B., I.M., C.A., J.F.V.), analysis and interpretation of data (G.M., G.G., V.C., K.L., A.B.), and drafting the article or revising it critically for important intellectual content (G.G., V.C., K.L., A.B.).

Please address correspondence to Vincent Costalat, MD, PhD, CHU Montpellier, Neuroradiology, Av Augustin Fliche, Montpellier, France; e-mail: v-costalat@chu-montpellier.fr

Indicates article with supplemental on-line table.

http://dx.doi.org/10.3174/ajnr.A3746

MATERIALS AND METHODS

Patient Selection

Ethical approval for this study was obtained by the local ethics committee in our institution after review of the stroke protocol. Patients with acute stroke were examined at admission by a senior stroke neurologist who assessed the severity of the neurologic deficit by using the NIHSS. An NIHSS score equal or superior to 8 was required for mechanical thrombectomy to be considered. Patients underwent comprehensive imaging in the acute phase, with MR imaging to delineate the extent of the ischemic lesion. In cases of MR imaging contraindication, CT, CTA, and CTP were carried out.

In patients with anterior circulation strokes, the ASPECT score was calculated on DWI MR imaging or CT to assess the extent of the ischemic core. Only patients with an ASPECT score of ≥5 were included, according to our institutional protocol[12] and the SAMURAI (Stroke Acute Management with Urgent Risk-factor Assessment and Improvement) study.[19]

In accordance with our institutional stroke protocol, patients presenting within 4.5 hours from symptom onset received a combined therapy associating IV fibrinolysis (rtPA 0.9 mg/kg) and mechanical thrombectomy. Patient presenting between 4.5 and 6 hours with anterior circulation strokes or presenting with IV fibrinolysis contraindication were treated with stand-alone thrombectomy. For patients with posterior circulation strokes, a combined approach was performed up to 24 hours after symptom onset, depending on the extent of the ischemic lesions. Extensive brain stem lesions (eg, bilateral complete involvement of the pons, mesencephalon, or diencephalic structures) were the main exclusion criteria in this location.

MR Imaging Protocol

MR imaging was performed by use of a 1.5T magnet (33 mT/m hypergradients; Intera, release 10; Philips Healthcare, Best, the Netherlands) with a phased-array head coil. First, a T2 gradient-echo was performed to screen for ICH. Then, DWI sequences B0, B500, and B1000 were acquired, as was an ADC map to identify the ischemic core. FLAIR and T2 were also used as surrogate markers of the time elapsed from symptom onset. A T1 contrast-enhanced MRA of the supra-aortic trunks and intra-cranial vessels was then obtained to screen for large-vessel occlusion. In cases of MR imaging contraindications, an unenhanced head CT, CTA, and CTP were performed. All MR and CT images were reviewed by 2 independent senior neuroradiologists who did not participate in the initial therapeutic management.

Devices

Stent retrievers were used as a first-line device. In 138 cases, the Solitaire FR revascularization device (Covidien, Irvine, California) was used. This device is a stent-based thrombectomy system with a closed-cell design and a longitudinal split section. Alternative stent retriever devices were used in 6 cases: the Revive[20] (Codman & Shurtleff, Raynham, Massachusetts) (4 cases) and the Trevo[21,22] (Stryker, Kalamazoo, Michigan) (2 cases).

Mechanical Thrombectomy Protocol

All procedures were performed via a femoral artery approach and with the patients under general anesthesia. For the anterior circulation, an 8F or 9F Merci balloon-guided catheter (BGC; Concentric Medical) was inserted through a sheath. For the posterior circulation, a 6F Envoy guiding catheter (Codman & Shurtleff) was placed through a sheath into the dominant, or navigable, vertebral artery. A 0.021-inch internal diameter microcatheter (Prowler Select Plus [Codman & Shurtleff] or Vasco 21 [Balt, Montmorency, France]) was navigated distal to the point of occlusion over a 0.014-inch steerable microwire. A microcatheter angiographic run was then carried out to define the vascular bed distal to the thrombus. The stent retriever was then introduced through the microcatheter and the device deployed across the occluding thrombus. The microcatheter distal marker was positioned at the exact level of the proximal marker of the stent retriever. After deployment, the stent retriever was maintained in place for approximately 3–7 minutes to allow full device expansion. The stent retriever was fully deployed in all cases. An angiographic run was performed to evaluate the degree of temporary recanalization. The fully deployed stent retriever and the delivery microcatheter were then gently pulled back together and recovered through the guiding catheter. During the retrieval, the BGC was inflated to interrupt anterograde flow. Manual aspiration with a 50-mL syringe was performed through the hemostatic valve during the retrieval to reverse the flow and to aspirate clot debris possibly lost in the guide catheter lumen. The integrity of the stent was consistently checked following each pass.

Successful recanalization was defined as TICI 2b or 3.[23] If the vessel was not reopened to at least TICI 2b with a maximum of 5 passes, then the treatment was considered failed. All TICI scores were independently reviewed by a second neuroradiologist and adjudicated in cases of disagreement. Neither IV heparin nor intra-arterial fibrinolytics were administered at any time during the procedure, even if the recanalization attempt was unsuccessful. Groin punctures were routinely closed with an Angio-Seal (St. Jude Medical, Minnetonka, Minnesota).

Should intracranial stenosis occur, complementary stand-alone angioplasty was preferred with use of a Gateway balloon (Stryker), or an UltraFlow balloon (Covidien) 2.5 mm. Inflation was cautiously done up to 6 atm. Following an angiographic control, stent placement was considered only if immediate restenosis of the target artery associated with immediate reocclusion occurred. In these cases, a Wingspan stent (Boston Scientific, Natick, Massachusetts) was chosen and sized according to the target vessel size. Antiplatelet management consisted of 500 mg of aspirin IV during the procedure, and double antiplatelet was discussed after the 24-hour CT control in view of any serious hemorrhagic complications.

Adverse Event Definition

The types of hemorrhagic complications were defined according to the European Co-operative Acute Stroke Study-II (ECASS II).[24] Symptomatic ICH was defined as parenchymatous hemorrhage (PH)1 or PH2 hematomas and a ≥4-point NIHSS score decline or death within the periprocedural period.

Embolic complications were defined as an angiographic occlusion in a previously unaffected vascular territory observed on the angiogram after clot removal and associated with new

ischemic changes on 24-hour postprocedural CT or MR imaging.

All 24-hour CT/MR imaging scans were reviewed by a second neuroradiologist and adjudicated in cases of disagreement.

Postoperative Management

A CT scan was performed at the end of the procedure to screen for immediate hemorrhagic transformation. Airway support was immediately discontinued after the procedure to allow prompt neurologic re-evaluation. Mechanical ventilation was maintained in cases of posterior circulation stroke. No antiplatelet or heparin was administered during the first 24 hours. An additional CT or MR imaging examination was performed 24 hours after the procedure. If no hemorrhage was present, aspirin 160 mg/day was administered. The length of stay was between 2 days and 1 month. The NIHSS score was then reported at discharge by a stroke practitioner.

Statistical Analysis

Patient characteristics were presented by use of median and range for continuous variables and frequencies and proportions for categoric variables. Statistical significance between recanalization failure and success and between complications and no complications was assessed by the Pearson χ^2 test for categoric variables and the Mann-Whitney *U* test or the Student *t* test for continuous variables. Baseline NIHSS score was entered as a continuous variable. The significance of adding or removing a variable from the logistic model was determined by the maximum likelihood ratio test. ORs and their 95% CIs were calculated. The goodness-of-fit of the models was assessed by use of the Hosmer and Lemeshow χ^2 test. A level of $P < .05$ was considered statistically significant. Statistical analysis was performed by use of SAS software, version 9 (SAS Institute, Cary, North Carolina).

RESULTS

Population

From August 2009 to November 2011, a total of 144 consecutive patients (70 women and 74 men) aged 26–91 years (median age, 70 years; mean age, 67 years) were treated. Mean baseline NIHSS score was 16.6 (median, 18; range, 3–36).

Acute MR Imaging

MR imaging was performed in 142 of 144 patients. Two patients had contraindications to MR imaging and were assessed by CT, CTA, and CTP. The mean DWI-derived ASPECT score was 6.3 (range, 3–10). In 109 patients (75.7%), the occlusion involved the anterior territory: MCA in 60 patients, ICA in 10 patients, ICA termination in 23 patients, and tandem occlusion in 16 patients. Acute occlusion of the basilar artery (BA) was noted in 35 patients (24.3%).

Protocol Deviation

Protocol deviations were observed in 18 cases (12.5%). Seven patients with an NIHSS score < 8 were included: 3 cases of a symptomatic BA occlusion and 4 cases of pertinent motor deficit in the anterior circulation. Eleven patients were treated despite an ASPECT score < 5. Among these patients (7 patients from the combined group, 4 from the stand-alone thrombectomy group), 3 (21.4%) underwent hemorrhagic transformation, from which 2 (18.2%) were symptomatic.

Relationship between perioperative mortality, failure, complications (embolic and hemorrhagic), and intracranial stenosis

Population	Perioperative Mortality (%)	*P* Value	Mean NIHSS at Discharge
Overall cohort	18.4		7.9
Failure	45	.003	14.6
Embolic complication	38.9	.0176	10.7
Hemorrhagic complication	45.5	.0236	14.2
Intracranial stenosis	57.1	.0176	16.3

Failure Rate

We noted 6 cases of TICI 2a (4.9%), 1 case of TICI 1 (0.7%), and 13 cases of TICI 0 (9%), which corresponds to an observed total failure rate of 13.9%. In our study, the mortality rate in failed thrombectomy cases (45%) was significantly higher than in the overall cohort (18.4%; $P = .003$). The overall rate of successful recanalization was 86.1% (TICI 3: 69.4%; TICI 2b: 16.7%).

Embolic and Hemorrhagic Complications

Embolic complications were observed in 18 patients (12.5%): 8 embolic complications (44.4%) were observed in the stand-alone thrombectomy group and 10 (55.6%) in the combined group ($P = .354$) (Table and On-line Table). When the clot was removed from the anterior circulation (MCA or ICA), we reported distal emboli within the anterior cerebral artery territories (6 cases) (Fig 2), distal M3-MCA (3 cases), and posterior cerebral arteries (3 cases). When the clot was removed from the BA, embolic complications were observed within the posterior inferior cerebellar artery (3 cases), the posterior cerebral arteries (2 cases), and the superior cerebellar artery (2 cases). Thirteen patients (72.2%) had clinical worsening including 7 deaths (38.9%), whereas the overall rate of periprocedural mortality was 18.4% ($P = .0176$). Overall hemorrhagic complications were noted in 30 cases (20.8%): 9 (18%) in the stand-alone thrombectomy group and 21 (22.3%) in the combined group ($P = .541$). We identified 4 subarachnoid hemorrhages, 6 hemorrhagic infarcts category 1 (HI1), 3 HI2, 9 PH1, and 8 PH 2 (Fig 1) according to the ECASS II classification.[24] Eleven patients (7.6%) had symptomatic ICH: 6 patients from the combined group and 5 patients from the stand-alone thrombectomy group. All ICHs were observed in the initial stroke territory. In our study, the mortality rate in patients with symptomatic ICH was 45.5% ($P = .0236$).

Other Periprocedural Complications

Technical complications were reported in 5 patients. In 1 patient, an in-stent thrombosis occurred 6 hours after stent deployment for an MCA dissection secondary to MCA stenosis angioplasty, resulting in clinical worsening. An iatrogenic extracranial ICA dissection resulted in an ICA occlusion, with the patient remaining asymptomatic because of good collaterals from the circle of Willis. An arterial perforation was reported in 1 patient, who died subsequently. This perforation was not caused by the thrombectomy device but, instead, by an MCA complementary angioplasty. Device fracture and spontaneous release of the stent retriever were also seen in 2 patients. In both cases, the device was left in place

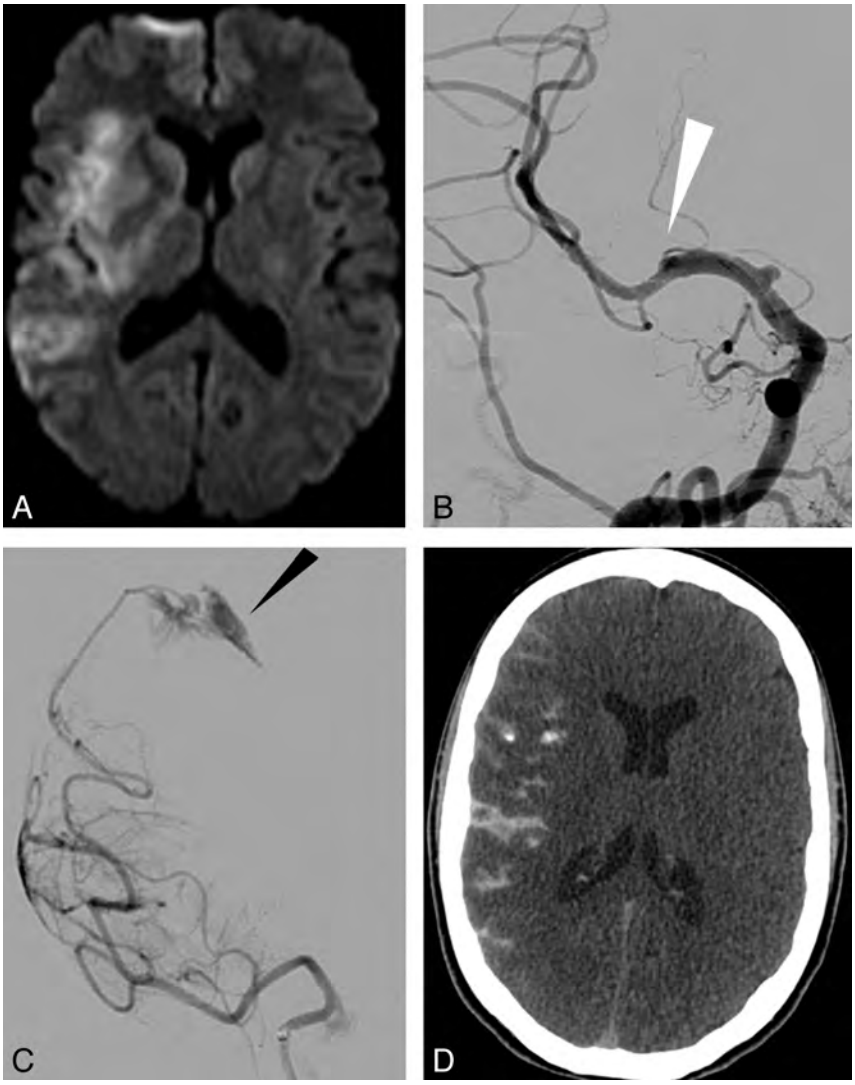

FIG 1. Rupture of a cortical pial vessel following selective injection via microcatheter. *A*, Initial DWI showing right MCA infarct (DWI ASPECT score, 5) without intracranial hemorrhage. *B*, Occlusion of right MCA (M2) (*white arrow*) seen on frontal angiogram. *C*, Selective injection via the microcatheter beyond the clot leading to rupture of a cortical pial vessel (*black arrow*). *D*, Immediate postoperative CT showing contrast within the subarachnoid space.

and the patient received long-term antiplatelet therapy with a good neurologic outcome at discharge.

No death or transfusion was related to groin puncture hematoma.

The rate of overall complications (including embolic complications, symptomatic ICH, and periprocedural complications) was 18.1%. The cumulative rate of failure, complication, and/or death during the perioperative period was 39.6%. Sixteen patients (11.8%) died without procedural complications and 9 (6.6%) secondary to a procedure-related event.

Intracranial Stenosis

Eight cases (5.5%) of intracranial stenosis were observed, including 3 stenoses of the BA and 5 of the MCA. The mean age of the intracranial stenosis patients was 74.4 years (age range, 55–86 years). In the elderly population (>70 years old), the overall mortality rate was 24.2%, and the mortality rate related to intracranial stenosis in this subgroup was 18.8%. Unsuccessful recanalization was observed in 7 (87.5%) of 8 cases. Angioplasties were performed in 3 of 7 cases of intracranial stenosis and provided a TICI 2b–3 recanalization in 1 case. Additional deployment of an intracranial stent was performed in 1 case of intracranial stenosis with an acute in-stent thrombosis 3 hours postprocedure. Periprocedural complications were reported in 28.6% of cases and were related to complications of angioplasty (1 dissection and 1 arterial rupture). The mortality rate in cases of intracranial stenosis was 50%.

Clinical Evaluation at Discharge

A total of 136 patients were assessed by a stroke practitioner at discharge. Mean NIHSS score at discharge was 7.9 (range, 0–25) in the overall cohort vs 10.7 in cases of embolic complications and 14.2 for hemorrhagic complications. In cases of thrombectomy failure, the mean NIHSS score was 14.6; in patients with intracranial stenosis, it was 16.3. At discharge, 25 deaths (18.4%) were reported (Table).

DISCUSSION

Recent studies (IMS III,[25] SYNTHESIS,[26] MR RESCUE trial[27]) did not observe superiority of endovascular approaches compared with standard intravenous rtPA treatment for large-vessel occlusion. However, these studies were conducted with first-generation devices, with almost no stent retriever. As recent studies[22,28,29] have reported, there is a significant superiority of stent retriever devices compared with "non-stent retriever" devices from a clinical and technical point of view. Hence, the results from these trials have not changed our current treatment protocol and practice, and we are pending the results of further trials such as THRACE (Trial and Cost Effectiveness Evaluation of Intra-arterial Thrombectomy in Acute Ischemic Stroke), SWIFT PRIME (Solitaire FR as Primary Treatment for Acute Ischemic Stroke), MRCLEAN (Endovascular treatment for acute ischemic stroke in the Netherlands), and PISTE (Pragmatic Ischaemic Stroke Thrombectomy Evaluation).

Recanalization Failure

The recanalization failure rate observed (13.9%) was roughly similar to the recent stent retriever literature (mean rate, 10.3%; range, 0%–33.3%).[15,20,22,28–31] It is not clear to date if IV and intra-arterial therapies are synergistic in achieving a higher recanalization rate.

In our study, IV thrombolytics were used in combination with mechanical thrombectomy in 65.3% of patients. In this group, the

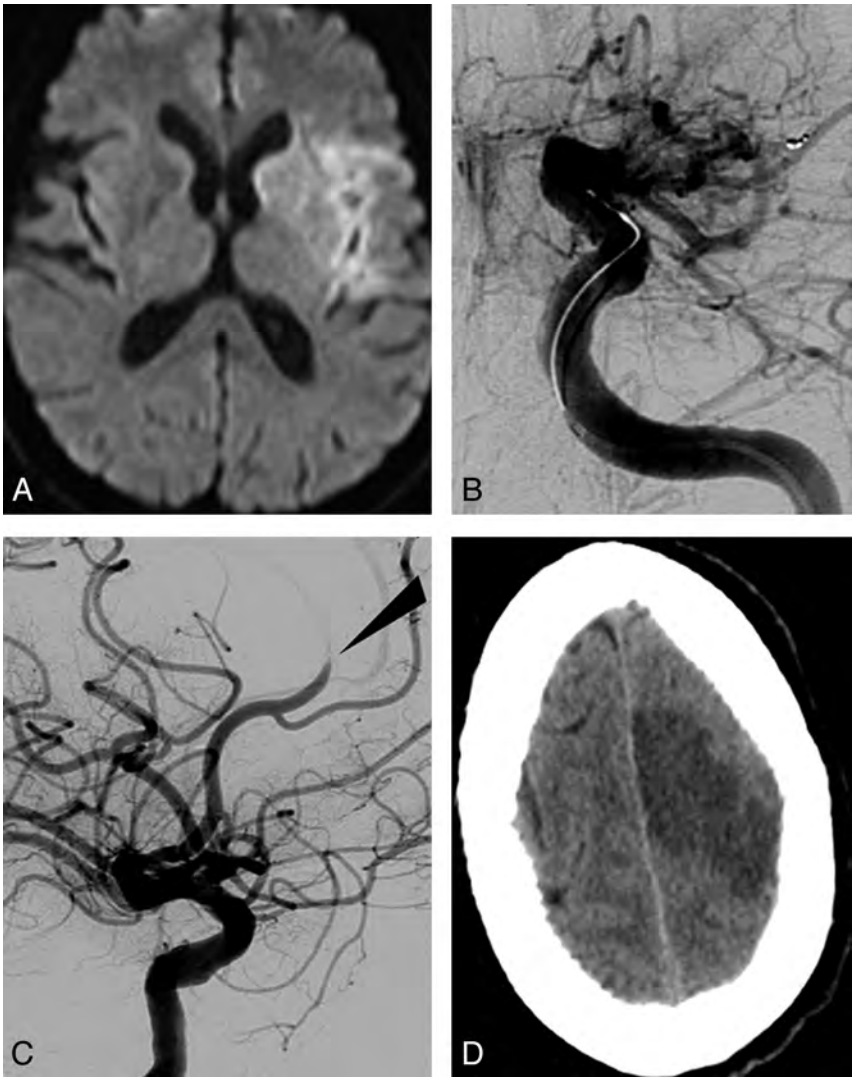

FIG 2. A thromboembolic occlusion of the left anterior cerebral artery after clot removal from the ipsilateral MCA. *A*, Initial DWI showing ischemic lesion in the left MCA territory (DWI ASPECT score, 7). *B*, Left ICA Townes projection angiogram showing terminal occlusion. *C*, Lateral projection angiogram after removal of the device allowing flow restoration within the MCA but embolic migration within the left anterior cerebral artery (*arrow*). *D*, New ischemic lesion seen on CT after the procedure within the left anterior cerebral artery territory.

recanalization failure rate was 14.9% vs 12% in patients treated by stand-alone thrombectomy ($P = .615$). This result suggests that IV therapy did not significantly influence the recanalization rate in acute thrombectomy cases by using a stent retriever. In a similar fashion, Dávalos et al[13] did not report any statistically significant difference between patients treated with combined therapy compared with the stand-alone thrombectomy group (failure rate, 14% vs 19%). On the contrary, Dorn et al[14] observed that the recanalization rate was higher when IV fibrinolysis was administered before mechanical thrombectomy. A reliable comparison between combined therapy and stand-alone thrombectomy is difficult to establish without a randomized trial. Actually, patients treated by stand-alone thrombectomy are selected following IV therapy exclusion criteria, resulting in a systematic selection bias. It is important to notice that the timing between these 2 therapies was not consistent and could reach several hours. In these conditions, we can hypothesize that IV therapy was not systematically fully efficient during mechanical treatment. It is interesting to note that Dávalos et al[13] reported a significantly better 3-month outcome (mRS $\leq$2) in patients treated by means of combined therapy compared with the stand-alone group, suggesting that IV therapy could play a role at a "microcirculatory level" on brain reperfusion, not visible on final DSA control.

The failure rate did not reach any statistical difference between the anterior circulation (12.3%) and the posterior circulation (17.1%) ($P = .535$), despite the obvious anatomic difference between these 2 territories and the lack of a BGC in the posterior circulation.

Embolic Complications

In our study, embolic complications occurred in 18 cases (12.5%) and seemed to be a major procedural issue of the technique despite such complications being rarely reported in the recent literature. For example, Castaño et al[11] and Roth et al[18] did not observe any embolic complications in their first experiences. Recently, Dorn et al[14] and Nogueira et al[22] observed a rate of embolic complications of 3.7% and 7%, respectively. In an experimental model of cerebrovascular occlusion, authors compared 5 thrombectomy devices[32] and concluded that the risk for embolic showers was influenced by the mechanism of action of the thrombectomy device. There was a significant increase in the number of large clot fragments with the Penumbra system (Penumbra, Alameda, California) compared with the Merci retriever. The Solitaire FR device produced larger fragments than the Waveguide system (OmniSonics Medical Technologies, Wilmington, Massachusetts). In our study, the mortality rate among patients who had embolic complications (38.9%) was higher than in the overall cohort (18.4%) ($P = .0176$). Eleven embolic events in 109 procedures were reported in the anterior circulation (10.1%) and 7 cases (20%) among 35 procedures in the posterior circulation, with no statistical difference but a slight tendency to a higher occurrence in the posterior circulation territory ($P = .144$), as was already suggested.[12] In the anterior circulation, Dávalos et al reported a significant role for BGCs in decreasing the incidence of collateral infarction in the anterior circulation. In the posterior circulation, in most circumstances, the bilateral supply from the contralateral vertebral artery prevents a complete blood flow reversal. The difference in embolic complication rates between the anterior and posterior circulation may also be explained by a less efficient aspiration in BA occlusion during clot removal.

No statistical differences in embolic complications were observed between the combined group and the stand-alone thrombectomy group ($P = .354$). Adjunctive fibrinolysis was not a significant protective factor as we may have initially expected.

Hemorrhagic Complications

Overall hemorrhagic complications occurred in 20.8% of patients, and symptomatic ICH was reported in 7.6% of patients. This rate (7.6%) was roughly similar to the recent stent retriever literature (mean rate, 8.7%; range, 0%–20%).[15,20,22,28–31] The rate was only 4% in the Solitaire retrospective multicenter study.[13] In our study, the mortality rate in the symptomatic ICH subgroup was significantly higher than in the overall cohort (45.5% vs 18.4%; $P = .0236$). It is not surprising that age was associated with an increased risk for ICH. Mean age in the hemorrhagic group was 72 years (median age, 74.5 years; age range, 40–89 years) vs a mean age of 66 years (median age, 68.5 years; age range, 26–90 years) in patients without hemorrhagic complication ($P = .043$). As observed in previous IV fibrinolysis studies,[33-36] age seemed to be an independent predictor of ICH in our series. ICH was not significantly different between the stand-alone and combined thrombectomy groups ($P = .615$) suggesting that IV lytics did not promote an increased rate of ICH. Time lapsed from symptom onset to successful recanalization was also not related to hemorrhagic transformation, possibly because patient selection was carried out by use of DWI MR imaging, hence excluding large brain infarction.

Initial infarct size and volume measured on DWI MR imaging were reported as independent factors associated with hemorrhagic transformation in acute ischemic stroke.[10,36,37] Actually, in our study, among 11 patients who had a DWI ASPECT score < 5, 3 (27.3%) had hemorrhagic complications, and 2 (18.2%) were symptomatic vs only 7.6% in the overall series ($P = .651$).

Intracranial Stenosis

In previous stent retriever thrombectomy studies,[11-17] intracranial stenoses were not discussed. In our series, intracranial stenoses were observed in 5.5% of patients and were linked with a high mortality rate (50%). The death rate in this subgroup of patients was significantly higher than in the overall cohort (18.4%; $P = .0176$) and may be related to a substantial number of failed recanalizations (87.5%) and periprocedural complications (28.6%). Multiple procedural clot removal attempts in such cases may further disrupt an instable plaque and irreversibly damage the vessel wall. Nowadays, MR imaging or CTA could easily detect intracranial stenosis when arteries remain permeable[38-40] but are still insufficient in diagnosing an underlying intracranial stenosis when the vessel is occluded.

Study Limitations

We acknowledge that our results need to be cautiously interpreted because they were derived from a single-center clinical experience. As with all continuous, prospectively collected clinical data, protocol deviations were observed (12.5%) but were reported in the study (DWI-derived ASPECT score and NIHSS inclusion). Also, interpretation of the angiographic and MR imaging results, though systematically carried out by 2 experienced neuroradiologists, were not analyzed by an independent core laboratory.

CONCLUSIONS

In this single-center prospective stent retriever study, recanalization failure was reported in 13.9% of patients. Embolic and symptomatic hemorrhagic complications were observed in 12.5% and 7.6%, respectively. The cumulative rate of failure, complication, and/or death was 39.6%. Mortality rate was 38.9% in cases of embolic events, 45.5% in cases of symptomatic ICH, and 57.1% in cases of intracranial stenosis. Age was an independent predictor of hemorrhagic complications. Concomitant fibrinolytic therapy did not influence the rates of recanalization, collateral embolic complications, or ICH occurrence.

Disclosures: Alain Bonafé—*UNRELATED: Consultancy:* Covidien. Vincent Costalat—*UNRELATED: Consultancy:* Covidien; *Payment for Lectures (including service on speaker bureaus):* ev3, J&J (Codman); *Payment for Development of Educational Presentations:* Covidien; *Travel/Accommodations/Meeting Expenses Unrelated to Activities Listed:* Covidien, Stryker, Codman.

REFERENCES

1. Molina CA, Montaner J, Arenillas JF, et al. **Differential pattern of tissue plasminogen activator-induced proximal middle cerebral artery recanalization among stroke subtypes.** *Stroke* 2004;35:486–90
2. Tandberg Askevold E, Naess H, Thomassen L. **Predictors for recanalization after intravenous thrombolysis in acute ischemic stroke.** *J Stroke Cerebrovasc Dis* 2007;16:21–24
3. Kimura K, Iguchi Y, Yamashita S, et al. **Atrial fibrillation as an independent predictor for no early recanalization after IV-t-PA in acute ischemic stroke.** *J Neurol Sci* 2008;267:57–61
4. Kimura K, Iguchi Y, Shibazaki K, et al. **Early stroke treatment with IV t-PA associated with early recanalization.** *J Neurol Sci* 2010; 295:53–57
5. Linfante I, Llinas RH, Selim M, et al. **Clinical and vascular outcome in internal carotid artery versus middle cerebral artery occlusions after intravenous tissue plasminogen activator.** *Stroke* 2002;33:2066–71
6. Rha JH, Saver JL. **The impact of recanalization on ischemic stroke outcome: a meta-analysis.** *Stroke* 2007;38:967–73
7. Zangerle A, Kiechl S, Spiegel M, et al. **Recanalization after thrombolysis in stroke patients: predictors and prognostic implications.** *Neurology* 2007;68:39–44
8. Kimura K, Sakamoto Y, Aoki J, et al. **Clinical and MRI predictors of no early recanalization within 1 hour after tissue-type plasminogen activator administration.** *Stroke* 2011;42:3150–55
9. Tanne D, Kasner SE, Demchuk AM, et al. **Markers of increased risk of intracerebral hemorrhage after intravenous recombinant tissue plasminogen activator therapy for acute ischemic stroke in clinical practice: the Multicenter rt-PA Stroke Survey.** *Circulation* 2002;105:1679–85
10. Singer OC, Humpich MC, Fiehler J, et al. **Risk for symptomatic intracerebral hemorrhage after thrombolysis assessed by diffusion-weighted magnetic resonance imaging.** *Ann Neurol* 2008;63:52–60
11. Castaño C, Dorado L, Guerrero C, et al. **Mechanical thrombectomy with the Solitaire AB device in large artery occlusions of the anterior circulation: a pilot study.** *Stroke* 2010;41:1836–40
12. Costalat V, Machi P, Lobotesis K, et al. **Rescue, combined, and stand-alone thrombectomy in the management of large vessel occlusion stroke using the Solitaire device: a prospective 50-patient single-center study: timing, safety, and efficacy.** *Stroke* 2011;42:1929–35
13. Dávalos A, Pereira VM, Chapot R, et al. **Retrospective multicenter study of Solitaire FR for revascularization in the treatment of acute ischemic stroke.** *Stroke* 2012;43:2699–705
14. Dorn F, Stehle S, Lockau H, et al. **Endovascular treatment of acute**

intracerebral artery occlusions with the Solitaire stent: single-centre experience with 108 recanalization procedures. *Cerebrovasc Dis* 2012;34:70–77
15. Koh JS, Lee SJ, Ryu CW, et al. **Safety and efficacy of mechanical thrombectomy with Solitaire stent retrieval for acute ischemic stroke: a systematic review.** *Neurointervention* 2012;7:1–9
16. Machi P, Costalat V, Lobotesis K, et al. **Solitaire FR thrombectomy system: immediate results in 56 consecutive acute ischemic stroke patients.** *J Neurointerv Surg* 2012;4:62–66
17. Stampfl S, Hartmann M, Ringleb PA, et al. **Stent placement for flow restoration in acute ischemic stroke: a single-center experience with the Solitaire stent system.** *AJNR Am J Neuroradiol* 2011;32:1245–48
18. Roth C, Papanagiotou P, Behnke S, et al. **Stent-assisted mechanical recanalization for treatment of acute intracerebral artery occlusions.** *Stroke* 2010;41:2559–67
19. Nezu T, Koga M, Nakagawara J, et al. **Early ischemic change on CT versus diffusion-weighted imaging for patients with stroke receiving intravenous recombinant tissue-type plasminogen activator therapy: Stroke Acute Management with Urgent Risk-factor Assessment and Improvement (SAMURAI) rt-PA registry.** *Stroke* 2011;42:2196–200
20. Rohde S, Haehnel S, Herweh C, et al. **Mechanical thrombectomy in acute embolic stroke: preliminary results with the Revive device.** *Stroke* 2011;42:2954–56
21. San Román L, Obach V, Blasco J, et al. **Single-center experience of cerebral artery thrombectomy using the TREVO device in 60 patients with acute ischemic stroke.** *Stroke* 2012;43:1657–59
22. Nogueira RG, Lutsep HL, Gupta R, et al. **Trevo versus Merci retrievers for thrombectomy revascularisation of large vessel occlusions in acute ischaemic stroke (TREVO 2): a randomised trial.** *Lancet* 2012;380:1231–40
23. Higashida RT, Furlan AJ, Roberts H, et al. **Trial design and reporting standards for intra-arterial cerebral thrombolysis for acute ischemic stroke.** *Stroke* 2003;34:e109–37
24. Hacke W, Kaste M, Fieschi C, et al. **Randomised double-blind placebo-controlled trial of thrombolytic therapy with intravenous alteplase in acute ischaemic stroke (ECASS II). Second European-Australasian Acute Stroke Study Investigators.** *Lancet* 1998;352:1245–51
25. Broderick JP, Palesch YY, Demchuk AM, et al. **Endovascular therapy after intravenous t-PA versus t-PA alone for stroke.** *N Engl J Med* 2013;368:893–903
26. Ciccone A, Valvassori L, Nichelatti M, et al. **Endovascular treatment for acute ischemic stroke.** *N Engl J Med* 2013;368:904–13
27. Kidwell CS, Jahan R, Alger JR, et al. **Design and rationale of the Mechanical Retrieval and Recanalization of Stroke Clots Using Embolectomy (MR RESCUE) Trial.** *Int J Stroke* 2014;9:110–16
28. Broussalis E, Trinka E, Hitzl W, et al. **Comparison of stent-retriever devices versus the Merci retriever for endovascular treatment of acute stroke.** *AJNR Am J Neuroradiol* 2013;34:366–72
29. Saver JL, Jahan R, Levy EI, et al. **Solitaire flow restoration device versus the Merci retriever in patients with acute ischaemic stroke (SWIFT): a randomised, parallel-group, non-inferiority trial.** *Lancet* 2012;380:1241–49
30. Ribo M, Molina CA, Jankowitz B, et al. **Stentrievers versus other endovascular treatment methods for acute stroke: comparison of procedural results and their relationship to outcomes.** *J Neurointerv Surg* 2013 May 28. [Epub ahead of print]
31. Mordasini P, Brekenfeld C, Byrne JV, et al. **Technical feasibility and application of mechanical thrombectomy with the Solitaire FR revascularization device in acute basilar artery occlusion.** *AJNR Am J Neuroradiol* 2013;34:159–63
32. Chueh JY, Wakhloo AK, Gounis MJ. **Effectiveness of mechanical endovascular thrombectomy in a model system of cerebrovascular occlusion.** *AJNR Am J Neuroradiol* 2012;33:1998–2003
33. Bluhmki E, Chamorro A, Davalos A, et al. **Stroke treatment with alteplase given 3.0–4.5 h after onset of acute ischaemic stroke (ECASS III): additional outcomes and subgroup analysis of a randomised controlled trial.** *Lancet Neurol* 2009;8:1095–102
34. Derex L, Nighoghossian N. **Intracerebral haemorrhage after thrombolysis for acute ischaemic stroke: an update.** *J Neurol Neurosurg Psychiatry* 2008;79:1093–99
35. **Intracerebral hemorrhage after intravenous t-PA therapy for ischemic stroke. The NINDS t-PA Stroke Study Group.** *Stroke* 1997;28:2109–18
36. Larrue V, von Kummer RR, Muller A, et al. **Risk factors for severe hemorrhagic transformation in ischemic stroke patients treated with recombinant tissue plasminogen activator: a secondary analysis of the European-Australasian Acute Stroke Study (ECASS II).** *Stroke* 2001;32:438–41
37. Sakamoto Y, Kimura K, Iguchi Y, et al. **Hemorrhagic transformation in acute cerebellar infarction.** *Cerebrovasc Dis* 2011;32:327–33
38. Xu WH, Li ML, Gao S, et al. **In vivo high-resolution MR imaging of symptomatic and asymptomatic middle cerebral artery atherosclerotic stenosis.** *Atherosclerosis* 2010;212:507–11
39. Chung GH, Kwak HS, Hwang SB, et al. **High resolution MR imaging in patients with symptomatic middle cerebral artery stenosis.** *Eur J Radiol* 2012;81:4069–74
40. Marquering HA, Nederkoorn PJ, Smagge L, et al. **Performance of semiautomatic assessment of carotid artery stenosis on CT angiography: clarification of differences with manual assessment.** *AJNR Am J Neuroradiol* 2012;33:747–54

Emergency Cervical Internal Carotid Artery Stenting in Combination with Intracranial Thrombectomy in Acute Stroke

S. Stampfl, P.A. Ringleb, M. Möhlenbruch, C. Hametner, C. Herweh, M. Pham, J. Bösel, S. Haehnel, M. Bendszus, and S. Rohde

ABSTRACT

BACKGROUND AND PURPOSE: In past years, thrombectomy has become a widely used procedure in interventional neuroradiology for the treatment of acute intracranial occlusions. However, in 10–20% of patients, there are additional occlusions or stenotic lesions of the ipsilateral cervical internal carotid artery. The purpose of this study was to evaluate the feasibility of emergency carotid artery stent placement in combination with intracranial thrombectomy and the clinical outcome of the treated patients.

MATERIALS AND METHODS: We analyzed clinical and angiographic data of patients who underwent emergency cervical ICA stent placement and intracranial thrombectomy with stent-retriever devices in our institution between November 2009 and July 2012. Recanalization was assessed according to the Thrombolysis in Cerebral-Infarction score. Clinical outcome was evaluated at discharge (NIHSS) and after 3 months (mRS).

RESULTS: Overall, 24 patients were treated. The mean age was 67.2 years; mean occlusion time, 230.2 minutes. On admission, the median NIHSS score was 18. In all patients, the Thrombolysis in Cerebral Infarction score was zero before the procedure. Stent implantation was feasible in all cases. In 15 patients (62.5%), a Thrombolysis in Cerebral Infarction score ≥ 2b could be achieved. Six patients (25%) improved ≥10 NIHSS points between admission and discharge. After 90 days, the median mRS score was 3.0. Seven patients (29.2%) had a good clinical outcome (mRS 0–2), and 4 patients (16.6%) died, 1 due to fatal intracranial hemorrhage. Overall, symptomatic intracranial hemorrhage occurred in 4 patients (16.6%).

CONCLUSIONS: Emergency ICA stent implantation was technically feasible in all patients, and the intracranial recanalization Thrombolysis in Cerebral Infarction score of ≥2b was reached in a high number of patients. Clinical outcome and mortality seem to be acceptable for a cohort with severe stroke. However, a high rate of symptomatic intracranial hemorrhage occurred in our study.

ABBREVIATION: ECASS = European Cooperative Acute Stroke Study

Stent-retriever devices play an increasing role in the treatment of acute ischemic stroke,[1-3] providing a high recanalization rate and a better functional outcome[4] compared with other recanalization devices. In approximately 10%–20% of patients with stroke,[5] additional ipsilateral high-grade ICA stenosis is present, which further complicates endovascular access and may lead to a delay in recanalization of the target vessel occlusion. On the other hand, patients with high-grade ICA stenosis might profit from pre-existing intracranial collaterals that—theoretically—can extend the time window for endovascular treatment in terms of beneficial clinical outcome. However, this hypothesis so far remains unproven either by experimental or clinical studies.

We prospectively collected clinical and angiographic data of patients with acute cerebral vessel occlusions of the anterior circulation and ipsilateral high-grade atherosclerotic stenosis or occlusion of the proximal/cervical ICA who underwent emergency ICA stent placement and intracranial thrombectomy with stent-retriever devices. We present the experience at our institution between November 2009 and July 2012.

MATERIALS AND METHODS

Inclusion Criteria and Patient Selection

Approval for prospective collection of clinical and interventional data was granted by the institutional review board.

We analyzed prospectively collected data of all patients with stroke who had embolic intracranial vessel occlusion of the anterior circulation and at the same time presented with atheroscle-

Received May 24, 2013; accepted after revision August 6.

From the Departments of Neuroradiology (S.S., M.M., C. Herweh, M.P., S.H., M.B., S.R.) and Neurology (P.A.R., C. Hametner, J.B.), University of Heidelberg, Heidelberg, Germany.

Please address correspondence to Sibylle Stampfl, MD, Im Neuenheimer Feld 400, 69120 Heidelberg, Germany; e-mail: sibyllestampfl@gmx.de

Indicates article with supplemental on-line table.

http://dx.doi.org/10.3174/ajnr.A3763

rosis-related high-grade cervical ICA stenosis or ICA occlusion. Patients with arterial dissections were excluded from this analysis. The eventual therapeutic procedure after cervical stent placement was intracranial endovascular recanalization with stent-retriever devices.

On admission, CT/CTA or MR imaging/MRA, including diffusion and perfusion imaging, was performed to evaluate the extension of the ischemic lesion and the potential tissue at risk (penumbra). Patients were selected for endovascular stroke treatment if they had an NIHSS score of ≥10 and CTA-proved vessel occlusion of the distal ICA or M1/2 segment and absence of early signs of an extensive and advanced infarction (more than one-third of the MCA territory) on CT- or MRA-proved vessel occlusion of the distal ICA or M1/2 segment, a DWI lesion less than one-third of the MCA territory, and/or a PWI/DWI mismatch of more than one-third on visual assessment.

Evaluation of Pretherapeutic Imaging Data

The above-mentioned CT and MR imaging inclusion criteria were noted. Furthermore, pretherapeutic CT or MR images were analyzed according to the ASPECTS study group.[6,7]

Interventional Procedure

All procedures were performed with the patient under general anesthesia. As vascular access, an 8F sheath was placed in the right common femoral artery. Then, an 8F guiding catheter was placed in the ipsilateral common carotid artery, and the cervical ICA stenosis was passed with a 0.014-inch microwire. A self-expanding stent (eg, Wallstent; Boston Scientific, Natick, Massachusetts) was advanced to cover the stenosis. After stent implantation, balloon dilation (Maverick balloon dilation catheter; Boston Scientific) was performed. If necessary, the stenosis was predilated with a percutaneous transarterial angioplasty balloon to allow fast access to the intracranial vasculature. If passage of the stenosis with an intermediate catheter was possible without stent placement, stent implantation was performed after thrombectomy. In case of complete cervical ICA occlusion due to underlying atherosclerosis, the occlusion was first crossed with a 0.027-inch microcatheter over a 0.014-inch microwire; afterward, predilation and carotid artery stent placement were performed as described above. We did not observe any case of spontaneous intracranial recanalization in patients with ICA and MCA occlusion immediately after ICA stent implantation.

For intracranial thrombectomy, an intermediate catheter (6F Neuron catheter; Penumbra, Alameda, California) was advanced through the cervical ICA and over the stent and positioned in the distal ICA as close to the thrombus as possible. A 0.027-inch microcatheter (eg, Rebar-18; Covidien, Irvine, California) was advanced through the thrombus, and the tip was placed distal to the thrombus. Then, a stent-retriever device (Solitaire; Covidien; or Revive; Codman Neurovascular, Raynham, Massachusetts) was deployed by pulling back the microcatheter. For thrombectomy, the device and microcatheter were simultaneously pulled back under continuous aspiration through the Neuron catheter. In case of incomplete recanalization, thrombectomy was repeated.

Evaluation of Angiographic Data

Angiographic images were analyzed regarding the following data: pretherapeutic level of ICA stenosis according to the North American Symptomatic Carotid Endarterectomy Trial method,[8] time between ICA stent implantation and flow restoration, time to flow restoration (time interval between the first diagnostic angiographic image and the first image with evidence of re-established perfusion within the occluded vessel segment), time to complete revascularization (time interval between the first diagnostic image and the completion angiogram), thrombus length, Thrombolysis in Cerebral Infarction score (score ranging from 0 = no perfusion to 3 = regular perfusion[9]) before and after the procedure, number of stent passes necessary for intracranial recanalization, and procedure-related complications. Successful recanalization was defined as TICI ≥ 2b. All angiographic images were evaluated in consensus by 2 neuroradiologists (S.S., S.R.).

Outcome Assessment

Follow-up CT imaging was performed 24–36 hours after the procedure or whenever clinical worsening occurred. Hemorrhage was classified according to the European Cooperative Acute Stroke Study (ECASS)-2 classification.[10]

Patients were assessed clinically on admission (NIHSS), at discharge (NIHSS, mRS), and after 90 days (mRS). Early clinical improvement was defined as NIHSS improvement of at least 10 points. Good clinical outcome was defined as mRS 0–2 at day 90. Outcome was assessed during an in-hospital visit or by a semistructured telephone interview by a neurologist not blinded to the initial treatment.

Statistics

Continuous data were collected in a data base and are described by median and interquartile range or as mean and SD in case of normal distribution. Statistical analysis was performed by GraphPad Prism 5.0 for OS X (GraphPad software, San Diego, California). For comparison of time to flow restoration in all patients with stroke and in patients with stroke with carotid stents, the nonparametric Mann-Whitney *U* Test was applied. A P value $< .05$ was statistically significant.

RESULTS

Overall, 136 patients with acute intracranial anterior circulation occlusion were treated between November 2009 and July 2012 by using stent-retriever devices. Twenty-four (17.6%) of these patients had an additional high-grade proximal stenosis (12 patients) or occlusion (12 patients) of the ipsilateral cervical ICA. Twenty-one patients were treated with ICA stent implantation and subsequent intracranial thrombectomy. Three patients underwent these treatments in reverse order. Stent implantation was technically feasible in all cases (details of each patient are shown in the Table and On-line Table).

In 17 patients, the glycoprotein IIb/IIIa receptor antagonist tirofiban was started before ICA stent implantation and was administered for 24–48 hours while an overlapping medication with aspirin, 100 mg/day, and clopidogrel, 75 mg/day, was initiated. In 5 patients, a loading dose of aspirin and clopidogrel was administered instead of tirofiban, and partial thromboplastin

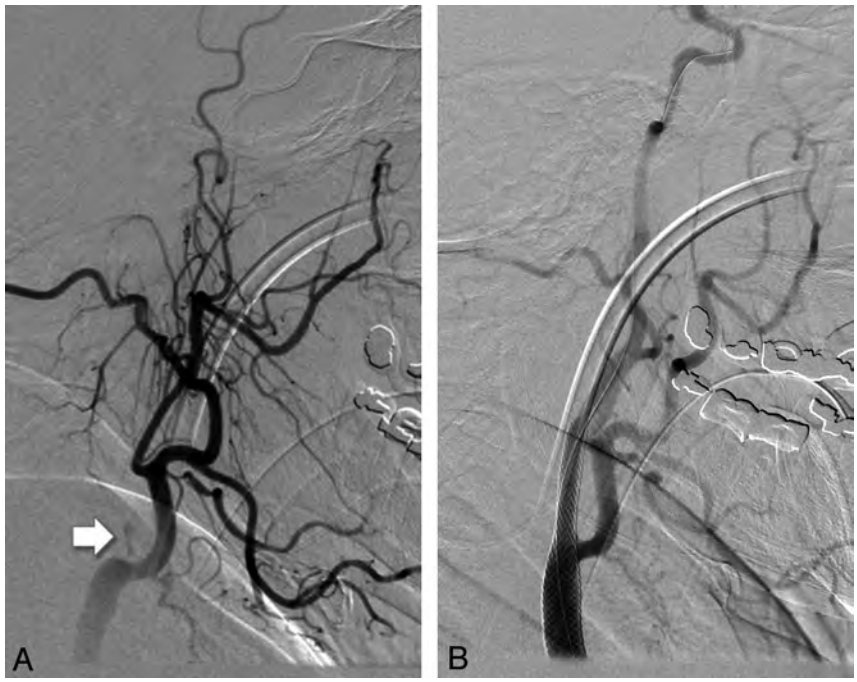

FIG 1. *A*, Occlusion of the cervical ICA close to the bifurcation (*arrow*). *B*, Successful reconstruction of the ICA lumen and sufficient antegrade flow after stent implantation and angioplasty.

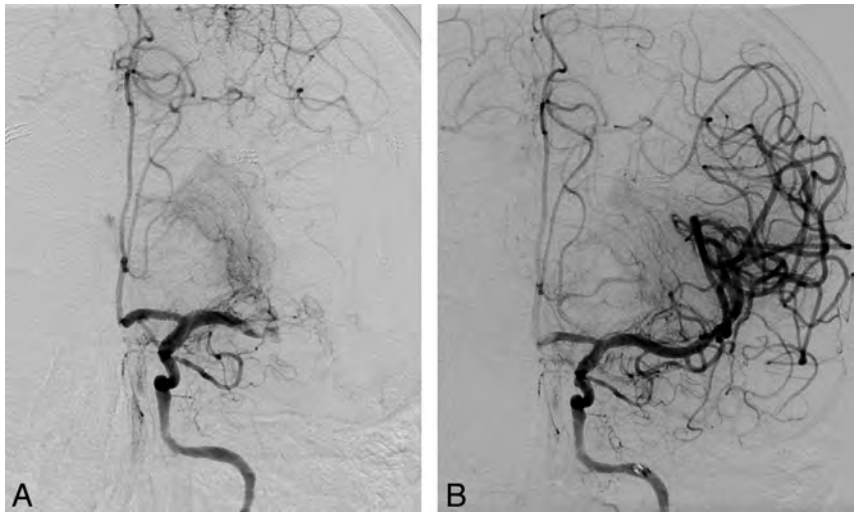

FIG 2. *A*, Intracranial angiogram shows a distal M1/M2 occlusion and good leptomeningeal collateralization via the anterior cerebral artery territory. *B*, After thrombectomy with the Revive device (1 device pass), complete recanalization of the M1/M2 segments could be achieved. Washout phenomenon in the anterior cerebral artery (A1 segment).

time-adjusted heparin was started. Two patients were already pretreated with aspirin and clopidogrel before the procedure, and additional heparin was initiated.

The mean age was 67.2 ± 10.1 years (range, 49–83; female/male, 3:21). The mean occlusion time was 230.2 ± 131.3 minutes (range, 134–643 minutes) in 15 patients. The patient with the longest occlusion time (643 minutes) presented with only mild symptoms at first (NIHSS 5), but his condition deteriorated within hours, despite IV thrombolysis, to NIHSS 12, and interventional recanalization was initiated. In 8 patients, the time of symptom onset was uncertain. In 1 patient, symptoms were mild for 3 days (NIHSS 4), and interventional recanalization was chosen after fluctuation and deterioration of his condition.

No patient had an ASPECTS score of <7 on pretherapeutic imaging evaluation. In all patients with CT imaging, early signs of infarction were mild and involved less than one-third of the MCA territory. In 1 patient undergoing MR imaging, the DWI lesion extent was estimated as one-third of the MCA territory, but with distinct PWI/DWI mismatch. In all other patients, the DWI lesion was less than one-third of the MCA territory. A PWI/DWI mismatch of more than one-third was found in all patients except 1 (in this patient, PWI was not performed due to agitation of the patient).

In all patients, cervical ICA changes visible on DSA resembled a typical atherosclerotic origin with various amounts of calcification, and acute stroke was caused by embolic occlusion of one of the major intracranial target vessels (MCA, $n = 11$; carotid T/MCA, $n = 13$).

In 22 patients, intravenous thrombolytic medication was administered prior to angiography according to the bridging concept (0.6 mg/kg body weight). In one of these patients, additional intra-arterial thrombolytic medication was injected through the microcatheter into an occluded MCA M2 branch. In 2 patients, only mechanical thrombectomy with stent-retriever devices and without bridging or intra-arterial lysis was performed.

Before the intracranial procedure, TICI was 0 in all patients. After the intervention, the median TICI was 2 (interquartile range, 2.0–3.0, [ie, TICI 0/1, $n = 0$; TICI 2a, $n = 9$; TICI 2b, $n = 4$; TICI 3, $n = 11$]). Thus, in 15 patients (62.5%), a TICI score of ≥2b could be achieved. A median of 2 stent-retriever passes was necessary to achieve TICI 2b/3 (interquartile range, 1.0–2.0).

For recanalization, the Solitaire stent was used in 4 patients and the Revive device, in 17 patients; in 3 patients, both devices were used. In 1 patient, permanent Solitaire stent deployment was performed to achieve sufficient revascularization of the MCA.

Intracranial flow restoration was achieved after 53.4 ± 20.5 minutes (range, 20–100 minutes). The mean time to recanalization was 89.8 ± 31.5 minutes (range, 45–177 minutes). The mean thrombus length was 15.9 ± 8.3 mm. Analysis of the time to flow restoration revealed that in patients who needed a carotid stent implantation, time to flow restoration was significantly longer

Overview of the imaging criteria of each patient[a]

Patient	Vessel Occlusion (CTA- or MRA-Proved)	Early Signs of Infarction Less Than One-Third of the MCA Territory on CT	DWI Lesion Less Than One-Third	PWI/DWI Mismatch More Than One-Third
1	(MRA)		+	+
2	(CTA)	+		
3	(CTA)	+		
4	(MRA)		+	+
5	(CTA)	+		
6	(MRA)		+	+
7	(CTA)	+		
8	(MRA)		+	+
9	(CTA)	+		
10	(CTA)	+		
11	(CTA)	+		
12	(MRA)		+	+
13	(CTA)	+		
14	(MRA)		+	+
15	(CTA)	+		
16	(CTA)	+		
17	(MRA)		+	+
18	(CTA)	+		
19	(MRA)		+	+
20	(MRA)		+	–
21	(CTA)	+		
22	(MRA)			+
23	(CTA)	+		
24	(CTA)	+		

Note:—+ indicates inclusion criteria met by patient; – indicates that no PWI was performed due to agitation of the patient.

[a] Imaging inclusion criteria for this analysis: All patients who were included in this analysis presented with an NIHSS score of ≥10 (2 patients after clinical deterioration) and were treated with cervical ICA stent implantation and intracranial thrombectomy. Furthermore, they met the following imaging inclusion criteria: NIHSS score ≥10 and CTA-proved vessel occlusion of the distal ICA or M1/2 segment and absence of early signs of an extensive and advanced infarction on CT, or MRA-proved vessel occlusion of the distal ICA or M1/2 segment, a DWI lesion less than 1/3 of the MCA territory, and/or a PWI/DWI mismatch of more than 1/3 on visual assessment.

than that in patients without stent implantation ($n = 112$), who underwent immediate thrombectomy with stent-retriever devices (53.4 ± 20.5 minutes versus 33.8 ± 23.7 minutes; $P < .0001$).

Clinical Outcome

On admission, the median initial NIHSS score was 18 (interquartile range, 15–22). Two patients (initial NIHSS scores of 4 and 5) were referred for interventional therapy only after fluctuation of symptoms and clinical deterioration. Six patients (25%) improved ≥10 NIHSS points between admission and discharge. After 90 days, the median mRS score was 3.0 (interquartile range, 2.0–5.0). Seven patients (29.2%) had a good clinical outcome (mRS 0–2), 4 patients (16.6%) died, 1 due to a fatal intracerebral bleeding. Among the patients with a good clinical outcome were 2 patients with TICI 2a recanalization.

If one applied the definition of good neurologic outcome according to the SWIFT (Solitaire FR with the intention for thrombectomy) study[4] (mRS ≤2 after 90 days, or NIHSS score improvement of ≥10 points), 8 patients (33.3%) met the criteria for a good neurologic outcome.

Complications

In one patient, extracranial internal carotid artery dissection distal to the ICA stent occurred after thrombectomy, which was treated with an additional Enterprise self-expanding stent implantation (Codman & Shurtleff).

In 3 patients, distal thrombus embolization occurred during the thrombectomy maneuver with the stent retriever (migration of thrombus material into distal MCA branches and anterior cerebral artery branches, respectively). No distal embolic complications related to the ICA stent implantation were observed.

Symptomatic intracranial hemorrhage (classified according to the ECASS-2 trial[10]) occurred in 4 patients (16.6%; 3 had received tirofiban, 1 had received a loading dose of aspirin and clopidogrel) and was fatal in one of them.

DISCUSSION

In acute ischemic stroke, fast recanalization of the occluded vessel is probably the most important precondition for favorable clinical outcome.[11,12] However, ≤20% of patients[5] with intracranial vessel occlusion have additional high-grade cervical ICA stenosis or even total occlusion. Tandem cervical ICA/MCA occlusions are associated with low recanalization rates despite systemic thrombolysis and often have a poor outcome.[13] Interventional procedures are a promising treatment option because a combination of ICA stent placement and intra-arterial thrombolysis seems to improve the outcome.[14]

To our knowledge, our study report represents the largest number of patients with stroke with cervical ICA stent placement and intracranial thrombectomy by using stent-retriever devices. Papanagiotou et al[15] described their experiences with emergency carotid stent placement and intracranial thrombectomy procedures in 22 patients, but these authors in addition to stent-retriever devices (Solitaire stent) used other devices (Penumbra system) for the intracranial procedure.

Most recently, Matsubara et al[16] published a report on 16 patients with acute cervical carotid occlusions caused by atherosclerosis, atrial fibrillation, or dissection. Ten of their patients had additional intracranial tandem occlusions. The patients were treated with various recanalization techniques. No stent retrievers were used. Similar to the present study, recanalization was successful in a high number of patients with cervical occlusion (81.3%). In 43.8% of their patients, successful extracranial and intracranial flow was reached. Although one-third of their whole patient cohort presented with a favorable clinical outcome, only 20% of their patients with cervical and intracranial occlusion reached an mRS score of 0–2, which is slightly lower than that in the present study. However, approximately 70% of their patients with successful extracranial and intracranial recanalization showed a favorable outcome, but none of the patients without successful extracranial or intracranial recanalization did. This finding clearly underlines the importance of technical success.

Malik et al[17] reported their experience with recanalization procedures of 77 patients with tandem occlusion. In contrast to our study, they used various recanalization devices and techniques. A high recanalization rate (75.3%) was reached.

Thrombectomy with stent-retriever devices resulted in TICI 2a (partial filling of the entire vascular territory) in 37.5% of our patients despite several thrombectomy attempts; successful recanalization (corresponding to TICI ≥ 2b) was achieved in 62.5%.

In agreement with the current literature,[15-18] emergency ICA stent implantation was technically successful in all our patients. Not surprising, ICA stent implantation leads to a prolonged procedure time until recanalization. However, in our analysis, the treatment time was increased by only 20 minutes, which underlines the good technical feasibility of the stent-placement procedure.

In our series, we did not observe any case of spontaneous intracranial recanalization in patients with ICA and MCA occlusion immediately after ICA stent implantation, though this has been described in the literature as a common finding.[17]

Given that most patients had a severe stroke (median NIHSS score of 18), it is remarkable that the mortality rate was relatively low (16.6%) compared with other series on tandem occlusion treatment (Malik et al, 24.7%).[17] However, 29.2% of our patients had an mRS of 0–2 after 3 months, which is lower than that described by Malik et al (41.6% good outcome).[17] Twenty-five percent of our patients improved ≥10 NIHSS points. If one applied the definition of good neurologic outcome according to the SWIFT study,[4] 8 patients (33.3%) met the criteria for a good neurologic outcome.

Because distinct atherosclerotic ICA changes were present in all patients, the relatively high survival rate might be due to good collateral blood supply in patients with long-standing ICA stenosis. However, further preprocedural imaging data would be necessary to support this hypothesis.

In carotid artery stent placement, antithrombotic medication is administered to prevent acute stent thrombosis. However, it bears a potential risk of intracranial hemorrhage. The antithrombotic treatment concept differs in the literature. In the study of Matsubara et al,[16] patients received a loading dose of aspirin and another antiplatelet drug, depending on the clinical conditions, if the postprocedural imaging showed no hemorrhage. The hemorrhage rate (6.3%) was low. The hemorrhage rate (10.4%) reported by Malik et al[17] was slightly higher but still lower than that in our study. In their study, glycoprotein IIb/IIIa inhibitor was administered before stent placement, and an oral load of clopidogrel and aspirin was initiated if postprocedure imaging showed no hemorrhage.[17] Later they changed their approach, and the patients received clopidogrel and aspirin before stent placement to avoid glycoprotein IIb/IIIa inhibition. However, they found no higher hemorrhage rate if patients were treated with glycoprotein IIb/IIIa inhibitor.

In our series, intracranial hemorrhage occurred in a high proportion of patients (16.6%), which was nearly triple the rates reported in the MR RESCUE[19] and the Interventional Management of Stroke 3 trials.[20] Although reperfusion trauma to a vascular territory that had been subjected to a long-term lower perfusion by the proximal stenosis might play a role, the high hemorrhage rate in our study might also be caused by the relatively aggressive antiplatelet therapy with full-dose tirofiban in most cases. Until 2012, our standard operation guidelines recommended the use of tirofiban when extracranial or intracranial stent placement was performed. Correspondingly, aspirin and clopidogrel were administered only in a minority of our patients. A recently published analysis of our patients with acute ischemic stroke in whom mechanical thrombectomy was performed revealed that additional treatment with tirofiban is associated with a worse outcome[21] due to increased rates of fatal intracerebral hemorrhage. This finding caused us to rethink our treatment strategy. We now have revised our standard operation guidelines and give IV aspirin and clopidogrel via a gastric tube. Another option might be to defer the administration of antiplatelet therapy until the infarction size can be assessed on posttreatment imaging and the hemorrhage risk can be estimated. Alternatively, the interventionalist could even try to avoid emergency ICA stent implantation in the acute phase and perform only balloon angioplasty. Thus, no antiplatelet therapy associated with the risk of hemorrhage would be required.

In our series, in most of our patients, ICA stent implantation was performed before intracranial thrombectomy. Three patients were treated in the reverse order. In these cases, the ICA stenosis could be passed with the intermediate catheter after balloon dilation. However, ICA stent implantation became necessary because of persisting flow reduction within the extracranial ICA after successful intracranial thrombectomy. This so-called reverse technique (intracranial thrombectomy first, then extracranial ICA stent implantation) has been described recently by Cohen et al.[22]

CONCLUSIONS

Emergency ICA stent implantation was technically feasible in all our patients, corresponding to other studies on endovascular tandem-occlusion treatment, and intracranial recanalization TICI ≥ 2b was reached in a high number of patients. The rate of favorable clinical outcome seems to be acceptable for such a cohort with severe stroke and is within the range of other endovascular stroke studies. However, in our series, a relatively high hemorrhage rate occurred.

Disclosures: Peter A. Ringleb—*UNRELATED*: *Consultancy*: Boehringer Ingelheim, *Comments*: less than €500 ($665.04 US), *Payment for Lectures (including service on Speakers Bureaus)*: Boehringer Ingelheim, Sanofi, PAION, Lilly, GlaxoSmithKline, Bayer Healthcare. Julian Bösel—*UNRELATED*: *Payment for Lectures (including service on Speakers Bureaus)*: total $5000, *Comments:* Covidien twice, talk on NIRS, satellite symposium; Sedana, twice, talk on AnaConDa Sedation Symposia; inviting hospitals or societies, 5 times; *Payment for Manuscript Preparation*: total $3000, *Comments*: reviews for intensive up2date, review for Current Opinion in Cardiovascular Therapy congress syllabus for Neurocritical Care Society meeting, *Travel/Accommodations/Meeting Expenses Unrelated to Activities Listed*: provided for several years by the medical societies (Deutsche Gesellschaft für Neurologie, German Neurological Society; Deutsche Gesellschaft für Neurointesiv- und Notfallmedizin, German Society for Neurological Intensive and Emergency Care; Deutsche interdisziplinäre Vereinigung für Intensivmedizin, German Interdisciplinary Association for Intensive Care; and the Neurocritical Care Society), *Comments*: accommodation and travel compensation when visiting conferences as an invited speaker, paid by inviting medical society (total $10,000). Martin Bendszus—*UNRELATED*: *Consultancy*: Codman Neurovascular, Novartis, and Bayer Healthcare (clarify), *Comments*: speaker honoraria for educational talks, *Other*: principal investigator for RIVER 4 study (terminated, no recompensation),* Codman Neurovascular.* Stefan Rohde—*UNRELATED*: *Payment for Lectures (including service on Speakers Bureaus)*: Codman Neurovascular, AB Medica. *Money paid to the institution.

REFERENCES

1. Castaño C, Dorado L, Guerrero C, et al. **Mechanical thrombectomy with the Solitaire AB device in large artery occlusions of the anterior circulation: a pilot study.** *Stroke* 2010;41:1836–40
2. Rohde S, Haehnel S, Herweh C, et al. **Mechanical thrombectomy in acute embolic stroke: preliminary results with the Revive device.** *Stroke* 2011;42:2954–56
3. Roth C, Papanagiotou P, Behnke S, et al. **Stent-assisted mechanical recanalization for treatment of acute intracerebral artery occlusions.** *Stroke* 2010;41:2559–67
4. Saver JL, Jahan R, Levy EI, et al. **Solitaire flow restoration device versus the Merci retriever in patients with acute ischaemic stroke (SWIFT): a randomised, parallel-group, non-inferiority trial.** *Lancet* 2012;380:1241–49
5. Grau AJ, Weimar C, Buggle F, et al. **Risk factors, outcome, and treatment in subtypes of ischemic stroke: the German stroke data bank.** *Stroke* 2001;32:2559–66
6. Barber PA, Demchuk AM, Zhang J, et al. **Validity and reliability of a quantitative computed tomography score in predicting outcome of hyperacute stroke before thrombolytic therapy: ASPECTS Study Group—Alberta Stroke Programme Early CT Score.** *Lancet* 2000;355:1670–74
7. Barber PA, Hill MD, Eliasziw M, et al. **Imaging of the brain in acute ischaemic stroke: comparison of computed tomography and magnetic resonance diffusion-weighted imaging.** *J Neurol Neurosurg Psychiatry* 2005;76:1528–33
8. Eliasziw M, Smith RF, Singh N, et al. **Further comments on the measurement of carotid stenosis from angiograms: North American Symptomatic Carotid Endarterectomy Trial (NASCET) Group.** *Stroke* 1994;25:2445–49
9. Higashida RT, Furlan AJ, Roberts H, et al. **Trial design and reporting standards for intra-arterial cerebral thrombolysis for acute ischemic stroke.** *Stroke* 2003;34:e109–137
10. Hacke W, Kaste M, Fieschi C, et al. **Randomised double-blind placebo-controlled trial of thrombolytic therapy with intravenous alteplase in acute ischaemic stroke (ECASS II): Second European-Australasian Acute Stroke Study Investigators.** *Lancet* 1998;352:1245–51
11. Khatri P, Abruzzo T, Yeatts SD, et al. **Good clinical outcome after ischemic stroke with successful revascularization is time-dependent.** *Neurology* 2009;73:1066–72
12. Rha JH, Saver JL. **The impact of recanalization on ischemic stroke outcome: a meta-analysis.** *Stroke* 2007;38:967–73
13. Rubiera M, Ribo M, Delgado-Mederos R, et al. **Tandem internal carotid artery/middle cerebral artery occlusion: an independent predictor of poor outcome after systemic thrombolysis.** *Stroke* 2006;37:2301–05
14. Kwak HS, Hwang SB, Jin GY, et al. **Predictors of functional outcome after emergency carotid artery stenting and intra-arterial thrombolysis for treatment of acute stroke associated with obstruction of the proximal internal carotid artery and tandem downstream occlusion.** *AJNR Am J Neuroradiol* 2013;34:841–46
15. Papanagiotou P, Roth C, Walter S, et al. **Carotid artery stenting in acute stroke.** *J Am Coll Cardiol* 2011;58:2363–69
16. Matsubara N, Miyachi S, Tsukamoto N, et al. **Endovascular intervention for acute cervical carotid artery occlusion.** *Acta Neurochir (Wien)* 2013;155:1115–23
17. Malik AM, Vora NA, Lin R, et al. **Endovascular treatment of tandem extracranial/intracranial anterior circulation occlusions: preliminary single-center experience.** *Stroke* 2011;42:1653–57
18. Jovin TG, Gupta R, Uchino K, et al. **Emergent stenting of extracranial internal carotid artery occlusion in acute stroke has a high revascularization rate.** *Stroke* 2005;36:2426–30
19. Kidwell CS, Jahan R, Gornbein J, et al. **A trial of imaging selection and endovascular treatment for ischemic stroke.** *N Engl J Med* 2013;368:914–23
20. Broderick JP, Palesch YY, Demchuk AM, et al. **Endovascular therapy after intravenous t-PA versus t-PA alone for stroke.** *N Engl J Med* 2013;368:893–903
21. Kellert L, Hametner C, Rohde S, et al. **Endovascular stroke therapy: tirofiban is associated with risk of fatal intracerebral hemorrhage and poor outcome.** *Stroke* 2013;44:1453–55
22. Cohen JE, Gomori M, Rajz G, et al. **Emergent stent-assisted angioplasty of extracranial internal carotid artery and intracranial stent-based thrombectomy in acute tandem occlusive disease: technical considerations.** *J Neurointerv Surg* 2013;5:440–46

The Outcome and Efficacy of Recanalization in Patients with Acute Internal Carotid Artery Occlusion

J.H. Kwak, L. Zhao, J.K. Kim, S. Park, D.-g. Lee, J.H. Shim, D.H. Lee, J.S. Kim, and D.C. Suh

ABSTRACT

BACKGROUND AND PURPOSE: Acute occlusion of the ICA is often associated with poor outcomes and severe neurologic deficits. This study was conducted to evaluate outcome of the occluded ICA and efficacy of recanalization under protective flow arrest.

MATERIALS AND METHODS: Fifty consecutive patients who underwent endovascular treatment for acute ICA occlusion were identified from the prospectively collected data base. We assessed $NIHSS_o$, occlusion type (cardioembolism vs atherosclerosis), occlusion level (supraclinoid-terminal, petrocavernous, or bulb-cervical), recanalization degree (TICI), and efficacy of recanalization (protective flow arrest vs nonprotection) leading to better outcome.

RESULTS: Successful recanalization (TICI $\geq$ 2) was obtained in 90% of patients and good recovery (mRS $\leq$ 2) in 60% of patients. Good outcome was related to National Institutes of Health Stroke Scale score on admission ($P < .001$), TICI ($P < .007$), occlusion type ($P = .022$), and occlusion level ($P = .038$). Poor initial patient status, less recanalization, cardioembolism, and supraclinoid-terminal occlusion were associated with poor prognosis. Application of protective flow arrest led to better outcome in the distal ICA segment than in the bulb-cervical segment.

CONCLUSIONS: In addition to the initial patient status and successful recanalization, the occlusion level or type of the occluded ICA could affect clinical outcome. In this study, treatment benefits of protective flow arrest were accentuated in patients with ICA occlusion above the bulb-cervical segment.

ABBREVIATIONS: ECIC = extracranial-intracranial; IMS III = Interventional Management of Stroke III trial; $NIHSS_o$ = National Institutes of Health Stroke Scale score on admission; TOAST = Trial of Org 10172 in Acute Stroke Treatment

Acute occlusion of the ICA is often associated with poor outcomes and severe neurologic deficits.[1,2] Acute ICA occlusions are more resistant than MCA occlusions to administration of intravenous tPA.[3,4] In the Trial of Org 10172 in Acute Stroke Treatment (TOAST), 10% of patients were diagnosed with ICA occlusion, which resulted in neurologic disability in 40% and mortality in 20% of patients.[5]

Intra-arterial mechanical thrombectomy has been increasingly used in the management of acute ischemic stroke with the recent introduction of stent retrievers (nondetachable microcatheter-based stentlike devices).[6-9] Despite anecdotal endovascular attempts, an effective management approach has not been well established for patients with acute ICA occlusion that is not applicable to intravenous and/or intra-arterial thrombolysis.[10-13] The aims of the present study were to investigate the outcome and factors associated with recanalization therapy in acute occlusion of the ICA and to assess the efficacy of proximal flow arrest.

MATERIALS AND METHODS

Between April 2007 and November 2011, intra-arterial recanalization therapy was performed on 50 consecutive patients who met the following criteria: 1) ICA occlusion presented with acute stroke, and 2) a small early infarct area (< one-third of vascular territory) on a DWI, with mismatched perfusion-diffusion. MR imaging–specific perfusion-diffusion mismatch was identified as having a mismatch larger than 20% measured visually from the relative mean transit time map and DWI.[14] Patients with ICA

Received May 20, 2013; accepted after revision August 12.

From the Department of Radiology and Research Institute of Radiology (J.H.K., L.Z., S.P., D.-g.L., J.H.S., D.H.L., D.C.S.) and Department of Neurology (J.S.K.), University of Ulsan, College of Medicine, Asan Medical Center, Seoul, Korea; Department of Radiology (J.H.K.), Daegu Fatima Hospital, Daegu, Korea; Department of Radiology (L.Z.), First Affiliated Hospital of Nanjing Medical University, Nanjing, China; and Department of Radiology (J.K.K.), Chung-Ang University, College of Medicine, Seoul, Korea.

Please address correspondence to Dae Chul Suh, MD, PhD, Department of Radiology, Asan Medical Center, University of Ulsan, College of Medicine, 86 Asanbyeongwon-Gil, Songpa-Gu, Seoul 138-736, Korea; e-mail: dcsuh@amc.seoul.kr

http://dx.doi.org/10.3174/ajnr.A3747

Table 1: Baseline characteristics of enrolled patients, subdivided depending on outcome

Parameter	Good (mRS ≤ 2) *n* = 30	Poor (mRS > 2) *n* = 20	Total *n* = 50	*P* Value
Age,[a] y	68 (56–71)	67 (56–77)	68 (56–72)	.684[b]
Sex, M/F	23/7	10/10	33/17	.051[c]
Risk factors				
Hypertension	19	10	29	.349[c]
Diabetes mellitus	9	9	18	.279[c]
Hyperlipidemia	10	6	16	.804[c]
Cardiac disease	9	11	20	.077[c]
Previous stroke	3	7	10	.067[c]
Family history	4	6	10	.171[c]
Smoking	11	5	16	.386[c]
Alcohol	14	8	22	.642[c]
Onset				.063[c]
<6 hours	10	12	22	
≥6 hours	20	8	28	
$NIHSS_o$[a]	6 (3–11)	15 (10–18)	10 (4–15)	<.001[b]
Occlusion level				.038[c]
Supraclinoid-terminal	6	8	14	
Petrocavernous	9	9	18	
Bulb-cervical	15	3	18	
Occlusion type				.022[c]
Cardioembolism	7	11	18	
Large-artery disease	23	9	32	
Flow arrest				.419[c]
Yes	17	9	26	
No	13	11	24	
TICI				.007[c]
≥2	30	15	45	
<2	0	5	5	

[a] Data expressed as median (interquartile range).
[b] Mann-Whitney test.
[c] The χ^2 test or the Fisher exact test.

occlusion with a history of transient ischemic attack or previous stroke in the subacute or chronic stages, intracranial occlusion beyond the ICA, or occlusion of the posterior circulation were excluded. Our institutional review board approved the design of the study and the use of clinical data, and all patients provided written informed consent.

Table 1 shows the clinical and angiographic data of patients with ICA occlusion. The following variables that may affect the rate of adverse events were included as possible risk factors: age; sex (men vs women); presence of vascular risk factors (hypertension, diabetes mellitus, hyperlipidemia, cardiac disease, stroke history, family history, smoking, and alcohol); symptom onset; NIHSS score on admission ($NIHSS_o$); occlusion level and type; application of protective transient flow arrest; and postprocedural TICI grades at the site of occlusion after revascularization.

Protective flow arrest with a proximal or distal protection balloon or manual neck vessel compression was applied at our institute. Various thrombectomy attempts, including aspiration or retrieval of an intravascular clot, were performed under proximal or distal balloon protection. We used a neck compression technique ($n = 3$) before a proximal protective balloon became available in our medical institute. The ipsilateral neck was manually compressed in the area of the carotid arterial pulsation or on the palpable guiding catheter in the carotid artery while aspiration was performed via a guiding catheter positioned in the ICA. Aspiration was done by applying continuous negative pressure by using a 30-cc syringe for approximately 10–15 seconds and was repeated 2 or 3 times during an approximately 30-second interval.[15]

Application of the protective flow arrest technique was added as a factor to the outcome analysis.

To analyze the occlusion level (site), we applied the embryologic segmental anatomy of the ICA.[16] The ICA was divided by the embryologic vascular remnants that can help identify the occlusion level and work as collateral channels, leading to subsequent embolism (Fig 1). The 50 patients were categorized according to occlusion level, based on the 3 most commonly encountered anatomic parts in the ICA segments: supraclinoid-terminal ($n = 14$), petrocavernous ($n = 18$), and bulb-cervical ($n = 18$).

Patients with acute stroke who presented with symptom onset of <6 hours ($n = 22$) were treated according to our institution's protocol by intravenous and/or intra-arterial thrombolytic therapies.[17] A total of 7 patients received IV tPA and subsequently underwent endovascular recanalization because there was no improvement in their status. The patients who presented with acute symptom onset of ≥6 hours ($n = 28$) were considered for recanalization on the basis of the extent of the infarct and diffusion-perfusion/symptom mismatch after discussion with neurologists. In those patients with low initial NIHSS scores, the recanalization procedure in our study was performed based on progressive or fluctuating symptoms ($n = 17$), or because of perfusion abnormality ($n = 24$).

The subtype classification of large-artery atherosclerosis ($n = 32$) or cardioembolism ($n = 18$) for ICA occlusion was based on the modified TOAST classification at the time of admission.[5] The pretherapeutic neurologic status of the patient was evaluated by $NIHSS_o$. The mRS was used to assess the final clinical outcome at 6 months (good outcome, mRS ≤ 2; poor outcome, mRS ≥ 3).

Recanalization Procedure

Fifty patients with occlusion of the ICA were treated with suction, angioplasty, and/or stent placement in conjunction with retrieval devices. All patients were given 200 mg of aspirin and a loading dose of 300 mg of clopidogrel before the procedure, if they were not already taking these medications. After the procedure, 100 mg of aspirin once daily was continued as a permanent medication. In addition, 75 mg of clopidogrel was given once daily for at least 6 months after the procedure.[18]

The procedural details were the same as we had described previously, except that a 9F sheath was used for the proximal protection balloon catheter.[15,18-23] Protective flow arrest methods included proximal balloon protection with or without distal balloon protection or manual neck compression. The distal balloon was introduced through a 4F catheter or the occluded segment after application of the proximal balloon.

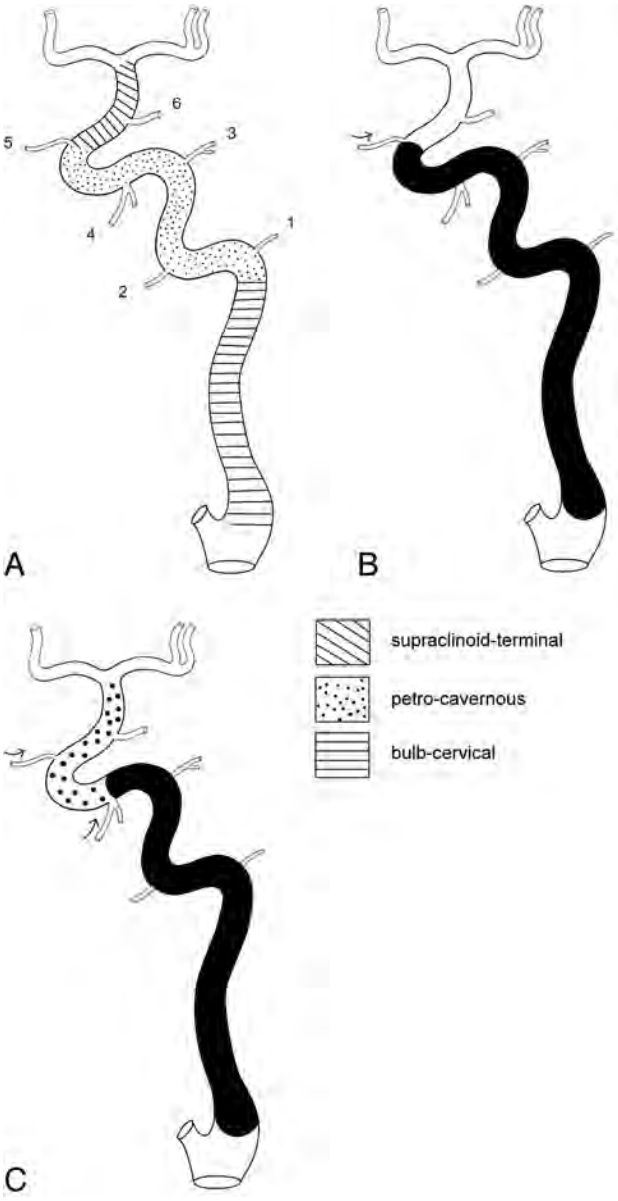

FIG 1. *A*, Division of the ICA segments into 3 parts based on embryologic classification (1 = caroticotympanic artery, 2 = mandibular artery, 3 = meningohypophyseal trunk, 4 = inferolateral trunk, 5 = ophthalmic artery, 6 = posterior communicating artery). When there is occlusion in the ICA (*B*), each branch between the segments may develop as a collateral, leading to thromboembolism by reopening the occluded vessel (*C*). Arrows in *B* and *C* are the direction of the flow. The inferolateral trunk plays a role in reopening the occluded the ICA segment and generating distal emboli.

TICI perfusion categories include grade 0 (no perfusion), grade I (penetration with minimal perfusion), grade II (partial perfusion), grade IIa (only partial filling; < two-thirds of the entire vascular territory), grade IIb (complete but slow filling of all of the expected vascular territory), and grade III (complete filling).[24] Although several studies have defined successful reperfusion as TICI IIb or greater, they used various cutoff values (50% vs 67%) for grade IIb, thus rendering comparisons across studies difficult or impossible.[25] Therefore, we defined TICI grade II–III as successful reperfusion.[25]

Basic Strategy of Recanalization According to Occlusion Levels

Proximal ICA Occlusion (Bulb-Cervical Segment). If there was an insufficient length of stump of the carotid bulb portion or if suction by proximal balloon catheter (eg, Optimo; Tokai Medical Products, Aichi, Japan) was ineffective, then a 4F catheter was passed along the 0.035-inch guidewire through the occluded segment and a distal balloon (eg, PercuSurge; Medtronic, Minneapolis, Minnesota) was introduced as shown in Fig 2*A*. Retrograde collateral filling of the segmental ICA anatomy as shown in Fig 1 was used as a guide for the subsequent procedure.

The location of the 4F catheter tip in the free lumen was identified by the suction of thrombotic debris in the distal segment beyond the occlusion and the regurgitation of blood. A protective distal balloon was introduced via the 4F catheter. Once protective distal occlusion was achieved, suction of the proximal ICA segment was followed by angioplasty and/or stent placement if there was any significant stenotic lesion. The ICA was irrigated by saline into the external carotid artery before balloon deflation to ensure that there was no debris in the ICA.

Distal ICA Occlusion (Petrocavernous Segment). Suction was applied via the proximal balloon catheter that was introduced in the cervical segment of the ICA (Fig 2*B*). If the suction was ineffective, then further clot retrieval was attempted by a Solitaire stent (Covidien, Irvine, California) or the Penumbra system (Penumbra, Alameda, California). If atherosclerotic stenosis remained after clot removal, then subsequent angioplasty and/or stent placement was performed under proximal balloon protection.

Occlusion of the Supraclinoid-Terminal Segment and/or an Intracranial Vessel. As was done with distal ICA occlusion, suction was applied via the proximal balloon catheter introduced in the cervical segment of the ICA. For residual intracranial vessel occlusion, further clot retrieval was attempted with a Solitaire or Penumbra catheter under proximal balloon protection (Fig 2*C*).

Statistical Analysis

We performed univariate analysis by using the χ^2 test or the Fisher exact test to assess the relationship between outcome and incontinuous independent variables. Mann-Whitney tests were used for continuous variables including age and $NIHSS_o$. Stratification analysis with the Cochran-Mantel-Haenszel test was used to assess the significant relationship between the potential risk factor and outcome, when there was a suspected confounding effect of another factor. All reported probability values were 2-sided, and *P* values of $< .05$ were considered statistically significant. We performed all statistical analyses by using SAS version 8.1 (SAS Institute, Cary, North Carolina).

RESULTS

Successful recanalization (TICI ≥ 2) was obtained in 45 (90%) of 50 patients, and good outcome (mRS ≤ 2) at 6 months was obtained in 30 (60%) of 50 patients. Good outcome was related to $NIHSS_o$ ($P < .001$), TICI ($P = .007$), occlusion type ($P = .022$), and occlusion level ($P = .038$) (Table 1). A lower $NIHSS_o$ and successful recanalization were significantly correlated with a good clinical outcome. Supraclinoid-terminal occlusion showed

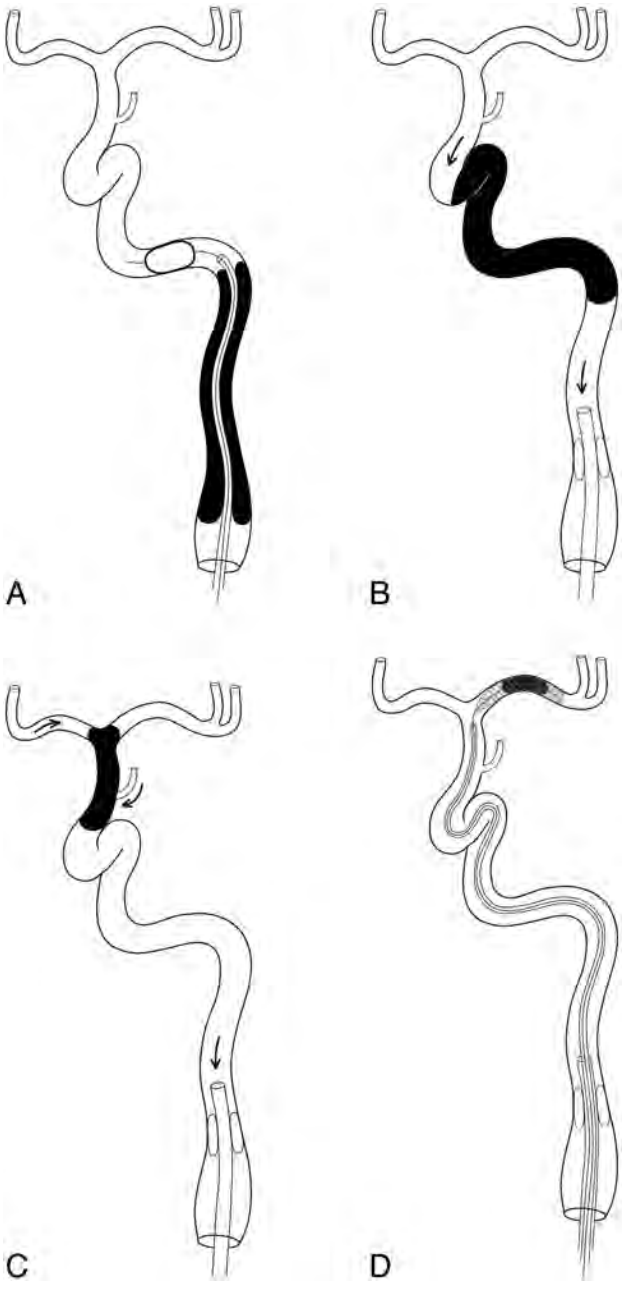

FIG 2. Schematic diagrams showing the protective flow arrest methods in each occluded level. *A*, A distal balloon was deployed beyond the bulb-cervical occlusion through a 4F catheter. Proximal balloons may be used together. Proximal flow arrest may be achieved by a proximal balloon catheter for petrocavernous (*B*) and supraclinoid-terminal (*C*) occlusions. Arrows in *B* and *C* are the flow direction when a negative pressure is applied by aspiration. There are 2 sources (the A1 and the posterior communicating artery) of the expected collateral channel in the supraclinoid-terminal segment. A fragmented or additional clot in the intracranial artery is subsequently retrieved by a stent retriever under proximal balloon protection (*D*).

poorer prognosis than petrocavernous or bulb-cervical occlusion. Results of stratification analysis (Table 2) revealed a significant correlation between application of flow arrest and clinical outcome with stratification according to occlusion levels ($P = .049$), that is, the application of protective flow arrest led to a better outcome in the distal ICA segment occlusion. On the other hand,

Table 2: Analysis of the relationship between application of protective flow arrest and clinical outcome with stratification according to occlusion levels

	Bulb (n = 18)		Above Bulb[a] (n = 32)	
	With Flow Arrest	Without Flow Arrest	With Flow Arrest	Without Flow Arrest
6 m mRS ≤ 2	4	11	13	2
6 m mRS > 2	1	2	8	9

Note:—The results of the Cochran-Mantel-Haenszel test and Cochran χ^2 value of 3.89 ($P = .049$) further verify a relationship between flow arrest and clinical outcome.
[a] Above bulb includes supraclinoid-terminal and petrocavernous segments.

outcome was irrelevant to the application of protective flow arrest in the bulb-cervical segment occlusion.

Five patients (10%) who had a failed recanalization (TICI < 2) showed poor clinical outcomes (mRS > 2) at 6 months. Patients with acute stroke (onset time < 6 hours) with ICA occlusion showed relatively poor clinical outcomes (55%; 12/22), despite relatively high recanalization rates (TICI ≥ 2; 82%; 18/22). Of the 22 patients who had ICA occlusion with onset time < 6 hours, 10 patients (45%) had a good clinical outcome and 5 patients (23%) died. These results were partially related to the fact that 17 (77%) of 22 patients with early onset (onset time < 6 hours) had a high NIHSS score (>10) compared with 6 (21%) of 28 patients with an onset time ≥6 hours ($P = .000$).

Thirty-four (94%) of 36 patients with bulb-cervical or petrocavernous ICA occlusion showed successful recanalization. In contrast, 11 (79%) of 14 patients with supraclinoid-terminal occlusion of the ICA showed successful recanalization, resulting in only 6 (43%) of 14 patients with a good outcome at 6 months. The initial patient status was poorer in cases of cardioembolism than in cases of large-artery disease (Fig 3). Large-artery disease was more common in the bulb-cervical segment compared with cardioembolism, which was more common in the supraclinoid-terminal segment of the ICA.

There were 3 patients (6%) with postprocedural symptomatic intracerebral hemorrhage. Six patients with intracerebral hemorrhage (12%) were asymptomatic. Two of the hemorrhages were related to massive infarcts. One was a massive hemorrhage that led to death. Of the 50 patients, 6 (12%) died within 6 months after the procedure. The cause of death was related to massive infarction ($n = 4$), intracranial hemorrhage ($n = 1$), or pneumonia-induced sepsis ($n = 1$).

DISCUSSION

Our study revealed that successful recanalization (TICI ≥ 2) was achieved in 45 (90%) of 50 patients and resulted in a good outcome (mRS > 2) after 6 months in 30 (60%) of 50 patients with acute ICA occlusion. Jovin et al[26] reported a favorable 30-day outcome (mRS ≤ 2) with endovascular treatment in 5 (33%) of 15 patients with acute ICA occlusion and 7 (88%) of 8 patients with subacute ICA occlusion. Using combined mechanical recanalization with aspiration and a stent retriever, Papanagiotou et al[10] obtained successful recanalization in 14 (63%) of 22 patients and a good outcome at 3 months in 13 (59%) of 22 patients. Although there are few large series of recanalization for patients with acute ICA occlusion, our results showed the possibility of an improved recanalization rate and good outcome among these patients.[22] Although the natural history of acute stroke with a pro-

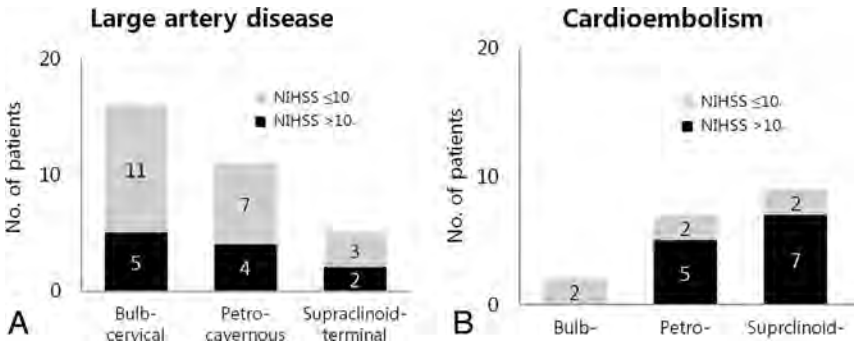

FIG 3. Different proportions of initial patient status according to the occlusion level based on the occlusion type (large-artery disease vs cardioembolism). There was a reversed trend of patient number for each occlusion type according to the lesion level. The initial status of patients with cardioembolism in the supraclinoid-terminal segment of the ICA was proportionally poorer than that of patients with large-artery disease.

gressive or fluctuating symptom pattern or perfusion abnormality in patients with low NIHSS is not completely known, recanalization may be warranted because mild or improving stroke may have poor short-term outcomes,[27] and acute ischemic stroke from occlusion of the ICA is one of the most devastating forms of acute ischemia, with only 2%–30% of patients achieving good recovery.[28]

Good outcome was related to initial patient status, postprocedural TICI grade, occlusion type, and occlusion level. The more favorable outcome may be related to good collateral circulation and small ischemic core or large penumbra lesion, because retrograde ICA filling, ophthalmic collaterals, or leptomeningeal collaterals are related to better short-term outcomes.[22,29,30] Assessment of occlusion level based on the segmental ICA anatomy as in our study could provide better anatomic confinement and allows the application of proximal and/or distal protection with flow arrest, which subsequently could play a role in improving the recanalization rate and resulting in good clinical outcome.[9,10] The rate of symptomatic intracerebral hemorrhage seen in our study was 6%, which was similar to 6.2% in the Interventional Management of Stroke III (IMS III) trial and 6% of fatal and nonfatal symptomatic intracranial hemorrhage in SYNTHESIS.[31,32]

Although the IMS III trial did not show any difference in functional independence (mRS ≤2) with endovascular therapy after intravenous tPA, compared with intravenous tPA alone, the ICA occlusion subgroup in the trial revealed the difference; the rate of partial or complete recanalization at 24 hours, as seen on CT angiograms at both baseline and at 24 hours, was 81% for an occlusion in the ICA in the endovascular therapy group, compared with 35% for an occlusion in the ICA in the intravenous tPA group.[32] In addition, the segmental location of the ICA occlusion and the mechanism of occlusion (cardioembolism vs atherosclerosis) were not specified in the IMS III and SYNTHESIS trials.[31,32] The MR RESCUE (Mechanical Retrieval and Recanalization of Stroke Clots Using Embolectomy) trial studied patients with NIHSS scores of 6–29 who had a large-vessel, anterior-circulation ischemic stroke and who were randomly assigned within 8 hours after the onset of symptoms to undergo either mechanical embolectomy or standard medical care.[33] However, the study used only the old version of recanalization devices (Merci [Concentric Medical, Mountain View, California] or Penumbra) without using Trevo (Stryker, Kalamazoo, Michigan) or Solitaire, both of which have revealed a better primary efficacy (61%) outcome (ie, successful recanalization without symptomatic intracranial hemorrhage) vs 21% with Merci.[34]

Because there is no standardized recanalization technique for ICA occlusion in patients with acute stroke, mechanical and/or intra-arterial thrombolysis for intracranial occlusion has been followed by angioplasty and/or stent placement, aspiration thrombectomy, or clot retrieval with various devices.[9-12,35] Among the factors affecting good outcome, the effect of revascularization (postprocedural TICI grade) may depend on the methodology used to improve the final luminal patency for each occlusion type and level. Among those methods, protective flow arrest applies simple suction that effectively aspirates the clot and prevents distal migration to the intracranial vessels during clot retrieval.[36] The angioplasty and/or stent placement performed in our study can be part of the recanalization procedure if the stent retriever is not effective and the indications can differ from those applied in SAMMPRIS (Stenting vs Aggressive Medical Management for Preventing Recurrent Stroke in Intracranial Stenosis), which included patients with TIA or nonsevere stroke occurring within 30 days of their enrollment and attributed to 70%–99% stenosis of a major intracranial artery.[37]

Because there is little stump for proper balloon engagement in bulb-cervical occlusion, a combination of proximal and distal protective balloons (as shown in Fig 2) may provide more protection against additional thromboemboli during the recanalization procedure. For petrocavernous and supraclinoid-terminal segment occlusion, proximal flow arrest alone may be applied to aspirate the clot and prevent distal thromboembolism during clot retrieval. The flow reversal technique or even manual neck compression may also be effective for protective proximal flow arrest.[9,12] Simple suction thrombectomy can be applied by using a proximal protection balloon with which the stent retriever is subsequently used.

Extracranial-intracranial (ECIC) bypass surgery in patients with symptomatic occlusion of the ICA was illustrated by a new operating technique and patients without naturally occurring collateral flow to maintain adequate circulation might benefit from ECIC bypass surgery. Recently, ECIC bypass surgery plus medical therapy was not found to reduce the risk for recurrent ipsilateral ischemic stroke compared with medical therapy alone.[38] ECIC bypass surgery may have limitations regarding response to a recent, symptomatic occlusion containing remarkable salvageable brain parenchyma at the time of symptom presentation.[39]

Our study had several limitations. First, the overall number of our study patients was relatively small; therefore, further analysis by categorization into small subgroups made it difficult to draw any definite conclusions. Second, the procedural methodology

used in our study was not homogeneous because various thrombectomy attempts, including aspiration or retrieval of an intravascular clot, were performed with or without proximal or distal balloon protection. Despite the use of currently available management strategies, the clinical and angiographic responses to therapy remain limited.[6] Therefore, further data must be added to support our conclusion, though it is difficult to perform a randomized controlled study because acute ICA occlusions presenting with severe stroke symptoms are relatively rare, even at high-volume stroke centers.

CONCLUSIONS

Our results showed that successful recanalization and a good outcome could be achieved by combined mechanical thrombectomy, especially under protective flow arrest. Good outcome was related to initial patient status, postprocedural TICI grade, occlusion type, and occlusion level. Our study also revealed that the application of proximal and/or distal protection with flow arrest helps to improve the recanalization rate and results in a good clinical outcome.

Disclosures: Deok Hee Lee—*UNRELATED: Board Membership:* Covidien, Comments: Asian clinical advisory board member; *Payment for Lectures (including service on speaker bureaus):* Codman; *Patents (planned, pending, or issued):* S&G Biotech; *Royalties:* S&G Biotech.

REFERENCES

1. Seet RC, Wijdicks EF, Rabinstein AA. **Stroke from acute cervical internal carotid artery occlusion: treatment results and predictors of outcome.** *Arch Neurol* 2012:1–6
2. Paciaroni M, Balucani C, Agnelli G, et al. **Systemic thrombolysis in patients with acute ischemic stroke and Internal Carotid ARtery Occlusion: the ICARO study.** *Stroke* 2012;43:125–30
3. Jansen O, von Kummer R, Forsting M, et al. **Thrombolytic therapy in acute occlusion of the intracranial internal carotid artery bifurcation.** *AJNR Am J Neuroradiol* 1995;16:1977–86
4. Linfante I, Llinas RH, Selim M, et al. **Clinical and vascular outcome in internal carotid artery versus middle cerebral artery occlusions after intravenous tissue plasminogen activator.** *Stroke* 2002;33:2066–71
5. Adams HP, Jr., Bendixen BH, Kappelle LJ, et al. **Classification of subtype of acute ischemic stroke. Definitions for use in a multicenter clinical trial. TOAST. Trial of Org 10172 in Acute Stroke Treatment.** *Stroke* 1993;24:35–41
6. Pierot L, van der Bom IM, Wakhloo AK. **Advances in stroke: advances in interventional neuroradiology.** *Stroke* 2012;43:310–13
7. Brinjikji W, Rabinstein AA, Kallmes DF, et al. **Patient outcomes with endovascular embolectomy therapy for acute ischemic stroke: a study of the National Inpatient Sample: 2006 to 2008.** *Stroke* 2011;42:1648–52
8. Costalat V, Machi P, Lobotesis K, et al. **Rescue, combined, and standalone thrombectomy in the management of large vessel occlusion stroke using the Solitaire device: a prospective 50-patient single-center study: timing, safety, and efficacy.** *Stroke* 2011;42:1929–35
9. Eesa M, Almekhlafi MA, Mitha AP, et al. **Manual aspiration thrombectomy through balloon-tipped guide catheter for rapid clot burden reduction in endovascular therapy for ICA L/T occlusion.** *Neuroradiology* 2012;54:1261–65
10. Papanagiotou P, Roth C, Walter S, et al. **Carotid artery stenting in acute stroke.** *J Am Coll Cardiol* 2011;58:2363–69
11. Hauck EF, Natarajan SK, Ohta H, et al. **Emergent endovascular recanalization for cervical internal carotid artery occlusion in patients presenting with acute stroke.** *Neurosurgery* 2011;69:899–907
12. Terada T, Okada H, Nanto M, et al. **Endovascular recanalization of the completely occluded internal carotid artery using a flow reversal system at the subacute to chronic stage.** *J Neurosurg* 2010;112:563–71
13. Thomas AJ, Gupta R, Tayal AH, et al. **Stenting and angioplasty of the symptomatic chronically occluded carotid artery.** *AJNR Am J Neuroradiol* 2007;28:168–71
14. Kang DW, Sohn SI, Hong KS, et al. **Reperfusion Therapy in Unclear-Onset Stroke Based on MRI Evaluation (RESTORE): a prospective multicenter study.** *Stroke* 2012;43:3278–83
15. Xu GF, Suh DC, Choi CG, et al. **Aspiration thrombectomy of acute complete carotid bulb occlusion.** *J Vasc Interv Radiol* 2005;16:539–42
16. Lasjaunias P, Berenstein A, Ter Brugge KG. **Skull base and maxillofacial region.** In: *Surgical Neuro-Angiography*, 2nd ed. Berlin: Springer-Verlag; 2001:261–90
17. Cho KH, Lee DH, Kwon SU, et al. **Factors and outcomes associated with recanalization timing after thrombolysis.** *Cerebrovasc Dis* 2012;33:255–61
18. Choi JW, Kim JK, Choi BS, et al. **Adjuvant revascularization of intracranial artery occlusion with angioplasty and/or stenting.** *Neuroradiology* 2009;51:33–43
19. Liu S, Jung JH, Kim SM, et al. **Simultaneous bilateral carotid stenting in high-risk patients.** *AJNR Am J Neuroradiol* 2010;31:1113–17
20. In HS, Lee HY, Park JY, et al. **Intracranial stenting in patients with atherosclerotic stenosis associated with various aneurysms in the same diseased arterial segment.** *AJNR Am J Neuroradiol* 2010;31:1895–98
21. Suh DC, Kim JK, Choi JW, et al. **Intracranial stenting of severe symptomatic intracranial stenosis: results of 100 consecutive patients.** *AJNR Am J Neuroradiol* 2008;29:781–85
22. Suh DC, Kim JK, Choi CG, et al. **Prognostic factors for neurologic outcome after endovascular revascularization of acute symptomatic occlusion of the internal carotid artery.** *AJNR Am J Neuroradiol* 2007;28:1167–71
23. Pyun HW, Suh DC, Kim JK, et al. **Concomitant multiple revascularizations in supra-aortic arteries: short-term results in 50 patients.** *AJNR Am J Neuroradiol* 2007;28:1895–901
24. Higashida RT, Furlan AJ, Roberts H, et al. **Trial design and reporting standards for intra-arterial cerebral thrombolysis for acute ischemic stroke.** *Stroke* 2003;34:e109–37
25. Suh SH, Cloft HJ, Fugate JE, et al. **Clarifying differences among Thrombolysis in Cerebral Infarction scale variants: Is the artery half open or half closed?** *Stroke* 2013;44:1166–68
26. Jovin TG, Gupta R, Uchino K, et al. **Emergent stenting of extracranial internal carotid artery occlusion in acute stroke has a high revascularization rate.** *Stroke* 2005;36:2426–30
27. Smith EE, Fonarow GC, Reeves MJ, et al. **Outcomes in mild or rapidly improving stroke not treated with intravenous recombinant tissue-type plasminogen activator: findings from Get With The Guidelines-Stroke.** *Stroke* 2011;42:3110–15
28. Fischer U, Mono ML, Schroth G, et al. **Endovascular therapy in 201 patients with acute symptomatic occlusion of the internal carotid artery.** *Eur J Neurol* 2013;20:1017–24, e87
29. Choi JW, Kim JK, Choi BS, et al. **Angiographic pattern of symptomatic severe M1 stenosis: comparison with presenting symptoms, infarct patterns, perfusion status, and outcome after recanalization.** *Cerebrovasc Dis* 2010;29:297–303
30. Liebeskind DS, Cotsonis GA, Saver JL, et al. **Collateral circulation in symptomatic intracranial atherosclerosis.** *J Cereb Blood Flow Metab* 2011;31:1293–301
31. Ciccone A, Valvassori L, Nichelatti M, et al. **Endovascular treatment for acute ischemic stroke.** *N Engl J Med* 2013;368:904–13
32. Broderick JP, Palesch YY, Demchuk AM, et al. **Endovascular therapy after intravenous t-PA versus t-PA alone for stroke.** *N Engl J Med* 2013;368:893–903
33. Kidwell CS, Jahan R, Gornbein J, et al. **A trial of imaging selection and endovascular treatment for ischemic stroke.** *N Engl J Med* 2013;368:914–23
34. Saver JL, Jahan R, Levy EI, et al. **Solitaire flow restoration device**

versus the Merci retriever in patients with acute ischaemic stroke (SWIFT): a randomised, parallel-group, non-inferiority trial. *Lancet* 2012;380:1241–49
35. Lü PH, Park JW, Park S, et al. **Intracranial stenting of subacute symptomatic atherosclerotic occlusion versus stenosis.** *Stroke* 2011;42:3470–76
36. Chueh JY, Wakhloo AK, Gounis MJ. **Effectiveness of mechanical endovascular thrombectomy in a model system of cerebrovascular occlusion.** *AJNR Am J Neuroradiol* 2012;33:1998–2003
37. Chimowitz MI, Lynn MJ, Turan TN, et al. **Design of the stenting and aggressive medical management for preventing recurrent stroke in intracranial stenosis trial.** *J Stroke Cerebrovasc Dis* 2011;20:357–68
38. Powers WJ, Clarke WR, Grubb RL, et al. **Extracranial-intracranial bypass surgery for stroke prevention in hemodynamic cerebral ischemia: the Carotid Occlusion Surgery Study randomized trial.** *JAMA* 2011;306:1983–92
39. Rodríguez-Hernández A, Josephson AS, Langer D, et al. **Bypass for the prevention of ischemic stroke.** *World Neurosurg* 2011;76(6 Suppl):S72–79

Correlation between Fissured Fibrous Cap and Contrast Enhancement: Preliminary Results with the Use of CTA and Histologic Validation

L. Saba, E. Tamponi, E. Raz, L. Lai, R. Montisci, M. Piga, and G. Faa

ABSTRACT

BACKGROUND AND PURPOSE: Previous studies demonstrated that carotid plaques analyzed by CTA can show contrast plaque enhancement. The purpose of this preliminary work was to evaluate the possible association between the fissured fibrous cap and contrast plaque enhancement.

MATERIALS AND METHODS: Forty-seven consecutive (men = 25; average age = 66.8 ± 9 years) symptomatic patients studied by use of a multidetector row CT scanner were prospectively analyzed. CTA was performed before and after contrast and radiation doses were recorded; analysis of contrast plaque enhancement was performed. Patients underwent carotid endarterectomy en bloc; histologic sections were prepared and evaluated for fissured fibrous cap and microvessel attenuation. The Mann-Whitney test was performed to evaluate the differences between the 2 groups. A multiple logistic regression analysis was performed to assess the effect of fissured fibrous cap and microvessel attenuation on contrast plaque enhancement. Receiver operating characteristic curve and area under the curve were also calculated.

RESULTS: Twelve patients had fissured fibrous cap. In 92% (11/12) of fissured fibrous cap–positive plaques, we found contrast plaque enhancement, whereas in 69% (24/35) of the plaques without fissured fibrous cap contrast plaque enhancement was found. The Mann-Whitney test showed a statistically significant difference between the contrast enhancement in plaques with fissured fibrous cap (Hounsfield units = 22.6) and without fissured fibrous cap (Hounsfield units = 12.9) ($P = .011$). On the regression analysis, both fissured fibrous cap and neovascularization were associated with contrast plaque enhancement ($P = .0366$ and $P = .0001$). The receiver operating characteristic curve confirmed an association between fissured fibrous cap and contrast plaque enhancement with an area under the curve of 0.749 ($P = .005$).

CONCLUSIONS: The presence of fissured fibrous cap is associated with contrast plaque enhancement. Histologic analysis showed that the presence of fissured fibrous cap is associated with a larger contrast plaque enhancement compared with the contrast plaque enhancement of plaques without fissured fibrous cap.

ABBREVIATIONS: CEA = carotid endarterectomy; CPE = carotid plaque enhancement; CTDI = CT dose index; DLP = dose-length product; FFC = fissured fibrous cap; ROC = receiver operating characteristic; HU = Hounsfield Units

The presence of fissured fibrous cap (FFC) in the carotid artery plaque is associated with an increased risk of cerebrovascular events, and therefore FFC is considered one element that makes a carotid plaque "vulnerable."[1-3] Identification of this condition is important to obtain a better stratification of stroke risk.[1]

The FFC has been studied by use of MR imaging, demonstrating the potential of MR imaging to detect the rupture of the fibrous cap,[4,5] with or without the use of gadolinium.[6,7] Recently, with the use of CTA and morphologic analysis of the carotid plaque, the FFC was documented.[8] Even though the rupture of FFC has been shown to be associated with enhancement on MR imaging,[7] this association has not yet been demonstrated by use of CT. The carotid plaque enhancement (CPE) on CTA is associated with plaque instability[9-11]; CPE is associated with microvessel attenuation, but the neovascularization alone cannot be the only factor because some plaques with high CPE do not show neovascularization.[9]

Our hypothesis is that the rupture of the FFC is an independent factor related to the CPE, and we aim to evaluate this association.

Received June 15, 2013; accepted after revision July 30.

From the Departments of Radiology (L.S., M.P.), Pathology (E.T., L.L., G.F.), and Vascular Surgery (R.M.), Azienda Ospedaliero Universitaria, Monserrato (Cagliari), Italy; Department of Radiology (E.R.), New York University School of Medicine, New York, New York; and Department of Neurology and Psychiatry (E.R.), Sapienza University of Rome, Italy.

Please address correspondence to Luca Saba, MD, Department of Radiology, Azienda Ospedaliero Universitaria (A.O.U.), di Cagliari–Polo di Monserrato s.s. 554 Monserrato (Cagliari) 09045, Italy; e-mail: lucasaba@tiscali.it

http://dx.doi.org/10.3174/ajnr.A3759

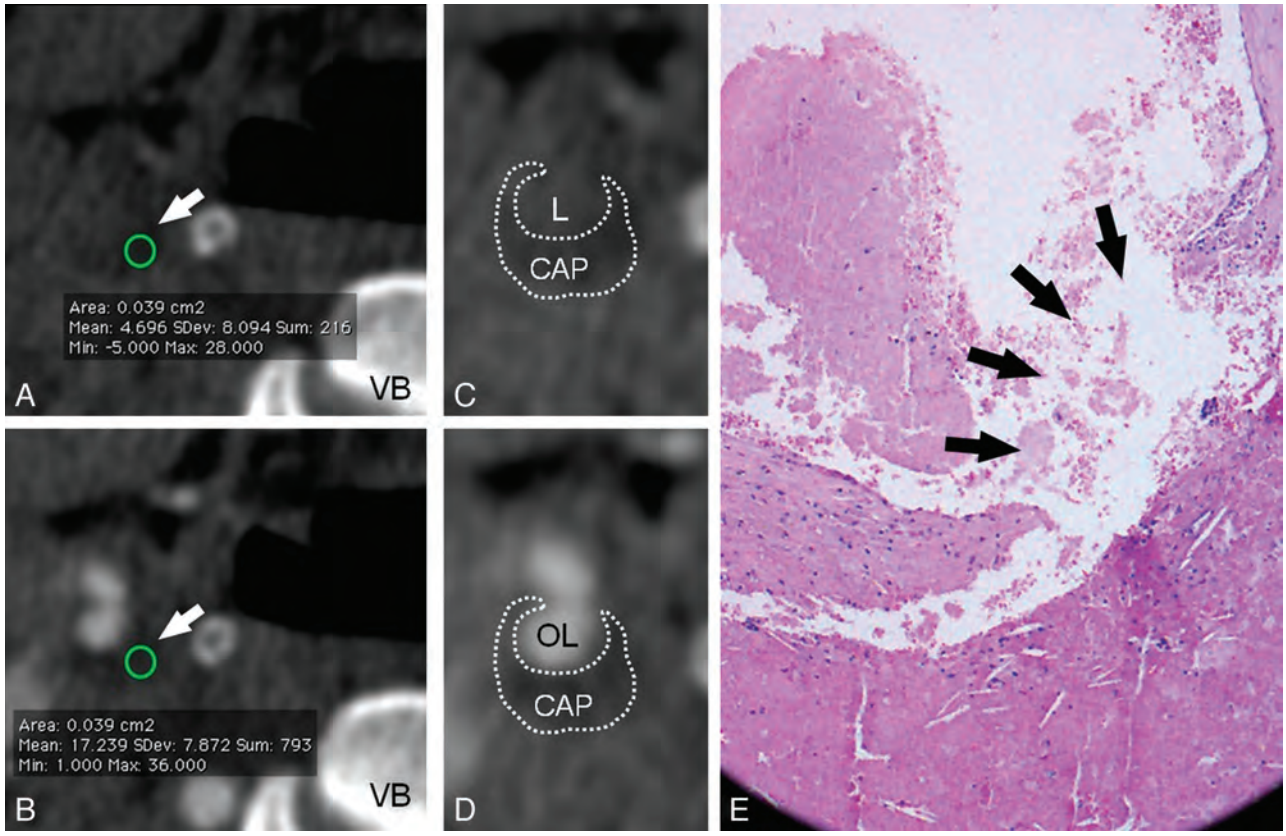

FIG 1. A 71-year-old male patient. In CT analysis, before *(A)* and after *(B)* contrast, the carotid artery plaque is visible (*white arrows*) and the CPE HU value is shown. The circles, indicated by the white arrows, represent the area of the plaque that was assessed (in this case, the area was 0.039 cm^2); in the basal scan, the average HU value was 4.696, whereas after administration of contrast material it was 17.239 (VB indicates vertebral body). In *C* and *D,* the same images as *A* and *B* are shown with a zoom factor of 150% and demonstrate the contour of the carotid artery plaque (CAP). In *C,* the patent lumen of the carotid is visible (L indicates lumen), whereas in *D,* the opacified patent lumen is also indicated (OL indicates opacified lumen). In the histologic section *(E),* the rupture of the FFC is noted (*black arrows*).

MATERIALS AND METHODS

Study Design and Patient Population

We obtained institutional review board approval for this study. Forty-seven consecutive symptomatic patients (men = 25; women = 22; mean age = 66.8 ± 9 years) were prospectively analyzed from May 2010 to March 2012. The mean time interval between CTA and the clinical episode (stroke or TIA) was 4 days (range, 1–12 days). We considered as an inclusion criterion that the carotid endarterectomy (CEA) was performed within 10 days after the CTA. A subgroup of the current population ($n = 29$) was included in a previous study.[9]

CT Technique

CT was performed with the use of a 16-row multidetector CT system (Brilliance, Philips, Best, The Netherlands) with a previously described protocol.[9] Briefly, the basal scan is performed, followed by the angiographic phase in the caudocranial direction. The volume of injected contrast is 80 mL (Ultravist 370; Bayer Schering Pharma, Berlin, Germany), with a flow rate of 5 mL/s. The precise timing of the injection is obtained with a bolus-tracking technique: the dynamic monitoring began 6 seconds after the beginning of the intravenous injection of contrast material. The delay between the acquisitions of each monitoring image was 1 second. When the threshold was reached (by using a threshold inside the region of interest set +90 Hounsfield units [HU] above the baseline as a trigger), the patient was instructed not to breathe; after an interval of 4 seconds, the CTA acquisition started in the caudocranial direction from the aortic arch to the circle of Willis, with a section thickness of 1.3 mm, increment 0.6 mm, matrix 512 × 512, FOV 16–19 cm, mAs 260–300, and kV 120–140. An intermediate reconstruction algorithm (C-filter) was used.

Carotid Plaque Enhancement Quantification

The CPE quantification was performed by use of a validated technique.[9-11] Two radiologists performed all measurements of HU (L.S. and E.R.) by using as window/level settings W850:L300.[12] Particular care was taken to obtain a correct registration between the basal phase and the enhanced phase (Fig 1*A*,-*B*). The HU quantification is obtained by use of a circular or elliptical region of interest (≥1 mm^2).The threshold to consider the CPE as present was a variation of ≥10 HU.[9]

Carotid Endarterectomy

CEA was performed by 2 vascular surgeons (R.M. and Robert Sanfilippo) by use of the en bloc technique (to reduce the manipulation of the carotid plaque and avoid the potential rupture/fragmentation of the plaque), by scoring the adventitia and outer media with a scalpel and removing the plaque as an intact tube. The criteria to perform carotid endarterectomy were based on the recommendations by the

NASCET and European Carotid Surgery Trial studies for symptomatic patients.[13-15]

Histologic Analysis of the Plaque

Histologic examination was performed by 2 observers (L.S. and E.R.) blinded to clinical-radiologic data. The plaque specimen was immediately fixed in formalin, and it was taken to the laboratory directly after the surgical procedure. None of the carotid endarterectomy specimens showed disruption of the luminal surface of the plaque. Carotid plaque was decalcified and embedded in paraffin wax. The portion of the specimen showing the carotid plaque was divided transversely in sections at 3-mm intervals that were air-dried at 60°C for 45 minutes. After this phase, paraffin was removed by xylol and the sections were hydrated. Finally, endogenous peroxidase activity was blocked by 2% H_2O_2. The 5-μm transverse sections were subjected to histologic examination to identify the plaque components, the fibrous cap, and its rupture (Fig 1*C*). The fibrous cap components such as attenuated and loose (proteoglycan) matrix, hemorrhage, neovasculature, calcification, and inflammatory cell infiltrate were analyzed, and the condition of FFC was identified by the loss of anatomic continuity (integrity) of the fibrous cap.[6] In addition, the neovascularization was assessed by analyzing the microvessel attenuation according to the methodology indicated by Saba et al.[9]

Table 1: Patient characteristics

Parameter	FFC	Non-FFC	*P* Value
Patients, *n*	12 (25.5%)	35 (74.5%)	NC
CPE, HU	22.6 ± 10.9	12.9 ± 9.4	.001
CPE, 95% CI, HU	12.8–33.1	10.2–20.8	NC
Age, y	67 ± 8	65 ± 9	.495
Sex, male	8 (67%)	17 (49%)	.278
Smoker	6 (55%)	19 (54%)	.938
Hypertension	7 (58%)	22 (63%)	.781
CAD	8 (67%)	19 (54%)	.454
Diabetes	3 (25%)	3 (9%)	.141
Dyslipidemia	7 (58%)	14 (40%)	.271
Statins and other drugs[a]	6 (50%)	14 (40%)	.545

Note:—CAD indicates coronary artery disease; NC, not calculable.
[a] Other lipid-lowering drugs.

Calculation of the Radiation Dose

For each examination, the CT dose index (CTDI), dose-length product (DLP), and length of the scans in centimeters was collected. The effective dose (measured in mSv) was also calculated by converting the DLP by use of the following conversion equation for CT of the neck: mSv = 0.0059 * DLP.[16]

Statistical Analysis

Continuous quantitative variables were expressed as mean ± standard deviations. The plaque HU values were averaged between the 2 radiologists, and the Bland-Altman statistic was performed. The Mann-Whitney test was used to test the differences between the 2 groups of patients, with and without FFC, and the nonparametric McNemar test was used to test the difference between the prevalence of FFC in carotid arteries with and without CPE. Receiver operating characteristic (ROC) curve analysis was also performed to test the association between the presence of FFC and CPE; the area under the curve was also calculated. Multiple logistic regression analysis was also performed to assess the effect of the FFC versus the microvessel attenuation. R software (www.r-project.org) was used for statistical analyses.

RESULTS

General Results

Demographic and CPE characteristics of the studied patients are shown in Table 1. In the 47 carotid arteries studied, 12 cases with FFC were found. In 92% (11/12) of the plaques with FFC we found CPE, whereas in only 69% (24/35) of the plaques without FFC, was CPE found and the McNemar test confirmed that there was a statistically significant difference ($P = .0001$) Bland-Altman analysis demonstrated very good concordance between readers, with a mean difference between them of 4%.

Mann-Whitney Test

The Mann-Whitney test showed a statistically significant difference between the amount of CPE in plaques with FFC (HU = 22.6 ± 10.9) and without FFC (HU = 12.9 ± 9.4) ($P = .011$) (Fig 2*A*).

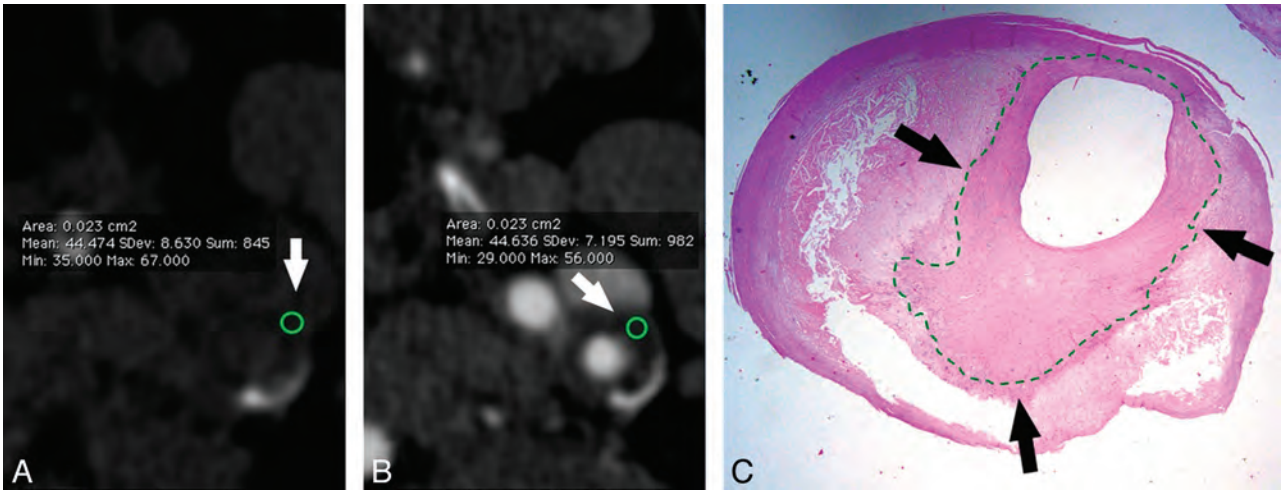

FIG 2. A 68-year-old male patient. In CT analysis, before *(A)* and after *(B)* contrast, the carotid artery plaque is visible (*white arrows*) and the CPE HU value is shown. The circles, indicated by the white arrows, represent the area of the plaque that was assessed; in the basal scan, the average HU value was 44.474, whereas after administration of contrast material it was 44.636. In this case, there was no contrast plaque enhancement. In the histologic section *(C)*, the thick fibrous cap is visible (*black arrows*).

ROC Curve Analysis

The ROC curve analysis (Fig 2*B*) confirmed an association between FFC and CPE, with an area under the curve of 0.749 (95% confidence interval = 0.601–0.864; $P = .005$; standard error = 0.089).

Multiple Logistic Regression Analysis

The multiple logistic regression analysis was performed to assess the effect of the FFC on the CPE by avoiding the confounding effect of the neovascularization (Table 2). We found that both FFC and neovascularization had a statistically significant association with the presence of CPE ($P = .0366$ and .0001, respectively).

Radiation Dose Analysis

The radiation dose analysis was performed in our cohort of patients, and the results are summarized in Table 3.

DISCUSSION

CTA is widely used for the imaging of carotid arteries; this technique allows for the study of plaque morphology and for the quantification and characterization of plaque composition with excellent detail. In CTA, carotid artery plaques may demonstrate the presence of contrast enhancement,[9-11] which is associated with the presence of cerebrovascular symptoms[10,11]; the reasons underlying the enhancement are otherwise unclear.

In our study, we found that the plaques with FFC enhance more often than do the plaques without FFC: in 92% of the plaques with FFC we found CPE, whereas in only 69% of the plaques without FFC, was CPE found ($P = .0001$). These results are also concordant with histologic and fluid-dynamic analyses that have clarified that the rupture of the FFC creates a breach into the lipid-rich necrotic core with blood flow that actively enters into the plaque by determining pro-thrombotic effects.[17,18] In the only case of FFC without CPE, the histologic sections were reanalyzed and an absence of lipid-rich necrotic core was detected. This fact suggests to us that the configuration of the core of the plaque may play a role: in these cases with a weak necrotic core, the rupture of the plaque may be associated with a blood invasion into the plaque, whereas in the case of more robust configuration, the rupture of the fibrous cap cannot be associated with intraplaque hemorrhage.

Moreover, we also found that the amount of CPE is larger in the plaques with FFC (22.6 versus 12.9; $P = .011$). This can be explained by the fact that the rupture of the fibrous cap allows the blood to massively enter into the plaque. ROC curve analysis confirmed an association between FFC and CPE (Fig 3). These results suggest that FFC is one of the factors that determine the enhancement of the plaque. It was demonstrated that the neovascularization of the plaque is associated with the presence of CPE, and this parameter may represent a confounding factor in the assessment of the effect of the FFC in CPE. Therefore, a multiple logistic

Table 2: Multiple logistic regression analysis

Independent Variables	Coefficient	Standard Error	*t*	*P* Value	*r*
(Constant)	0.23552				
FFC	0.25401	0.1178	2.156	.0366	0.208
Neovascularization	0.19714	0.04244	4.645	<.0001	0.539

Table 3: Radiation dose parameters of the population for the basal or contrast-enhanced phase

	n	Mean	95% CI	SD	Minimum	Maximum	2.5–97.5 Percentiles
CTDI, mGy	47	11.657	11.510–11.805	0.5021	10.9	13	11.035–12.933
DLP, mGy*cm	47	348.113	341.502–354.725	22.5172	306.23	415	307.425–400.353
Effective dose, mSv	47	2.054	2.015–2.093	0.1329	1.807	2.449	1.814–2.362
Length	47	29.866	29.416–30.316	1.5339	27.1	34.2	27.370–33.525

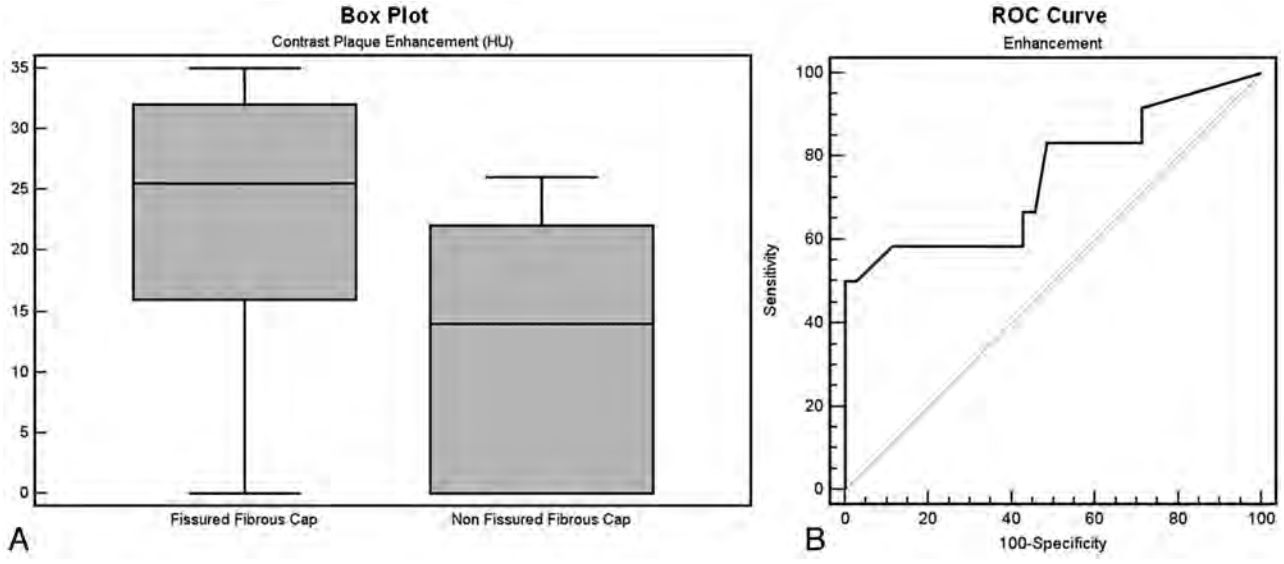

FIG 3. Boxplot analysis shows the difference in CPE between the group of patients with FFC and the patients without FFC *(A)*; the ROC curve shows the association between FFC and CPE *(B)*.

regression analysis was performed, and this confirmed that both FFC and neovascularization had a statistically significant association with the presence of CPE ($P = .0366$ and .0001, respectively) and that they independently can determine the presence of CPE. These results may explain why in previous analysis,[9] plaques with low levels of neovascularization had a large CPE. In our study, notably, the 2 groups of patients, with and without rupture of the FFC, were similar with regard to risk factors for carotid artery disease (Table 1). A similar result has been described with the use of MR imaging,[7] but the description of this finding by use of CT has obvious consequences on the usefulness of this evaluation in clinical practice. The results are also concordant with histologic and fluid-dynamic analyses that have clarified that the rupture of the FFC creates a breach into the lipid-rich necrotic core with the blood flow that actively enters into the plaque by determining pro-thrombotic effects.[17,18]

In the past years, several investigations have demonstrated the potentialy of MR in the assessment of FFC status.[1,2,6,7] However in several institutions, CTA is widely used in the assessment of the carotid artery status, in particular in emergency settings[19] or for those subjects with contraindications to MR imaging such as claustrophobic patients or patients with pacemakers. Some advantages of CT are the short time of the procedure (the CT acquisition requires only few seconds) and the excellent spatial resolution that can reach 0.3 mm isotropic voxels. In recent years, several investigations have demonstrated the potential of CT in the assessment of carotid artery plaque composition[20,21] by suggesting that some parameters, easily detectable with CT, are important for stroke risk stratification. With the current study, we showed that the presence of FFC is associated with contrast plaque enhancement and that this should be considered a further useful element for the stratification of stroke risk. It is not our opinion that the CTA should be performed to merely test the presence or absence of the CPE; once the CTA is performed, we think that this element should be assessed.

The 2 main disadvantages of CTA are the nephrotoxicity and radiation dose. To reduce the nephrotoxicity, we are currently using the "bolus technique," with a reduced volume of contrast material (80 mL) injected at a high flow rate. In the future, it is likely that the volume of the injected contrast material will be further reduced, thanks to the potential and velocity of the newer CT scanners. The radiation dose delivered to the patient is the second main issue related to the use of CT. In our cohort of patients, we had a mean CTDI of 11.657 mGy, which is a value similar to another recent publication where the single-source CT was used[22] (12.5 mGy); the effective dose for each acquisition is similar. It is important to underline that there is an evolution with the new CT scanners, in particular the dual-energy systems that allow performing examinations with similar image quality and lower radiation dose compared with single-source CT.[22]

In this study, there are some limitations: the first is the number of analyzed patients ($n = 47$), which does not allow us to obtain a strong statistical analysis with tight confidence intervals; for this reason, the current results should be considered as preliminary results that must be confirmed in a larger population. The second limitation of this study is the potential plaque rupture during the surgeon's manipulation of the carotid arteries while performing the carotid endarterectomy. However, it is our hypothesis that this can be considered as a minor limitation because our surgeons used particular care in the CEA procedure; to reduce this effect, an ex vivo CEA should be performed.

CONCLUSIONS

The results of this preliminary study indicated that the presence of FFC is associated with CPE. Histologic analysis showed that the presence of FFC is associated with a larger CPE compared with the CPE of plaques without FFC.

REFERENCES

1. Hatsukami TS, Yuan C. **MRI in the early identification and classification of high-risk atherosclerotic carotid plaques.** *Imaging Med* 2010;2:63–75
2. Yuan C, Zhang SX, Polissar NL, et al. **Identification of fibrous cap rupture with magnetic resonance imaging is highly associated with recent transient ischemic attack or stroke.** *Circulation* 2002;105:181–85
3. Takaya N, Yuan C, Chu B, et al. **Association between carotid plaque characteristics and subsequent ischemic cerebrovascular events: a prospective assessment with MRI: initial results.** *Stroke* 2006;37:818–23
4. Saba L, Potters F, van der Lugt A, et al. **Imaging of the fibrous cap in atherosclerotic carotid plaque.** *Cardiovasc Intervent Radiol* 2010;33:681–89
5. Watanabe Y, Nagayama M. **MR plaque imaging of the carotid artery.** *Neuroradiology* 2010;52:253–74
6. Hatsukami TS, Ross R, Polissar NL, et al. **Visualization of fibrous cap thickness and rupture in human atherosclerotic carotid plaque in vivo with high-resolution magnetic resonance imaging.** *Circulation* 2000;102:959–64
7. Cai J, Hatsukami TS, Ferguson MS, et al. **In vivo quantitative measurement of intact fibrous cap and lipid-rich necrotic core size in atherosclerotic carotid plaque: comparison of high-resolution, contrast-enhanced magnetic resonance imaging and histology.** *Circulation* 2005;112:3437–44
8. Saba L, Mallarini G. **Fissured fibrous cap of vulnerable carotid plaques and symptomaticity: are they correlated? Preliminary results by using multi-detector-row CT angiography.** *Cerebrovasc Dis* 2009;27:322–27
9. Saba L, Lai ML, Montisci R, et al. **Association between carotid plaque enhancement shown by multidetector CT angiography and histologically validated microvessel density.** *Eur Radiol* 2012;22:2237–45
10. Saba L, Piga M, Raz E, et al. **Carotid artery plaque classification: does contrast enhancement play a significant role?** *AJNR Am J Neuroradiol* 2012;33:1814–17
11. Saba L, Mallarini G. **Carotid plaque enhancement and symptom correlations: an evaluation by using multidetector row CT angiography.** *AJNR Am J Neuroradiol* 2011;32:1919–25
12. Saba L, Mallarini G. **MDCTA in the study of carotid plaque stenosis degree: evaluation of inter-observer agreement.** *AJR Am J Roentgenol* 2008;190:W41–46
13. North American Symptomatic Carotid Endarterectomy Trial Collaborators. **Beneficial effect of carotid endarterectomy in symptomatic patients with high-grade stenosis.** *N Engl J Med* 1991;325:445–53
14. Barnett HJ, Taylor DW, Eliasziw M, et al. **Benefit of carotid endarterectomy in patients with symptomatic moderate or severe stenosis: North American Symptomatic Carotid Endarterectomy Trial Collaborators.** *N Engl J Med* 1998;339:1415–25
15. Rothwell PM, Eliasziw M, Gutnikov SA. **Analysis of pooled data from the randomised controlled trials of endarterectomy for symptomatic carotid stenosis.** *Lancet* 2003;361:107–16
16. Bongartz G, Golding SJ, Jurik AG. **CT quality criteria.** Luxembourg: European Commission; 2004

17. Redgrave JN, Gallagher P, Lovett JK, et al. **Critical cap thickness and rupture in symptomatic carotid plaques: the Oxford Plaque Study.** *Stroke* 2008;39:1722–9
18. Cicha I, Wörner A, Urschel K, et al. **Carotid plaque vulnerability: a positive feedback between hemodynamic and biochemical mechanisms.** *Stroke* 2011;42:3502–10
19. Magge R, Lau BC, Soares BP, et al. **Clinical risk factors and CT imaging features of carotid atherosclerotic plaques as predictors of new incident carotid ischemic stroke: a retrospective cohort study.** *AJNR Am J Neuroradiol* 2013;34:402–09
20. Saba L, Sanfilippo R, Sannia S, et al. **Association between carotid artery plaque volume, composition, and ulceration: a retrospective assessment with MDCT.** *AJR Am J Roentgenol* 2012;199:151–56
21. van Gils MJ, Vukadinovic D, van Dijk AC, et al. **Carotid atherosclerotic plaque progression and change in plaque composition over time: a 5-year follow-up study using serial CT angiography.** *AJNR Am J Neuroradiol* 2012;33:1267–73
22. Paul J, Mbalisike EC, Nour-Eldin NE, et al. **Dual-source 128-slice MDCT neck: radiation dose and image quality estimation of three different protocols.** *Eur J Radiol* 2013;82:787–96

Can Doppler Flow Parameters of Carotid Stenosis Predict the Occurrence of New Ischemic Brain Lesions Detected by Diffusion-Weighted MR Imaging after Filter-Protected Internal Carotid Artery Stenting?

Y. Gunduz, R. Akdemir, L.T. Ayhan, and N. Keser

ABSTRACT

BACKGROUND AND PURPOSE: Carotid angioplasty and stent placement are increasingly being used for the treatment of symptomatic and asymptomatic carotid artery disease. Carotid angioplasty and stent placement carry an inherent risk of distal cerebral embolization, precipitating new brain ischemic lesions and neurologic symptoms. Our purpose was to evaluate the frequency of new ischemic lesions found on diffusion-weighted imaging after protected carotid angioplasty and stent placement and to determine the association of new lesions with ICA Doppler flow parameters.

MATERIALS AND METHODS: Fifty-two patients (mean age, 68 ± 11 years) with 50%–69% ($n = 20$, group 1) and ≥70% ($n = 32$, group 2) internal carotid artery stenosis underwent carotid angioplasty and stent placement with distal filter protection. DWI was performed before and 48 hours after carotid angioplasty and stent placement.

RESULTS: Thirty-three (63.4%) patients showed new lesions. The average number of new postprocedural lesions was 3.4 per patient. Most of the postprocedural lesions were <5 mm (range, 3–23 mm), cortical and corticosubcortical, and clinically silent. Group 2 had a significantly higher number of new lesions compared with group 1 ($P < .001$). A significant relationship was found between ICA Doppler flow parameters and the appearance of new lesions.

CONCLUSIONS: The appearance of new ischemic lesions was significantly related to the Doppler flow parameters, particularly peak systolic velocity.

ABBREVIATIONS: CAS = carotid artery stenting; CCA = common carotid artery; EDV = end-diastolic velocity; PSV = peak systolic velocity

Stroke is the most common life-threatening neurologic disorder and the most important single cause of disability.[1,2] Carotid artery stenosis, a major risk factor for stroke, and distal embolization, arising from degenerative breakdown or thrombotic occlusion of complex plaques, are important mechanisms of stroke in patients with atherosclerotic internal carotid artery stenosis.[3-6] Duplex sonography is currently the principal and, undoubtedly, the most accurate noninvasive and inexpensive diagnostic technique available for the evaluation of internal carotid artery stenosis. It provides information about the presence and severity of carotid stenosis, the velocity and characteristics of blood flow, and plaque morphology.[7-10]

Carotid angioplasty and stent placement for severe internal carotid artery stenosis have been introduced as a safe alternative to medical and/or surgical treatment in patients at high risk for surgical procedures.[11,12] However, there is still a major concern regarding its safety because of the risk of distal cerebral embolization during the procedure. Recent technical refinements, therefore, have led to the widespread use of carotid artery stenting (CAS) with cerebral-protection devices, markedly reducing thromboembolic complication rates.[13] Diffusion-weighted MR imaging is a very sensitive and specific technique for diagnosing cerebral ischemia.[14,15] It has been used to detect structural damage of the brain due to cerebral embolism after cerebral angiography, neurointerventional procedures, and carotid endarterectomy.[16,17]

The purpose of our study was to assess, with DWI, the number, size, and location of new brain lesions after protected CAS and to evaluate the association of these new lesion deficits and Doppler flow parameters of ICA.

MATERIALS AND METHODS

Study Population

From July 2010 to April 2013, 72 patients with sonographically significant lesions (diameter stenosis of ≥50%) underwent elective carotid angiography and stent placement in the ICA (40 right,

Received May 30, 2013; accepted after revision August 12.

From the Departments of Radiology (Y.G., L.T.A.) and Cardiology (R.A., N.K.), Sakarya University Medical Faculty, Sakarya, Turkey.

Please address correspondence to Yasemin Gunduz, MD, Department of Radiology, Sakarya University Medical Faculty, 54100, Sakarya, Turkey; e-mail: dryaseminggunduz@yahoo.com

http://dx.doi.org/10.3174/ajnr.A3904

32 left), of which 52 consecutive patients were enrolled and 20 patients were excluded from this study.

The following conditions were exclusion criteria: patients who underwent an urgent carotid artery stent placement for severe neurologic symptoms; those with disabling stroke; lack of compliance; prior carotid intervention; contralateral ICA occlusion; history of heart failure and myocardial infarction 72 hours before CAS; significant thyroid, renal, or hepatic dysfunction; incomplete or poor-quality MR imaging data; and any contraindication for MR imaging examination (pacemaker, claustrophobia).

The carotid angiograms were reviewed by an experienced cardiologist, who determined the severity of each lesion according to the criteria of the North American Symptomatic Carotid Endarterectomy Trial.[18] According to our research protocol, the carotid artery was stented in asymptomatic patients with ≥80% stenosis of the extracranial carotid artery and in symptomatic patients with ≥70% stenosis.

Neurologic examination was performed before and after CAS by an experienced neurologist who was not involved in the CAS procedure. Patients were considered symptomatic in case of a transient ischemic attack, a retinal ischemic event, or an ischemic stroke within the territory of the narrowed carotid artery.

In addition, baseline risk factors for atherosclerosis, age, sex, hypertension, hyperlipidemia, diabetes mellitus, history of ischemic heart disease, and smoking were investigated for each patient.

The study, which complied with the Declaration of Helsinki, was approved by the local ethics committee, and all patients enrolled in the study gave written informed consent.

Carotid Ultrasonography

Baseline carotid ultrasonography was performed between 1 and 30 days before carotid angiography. All participants were examined after a 10-minute rest period to minimize the changes in blood pressure and heart rate to avoid influencing the Doppler parameters. Atherosclerosis of the carotid arteries was assessed by a radiologist who was blinded to the clinical data by using the same Doppler ultrasound device (Aplio MX; Toshiba Medical Systems, Tokyo, Japan). All patients were evaluated initially preprocedurally and postprocedurally with duplex ultrasonography of the ipsi- and contralateral common carotid artery (CCA) and ICA.

ICA atherosclerosis was evaluated by the maximum percentage of diameter reduction recorded by B-mode sonography and by the peak systolic velocity (PSV), end-diastolic velocity (EDV), and ICA/CCA PSV ratio per Doppler ultrasound. Lesion severity was defined as the greatest stenosis observed on either the right or left ICA. Sonography and Doppler findings were classified into 2 categories[19]:

1) Clinically insignificant: ICA stenosis of <50% (normal and noncritical). PSV < 125 cm/s with no signs of the presence of a sonographic atherosclerotic lesion (no plaque or intimal thickening is visible sonographically), correlating to additional criteria, including ICA/CCA PSV ratio < 2.0 and ICA EDV < 40 cm/s.
2) Clinically significant: a) ICA stenosis of 50%–69% (PSV = 125–230 cm/s and the presence of a sonographic atherosclerotic lesion). Additional criteria include an ICA/CCA PSV ratio of 2.0–4.0 and ICA EDV of 40–100 cm/s. b) ICA stenosis of ≥70%, but less than near-occlusion (PSV is >230 cm/s and the presence of a sonographic atherosclerotic lesion). Additional criteria include an ICA/CCA PSV ratio > 4 and ICA EDV > 100 cm/s (Fig 1).

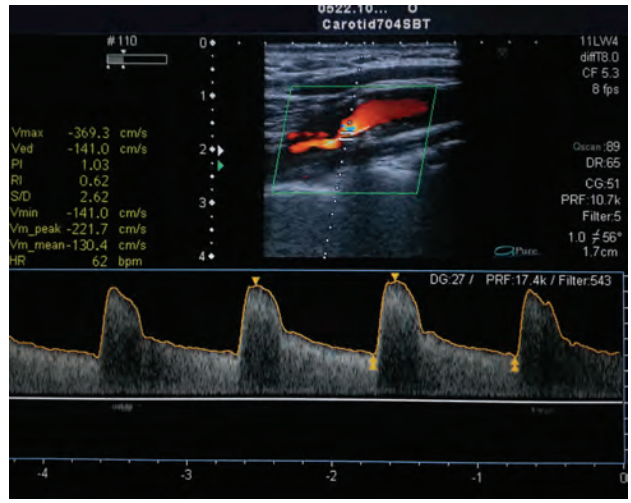

FIG 1. Patient 27, with ≥70% stenosis of the left ICA. Duplex ultrasound image of the ICA shows a high PSV (369 cm/s) and color flow turbulence immediately distal to the stenotic segment, broadening of the pulse wave Doppler spectrum, and a high end-diastolic velocity (141 cm/s).

Patients with total or near-occlusion (defined as 0 PSV and no visible flow total or near-occlusion) were excluded.

Fifty-two patients with 50%–69% ($n = 20$, group 1) and 70%–99% ($n = 32$, group 2) ICA stenosis were treated with protected CAS following a prospective protocol.

Carotid Angiography and Carotid Artery Stent Placement Protocol

All procedures were performed by the femoral approach by using the standard Judikins technique. At least 2 projections of the carotid artery stenosis were obtained for the calculations of vessel diameter and degree of stenosis.

CAS was performed by an experienced interventional cardiologist by using a 0.014-inch platform with a distal embolus protection device (Emboshield NAV6; Abbott Laboratories, Abbott Park, Illinois). The appropriate length and diameter of self-expandable carotid stents (Xact; Abbott Laboratories) were used throughout the study. All stents were implanted from the ICA to the CCA. In case of technical difficulties with primary stent placement, the lesion was predilated before stent placement. After deployment, all stents were dilated with a 5.0- or 6.0-mm balloon (Falcon Grande; Invatec, Roncadelle, Italy). The filter was retrieved through a 4.3F dedicated catheter. A completion angiogram was obtained after removing the protection device. Patients were monitored in the recovery room and, barring any complication, were discharged in 3 days. The procedure was performed by the same experienced operator by using the same stent and the same filter (Fig 2), to keep any potential bias as low as possible.

MR Imaging Protocol

MR imaging was performed 48 hours before and after stent placement and at any time in case of neurologic deterioration (1.5T whole-body scanner, with a dedicated head coil; Signa Horizon; GE Healthcare, Milwaukee, Wisconsin).

DWI scans and the apparent diffusion coefficient maps were used to detect new acute ischemic lesions. A new lesion after CAS was defined as a focal hyperintense area detected by the fluid-

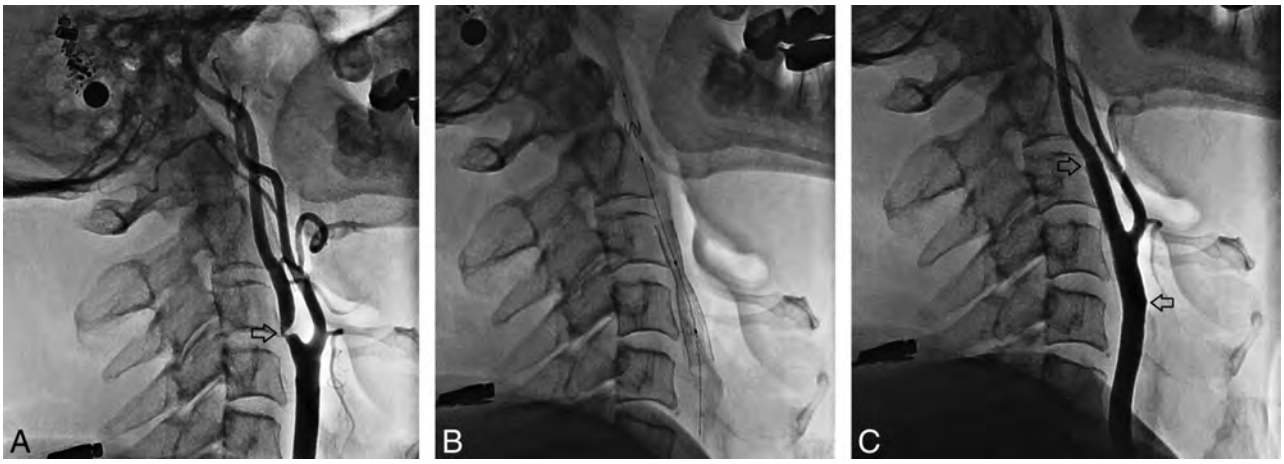

FIG 2. Patient 15. Angiographic sequence of carotid stent placement (a 65-year-old male patient who presented with right hemiplegia and hemiparesis). *A*, Baseline angiography (*arrow* indicates the ICA and CCA) shows 80% ICA stenosis. *B*, A filter was placed. The stent was then extended from the ICA into the CCA. *C*, Angiography after the procedure (*arrows* indicate ICA patency).

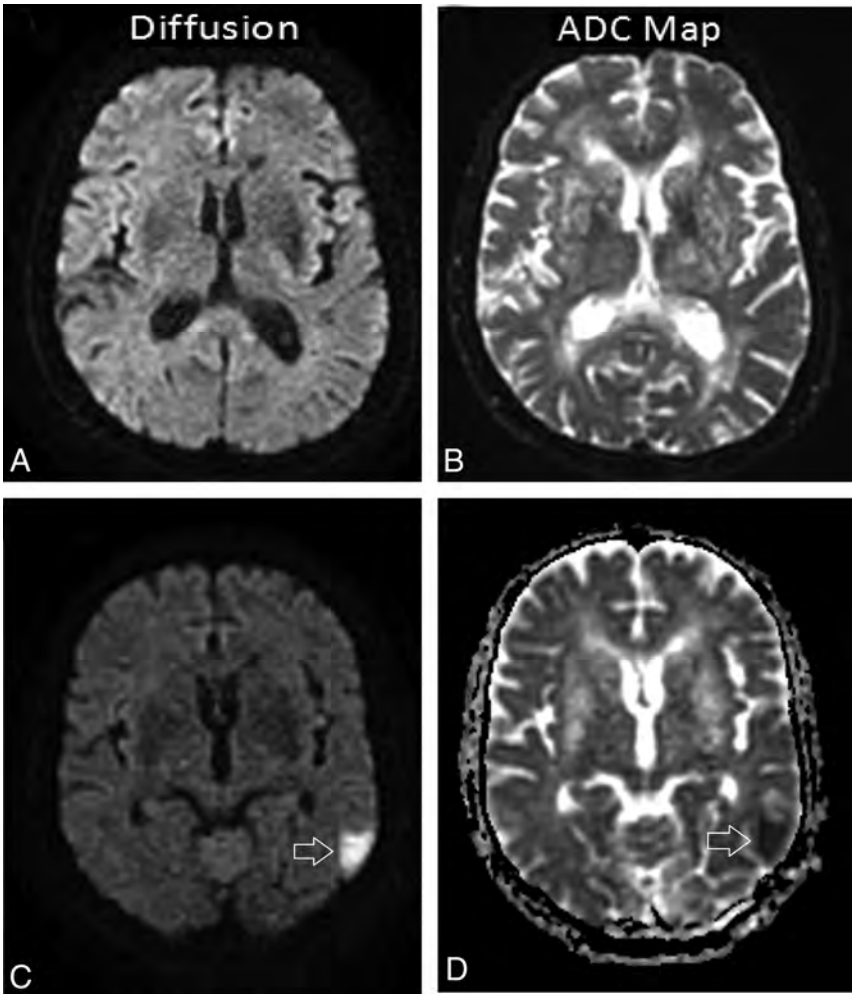

FIG 3. Patient 9, a 58-year-old woman with asymptomatic stenosis (≥80%) of the right ICA. DWI and ADC map images in the 2 days before and the second day after filter-protected stent placement. *A* and *B*, No visible lesion is seen on both images. *C* and *D*, Poststent images demonstrate a single new ischemic lesion in the contralateral temporoparietal cortex (the lesion was hyperintense on the DWI and hypointense on the corresponding ADC map, *arrowhead*).

attenuated inversion recovery sequence, corresponding to a restricted diffusion signal in the DWI sequence and confirmed by apparent diffusion coefficient mapping to rule out shinethrough artifacts. The diffusion-weighted sequence was performed with 2 levels of diffusion sensitization: $b = 0$ and $b = 1000$ s/mm^2. The higher level of diffusion sensitization was replicated in each of the 3 principal gradient directions (x, y, and z planes). The diffusion-weighted images from each of the 3 diffusion-sensitized acquisitions were separately displayed for analysis. Besides DWI, other sequences, which comprised the axial spin-echo T1-weighted image, the fast spin-echo T1-weighted image, the fast spin-echo T2-weighted image, the FLAIR image, the perfusion image, and the contrast-enhanced spin-echo T1-weighted image, were included (Fig 3). On each scan, the number and distribution (cortical, subcortical, or deep white matter) of lesions were recorded. Lesions were classified into 3 groups according to size (<5 mm, 5–10 mm, >10 mm).

Two radiologists counted and recorded the number of new high-signal intensities in the cerebral hemispheres by comparing the pre- and postprocedural DWIs for each CAS procedure without any knowledge of the clinical status.

Concomitant Medical Therapy

All patients were treated with aspirin, 100 mg/day, plus clopidogrel, 75 mg/day, for at least 7 days before CAS and 1 month

Table 1: Baseline characteristics of study patients

Baseline Characteristics	(*n* = 52)
Mean age (yr)	68 ± 11 (53–81)
Male/Female (No.)	37:15
Diabetes mellitus (%)	32
Smoking (%)	42
Hypertension (%)	66
Dyslipidemia (%)	77
Symptomatic (%-No.)	75–39
Coronary artery disease (%)	48
Internal carotid artery, right (*n*)	24
50–69% Stenosis (treated vessel)	20
≥70% Stenosis	32
Mean stenosis, preprocedure (%)	81 ± 21
Mean stenosis, postprocedure (%)	12 ± 7
DWI lesion count per patient (preprocedural)	2.8 ± 1.2
DWI lesion count (new) per patient (postprocedural)	3.4 ± 0.7
Mean lesion length (mm)	16.4 ± 5.1
Mean duration of procedure (min)	29 ± 12

afterward. During CAS, patients received intravenous heparin (5000–10,000 U) to maintain activated clotting time between 250 and 300 seconds. Just before the poststenting dilation phase, atropine (0.5–1 mg IV) was given to most patients to reduce bradycardia and hypotension potentially associated with carotid dilation.

Statistical Analysis

Statistical evaluation was performed by using the Statistical Package for the Social Sciences, Version 17.0, software package for Windows (IBM, Armonk, New York). Quantitative variables are given as mean ± SD, and qualitative variables are expressed as frequency and percentage. Groups were compared by using the Student *t* test for continuous variables and the χ^2 test for categoric variables. When >2 groups were compared for parameters, analysis of variance was used; post hoc analysis was performed by using the Tukey honest significant difference test. Logistic regression models were fitted for new brain lesions detected by DWI–MR frequency and extension as the dependent variable, with adjustment for Doppler parameters of ICA, age, sex, smoking status, hypertension, diabetes mellitus, and hyperlipidemia. For all analyses, a 2-tailed $P \leq .05$ was considered statistically significant.

RESULTS

In this prospective study, we also analyzed angiographic carotid stenosis on the basis of the North American Symptomatic Carotid Endarterectomy Trial criteria.[17] Seventy-two patients underwent elective stent placement in the ICA, of which 52 consecutive patients were enrolled and 20 patients were excluded from the study.

The mean age of the patients was 68 ± 11 years (range, 53–83 years). Coronary artery disease was present in 48% of the patients ($n = 25$), 66% ($n = 29$) had a history of hypertension, 32% ($n = 18$) had diabetes mellitus, 77% ($n = 40$) had a history of dyslipidemia, 42% ($n = 22$) were smokers, and 75% ($n = 39$) were symptomatic. The demographic and clinical characteristics of the patients are presented in Table 1.

Among the patients who underwent carotid stent placement, the preprocedural PSV, EDV, and ICA/CCA ratio in the treated internal carotid artery were 290 ± 57 cm/s, 109 ± 31 cm/s, and 4.0 ± 2.1; and after stent placement, they were 77 ± 24 cm/s, 34 ± 10 cm/s, and 1.4 ± 0.9, respectively. In addition, the preprocedural PSV, EDV, and resistive index in the ipsilateral CCA were 121 ± 41 cm/s, 31 ± 11 cm/s, and 0.75 ± 0.38, whereas after stent placement, they were 107 ± 15 cm/s, 28 ± 7 cm/s, and 0.77 ± 0.38, respectively. A marked decrease in ICA flow parameters was determined, and there was a statistically significant change from before to after ipsilateral stent placement; however, CCA flow parameters (PSV, EDV, and resistive index) did not change after ipsilateral ICA stent placement (Table 2).

Table 2: Comparison of pre- and postprocedural Doppler flow parameters of ICA and CCA

	Preprocedural Doppler Flow	Postprocedural Doppler Flow	*P* Value
ICA PSV (cm/s)	290 ± 57	77 ± 24	<.001
ICA EDV (cm/s)	109 ± 31	34 ± 10	<.001
ICA-CCA ratio	4.0 ± 2.1	1.4 ± 0.9	<.001
CCA PSV (cm/s)	121 ± 41	107 ± 15	.098
CCA EDV (cm/s)	31 ± 11	28 ± 7	.441
CCA RI	0.75 ± 0.38	0.77 ± 0.38	.631

Note:—RI indicates resistive index.

When groups 1 and 2 were compared, the treated internal carotid artery PSV, EDV, and ICA/CCA ratio (212 ± 25 cm/s, 77 ± 19 cm/s, 3.3 ± 0.9, respectively) were significantly lower in group 1 than in group 2 (351 ± 61 cm/s, 133 ± 38 cm/s, 4.8 ± 1.9, respectively). In contrast, the symptomatic patients' number, side of intervention, and carotid plaque length were not significantly different in group 1 versus group 2 patients (Table 3). In addition, sex, hypertension, diabetes, dyslipidemia, and smoking were not significantly different between the 2 groups.

Before the procedure, diffusion-weighted MR images revealed cerebral lesions in 39 (75%) of 52 cases. The average number of preprocedural lesions was 2.8 per patient. After the procedure, new ipsilateral lesions were seen in 29 (55.7%) of 52 cases, and new contralateral lesions were seen in 4 (7.6%). The average number of new postprocedural lesions was 3.4 per patient. Eighteen (54.5%) postprocedural lesions had a diameter of <5 mm, 8 (24.2%) had a diameter of 5–10 mm, and 7 (21.2%) had a diameter of >10 mm on diffusion-weighted images. The size of the lesions in these patients varied from 3 to 23 mm. Twenty-one (63.6%) postprocedural lesions occurred in the cortical and subcortical areas of the brain, and 12 (36.4%) postprocedural lesions were in the deep brain areas. In 29 patients, these new lesions were clinically silent. Four patients, who had new lesions on postprocedural MR images, experienced adverse neurologic events during or immediately after the intervention: 2 patients had a minor stroke, 1 patient had a transient ischemic attack, and 1 patient had transient monocular blindness. There were no deaths or major strokes during the procedure.

When groups 1 and 2 were compared, pre- and postprocedural DWI lesion count per patient and number of patients with new lesions (1.4 ± 0.7, 2.2 ± 19 cm/s, 7, respectively) were significantly lower in group 1 than in group 2 (5.1 ± 0.9, 4.7 ± 2.3 cm/s, 26, respectively). In contrast, symptomatic patients' number, side of intervention, and carotid plaque length did not differ significantly between group 1 and group 2 patients (Table 3). Univariate

Table 3: Comparison of patients with ICA stenosis 50%–69% and >70%; correlation of preprocedural Doppler flow parameters of carotid stenosis and new ischemic brain lesions on DWI after internal carotid artery stenting

Characteristics	50%–69% Stenosis (*n* = 20)	≥70% Stenosis (*n* = 32)	Univariate Analysis, *P* Value	Multivariate Analysis	
				OR	*P* Value
ICA PSV (cm/s)	212 ± 25	351 ± 61	<.001	1.421	<.001
ICA EDV (cm/s)	77 ± 19	133 ± 38	.003	1.024	.021
ICA-CCA ratio	3.3 ± 0.9	4.8 ± 1.9	.007	1.009	.038
Symptomatic (%, No.)	55%–11	87.5%–28	.169	–	–
Patients with new lesions (No.)	7	26	.013	–	–
DWI lesion count per patient (preprocedural)	1.4 ± 0.7	5.1 ± 1.9	<.001	–	–
DWI lesion count (new) per patient (postprocedural)	2.1 ± 0.9	4.7 ± 2.3	<.001	–	–
Side of intervention, right (No.)	10	14	–	–	–
Mean lesion length (mm)	14.8 ± 3.8	17.6 ± 6.1	.451	–	–

analysis revealed that there was no significant correlation between the occurrence of a new DWI lesion and either age, presence of CAD, hypertension, diabetes mellitus, smoking, or hyperlipidemia ($P > .05$). Multivariate analysis revealed a significant correlation between ICA flow parameters, especially PSV, and each of the DWI lesion counts per patient (pre- and postprocedural, Table 3).

Furthermore, technical success (<30% post-CAS diameter stenosis) was achieved in all patients, and postprocedural angiography demonstrated a patent ICA in all patients (Fig 1). The percentage diameter stenosis of the ICA decreased from 81 ± 21% preprocedure to 12 ± 7% postprocedure. Neither dissection nor spasm severe enough to produce ICA flow impairment was observed.

DISCUSSION

We found that Doppler flow parameters (especially PSV) of internal carotid artery stenosis were significantly correlated with periprocedural ischemic events associated with carotid stent placement. In contrast, known atherosclerotic risk factors (age, presence of CAD, hypertension, diabetes mellitus, and hyperlipidemia) were not significantly associated with new DWI lesions. This finding suggests that PSV is an important flow parameter, more specifically applying to stenosis, and a predictive marker of ischemic cerebral lesions.

Several investigators, by using DWI to detect clinically silent embolic lesions after protected CAS, have reported new DWI lesions over a wide range, from 17.3% to 73%.[20] Furthermore, the results from transcranial Doppler monitoring and experimental studies show that embolization may occur in nearly all stent-implantation procedures in the carotid artery.[21] The rate of new DWI lesions in our study was similar compared with these other studies. Of 52 patients, 63% had new lesions after CAS with distal filter protection, and new ischemic lesions were detected in the treated vascular territory in 55% of the patients. Because the protective function of filters is limited to treated vessels, and a certain number of embolic events ipsi- and contralateral to the treated vessels are probably sourced from endovascular procedures,[13] these findings cast doubt on the efficacy of the routine use of filter-type cerebral protection devices.

Clearly, the more complete evaluation of brain injury performed at least 48 hours postprocedure is to be preferred if one is examining the incidence of new lesions on DWI.[22,23] We also used diffusion-weighted MR imaging within 48 hours before and after the procedure. The mean number of new lesions inside the treated vascular territory in our study (3.4 per patient) was higher compared with the reported incidence of between 1.42 and 2.8.[13,20] In agreement with these results, most were at the cortical and corticosubcortical area and <5 mm. The clinical importance of asymptomatic cerebral microemboli is still unclear.[16,21] In our series, most of (29 of 33) the patients with new postprocedural DWI lesions were neurologically asymptomatic, and only the neurologic status of 4 patients changed within 48 hours after CAS.

In patients with carotid stenosis, microembolism has been related to the degree of carotid narrowing and to the ulcerated appearance of the plaque.[6,24,25] Sterpetti et al[26] examined prospectively 214 consecutive patients referred to a vascular laboratory and found that a degree of stenosis of >50% was an independent predictor of new cerebrovascular events. Until now, to our knowledge, no study has been published that specifically evaluated the relationship between DWI findings after protected CAS and Doppler flow parameters of ICA. We found a significant relationship between ICA Doppler flow parameters, especially PSV, and the appearance of new lesions. Moreover, patients with ≥70% stenosis had a significantly higher number of new lesions compared with patients with 50%–69% stenosis. The most plausible reason for the relation between the frequency of ischemic lesions and Doppler flows of the stenotic ICA segment is that the higher the flow of stenotic ICA, the more plaque formation and solid emboli source.

The present study shows that known cardiovascular risk factors such as age, blood pressure, and cholesterol levels were not significantly related to ischemic cerebrovascular events detected by DWI. However, PSV, EDV, and the ICA/CCA ratio and pre- and postprocedural DWI lesions per patient were significantly different in univariate analysis. Most interesting, in multivariate analysis, these Doppler parameters were significant predictors of cerebrovascular events. Thus, in our opinion, an accurate determination of Doppler flow data of carotid artery stenosis may be useful to plan medical or/and interventional therapy for the primary as well as for secondary prevention of cerebrovascular events.

Limitations

This is a single-center study. In line with our finding, the use of cerebral protection devices does not appear to significantly reduce the number of new ipsilateral DWI lesions after CAS. The number of patients, however, was too small to allow investigation by using

a full regression model, though association between the occurrence of new DWI lesions and Doppler flow characteristics and cross-validation may be needed.

CONCLUSIONS

Our data showed that CAS is associated with a high number of new ischemic lesions at cerebral MR imaging, of which most are clinically silent. We believe that the use of Doppler parameters plays a crucial role in the accurate assessment of the degree of ICA stenosis and in the prediction of new ischemic DWI lesions. The examination of a larger patient population and the analysis of Doppler flow parameters showing varying degrees of stenosis may allow identification of patients who have a high rate of positive findings on postprocedural diffusion-weighted images.

REFERENCES

1. Poungvarin N. **Stroke in the developing world.** *Lancet* 1998; 352(suppl 3):SIII19–22
2. Alam I, Haider I, Wahab F, et al. **Risk factors stratification in 100 patients of acute stroke.** *J Postgrad Med Inst* 2004;18:583–91
3. Strickman NE, Loyalka P. **Carotid artery stenosis: an endovascular specialist's perspective.** *Tex Heart Inst J* 2005;32:318–22
4. Siebler M, Sitzer M, Rose G, et al. **Silent cerebral embolism caused by neurologically symptomatic high-grade carotid stenosis.** *Brain* 1993;116:1005–15
5. Siebler M, Kleinschmidt A, Sitzer M, et al. **Cerebral microembolism in symptomatic and asymptomatic high-grade internal carotid artery stenosis.** *Neurology* 1994;44:615–18
6. Sitzer M, Muller W, Siebler M, et al. **Plaque ulceration and lumen thrombus are the main sources of cerebral microemboli in high-grade internal carotid artery stenosis.** *Stroke* 1995;26:1231–33
7. Heijenbrok-Kal MH, Nederkoorn PJ, Buskens E, et al. **Diagnostic performance of duplex ultrasound in patients suspected of carotid artery disease: the ipsilateral versus contralateral artery.** *Stroke* 2005;36:2105–09
8. Ota H, Takase K, Rikimaru H, et al. **Quantitative vascular measurements in arterial occlusive disease.** *Radiographics* 2005;25:1141–58
9. Shaikh NA, Bhatty S, Irfan M, et al. **Frequency, characteristics and risk factors of carotid artery stenosis in ischaemic stroke patients at Civil Hospital Karachi.** *J Pak Med Assoc* 2010;60:8–12
10. Tahmasebpour HR, Buckley AR, Cooperberg PL, et al. **Sonographic examination of the carotid arteries.** *Radiographics* 2005;25:1561–75
11. Demarin V, Lovrencić-Huzjan A, Basić S, et al. **Croatian Society for Neurovascular Disorders; Croatian Society of Neurology; Croatian Society of Ultrasound in Medicine and Biology; Croatian Society of Radiology; Croatian Society of Vascular Surgery; Croatian Society of Neurosurgery: recommendations for the management of patients with carotid stenosis**. *Acta Clin Croat* 2010;49:101–18
12. Liapis CD, Bell PR, Mikhailidis D, et al, for the ESVS Guidelines Collaborators**. ESVS guidelines: invasive treatment for carotid stenosis: indications, techniques.** *Eur J Vasc Endovasc Surg* 2009; 37(4 Suppl):1–19
13. Piñero P, González A, Mayol A, et al. **Silent ischemia after neuroprotected percutaneous carotid stenting: a diffusion-weighted MRI study.** *AJNR Am J Neuroradiol* 2006;27:1338–45
14. Marks MP, De Crespigny A, Lentz D, et al. **Acute and chronic stroke: navigated spin-echo diffusion-weighted MR imaging.** *Radiology* 1996;199:403-08
15. González RG, Schaefer PW, Buonanno FS, et al. **Diffusion-weighted MR imaging: diagnostic accuracy in patients imaged within 6 hours of stroke symptom onset.** *Radiology* 1999; 210:155-62
16. Bendszus M, Koltzenburg M, Burger R, et al. **Silent embolism in diagnostic cerebral angiography and neurointerventional procedures: a prospective study.** *Lancet* 1999;354:1594–97
17. Britt PM, Heiserman JE, Snider RM, et al. **Incidence of postangiographic abnormalities revealed by diffusion-weighted MR imaging.** *AJNR Am J Neuroradiol* 2000;21:55–59
18. North American Symptomatic Carotid Endarterectomy Trial Collaborators. **Beneficial effect of carotid endarterectomy in symptomatic patients with high-grade carotid stenosis.** *N Engl J Med* 1991;325:445–53
19. Grant EG, Benson CB, Moneta GL, et al. **Carotid artery stenosis: gray-scale and Doppler US diagnosis—Society of Radiologists in Ultrasound Consensus Conference.** *Radiology* 2003;229:340–46
20. Stojanov D, Ilic M, Bosnjakovic P, et al. **New ischemic brain lesions on diffusion-weighted MRI after carotid artery stenting with filter protection: frequency and relationship with plaque morphology.** *AJNR Am J Neuroradiol* 2012;33:708–14
21. Jaeger HJ, Mathias KD, Hauth E, et al. **Cerebral ischemia detected with diffusion-weighted MR imaging after stent implantation in the carotid artery.** *AJNR Am J Neuroradiol* 2002;23:200–07
22. Kastrup A, Nagele T, Groschel K, et al. **Incidence of new brain lesions after carotid stenting with and without cerebral protection.** *Stroke* 2006;37:2312–16
23. du Mesnil de Rochemont R, Schneider S, Yan B, et al. **Diffusion-weighted MR imaging lesions after filter-protected stenting of high-grade symptomatic carotid artery stenoses.** *AJNR Am J Neuroradiol* 2006;27:1321–25
24. Eicke B, von Lorentz J, Paulus W. **Embolus detection in different degrees of carotid disease.** *Neurol Res* 1995;17:181–84
25. Valton L, Larrue V, Arrué P, et al. **Asymptomatic cerebral embolic signals in patients with carotid stenosis: correlation with appearance of plaque ulceration on angiography.** *Stroke* 1995;26:813–15
26. Sterpetti AV, Schultz RD, Feldhaus RJ, et al. **Ultrasonographic features of carotid plaque and the risk of subsequent neurologic deficits.** *Surgery* 1988;104:652–60

Predicting Carotid Plaque Characteristics Using Quantitative Color-Coded T1-Weighted MR Plaque Imaging: Correlation with Carotid Endarterectomy Specimens

S. Narumi, M. Sasaki, H. Ohba, K. Ogasawara, M. Kobayashi, T. Natori, J. Hitomi, H. Itagaki, T. Takahashi, and Y. Terayama

ABSTRACT

BACKGROUND AND PURPOSE: MR plaque imaging is used to evaluate the risk of embolic complications during carotid endarterectomy and carotid artery stent placement. However, its performance for characterizing intraplaque components has varied across studies and is generally suboptimal. Hence, we correlated MR imaging results with histologic findings to determine whether a combination of high-contrast T1-weighted imaging and quantitative image analysis could readily determine plaque characteristics.

MATERIALS AND METHODS: We prospectively examined 40 consecutive patients before carotid endarterectomy by using a 1.5T scanner and axial T1-weighted spin-echo images under optimized scanning conditions. The percentage areas of intraplaque fibrous tissue, lipid/necrosis, and hemorrhage were calculated automatically by using the software with previously reported cutoff values and were compared with those of the specimens. The thickness of the fibrous cap was also measured manually.

RESULTS: The percentage areas of fibrous, lipid/necrotic, and hemorrhagic components were 5.7%–98.7%, 1.3%–65.7%, and 0%–82.0%, respectively, as determined by the MR images, whereas the corresponding values were 4.8%–92.3%, 7.0%–93.8%, and 0%–70.4%, respectively, as determined by histologic examination. Significant positive correlation and agreement were observed between MR images and histologic specimens (r = 0.92, 0.79, and 0.92; intraclass correlation coefficients = 0.91, 0.67, and 0.89; respectively). Thickness of the fibrous caps on MR images (0.21–0.87 mm) and in the specimens (0.14–0.83 mm) also showed positive correlation and agreement (r = 0.61, intraclass correlation coefficient = 0.59).

CONCLUSIONS: Quantitative analysis of high-contrast T1-weighted images can accurately evaluate the composition of carotid plaques in carotid endarterectomy candidates.

ABBREVIATIONS: ICC = intraclass correlation coefficient; SE = spin-echo

Estimation of the composition of carotid plaques is important to help identify the risk of embolic events during carotid endarterectomy or carotid artery stent placement. Ultrasonography has commonly been used for this purpose, but it is not useful in cases of extensive calcification or if the plaque is in a higher location; furthermore, ultrasonography lacks reliable and versatile quantitative metrics.[1-4] Thus, as a complement to ultrasonography, MR plaque imaging is now widely used to estimate plaque composition. However, plaque characterization remains unsatisfactory, presumably owing to the deterioration of image contrast, secondary to inappropriate scanning techniques and/or protocols.[5] Recently, a nongated T1-weighted spin-echo (SE) technique with appropriately fixed scanning parameters was reported to improve and stabilize intraplaque contrast, compared with a cardiac-gated black-blood fast spin-echo technique in which T1-weighting tended to be attenuated and fluctuated according to a heart-rate-dependent setting of the TR.[6] The nongated T1-weighted spin-echo method has been found to allow accurate estimation of the main plaque components with minimal overlap,[7] suggesting potential advantages over other imaging modalities in terms of plaque characterization. However, quantitative evaluation of intraplaque composition has not been achieved by this method. Hence, in the present study, we used a quantitative color-coded image-analysis software to characterize intraplaque distribution by percentage

Received April 23, 2013; accepted after revision July 27.

From the Department of Neurology and Gerontology (S.N., H.O., T.N., Y.T.), Institute for Biomedical Sciences (M.S.), Department of Neurosurgery (K.O., M.K.), and Department of Anatomy (J.H.), Iwate Medical University, Morioka, Japan; and Hitachi Medical Corporation (H.I., T.T.), Tokyo, Japan.

This work was partly supported by a Grant-in-Aid for Strategic Medical Science Research from the Ministry of Education, Culture, Sports, Science and Technology of Japan.

Please address correspondence to Shinsuke Narumi, MD, Department of Neurology, Iwate Medical University, 19-1 Uchimaru, Morioka 020-8505, Japan; e-mail: snarumi@iwate-med.ac.jp

http://dx.doi.org/10.3174/ajnr.A3741

area of fibrous, lipid/necrotic, and hemorrhagic tissues and to determine the accuracy of this method for predicting plaque characteristics by correlating the results with histologic findings from the carotid endarterectomy specimens.

MATERIALS AND METHODS

Patients

From April 2009 to July 2010, we prospectively examined 40 consecutive male patients (age range, 59–82 years; mean age, 69.5 years) with stenosis of the cervical internal carotid artery, all of whom underwent carotid endarterectomy. Of these patients, 30 had symptomatic stenosis of ≥70%, and 10 others had asymptomatic stenosis of ≥80%. The clinical profiles of the patients included hypertension in 38 patients, hyperlipidemia in 22, and diabetes mellitus in 13. All of the study examinations were carried out after obtaining approval from the institutional review board and written informed consent from the patients.

Imaging Protocol

Axial 2D SE T1-weighted images of the affected carotid bifurcation were obtained by using a 1.5T MR imaging scanner (Echelon Vega; Hitachi Medical, Tokyo, Japan) and an 8-channel neurovascular coil. The pulse sequence parameters were as follows: TR/ TE, 500 /12 ms; FOV, 18 cm; section thickness, 4.0 mm with an intersection gap of 1 mm; number of sections, 9; and NEX, 2. A radial *k*-space acquisition technique with self-navigation, which is similar to the periodically rotated overlapping parallel lines with enhanced reconstruction method, was used for motion correction.[8] In this technique, 40 radially rotating blades with 10 parallel phase-encoding lines and readout encoding of 256 steps, which caused oversampling at the center of the *k*-space, were obtained (acquisition time: 6 minutes 46 seconds), and mutual phase corrections among the blades were performed as a self-navigation for compensating nonrigid motions. After rebinning to Cartesian coordinates with zero-fill interpolation, images with a matrix size of 512 × 512 (apparent pixel size, 0.35 × 0.35 mm) were obtained. Chemical shift selective saturation pulses within the planes and nonselective saturation pulses at the superior and inferior sides were used as fat-suppression and black-blood techniques, respectively. The section direction was carefully set in a plane perpendicular to the long axis of the carotid bifurcation on sagittal 2D phase-contrast MR angiographic images.

Histologic Preparation

Specimens excised en bloc from the affected carotid arteries were submitted for histologic evaluation. The specimens were fixed in formaldehyde, and transverse sections of the carotid bifurcations that were carefully cut to correspond in direction and position to those of the MR images were obtained. During histologic preparation, hematoxylin-eosin, Masson trichrome, and antiglycophorin-A stains were applied to paraffin-embedded 7-μm-thick sections.

Data Processing and Statistical Analyses

Data processing was performed by one of the authors (S.N.) who was blinded to the clinical and imaging findings. The MR image data the from the DICOM files for the sections of the maximum plaque size were transferred to the plaque analysis software package (PlaqueViewer; Hitachi Medical), which automatically divided internal areas of the plaques into 3 color-coded components (ie, fibrous tissue, green; lipid/necrosis, yellow; and hemorrhage, red) according to the contrast ratios of the plaques to the adjacent muscle, with the cutoff values of 1.17 (fibrous versus lipid/necrosis) and 1.55 (lipid/necrosis versus hemorrhage) that were obtained in a previous study.[7] Next, the percentage areas of each component were automatically calculated. In addition, in patients with yellow and/or red areas within the plaques suggesting lipid/necrotic and/or hemorrhagic components, the thickness of the fibrous cap, shown as the green area between the yellow/red area and the adjacent arterial lumen, was manually measured on the color-coded images 3 times by using a linear cursor and the values were averaged.

On the specimen sections that corresponded to the MR images, the same blinded operator measured areas of fibrous, lipid/necrotic, and hemorrhagic tissue as well as the thicknesses of fibrous caps 3 times through a manual tracing method by using a software package (ImageJ, Version 1.44; National Institutes of Health, Bethesda, Maryland), and the values were averaged.

For statistical analyses, Pearson correlation coefficients (*r*) and intraclass correlation coefficients (ICCs) were assessed to determine correlation and agreement between the percentage areas of each component and the thickness of the fibrous caps in the color-coded MR images and the specimens. The ICC was also used to determine intraoperator agreements for the manual measurements.

Percentage of areas of intraplaque components and fibrous cap thicknesses on color-coded MR images and histologic specimens[a]

	MR Images	Specimens	*r*	ICC
Fibrous tissue (%)	5.7–98.7 (24.7)	4.8–92.3 (21.0)	0.92	0.91
Lipid/necrosis (%)	1.3–65.7 (22.2)	7.0–93.8 (33.8)	0.79	0.67
Hemorrhage (%)	0–82.0 (41.0)	0–70.4 (35.8)	0.92	0.89
Fibrous cap (mm)	0.21–0.87 (0.47)	0.14–0.83 (0.45)	0.61	0.59

Note:—*r* indicates the Pearson correlation coefficient.
[a] Data are presented as range (median).

RESULTS

Six patients were excluded because of substantial motion artifacts, and the remaining 34 patients (mean age, 70.2 years) were eligible for further analysis. The ICCs of manual measurements for MR images and histologic specimens were 0.99 and 0.99, respectively, indicating excellent intraoperator agreements.

The percentage areas of fibrous tissue, lipid/necrosis, and hemorrhage on the color-coded MR images ranged from 5.7% to 98.7% (median, 24.7%), 1.3% to 65.7% (22.2%), and 0% to 82.0% (41.0%), respectively, while those on the histologic specimens ranged from 4.8% to 92.3% (21.0%), 7.0% to 93.8% (33.8%), and 0% to 70.4% (35.8%), respectively. Excellent or good positive correlation and agreement were observed between the color-coded maps and the specimens ($r = 0.92$, 0.79, and 0.92; ICC = 0.91, 0.67, and 0.89, respectively) (Table and Figs 1 and 2).

The thickness of the fibrous caps on MR images was measurable in 25 patients and ranged from 0.21 to 0.87 mm (median, 0.47 mm), while that in the corresponding histologic specimens

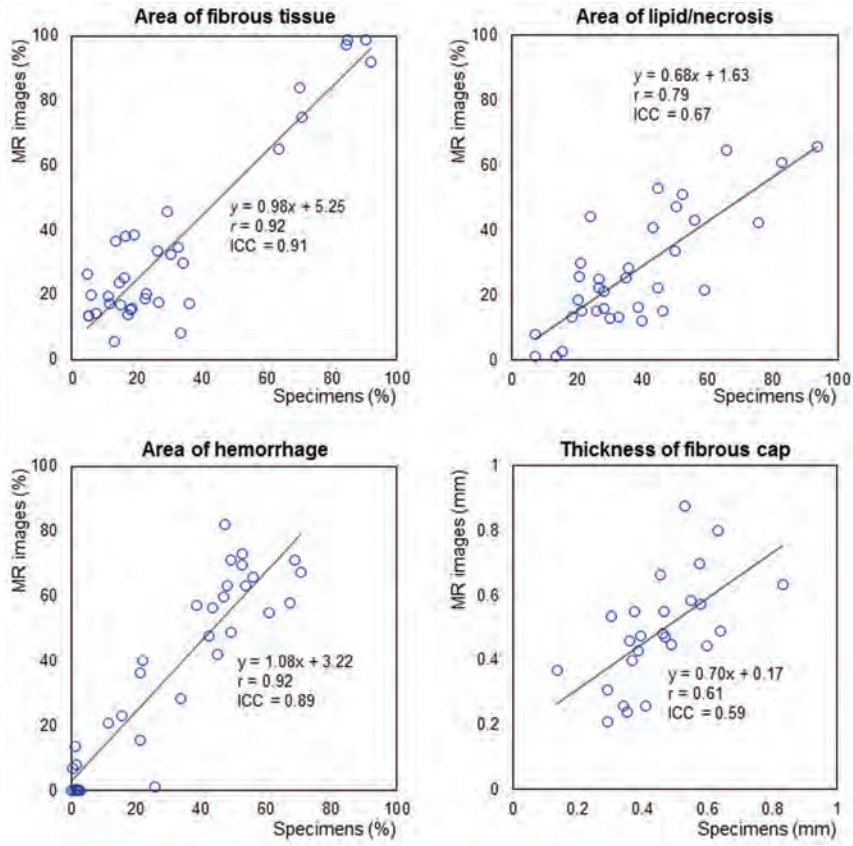

FIG 1. Correlation and agreement between percentage area of intraplaque components and fibrous cap thickness observed in MR images and histologic specimens. Excellent positive correlation and agreement were observed between the percentage areas of the fibrous tissue and hemorrhagic areas within the plaque determined on MR images and histologic specimens. Percentage areas of lipid/necrosis and thickness of the fibrous cap also showed good correlation and agreement. *r* indicates the Pearson correlation coefficient.

was 0.14–0.83 mm (0.45 mm), and these results also showed positive correlation and agreement ($r = 0.61$, ICC = 0.59) (Table and Figs 1 and 2).

DISCUSSION

Unstable (or vulnerable) plaques are usually defined as plaques mainly consisting of lipid/necrosis or hemorrhage with a thin fibrous cap because plaque rupture and subsequent release of embolic materials into distal blood flow can more easily occur in these plaques than in more stable plaques consisting mainly of fibrous tissue.[9-11] Several imaging modalities have been used to detect unstable plaques by characterizing intraplaque features. Unstable plaques are characterized by mobility and/or low echogenicity on ultrasonography, low attenuation on CT, and hyperintensity on MR imaging.[1-7,11-15] However, the diagnostic performance of all of these modalities varies considerably and remains imperfect.

In this study, we used SE T1-weighted MR images as the source data for quantitative evaluation of carotid plaques. Various imaging protocols and techniques have been applied in MR plaque imaging, and the results in previous reports have varied.[5,7,10-13,16,17] Of these protocols, an electrocardiograph-gated 2D fast SE technique with a black-blood method is commonly applied.[10,16] However, this method is generally complicated and time-consuming and can obtain only a few sections of imaging. In this method, moreover, the heart rate of patients forces the TR to be inappropriate, resulting in deterioration of image contrast.[6,7,17] A magnetization-prepared rapid acquisition of gradient echo technique has also been widely used.[18,19] In this technique, however, an inversion pulse for suppressing the blood signal is nonspecific and can attenuate the signal of the lipid/necrotic component that has T1 relaxation times similar to those of blood.

Source images of 3D time-of-flight MR angiography have also been used in several studies.[10,17,20,21] This technique can provide stable T1-related contrast but no black-blood effects, suggesting that it would be unsuitable for quantitative analysis based on signal intensity. Recently, a direct comparison of the 4 techniques revealed that the T1-weighted SE technique showed excellent intraplaque contrast and could accurately characterize the main intraplaque components.[17] Furthermore, the T1-weighted SE technique combined with the quantitative color map software package is reported to allow clinicians to monitor changes in intraplaque components during medical treatment.[22] Hence, we selected a T1-weighted SE technique from among the various MR imaging options to obtain source images for automated quantitative analysis of intraplaque composition. We believe this choice is one of the factors that allowed this study to achieve good correlation and agreement of MR imaging and histologic findings, and these results are comparable with those of previous studies in which multicontrast MR images were used.[16,17]

In addition to automated estimation of intraplaque components, we attempted to measure the thickness of the fibrous caps because the caps are also considered important for predicting vulnerability of carotid plaques. As a rule, ruptured plaques tend to have thin fibrous caps compared with unruptured plaques.[23-25] In previous studies, high-resolution source images of 3D time-of-flight MR angiography or contrast-enhanced T1-weighted images have been evaluated to estimate fibrous cap thickness and have provided good correlation and agreement with histologic findings[26]; compared with the findings of these studies, our results were unsatisfactory, presumably owing to limited contrast between lipid/necrotic and fibrous tissues and low spatial resolution. Nonetheless, the method was noninvasive and simple.

This study has several limitations. First, only a nongated T1-weighted SE sequence was used for the quantitative analyses, because this sequence showed the best performances to characterize intraplaque components compared with other various T1-weighted, proton-attenuation-weighted, and T2-weighted se-

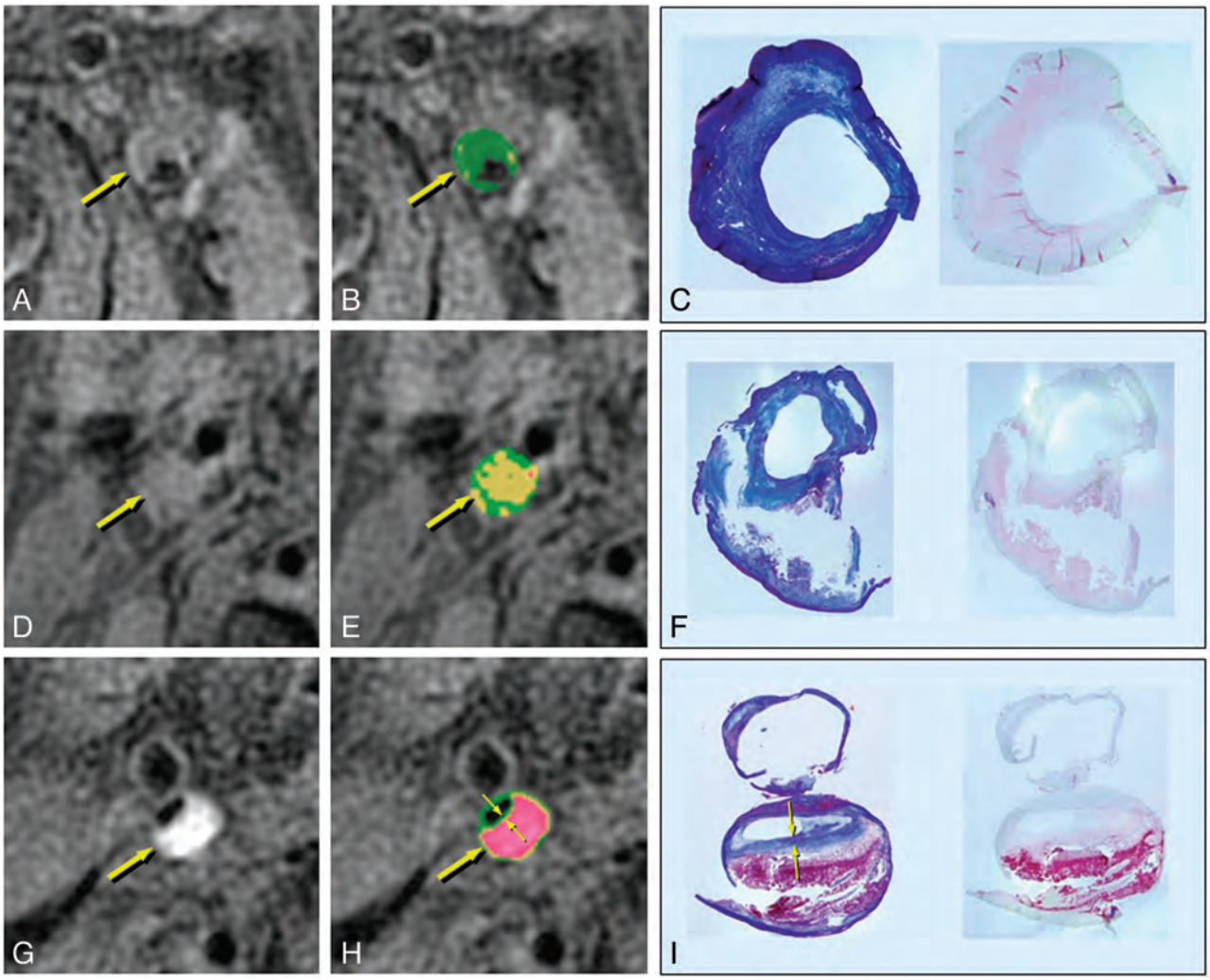

FIG 2. MR imaging and histologic findings of the carotid plaques. *A*, *D*, *G*, T1-weighted images. *B*, *E*, *H*, Color-coded maps. *C*, *F*, *I*, Corresponding histologic specimens (left, Masson trichrome staining; right, antiglycophorin-A staining). *A–C*, Left carotid stenosis in a 70-year-old man. The plaque shows isointensity to adjacent muscle on the T1-weighted image (*A*, *arrow*) and is mainly green on the color-coded map (*B*, *arrow*), suggesting a fibrous composition. On histologic examination, the corresponding plaque specimens consist mainly of thick fibrous tissue (*C* and *D*). The percentage areas of the fibrous, lipid/necrotic, and hemorrhagic components are 97%, 3%, and 0%, respectively, on MR images and 85%, 15%, and 0%, respectively, in the histologic specimens. *D–F*, Right carotid stenosis in a 68-year-old man. The plaque shows slight hyperintensity on the T1-weighted image (*D*, *arrow*) and is mainly yellow on the color map (*E*, *arrow*), suggesting a lipid-rich plaque. The corresponding plaque specimens contained lipid and necrotic tissue that flowed out of the specimen during the tissue preparation (*F*). The percentage areas of the fibrous, lipid/necrotic, and hemorrhagic components are 35%, 64%, and 1%, respectively, on the MR images, and 33%, 66%, and 1%, respectively, in the corresponding specimens. *G–I*, Right carotid stenosis in a 74-year-old man. The plaque shows marked hyperintensity on the T1-weighted image (*G*, *arrow*) and red on the color map (*H*, *arrow*), suggesting intraplaque hemorrhage. In the corresponding pathology specimens, the plaque contains massive hemorrhage with a thin fibrous cap (*I*). The percentage areas of fibrous, lipid/necrotic, and hemorrhagic components are 17%, 13%, and 70%, respectively, on MR imaging, and 15%, 33%, and 52%, respectively, in the specimens. The fibrous cap thicknesses on the MR images (*H*, *small arrows*) and in the specimen (*I*, *small arrows*) are 0.47 and 0.39 mm, respectively. (*C,F,* and *I*, 3x magnification.)

quences and was eligible for quantitative analyses in the previous studies.[6,7,17,22] On T1-weighted images, the contrast between fibrous and hemorrhagic components is evident because the latter usually has very short T1 relaxation times. In contrast, even when using the most appropriate sequence, the difference in signal intensity between fibrous and lipid/necrotic components tends to be subtle because the T1 relaxation times of these components are similar. This phenomenon can lead to underestimation of the extent of lipid/necrotic tissue and, presumably, is the reason for diminished correlation and agreement for lipid/necrotic areas between MR images and histology specimens in the present study. This issue might be resolved by combining T1-weighted images with other images (eg, T2-weighted images) on which lipid and necrosis show marked hyperintensity compared with fibrous tissues.[5,7] For this purpose, a sophisticated program that can handle multiple source data is needed, which we are now developing.

Second, we did not assess the calcific component, which is said to be one of the stable components, of the plaques because calcific regions are barely visualized on MR images by the SE technique used in this study, which is known to be insensitive to calcification; furthermore, the histologic specimens were decalcified during preparation. This limitation may lead to substantial error in the automated analyses applied in this study. To overcome this limitation, susceptibility-sensitive MR imaging techniques such

as T2*-weighted imaging, as well as tissue preparation without decalcification, will be needed.

Another limitation involves a technical issue. In this study, 2D images with relatively low spatial resolution were obtained by using the 1.5T scanner and a standard neurovascular coil, and this could have caused substantial errors in quantitative analysis and manual measurement owing to partial volume effects and spatial mismatches with the histologic sections of the specimen. To improve the precision of quantitative analysis of plaque composition and fibrous cap thickness as well as the spatial correspondence between the MR and histologic images, high-field MR imaging scanners and sophisticated 3D imaging techniques with excellent contrast (eg, 3D-T1-weighted FSE), which we are planning to use, are required.[27] Finally, we did not investigate whether the quantitative imaging findings correlate with stroke or other adverse events during or after carotid endarterectomy or whether these findings are different between symptomatic or asymptomatic patients because these issues are beyond the scope of this study. Hence, this study provided no direct evidence for prediction of stroke events and perisurgical complications, though the results suggest that the method we used is promising for this purpose. A prospective study to investigate this issue is now ongoing with a larger cohort and the similar imaging protocols.

CONCLUSIONS

Quantitative color-coded analyses applying nongated T1-weighted SE images can readily predict the composition of carotid plaques, particularly the percent areas of fibrous and hemorrhagic components, in patients who are carotid endarterectomy candidates.

Disclosures: Shinsuke Narumi—*RELATED*: *Grant*: Grant-in-Aid for Strategic Medical Science Research and Grants-in-Aid for Science Research (22890169) from the Ministry of Education, Culture, Sports, Science and Technology of Japan.* Makoto Sasaki—*RELATED*: *Grant*: Grant-in-Aid for Strategic Medical Science Research from the Ministry of Education, Culture, Sports, Science and Technology of Japan,* *Consulting Fee or Honorarium*: Hitachi Medical, *Comments*: M.S. is a consultant for Hitachi Medical Corporation and has received honoraria from them, *UNRELATED*: *Consultancy*: Lundbek, *Payment for Lectures (including service on Speakers Bureaus)*: GE Healthcare, Daiichi, Mitsubishi, Ohtsuka, Sanofi, Johnson & Johnson, Ezai. Jiro Hitomi—*UNRELATED*: *Grants/Grants Pending*: Japanese Ministry of Health, Labour, and Welfare,* *Comments*: projects for the promotion of the indigenous creation and development of innovative medical devices in the Tohoku area. Tetsuhiko Takahashi—*UNRELATED*: *Employment*: Hitachi Medical Corporation. Yasuo Terayama—*UNRELATED*: *Grants/Grants Pending*: Grant-in-Aid for Scientific Research,* Health Labour Sciences Research Grant,* *Payment for Lectures (including service on Speakers Bureaus)*: Sanofi K.K., Otsuka Pharmaceutical. Hiryuki Itagaki is an employee of Hitachi Medical Corporation. *Money paid to the institution.

REFERENCES

1. Waki H, Masuyama T, Mori H, et al. **Ultrasonic tissue characterization of the atherosclerotic carotid artery: histological correlates or carotid integrated backscatter.** *Circulation* 2003;67:1013–16
2. Sztajzel R, Momjian S, Momjian-Mayor I, et al. **Stratified gray-scale median analysis and color mapping of the carotid plaque: correlation with endarterectomy specimen histology of 28 patients.** *Stroke* 2005;36:741–45
3. Mathiesen EB, Bonaa KH, Joakimsen O. **Echolucent plaques are associated with high risk of ischemic cerebrovascular events in carotid stenosis: the Tromsø study.** *Circulation* 2001;103:2171–75
4. Kagawa R, Moritake K, Shima T, et al. **Validity of B-mode ultrasonographic findings in patients undergoing carotid endarterectomy in comparison with angiographic and clinicopathologic features.** *Stroke* 1996;27:700–05
5. Watanabe Y, Nagayama M, Suga T, et al. **Characterization of atherosclerotic plaque of carotid arteries with histopathological correlation: vascular wall MR imaging vs. color Doppler ultrasonography (US).** *J Magn Reson Imaging* 2008;28:478–85
6. Narumi S, Sasaki M, Ohba H, et al. **Altered carotid plaque signal among different repetition times on T1-weighted magnetic resonance plaque imaging with self-navigated radial-scan technique.** *Neuroradiology* 2010;52:285–90
7. Narumi S, Sasaki M, Ohba H, et al. **Prediction of carotid plaque characteristics using non-gated MR imaging: correlation with endarterectomy specimens.** *AJNR Am J Neuroradiol* 2013;34:191–97
8. Pipe JG. **Motion correction with PROPELLER MRI: application to head motion and free-breathing cardiac imaging.** *Magn Reson Med* 1999;42:963–69
9. Altaf N, MacSweeney ST, Gladman J, et al. **Carotid intraplaque hemorrhage predicts recurrent symptoms in patients with high-grade carotid stenosis.** *Stroke* 2007;38:1633–35
10. Takaya N, Yuan C, Chu B, et al. **Association between carotid plaque characteristics and subsequent ischemic cerebrovascular events: a prospective assessment with MRI–initial results.** *Stroke* 2006;37:818–23
11. Yoshida K, Narumi O, Chin M, et al. **Characterization of carotid atherosclerosis and detection of soft plaque with use of black-blood MR imaging.** *AJNR Am J Neuroradiol* 2008;29:868–74
12. Fabiano S, Mancino S, Stefanini M, et al. **High-resolution multicontrast-weighted MR imaging from human carotid endarterectomy specimens to assess carotid plaque components.** *Eur Radiol* 2008;18:2912–21
13. Cappendijk VC, Cleutjens KB, Kessels AG, et al. **Assessment of human atherosclerotic carotid plaque components with multisequence MR imaging: initial experience.** *Radiology* 2005;234:487–92
14. Oliver TB, Lammie GA, Wright AR, et al. **Atherosclerotic plaque at the carotid bifurcation: CT angiographic appearance with histopathologic correlation.** *AJNR Am J Neuroradiol* 1999;20:897–901
15. Culebras A, Magana R, Cacayorin ED. **Computed tomography of the cervical carotid artery: significance of the lucent defect.** *Stroke* 1988;19:723–27
16. Chu B, Kampschulte A, Ferguson MS, et al. **Hemorrhage in the atherosclerotic carotid plaque: a high-resolution MRI study.** *Stroke* 2004;35:1079–84
17. Saito A, Sasaki M, Ogasawara K, et al. **Carotid plaque signal differences among four kinds of T1-weighted magnetic resonance imaging techniques: a histopathological correlation study.** *Neuroradiology* 2012;54:1187–94
18. Yamada N, Higashi M, Otsubo R, et al. **Association between signal hyperintensity on T1-weighted MR imaging of carotid plaques and ipsilateral ischemic events.** *AJNR Am J Neuroradiol* 2007;28:287–92
19. Moody AR, Murphy RE, Morgan PS, et al. **Characterization of complicated carotid plaque with magnetic resonance direct thrombus imaging in patients with cerebral ischemia.** *Circulation* 2003;107:3047–52
20. Yoshimura S, Yamada K, Kawasaki M, et al. **High-intensity signal on time-of-flight magnetic resonance angiography indicates carotid plaques at high risk for cerebral embolism during stenting.** *Stroke* 2011;42:3132–37
21. Qiao Y, Etesami M, Malhotra S, et al. **Identification of intraplaque hemorrhage on MR angiography images: a comparison of contrast-enhanced mask and time-of-flight techniques.** *AJNR Am J Neuroradiol* 2011;32:454–59
22. Yamaguchi M, Sasaki M, Ohba H, et al. **Quantitative assessment of changes in carotid plaques during cilostazol administration using three-dimensional ultrasonography and non-gated magnetic resonance plaque imaging.** *Neuroradiology* 2012;54:939–45
23. Yuan C, Zhang SX, Polissar NL, et al. **Identification of fibrous cap rupture with magnetic resonance imaging is highly associated with**

recent transient ischemic attack or stroke. *Circulation* 2002; 105:181–85
24. Redgrave JN, Gallagher P, Lovett JK, et al. **Critical cap thickness and rupture in symptomatic carotid plaques: the Oxford plaque study.** *Stroke* 2008;39:1722–29
25. Trivedi RA, U-King-Im JM, Graves MJ, et al. **MRI-derived measurements of fibrous-cap and lipid-core thickness: the potential for identifying vulnerable carotid plaques in vivo.** *Neuroradiology* 2004;46:738–43
26. Cai J, Hatsukami TS, Ferguson MS, et al. **In vivo quantitative measurement of intact fibrous cap and lipid-rich necrotic core size in atherosclerotic carotid plaque: comparison of high-resolution, contrast-enhanced magnetic resonance imaging and histology.** *Circulation* 2005;112:3437–44
27. Balu N, Chu B, Hatsukami TS, et al. **Comparison between 2D and 3D high-resolution black-blood techniques for carotid artery wall imaging in clinically significant atherosclerosis.** *J Magn Reson Imaging* 2008;27:918–24

Craniopharyngeal Canal and Its Spectrum of Pathology

T.A. Abele, K.L. Salzman, H.R. Harnsberger, and C.M. Glastonbury

ABSTRACT

BACKGROUND AND PURPOSE: The craniopharyngeal canal is a rare, well-corticated defect through the midline of the sphenoid bone from the sellar floor to the anterosuperior nasopharyngeal roof. We reviewed a series of craniopharyngeal canals to determine a system of classification that might better our understanding of this entity, highlight the range of associated pathologic conditions, and optimize patient treatment.

MATERIALS AND METHODS: Available MR imaging, CT, and clinical data (from 1989–2013) of 29 patients (10 female, 15 male, 4 unknown; median age, 4 years; age range, 1 day–65 years) with craniopharyngeal canals were retrospectively examined. Qualitative assessment included orthotopic or ectopic adenohypophysis and the presence of a tumor and/or cephalocele. The midpoint anteroposterior diameter was measured. Clinical and imaging data were evaluated for pituitary dysfunction and accompanying anomalies.

RESULTS: Craniopharyngeal canals were qualitatively separated into 3 types: incidental canals (type 1); canals with ectopic adenohypophysis (type 2); and canals containing cephaloceles (type 3A), tumors (type 3B), or both (type 3C), including pituitary adenoma, craniopharyngioma, dermoid, teratoma, and glioma. Quantitative evaluation showed a significant difference ($P < .0001$) in the anteroposterior diameters of type 1 canals (median, 0.8; range, 0.7–1.1 mm), type 2 canals (median, 3.9, range, 3.5–4.4 mm), and type 3 canals (median, 9.0; range, 5.9–31.0 mm) imparting small, medium, and large descriptors. Canals with cephaloceles all contained an ectopic adenohypophysis. The craniopharyngeal canals were associated with pituitary dysfunction (6/29) and congenital anomalies (8/29).

CONCLUSIONS: Accurate diagnosis and classification of craniopharyngeal canals are valuable to characterize lesions requiring surgery, identify patients with potential pituitary dysfunction, and avoid iatrogenic hypopituitarism or CSF leak during surgical resection of nasopharyngeal masses.

ABBREVIATIONS: AP = anteroposterior; CPC = craniopharyngeal canal

The craniopharyngeal canal (CPC) is a rare, well-corticated defect of the midline sphenoid body from the sellar floor to the nasopharynx. Although embryogenesis of the canal has been disputed, evidence supports its origin from incomplete closure of the Rathke pouch, the precursor of the adenohypophysis.[1-3] Since the arrival of modern cross-sectional imaging, the literature on CPCs has been limited to case reports and a few small case series, which describe variably sized canals and a range of associated lesions.[2,4-13] CPC is a rare but important entity to recognize in the evaluation of nasopharyngeal or midline skull base lesions. Correct diagnosis may indicate pituitary dysfunction, obviate the need for surgery, and prevent iatrogenic hypopituitarism or CSF leak.

CPCs have previously been described as either small[14] (<1.5 mm diameter) or large[4] with or without mass; however, this binary division does not fully characterize its range. In this retrospective review of 29 patients with CPCs, we use quantitative and qualitative imaging features to provide a new system of classification, which divides the malformation into 3 types that more accurately describe size and associated pathologic appearance: small incidental canals (type 1); medium-sized canals containing ectopic (inferiorly displaced) adenohypophysis (type 2); and large canals with associated cephaloceles (type 3A), tumors of the adenohypophysis and associated embryonic tissues (type 3B), or both (type 3C). In addition, we examine the embryology and relevant

Received June 27, 2013; accepted after revision August 15.

From the Department of Radiology (T.A.A., K.L.S., H.R.H.), University of Utah, Salt Lake City, Utah; and Department of Radiology (C.M.G.) University of California, San Francisco, San Francisco, California.

Paper previously presented at: Annual Meeting of the American Society of Neuroradiology, May 23, 2013; San Diego, California.

Please address correspondence to Travis A. Abele, MD, Department of Radiology, University of Utah, 30 North 1900 East #1A071, Salt Lake City, UT 84132; e-mail: travis.abele@hsc.utah.edu

Indicates article with supplemental on-line tables.

http://dx.doi.org/10.3174/ajnr.A3745

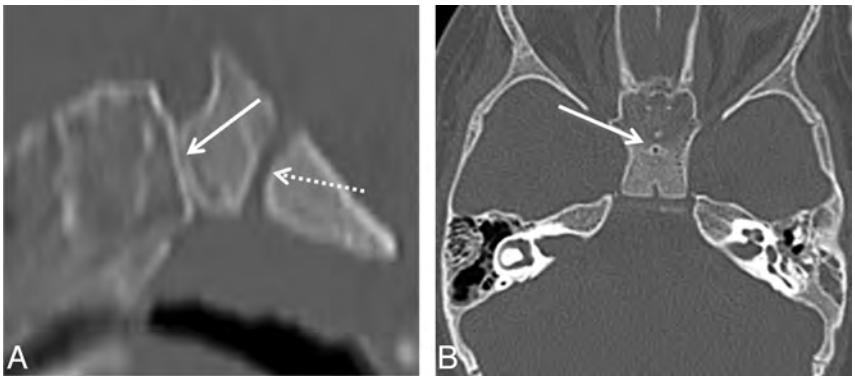

FIG 1. A 15-month-old girl with a history of trauma and type 1 CPC. *A*, Sagittal CT reconstruction shows the classic appearance of a small incidental CPC (*arrow*). Note its extent from the sella turcica to the roof of the nasopharynx. The spheno-occipital synchondrosis (*dashed arrow*) is visualized in its normal position posterior and inferior to the sella. *B*, Axial CT image shows well-corticated CPC (*arrow*) in the midline of the sphenoid body.

literature of the CPC to refine understanding of this rare entity and its associated congenital anomalies and neoplasms.

MATERIALS AND METHODS

In our study, which was approved by our institutional review board and is compliant with the Health Insurance Portability and Accountability Act, 2 neuroradiologists with Certificates of Added Qualification and a neuroradiology fellow retrospectively examined available clinical and imaging data of a series of radiologically proven CPCs reviewed or treated at the University of Utah during the past 25 years (1989–2013). Radiologic diagnosis of CPC was defined as a bony channel extending from the floor of the sella turcica to the inferior border of the sphenoid body. All patients underwent cross-sectional imaging studies: CT, MR imaging, or both.

Qualitative imaging evaluation was based on 2 criteria: 1) orthotopic or ectopic position of the adenohypophysis, and 2) cephalocele and/or neoplasm within the canal. These criteria were then used to divide the CPCs into 3 types: incidental canals with orthotopic adenohypophysis and no cephalocele or tumor (type 1); canals with ectopic (inferiorly displaced) adenohypophysis but no associated cephalocele or tumor (type 2); and canals with associated cephalocele (type 3A), tumor (type 3B), or both (type 3C). Neurohypophysis location was documented when identified. Cephalocele was defined as herniation of the meninges and CSF contents into the CPC with or without herniation of the pituitary gland and its associated structures.

We performed quantitative evaluation by measuring the anteroposterior (AP) diameter at the midpoint of the CPC from the anterior to posterior wall of the canal on a sagittal MR imaging sequence or CT reconstruction. When a neoplasm obliterated the walls of the CPC, the anterior and posterior margins of the tumor were used as a surrogate measure of the canal diameter. All measurement data were expressed as median and range. One-way ANOVA was used to assess statistically significant difference among AP diameter measurements of the 3 qualitative types of CPCs.

Clinical information was compiled via a retrospective chart review and included available demographic information, presenting symptoms, the presence of pituitary dysfunction, pathologic features, or the presence of other congenital anomalies. Patients without symptoms of pituitary dysfunction were presumed to have normal pituitary function. All tumors were resected, and diagnosis was based on pathologic analysis.

RESULTS

Twenty-nine patients (age range, 1 day–65 years; median age, 4 years) had radiologically identified CPCs on CT (3 patients), MR imaging (15 patients), or both CT and MR imaging (11 patients). Ten patients were female, 15 male, and in 4 patients, sex was not provided in available clinical data. Of 29 patients, 9 (31%) had type 1 incidental canals with orthotopic adenohypophysis and no cephalocele or tumor. Type 2 CPCs with ectopic adenohypophysis and no associated cephalocele or tumor were seen in 7 (24%) of 29 patients. Forty-five percent (13/29) of patients had type 3 CPCs associated with cephaloceles (4/29, type 3A), tumors (7/29, type 3B), or both (2/29, type 3C) including pituitary adenoma, craniopharyngioma, dermoid, teratoma, and glioma.

The AP diameter of each qualitative CPC type were as follows: type 1 canals: median, 0.8; range, 0.7–1.1 mm; type 2 canals: median, 3.9; range, 3.5–4.4 mm; and type 3 canals: median, 9.0; range, 5.9–31.0 mm. ANOVA analysis demonstrated statistically significant difference ($P < .0001$) among the AP diameter measurements of each type of CPC, thus imparting size descriptors: small, medium, and large. There was no significant difference between the AP diameters of the type 3A, 3B, and 3C canals.

Pituitary dysfunction was documented in 6 (21%) of all 29 CPCs and in 6 (30%) of the 20 type 2 and type 3 canals. Hormone abnormalities included generalized hypopituitarism (2 patients), partial hypopituitarism, diabetes insipidus, and growth hormone deficiency (2 patients). Other congenital anomalies were seen in 8 of 29 patients with no predilection for type of CPC. Patient data are summarized in On-line Table 1, and complete patient data are provided in On-line Table 2.

Type 1 small, incidental CPCs with orthotopic adenohypophysis (Fig 1) demonstrated a well-corticated channel on CT extending from the inferior floor of the sella turcica to the inferior border of the midline sphenoid body and measured ≥1.1 mm in AP diameter. On MR imaging, they showed the same midline path through the sphenoid bone with variable internal signal. These patients underwent imaging for symptoms unrelated to the CPC, such as sinus disease and trauma; however, some patients were known to have congenital anomalies including PHACE (posterior fossa malformations, hemangiomas, arterial abnormalities, cardiac defects, eye abnormalities) syndrome,[15] Blake remnant, duplicated pituitary gland, and congenital cleft lip or cleft palate. The patient with the duplicated pituitary gland also had a nasopharyngeal teratoma, which did not involve the CPC. None of the patients with type 1 CPCs had pituitary dysfunction or contained ectopic pituitary tissue, cephalocele, or tumor.

Type 2 medium-sized CPCs presented as well-corticated channels (3.5–4.4 mm AP diameter) on CT and, on MR imaging,

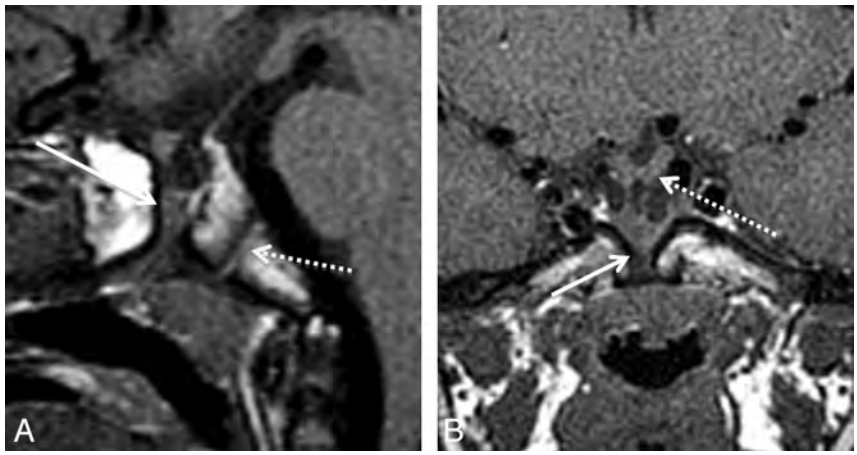

FIG 2. A 4-year-old boy with hypopituitarism and a type 2 CPC. *A*, Sagittal T1 MR image shows a medium-sized canal with ectopic, inferiorly displaced pituitary tissue (*arrow*). The AP diameter of this canal measured 3.5 mm. Note the normal spheno-occipital synchondrosis (*dashed arrow*). *B*, Coronal T1 MR image demonstrates soft tissue within the CPC (*arrow*). There is mild inferior displacement of the optic chiasm (*dashed arrow*) and infundibular recess of the third ventricle.

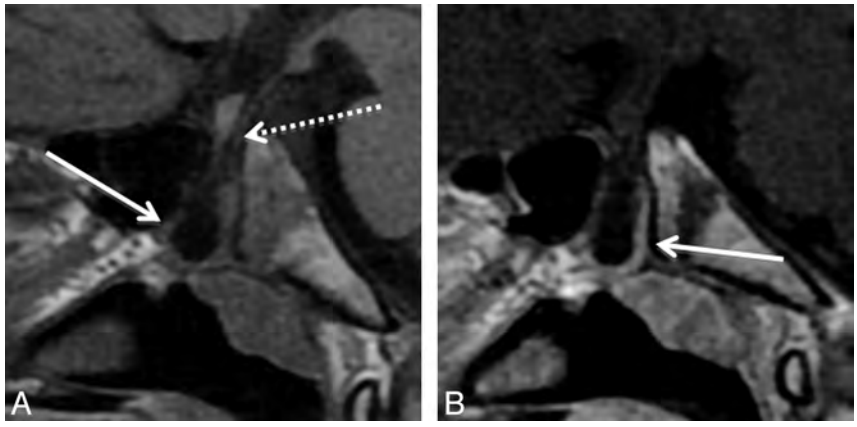

FIG 3. A 10-year-old boy with growth hormone deficiency and short stature with a type 3A CPC. *A*, Sagittal T1 MR image shows a large CPC containing a cephalocele with herniated adenohypophysis (*arrow*) and CSF. Note displacement of the infundibular recess of the third ventricle (*dashed arrow*). *B*, Sagittal T1 postcontrast MR image shows enhancement of the adenohypophysis (*arrow*), which, in our 4 type 3A canals, was invariably positioned along the posterior and/or inferior aspect of the cephalocele.

contained inferiorly located ectopic adenohypophysis (Fig 2). Adenohypophysis was identified and was distinguished from tumor on MR imaging by a characteristic homogeneous T1 signal isointense to the brain and homogeneous enhancement. Other characteristic features were the location of the dorsal T1 hyperintense neurohypophysis and infundibular stalk extending to the superior surface of the adenohypophysis. Of 7 patients, 4 also had inferiorly located neurohypophysis. One medium-sized canal had orthotopic neurohypophysis, and in another case, the neurohypophysis was not identified. One type 2 CPC was partially patent on sagittal T1-weighted MR imaging and had suprasellar ectopic posterior pituitary tissue inferior to the hypothalamus. Type 2 CPCs were found in patients who clinically presented with pituitary dysfunction (2/7), headache, coloboma, and hydrocephalus. The patient with hydrocephalus had congenital abnormalities, including cortical dysplasia, absent right ICA, and schizencephaly. Other congenital anomalies included holoprosencephaly and coloboma.

The 4 type 3A large CPCs containing only cephalocele demonstrated well-corticated channels on CT that, on MR imaging, contained CSF; meninges; ectopic adenohypophysis (4/4); the pituitary infundibulum; infundibular recess of the third ventricle; and, in 1 case, an associated arachnoid cyst (Fig 3). The 4 patients with type 3A CPCs presented with growth hormone deficiency, generalized hypopituitarism, diabetes insipidus, or meningitis. These patients had no other documented congenital anomalies.

Type 3B large CPCs containing tumors consisted of 2 gliomas, 1 dermoid, 1 teratoma, 1 craniopharyngioma, and 2 adenomas. Type 3C large CPCs containing tumor and cephalocele consisted of 2 dermoids (Fig 4). Most tumors had a large portion of their mass within the CPC. One of the nasopharyngeal gliomas extended intracranially into the sella turcica, and the other glioma passed superiorly through the canal into the suprasellar space (Fig 4*B*). In both type 3C and 2 type 3B CPCs, there was ectopic adenohypophysis. In the cases of craniopharyngioma and adenoma, which obliterated the canal walls, the adenohypophysis was orthotopic. Of the 9 type 3B and type 3C CPCs, 4 presented as a nasopharyngeal mass, and 1 presented with growth hormone deficiency. The 1 patient with teratoma had a duplicated pituitary gland. Otherwise, there were no documented associated congenital anomalies in type 3 large canals.

DISCUSSION

The CPC is a rare, well-corticated defect of the midline sphenoid body extending from the floor of the sella turcica to the roof of the nasopharynx.[14] To our knowledge, our study is the largest series of CPCs since the advent of cross-sectional imaging. On the basis of quantitative and qualitative features, CPCs can be classified into 3 types: small incidental canals (type 1); medium-sized canals with ectopic pituitary tissue (type 2); and large canals containing cephaloceles (type 3A), tumors (type 3B), or both (type 3C). Identification and classification of CPCs have prognostic and therapeutic implications. Type 1 small incidental canals are benign but may be found in patients with other craniofacial or neural congenital anomalies. Type 2 medium-sized canals and type 3A large canals with cephaloceles are associated with ectopic adenohypophysis and possible pituitary dysfunction. Type 3 large CPCs containing tumors and/or cephaloceles often contain ectopic pituitary tissue within the nasopharynx; thus, care should be taken during surgery to avoid iatrogenic hypopituitarism and/or CSF leak. Compared with the previous division of small benign CPCs[14] or large CPCs

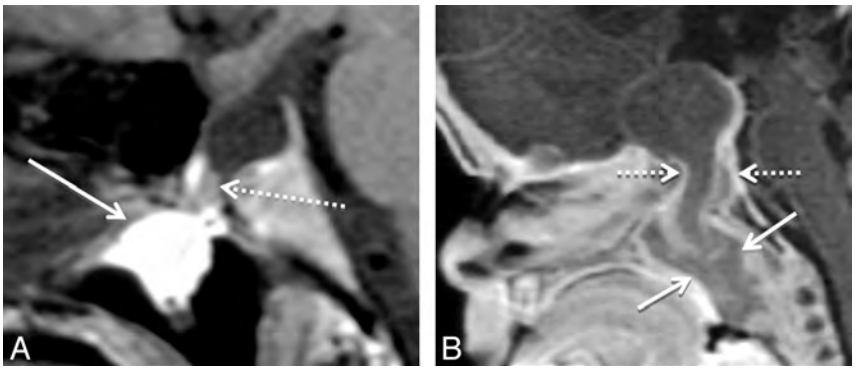

FIG 4. Two different patients with type 3 large CPCs containing tumor. *A*, Sagittal T1 MR image shows a large CPC containing portions of a T1 hyperintense dermoid (*arrow*) in a 30-year-old woman who presented with a nasopharyngeal mass. Note the associated cephalocele with herniated CSF and the adenohypophysis (*dashed arrow*). This is a type 3B CPC. *B*, Sagittal T1 postcontrast MR image in an 8-week-old girl who underwent imaging for a nasopharyngeal mass demonstrates a nasopharyngeal glioma (*arrows*), with mild enhancement extending into the suprasellar space through a large CPC (*dashed arrows*). This is a type 3C CPC.

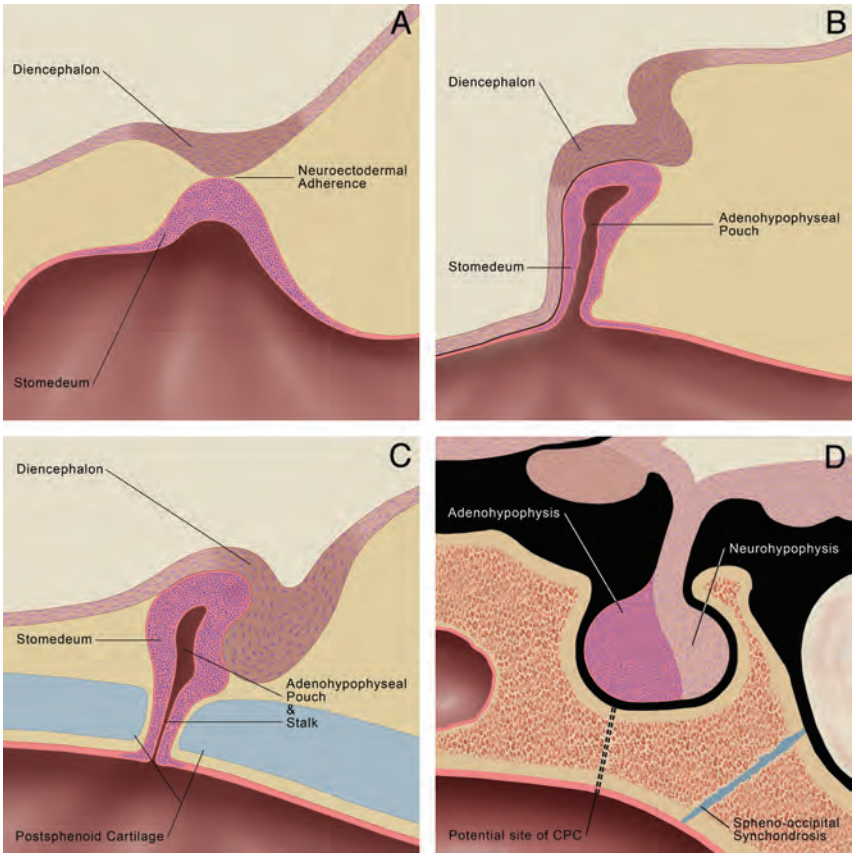

FIG 5. Embryology of the normal pituitary gland. *A*, At 3–4 weeks of gestation, the neuroectodermal adherence develops at a point of contact between the diencephalon (neurohypophyseal anlage) and roof of the stomodeum (adenohypophyseal anlage). *B*, At 4–5 weeks, the neuroectodermal adherence migrates dorsally forming the adenohypophyseal (Rathke) pouch, while the diencephalon migrates dorsal to the stomodeum to assume the position of the future neurohypophysis. The adenohypophyseal pouch elongates forming a stalk at its ventral aspect at 5–6 weeks (not shown). *C*, At 6–7 weeks, the postsphenoid cartilage develops, which results in obliteration of the adenohypophyseal stalk. *D*, In this illustration of the infant pituitary gland and sella, a dotted line traces the path of the potential CPC, which is believed to arise from nonobliteration of the adenohypophyseal stalk. The spheno-occipital synchondrosis (*illustrated in blue*) does not close until approximately age 16 years and mimics the CPC in children. Graphic illustrations used with permission from Amirsys.

with associated nasopharyngeal masses and craniofacial malformations,[4] our classification provides a more nuanced characterization of the CPC with the inclusion of medium-sized type 2 canals and subdivision of large type 3 canals.

From our data, a nasopharyngeal mass should raise the suspicion for a type 3 CPC, and pituitary dysfunction may suggest a type 2 or 3 CPC. CT is sufficient to characterize type 1 CPCs, unless there is suspicion for associated craniofacial congenital anomalies. MR imaging, however, is the best for evaluation of ectopic adenohypophysis in type 2 CPCs and cephalocele and/or tumor in type 3 CPCs due to its superior contrast resolution.

The CPC is postulated to arise from an error in the normal development of the pituitary gland (Fig 5). The pituitary gland originates from a single embryologic neuroectodermal adherence formed by fusion of the roof of the stomodeum (adenohypophysis anlage) and floor of the diencephalon (neurohypophysis anlage).[16] At approximately the fourth week of gestation, the forebrain grows rostrocaudally and mesoderm proliferates ventrolaterally around the neuroectodermal adherence, causing the adherence to migrate dorsally and form an invagination, called the adenohypophyseal (Rathke) pouch.[16,17] During the fifth and sixth weeks of gestation, the adenohypophyseal pouch elongates, forming a narrow stalk between it and the stomodeum.[18] At approximately the sixth to seventh weeks of gestation, the cartilaginous sphenoid skull base develops, obliterating this adenohypophyseal stalk.[18,19] The sphenoid cartilage is composed of 2 paired presphenoid and 2 paired postsphenoid cartilages. The presphenoid cartilages fuse and later form the anterior sphenoid body, and the postsphenoid cartilages fuse to form the basisphenoid cartilage, which later becomes the posterior sphenoid body and sella turcica.[20] Defective fusion of the postsphenoid cartilages results in nonobliteration of the stalk between the adenohypophyseal pouch and the stomodeum and a residual canal extending from the sella turcica to the pharynx, named the CPC.

Two case series from the mid-20th century proposed that the CPC is merely a remnant of a vascular channel. Arey[14]

came to this conclusion when, after examining the sphenoid bone of 17 embryonic specimens for persistence of a CPC containing pituitary tissue, he only found channels for blood vessels. Lowman et al[21] radiographically identified 2 complete CPCs in 400 neonate sphenoid bone specimens, but when he histologically analyzed the specimens, he found only vascular channels without evidence of "squamous or ciliated epithelium." Both authors erroneously concluded that the absence of evidence for the pituitary origin of the CPC suggests that it does not arise from the embryologic pituitary.

Subsequent studies make a strong case for the pituitary origin. Kjaer and Fischer-Hansen[1] used modern immunohistochemistry to demonstrate adenohypophyseal tissue within the CPC of 6 fetuses with holoprosencephaly or anencephaly. Moreover, Kjaer and Fischer-Hansen noted that the postsphenoid bone is nearly always malformed in holoprosencephaly and invariably malformed in anencephaly, supporting an association between malformation of the cartilaginous sphenoid skull base and persistence of the CPC. Hori et al[3] evaluated nasopharyngeal pituitary tissue of fetal specimens and demonstrated adenohypophyseal tissue in a CPC. These authors also performed a meta-analysis showing that 24 of 27 ectopic pituitary adenomas in the literature occurred in either the sphenoid sinus or the clivus. Hori et al[3] believed this evidence for the persistence of pharyngeal pituitary tissue into adulthood; however, one could more convincingly propose, given the nonaggressive nature of pituitary adenomas, that the bony location of these ectopic adenomas supports pituitary tissue within a CPC rather than in the pharynx. The same conclusion can be made from the craniopharyngioma and adenomas in our series and case reports of ectopic intrasphenoid pituitary neoplasms in the literature.[2,12,13]

The characteristics of our type 1 small incidental CPCs are similar to those of the meta-analysis performed by Arey.[14] Of 8338 skulls in 11 studies, 35 CPCs were identified, yielding a prevalence of 0.42%. Each canal extended from the sella turcica to the basal surface of the sphenoid bone, was surrounded by "compact" bone, and measured $<$ 1.5 mm. These features are comparable to our type 1 canals, which were delimited by cortical bone and measured 0.7–1.1 mm in AP diameter. Small CPCs were first systematically evaluated by Landzert (who coined the term craniopharyngeal canal) in 1868. He identified a complete bony sphenoid canal the width of a bristle in 10 (10%) of 100 anatomic specimens from infants up to 8 months old.[14] A study in 1903 showed similar prevalence (18/200) in infants younger than 3 months old.[14] Comparing these data with Arey's frequency of 0.42% raises the question of whether some CPCs obliterate in early childhood. To our knowledge, no studies have investigated this matter.

An in vivo type 2 medium-sized CPC with ectopic pituitary tissue was first reported in 1949 by Wilkerson and Cayce,[22] in which a 19-year-old woman had a 3–5 mm diameter canal at the base of the sphenoid discovered during choanal atresia surgery. The canal was radiographed during extensive probing, and the patient subsequently experienced hypothyroidism and secondary amenorrhea. This development is not surprising given the presence of ectopic adenohypophysis in all type 2 CPCs in our series. Two recent case reports discuss medium-sized CPCs with ectopic pituitary tissue. One had an associated hypothalamic hamartoma, measured $>$ 1.5 mm in diameter (exact measurement not provided), and had inferior ectopic adenohypophysis on MR imaging.[11] Currarino et al[4] reported the other medium-sized CPC in their article on "large craniopharyngeal canals." One of their 2 cases described a male infant with a 3-mm diameter CPC containing mildly displaced adenohypophysis (as demonstrated in the figures) but no pituitary dysfunction. This patient also had congenital anomalies, including cleft lip and palate, hypertelorism, and orbital hypoplasia. Type 2 CPCs are important to recognize not only for their apparent association with congenital abnormalities but also for the detection of related pituitary dysfunction. In our series, 2 of 7 type 2 CPCs had pituitary dysfunction. We postulate the cause to be ectopic pituitary tissue, as our type 3A large CPCs with cephaloceles and more displaced pituitary tissue had a higher rate of pituitary deficiency (4/6) than the type 2 canals.

A case of type 3A large CPC containing cephalocele and ectopic pituitary tissue was first described by Klinkosch in 1764, in which a neonate had a 5-mm wide passage extending through the middle of the sphenoid that contained prolapsed dura and an ectopic pituitary gland.[14] Recent case reports of large CPCs with cephaloceles containing ectopic pituitary tissue describe canals measuring 10–13 mm in diameter.[8,9,23,24] One patient presented with recurrent meningitis (as in our series), and 2 patients had colobomas, believed to result from stretching of the optic nerves into the cephalocele.[23-25] Three of 4 large CPCs in the literature that were identified before surgery had pituitary dysfunction, reflecting our 75% prevalence in large canals.[9,23] Hughes et al[8] described 2 patients with large CPCs and cephaloceles who presented with suspected iatrogenic hypopituitarism after resection of nasopharyngeal "masses." This finding underscores the importance of recognizing cephaloceles and ectopic pituitary tissue in type 3A CPCs to avoid CSF leak and/or pituitary resection during nasopharyngeal mass surgery.

Fewer than 25 cases of ectopic pituitary adenomas are reported within the sphenoid sinus, presumed to originate within type 3B CPCs. Most of these lesions presented due to mass effect (as in 1 of our 2 cases) or ectopic hormone secretion.[2,26] Reports of infrasellar craniopharyngiomas are rarer, with at least 5 reported in the modern literature.[13,27-30] An infrasellar location separate from the sella turcica is important to recognize because it indicates that the craniopharyngioma originated within a type 3B CPC rather than invading the skull base inferiorly from a sellar origin.

Dermoids, teratomas, and gliomas are uncommon lesions of the nasopharynx.[31,32] Nasopharyngeal teratoma can be associated with duplication of the adenohypophysis, as in our case.[33] The epignathus type of teratoma is a large neoplasm that fills the oral cavity and has been reported in association with a CPC.[5] Nasopharyngeal glioma is a rare entity composed of heterotopic neuroglial tissue. Although there are reported cases of nasopharyngeal gliomas associated with midline skull base defects, none are explicitly associated with CPCs or extend intracranially as our cases did.[32] As in type 3 CPCs with cephalocele, identifying intracranial extension of a dermoid, teratoma, or glioma into a type 3 CPC is important for surgical planning to avoid inadvertent CSF leak and potential meningitis.

Limitations of this series were its relatively small size and retrospective nature. In addition, because many of the cases were

referred for evaluation from outside institutions, we had no control of the quality or protocol of the imaging examinations and completeness of the clinical data.

CONCLUSIONS

CPCs can be classified into 3 types, which have therapeutic and prognostic implications: small incidental canals (type 1); medium-sized canals with ectopic adenohypophysis (type 2); and large canals containing cephaloceles (type 3A), tumors (type 3B), or both (type 3C). Type 2 CPCs and type 3A large canals with cephaloceles have ectopic adenohypophysis and should alert the clinician to possible pituitary dysfunction. Type 3 large CPCs associated with tumors and/or cephaloceles often contain ectopic pituitary tissue within the nasopharynx or have continuity with the dural meninges; thus, care should be taken during surgery to avoid iatrogenic hypopituitarism and/or CSF leak.

Disclosures: Karen L. Salzman—*UNRELATED: Consultancy:* Amirsys Publishing; *Royalties:* Amirsys Publishing. H. Ric Harnsberger—*Employment:* Amirsys; *Royalties:* Amirsys; *Stock/Stock Options:* Amirsys. Christine M. Glastonbury—*UNRELATED: Consultancy:* Amirsys; *Royalties:* Amirsys; *Stock/Stock Options:* Amirsys.

REFERENCES

1. Kjaer I, Fischer-Hansen B. **Human fetal pituitary gland in holoprosencephaly and anencephaly.** *J Craniofac Genet Dev Biol* 1995;15:222–29
2. Kaushik C, Ramakrishnaiah R, Angtuaco EJ. **Ectopic pituitary adenoma in persistent craniopharyngeal canal: case report and literature review.** *J Comput Assist Tomogr* 2010;34:612–14
3. Hori A, Schmidt D, Rickels E. **Pharyngeal pituitary: development, malformation, and tumorigenesis.** *Acta Neuropathol* 1999;98:262–72
4. Currarino G, Maravilla KR, Salyer KE. **Transsphenoidal canal (large craniopharyngeal canal) and its pathologic implications.** *AJNR Am J Neuroradiol* 1985;6:39–43
5. Cohen R, Nelson MD, Segall HD. **Epignathic teratoma associated with craniopharyngeal canal.** *AJNR Am J Neuroradiol* 1989;10:652
6. Rottenberg GT, Chong WK, Powell M, et al. **Cyst formation of the craniopharyngeal duct.** *Clinical Radiol* 1994;49:126–29
7. Kjaer I, Russell BG. **The craniopharyngeal canal indicating the presence of pharyngeal adenopituitary tissue.** *Eur J Radiol* 1995;20:212–14
8. Hughes ML, Carty AT, White FE. **Persistent hypophyseal (craniopharyngeal) canal.** *Br J Radiol* 1999;72:204–06
9. Ekinci G, Kiliç T, Baltacioğlu F, et al. **Transsphenoidal (large craniopharyngeal) canal associated with a normally functioning pituitary gland and nasopharyngeal extension, hyperprolactinemia, and hypothalamic hamartoma.** *AJR Am J Roentgenol* 2003;180:76–77
10. Marsot-Dupuch K, Smoker WR, Grauer W. **A rare expression of neural crest disorders: an intrasphenoidal development of the anterior pituitary gland.** *AJNR Am J Neuroradiol* 2004;25:285–88
11. Kizilkilic O, Yalcin O, Yildirim T, et al. **Hypothalamic hamartoma associated with a craniopharyngeal canal.** *AJNR Am J Neuroradiol* 2005;26:65–67
12. Megdiche-Bazarbacha H, Ben Hammouda K, Aicha AB, et al. **Intrasphenoidal Rathke cleft cyst.** *AJNR Am J Neuroradiol* 2006;27:1098–1100
13. Nourbakhsh A, Brown B, Vannemreddy P, et al. **Extracranial infrasellar ectopic craniopharyngioma: a case report and review of the literature.** *Skull Base* 2010;20:475–80
14. Arey LB. **The craniopharyngeal canal reviewed and reinterpreted.** *Anat Rec* 1950;106:1–16
15. Frieden IJ, Reese V, Cohen D. **PHACE syndrome. The association of posterior fossa brain malformations, hemangiomas, arterial anomalies, coarctation of the aorta and cardiac defects, and eye abnormalities.** *Arch Dermatol* 1996;132:307–11
16. Gilbert MS. **Some factors influencing the early development of the mammalian hypophysis.** *Anat Rec* 1935;62:337–59
17. Müller F, O'Rahilly R. **The development of the human brain from a closed neural tube at stage 13.** *Anat Embryol* 1988;177:203–24
18. Ikeda H, Suzuki J, Sasano N, et al. **The development and morphogenesis of the human pituitary gland.** *Anat Embryol* 1988;178:327–36
19. Kollias SS, Ball WS, Prenger EC. **Review of the embryologic development of the pituitary gland and report of a case of hypophyseal duplication detected by MRI.** *Neuroradiology* 1995;37:3–12
20. Sperber GH, Sperber SM, Guttmann GD. *Craniofacial Embryogenetics and Development.* Shelton, Connecticut: People's Medical Publishing House-USA; 2010:105–13
21. Lowman RM, Robinson F, McAllister WB. **The craniopharyngeal canal.** *Acta Radiol Diagn (Stockh)* 1966;5:41–54
22. Wilkerson WW, Cayce LF. **Persistent craniopharyngeal canal in a living adult.** *Laryngoscope* 1949;59:381–96
23. Blustajn J, Netchine I, Frédy D, et al. **Dysgenesis of the internal carotid artery associated with transsphenoidal encephalocele: a neural crest syndrome?** *AJNR Am J Neuroradiol* 1999;20:1154–57
24. Pinilla-Arias D, Hinojosa J, Esparza J, et al. **Recurrent meningitis and persistence of craniopharyngeal canal: case report.** *Neurocirugia* 2009;20:50–53
25. Goldhammer Y, Smith JL. **Optic nerve anomalies in basal encephalocele.** *Arch Ophthalmol* 1975;93:115–18
26. Pasquini E, Faustini-Fustini M, Sciarretta V, et al. **Ectopic TSH-secreting pituitary adenoma of the vomerosphenoidal junction.** *Eur J Endocrinol* 2003;148:253–57
27. Arndt S, Wiech T, Mader I, et al. **Entire infrasellar craniopharyngioma simulating clival chordoma.** *Otolaryngol Head Neck Surg* 2007;137:981–83
28. Benitez WI, Sartor KJ, Angtuaco EJ. **Craniopharyngioma presenting as a nasopharyngeal mass: CT and MR findings.** *J Comput Assist Tomogr* 1988;12:1068–72
29. Byrne MN, Sessions DG. **Nasopharyngeal craniopharyngioma. Case report and literature review.** *Ann Otol Rhinol Laryngol* 1990;99:633–39
30. Lewin R, Ruffolo E, Saraceno C. **Craniopharyngioma arising in the pharyngeal hypophysis.** *South Med J* 1984;77:1519–23
31. Coppit GL 3rd, Perkins JA, Manning SC. **Nasopharyngeal teratomas and dermoids: a review of the literature and case series.** *Int J Pediatr Otorhinolaryngol* 2000;52:219–27
32. Husein OF, Collins M, Kang DR. **Neuroglial heterotopia causing neonatal airway obstruction: presentation, management, and literature review.** *Eur J Pediatr* 2008;167:1351–55
33. Manjila S, Miller EA, Vadera S, et al. **Duplication of the pituitary gland associated with multiple blastogenesis defects: duplication of the pituitary gland (DPG)-plus syndrome. Case report and review of literature.** *Surg Neurol Int* 2012;3:23

An Exponential Growth in Incidence of Thyroid Cancer: Trends and Impact of CT Imaging

J.K. Hoang, K.R. Choudhury, J.D. Eastwood, R.M. Esclamado, G.H. Lyman, T.M. Shattuck, and X.V. Nguyen

ABSTRACT

BACKGROUND AND PURPOSE: Workup of incidental thyroid nodules detected on CT imaging could be contributing to the increased diagnosis of small thyroid cancers. The purpose of this study was to evaluate recent trends in the incidence of thyroid cancer, and to determine the relationship between annual CT imaging volume and rate of thyroid cancer diagnosis.

MATERIALS AND METHODS: This retrospective cohort study used data bases for thyroid cancer and CT imaging volume. Thyroid cancer data from 1983–2009 were obtained from the Surveillance, Epidemiology, and End Results data base. National Council of Radiation Protection and Measurements Report No. 160 provided data on hospital and nonhospital CT imaging volume for 1993–2006. Trends in thyroid cancer were modeled for overall incidence on the basis of patient age, tumor histologic features, and tumor size and stage. Linear regression analysis was performed to evaluate the strength of the relationship between annual CT scan volume and the incidence of thyroid cancer by tumor size and histologic type.

RESULTS: In 2009, the incidence of thyroid cancer was 14 per 100,000, which represented a 1.9-fold increase compared with 2000. The growth in incidence was exponential compared with a minimal linear increase in thyroid cancer mortality rate. The subgroup with the greatest change was subcentimeter papillary carcinoma, with doubling in incidence approximately every 6.2 years. The linear relationship between annual CT scan volume and the incidence of subcentimeter papillary carcinoma was very strong ($R^2 = 0.98$; $P < .0001$).

CONCLUSIONS: The incidence of subcentimeter papillary carcinoma is growing at an exponential rate without significant change in mortality rate. The strong linear relationship between new cases of subcentimeter papillary carcinomas and the number of CT scans per year suggests that an increase in CT scans may increase the detection of incidental thyroid cancers.

ABBREVIATIONS: NCRP = National Council on Radiation Protection; SEER = Surveillance, Epidemiology, and End Results

The incidence of thyroid cancer is increasing in the United States. A study published by Davies and Welch[1] found that from 1973–2002, the incidence of thyroid carcinoma more than doubled. They reported that 87% of the increase in discovered cancers was attributable to tumors that were 2 cm or smaller, and despite earlier diagnosis, there was no change in mortality. These results provided compelling evidence for an "apparent" increase in cancer derived from increased use of diagnostic imaging tests, rather than a true increase in the biologic occurrence of thyroid cancer. This pattern of increased diagnosis of a silent reservoir of disease with an indolent natural history is similar to the epidemiologic changes in prostate cancer that occurred with prostatic-specific antigen and digital rectal examination–based screening.[2] Davies and Welch[1] and McLeod et al[3] proposed that advances in sonography and fine-needle aspiration were leading to an increased diagnosis of subclinical (ie, small, impalpable) thyroid cancers that would otherwise remain asymptomatic during a patient's lifetime and not increase mortality rates. Epidemiologists have labeled this situation "overdiagnosis."[1,4]

In recent years, 2 factors may have strongly influenced the work-up of subclinical thyroid nodules and, thus, the incidence of thyroid cancer. First, several societies, including the Society of Radiologists in Ultrasound and American Thyroid Association, published sonographic guidelines for biopsy of thyroid nodules on the basis of best available evidence and expert opinion.[5,6] These societies raised concern that their recommendations could

Received May 31, 2013; accepted after revision August 5.

From the Departments of Radiology (J.K.H., K.R.C., J.D.E.), Radiation Oncology (J.K.H.), and Pathology (T.S.), Division of Otolaryngology Head and Neck Surgery (R.M.E.), and Department of Medicine (G.H.L.), Division of Oncology, Duke University Medical Center, Durham, North Carolina; and Department of Radiology (X.V.N.), The Ohio State University Wexner Medical Center, Columbus, Ohio.

Please address correspondence to Jenny K. Hoang, Department of Radiology, Division of Neuroradiology, Duke University Medical Center, Box 3808, Erwin Rd, Durham, NC 27710; e-mail: jennykh@gmail.com; jennykh@gmail.com

Indicates article with supplemental on-line appendix.

http://dx.doi.org/10.3174/ajnr.A3743

increase the biopsy rate of thyroid nodules and the incidence of thyroid cancer.[5] Second, the use of diagnostic imaging has changed substantially in recent years. In particular, the use of CT has increased rapidly in the United States, at a rate greater than sonography imaging.[7-9] A study of nationwide emergency department imaging use from 2000–2008 found that the use of sonography increased by 95%, whereas CT increased by 227%. In addition, CT made up 29% of emergency department imaging, but sonography comprised only 4%. CT scans of the neck, cervical spine, and/or chest can include the thyroid gland and may be a source for the detection of incidental thyroid nodules that subsequently receive work-up and biopsy.

The aim of our study was to evaluate the recent trends in the incidence of thyroid cancer, and to determine the relationship between annual CT imaging volume and thyroid cancer incidence. Our hypothesis was that the incidence of subclinical thyroid cancers has continued to increase, and that the increase in thyroid cancers correlates strongly with the volume of CT imaging.

MATERIALS AND METHODS

This retrospective cohort study evaluated 2 large data bases for thyroid cancer and CT imaging volume. The study was approved by our institutional review board.

Data Sources and Analysis

Data on thyroid cancer incidence and survival for thyroid cancer were obtained from the National Cancer Institute's Surveillance, Epidemiology, and End Results (SEER) data base. The SEER program collects cancer data from multiple population-based registries, with the 9 registries that were active throughout this interval comprising 10% of the US population. Available data from 1983–2009 included patient sex, age, and follow-up, as well as tumor size, histologic features, and staging.

Data on CT imaging volume were obtained from the National Council on Radiation Protection (NCRP) and Measurements Report No. 160.[10] The report provides the annual number of CT procedures in both hospital and nonhospital facilities in the United States from 1993–2006.

Statistical Analyses

Trends in Incidence and Mortality. Trends in thyroid cancer were modeled for overall incidence and mortality. Incidence was also modeled as a function of patient age, as well as tumor histologic features, size, and stage, to determine the characteristics of the tumors that are increasing in incidence. The number of new cases annually was assumed to have a Poisson distribution, and a multivariate log-linear model was proposed for the mean incidence to determine variables influencing the rate of change in incidence (On-line Appendix A). The models were fitted based on maximal likelihood by use of iteratively reweighted least squares.

Relationship of CT Imaging and Thyroid Cancer. Trends in CT volume were modeled to describe growth in CT as an exponential function of time, fitted by log-linear regression. The slope of the fitted regression line is interpreted as the annual rate of increase in CT volume.

We fit a linear regression model to evaluate the relative impact of annual CT imaging volume on the incidence of thyroid cancer for 1993–2006, as influenced by tumor size and histologic appearance. A linear regression model was chosen because we aimed to describe the dependence of new cases of thyroid cancer on the number of CT scans for matched years. If incidental nodules seen on CT led to a diagnosis of thyroid cancer, then we would expect cancer incidence to increase proportionately with CT scans.

The model was as follows:

$$y_s(t) = \mu + \mu_s + bc(t) + b_s c(t) + \varepsilon_s(t)$$

where $y_s(t)$ is the number of cases of thyroid cancer of size s (<10 mm, 10–14 mm, 15–19 mm, 20–29 mm, 30–39 mm, or >40 mm,) in year t and $c(t)$ is the total number of CT scans in year t. The model explains the number of cases in μ, the baseline number of cases of size < 10 mm in 1993, b, the rate of increase in cases per million extra CT cases for size < 10 mm, μ_s, the change in number of cases of size s (relative to baseline) in 1993, and b_s, the change in rate of increase for cases of size s (relative to baseline). The slope of the model (b) for tumor size was of particular interest because we would expect the slope to be higher for smaller cancers if incidental nodules seen on CT are contributing to the increase in diagnosis of thyroid cancer.

Statistical analyses were performed with SeerStat 7.1.0 (National Cancer Institute, Bethesda, Maryland) and R package (www.r-project.org). For all tests, a P value < .05 was considered statistically significant.

RESULTS

Trends in Incidence and Mortality

A total of 52,930 cases of thyroid cancer were diagnosed in the 9 SEER geographic areas from 1983–2009. In 2009, the incidence of thyroid cancer was 14 per 100,000, which was a 1.9-fold increase compared with the year 2000 (Table 1). The trend in thyroid cancer incidence during this period seems to be exponential (Fig 1). By contrast, the trends in mortality and population growth seem approximately linear (Fig 1) and relatively much slower during the same period.

Variables Influencing Trends

Papillary carcinoma was the most common histologic type, comprising 88% of thyroid cancers in 2009 (Table 1) and having an exponential rate of growth in incidence (Fig 1). An exponential model was able to explain 96% of the variability (null deviance) in the data, suggesting an excellent fit (On-line Appendix B). The variable that most significantly influenced the increase in incidence was tumor size < 10 mm. For papillary carcinoma with size < 10 mm, the growth in incidence per year was 11.8%, which translates into a doubling in incidence every 6.2 years (Fig 2).

Baseline rates of growth in incidence for other histologic types were considerably lower: follicular, 3.8% (95% CI, 2.4–5.1); medullary, 4.0% (95% CI, 1.2–6.6); and anaplastic, 1.5% (95% CI, −21% to 18%).

Relationship of CT Imaging and Thyroid Cancer

The rate of increase in CT scan volume per year was not linear. From 1993–1999, the number of CT scans per year increased from 18.3 to 30.6 million per year (12.3-million increase). In the same

Table 1: Thyroid carcinoma overall incidence and mortality, stratified by patient sex and tumor characteristics

	Year				
	1990	1993	2000	2006	2009
Total incidence	5.43	5.58	7.53	11.1	14.1
Total mortality	0.37	0.49	0.55	0.48	0.5
Incidence in subgroups					
Sex					
Male	2.87	3.58	3.98	5.74	6.84
Female	7.89	7.54	10.98	16.35	21.2
Tumor histology					
Papillary	4.29 (79%)	4.31 (77%)	6.36 (84%)	9.51 (86%)	12.47 (88%)
Follicular	0.75 (14%)	0.83 (15%)	0.79 (10%)	1.09 (10%)	1.14 (8%)
Medullary	0.13 (2%)	0.2 (4%)	0.19 (3%)	0.2 (2%)	0.21 (1%)
Anaplastic	0.04 (1%)	0.09 (2%)	0.05 (1%)	0.06 (1%)	0.11 (1%)
Other	0.22 (4%)	0.16 (3%)	0.14 (2%)	0.23 (2%)	0.18 (1%)
Tumor size					
<10 mm	0.71 (13%)	0.82 (15%)	1.47 (20%)	3.15 (28%)	4.38 (31%)
10–14 mm	0.57 (10%)	0.55 (10%)	0.85 (11%)	1.6 (14%)	2.15 (15%)
15–19 mm	0.55 (10%)	0.61 (11%)	0.89 (12%)	1.36 (12%)	1.86 (13%)
20–29 mm	0.99 (18%)	1.04 (19%)	1.35 (18%)	1.79 (16%)	2.14 (15%)
30–39 mm	0.51 (9%)	0.56 (10%)	0.66 (9%)	0.96 (9%)	1.22 (9%)
≥40 mm	0.61 (11%)	0.68 (12%)	0.86 (11%)	1.4 (13%)	1.57 (11%)
Tumor stage					
Localized or unstaged	2.97 (55%)	3.05 (55%)	4.49 (60%)	7.12 (64%)	9.09 (64%)
Regional	2.04 (38%)	2.14 (38%)	2.61 (35%)	3.49 (31%)	4.33 (31%)
Distant	0.42 (8%)	0.4 (7%)	0.42 (6%)	0.49 (4%)	0.68 (5%)

Note:—Incidence is expressed as the number of new cases per 100,000 people per year. The numbers in parentheses are percentages of the total incidence. The years 1993–2006 represent the period for which annual CT volume data are also available.

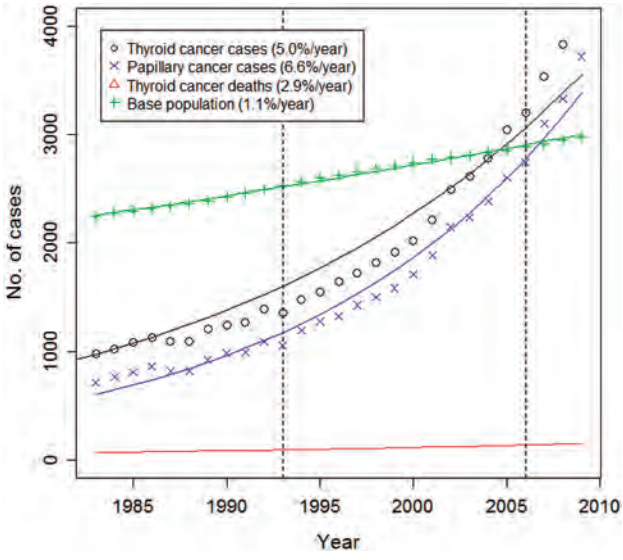

FIG 1. Trends in incidence and mortality of thyroid carcinoma. The rate of increase in incidence (%) per year is shown for thyroid cancer, papillary cancer, thyroid cancer deaths, and the size of the population. The base population is expressed in units of persons $\times 10^{-4}$. All of the trend lines were fitted to an exponential function, but the low growth rates for base population and thyroid deaths could be approximated by linear growth curves. Dashed vertical lines indicate the period of 1993–2006 for which annual CT volume data were also available.

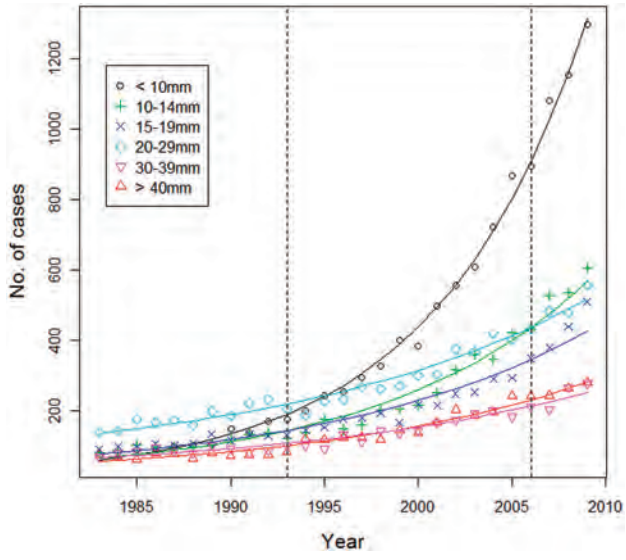

FIG 2. Trends in the number of new cases per year of papillary carcinoma by size. Symbols show observed values. Lines show fit from multivariate log-linear model for incidence (On-line Appendix B). Dashed vertical lines indicate the period of 1993–2006 for which annual CT volume data were also available.

period from 2000–2006, CT volume per year had increased from 34.9 to 62.0 million, which represented an increase of 27.1 million scans. This finding represents a growth in CT scans of 10% per year.

The NCRP report did not provide the proportion of studies for each body region by year but did include the proportion of CT procedures for various body categories for 3 selected years for its 4 largest datasets (commercial [IMV Benchmark report], Medicare, Veterans Affairs, and Large National Employer Plan). The IMV Benchmark report data represented the largest contribution to the data base (75% of CT scans in 2003). According to this dataset, the proportion of studies attributed to head and neck and chest imaging from 1998 to 2006 was stable. Head and neck CT in 1998, 2003, and 2006 comprised 32%, 31%, and 29% of CT studies, respectively. Chest CT in 1998, 2003, and 2006 comprised 17%, 16%, and 16% of CT studies, respectively.

Linear regression analysis of new cases of thyroid cancer and

Table 2: Estimated coefficients for linear regression model for papillary thyroid cancer incidence

	Estimate	Std. Error	*T* Value	Pr (< |t|)
Baseline intercept[a]	178.79	9.05	19.75	<.0001
Baseline slope CT[b]	15.6	0.39	39.84	<.0001
Diff. intercept size[c]				
10–14 mm	−52.93	12.8	−4.13	.0001
15–19 mm	−37.7	12.8	−2.94	.0043
20–29 mm	29.41	12.8	2.3	.0245
30–39 mm	−74.14	12.8	−5.79	<.0001
>40 mm	−77.87	12.8	−6.08	<.0001
Diff. slope CT:size[d]				
10–14 mm	−12.47	0.55	−22.52	<.0001
15–19 mm	−8.72	0.55	−15.75	<.0001
20–29 mm	−11.5	0.55	−20.77	<.0001
30–39 mm	−10.28	0.55	−18.57	<.0001
>40 mm	−13.12	0.55	−23.69	<.0001

Note:—The estimated coefficients indicate how changes in CT imaging volume, tumor size, and interaction between these 2 factors would affect thyroid cancer incidence compared with the baseline number of cases of size < 10 mm in 1993.

[a] Baseline intercept term is the estimated incidence in the year 1993.

[b] Baseline slope CT refers to the rate of increase in cases per million CT scans for tumors < 10 mm since 1993.

[c] Diff. intercept size indicates how much the intercept changes for other sized tumors.

[d] Diff. slope CT:size indicates how much the slope changes for other sized tumors. A negative estimate value indicates that the intercept or slope would be lower than for the baseline case of size < 10 mm.

CT volume by year demonstrated that the model fit the data very well. R^2 represents the proportion of variability of the data that could be explained by linear regression. For papillary cancers, the R^2 was 0.98, whereas for other cancers, the R^2 was 0.96. Our interest is primarily in the slope of the fitted lines, ie, the rate of increase in incidence per million CT scans. The highest rate of increase was for papillary tumors < 10 mm in size (Table 2). Slopes for all other sizes were 2.3–6.2 times lower (Table 2). For papillary cancers, the rate of growth in incidence (slopes) generally decreased with increase in size (Table 2 and Fig 3*A*). For nonpapillary cancers, the picture is the opposite: if anything, slopes increased with higher sizes (Fig 3*B*).

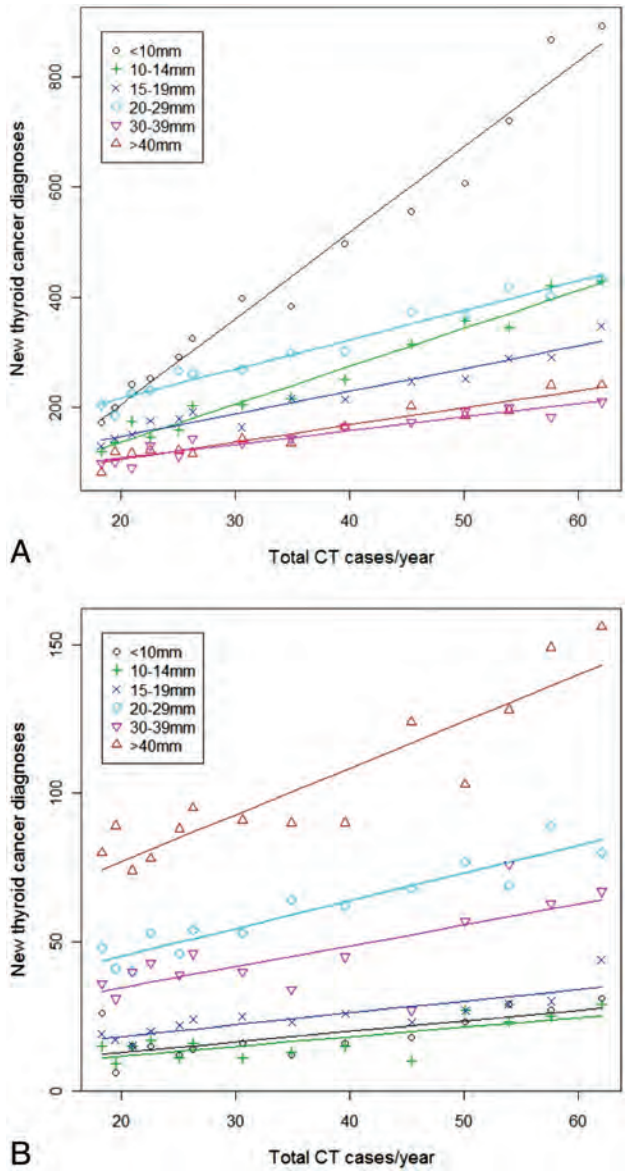

FIG 3. Relationship between annual CT scans and incidence of thyroid cancer for (*A*) papillary carcinoma and (*B*) nonpapillary carcinoma. The CT cases represents million cases per year.

DISCUSSION

Although it took 30 years for the incidence of thyroid cancer to double before 2002,[1] we found that the number of new diagnoses nearly doubled between the years 2000 and 2009 without significant change in mortality rate. Our observation that subcentimeter, and hence impalpable, thyroid cancers are growing at the greatest rate agrees with a body of literature that proposes imaging could be leading to the increased diagnosis of small thyroid cancers.[1,11,12]

The influence of imaging on the detection of thyroid cancer began with the use of sonography and sonography-guided fine-needle biopsy in the 1980s. The incidence continued to increase as sonography machines became more widely used in the clinician's office.[13] This study generates a hypothesis that the current trends could also be related to CT imaging in addition to sonography. Our data show a parallel increase in the use of diagnostic CT and cases of thyroid cancer, especially for subcentimeter papillary carcinoma. Although regression analyses do not infer causality, the linear model fits very well and has led us to consider 2 scenarios in which CT scanning could lead to a diagnosis of thyroid cancer. The first is that an increase in CT imaging detects more incidental thyroid nodules that receive work-up leading to the subsequent diagnosis of cancer. Alternatively, the microcarcinoma may not have been seen on the initial CT, but work-up of another nodule detected on CT could lead to detection of the microcarcinoma on thyroid sonography or in a diagnostic lobectomy surgical specimen.[14]

In our study, larger thyroid cancers (>20 mm) are also increasing, albeit at a lower rate than cancers <10 mm. Chen et al[15] argued that diagnostic scrutiny from imaging would not account for the increase in larger thyroid cancers. We suggest that CT imaging could lead to the incidental diagnosis of larger cancers, as large nodules may be asymptomatic because of deep location in the posterior aspect of the thyroid or because of large body habitus. Wiest et al[16] found that 52% of thyroid nodules >2 cm were not palpable by experienced physician examiners. Furthermore, it is known from retrospective studies that incidental thyroid nod-

ules can be >2 cm. Hobbs et al[17] studied the presentation of thyroid nodules having sonography-guided biopsy, and found that nodules detected incidentally on imaging had a mean size of 26 mm (standard deviation, 17 mm). In our study, the relationship between annual CT volume and the incidence of papillary carcinomas that were >2 cm also fit the linear regression model well, but the rate of increase in incidence per million scans was 3–6 times lower than for subcentimeter papillary carcinoma.

It is also plausible that the relationship between CT and thyroid cancer is in reverse order to our main hypothesis: An increased incidence of thyroid cancer may be causing an increase in CT scans. The effect may represent use of CT for work-up of known thyroid cancer. Against this alternative hypothesis is that sonography is used far more frequently to evaluate newly diagnosed thyroid cancers than CT. CT scans are only obtained in newly diagnosed thyroid cancer for large tumors that may be invading the trachea or carotid artery, or have substernal extension. In fact, the American Thyroid Association strongly recommends against preoperative CT and MR imaging for thyroid cancer.[6] The second argument against thyroid cancer causing an increase in CT use is the observation of the linear regression results for nonpapillary carcinoma. The linear regression slopes for different tumor sizes show a higher slope for larger nonpapillary cancers than smaller nonpapillary cancers, indicating that for a given CT scan, there are more larger cancers than smaller cancers. If the x- and y-axes were reversed for the hypothesis that thyroid cancers led to CT scans, there would be less CT scans for a given number of larger nonpapillary cancers than smaller nonpapillary cancers. The opposite would be expected for large invasive anaplastic and medullary cancers—large tumors are more likely to require CT for evaluation of local invasion. Thus, it is unlikely that CT work-up is the major explanation for the relationship between CT scans and thyroid cancer.

A less likely alternative explanation for the linear relationship between thyroid cancer and CT is that radiation exposure from CT scanning is causing thyroid cancer. The mean radiation dose to the thyroid from a CT scan of the neck ranges from 17–34 mGy, which is within the range that may increase the risk for thyroid cancer in children.[18-20] However, most people receiving neck CT scans are older adults, and the risk for cancer from radiation exposure decreases sharply with increasing age.[21] Pooled analyses of studies of thyroid cancer in patients exposed to radiation found that there was little risk for excess cancer when exposure was after age 20 years.[22] The International Commission on Radiological Protection also estimates that the relative risk for thyroid cancer decreases by 57% for each decade of life.[23] Patients having a CT scan of the cervical spine are often in a younger age group, but they are still mostly adults. In a large multicenter cervical spine trauma study, the mean age of patients having cervical spine imaging for trauma was 37 years.[24] Furthermore, radiation-induced malignant disease occurs decades after the radiation exposure. Kikuchi et al[25] studied patients with therapeutic radiation exposure to the neck and found that the mean latency period for thyroid cancer was 28 years. Thus, the more dramatic increase in CT scans in the US population that has occurred in the last 10 years should not affect the incidence of thyroid cancer until future years.

Our study had several limitations. First, the SEER data base did not provide information on how the tumors were diagnosed. The impact of other potential sources of occult papillary microcarcinomas, such as thyroidectomies for benign indications or a change in pathologic technique or classification, cannot be measured for these data.[26,27] Second, the data bases for thyroid cancer and CT volume were not exactly matched. The patients in the SEER data base represent 10% of the US population, whereas the NCRP CT data base is for the entire US population. Third, it was not possible to exclude CT studies that do not image the thyroid from the NCRP CT data base. To use the available data, we assumed that the proportion of studies that included the neck had increased at the same rate with time. In addition, we could not exclude repeated studies performed in the same patient or multiple scans performed in the same session. These 2 limitations of the NCRP data base could be overcome by obtaining CT use data from the Medicare data base, but the Medicare data base only includes patients 65 years and older and would not account for correlation with younger patients. This would have been a major limitation because our results found that the greatest growth in thyroid cancer incidence was seen in the 50- to 64-year-old group.

Although our analysis cannot prove causation, this relationship may help to focus future work on testing the hypothesis that CT scans contribute to the increased detection of incidental thyroid nodules leading to an increased incidence in thyroid cancer. Until then, we should improve on current practices by developing evidence-based and cost-effective guidelines for the work-up of incidental thyroid nodules seen on CT. Currently thyroid nodules are seen in 1 in 6 CT neck studies.[21,28] The radiologist's approach to reporting incidental thyroid nodules on CT can vary because CT cannot differentiate between a benign and malignant nodule, and there is a lack of clear guidelines for work-up.[21,29]

CONCLUSIONS

The incidence of subcentimeter papillary carcinoma is growing at an exponential rate without significant change in mortality rate. There is a very strong linear relationship between new cases of subcentimeter papillary carcinomas and the number of CT scans per year. This trend suggests that an increase in CT scans may increase the detection of incidental thyroid cancers.

Disclosures: Gary Lyman—*UNRELATED: Grants/Grants Pending:* Amgen,* Comments: PI on research grant to Duke University. **Money paid to institution.*

REFERENCES

1. Davies L, Welch HG. **Increasing incidence of thyroid cancer in the United States, 1973–2002.** *JAMA* 2006;295:2164–67
2. Sandhu GS, Andriole GL. **Overdiagnosis of prostate cancer.** *J Natl Cancer Inst Monogr* 2012;2012:146–51
3. McLeod DS, Sawka AM, Cooper DS. **Controversies in primary treatment of low-risk papillary thyroid cancer.** *Lancet* 2013;381:1046–57
4. Etzioni R, Penson DF, Legler JM, et al. **Overdiagnosis due to prostate-specific antigen screening: lessons from U.S. prostate cancer incidence trends.** *J Natl Cancer Inst* 2002;94:981–90
5. Frates MC, Benson CB, Charboneau JW, et al. **Management of thyroid nodules detected at US: Society of Radiologists in Ultrasound consensus conference statement.** *Radiology* 2005;237:794–800
6. Cooper DS, Doherty GM, Haugen BR, et al. **Revised American Thyroid Association management guidelines for patients with thyroid**

nodules and differentiated thyroid cancer. *Thyroid* 2009;19: 1167–214
7. Matin A, Bates DW, Sussman A, et al. **Inpatient radiology utilization: trends over the past decade.** *AJR Am J Roentgenol* 2006;186:7–11
8. Rao VM, Levin DC, Parker L, et al. **Trends in utilization rates of the various imaging modalities in emergency departments: nationwide Medicare data from 2000 to 2008.** *J Am Coll Radiol* 2011;8:706–09
9. Broder J, Warshauer DM. **Increasing utilization of computed tomography in the adult emergency department, 2000–2005.** *Emerg Radiol* 2006;13:25–30
10. National Council on Radiation Protection and Measurements., National Council on Radiation Protection and Measurements. Scientific Committee 6–2 on Radiation Exposure of the U.S. Population. *Ionizing Radiation Exposure of the Population of the United States.* Bethesda, MD: National Council on Radiation Protection and Measurements; 2009
11. Hughes DT, Haymart MR, Miller BS, et al. **The most commonly occurring papillary thyroid cancer in the United States is now a microcarcinoma in a patient older than 45 years.** *Thyroid* 2011; 21:231–36
12. Pellegriti G, Frasca F, Regalbuto C, et al. **Worldwide increasing incidence of thyroid cancer: update on epidemiology and risk factors.** *J Cancer Epidemiol* 2013;2013:965212
13. Moore CL, Copel JA. **Point-of-care ultrasonography.** *N Engl J Med* 2011;364:749–57
14. Kim DW, Kim SH, Jung SJ. **Successful sonography-guided fine-needle aspiration biopsy of a 1-millimeter-diameter papillary thyroid microcarcinoma.** *AJNR Am J Neuroradiol* 2010;31:1082–84
15. Chen AY, Jemal A, Ward EM. **Increasing incidence of differentiated thyroid cancer in the United States, 1988–2005.** *Cancer* 2009; 115:3801–07
16. Wiest PW, Hartshorne MF, Inskip PD, et al. **Thyroid palpation versus high-resolution thyroid ultrasonography in the detection of nodules.** *J Ultrasound Med* 1998;17:487–96
17. Hobbs H, Bahl M, Nelson RC, et al. **Incidental thyroid nodules detected on imaging: can workup be reduced by using the SRU recommendations and the 3-tier system?** *AJR Am J Roentgenol* 2014. In press.
18. Hoang JK, Yoshizumi TT, Nguyen G, et al. **Variation in tube voltage for adult neck MDCT: effect on radiation dose and image quality.** *AJR Am J Roentgenol* 2012;198:621–27
19. Leswick DA, Hunt MM, Webster ST, et al. **Thyroid shields versus z-axis automatic tube current modulation for dose reduction at neck CT.** *Radiology* 2008;249:572–80
20. Mazonakis M, Tzedakis A, Damilakis J, et al. **Thyroid dose from common head and neck CT examinations in children: is there an excess risk for thyroid cancer induction?** *Eur Radiol* 2007; 17:1352–57
21. Nguyen XV, Choudhury KR, Eastwood JD, et al. **Incidental thyroid nodules on CT: evaluation of 2 risk-categorization methods for work-up of nodules.** *AJNR Am J Neuroradiol* 2013;34:1812–17
22. Ron E, Lubin JH, Shore RE, et al. **Thyroid cancer after exposure to external radiation: a pooled analysis of seven studies.** *Radiat Res* 1995;141:259–77
23. **The 2007 Recommendations of the International Commission on Radiological Protection. ICRP publication 103.** *Ann ICRP* 2007; 37:1–332
24. Hoffman JR, Mower WR, Wolfson AB, et al. **Validity of a set of clinical criteria to rule out injury to the cervical spine in patients with blunt trauma. National Emergency X-Radiography Utilization Study Group.** *N Engl J Med* 2000;343:94–99
25. Kikuchi S, Perrier ND, Ituarte P, et al. **Latency period of thyroid neoplasia after radiation exposure.** *Ann Surg* 2004;239:536–43
26. Salajegheh A, Petcu EB, Smith RA, et al. **Follicular variant of papillary thyroid carcinoma: a diagnostic challenge for clinicians and pathologists.** *Postgrad Med J* 2008;84:78–82
27. de Matos LL, Del Giglio AB, Matsubayashi CO, et al. **Expression of CK-19, galectin-3 and HBME-1 in the differentiation of thyroid lesions: systematic review and diagnostic meta-analysis.** *Diagn Pathol* 2012;7:97
28. Yousem DM, Huang T, Loevner LA, et al. **Clinical and economic impact of incidental thyroid lesions found with CT and MR.** *AJNR Am J Neuroradiol* 1997;18:1423–28
29. Shetty SK, Maher MM, Hahn PF, et al. **Significance of incidental thyroid lesions detected on CT: correlation among CT, sonography, and pathology.** *AJR Am J Roentgenol* 2006;187:1349–56

Spontaneous Lateral Sphenoid Cephaloceles: Anatomic Factors Contributing to Pathogenesis and Proposed Classification

F. Settecase, H.R. Harnsberger, M.A. Michel, P. Chapman, and C.M. Glastonbury

ABSTRACT

SUMMARY: Spontaneous lateral sphenoid cephaloceles arise from bony defects in the lateral sphenoid, in the absence of predisposing factors such as trauma, surgery, mass, or congenital skull base malformation. We reviewed CT and MR imaging findings and clinical data of 26 patients with spontaneous lateral sphenoid cephaloceles to better understand anatomic contributions to pathogenesis, varying clinical and imaging manifestations, and descriptive terminology. Two types of spontaneous lateral sphenoid cephaloceles were identified. In 15 of 26 patients, a type 1 spontaneous lateral sphenoid cephalocele was noted, herniating into a pneumatized lateral recess of the sphenoid sinus, and typically presenting with CSF leak and/or headache. In 11 of 26 patients, a type 2 spontaneous lateral sphenoid cephalocele was noted, isolated to the greater sphenoid wing without extension into the sphenoid sinus, presenting with seizures, headaches, meningitis, cranial neuropathy, or detected incidentally. All patients had sphenoid arachnoid pits, and 61% of patients had an empty or partially empty sella, suggesting that altered CSF dynamics may play a role in their genesis.

ABBREVIATIONS: AbAGs = aberrant arachnoid granulations; GWS = greater wing of the sphenoid; IIH = idiopathic intracranial hypertension; SLSC = spontaneous lateral sphenoid cephalocele; SS = sphenoid sinus

Cephalocele is a hypernymous term describing a herniation of intracranial contents through a bony defect in the skull base or calvaria, such as meninges and CSF (meningocele), and sometimes brain tissue (meningoencephalocele or encephalocele). Cephaloceles may be congenital with failure of normal skull base development, or related to prior trauma, surgery, tumors, sphenoid dysplasia in neurofibromatosis type 2, or osteoradionecrosis. In the absence of the aforementioned predisposing factors, cephaloceles are referred to as spontaneous. Although spontaneous cephaloceles are believed to be rare, they are likely more common than previously reported[1-4] and may have confusing imaging manifestations. A subset of spontaneous cephaloceles occurs off midline in the lateral sphenoid bone, and has been referred to as spontaneous lateral sphenoid cephaloceles (SLSCs). Left untreated, these lesions may pose a risk for ascending infection and meningitis[1,5] and may be a cause of seizures and headaches.

The literature has focused on a subset of patients with SLSCs presenting with CSF leak, most likely because this is a common presentation, and patients with CSF leaks share a similar treatment approach. The etiopathogenesis of spontaneous lateral sphenoid CSF leaks was initially postulated to result from a persistence of a Sternberg canal.[6-8] An interplay of physiologic and other anatomic factors is now more widely favored, based on CT and MR imaging observations of associations with pneumatization of the lateral recess of the sphenoid sinus (SS),[3,9,10] arachnoid pits, and an empty or partially empty sella.[1-3,9,11-17] Sharing not only similarities in associated imaging signs[18] as well as common clinical and demographic features of female sex, middle age, and obesity, spontaneous skull base CSF leaks have been also postulated to represent a rare manifestation of idiopathic intracranial hypertension (IIH).[1,3,13-18] Limiting analysis to the subset of patients with lesions presenting with CSF leaks, however, may result in an incomplete understanding of the etiopathogenesis of these lesions.

In this study, we retrospectively review CT and MR imaging findings and clinical presentation of patients with SLSCs. We specifically sought to better understand the anatomical factors contributing to pathogenesis, varying clinical presentations and imaging findings, and clarify the current descriptive terminology of these lesions.

Received June 4, 2013; accepted after revision August 14.

From the Department of Radiology and Biomedical Imaging (F.S., C.M.G.) University of California, San Francisco, San Francisco, California; Department of Radiology (H.R.H.), University of Utah, Salt Lake City, Utah; Department of Radiology (M.A.M.), Medical College of Wisconsin, Milwaukee, Wisconsin; and Department of Radiology (P.C.), University of Alabama, Birmingham, Alabama.

Paper previously presented at: 45th Annual Meeting of the American Society of Head and Neck Radiology, September 7–11th, 2011; San Diego, California.

Please address correspondence to Fabio Settecase, MD, MSc, FRCPC, Department of Radiology and Biomedical Imaging, University of California, San Francisco, 505 Parnassus Ave, L358, San Francisco, CA 94143; e-mail: fabio.settecase@utoronto.ca

http://dx.doi.org/10.3174/ajnr.A3744

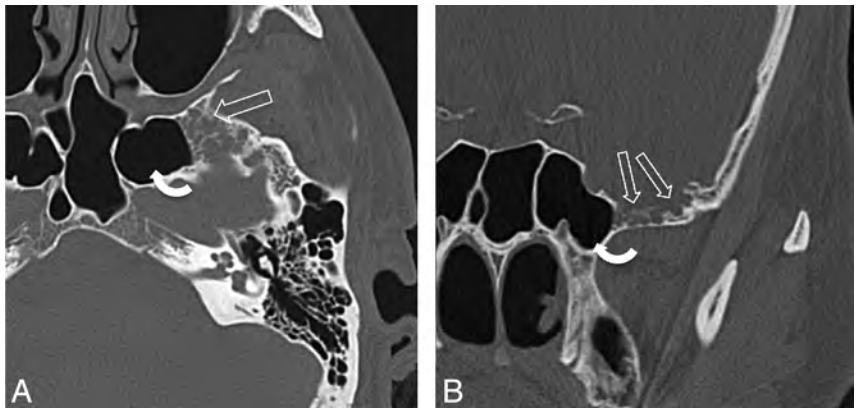

FIG 1. A 43-year-old man presenting with headaches (patient 20). *A*, Axial bone CT image through the mid SS shows multiple ovoid bony defects in the greater wing of the sphenoid bone representing arachnoid pits due to aberrant arachnoid granulations (*open arrows*). This patient also has extensive pneumatization of the lateral recesses of the SS (*curved arrow*). *B*, Coronal CT image of the same patient as in panel *A*, again demonstrating multiple arachnoid pits in the GWS (*open arrows*). A cephalocele was seen on MR imaging (not shown here).

MATERIALS AND METHODS

A retrospective review of 4 university hospital imaging archives identified 29 patients with SLSCs who underwent imaging between 2000 and 2012. Search terms included *sphenoid cephalocele*, *sphenoid meningocele*, and *sphenoid encephalocele*. As a retrospective chart and imaging review, this study was exempted from informed patient consent by the institutional review board. Diagnosis was established by imaging findings and was confirmed with direct visualization in surgically repaired cases. Exclusion criteria included a history of head trauma, previous skull base or SS surgery, tumor, and known congenital malformation of the skull base. Three patients were excluded based on the presence of a pineal gland tumor, a history of previous head trauma, and multiple previous skull base surgeries.

Imaging was reviewed by a single reader (F.S.), a fellowship-trained neuroradiologist, who was blinded to clinical information at the time of the imaging review. CT and MR imaging of 26 patients were reviewed, with particular attention to SLSC location, presence of arachnoid pits, degree of pneumatization of the lateral recesses of the SS, and the presence of an empty or partially empty sella. Arachnoid pits were identified based on their appearance, as previously described and illustrated,[3,9,10] which consists of focal lobulated or multilobulated outward concave bony areas along the inner table of the greater wing of the sphenoid on CT and/or MR imaging (Fig 1). On MR imaging, the contents of the arachnoid pits appear isointense to CSF. Pneumatization of the lateral recesses of the SS was defined as extension of the air-filled SSs inferolaterally into the sphenoid body/greater sphenoid wing junction, caudal to the foramen rotundum, anteroinferior to the foramen ovale, and often extending into the pterygoid plates.

Imaging studies were acquired according to institutional protocols and presenting symptoms, and consisted of 1 or more of the following: routine head CT; multidetector CT of the sinuses acquired in the axial plane, and reconstructed in sagittal and coronal planes; MR imaging of the head at 1.5T or 3T, including axial and coronal T1-weighted with and without intravenous contrast material, and coronal T2-weighted fast spin-echo and steady-state free precession sequences, by use of a standard head coil. CT cisternography was also reviewed in cases where it was performed.

Clinical notes were reviewed for patient characteristics. The presenting symptom of CSF leak was confirmed by B2 transferrin and was visualized on CT cisternography in 3 patients.

RESULTS

A total of 26 patients (16 women, 10 men) with 28 SLSCs were identified. The clinical and imaging findings are summarized in the accompanying Table.

Clinical Findings

Patients ranged in age from 20–76 years with an average age of 49 ± 15 years. Of the 26 patients, the most common clinical presentations were CSF leak in 12 (46%), headache in 7 (27%), and seizures in 7 (27%). One patient with headaches and CSF rhinorrhea also had meningitis at presentation. One patient each presented with cranial neuropathy, nasal fullness, and proptosis, and in a single patient, an SLSC was an incidental imaging finding (Table).

Imaging Findings

Nineteen patients had both MR imaging and CT available for review, 4 patients had only CT imaging performed, and 3 patients had only MR imaging. Five patients underwent additional imaging with CT cisternography. The following imaging observations were made with reference to the patient group: the presence of arachnoid pits, SLSCs, pneumatization of the lateral recess of the SSs, and an empty or partially empty sella. These characteristics are described in detail below.

Presence of Arachnoid Pits

Arachnoid pits were present in all 26 patients with SLSCs, and all patients had 1 or more arachnoid pits that were noncontiguous with the SLSC, either on the same or contralateral side (Figs 1–3). Size varied from 1–2 mm to > 1 cm in size. The arachnoid pits involved the inner table of the medial greater wing of the sphenoid (GWS) in the middle cranial fossa, lateral to the foramen rotundum and anterior to the foramen ovale. In some cases, arachnoid pits extended laterally along the inner table of the squamosal temporal bone.

Spontaneous Lateral Sphenoid Cephaloceles

CT and MR imaging depicted 28 SLSCs in 26 patients: 12 on the left side, 12 on the right, and bilaterally in 2 patients. On CT, a SLSC appears as a focal dehiscence of bone (Figs 2 and 3) with soft tissue or fluid attenuation herniating into the defect, often mimicking a mucous retention cyst. The contents of the cephalocele were better demonstrated on MR imaging or CT cisternography (Figs 2*B* and 3*B*). Meninges were seen herniating through the defect as a thin dark line on T2 imaging. CSF was characteristi-

Patient characteristics, clinical information, and imaging findings

Patient	Age	Sex	Presenting Symptom(s)	Arachnoid Pits	Pneumatization of Lateral Recesses of SS	Site of Cephalocele	Side of Defect	Empty or PE Sella
1	55	M	CSF rhinorrhea	Yes	Yes	SS	R	Yes
2	48	M	Chronic sinusitis	Yes	Yes	SS	R	Yes
3	49	F	Seizures	Yes	Yes	SS	L	No
4	54	F	CSF rhinorrhea and headache	Yes	Yes	SS	R	Yes
5	54	F	CSF rhinorrhea and headache	Yes	Yes	SS	R	Yes
6	59	F	CSF rhinorrhea	Yes	Yes	SS	R	Yes
7	55	M	CSF rhinorrhea	Yes	Yes	SS	R	Yes
8	75	F	CSF rhinorrhea	Yes	Yes	SS	L	Yes
9	76	F	Headache	Yes	Yes	SS	L	No
10	63	F	CSF rhinorrhea and headache	Yes	Yes	SS	L	No
11	32	F	CSF rhinorrhea	Yes	Yes	SS	L	No
12	57	F	CSF rhinorrhea	Yes	Yes	SS	R	No
13	57	F	CSF rhinorrhea	Yes	Yes	SS	L	Yes
14	52	M	CSF rhinorrhea	Yes	Yes	SS	R	Yes
15	29	M	Seizures	Yes	No	GWS	R	No
16	53	F	Nasal fullness	Yes	Yes	GWS	R	No
17	50	M	Seizures	Yes	No	GWS	R	No
18	20	M	Seizures	Yes	No	GWS	L	No
19	34	M	Meningitis, seizures, and CSF rhinorrhea	Yes	Yes	SS	R	Yes
20	43	M	Headaches	Yes	Yes	GWS	B	Yes
21	27	M	Seizures	Yes	No	GWS	B	NK
22	67	F	Seizures	Yes	Yes	GWS	L	Yes
23	65	F	Incidental (imaging for decreased vision in right eye)	Yes	Yes	GWS	L	No
24	26	F	Headaches	Yes	No	GWS and clivus	L	NK
25	26	F	Proptosis	Yes	No	GWS	L	Yes
26	45	F	Headache and infraorbital nerve symptoms	Yes	No	GWS	L	NK

Note:—B indicates bilateral; L, left; NK, not known; PE, partially empty; R, right.

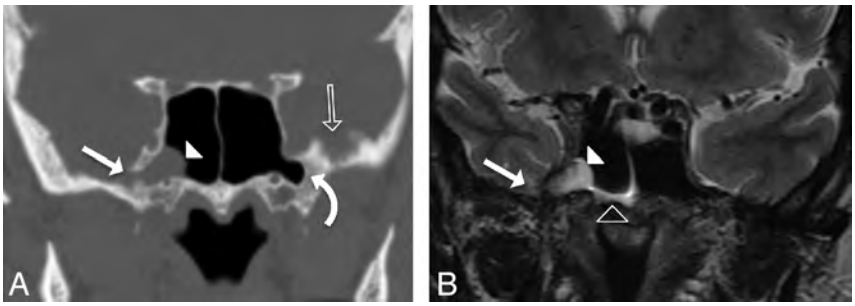

FIG 2. A 59-year-old woman presenting with CSF rhinorrhea (patient 6). *A*, Coronal CT image in bone windows showing focal bony dehiscence of the lateral wall of the right SS (*solid arrow*), with soft tissue attenuation herniating into the SS through the defect (*arrowhead*). Note the presence of arachnoid pits along the inner table of the contralateral GWS (*open arrow*) and bilateral pneumatization of the lateral sphenoid recesses (*curved arrow*). *B*, Coronal T2-weighted image demonstrating the contents of the herniation from panel *A* as a cephalocele composed of meninges, CSF, and a portion of the right mesial temporal lobe (*solid arrowhead*). Note the CSF fluid level within the right SS (*open arrowhead*). This type 1 SLSC best illustrates the ability of these lesions to simulate a mucous retention cyst.

cally T2 hyperintense or filled with intrathecal contrast on CT cisternography. The soft tissue herniating through the defect was contiguous with brain parenchyma, which allowed for a specific diagnosis of a cephalocele. The herniated brain typically followed T1 and T2 signal characteristics of normal brain parenchyma. In some cases, white matter T2 hyperintensity was seen within the involved temporal lobe, suggesting edema and/or gliosis (Fig 3*B*).

Of 28 SLSCs, 15 (54%) involved a bony defect of the lateral wall of the SS, resulting in herniation of the cephalocele into the SS. In 13 of 28 SLSCs, the cephalocele herniated through a bony defect of the GWS that did not involve the wall of the SS (Fig 3). The CT appearance often mimicked an aggressive lytic lesion of the sphenoid bone. As with SLSCs extending into the SS, MR imaging signal characteristics of these cephaloceles followed those of CSF and brain tissue, which allowed for a specific diagnosis.

Degree of Pneumatization of the Lateral Recess of the Sphenoid Sinuses

Pneumatization of the lateral recesses of the SS was present in 19 (73%) of 26 patients. The lateral recess of the SS was the site of the cephalocele in 15 (54%) of 28 cephaloceles, with all 15 of these demonstrating pneumatization of the lateral recess of the SS (Table and Fig 2). The other 13 cephaloceles involved the GWS lateral to the SS (Fig 3).

Empty or Partially Empty Sella

Imaging through the sella was available in 23 (88%) of 26 patients. An empty or partially empty sella was noted in 14 (61%) of these 23 patients (Table).

DISCUSSION

The clinical presentation of SLSCs is varied. The literature has focused on a subset of patients presenting with CSF leak, most likely because this is a common presentation, and patients with CSF leaks share similar treatment approaches. In our study, how-

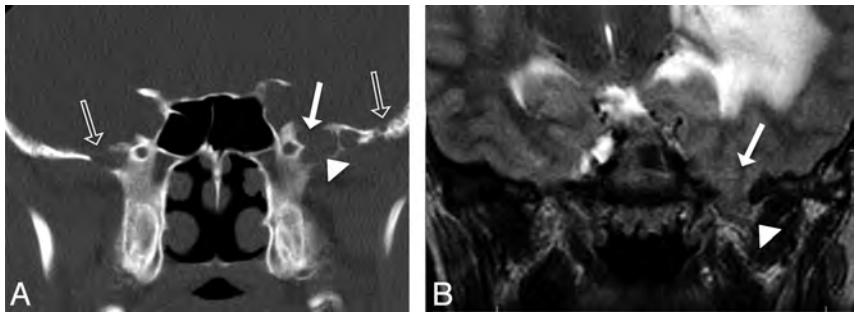

FIG 3. A 27-year-old man presenting with seizures (patient 21). *A*, Coronal CT image shows absence of pneumatization of the lateral sphenoid recesses, but focal dehiscence of inner table of the left greater sphenoid wing (*solid arrow*) with soft tissue attenuation herniating into the defect (*solid arrowhead*). Note the presence of arachnoid pits along the inner table of both the ipsilateral and contralateral GWS (*open arrows*). *B*, Coronal T2-weighted image demonstrating brain parenchyma (*solid arrowhead*) herniating through the bony defect in the GWS (*solid arrow*). Also, note the T2 hyperintensity and mass effect within the left temporal lobe. This patient was found to also have a left occipital dural capillary hemangioma, which, in addition to the white matter T2 abnormality, may have increased intracranial CSF pressure causing enlargement of arachnoid pits bilaterally and subsequent development of a type 2 SLSC seen here.

ever, only 46% of patients with SLSCs presented with a CSF leak. This study illustrates that the clinical presentation of a SLSC largely depends on the location of the bony defect, and that SLSCs can be divided into 2 subtypes. Type 1 SLSC herniates into a pneumatized lateral recess of the SS. Patients with this subtype typically present with a CSF leak and/or headache. Type 2 SLSC herniates into the GWS and not into the SS. In this subtype, the SS lateral recess is usually not pneumatized. Type 2 SLSCs most commonly present with seizures and/or headaches, but they can also be found incidentally and may result in diagnostic confusion (Table).

The development of a spontaneous lateral sphenoid CSF leak was initially postulated to be related to a congenital bony defect in the lateral wall of the SS first described by Sternberg in 1888.[6] Although the Sternberg canal was reported to persist to adulthood in 4% of patients in an anatomic study,[6] this canal underlies the cavernous sinus, whereas SLSCs occur lateral to the foramen rotundum,[10] a finding confirmed in this study. Moreover, a congenital cause is unlikely, because SS pneumatization occurs in later childhood. SLSCs are not accompanied by brain malformations as with true congenital meningocele/meningoencephaloceles,[9] SLSCs are smaller in size and occasionally multiple and bilateral,[9] and patients present during adulthood.[3,9,10]

The etiopathogenesis of lateral sphenoid CSF leaks is now more widely thought to result from a combination of physiologic and anatomic factors, based on CT and MR imaging observations in these patients of associations with arachnoid pits, an empty or partially empty sella, and pneumatization of the lateral recess of the SS. The presence of arachnoid pits in all patients with SLSC in our study, as well as an association with an empty or partially empty sella and with pneumatization of the lateral recess of the SS, is consistent with prior studies on subsets of patients with SLSCs presenting with CSF leaks.[3,9,10]

The most important mechanism underlying the development of SLSCs is likely related to altered CSF dynamics in aberrant arachnoid granulations.[14] Arachnoid granulations are found along the dura and are commonly seen projecting into the dural venous sinuses. They contain arachnoid villi, which are responsible for CSF reabsorption. Less commonly, they can be seen along the calvaria or skull base outside of a dural venous sinus, for instance, along the middle cranial fossa. Outside the dural venous sinuses, they have been termed aberrant arachnoid granulations (AbAGs). AbAGs result in small concave pits in the inner table of the calvaria (Fig 1), best seen on thin-section CT coronal reformats, giving rise to the descriptive term arachnoid pit.[9] On MR imaging, the arachnoid pits follow CSF intensity, and arachnoid strands may occasionally be visible. No postcontrast enhancement is typically seen. The incidence of arachnoid pits in 1000 patients without CSF leak undergoing sinus CT was reported to be 23%.[10] In most cases, arachnoid pits are asymptomatic and incidental; however, in the setting of persistently elevated or large-fluctuation CSF pressure, egress of CSF from the AbAGs may be impaired by their location outside a dural venous sinus. This may lead to progressive enlargement and scalloping of the underlying bone.[9] Arachnoid pits may appear unilocular or multilocular and may mimic a multicystic bone lesion on CT (Figs 1–3), though their characteristic location along the middle cranial fossa is a helpful distinguishing feature. Further enlargement may eventually result in a bony dehiscence, especially if the underlying sphenoid bony substrate is inherently thin to begin with.

The association of SLSCs with pneumatization of the lateral recesses of the SS may be related to the thinning of the SS wall caused by the pneumatization, in addition to the tendency of arachnoid pits to occur along the inner table of the greater sphenoid wing (Figs 1 and 2). The extent of normal pneumatization of the SS is variable in the general population. Pneumatization of the lateral recess of the SS is seen in 23%–43% of healthy adults.[3,9,10,13,16] In this study, pneumatization of the lateral recess of the SS was present in 19 (74%) of 26 patients, and in all 12 patients presenting with CSF rhinorrhea. Previous studies of spontaneous lateral sphenoid CSF leaks found pneumatization of the lateral recess of the SS in 91%–100%.[9,10] However, SLSC herniation into the SS may not always necessarily result in CSF leak at presentation, as seen in 3 patients in our study (Table).

In addition to arachnoid pits, further suggestive evidence of altered CSF hydrodynamics in patients with SLSCs is an association with an empty or partially empty sella.[1-3,9,11-17] In our study, the prevalence of an empty or partially empty sella was 61%, in keeping with prior studies of patients with spontaneous SS CSF leaks.[3,9,17] In contrast, the prevalence of an empty sella in the general population is estimated to be 5%–6%.[19] Sharing not only similarities in associated imaging signs[18] as well as common clinical and demographic features of female sex, middle age, and obesity, spontaneous skull base CSF leaks and cephaloceles have been postulated to represent a rare manifestation of idiopathic intracranial hypertension in retrospective cohort studies.[1,3,13-18,20] Furthermore, patients with spontaneous CSF leaks have histori-

cally had a significantly lower repair success rate and a 25%–87% recurrence rate compared with other types of CSF leaks.[17,21,22] Both elevated intracranial pressure and predisposing osseous thinning at the skull base have also been implicated in the formation of spontaneous cephaloceles and CSF leaks involving the anterior cranial fossa and temporal bone. Although arachnoid pits have not been commonly described in association with ethmoid/cribriform plate cephaloceles and CSF leaks,[3] the predisposition may be related to the inherently decreased thickness of the cribriform plate. Spontaneous cephaloceles and/or CSF otorrhea involving the tegmen tympani, roof of the Eustachian tube, jugular foramen, and the posterior plate of the temporal bone between the sigmoid sinus and the bony labyrinth have also been reported, with arachnoid pits causing progressive scalloping of the temporal bone postulated as a cause.[1-3,5,12-16,23-36] These skull base regions must also be assessed any patient presenting with an SLSC, as there may be multiple cephaloceles at presentation, and on follow-up imaging, especially in patients with persistently elevated CSF pressure or IIH.

Prompt repair of a SLSC defect in patients with CSF leaks is important, as delay in treatment may result in ascending infection (meningitis, encephalitis, or abscess),[1,5] with an annual and long-term risk for meningitis of 10% and 40%, respectively.[11] If the SLSC extends into the SS (type 1), endoscopic repair is usually preferred because it affords good visualization while being less traumatic and has a superior success rate to transcranial approaches.[12,37,38] In this study, seizure was found to be a more common presentation of type 2 SLSCs (5/7 patients presenting with seizures had a type 2 SLSC) and only 1 of these 7 patients presented with a CSF leak. The cause of increased seizure incidence in type 2 SLSCs is unknown; however, this may be related to relative delay in diagnosis or the lack of decompression of herniated brain tissue into the SS. Patients with an untreated type 2 SLSC presenting with seizures may be at risk for continued seizure activity. Type 2 SLSCs may be treated medically or surgically repaired by use of a transcranial approach, but only after clinical confirmation of the SLSC as a distinct seizure focus, source of headaches, or other symptoms, because some SLSCs may be detected incidentally on imaging (Table).

Our study had several important limitations. As a retrospective study, a selection bias may have been present in the patients included in this study. Endoscopic or pathologic confirmation of lesions suspected to represent cephaloceles on imaging was not available for all patients included in this study. Indirect confirmation was available, however, for the 12 patients with documented CSF rhinorrhea. In others, MR imaging appearance was pathognomonic. Because of limited follow-up data, clinical confirmation of the cause of symptoms other than CSF rhinorrhea, such as seizures or headaches, was also limited. In addition, inference on the role of altered CSF hydrodynamics and/or IIH in the etiopathogenesis of SLSCs in this study was limited because of incomplete clinical data relating to patient body habitus, obesity, papilledema, history of IIH, or CSF opening pressure measurements. The association of SLSCs with clinical as well as imaging signs of increased intracranial pressure, such as papilledema, optic nerve-sheath complex enlargement, and narrowing of the dural venous sinuses, in addition to an empty or partially empty sella, should be addressed in a prospective study.

CONCLUSIONS

We propose a classification of SLSCs into 2 types determined by their location. A type 1 SLSC herniates into a pneumatized SS lateral recess and may simulate a mucous retention cyst on CT. This subtype typically presents with CSF leak and/or headache and may be amenable to transphenoidal endoscopic repair. A type 2 SLSC herniates into or through the greater wing of the sphenoid with GWS scalloping or defect, and may have a confusing imaging appearance. Patients with this subtype most frequently present with seizure or headache, and surgical repair requires a transcranial approach. The presence of arachnoid pits in all patients and an association of both types of SLSC with an empty or partially empty sella suggest that altered CSF flow dynamics may play an important role in the pathogenesis.

Disclosures: Michelle Michel—*UNRELATED: Consultancy:* Amirsys; *Payment for Lectures (including service on speaker bureaus):* iiCME; *Royalties:* Amirsys; *Travel/Accommodations/Meeting Expenses Unrelated to Activities Listed:* iiCMHE. Christine M. Glastonbury—*UNRELATED: Royalties:* Amirsys, Comments: Royalties from books; *Payment for Development of Educational Presentations:* Amirsys, Comments: StatDx material; *Stock/Stock Options:* Amirsys, Comments: Family trust.

REFERENCES

1. Lloyd KM, DelGaudio JM, Hudgins PA. **Imaging of skull base cerebrospinal fluid leaks in adults.** *Radiology* 2008;248:725–36
2. Lopatin AS, Kapitanov DN, Potapov AA. **Endonasal endoscopic repair of spontaneous cerebrospinal fluid leaks.** *Arch Otolaryngol Head Neck Surg* 2003;129:859–63
3. Schuknecht B, Simmen D, Briner HR, et al. **Nontraumatic skull base defects with spontaneous CSF rhinorrhea and arachnoid herniation: imaging findings and correlation with endoscopic sinus surgery in 27 patients.** *AJNR Am J Neuroradiol* 2008;29:542–49
4. Alonso RC, de la Peña MJ, Caicoya AG, et al. **Spontaneous skull base meningoencephaloceles and cerebrospinal fluid fistulas.** *Radiographics* 2013;33:553–70
5. Meco C, Oberascher G. **Comprehensive algorithm for skull base dural lesion and cerebrospinal fluid fistula diagnosis.** *Laryngoscope* 2004;114:991–99
6. Sternberg M. **Ein bisher nicht beschriebener Kanal im Keilbein des Menschen.** *Anat Anz* 1888;23:784–86
7. Schick B, Brors D, Prescher A. **Sternberg's canal–cause of congenital sphenoidal meningocele.** *Eur Arch Otorhinolaryngol* 2000;257:430–32
8. Castelnuovo P, Dallan I, Pistochini A, et al. **Endonasal endoscopic repair of Sternberg's canal cerebrospinal fluid leaks.** *Laryngoscope* 2007;117:345–49
9. Shetty PG, Shroff MM, Fatterpekar GM, et al. **A retrospective analysis of spontaneous sphenoid sinus fistula: MR and CT findings.** *AJNR Am J Neuroradiol* 2000;21:337–42
10. Barañano CF, Curé J, Palmer JN, et al. **Sternberg's canal: fact or fiction?** *Am J Rhinol Allergy* 2009;23:167–71
11. La Fata V, McLean N, Wise SK, et al. **CSF leaks: correlation of high-resolution CT and multiplanar reformations with intraoperative endoscopic findings.** *AJNR Am J Neuroradiol* 2008;29:536–41
12. Mirza S, Thaper A, McClelland L, et al. **Sinonasal cerebrospinal fluid leaks: management of 97 patients over 10 years.** *Laryngoscope* 2005;115:1774–77
13. Woodworth BA, Palmer JN. **Spontaneous cerebrospinal fluid leaks.** *Curr Opin Otolaryngol Head Neck Surg* 2009;17:59–65
14. Schlosser RJ, Woodworth BA, Wilensky EM, et al. **Spontaneous cerebrospinal fluid leaks: a variant of benign intracranial hypertension.** *Ann Otol Rhinol Laryngol* 2006;115:495–500

15. Silver RI, Moonis G, Schlosser RJ, et al. **Radiographic signs of elevated intracranial pressure in idiopathic cerebrospinal fluid leaks: a possible presentation of idiopathic intracranial hypertension.** *Am J Rhinol* 2007;21:257–61
16. Woodworth BA, Prince A, Chiu AG, et al. **Spontaneous CSF leaks: a paradigm for definitive repair and management of intracranial hypertension.** *Otolaryngol Head Neck Surg* 2008;138:715–20
17. Schlosser RJ, Bolger WE. **Significance of empty sella in cerebrospinal fluid leaks.** *Otolaryngol Head Neck Surg* 2003;128:32–38
18. Prichard CN, Isaacson B, Oghalai JS, et al. **Adult spontaneous CSF otorrhea: correlation with radiographic empty sella.** *Otolaryngol Head Neck Surg* 2006;134:767–71
19. Garcīa-Uria J, Ley L, Parajõn A, et al. **Spontaneous cerebrospinal fluid fistulae associated with empty sellae: surgical treatment and long-term results.** *Neurosurgery* 1999;45:766–73; discussion 773–74
20. Wang EW, Vandergrift WA 3rd, Schlosser RJ. **Spontaneous CSF leaks.** *Otolaryngol Clin North Am* 2011;44:845–56, vii
21. Schlosser RJ, Wilensky EM, Grady MS, et al. **Cerebrospinal fluid pressure monitoring after repair of cerebrospinal fluid leaks.** *Otolaryngol Head Neck Surg* 2004;130:443–48
22. Schlosser RJ, Wilensky EM, Grady MS, et al. **Elevated intracranial pressures in spontaneous cerebrospinal fluid leaks.** *Am J Rhinol* 2003;17:191–95
23. Connor SE. **Imaging of skull-base cephalocoeles and cerebrospinal fluid leaks.** *Clin Radiol* 2010;65:832–41
24. Gacek RR, Gacek MR, Tart R. **Adult spontaneous cerebrospinal fluid otorrhea: diagnosis and management.** *Am J Otol* 1999;20:770–76
25. Goddard JC, Meyer T, Nguyen S, et al. **New considerations in the cause of spontaneous cerebrospinal fluid otorrhea.** *Otol Neurotol* 2010;31:940–45
26. Wind JJ, Caputy AJ, Roberti F. **Spontaneous encephaloceles of the temporal lobe.** *Neurosurg Focus* 2008;25:E11
27. Arai A, Mizukawa K, Nishihara M, et al. **Spontaneous cerebrospinal fluid rhinorrhea associated with a far lateral temporal encephalocele–case report.** *Neurol Med Chir (Tokyo)* 2010;50:243–45
28. May JS, Mikus JL, Matthews BL, et al. **Spontaneous cerebrospinal fluid otorrhea from defects of the temporal bone: a rare entity?** *Am J Otol* 1995;16:765–71
29. Papanikolaou V, Bibas A, Ferekidis E, et al. **Idiopathic temporal bone encephalocele.** *Skull Base* 2007;17:311–16
30. Shetty PG, Shroff MM, Sahani DV, et al. **Evaluation of high-resolution CT and MR cisternography in the diagnosis of cerebrospinal fluid fistula.** *AJNR Am J Neuroradiol* 1998;19:633–39
31. Stone JA, Castillo M, Neelon B, et al. **Evaluation of CSF leaks: high-resolution CT compared with contrast-enhanced CT and radionuclide cisternography.** *AJNR Am J Neuroradiol* 1999;20:706–12
32. Sillers MJ, Morgan CE, el Gammal T. **Magnetic resonance cisternography and thin coronal computerized tomography in the evaluation of cerebrospinal fluid rhinorrhea.** *Am J Rhinol* 1997;11:387–92
33. Ommaya AK, Di Chiro G, Baldwin M, et al. **Non-traumatic cerebrospinal fluid rhinorrhoea.** *J Neurol Neurosurg Psychiatry* 1968;31:214–25
34. Hooper AC. **Sphenoidal defects–a possible cause of cerebrospinal fluid rhinorrhoea.** *J Neurol Neurosurg Psychiatry* 1971;34:739–42
35. Lang J *Clinical Anatomy of the Nose, Nasal Cavity and Paranasal Sinuses.* New York: Thieme Stuttgart;1989:121
36. Gacek RR. **Arachnoid granulation cerebrospinal fluid otorrhea.** *Ann Otol Rhinol Laryngol* 1990;99:854–62
37. Castelnuovo P, Dallan I, Battaglia P, et al. **Endoscopic endonasal skull base surgery: past, present and future.** *Eur Arch Otorhinolaryngol* 2010;267:649–63
38. Nyquist GG, Anand VK, Mehra S, et al. **Endoscopic endonasal repair of anterior skull base non-traumatic cerebrospinal fluid leaks, meningoceles, and encephaloceles.** *J Neurosurg* 2010;113:961–66

Role of Diffusion Tensor Imaging as an Independent Predictor of Cognitive and Language Development in Extremely Low-Birth-Weight Infants

U. Pogribna, K. Burson, R.E. Lasky, P.A. Narayana, P.W. Evans, and N.A. Parikh

ABSTRACT

BACKGROUND AND PURPOSE: Diffusion tensor imaging at term can predict later development of cerebral palsy. Less is known about its ability to independently predict cognitive and language development in extremely preterm infants. The goals of the study were to investigate the following: 1) whether regional DTI measures at term-equivalent age in extremely low-birth-weight infants (birth weight, ≤1000 g) are predictive of Bayley III developmental scores at 18- to 22-months' corrected age, and 2) to compare white matter microstructural development at term and neurodevelopmental outcomes of extremely low-birth-weight infants with healthy term controls.

MATERIALS AND METHODS: Fractional anisotropy and mean diffusivity in 7 vulnerable cerebral regions were measured in 42 extremely low-birth-weight and 16 term infants with high-quality DTI scans. The Bayley mental scale score (average of cognitive and language scale scores) was the primary outcome of interest with individual scores serving as secondary outcomes. Multiple linear regression modeling was used to identify the incremental ability of DTI measures to predict Bayley scores over known predictors.

RESULTS: Compared with healthy term infants, extremely low-birth-weight infants exhibited significantly higher mean diffusivity and lower fractional anisotropy in 6 of 7 regions. At 18- to 22-months' corrected age, 39 extremely low-birth-weight infants (93%) and 14 term infants (88%) had undergone neurodevelopmental assessments. Although not statistically significant, extremely low-birth-weight infants averaged 7–9 points lower on Bayley subtests than term controls. In multivariable analyses, centrum semiovale mean diffusivity was a significant predictor of mental and language scale scores, and subventricular zone fractional anisotropy was a significant predictor of cognitive scale scores. A 10% increase in centrum semiovale mean diffusivity was associated with a 4.6 (95% CI, 1.6–7.6) point lower mental scale score (adjusted $R^2 = 0.341$, $P = .001$).

CONCLUSIONS: In our extremely low-birth-weight cohort, DTI was an independent predictor of later cognitive and language development.

ABBREVIATIONS: ELBW = extremely low-birth-weight (≤1000 g birth weight); FA = fractional anisotropy; GA = gestational age; MD = mean diffusivity

Up to 50% of extremely preterm infants are diagnosed with cognitive impairment by school age.[1] While cerebral white matter abnormalities visible on cranial sonography account for an important proportion of those with later impairment, nearly 30% with no abnormality on sonography develop impairment.[2] The increasingly common finding of diffuse noncystic white matter signal abnormalities, primarily visible only by using conventional brain MR imaging, has been linked with later cognitive impairment.[3-5] However, neurodevelopmental outcome prediction by using qualitative conventional MR imaging at term-equivalent age remains suboptimal.[5-7] More accurate risk prediction at term

Received May 30, 2013; accepted after revision July 24.

From the Division of Neonatology (U.P., K.B., R.E.L., P.W.E., N.A.P.), Department of Pediatrics, and Department of Radiology (P.A.N.), University of Texas Health Science Center, Houston, Texas; Center for Perinatal Research (N.A.P.), The Research Institute at Nationwide Children's Hospital, Columbus, Ohio; and Department of Pediatrics (N.A.P.), Ohio State University College of Medicine, Columbus, Ohio.

Author contributions: conceived and designed the experiments: N.A.P., R.E.L., P.A.N.; performed the experiments: N.A.P., K.B., P.W.E., U.P.; analyzed the data: U.P., N.A.P.; wrote the paper: U.P., N.A.P.; critically reviewed the paper: U.P., K.B., R.E.L., P.A.N., P.W.E., N.A.P.

This work was supported by the National Center for Research Resources grant UL1 RR024148 (University of Texas Health Science Center at Houston Center for Clinical and Translational Sciences) and the National Center for Research Resources/Eunice Shriver Kennedy National Institute of Child Health & Human Development, grant UL1 RR024148-04S3 (Best Pharmaceuticals for Children Act). The 3T scanner was partially funded by National Center for Research Resources/National Institutes of Health through a grant to P.A.N. (grant S10 RR19186). The funding agencies played no role in the design, conduct, or analysis of the trial. The authors take full responsibility for the integrity of the data and analyses.

Paper previously presented at: Neonatology General Poster Session at the Pediatric Academic Societies Annual Meeting, May 4–7, 2013; Washington, DC (Abstract, Publication 3832.535).

Please address correspondence to Nehal A. Parikh, D.O., M.S., Center for Perinatal Research, Research Building III, 575 Children's Crossroad, Columbus, OH 43215; e-mail: Nehal.Parikh@NationwideChildrens.org

Indicates open access to non-subscribers at www.ajnr.org

http://dx.doi.org/10.3174/ajnr.A3725

could facilitate targeted intensive early intervention therapies and novel neuroprotection trials.

Recent MR imaging advances permit quantification of water diffusion and anisotropy in vivo by using DTI. This advancement has facilitated sensitive detection of microstructural white matter injury and aberrant brain development in extremely preterm infants, making DTI a powerful diagnostic tool and potential early imaging biomarker for cognitive and other neurodevelopmental impairments.[8-11] There is emerging evidence that DTI can predict neurodevelopmental impairments in very low-birth-weight (≤1500 g) infants.[12-15] However, studies in more immature extremely low-birth-weight (≤1000 g) (ELBW) populations are lacking, and the incremental benefits of DTI over conventional MR imaging remain poorly defined. The goals of our study were 2-fold: 1) to investigate whether regional abnormalities on DTI at term-equivalent age in ELBW infants are independent predictors, over known clinical predictors, of standardized cognitive and language scores at 18- to 22-months' corrected age; and 2) to compare white matter microstructural development at term and neurodevelopmental outcomes of ELBW infants with healthy term controls at 18- to 22-months' corrected age by using the newer Bayley Scales of Infant and Toddler Development III.[16]

MATERIALS AND METHODS

Participants

Fifty ELBW and 16 healthy term infants from the Children's Memorial Hermann Hospital neonatal intensive care unit and neonate nursery, respectively, were enrolled to undergo brain DTI at 38 weeks' postmenstrual age or before discharge, if discharge was earlier. Dates of enrollment for ELBW and term infants were May 2007 to July 2009 and July 2008 to January 2010, respectively. The main eligibility criteria for ELBW infants were a birth weight ≤1000 g and survival to 34 weeks postmenstrual age or greater and, for term infants, gestational age (GA) of ≥37 weeks and birth weight appropriate for GA. ELBW infants with known congenital CNS anomalies or who were mechanically ventilated with unstable clinical status at the time of enrollment were excluded. Term infants with any history of perinatal distress or complications or ≥42 weeks' GA were excluded. Institutional review board approval and informed consent were obtained before enrollment.

Image Acquisition and Processing

We used a 3T Achieva scanner (Philips Healthcare, Best, the Netherlands), equipped with a 32-channel receiver and a gradient system capable of producing gradient amplitudes of 80 mT/m with a slew rate of 200 T/m/s for all MR imaging. An 8-channel phased array head coil was used for data acquisition. The DTI protocol consisted of a single-shot, spin-echo planar sequence with TR/TE, 6000/61 ms; in-plane resolution, 1.6 × 1.6 mm^2; FOV, 180 mm^2; 128 × 128 matrix; and 2-mm contiguous sections. Fifteen directions of diffusion gradients were used with a b-value of 800 s/mm^2; low b-value = 0; sensitivity encoding factor = 2. The imaging parameters for the proton-attenuation/T2-weighted scan were the following: TE1, 9 ms; TE2, 175 ms; TR, 10,000 ms; flip angle, 90°; FOV, 180 × 180 mm^2; 256 × 256 mm^2 matrix; section thickness, 2 mm. Sagittal T1, axial FLAIR, axial MPRAGE, coronal T2, and axial gradient-recalled echo sequences were also obtained. Total acquisition time was 4 minutes for the DTI sequence and 25 additional minutes for the conventional sequences. Total imaging time, including repeated sequences, took approximately 1 hour on average.

Patients were fed and swaddled before MR imaging scans. MedVac infant vacuum splint (CFI Medical Solutions, Fenton, Michigan), Insta-Puffy Silicone Earplugs (E.A.R. Inc, Boulder, Colorado), and Natus Mini Muffs (Natus Medical, San Carlos, California) were used for restraint and noise reduction. No sedation was given. All scans were supervised by an experienced neonatologist and a neonatal research nurse.

Image postprocessing and tensor calculations were performed by using MRIStudio software, Version 3.0.3 (Johns Hopkins University, Baltimore, Maryland; http://cmrm.med.jhmi.edu).[17] Regions of interest were selected on the basis of prior published data.[18,19] The following white matter ROIs were selected for further analysis: anterior and posterior limbs of the internal capsule, frontal and occipital periventricular zones, the centrum semiovale, the genu and splenium of the corpus callosum, and the subventricular zone. To minimize variability in region-of-interest placement, we used ImageJ, Version 1.44p (National Institutes of Health; http://imagej.nih.gov/ij) for development and placement of region-of-interest templates (1 for each region of interest) in the native space (Fig 1). All analyses were blinded to clinical variables and cranial sonography and anatomic MR imaging findings. Fractional anisotropy (FA) and mean diffusivity (MD) were measured for each region of interest.

Follow-Up and Developmental Assessment

Standardized follow-up assessments of ELBW and term infants were completed at 18- to 22-months' corrected age in the High-Risk Infant Follow-up Clinic at the University of Texas Health Science Center at Houston. During the follow-up visit, all patients had a complete neurologic physical examination to assess gross motor function and ascertain the presence of cerebral palsy by standardized Eunice Kennedy Shriver National Institute of Child Health and Human Development (NICHD) Neonatal Research Network examiners. The Bayley Scales of Infant and Toddler Development III[16] cognitive and language subtests (scale of 50 to 150; mean of 100; 150 indicating the most advanced development) were administered by a masked, certified examiner.

Data Analysis

Detailed data that included demographics, maternal, perinatal, and neonatal history were prospectively collected for all enrolled ELBW infants during their hospitalization. Additional data in regard to demographics and socioeconomic and health statuses were also collected for infants during their follow-up period. All data were entered into a secure data base with error checks by qualified neonatal research nurses. All unique identifiers were removed to protect privacy and to blind investigators to clinical history.

STATA/IC 12 (StataCorp, College Station, Texas) was used for all data analyses. Two-sample *t* tests, χ^2 tests, and Fisher exact tests were used to describe and compare demographic characteristics of ELBW and term infants, as appropriate. Intrarater reliability

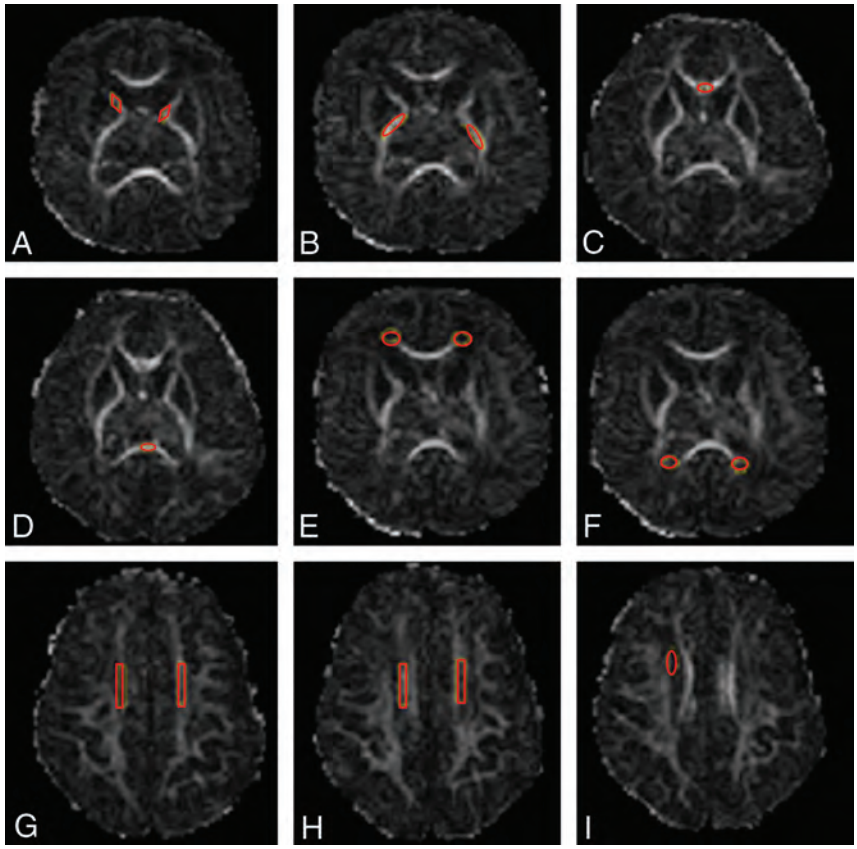

FIG 1. Region-of-interest templates and placements shown on FA maps. *A*, Anterior limb of the internal capsule, *B*, Posterior limb of the internal capsule. *C* and *D*, Corpus callosum, genu and splenium. *E*, Frontal periventricular zone. *F*, Occipital periventricular zone. *G* and *H*, Centrum semiovale at 2 consecutive levels. *I*, Subventricular zone (right-sided). The same templates were used for all scans.

for region-of-interest placements was assessed by using intraclass correlation coefficients on 17 randomly selected ELBW cases.

The mental scale score (the average of cognitive and language scale scores) on Bayley III was the primary outcome of interest. This average score is an overall composite of cognitive and language abilities and permits comparison with the Bayley II mental scale score.[20] Bayley III cognitive and language scale scores were also evaluated independently as secondary outcomes. Bayley III scores (mental, cognitive, and language) and FA and MD measures for each region of interest were compared between term and ELBW infants by using a 2-sample *t* test or a Wilcoxon Mann-Whitney test, as appropriate.

Postmenstrual age was significantly associated with several regional diffusion measures as well as neurodevelopmental outcomes. As such, all regression analyses were controlled for this important confounder. Only regions in which FA and MD were significantly different in ELBW infants compared with term controls were selected for correlation with Bayley III outcomes. Univariate analyses for each region of interest were correlated with mental, cognitive, and language scale scores in separate analyses. Multiple regression modeling was used to identify the incremental and independent ability of DTI measures to predict Bayley III scores. All significant FA and MD ROIs ($P < .05$) were further analyzed in adjusted, multiple regression models. Each multiple regression model was adjusted for birth weight, white matter injury on cranial sonography (presence of ventriculomegaly with or without blood in the ventricles, echodense lesions in the parenchyma, cystic periventricular leukomalacia, and/or a porencephalic cyst evident on cranial ultrasound before 28 days of life), and abnormal conventional MR imaging findings at term (the presence of signal abnormalities, brain atrophy, and/or abnormal gray matter or white matter maturation for age). All assumptions of linear regression were met. In the final models, $P < .05$ was considered significant. All model results are presented as adjusted R^2 values, which represent the proportion of variability in the outcome explained by the model and regression coefficients, with corresponding 95% confidence intervals. Bootstrapping was used to assess the internal validity of the final adjusted models.

RESULTS

Forty-eight of 50 (96%) ELBW infants and 14 of 16 (88%) term infants returned for follow-up at 18- to 22-months' corrected age. Forty-two of these 48 ELBW infants and all 14 of the term infants had high-quality DTI scans free of motion artifacts. Complete Bayley testing was unavailable in 3 ELBW (2 had only cognitive scores) and 2 term infants due to behavioral problems, resulting in the final sample size of 39 ELBW and 12 term infants with complete follow-up and high-quality DTI scans. Demographic and clinical characteristics of these infants are presented in Table 1. ELBW infants were significantly smaller for GA (range, 23–30 weeks) and weight (range, 468–1000 g) than their term counterparts; however, postmenstrual age at MR imaging was similar between groups. Both groups were similar in regard to race and insurance status at birth and at follow-up. The 6 ELBW infants excluded secondary to motion artifacts were similar in a majority of key demographic and clinical variables and Bayley scores compared with those with complete follow-up data.

Cerebral palsy was diagnosed in 4 of 39 (10%) ELBW infants but in none of the term infants at 18- to 22-months' corrected age. Cerebral palsy was not considered as an outcome measure due to our limited study power (Table 1).

Bayley III subtest scores are presented in Table 2. The mean age at follow-up was 20.8 ± 3.8 and 20.8 ± 1.9 months' corrected age for preterm and term infants, respectively. The mean cognitive score for term controls was close to the test norm of 100 points, but the mean language score was approximately 5 points lower. Although not statistically significant, ELBW infants averaged 7–9 points lower than healthy term controls on the Bayley subtests.

Compared with healthy term infants, ELBW infants exhibited

Table 1: Demographic and clinical characteristics of study infants

	Term (*n* = 12) (Mean) (SD) or (%)	ELBW (*n* = 39) (Mean) (SD) or (%)
Maternal age (yr)	23.6 (5.6)	27.9 (4.9)[a]
GA at birth (wk)	38.6 (1.1)	25.6 (1.5)[a]
Birth weight (g)	3159.8 (428.0)	768.6 (147.6)[a]
PMA at MRI (wk)	38.9 (1.1)	38.4 (2.3)
Male	33%	54%
Race: white	42%	46%
Private or mix of private/public medical insurance	33%	44%
Maternal education: college degree or greater	50%	72%
Antenatal steroids given (full course of betamethasone)	N/A	62%
Small for GA (<10th percentile)	0%	18%[a]
Delivery room resuscitation		
Intubation at birth	N/A	92%
Resuscitation drug given	N/A	3%
Bronchopulmonary dysplasia	N/A	85%
Late-onset sepsis (± culture)	N/A	67%
Culture proven late-onset sepsis	N/A	28%
Necrotizing enterocolitis	N/A	3%
Major surgery (with general anesthesia)	N/A	26%
Severe retinopathy of prematurity	N/A	21%
White matter injury on cranial ultrasound[b]	N/A	21%
Abnormal conventional MRI findings at term[c]	N/A	66%
Child's insurance status at time of follow-up		
Private	33%	37%
Public medical insurance	67%	63%
Household income ≥$50,000 at follow-up	33%	32%

Note:—PMA indicates postmenstrual age; N/A, not applicable.

[a] $P < .05$.

[b] Defined as any presence of ventriculomegaly with or without blood in the ventricles, echodense lesions in the parenchyma, cystic periventricular leukomalacia, and/or a porencephalic cyst evident on cranial ultrasound prior to 28 days of life.

[c] Defined as the presence of signal abnormalities, brain atrophy, and/or abnormal gray matter or white matter maturation for age.

Table 2: Developmental outcome comparisons of term and ELBW infants

Developmental Outcome	Term (*n* = 12) (Mean) (SD) or (%)	ELBW (*n* = 39) (Mean) (SD) or (%)	*P* Value
Cerebral palsy	0%	10%	N/A
Bayley III mental scale score	96.4 (15.4)	88.5 (16.6)	.16
Bayley III cognitive scale score	99.2 (17.8)	92.6 (15.3)	.46
Bayley III language scale score	94.9 (16.4)	86.2 (18.6)	.21

Note:—N/A indicates not applicable.

significantly higher MD and lower FA in 6 of the 7 selected brain regions (Fig 2). Mean FA and MD for term infants were 0.143 ± 0.037 and $1.232 \times 10^{-3} \pm 0.099 \times 10^{-3}$, respectively, in the subventricular zone and 0.157 ± 0.031 and $1.530 \times 10^{-3} \pm 0.118 \times 10^{-3}$, respectively, in the centrum semiovale. For ELBW infants, mean FA and MD in the subventricular zone were 0.118 ± 0.031 and $1.577 \times 10^{-3} \pm 0.348 \times 10^{-3}$; and in the centrum semiovale, they were 0.126 ± 0.028 and $1.812 \times 10^{-3} \pm 0.153 \times 10^{-3}$, respectively. The intrarater intraclass correlation coefficient for region-of-interest placements was 0.93. In univariate analyses, subventricular zone FA had a significant positive association with mental and cognitive scale scores; the centrum semiovale and subventricular zone MD had a negative association with mental, cognitive, and language scale scores (Table 3). As such, lower FA or higher MD values in these 2 regions were associated with lower Bayley III scores. White matter injury on cranial sonography performed within the first 28 days of birth was also a significant predictor of all 3 Bayley III scores. Abnormal conventional MR imaging findings (abnormalities in maturation or myelination, atrophy, and structural lesions) at term were a significant predictor of adverse Bayley mental and language scale scores but not cognitive scale scores at 18- to 22-months' corrected age. No associations between birth weight and Bayley III scores were found in the ELBW cohort.

Centrum semiovale MD and subventricular zone FA remained significant independent predictors of Bayley III scores in the adjusted multiple-regression models. Centrum semiovale MD was the only significant predictor of mental scale scores, our primary outcome (Table 4). In secondary analyses, centrum semiovale MD was predictive of language scale scores, and lower subventricular zone FA values were predictive of adverse cognitive scale scores on the Bayley scale (Table 4). In clinical terms, a 10% increase in centrum semiovale MD was associated with a −4.6 (95% CI, −7.6 to −1.6) point decrease on mental scale scores and a −4.6 (95% CI, −8.0 to −1.2) point decrease on language scale scores. Similarly, a 10% increase in subventricular zone FA correlated with a 24.5 (95% CI, 9.6–39.3) point increase on the Bayley III cognitive scale score. Most interesting, of the adjusted factors, only white matter injury on cranial sonography remained a significant predictor of lower mental and cognitive scale scores in multivariable regression modeling. Bootstrapping confirmed the internal validity of the 3 adjusted prediction models.

DISCUSSION

We identified 2 independent regional biomarkers of cognitive and language development in a prospective cohort of ELBW infants imaged at term-equivalent age. Our findings are consistent with emerging evidence of the utility of DTI microstructural abnormalities at term for prediction of neurodevelopmental impairment in very low-birth-weight preterm infants.[9,12-14] Our data support the value of DTI in ELBW infants and suggest that FA and MD are independent predictive biomarkers of early cognitive and language development, in addition to cranial sonography and conventional MR imaging measures.

Cerebral palsy and results of standardized neurodevelopmental assessments are now the most commonly reported outcome measures in studies of preterm infants. Our small sample size, however, precluded us from testing cerebral palsy as an end point. Cognitive and language assessments may be considered the most clinically meaningful outcomes, with up to 50% of ELBW infants developing cognitive impairments by 2 years of age.[1] Mental scale scores and language and cognitive scale scores on the Bayley III were our primary and secondary outcomes of interest, respec-

tively, serving as markers of functional brain development in our cohort of ELBW infants. Several studies have found similar associations between DTI and cognitive and language development, though these studies were completed in older preterm infants during childhood and adolescence.[21-23]

Our study is one of a few that has attempted to correlate early DTI measurements at term with later cognitive development.[21-23] The subventricular zone and centrum semiovale were 2 vulnerable regions of particular interest—abnormalities in fractional anisotropy (lower values) and mean diffusivity (higher values) in these regions were associated with lower mental, cognitive, and language scale scores. These abnormalities remained significant predictors of Bayley III scores, even after adjustment for known adverse predictors of outcome (Table 3). Because diffuse excessive high signal abnormalities are especially common in the centrum semiovale, our results provide additional evidence that such diffuse white matter abnormalities are predictive of cognitive impairment.[4,5,13] Even relatively small changes (10%)—equivalent to 1.1–3.5 weeks of brain maturation[24]—in fractional anisotropy or mean diffusivity, respectively, were associated with clinically meaningful effects on Bayley scores at 18- to 22- months' corrected age. Our results highlight the importance of measuring both MD and FA in vulnerable regions, and differences we observed in correlations with outcome suggest differences in underlying white matter pathology. Mean diffusivity measures the average water diffusion, and high values are believed to reflect destruction of tissue architecture. In contrast, FA values reflect the degree of water anisotropy along different axes; decreased tissue anisotropy likely reflects tissue degeneration.[25]

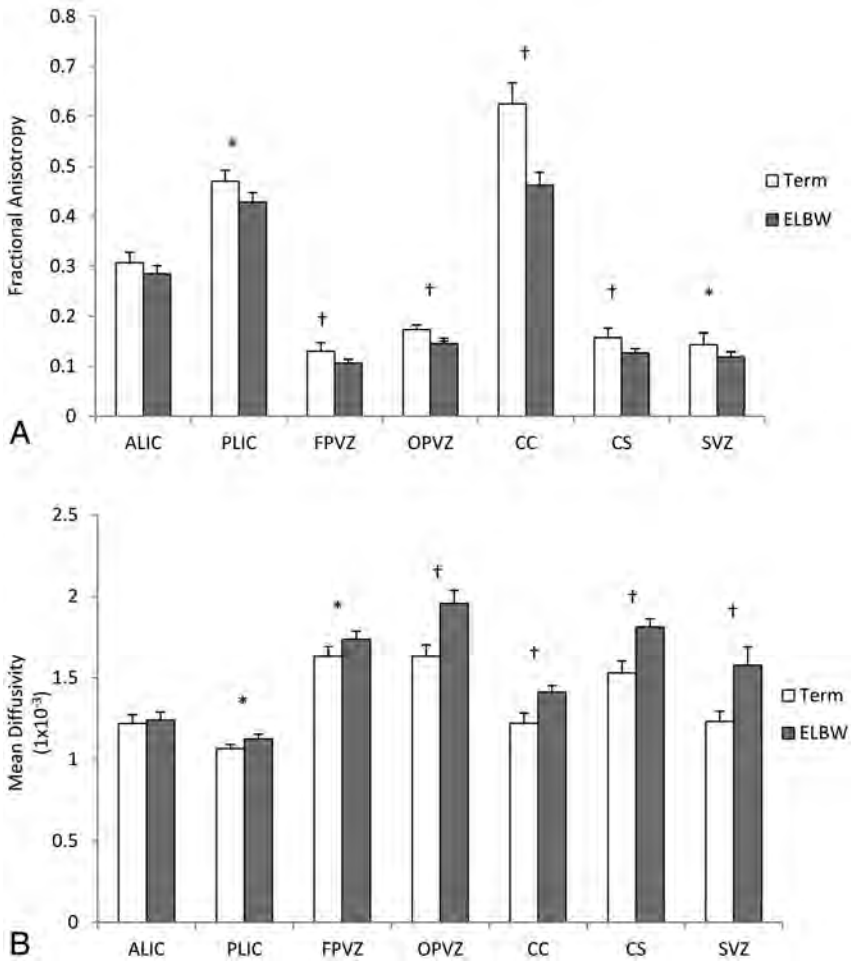

FIG 2. Comparison of mean (SD) fractional anisotropy (*A*) and mean diffusivity (SD) (*B*) in term (white) and ELBW (gray) infants in selected regions of interest. Asterisk indicates $P < .05$; dagger, $P < .01$; ALIC, anterior limb of the internal capsule; PLIC, posterior limb of the internal capsule; FPVZ, frontal periventricular zone; OPVZ, occipital periventricular zone; CC, corpus callosum; CS, centrum semiovale; SVZ, subventricular zone.

In addition to numerous animal models of CNS diseases,[26,27] there are now human fetal[28] and adult studies[29,30] that have demonstrated accurate correlations between DTI microstructural measures and histopathology measures. Increasing fractional anisotropy and decreasing mean diffusivity are markers of improved axonal organization and white matter myelination and are associated with increasing brain development.[31] Multiple studies to date, however, have shown that preterm infants exhibit both macro- and microstructural differences in their white matter organization, often irrespective of underlying injury, compared with healthy term infants; such differences persist into early childhood, adolescence, and even adulthood.[18,23,24,32] In their study, Shim et al[33] observed that chronic lung disease and postnatal infection in preterm infants were independently correlated with altered FA in the posterior limb of the internal capsule and corpus callosum, suggesting that factors other than prematurity

Table 3: Univariate analyses of DTI and clinical variables and their association with Bayley III scores at 18- to 22-months' corrected age in ELBW infants

Variable	Mental Score		Cognitive Score		Language Score	
	Coefficient (95% CI)	*P*	Coefficient (95% CI)	*P*	Coefficient (95% CI)	*P*
FA subventricular zone	179.4 (13.8–345.0)	.04	219.4 (62.8–376.1)	.01	141.1 (−57.1–339.2)	.16
MD subventricular zone	−18.9 (−33.4 to −4.3)	.01	−17.5 (−32.0 to −3.1)	.02	−20.2 (−37.1 to −3.3)	.02
MD centrum semiovale	−55.8 (−86.7 to −24.9)	.001	−51.4 (−82.3 to −20.4)	.002	−60.2 (−96.3 to −24.1)	.002
Birth weight	0.01 (−0.02–0.1)	.42	0.01 (−0.03–0.04)	.80	0.01 (−0.03-.04)	.80
White matter injury on cranial US	−16.8 (−29.1 to −4.5)	.01	−15.7 (−27.9 to −3.5)	.01	−15.7 (−27.9 to −3.5)	.01
Abnormal findings on conventional MRI	−11.6 (−22.3 to −0.9)	.03	−5.8 (−16.8–5.1)	.29	−5.8 (−16.8 to 5.1)	.29

Note:—US indicates ultrasound.

Table 4: Abnormalities in MD and FA and their association with Bayley III scores at 18–22 months corrected age in ELBW infants

Clinical/DTI Variable	Coefficient (95% CI)	*P*
A) Mental scale score (adjusted R^2 0.34/model P 0.001)		
MD centrum semiovale	−45.7 (−75.6 to −15.7)	.004
Birth weight	0.01 (−0.02–0.04)	.41
White matter injury on ultrasound	−12.5 (−23.9 to −1.0)	.03
Abnormal MRI findings at term	−5.0 (−14.9–4.8)	.31
B) Language scale score (adjusted R^2 0.37/model P 0.001)		
MD centrum semiovale	−46.4 (−80.1 to −12.8)	.01
Birth weight	0.02 (−0.02–0.054)	.28
White matter injury on ultrasound	−12.0 (−24.9–1.0)	.07
Abnormal MRI at term	−10.5 (−21.7–0.7)	.07
C) Cognitive scale score (adjusted R^2 0.30/model P 0.003)		
FA subventricular zone	244.6 (96.1–393.1)	.002
Birth weight	0.01 (−0.02–0.05)	.40
White matter injury on ultrasound	−14.0 (−25.5 to −2.6)	.02
Abnormal findings on MRI at term	−5.5 (−15.6–4.6)	.28

alone may affect brain microstructure in preterm infants. Similarly, we have found an independent association between increasing duration of mechanical ventilation (our proxy for chronic lung disease) and delayed maturation (increased MD) of the occipital periventricular zone and centrum semiovale.[34]

Studies in more mature preterm infants found FA and MD to be sensitive markers of microstructural white matter abnormalities and significantly associated with neurodevelopmental impairments.[9,13,14] For example, Krishnan et al[13] observed increasing centrum semiovale MD to be associated with a decreasing developmental quotient in infants ≤34 weeks' GA at birth, similar to our primary outcome findings. However, van Kooij et al[14] reported a significant association between corpus callosum FA and Bayley III cognitive scores in infants <31 weeks' GA, a finding we were not able to validate. Study differences in DTI acquisition and processing methodology (eg, region of interest–based versus whole-brain analyses) and cohort characteristics may well explain such a difference in results. Our data further highlight the importance of DTI measures as early imaging biomarkers and useful adjuncts to conventional neuroimaging to predict cognitive and language development, particularly in the smallest and most vulnerable infants.

The main characteristics of our study included a high-risk population, consistent and reproducible DTI measurements by using robust postprocessing methods, high-resolution 3T imaging, internal validation by using bootstrap, and high follow-up rates. However, our relatively small sample size may have resulted in type II errors (false-negatives). In particular, the lack of a statistical difference in neurodevelopmental scores we observed between ELBW and term infants may have been largely affected by our limited study power. Our decision to avoid sedation for MR imaging in any of the study infants likely contributed to the 10% rate of excessive motion artifacts and case exclusions. Additionally, 18- to 22-months' corrected age is a relatively early follow-up interval for cognitive assessments because these appear to be more accurate at school age.[35] Despite these limitations, our DTI biomarkers accounted for a sizable percentage of the variance in cognitive and language scores, in addition to qualitative neuroimaging approaches, and warrant validation in a larger cohort with school-age follow-up.

CONCLUSIONS

In this prospective cohort study of ELBW infants, DTI microstructural biomarkers at term-equivalent age were independent predictors, in addition to known clinical and imaging risk factors, of cognitive and language development at 18- to 22-months' corrected age. Larger cohort studies with longer follow-up are needed to further assess the predictive validity of DTI measures as early imaging biomarkers of functional impairments in extremely preterm infants.

ACKNOWLEDGMENTS

We sincerely thank Vipulkumar S. Patel for assistance with MR imaging data acquisition as well as the families and nurses that made this study possible.

Disclosures: Ponnada A. Narayana—*RELATED*: *Grant*: National Institutes of Health,* *UNRELATED*: *Grants/Grants Pending*: National Institutes of Health.* Nehal A. Parikh—*RELATED*: *Grant*: Eunice Kennedy Shriver National Institute of Child Health and Human Development,* National Center for Research Resources,* *Comments*: grants UL1 RR024148 and UL1 RR024148-04S3. *Money paid to the institution.

REFERENCES

1. Potharst ES, van Wassenaer AG, Houtzager BA, et al. **High incidence of multi-domain disabilities in very preterm children at five years of age.** *J Pediatr* 2011;159:79–85
2. Laptook AR, O'Shea TM, Shankaran S, et al, for the NICHD Neonatal Network. **Adverse neurodevelopmental outcomes among extremely low birth weight infants with a normal head ultrasound: prevalence and antecedents.** *Pediatrics* 2005;115:673–80
3. Volpe JJ. **Cerebral white matter injury of the premature infant: more common than you think.** *Pediatrics* 2003;112:176–80
4. Dyet LE, Kennea N, Counsell SJ, et al. **Natural history of brain lesions in extremely preterm infants studied with serial magnetic resonance imaging from birth and neurodevelopmental assessment.** *Pediatrics* 2006;118:536–48
5. Iwata S, Nakamura T, Hizume E, et al. **Qualitative brain MRI at term and cognitive outcomes at 9 years after very preterm birth.** *Pediatrics* 2012;129:e1138–47
6. Woodward LJ, Anderson PJ, Austin NC, et al. **Neonatal MRI to predict neurodevelopmental outcomes in preterm infants.** *N Engl J Med* 2006;355:685–94
7. Nongena P, Ederies A, Azzopardi DV, et al. **Confidence in the prediction of neurodevelopmental outcome by cranial ultrasound and MRI in preterm infants.** *Arch Dis Child Fetal Neonatal Ed* 2010;95:F388–90
8. Ment LR, Hintz D, Hüppi PS. **Imaging biomarkers of outcome in the developing preterm brain.** *Lancet Neurol* 2009;8:1042–55
9. Arzoumanian Y, Mirmiran M, Barnes PD, et al. **Diffusion tensor brain imaging findings at term-equivalent age may predict neurologic abnormalities in low birth weight preterm infants.** *AJNR Am J Neuroradiol* 2003;24:1646–53
10. Hüppi PS, Dubois J. **Diffusion tensor imaging of brain development.** *Semin Fetal Neonatal Med* 2006;11:489–97
11. Liu Y, Aeby A, Baleriaux D, et al. **White matter abnormalities are related to microstructural changes in preterm neonates at term-equivalent age: a diffusion tensor imaging and probabilistic tractography study.** *AJNR Am J Neuroradiol* 2012;33:839–45
12. Rose J, Butler EE, Lamont LE, et al. **Neonatal brain structure on MRI and diffusion tensor imaging, sex, and neurodevelopment in very-low-birthweight preterm children.** *Dev Med Child Neurol* 2009;51:526–35
13. Krishnan ML, Dyet LE, Boardman JP, et al. **Relationship between**

white matter apparent diffusion coefficients in preterm infants at term-equivalent age and developmental outcome at 2 years. *Pediatrics* 2007;120:e604–09
14. van Kooij BJ, de Vries LS, Ball G, et al. **Neonatal tract-based spatial statistics findings and outcome in preterm infants.** *AJNR Am J Neuroradiol* 2012;33:188–94
15. Counsell SJ, Edwards AD, Chew ATM, et al. **Specific relations between neurodevelopmental abilities and white matter microstructure in children born preterm.** *Brain* 2008;131:3201–08
16. Bayley N. *Bayley Scales of Infant and Toddler Development.* 3rd ed. San Antonio, Texas: Psychological Corporation; 2005
17. Jiang H, van Zijl PC, Kim J, et al. **DtiStudio: resource program for diffusion tensor computation and fiber bundle tracking.** *Comput Methods Programs Biomed* 2006;81:106–16
18. Anjari M, Srinivasan L, Allsop JM, et al. **Diffusion tensor imaging with tract-based spatial statistics reveals local white matter abnormalities in preterm infants.** *Neuroimage* 2007;35:1021–27
19. Boardman JP, Craven C, Valappil S, et al. **A common neonatal image phenotype predicts adverse neurodevelopmental outcome in children born preterm.** *Neuroimage* 2010;52:409–14
20. Moore T, Johnson S, Haider S, et al. **Relationship between test scores using the second and third editions of the Bayley Scales in extremely preterm children.** *J Pediatr* 2012;160:553–58
21. Feldman HM, Lee ES, Yeatman JD, et al. **Language and reading skills in school-aged children and adolescents born preterm are associated with white matter properties on diffusion tensor imaging.** *Neuropsychologia* 2012;50:3348–62
22. Feldman HM, Lee ES, Loe IM, et al. **White matter microstructure on diffusion tensor imaging is associated with conventional magnetic resonance imaging findings and cognitive function in adolescents born preterm.** *Dev Med Child Neurol* 2012;54:809–14
23. Eikenes L, Lohaugen GC, Brubakk AM, et al. **Young adults born preterm with very low birth weight demonstrate widespread white matter alterations on brain DTI.** *Neuroimage* 2011;54:1774–85
24. Partridge SC, Mukherjee P, Henr RG, et al. **Diffusion tensor imaging: serial quantitation of white matter tract maturity in premature newborns.** *Neuroimage* 2004;22:1302–14
25. Ito M, Watanabe H, Kawai Y, et al. **Usefulness of combined fractional anisotropy and apparent diffusion coefficient values for detection of involvement in multiple system atrophy.** *J Neurol Neurosurg Psychiatry* 2007;78:722–28
26. Mori S, Zhang J. **Principles of diffusion tensor imaging and its applications to basic neuroscience research.** *Neuron* 2006;51:527–39
27. Budde MD, Kim JH, Liang HF, et al. **Toward accurate diagnosis of white matter pathology using diffusion tensor imaging.** *Magn Reson Med* 2007;57:688–95
28. Gupta RK, Hasan KM, Trivedi R, et al. **Diffusion tensor imaging of the developing human cerebrum.** *J Neurosci Res* 2005;81:172–78
29. Stadlbauer A, Ganslandt O, Buslei R, et al. **Gliomas: histopathologic evaluation of changes in directionality and magnitude of water diffusion at diffusion-tensor MR imaging.** *Radiology* 2006:240;803–10
30. Concha L, Livy DJ, Beaulieu C, et al. **In vivo diffusion tensor imaging and histopathology of the fimbria-fornix in temporal lobe epilepsy.** *J Neurosci* 2010;30:996–1002
31. Hüppi PS, Murphy B, Maier SE, et al. **Microstructural brain development after perinatal cerebral white matter injury assessed by diffusion tensor magnetic resonance imaging.** *Pediatrics* 2001;107:455–60
32. Nagy A, Ashburner J, Andersson J, et al. **Structural correlates of preterm birth in the adolescent brain.** *Pediatrics* 2009;124:e964–72
33. Shim SY, Jeong HJ, Son DW, et al. **Altered microstructure of white matter except the corpus callosum is independent of prematurity.** *Neonatology* 2012;102:309–15
34. Pogribna U, Yu X, Burson K, et al. **Perinatal clinical antecedents of white matter microstructural abnormalities on diffusion tensor imaging in extremely preterm infants.** *PLoS One.* In press
35. Hack M, Taylor HG, Drotar D, et al. **Poor predictive validity of the Bayley Scales of Infant Development for cognitive function of extremely low birth weight children at school age.** *Pediatrics* 2005;116:333–41

MR Imaging Evaluation of Inferior Olivary Nuclei: Comparison of Postoperative Subjects with and without Posterior Fossa Syndrome

Z. Patay, J. Enterkin, J.H. Harreld, Y. Yuan, U. Löbel, Z. Rumboldt, R. Khan, and F. Boop

ABSTRACT

BACKGROUND AND PURPOSE: Posterior fossa syndrome is a severe postoperative complication occurring in up to 29% of children undergoing posterior fossa tumor resection; it is most likely caused by bilateral damage to the proximal efferent cerebellar pathways, whose fibers contribute to the Guillain-Mollaret triangle. When the triangle is disrupted, hypertrophic olivary degeneration develops. We hypothesized that MR imaging patterns of inferior olivary nucleus changes reflect patterns of damage to the proximal efferent cerebellar pathways and show association with clinical findings, in particular the presence or absence of posterior fossa syndrome.

MATERIALS AND METHODS: We performed blinded, randomized longitudinal MR imaging analyses of the inferior olivary nuclei of 12 children with and 12 without posterior fossa syndrome after surgery for midline intraventricular tumor in the posterior fossa. The Fisher exact test was performed to investigate the association between posterior fossa syndrome and hypertrophic olivary degeneration on MR imaging. The sensitivity and specificity of MR imaging findings of bilateral hypertrophic olivary degeneration for posterior fossa syndrome were measured.

RESULTS: Of the 12 patients with posterior fossa syndrome, 9 had bilateral inferior olivary nucleus abnormalities. The 12 patients without posterior fossa syndrome had either unilateral or no inferior olivary nucleus abnormalities. The association of posterior fossa syndrome and hypertrophic olivary degeneration was statistically significant ($P < .0001$).

CONCLUSIONS: Hypertrophic olivary degeneration may be a surrogate imaging indicator for damage to the contralateral proximal efferent cerebellar pathway. In the appropriate clinical setting, bilateral hypertrophic olivary degeneration may be a sensitive and specific indicator of posterior fossa syndrome.

ABBREVIATIONS: HOD = hypertrophic olivary degeneration; ION = inferior olivary nucleus; pECP = proximal efferent cerebellar pathway; PFS = posterior fossa syndrome

Posterior fossa syndrome (PFS), a complication of posterior fossa surgery,[1,2] occurs in 11%–29% of patients undergoing posterior fossa tumor resection.[3] Although the definition of the "all-inclusive" PFS is broad and comprises complex neurobehavioral and motor symptoms, cerebellar mutism is at the core of the diagnosis.[4]

Growing evidence suggests that PFS is the result of bilateral damage to the proximal efferent cerebellar pathways (pECPs) along the dentatorubrothalamocortical pathway.[5-13] This relationship was initially observed as cerebellar mutism after stereotactic ablation of the bilateral dentate nuclei.[14] Reversed cerebellocerebral diaschisis, in which deprivation of the cerebral cortex from cerebellar input due to bilateral pECP damage results in a frontally predominant drop of cerebral cortical perfusion, has been proposed to be the mechanism of PFS, and cerebellar mutism is thought to be a form of speech apraxia.[9] During the months following surgery, speech and the associated neurologic deficits usually improve, but those rarely if ever completely normalize. This outcome suggests a profound disturbance of complex neural systems, with significant implications for the long-term quality of life of the steadily increasing number of survivors.[15]

Damage anywhere along the dentatorubrothalamocortical pathway may lead to a speech disorder, and damage to the dentate nuclei in particular has repeatedly been cited as a cause of cerebellar mutism,[5,10,16,17] which can occur after injury along the superior cerebellar peduncles,[8] brachium pontis/conjunctivum,[6,18]

Received May 15, 2012; accepted after revision August 21.

From the Departments of Radiological Sciences (Z.P., J.H.H., U.L.), Biostatistics (Y.Y.), Pediatrics (R.K.), and Surgery (F.B.), St. Jude Children's Research Hospital, Memphis, Tennessee; and Department of Radiology (J.E., Z.R.), Medical University of South Carolina, Charleston, South Carolina.

This work was supported in part by grant no. CA21765 from the National Cancer Institute and by the American Lebanese Syrian Associated Charities.

Please address correspondence to Zoltan Patay, MD, PhD, Department of Radiological Sciences, St. Jude Children's Research Hospital, 262 Danny Thomas Pl, Mail Stop 210, Memphis, TN 38105; e-mail: zoltan.patay@stjude.org

Indicates open access to non-subscribers at www.ajnr.org

http://dx.doi.org/10.3174/ajnr.A3762

bilateral thalamic tracts,[11] or the frontal lobes.[19-21] Given that the dentate nuclei, superior cerebellar peduncles, and mesencephalic tegmental decussation often lie adjacent to and may, therefore, be invaded by midline intraventricular posterior fossa tumors, these structures are the ones most prone to injury during aggressive tumor resection.

The efferent cerebellar tracts that pass through the superior cerebellar peduncles[3] are adjacent to and involve fibers associated with the dentatorubral segment of the Guillain-Mollaret triangle.[22] The Guillain-Mollaret triangle is composed of an ipsilateral red nucleus and inferior olivary nucleus (ION), which are connected by the central tegmental tract, and a contralateral dentate nucleus, which is connected through the superior (dentatorubral) and inferior cerebellar (dentato-olivary) peduncles (Fig 1).

Disrupting the Guillain-Mollaret triangle leads to degeneration of the ION,[23-26] resulting in visible changes in both the pathologic evaluation and MR imaging findings.[27,28] Specifically, damage to the dentate nucleus, superior cerebellar peduncle, or both leads to contralateral hypertrophic olivary degeneration (HOD), but damage to the tegmental tracts leads to ipsilateral HOD.

The purpose of this study was to determine whether MR imaging findings of children with PFS could be used to validate the clinical diagnosis of PFS. We hypothesized that patterns of hypertrophic degeneration in the inferior olivary nuclei reflect patterns of damage to the pECPs and that these patterns would show an association with clinical findings, in particular with the presence or absence of PFS.

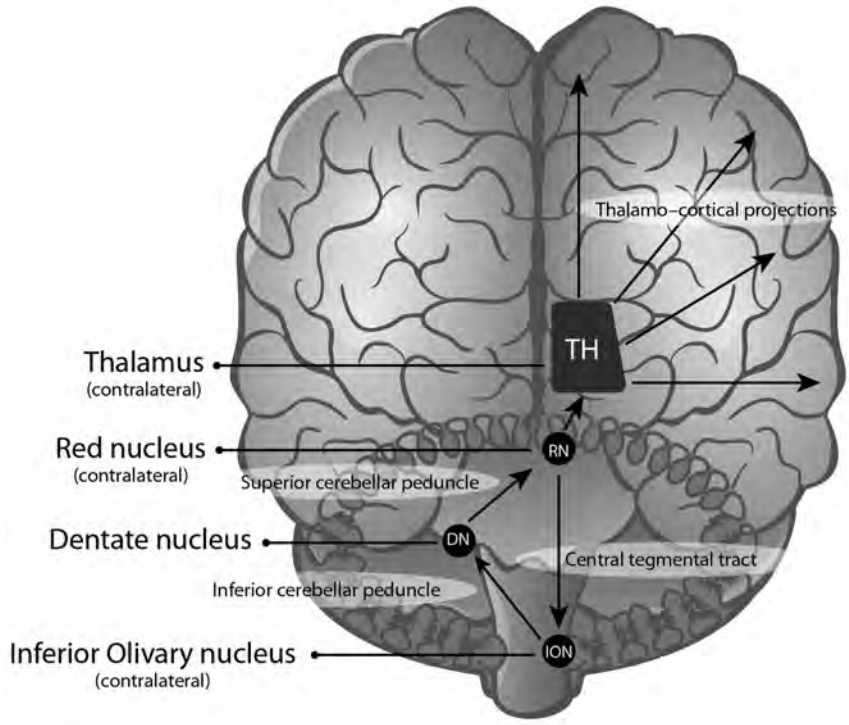

FIG 1. The Guillain-Mollaret triangle and dentatorubrothalamocortical projections.

MATERIALS AND METHODS

Patients and Study Design

We retrospectively evaluated ION changes on MR imaging of children with and without PFS after posterior fossa surgery for midline intraventricular tumor. Patients were selected from an institutional review board–approved, prospectively designed clinical trial of those with newly diagnosed medulloblastoma, supratentorial primitive neuroectodermal, or atypical teratoid/rhabdoid tumors. Patient/guardian consent was obtained before enrollment in the clinical trial. Twenty-four patients were selected. All were boys with a mean age of 9 ± 3.2 years. Of the 24 patients, 12 had a recorded clinical diagnosis of PFS, which required the presence of complete mutism in the early postoperative period that lasted at least 24 hours and was

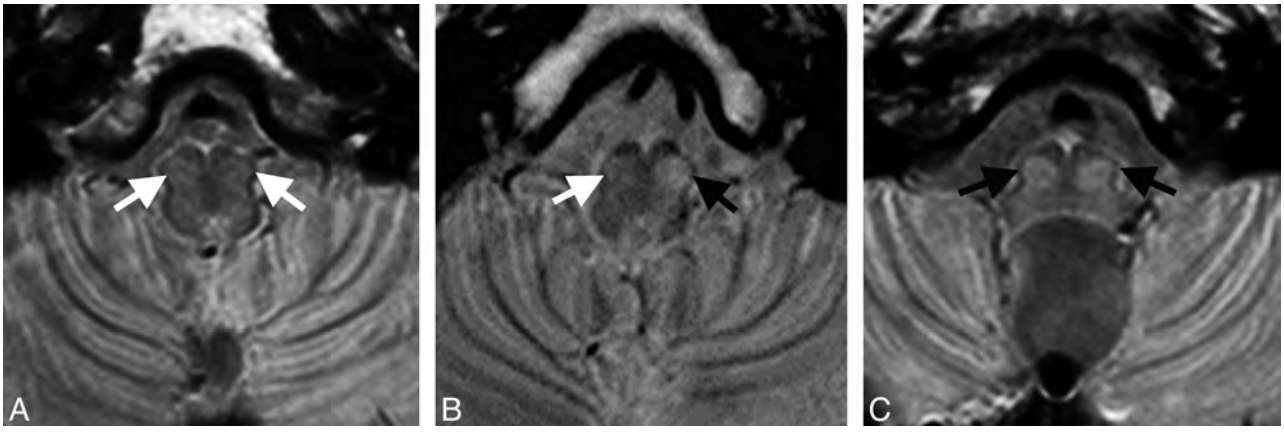

FIG 2. Transverse proton attenuation–weighted images illustrating the MR imaging appearance of normal IONs (*A*, *white arrows*) and unilateral (*B*, *black arrow*) and bilateral (*C*, *black arrows*) HOD in patients approximately 4 months after surgery for midline posterior fossa tumors. Note that with this imaging technique, normal IONs (*white arrows*) are barely recognizable, but in abnormal conditions, their conspicuity is markedly increased, allowing confident identification of HOD in most cases.

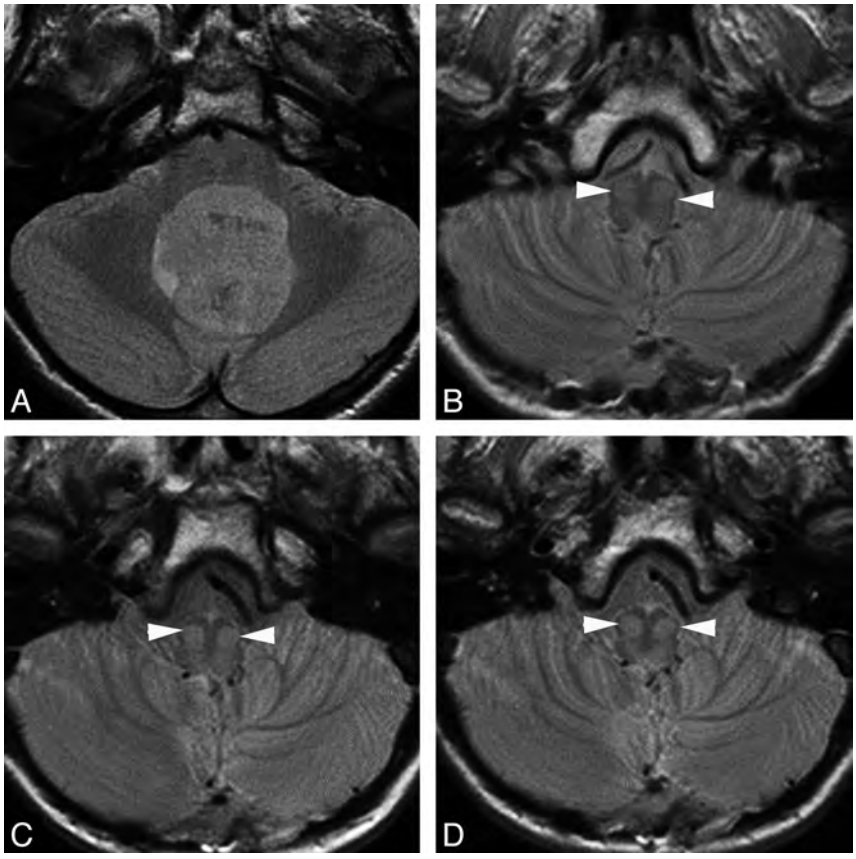

FIG 3. Transverse proton attenuation–weighted images showing chronologic changes (increasing conspicuity) within the bilateral inferior olivary nuclei (*white arrowheads*) in a patient with PFS during the first year after surgery. *A*, Preoperative study. *B*, At 1-month follow-up. *C*, At 6-month follow-up. *D*, At 10-month follow-up.

not explained by any other cause such as medication. For comparison, 12 age- and sex-matched patients without PFS were selected as controls. All patients, regardless of clinical PFS status, were evaluated for associated cerebellar signs and symptoms. Of the 12 patients with PFS, 11 had medulloblastoma and 1 had an atypical teratoid/rhabdoid tumor. Of the 12 patients without PFS, all had medulloblastomas.

MR Imaging

Postoperative follow-up studies included standardized axial long-TR imaging (proton attenuation and T2-weighted), in addition to multiplanar nonenhanced and contrast-enhanced T1-weighted, axial contrast-enhanced FLAIR, and diffusion-weighted imaging. The geometric parameters for the long-TR imaging sequences (used for evaluation of the ION) were identical: number of sections = 31, section thickness = 5 mm, FOV read = 210 mm, FOV phase = 100%. Other parameters for the proton attenuation and T2-weighted sequence were the following: TR = 4500 ms; TE1 = 13 ms; TE2 = 105 ms; turbo factor = 5; bandwidth = 98 Hz/px; and for FLAIR: TR = 10,000 ms; TI = 2500 ms; TE = 103 ms; turbo factor = 21; bandwidth = 130 Hz/px. In compliance with protocol requirements, all studies were performed on 1.5T magnets (Magnetom Avanto; Siemens, Erlangen, Germany) at the same center by using a 4-channel, circularly polarized head array coil. Average follow-up was 38 ± 20 months, and each patient had an average of 14 ± 5 follow-up studies.

Image Analysis

Blinded, randomized analysis of MR images was performed by a senior attending neuroradiologist. Specific attention was given to the bilateral IONs on long-TR images. The IONs were evaluated for volume and signal changes independently. An abnormality was deemed to be HOD if it met the following criteria: 1) Both hypertrophy and signal changes (T2 prolongation) were present; 2) the hypertrophic component was modest or absent, but the signal changes were unequivocal. The findings within each ION for both T2- and proton attenuation–weighted sequences were classified as follows: 0 = no visible abnormality, 1 = questionable abnormally high signal within the hilum or entire nucleus with or without volume changes, or 2 = definite abnormally high signal within the hilum or entire nucleus with or without volume changes. A score of 2 at any point during the postoperative follow-up qualified the respective ION for HOD status. Patients were subsequently categorized as having definite bilateral HOD, definite unilateral HOD, or no HOD.

Statistical Analysis

Statistical analysis was performed by using SAS 9.2 software (SAS Institute, Cary, North Carolina). The Fisher exact test was performed to investigate the association of HOD-related MR imaging abnormalities with PFS. The sensitivity and specificity of HOD as an indicator of PFS were calculated by using the clinical diagnosis of PFS as the criterion standard (true-positive).

RESULTS

Of the 12 patients with clinically diagnosed PFS, 9 had bilateral HOD on MR imaging and 2 had definitive unilateral HOD changes (1 with questionable contralateral involvement), and 1 had no abnormal MR imaging findings that were consistent with HOD. Conversely, 10 of the 12 patients without PFS had no HOD-suggestive findings on MR imaging, and 2 had unilateral HOD. In cases of unilateral HOD, patients with PFS had HOD on the right side, and patients without PFS had it on the left. The earliest time when definite bilateral HOD was seen in our patients was 1 month from surgery, and the longest interval between surgery and the appearance of definite bilateral HOD was 5.5 months (mean, 3.5 months).

The clinical features of all 24 patients are summarized in the Table. All 12 patients with postoperative mutism had severe cerebellar syndrome with dysmetria and ataxia. All patients without PFS had some degree of cerebellar dysfunction without mutism, and 5 were quite severely affected. The 2 patients with clinical PFS but only unilateral HOD had mild postoperative dysmetria and

Clinical features of patients with and without posterior fossa syndrome

Variable	PFS (*n* = 12)	Non-PFS (*n* = 12)
Mutism >24 hours	12	0
Immediate postoperative		
Mild-to-moderate dysmetria	7	2
Severe dysmetria	5	0
Mild-to-moderate ataxia	0	7
Severe ataxia	12	2
At last follow-up[a]		
Mild-to-moderate dysmetria	2	0
Severe dysmetria	1	0
Mild-to-moderate ataxia	7	5
Severe ataxia	5	1

Note:—Dysmetria: incoordination of limbs with either some (i.e., mild to moderate) or complete (i.e., severe) impairment of function. Ataxia: impaired ability to sit and walk with independent mobility retained (mild to moderate) or with mobility assistance required (severe).

[a] Time to last follow-up evaluation: 3–99 months.

severe ataxia. The 2 patients who had unilateral HOD without clinical PFS had mild postoperative dysmetria and mild ataxia.

The fact that 100% of patients with bilateral HOD changes had PFS and 0% of patients without PFS had such changes suggests that the presence of bilateral HOD is associated with PFS. The results of the Fisher exact test confirmed the strong association between bilateral HOD and clinical PFS ($P < .0001$). These findings also indicated a false-positive MR imaging rate of 0% (0/9) for bilateral HOD because all patients with bilateral HOD indeed had PFS. The false-negative MR imaging rate was 25% (3/12). In this clinical setting, MR imaging findings of bilateral HOD were 75% sensitive and 100% specific for the diagnosis of PFS. With bilateral HOD as a putative indicator of PFS, the positive predictive value of bilateral HOD is 100% and the negative predictive value of the absence of HOD is 80%.

DISCUSSION

As previously stated, damage to the bilateral pECPs is the most widely accepted cause of postoperative PFS and cerebellar mutism.[5,8-12] Because of the anatomic overlap between the first segments of the dentatorubrothalamocortical pathway and the Guillain-Mollaret triangle, damage to the pECP leads to contralateral HOD.[23-28] Therefore, damage to the bilateral pECPs should lead to the development of bilateral HOD on MR imaging, which may serve as a delayed surrogate imaging indicator of PFS. Indeed, the 100% positive predictive value yields a high confidence that a positive result (obtained by using bilateral HOD as a classifier) is truly indicative of PFS.

Although bilateral HOD has previously been associated with linguistic pathway abnormalities,[29-32] we could not find any report of cerebellar mutism and linguistic abnormalities attributed to bilateral damage of the pECPs and with subsequent HOD in the ION. Most of the described cases in which unilateral HOD was observed on imaging did not have associated linguistic category findings,[33-37] though this was described in at least 1 study.[38]

Bilateral HOD was not present in every case of clinically diagnosed PFS in our cohort. This divergence could be due to inconsistencies in the clinical diagnostic criteria because despite all ongoing effort and research, the diagnosis of PFS is sometimes still a judgment call, dependent on the investigator's experience. Our criteria of prolonged mutism and severe associated cerebellar syndrome with ataxia were used to differentiate PFS from other causes of postoperative speech disorders, including damage to the lower cranial nerves,[13] psychological issues,[39] and medication-induced deficits. Indeed, at least one of our patients with PFS without bilateral HOD on MR imaging was described in the medical records as having immediate mutism following anesthesia recovery, a presentation that is not typical of cerebellar mutism, which generally appears an average of 1.7 days after surgery.[3,5,40] In fact, the immediate onset of mutism may indicate a bulbar abnormality from direct, inadvertent surgical injury to the lower cranial nerve nuclei[13] rather than true cerebellar mutism in the context of PFS. We, therefore, recognize the challenges of differentiating cerebellar mutism from other forms of transient speech arrests in these patients during the postoperative period when other compounding clinical considerations occur concurrently.

Another reason that bilateral HOD was not always present in patients with PFS is that surgical damage is not necessarily a binary, all-or-none phenomenon. In other words, the magnitude of damage to the pECP that is needed to cause a critical drop of cerebellar input to the supratentorial brain may be different from the amount of damage leading the later to visible MR imaging changes of HOD. For example, one may hypothesize that most of the bilateral pECP fibers need to be destroyed to result in bilateral HOD, but somewhat less damage may be sufficient to cause a global frontal lobe dysfunction and resultant speech apraxia (ie, cerebellar mutism). Indeed, the 2 mechanisms causing PFS and HOD are likely different: one leading to frontal lobe dysfunction and mutism through reversed cerebellocerebral diaschisis; the other, to a peculiar form of degeneration associated with initial hypertrophy through a trans-synaptic mechanism with as yet poorly understood neurologic correlates.

Another unique clinical aspect of bilateral HOD in our patient cohort was the absence of palatal myoclonus in all patients, though this neurologic sign is commonly seen associated with HOD. The reason for this discrepancy is unclear. However, given that our cohort's lesions occurred in the specific circumstance of posterior fossa surgery and consistently in a specific location (ie, pECP) but other lesions in the literature often involved injury to the second, descending (rubro-olivary) segment of the Guillain-Mollaret triangle, an unidentified anatomic explanation may exist, such as involvement of brain stem structures immediately adjacent to the descending tegmental tracts in the development of palatal myoclonus.

The MR imaging signs and evolution of HOD-type changes are well-described, with pathologic evaluation first revealing 6 distinct stages after destruction of the central tegmental tracts: no olivary changes (within 24 hours), olivary amiculum degeneration (typically 2–7 days), olivary hypertrophy (approximately 3 weeks), culminant olivary enlargement (approximately 8.5 months), olivary pseudohypertrophy (9.5 months), and olivary atrophy (after a few years).[28] These findings were later classified into 3 stages on the basis of MR imaging of other cases and analysis of cases in the literature.[27,34] The first is seen with T2 and proton attenuation signal hyperintensity without hypertrophy and may occur as early as 4 weeks after injury. The second stage demonstrates hypertrophy starting approximately 4 months after injury extending until hypertrophy resolves approximately 3–4

years later. The third and final stage exhibits resolved hypertrophy with persistent high T2 and proton attenuation signal intensity and is noted to persist indefinitely. These concur with our observations.

We were fortunate that our retrospective analysis was performed on patients whose clinical imaging protocol had included both axial T2 and proton attenuation imaging. The proton attenuation sequence was often the most conclusive imaging sequence, especially on the earlier postoperative follow-up studies, as previously reported by others.[41] However, our imaging protocol was not optimized to evaluate the ION, an area that is somewhat difficult to visualize on routine imaging and is often prone to artifacts. Our protocol was also limited by section thickness, which was routinely 5 mm. Because the olivary body measures approximately 1.25 cm, with the ION being in the bottom portion, only 1 or 2 sections could generally be obtained to evaluate the region of interest on traditional 5-mm imaging, with the possibility of significant partial volume averaging effects.

Our finding of unilateral HOD in patients with and without PFS may be due to the proposed process of 1 cerebellar hemisphere normally providing asymmetric input toward speech. There is no consensus in the literature as to which side provides more input, with an earlier article implicating the left cerebellar hemisphere[42] and more recent articles implicating the right.[43-47] In cases in which we detected unilateral HOD, patients with PFS had unilateral right HOD, and patients without PFS had unilateral left HOD. Other articles described inconclusive findings.[38,48] Given the inconsistency between literature reports, it is possible that interindividual variations determine the dominant cerebellar hemisphere for speech and language production. Alternatively, complete damage to the dominant side may lead to PFS, even if damage to the subdominant pECP is partial, hence insufficient to cause corresponding HOD. This result would explain the few exceptions of clinical-imaging discrepancies (ie, clinical PFS syndrome in conjunction with unilateral HOD only).

Although bilateral HOD is not 100% sensitive for detecting PFS, these findings suggest that a threshold of damage to the pECPs is required for both MR imaging and clinical perceptibility. Future studies evaluating the degree of damage to the pECPs and defining PFS diagnostic criteria in a larger patient cohort with detailed clinical evaluation will be the next step in understanding this complex syndrome. Our data demonstrate that changes of HOD on MR imaging may be used in the future as an objective though a posteriori criterion in the diagnosis of PFS and may help clarify the definition of the clinical syndrome. Future evaluation will include prospective analysis of a larger cohort of patients with posterior fossa surgery who have PFS, with more robust diagnostic information (optimized imaging of the Guillain-Mollaret triangle and pECPs) and structured clinical information acquired and evaluated by experienced investigators to formulate standardized clinical and imaging diagnostic criteria for this complex, challenging syndrome.

CONCLUSIONS

Damage to the pECP manifests as contralateral HOD through disruption of the Guillain-Mollaret triangle and subsequent trans-synaptic degeneration. We provide objective imaging data demonstrating that damage to the bilateral pECPs manifests as bilateral HOD. Our false-positive MR imaging rate for bilateral HOD was 0%; hence, bilateral HOD may be a delayed but reliable surrogate imaging marker for PFS. Therefore, MR imaging findings, especially those obtained by using imaging protocols that are optimized for the visualization of the ION, can be useful criteria in the diagnosis of PFS as a more robust definition is developed. Our findings contribute to the growing body of evidence supporting the role of bilateral pECP damage in the pathogenesis of postoperative PFS.

ACKNOWLEDGMENTS

The authors thank Cherise M. Guess, PhD, ELS, for reviewing and editing the manuscript.

Disclosures: Zoltan Patay—*UNRELATED*: *Grants/Grants Pending*: American Lebanese Syrian Associated Charities,* National Cancer Institute,* *Comments*: The American Lebanese Syrian Associated Charities is the fundraising arm of St. Jude Children's Research Hospital; therefore, most research conducted at St. Jude is "funded" to some extent by the American Lebanese Syrian Associated Charities; St. Jude Children's Research Hospital is also a "Comprehensive Cancer Center" receiving a grant from the National Cancer Institute, *Travel/Accommodations/Meeting Expenses Unrelated to Activities Listed*: ERASMUS Course, European Course of Pediatric Neuroradiology, European Society of Neuroradiology, São Paulo Radiology Society, Kuwait Radiology Society, Hungarian Neuroradiology Society, *Comments*: travel and accommodation expense coverage for presenting educational and/or invited lectures at courses or annual scientific meetings (no honoraria). Jacob Enterkin—*UNRELATED*: *Travel/Accommodations/Meeting Expenses Unrelated to Activities Listed*: Medical University of South Carolina, *Comments*: received reimbursement to attend the American Society of Spine Radiology Annual Symposium in February 2013 to present a paper. As a neuroradiology fellow, 1 meeting is reimbursed. Zoran Rumboldt—*UNRELATED*: *Grants/Grants Pending*: Siemens,* *Comments*: CT Perfusion for Head and Neck Cancer, *Travel/Accommodations/Meeting Expenses Unrelated to Activities Listed*: Siemens, Bracco. Frederick Boop—*UNRELATED*: *Board Membership*: Secretary, American Association of Neurological Surgeons.* *Money paid to the institution.

REFERENCES

1. Hirsch JF, Renier D, Czernichow P, et al. **Medulloblastoma in childhood: survival and functional results.** *Acta Neurochir (Wien)* 1979;48:1–15
2. Stein BM, Fraser RA, Tenner MS. **Normal pressure hydrocephalus: complication of posterior fossa surgery in children.** *Pediatrics* 1972;49:50–58
3. Gudrunardottir T, Sehested A, Juhler M, et al. **Cerebellar mutism: review of the literature.** *Childs Nerv Syst* 2011;27:355–63
4. Gudrunardottir T, Sehested A, Juhler M, et al. **Cerebellar mutism: definitions, classification and grading of symptoms.** *Childs Nerv Syst* 2011;27:1361–63
5. Erşahin Y, Mutluer S, Cağli S, et al. **Cerebellar mutism: report of seven cases and review of the literature.** *Neurosurgery* 1996;38:60–65, discussion 66
6. Pollack IF, Polinko P, Albright AL, et al. **Mutism and pseudobulbar symptoms after resection of posterior fossa tumors in children: incidence and pathophysiology.** *Neurosurgery* 1995;37:885–93
7. Riva D, Giorgi C. **The cerebellum contributes to higher functions during development: evidence from a series of children surgically treated for posterior fossa tumours.** *Brain* 2000;123(pt 5):1051–61
8. Morris EB, Phillips NS, Laningham FH, et al. **Proximal dentatothalamocortical tract involvement in posterior fossa syndrome.** *Brain* 2009;132:3087–95
9. Miller NG, Reddick WE, Kocak M, et al. **Cerebellocerebral diaschisis is the likely mechanism of postsurgical posterior fossa syndrome in pediatric patients with midline cerebellar tumors.** *AJNR Am J Neuroradiol* 2010;31:288–94
10. Puget S, Boddaert N, Viguier D, et al. **Injuries to inferior vermis and dentate nuclei predict poor neurological and neuropsychological**

outcome in children with malignant posterior fossa tumors. *Cancer* 2009;115:1338–47
11. Crutchfield JS, Sawaya R, Meyers CA, et al. **Postoperative mutism in neurosurgery: report of two cases.** *J Neurosurg* 1994;81:115–21
12. Koh S, Turkel SB, Baram TZ. **Cerebellar mutism in children: report of six cases and potential mechanisms.** *Pediatr Neurol* 1997;16:218–19
13. Robertson PL, Muraszko KM, Holmes EJ, et al. **Incidence and severity of postoperative cerebellar mutism syndrome in children with medulloblastoma: a prospective study by the Children's Oncology Group.** *J Neurosurg* 2006;105:444–51
14. Fraioli B, Guidetti. **Effects of stereotactic lesions of the dentate nucleus of the cerebellum in man.** *Appl Neurophysiol* 1975;38:81–90
15. Steinbok P, Cochrane DD, Perrin R, et al. **Mutism after posterior fossa tumour resection in children: incomplete recovery on long-term follow-up.** *Pediatr Neurosurg* 2003;39:179–83
16. Kusano Y, Tanaka Y, Takasuna H, et al. **Transient cerebellar mutism caused by bilateral damage to the dentate nuclei after the second posterior fossa surgery: case report.** *J Neurosurg* 2006;104:329–31
17. Rekate HL, Grubb RL, Aram DM, et al. **Muteness of cerebellar origin.** *Arch Neurol* 1985;42:697–98
18. Pollack IF. **Posterior fossa syndrome.** *Int Rev Neurobiol* 1997;41:411–32
19. Devinsky O, Morrell MJ, Vogt BA. **Contributions of anterior cingulate cortex to behaviour.** *Brain* 1995;118(pt 1):279–306
20. Nagaratnam N, Nagaratnam K, Ng K, et al. **Akinetic mutism following stroke.** *J Clin Neurosci* 2004;11:25–30
21. Tahta K, Cirak B, Pakdemirli E, et al. **Postoperative mutism after removal of an anterior falcine meningioma.** *J Clin Neurosci* 2007;14:793–96
22. Guillain G, Mollaret P. **Deux *cas de* myoclonies synchrones et rythmées vélo-pharyngo-laryngo-oculo-diaphragmatiques.** *Rev Neurol* 1931;12:545–66
23. Gautier JC, Blackwood W. **Enlargement of the inferior olivary nucleus in association with lesions of the central tegmental tract or dentate nucleus.** *Brain* 1961;84:341–61
24. Jellinger K. **Hypertrophy of the inferior olives. Report on 29 cases.** *Z Neurol* 1973;205:153–74
25. Krings T, Foltys H, Meister IG, et al. **Hypertrophic olivary degeneration following pontine haemorrhage: hypertensive crisis or cavernous haemangioma bleeding?** *J Neurol Neurosurg Psychiatry* 2003;74:797–99
26. Uchino A, Hasuo K, Uchida K, et al. **Olivary degeneration after cerebellar or brain stem haemorrhage: MRI.** *Neuroradiology* 1993;35:335–38
27. Goyal M, Versnick E, Tuite P, et al. **Hypertrophic olivary degeneration: metaanalysis of the temporal evolution of MR findings.** *AJNR Am J Neuroradiol* 2000;21:1073–77
28. Goto N, Kaneko M. **Olivary enlargement: chronological and morphometric analyses.** *Acta Neuropathol* 1981;54:275–82
29. Gerace C, Fele MR, Luna R, et al. **Neurological picture: bilateral hypertrophic olivary degeneration.** *J Neurol Neurosurg Psychiatry* 2006;77:73
30. Rieder CR, Reboucas RG, Ferreira MP. **Holmes tremor in association with bilateral hypertrophic olivary degeneration and palatal tremor: chronological considerations—case report.** *Arq Neuropsiquiatr* 2003;61:473–77
31. Vaidhyanath R, Thomas A, Messios N. **Bilateral hypertrophic olivary degeneration following surgical resection of a posterior fossa epidermoid cyst.** *Br J Radiol* 2010;83:e211–215
32. Shepherd GM, Tauboll E, Bakke SJ, et al. **Midbrain tremor and hypertrophic olivary degeneration after pontine hemorrhage.** *Mov Disord* 1997;12:432–37
33. Akar S, Drappatz J, Hsu L, et al. **Hypertrophic olivary degeneration after resection of a cerebellar tumor.** *J Neurooncol* 2008;87:341–45
34. Birbamer G, Buchberger W, Kampfl A, et al. **Early detection of post-traumatic olivary hypertrophy by MRI.** *J Neurol* 1993;240:407–09
35. Macht S, Hänggi D, Turowski B. **Hypertrophic olivary degeneration following pontine cavernoma hemorrhage: a typical change accompanying lesions in the Guillain-Mollaret triangle.** *Klin Neuroradiol* 2009;19:235–37
36. Phatouros CC, McConachie NS. **Hypertrophic olivary degeneration: case report in a child.** *Pediatr Radiol* 1998;28:830–31
37. Salamon-Murayama N, Russell EJ, Rabin BM. **Diagnosis please: case 17—hypertrophic olivary degeneration secondary to pontine hemorrhage.** *Radiology* 1999;213:814–17
38. Ash L, Srinivasan A. **Case of the season: hypertrophic olivary degeneration.** *Semin Roentgenol* 2008;43:171–72
39. Ferrante L, Mastronardi L, Acqui M, et al. **Mutism after posterior fossa surgery in children: report of three cases.** *J Neurosurg* 1990;72:959–63
40. Gelabert-González M, Fernández-Villa J. **Mutism after posterior fossa surgery: review of the literature.** *Clin Neurol Neurosurg* 2001;103:111–14
41. Yokota T, Hirashima F, Furukawa T, et al. **MRI findings of inferior olives in palatal myoclonus.** *J Neurol* 1989;236:115–16
42. Lechtenberg R, Gilman S. **Speech disorders in cerebellar disease.** *Ann Neurol* 1978;3:285–90
43. Gebhart AL, Petersen SE, Thach WT. **Role of the posterolateral cerebellum in language.** *Ann N Y Acad Sci* 2002;978:318–33
44. Stoodley CJ, Schmahmann JD. **Functional topography in the human cerebellum: a meta-analysis of neuroimaging studies.** *Neuroimage* 2009;44:489–501
45. Baillieux H, De Smet HJ, Paquier PF, et al. **Cerebellar neurocognition: insights into the bottom of the brain.** *Clin Neurol Neurosurg* 2008;110:763–73
46. Ackermann H, Mathiak K, Ivry RB. **Temporal organization of "internal speech" as a basis for cerebellar modulation of cognitive functions.** *Behav Cogn Neurosci Rev* 2004;3:14–22
47. Fiez JA, Petersen SE, Cheney MK, et al. **Impaired non-motor learning and error detection associated with cerebellar damage: a single case study.** *Brain* 1992;11(pt 1):155–78
48. Bruno MK, Wooten GF. **Hypertrophic olivary degeneration.** *Arch Neurol* 2012;69:274–75

Time-Dependent Structural Changes of the Dentatothalamic Pathway in Children Treated for Posterior Fossa Tumor

S. Perreault, R.M. Lober, S. Cheshier, S. Partap, M.S. Edwards, and K.W. Yeom

ABSTRACT

BACKGROUND AND PURPOSE: Injury to the dentatothalamic pathway that originates in the cerebellum has been suggested as a mechanism for neurologic complications in children treated for posterior fossa tumors. We hypothesized that time-dependent changes occur in the dentatothalamic pathway.

MATERIALS AND METHODS: Diffusion tensor evaluation was performed in 14 children (median age, 4.1 years; age range, 1–20 years) who underwent serial MR imaging at 3T as part of routine follow-up after posterior fossa tumor resection with or without adjuvant therapy. Tensor metrics were obtained in the acute (≤1 week), subacute (1 to <6 months), and chronic (≥6 months) periods after surgery. We evaluated the following dentatothalamic constituents: bilateral dentate nuclei, cerebellar white matter, and superior cerebellar peduncles. Serial dentate nuclei volumes were also obtained and compared with the patient's baseline.

RESULTS: The most significant tensor changes to the superior cerebellar peduncles and cerebellar white matter occurred in the subacute period, regardless of the tumor pathology or therapy regimen, with signs of recovery in the chronic period. However, chronic volume loss and reduced mean diffusivity were observed in the dentate nuclei and did not reverse. This atrophy was associated with radiation therapy and symptoms of ataxia.

CONCLUSIONS: Longitudinal diffusion MR imaging in children treated for posterior fossa tumors showed time-dependent tensor changes in components of the dentatothalamic pathway that suggest evolution of structural damage with inflammation and recovery of tissue directionality. However, the dentate nuclei did not show tensor or volumetric recovery, suggesting that the injury may be chronic.

ABBREVIATIONS: DTT = dentatothalamic; FA = fractional anisotropy; $\lambda_{\|}$ = perpendicular diffusivity; MD = mean diffusivity; PF = posterior fossa; PFS = posterior fossa syndrome; SCP = superior cerebellar peduncles; $\lambda_{\|}$ = parallel diffusivity

Posterior fossa (PF) tumors represent a significant number of pediatric brain tumors and largely comprise pilocytic astrocytoma, medulloblastoma, and ependymoma.[1] Despite an increase in survival from advances in therapy, many survivors of PF tumors have cognitive and various forms of cerebellar dysfunction thought to reflect brain injury incurred by a combination of tumor and treatment.[2-4] Given its important role not only in motor coordination but also in cognition, injuries to the cerebellum and, more specifically, the cerebrocerebellar pathway have been proposed as possible mechanisms.[5-7]

One such pathway, the dentatothalamic (DTT) tract, has been shown to display a role in linguistic and cognitive functions.[8-10] The DTT tract contains axons that originate in the dentate nucleus of the cerebellum, project through the ipsilateral superior cerebellar peduncle (SCP), decussate in the dorsal midbrain, and then terminate in the contralateral ventrolateral nucleus of the thalamus. From there, the axons project to the primary motor cortex as well as secondary and tertiary association areas within the frontal and parietal lobes.[11]

Studies have shown that injury to the DTT tract and associated degeneration may be implicated in cognitive and behavioral deficits as well as the development of posterior fossa syndrome (PFS), a unique constellation of symptoms including speech impairment, emotional lability, hypotonia, and ataxia.[12-15] Recent studies have used diffusion MR imaging to evaluate DTT pathways in patients treated for PF tumors but have reported variable DTI metric results.[12,13,16,17] A possible explanation might be that associated axonal degeneration, tissue inflammation, and repair that occur after injury are not static but evolve in a time-depen-

Received July 3, 2013; accepted after revision July 28.

From the Departments of Neurology (S. Perreault, S. Partap), Neurosurgery (R.M.L., S.C., M.S.E.), and Radiology (K.W.Y.), Lucile Packard Children's Hospital at Stanford, Palo Alto, California.

Please address correspondence to Kristen W. Yeom, MD, Department of Radiology, Lucile Packard Children's Hospital at Stanford, 725 Welch Rd, Room 0511A, Palo Alto, CA 94304; e-mail: kyeom@stanford.edu

Indicates article with supplemental on-line tables

http://dx.doi.org/10.3174/ajnr.A3735

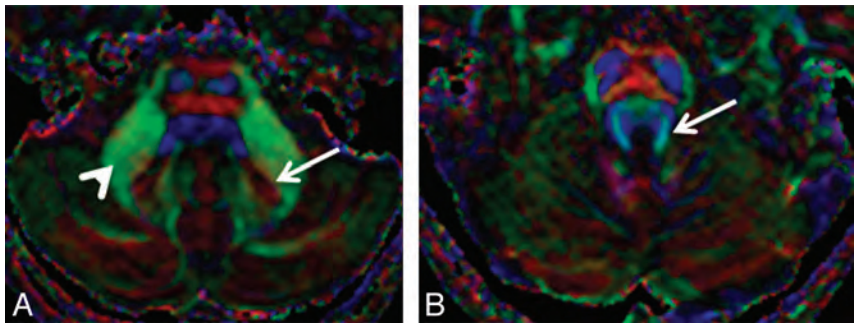

FIG 1. Eigenvector color maps. *A*, Long arrow indicates the dentate nucleus; arrowhead, the cerebellar white matter at the level of middle cerebellar peduncle. *B*, Long arrow indicates the superior cerebellar peduncle.

Clinical features of posterior fossa tumor patients

Patient Characteristics	No. (%)
Age at initial diagnosis (yr)	
Median	4.1
Range	1–20
Sex	
Male	9 (64)
Female	5 (36)
Diagnosis	
Medulloblastoma	7 (50)
Pilocytic astrocytoma	4 (29)
Ependymoma	2 (14)
Choroid plexus papilloma	1 (7)
Treatment modalities	
Surgery only	5 (36)
Surgery/chemotherapy	2 (14)
Surgery/chemotherapy/radiation therapy	7 (50)
Postoperative neurologic status	
Ataxia	8 (57)
Hemiplegia	5 (36)
No sequelae	5 (36)
Posterior fossa syndrome	3 (21)

dent manner.[18-20] A study that investigates temporally relevant tissue changes might provide insight into cerebellar injury and its evolution in children who undergo PF tumor therapy. We hypothesized that time-dependent changes occur in the DTT pathway as measured by DTI metrics and dentate nuclei volume in children treated for PF tumors.

MATERIALS AND METHODS

Subjects

All patients presenting with treatment-naïve PF tumor at our children's hospital between January 2010 and May 2012 were retrospectively reviewed after approval by the institutional review board (protocol 4223; No. 4947). The study cohort was identified by using the following inclusion criteria: The patient underwent DTI at 3T as part of routine tumor evaluation, subsequently underwent surgical resection of the tumor, and underwent a baseline DTI ≤1 week after surgery and follow-up DTI at least 1 month after surgery. Information regarding age at diagnosis, sex, tumor pathology, the presence of PFS or other neurologic complications, and postoperative clinical status at 1 month after surgery was collected. The time points for analysis after surgery were defined in the following manner: acute period (≤1 week after surgery), the subacute period (between 1 month and <6 months after surgery), and the chronic period (≥6 months after surgery).

Image Acquisition

A generalized autocalibrating partially parallel acquisition DTI was obtained at 3T MR imaging (Discovery 750; GE Healthcare, Milwaukee, Wisconsin) with an 8-channel head coil and a twice-refocused generalized autocalibrating parallel acquisitions diffusion tensor echo-planar imaging sequence (acquisition matrix = 128 ×128, acceleration factor = 3, NEX = 3, 25 isotropically distributed diffusion directions with b = 1000 s/mm^2, 5 b = 0 images, section thickness/gap = 3/0 mm, FOV = 20–24 cm) by using the reconstruction and motion-correction methods previously described.[21]

Imaging Analysis of DTT Pathway

Mean diffusivity (MD) and fractional anisotropy (FA) were obtained by using the region-of-interest analysis. These regions included the following: bilateral dentate nuclei, cerebellar white matter at the level of the middle cerebellar peduncle, and the SCP. One investigator (S. Perreault), blinded to clinical information, selected ROIs (Fig 1). Structures were first identified by using a combination of T1- and T2-weighted images and color eigenvector DTI maps and then were cross-referenced to the ADC (mean diffusivity) and FA maps. The ROIs were adjusted on the basis of the anatomy of each patient. For example, the ROIs for the SCP were ellipsoid and measured approximately 10 mm^2. The ROIs for the cerebellar white matter at the level of the middle cerebellar peduncle were circular and measured approximately 30 mm^2. Proper placement of the ROIs was confirmed independently by a blinded board-certified pediatric neuroradiologist (K.W.Y).

Bilateral dentate nuclei delineations conformed to their size and were performed by using the eigenvector color maps. Volume was measured by calculating the area within a region of interest multiplied by the 3-mm section thickness, similar to the method described by Du et al.[22]

Statistical Analyses

Statistical analyses were performed with the Statistical Package for the Social Sciences, Version 20.0 (IBM, Armonk, New York). Statistical analyses were conducted by using the Fisher exact test (2-tailed), Friedman 2-way analysis of variance by rank for related samples, and the Wilcoxon signed rank test for related samples. A general linear model was used to determine significant independent factors.

RESULTS

Patients with PF Tumor

Fourteen patients met the inclusion criteria and were included in the study. Median age at diagnosis was 4.1 years (age range, 1–20 years) (Table). Our patient cohort underwent 45 DTIs (median = 3 per patient; range, 2–4). The median time of DTI acquisition in the acute period was 3 days after surgery (range, 1–7 days); in the subacute period, 2.8 months after surgery (range, 1.2–5.8

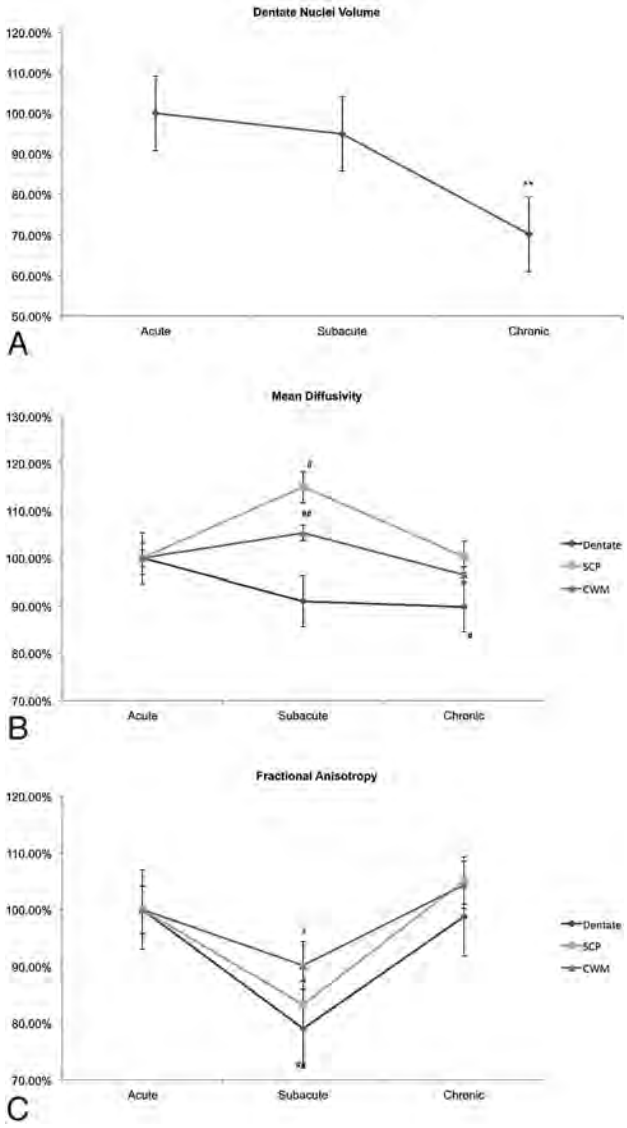

FIG 2. Mean variation from baseline of dentate nuclei volume, mean diffusivity, and fractional anisotropy during the acute, subacute, and chronic periods. *A*, Dentate nuclei volume variation. *B*, Mean diffusivity variation. *C*, Fractional anisotropy variation. CWM indicates cerebellar white matter. Error bars represent standard error of the mean. Double asterisks indicate Friedman 2-way analysis of variance by rank for related samples ($P < .01$); number sign, Wilcoxon signed rank test for related samples (double number sign, $P = .01$; number sign, $P \leq .05$).

months); and in the chronic period, 15.5 months after surgery (range, 6–29.4 months).

Medulloblastoma was the most frequent diagnosis with 7 patients (50%), followed by pilocytic astrocytoma ($n = 4$, 29%), ependymoma ($n = 2$, 14%), and choroid plexus papilloma ($n = 1$, 7%). No significant age difference was seen between medulloblastoma and other tumor groups (5.15 ± 3.2 versus 6.14 ±4.8 years, $P = .7$). Five patients (36%) underwent surgery only, 2 patients received chemotherapy after surgery (14%), and 7 patients (50%) received chemotherapy plus radiation therapy after initial tumor resection (Table). Three patients developed PFS in the postoperative period. One month after resection, 9 patients (64%) had either ataxia or hemiplegia and 5 patients had no sequelae.

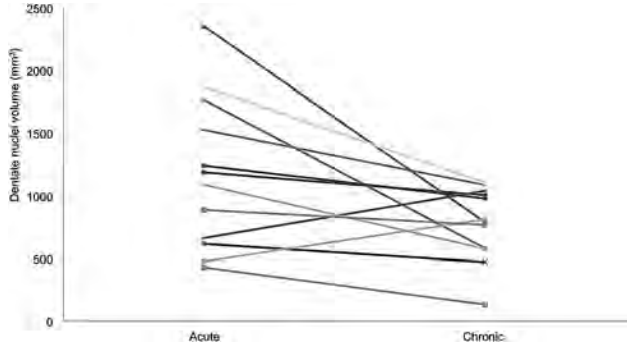

FIG 3. Combined dentate nuclei volume during the acute period compared with the chronic period for each patient.

Dentate Nuclei Volume

Among the patients with PF tumors, dentate nuclei volume remained stable in the acute and subacute periods but showed significant volume loss in the chronic period (389.3 mm^3 compared with 554.9 mm^3, $P = .007$) (Figs 2*A* and 3, On-line Table 1).

Mean Diffusivity

MD of the SCP increased and cerebellar white matter trended higher from the acute-to-subacute periods with a return close to postoperative baseline in the chronic time point (Fig 2*B*, On-line Table 1). The decrease in MD of the dentate nuclei was not significant between the acute and subacute periods but showed significant decrease in the chronic period (Fig 2*B*, On-line Table 1).

Fractional Anisotropy

The FA significantly decreased from the acute-to-subacute periods in the dentate nuclei and in the SCP but returned to the postoperative level during the chronic period. The FA of the cerebellar white matter trended lower from the acute-to-subacute periods and returned to the postoperative level during the chronic period (Fig 2*C*, On-line Table 1).

Tumor Group Differences

Tumor types, differences in treatment regimen, or neurologic sequelae were not associated with differences in MD or FA ($P > .3$).

All patients showed reduced total volume of the dentate nuclei except for 2 patients who had undergone surgery only for pilocytic astrocytomas and did not have any clinical sequelae. These patients with pilocytic astrocytoma did not have a significant change in dentate nuclei volume during the observation period (On-line Table 2). Factors associated with dentate nuclei atrophy were medulloblastoma, radiation therapy, presence of ataxia, and posterior fossa syndrome (On-line Table 2). With a general linear model, only radiation therapy and ataxia were related to atrophy of the dentate nuclei (partial eta squared, 0.22, $P = .03$ and .02, respectively). Tumor types and PFS did not contribute significantly to the model.

DISCUSSION

Our results showed that the most significant tensor changes to the SCP and cerebellar white matter occurred in the subacute period, or in the 1–6 months following PF tumor resection. Patients with PF tumors other than pilocytic astrocytoma showed significant volume loss and decrease in mean diffusivity of the dentate nuclei

in the chronic period. The presence of ataxia and prior radiation were positively associated with the presence of dentate nuclei atrophy. To our knowledge, this is the first study to examine longitudinal tensor and volumetric changes of the key components of the DTT pathway in children treated for PF tumors.

Prior studies have reported the sensitivity of diffusion MR imaging to axonal injury and have shown diffusion changes distal to the site of the lesion,[23-25] suggesting detection of Wallerian degeneration, which occurs when axons are separated from their cell body.[26] The DTT tract is the main outflow of the cerebellum, and it has been suggested that injury to the cerebellum and degeneration of this cerebrocerebellar pathway may be involved in cognitive dysfunction and PFS.[13,27-29] More recently, DTI metrics have shown tensor changes in the DTT pathway in patients treated for PF tumor, suggesting that DTI may be more robust than conventional MR imaging in probing structural damage.[12,13,16,30]

While prior studies have reported decreased FA of the SCP or increased MD of the cerebellar white matter in patients with PFS when examined at variable single-time points, our results show that the tensor changes may not be limited to those with symptoms of PFS.[13,16] In fact, when assessed longitudinally, all patients with treated PF tumors showed tensor changes at 1–6 months after surgery. These tensor changes (reduced FA and increased MD) showed significant improvement in the chronic period within both the SCP and the cerebellar white matter. Such tensor patterns suggest that tissue breakdown, inflammation, repair, or other injury-related features might be time-dependent. As previously described in animal models, axonal degeneration can occur as early as 30 minutes from the time of insult, with centrifugal disintegration and fragmentation of the axonal cytoskeleton and concomitant breakdown of the myelin sheaths.[18,20] Weeks later, inflammatory cells begin phagocytosis of the myelin and axon debris, a process that can last for many months.[18]

Reduced FA and increased MD may be explained by reduced axonal directionality and more uniform spatial water displacement that result from the breakdown of barriers that normally hinder water diffusion.[31,32] Studies have also shown that reduced FA or changes in MD can be attributed to a combination of reduced diffusivity parallel ($\lambda_{\parallel}$) to the principal axis of the fibers, which might arise from additional barriers imposed by axonal beading, bulges, fragmentation, and increased perpendicular diffusivity ($\lambda_{\perp}$), which might be seen with increased water mobility in perpendicular direction with myelin loss.[32-39]

Our study is consistent with a prior study by Concha et al,[40] which reported more significant tensor changes (lower FA and higher MD) at 2 months compared with 1 week after callosotomy in patients with epilepsy and similar time-dependent diffusion changes in the animal models of spinal injury.[23,41] In those studies, further assessment revealed decreased $\lambda_{\parallel}$ in the acute period (1 week) and elevated $\lambda_{\perp}$ at a later time (21 days to 2 months) after injury.[23,40,41] Given that $\lambda_{\parallel}$ may be more sensitive to axonal degeneration, whereas $\lambda_{\perp}$ changes may be driven by myelin effects, these studies suggested that varying contributions from axonal degeneration and myelin breakdown along different time points likely impacted temporal tensor differences, including both FA and MD.[23,40,41] Other studies have also suggested that an increase in $\lambda_{\perp}$ may drive the reduction in FA that occurs at a later time point in axonal degeneration.[42-44]

While individual FA and MD are not sufficient to differentiate axonal-versus-myelin degeneration, a pronounced reduction in FA and an increase in MD in the subacute period likely reflect the combined effects of active or ongoing myelin breakdown and inflammation after initial cerebellar injury.

Clinical factors associated with progressive decrease in dentate nuclei volume were radiation therapy, medulloblastoma (which often includes radiation as part of standard care), and symptoms of ataxia and PFS, whereas tensor changes occurred globally in all patients who underwent PF surgery. These findings suggest that the dentate nuclei may be particularly sensitive to the effects of radiation, with resultant injury and gliosis, as reflected by progressive volume loss and a decrease in MD. Symptoms of ataxia and PFS possibly reflect some aspect of dentate nuclei dysfunction. In comparison, tensor changes were seen in our general PF tumor cohort and may represent nonspecific sequelae of global cerebellar injury that combine tumor mass effect, edema, surgical manipulation, various therapy-induced excitotoxic events, inflammation, and local reactive tissue changes. This finding is also consistent with a prior report that did not find significant tensor differences among patients with PF tumor who underwent surgery only versus those who underwent surgery and radiation therapy.[12]

Given that an individual child's baseline myelination status, axonal density, and axonal diameter could influence diffusion metrics, each patient served as his or her own control in our longitudinal analysis. Although preoperative MR imaging might provide additional information, this was not feasible due to gross anatomic distortion by tumor, which would have rendered inaccurate measurements.

Despite certain limitations, this is the first study to demonstrate time-relevant structural changes that occur to the DTT pathway in children who have undergone therapy for PF tumors. Future studies that combine longitudinal DTT changes and cerebral connectivity could provide additional insight into treatment-related neurotoxicity and associated neurologic complications in children treated for PF tumors.

CONCLUSIONS

Longitudinal diffusion MR imaging in children treated for PF tumors showed time-dependent tensor changes in the components of the DTT pathway that suggest evolving structural damage, inflammation, and signs of tissue restoration and directionality. However, the dentate nuclei showed progressive atrophy and a decrease in MD in the chronic period. This volume loss was most significant in children treated with radiation therapy and symptoms of ataxia.

Disclosures: Sébastien Perreault—*UNRELATED*: *Grants/Grants Pending*: Fonds de la recherche en santé du Québec, *Comments*: fellowship grant.

REFERENCES

1. Arora RS, Alston RD, Eden TO, et al. **Age-incidence patterns of primary CNS tumors in children, adolescents, and adults in England.** *Neuro Oncol* 2009;11:403–13

2. Rønning C, Sundet K, Due-Tonnessen B, et al. **Persistent cognitive dysfunction secondary to cerebellar injury in patients treated for posterior fossa tumors in childhood.** *Pediatr Neurosurg* 2005; 41:15–21
3. Mabbott DJ, Penkman L, Witol A, et al. **Core neurocognitive functions in children treated for posterior fossa tumors.** *Neuropsychology* 2008;22:159–68
4. Spiegler BJ, Bouffet E, Greenberg ML, et al. **Change in neurocognitive functioning after treatment with cranial radiation in childhood.** *J Clin Oncol* 2004;22:706–13
5. Timmann D, Daum I. **Cerebellar contributions to cognitive functions: a progress report after two decades of research.** *Cerebellum* 2007;6:159–62
6. Kim SG, Ugurbil K, Strick PL. **Activation of a cerebellar output nucleus during cognitive processing.** *Science* 1994;265:949–51
7. Leiner HC, Leiner AL, Dow RS. **Cognitive and language functions of the human cerebellum.** *Trends Neurosci* 1993;16:444–47
8. Marx JJ, Iannetti GD, Thomke F, et al. **Topodiagnostic implications of hemiataxia: an MRI-based brainstem mapping analysis.** *Neuroimage* 2008;39:1625–32
9. Schmahmann JD, Sherman JC. **The cerebellar cognitive affective syndrome.** *Brain* 1998;121(pt 4):561–79
10. Müller RA, Chugani DC, Behen ME, et al. **Impairment of dentato-thalamo-cortical pathway in autistic men: language activation data from positron emission tomography.** *Neurosci Lett* 1998;245:1–4
11. Kwon HG, Hong JH, Hong CP, et al. **Dentatorubrothalamic tract in human brain: diffusion tensor tractography study.** *Neuroradiology* 2011;53:787–91
12. Law N, Bouffet E, Laughlin S, et al. **Cerebello-thalamo-cerebral connections in pediatric brain tumor patients: impact on working memory.** *Neuroimage* 2011;56:2238–48
13. Morris EB, Phillips NS, Laningham FH, et al. **Proximal dentato-thalamocortical tract involvement in posterior fossa syndrome.** *Brain* 2009;132:3087–95
14. Robertson PL, Muraszko KM, Holmes EJ, et al. **Incidence and severity of postoperative cerebellar mutism syndrome in children with medulloblastoma: a prospective study by the Children's Oncology Group.** *J Neurosurg* 2006;105:444–51
15. Huber JF, Bradley K, Spiegler BJ, et al. **Long-term effects of transient cerebellar mutism after cerebellar astrocytoma or medulloblastoma tumor resection in childhood.** *Childs Nerv Syst* 2006;22:132–38
16. Law N, Greenberg M, Bouffet E, et al. **Clinical and neuroanatomical predictors of cerebellar mutism syndrome.** *Neuro Oncol* 2012;14: 1294–303
17. Lober RM, Perreault S, Partap S, et al. **Injury to dentate nuclei and efferent fibers by pediatric posterior fossa tumors.** *Neuro Oncol* 2012;14(suppl 1):132
18. George R, Griffin JW. **The proximo-distal spread of axonal degeneration in the dorsal columns of the rat.** *J Neurocytol* 1994;23:657–67
19. George R, Griffin JW. **Delayed macrophage responses and myelin clearance during Wallerian degeneration in the central nervous system: the dorsal radiculotomy model.** *Exp Neurol* 1994;129: 225–36
20. Kerschensteiner M, Schwab ME, Lichtman JW, et al. **In vivo imaging of axonal degeneration and regeneration in the injured spinal cord.** *Nat Med* 2005;11:572–77
21. Skare S, Newbould RD, Clayton DB, et al. **Clinical multishot DW-EPI through parallel imaging with considerations of susceptibility, motion, and noise.** *Magn Reson Med* 2007;57:881–90
22. Du AX, Cuzzocreo JL, Landman BA, et al. **Diffusion tensor imaging reveals disease-specific deep cerebellar nuclear changes in cerebellar degeneration.** *J Neurol* 2010;257:1406–08
23. Cohen-Adad J, Leblond H, Delivet-Mongrain H, et al. **Wallerian degeneration after spinal cord lesions in cats detected with diffusion tensor imaging.** *Neuroimage* 2011;57:1068–76
24. Cohen-Adad J, Benali H, Hoge RD, et al. **In vivo DTI of the healthy and injured cat spinal cord at high spatial and angular resolution.** *Neuroimage* 2008;40:685–97
25. DeBoy CA, Zhang J, Dike S, et al. **High-resolution diffusion tensor imaging of axonal damage in focal inflammatory and demyelinating lesions in rat spinal cord.** *Brain* 2007;130:2199–210
26. Beirowski B, Adalbert R, Wagner D, et al. **The progressive nature of Wallerian degeneration in wild-type and slow Wallerian degeneration (WldS) nerves.** *BMC Neurosci* 2005;6:6
27. McMillan HJ, Keene DL, Matzinger MA, et al. **Brainstem compression: a predictor of postoperative cerebellar mutism.** *Childs Nerv Syst* 2009;25:677–81
28. Ogiwara H, Dipatri AJ Jr, Bowman RM, et al. **Diffuse postoperative cerebellar swelling in medulloblastoma: report of two cases.** *Childs Nerv Syst* 2011;27:743–47
29. Rao VK, Haridas A, Nguyen TT, et al. **Symptomatic cerebral vasospasm following resection of a medulloblastoma in a child.** *Neurocrit Care* 2013;18:84–88
30. Beaulieu C. **The basis of anisotropic water diffusion in the nervous system: a technical review.** *NMR Biomed* 2002;15:435–55
31. Beaulieu C, Does MD, Snyder RE, et al. **Changes in water diffusion due to Wallerian degeneration in peripheral nerve.** *Magn Reson Med* 1996;36:627–31
32. Song SK, Yoshino J, Le TQ, et al. **Demyelination increases radial diffusivity in corpus callosum of mouse brain.** *Neuroimage* 2005;26:132–40
33. Ochs S, Pourmand R, Jersild RA Jr, et al. **The origin and nature of beading: a reversible transformation of the shape of nerve fibers.** *Prog Neurobiol* 1997;52:391–426
34. Budde MD, Kim JH, Liang HF, et al. **Axonal injury detected by in vivo diffusion tensor imaging correlates with neurological disability in a mouse model of multiple sclerosis.** *NMR Biomed* 2008; 21:589–97
35. Budde MD, Xie M, Cross AH, et al. **Axial diffusivity is the primary correlate of axonal injury in the experimental autoimmune encephalomyelitis spinal cord: a quantitative pixelwise analysis.** *J Neurosci* 2009;29:2805–13
36. Kim JH, Loy DN, Liang HF, et al. **Noninvasive diffusion tensor imaging of evolving white matter pathology in a mouse model of acute spinal cord injury.** *Magn Reson Med* 2007;58:253–60
37. Mac Donald CL, Dikranian K, Bayly P, et al. **Diffusion tensor imaging reliably detects experimental traumatic axonal injury and indicates approximate time of injury.** *J Neurosci* 2007;27:11869–76
38. Song SK, Sun SW, Ramsbottom MJ, et al. **Dysmyelination revealed through MRI as increased radial (but unchanged axial) diffusion of water.** *Neuroimage* 2002;17:1429–36
39. Zhang J, Jones M, DeBoy CA, et al. **Diffusion tensor magnetic resonance imaging of Wallerian degeneration in rat spinal cord after dorsal root axotomy.** *J Neurosci* 2009;29:3160–71
40. Concha L, Gross DW, Wheatley BM, et al. **Diffusion tensor imaging of time-dependent axonal and myelin degradation after corpus callosotomy in epilepsy patients.** *Neuroimage* 2006;32:1090–99
41. Farrell JA, Zhang J, Jones MV, et al. **Q-space and conventional diffusion imaging of axon and myelin damage in the rat spinal cord after axotomy.** *Magn Reson Med* 2010;63:1323–35
42. Wieshmann UC, Symms MR, Clark CA, et al. **Wallerian degeneration in the optic radiation after temporal lobectomy demonstrated in vivo with diffusion tensor imaging.** *Epilepsia* 1999;40:1155–58
43. Werring DJ, Toosy AT, Clark CA, et al. **Diffusion tensor imaging can detect and quantify corticospinal tract degeneration after stroke.** *J Neurol Neurosurg Psychiatry* 2000;69:269–72
44. Thomalla G, Glauche V, Weiller C, et al. **Time course of Wallerian degeneration after ischaemic stroke revealed by diffusion tensor imaging.** *J Neurol Neurosurg Psychiatry* 2005;76:266–68

Diffusional Kurtosis Imaging of the Developing Brain

A. Paydar, E. Fieremans, J.I. Nwankwo, M. Lazar, H.D. Sheth, V. Adisetiyo, J.A. Helpern, J.H. Jensen, and S.S. Milla

ABSTRACT

BACKGROUND AND PURPOSE: Diffusional kurtosis imaging is an extension of DTI but includes non-Gaussian diffusion effects, allowing more comprehensive characterization of microstructural changes during brain development. Our purpose was to use diffusional kurtosis imaging to measure age-related microstructural changes in both the WM and GM of the developing human brain.

MATERIALS AND METHODS: Diffusional kurtosis imaging was performed in 59 subjects ranging from birth to 4 years 7 months of age. Diffusion metrics, fractional anisotropy, and mean kurtosis were collected from VOIs within multiple WM and GM structures and subsequently analyzed with respect to age. Diffusional kurtosis tractography images at various stages of development were also generated.

RESULTS: Fractional anisotropy and mean kurtosis both showed age-related increases in all WM regions, reflecting progression of diffusional anisotropy throughout development, predominantly in the first 2 years of life (eg, 70% and 157% increase in fractional anisotropy and mean kurtosis, respectively, from birth to 2 years for the splenium). However, mean kurtosis detected continued microstructural changes in WM past the fractional anisotropy plateau, accounting for more delayed isotropic changes (eg, 90% of maximum fractional anisotropy was reached at 5 months, whereas 90% of maximum mean kurtosis occurred at 18 months for the external capsule). Mean kurtosis may also provide greater characterization of GM maturation (eg, the putamen showed no change in fractional anisotropy but an 81% change in mean kurtosis from birth to 4 years 7 months).

CONCLUSIONS: Mean kurtosis detects significant microstructural changes consistent with known patterns of brain maturation. In comparison with fractional anisotropy, mean kurtosis may offer a more comprehensive evaluation of age-related microstructural changes in both WM and GM and is potentially a valuable technique for studying brain development.

ABBREVIATIONS: DKI = diffusional kurtosis imaging; FA = fractional anisotropy; IC = internal capsule; max = maximum; MK = mean kurtosis

MR imaging has become the criterion standard for noninvasive high-resolution brain imaging in the pediatric population. Macrostructural changes that take place within the brain during maturation have been well documented by conventional MR imaging techniques in both normal and pathologic states.[1-6] However, these conventional techniques are limited in their ability to quantify developmental changes that occur at the microstructural level. Therefore, in vivo characterization and accurate diagnosis of microstructural abnormalities currently remain challenging.

During brain development, many cellular processes can affect water diffusion properties. WM myelination and maturation, axonal growth and development, and changes in axonal membrane permeability can affect free water diffusion.[7] Indeed, DWI has been used to detect many of these microstructural changes that occur during brain maturation.[8] In particular, the widely used DTI technique has been shown to be sensitive to age-related microstructural changes in both rodent and human models.[5,7,9-11]

DTI describes restricted diffusion in the brain by estimating the diffusion tensor, whereby the principal diffusion tensor eigenvector tends to be directed parallel to axonal bundles (axial direc-

Received June 29, 2013; accepted after revision August 14.

From the Department of Radiology (A.P., E.F., J.I.N., M.L., H.D.S., V.A., S.S.M.), Center for Biomedical Imaging, New York University School of Medicine, New York, New York; and Department of Radiology and Radiological Science (J.A.H., J.H.J.), Center for Biomedical Imaging, Medical University of South Carolina, Charleston, South Carolina.

The authors do not have a direct financial/commercial interest or financial involvement with any organization.

Preliminary data from this research previously presented at: Annual Meeting of the American Society of Neuroradiology and the Foundation of the ASNR Symposium, April 16–21, 2012; New York, New York.

Please address correspondence to Amir Paydar, MD, Department of Radiology-Neuroradiology Section, Center for Biomedical Imaging, NYU Langone Medical Center, 660 First Ave, 3rd Fl, New York, NY 10016; e-mail: amir.paydar@nyumc.org

http://dx.doi.org/10.3174/ajnr.A3764

tion) and the other eigenvectors are perpendicular to the axons (radial direction).[12] The diffusivities corresponding to these directions are referred to as axial diffusivity and radial diffusivity, respectively.[12,13] It has been proposed that axial diffusivity characterizes axonal architecture, while radial diffusivity reflects myelin integrity,[9,12,14] though such simplified interpretations should be regarded with caution.[15] From diffusion tensor eigenvalues, fractional anisotropy (FA), which is a primary index of diffusional directionality, may be calculated. FA values range from zero to 1, where zero implies an isotropic environment with similar diffusion in all directions and 1 implies diffusion along only 1 axis.[13,16] By using these diffusion tensor eigenvectors, one can evaluate the anisotropic neuroarchitectural orientation of WM fiber tracts. Accordingly, DTI is an excellent tool for investigating the age-related increase in anisotropy that occurs within the network of WM tracks as a result of myelination.[5,9,17] However, DTI is based on a Gaussian approximation of water diffusion, which limits its sensitivity to diffusional and microstructural properties of biologic tissues.[18]

Recently, diffusion-weighted techniques that exploit diffusional non-Gaussianity have been developed, including high-angular-resolution diffusion imaging, diffusion spectrum imaging, and diffusional kurtosis imaging (DKI).[19-22] These techniques take into account the non-Gaussian diffusional properties of water motion in complex media and are, therefore, more comprehensive in evaluating brain tissue microstructural complexity.[9,19,23] The DKI technique is a clinically feasible extension of the traditional DTI model while maintaining the ability to estimate all the standard diffusion tensor metrics, including axial diffusivity, radial diffusivity, and FA,[19,20,24] but with improved accuracy.[18] DKI requires at least 2 nonzero b-values and 15 diffusion gradient directions (compared with 1 nonzero b-value and 6 directions for DTI), thereby affording a higher angle resolution of diffusion acquisition.[18,19,23] Moreover, DKI provides an additional metric that quantifies non-Gaussian diffusion termed diffusional kurtosis, *K*. This metric is defined by the equation

$$K = \frac{M_4}{M_2^2} - 3$$

where K represents excess kurtosis and M_n is the nth-order diffusion displacement moment; in a purely Gaussian distribution, $K = 0$.[19] Accordingly, K is a measure that quantifies the deviation of the water diffusion profile from a Gaussian distribution, potentially allowing sensitivity to underlying microstructural barriers not detected by the standard diffusion tensor metrics. By using this parameter, one can generate the metrics axial kurtosis, radial kurtosis, and mean kurtosis (MK), which are the kurtosis counterparts of axial diffusivity, radial diffusivity, and FA, respectively.

In this human study, we used DKI to quantify microstructural changes that occur in both WM and GM during the first 5 years of life, when the brain is in its most active stage of development. We hypothesize that owing to their sensitivity for the detection of microstructural changes in both anisotropic and isotropic environments,[10,19] the kurtosis metrics of DKI (particularly MK) may provide additional information about brain maturation compared with that obtainable with conventional diffusion tensor metrics (specifically FA). Therefore, DKI has the potential to improve the evaluation of the developing brain in both normal and pathologic states.

MATERIALS AND METHODS

An institutional review board–approved retrospective review was initiated by obtaining a comprehensive data base of brain MRI in 59 pediatric subjects (31 female, 28 male) who underwent DKI imaging as part of a routine MR imaging examination under sedation at a major university medical center from June 2009 to October 2010. Subject or parental informed consent was waived because it was not required by the institutional review board. The age range of our subjects was birth (ie, day 1 of life) to 4 years 7 months (ie, 1689 days of age). Subjects who underwent brain MR imaging for non-neurologic indications (eg, facial hemangiomas, orbital lesions, sinonasal abnormalities, vomiting, weight loss, precocious puberty) were included in this study. However, premature infants and subjects who had medical histories with possibly related intracranial/neurologic manifestations (eg, seizures or delayed myelination) were excluded from this study. All the included examination findings were interpreted as normal by fellowship-trained board-certified neuroradiologists. MR imaging examinations that demonstrated any intracranial pathology or were considered of low quality due to motion artifacts, oblique positioning, or a low signal-to-noise ratio were also excluded. All MR imaging examination findings were re-evaluated by a board-certified pediatric neuroradiologist for normalcy before inclusion.

All studies were performed on a 1.5T MR imaging scanner (Magnetom Avanto; Siemens, Erlangen, Germany). A body coil was used for transmission of the signal and an 8-channel head coil was used to receive the signal. Diffusion-weighted data were obtained using an axial fat-suppressed single-shot echo-planar sequence with the following imaging parameters: TR/TE = 4500/96 ms; matrix size = 78–82 × 78–82 × 28–34; voxel size = 2.2–2.8 × 2.2–2.8 × 4–5 mm^3 (ie, section thickness = 4–5 mm, without an intersection gap); generalized autocalibrating partially parallel acquisitions acceleration factor = 2; acquisition time = 4 minutes 48 seconds; diffusion directions = 30; b-values = 0, 1000, and 2000 s/mm^2. Of note, maximum b-values of approximately 2000 s/mm^2 are needed for the diffusion signal to be sensitive to non-Gaussian effects and to quantify accurate kurtosis values.[19,23]

DKI data were processed by using in-house software called the Diffusional Kurtosis Estimator (http://www.nitrc.org/projects/dke). Subsequently, the diffusion and kurtosis tensors were calculated on a voxel-by-voxel basis to produce skull-stripped parametric gray-scale maps for FA and MK.[19,25] Sample transaxial sections from FA and MK maps for the youngest and oldest subjects are portrayed in Fig 1*A* and -*B*.

Using MRIcron (http://www.sph.sc.edu/comd/rorden/mricro.html), we drew VOIs directly on multiple FA map transverse sections for volumetric analysis. VOIs were drawn on 9 different anatomic WM and GM structures, including the genu and splenium of the corpus callosum, frontal WM, parietal WM, anterior and poster limbs of the internal capsule (IC), external capsule, thalamus, and putamen (Fig 1*C*). VOI drawing was performed by a neuroradiology fellow, fourth-year radiology res-

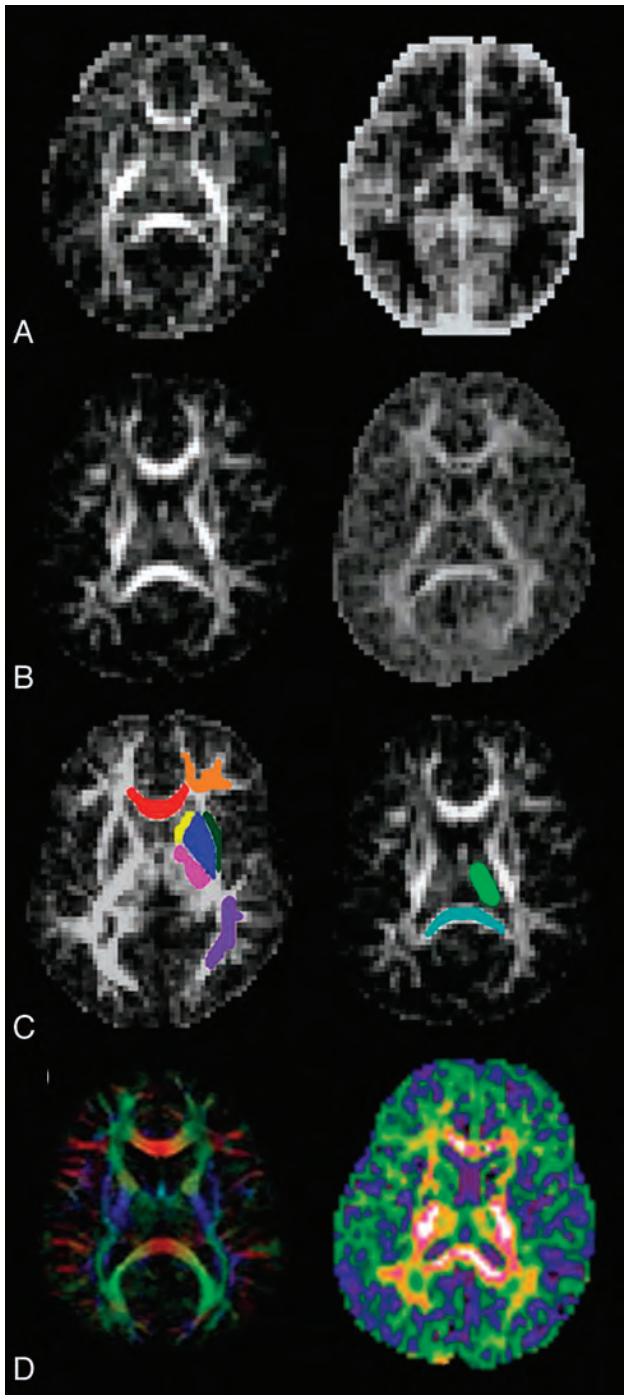

FIG 1. *A*, Transaxial FA (left) and MK (right) maps at birth. *B*, Transaxial FA (left) and MK (right) maps at 4 years 7 months. *C*, Examples of VOIs drawn on transaxial FA maps over the genu (red), frontal WM (orange), parietal WM (purple), putamen (blue), anterior IC (yellow), posterior IC (pink), external capsule (dark green), thalamus (light green), and splenium (cyan). *D*, Transaxial FA (left) and MK (right) color maps.

ident, and a second-year medical student. To control for interobserver variability, we assigned each of these investigators to draw all of the VOIs for any given anatomic structure for all the subjects. All VOIs were later carefully reviewed by a single board-certified pediatric neuroradiologist to further minimize interobserver variability. VOIs were then applied to the parametric maps in Matlab (MathWorks, Natick, Massachusetts) to calculate the mean FA and MK values for each VOI.

Thereafter, the mean FA and MK for each VOI were analyzed for each subject and correlated with age by fitting each parameter value P to a nonlinear monoexponential plus a constant, $P = ae^{-bX} + c$, where X is age and a, b, c are fitting parameters. Using this function, we generated regression curves for both FA and MK values for all 9 VOIs in Matlab (Figs 2–5). Coefficient of determination (R^2) values were also calculated to demonstrate the quality of the exponential fit for the FA and MK regression curves (Table). In addition, to compare developmental timing parameters for all 9 WM and GM VOIs, we first defined the developmental plateau for both FA and MK values at the asymptotes of the exponential curves and labeled them as FA_{max} and MK_{max}, respectively (Table). Using these FA_{max} and MK_{max} values, we calculated percentage changes in both FA and MK metrics at 2 years and 4 years 7 months of age. Finally, the specific ages at which 90% of FA_{max} and MK_{max} were reached since birth were estimated for all VOIs.

DKI tractography was performed for the newborn, 6 month, 11 month, and 2 year 1 month subjects (Fig 6). Complex orientation distribution function profiles were obtained at all brain voxels with $MK > 0.1$,[26] and fiber directions at each voxel were estimated by using the maxima of the orientation distribution function profiles. VOIs for the genu, splenium, anterior IC, posterior IC, and external capsule were used as seeds to generate fiber trajectories by using a fiber assignment by continuous tracking approach.[27] Fiber tracts were terminated if they reached regions with $FA < 0.1$ (for subjects at least several months of age) or $FA < 0.05$ (for the neonate subject) or if the angle between 2 consecutive steps was $>45°$. Only tracts with lengths larger than 30 mm were retained in the final image.

RESULTS

Figures 2–5 show the data points for the 59 subjects with the corresponding regression curves, demonstrating the progressive changes in the FA and MK values for all 9 WM and GM regions as a function of age from birth to 4 years 7 months. Figure 2 shows the FA curves as manifested by a change in the FA value with time in all 7 WM regions. There is an exponential increase in FA during the course of development within all WM structures, most appreciable within the first 2 years. Figure 3 shows the MK curves, demonstrating a change in the MK value with time in the same 7 WM regions. There is also a steady increase in MK with time within all WM structures, also most evident in the first 2 years.

The corpus callosum demonstrates relatively higher FA and MK values compared with the other WM regions, the splenium more so than the genu. Differences in the sloping of both FA and MK curves are also seen between the splenium and genu. The splenium shows an earlier percentage rise in both FA and MK compared with the genu. In addition, 90% of the developmental plateaus for both FA and MK curves (ie, 90% of FA_{max} and MK_{max}) are reached at an earlier age for the splenium (9 and 15 months) than for the genu (16 and 19 months; Table).

Important temporal differences are also observed between FA and MK curves. As demonstrated in the Table, MK developmental plateaus are reached at later ages than those for FA in all WM regions. Percentage change in FA reaches its asymptote at approximately 2 years of age, while percentage change in MK continues beyond the 2-year mark. In addition, in all WM

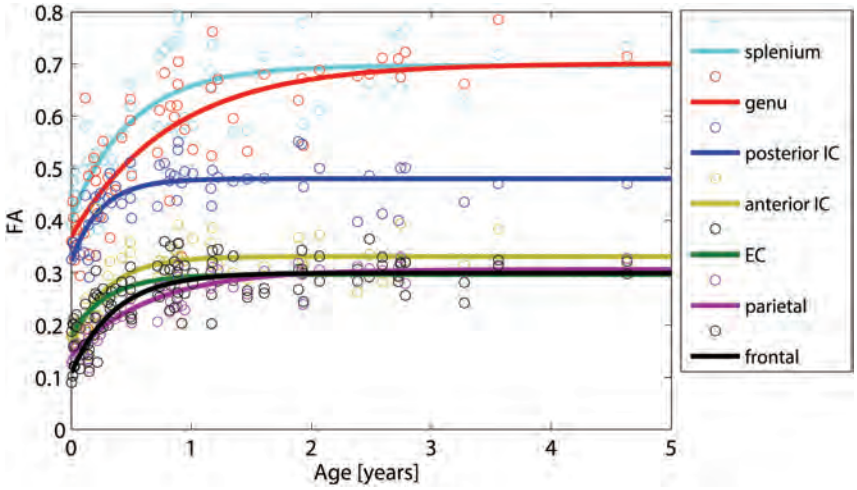

FIG 2. FA curves demonstrate a change in FA value as a function of age in all 7 WM regions.

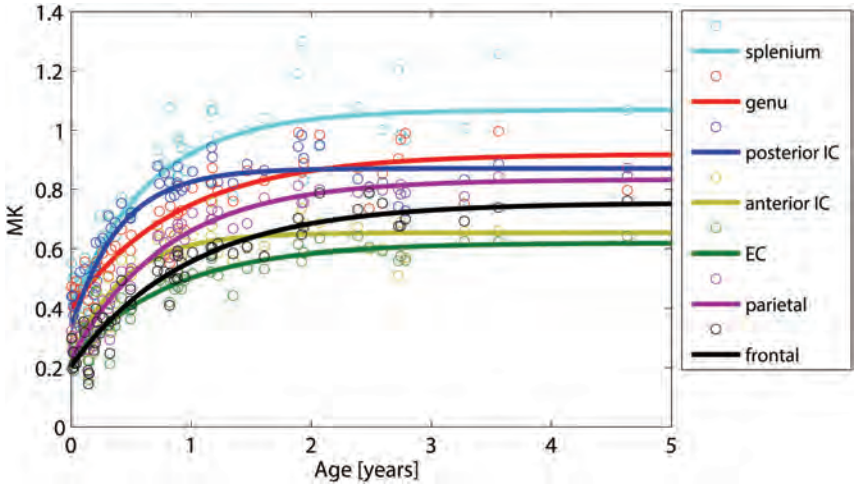

FIG 3. MK curves demonstrate a change in MK value as a function of age in all 7 WM regions.

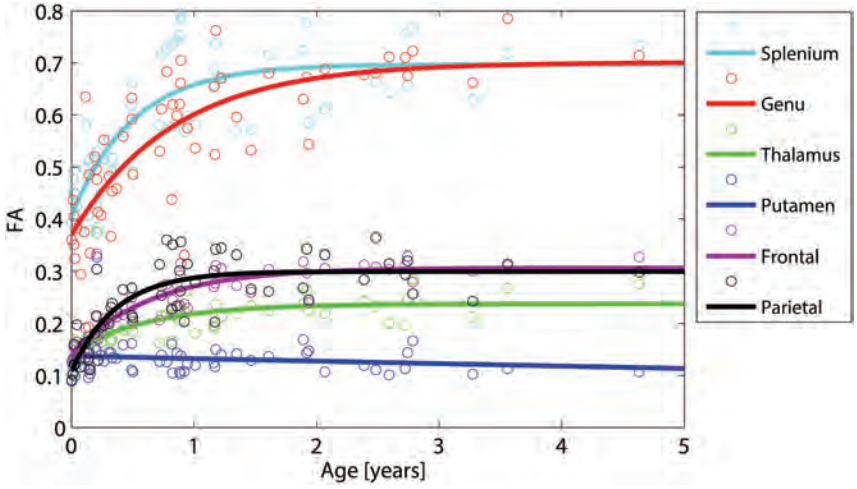

FIG 4. FA curves demonstrate a change in FA values as a function of age in 2 GM regions (thalamus and putamen); FA curves for 4 WM regions from Fig 3 are also included in this graph for comparison.

locations, 90% of MK_{max} is reached at a later age (eg, at 18 months in the external capsule) than 90% of FA_{max} (eg, 5 months in the external capsule).

Figures 4 and 5 show the FA and MK curves for the 2 GM regions, the thalamus and putamen; FA and MK curves for the subcortical WM regions and the corpus callosum are also included in these graphs for comparison. No detectible change in FA is seen in the putamen with time. In contrast, there is up to an 81% change in MK detected within the putamen from birth to 4 years 7 months (Table). Notably, the FA curve for the thalamus demonstrates a slight percentage increase in FA (63% at 2 years and 66% at 4 years 7 months). On the other hand, the MK curve for the thalamus shows a much more substantial increase in MK (136% at 2 years and 137% at 4 years 7 months).

DKI tractography images in Fig 6 qualitatively illustrate the progressive increase in volume and coherent orientation of WM fibers within the genu, splenium, anterior IC, posterior IC, and external capsule WM structures from birth to 2 years 1 month of age.

DISCUSSION

With respect to conventional DTI, DKI has been shown to provide additional information about microstructural changes in the developing brain. A previous rodent study ascertained that DKI offers a more sensitive evaluation of the microstructural complexity of both WM and GM at 3 stages of brain development compared with DTI.[10] We were able to document similar findings in the human brain.

In our study, a progressive rise in FA throughout all WM regions reflects the increase in anisotropy in WM tracts as myelination progresses. This phenomenon has also been well-documented in prior investigations.[10,11] Notably, this trend is most evident in the first 2 years, when myelination is the dominant contributor to the increase in the microstructural complexity of WM. In addition, the relatively higher FA in the corpus callosum throughout all ages may be attributed to its more tightly packed and anisotropic architecture.[5,9,10,28] We also observed that the increase in FA and the age at which FA peaks both occur relatively earlier in the splenium than in the genu, in keeping with the well-known caudorostral pattern of myelination of the corpus callosum during maturation.[1,4,7,11,28,29]

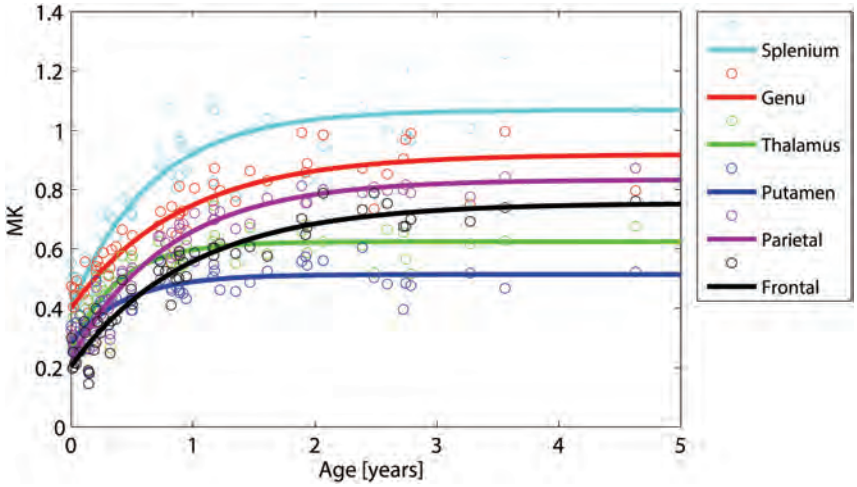

FIG 5. MK curves demonstrate a change in MK values as a function of age in 2 GM regions (thalamus and putamen); MK curves for 4 WM regions from Fig 4 are also included in this graph for comparison.

MK, like FA, increases in all WM regions, suggesting that DKI can detect the age-related increase in anisotropy as well, likely also predominantly as a function of myelination. DKI tractography images (Fig 6) display this age-related increase in anisotropy within central WM tracts, as reflected by the increase in tract coherence with age. However, our DKI data also show that MK continues to rise beyond the 2-year mark and plateaus at later ages than FA does in all WM locations. This trend indicates that DKI can further resolve isotropic diffusion barriers that continue to develop in the WM even after myelination and axonal packing have already peaked. Speculatively, these barriers may form partly as a result of an increase in the complexity of intrinsic cellular processes and extracellular matrices,[18-20] axonal pruning,[10] and functional reorganization of myelin to allow the progressive increase in axon conduction velocities,[11,30,31] all of which continue to occur during later stages of development. Another concept that may explain this trend is the continued maturation of crossing fibers in WM during later childhood. DTI is limited in the evaluation of both anisotropy and directionality of crossing fibers because the diffusion tensor can only resolve a singlefiber orientation within each voxel.[10,21,22] While FA is diminished inside voxels containing crossing fibers, MK can better define the multidirectional environment inside these voxels. This intrinsic property is also validated with tractography. Via the application of the orientation distribution function, fiber tracking with DKI has been shown to better account for the presence of these crossing fibers.[26] DTI and DKI tractography images in Fig 7 visually demonstrate this concept by displaying the higher sensitivity of DKI for crossing-fiber resolution. In conclusion, as isotropic diffusion barriers and more complex fiber patterns continue to materialize in the WM after myelination has already been established, a non-Gaussian diffusion approach may better characterize these more delayed developmental changes.

Our study also supports the hypothesis that DKI is sensitive to age-related microstructural changes that occur in the isotropic GM, for which DTI has previously been shown to have limited sensitivity.[9,10] In the putamen, there is no appreciable change in FA throughout the first 4 years 7 months of life, corresponding to the complete lack of anisotropic architecture of the putamen. However, a slight increase in FA is seen in the thalamus with time, mainly because the thalamus, though predominantly a GM structure, has a sizeable fraction of linear axonal WM tracts and therefore an element of internal anisotropy.[9] On the other hand, there is a steady rise in MK in both the putamen and thalamus with time, accounting for other specific isotropic changes that occur in these GM structures throughout development. In theory, these isotropic diffusion barriers to which MK is sensitive probably emerge as a result of a progressive increase in macromolecular concentration and a decrease in tissue water content as GM matures.[9] Other specific cytoarchitectural changes that affect MK-sensitive isotropic diffusion behaviors in the developing GM may include the proliferation of cell membranes and organelles, the transition of radial glial cells to astrocytic neuropil, the addition of basal dendrites, and cell packing.[9,10,14] Therefore, compared with FA, MK can better resolve the progression of GM organization with respect to age by accounting for other isotropic microstructural barriers that form at the cellular level.

Relative change in FA and MK from birth to 4 years 7 months at all anatomic locations

	FA				MK			
Anatomic Location	R^2[a]	% Δ (Birth to 2 yr)[b]	% Δ (Birth to 4 yr 7 mo)[c]	90% of FA_{max} (mo)[d]	R^2[a]	% Δ (Birth to 2 yr)[b]	% Δ (Birth to 4 yr 7 mo)[c]	90% of MK_{max} (mo)[d]
Splenium	0.66	70	71	9	0.82	157	165	15
Genu	0.63	81	89	16	0.85	115	129	19
Frontal WM	0.69	172	173	8	0.92	233	265	23
Parietal WM	0.77	111	116	13	0.94	236	257	19
Anterior IC	0.62	103	103	6	0.85	182	184	10
Posterior IC	0.61	48	48	4	0.84	158	159	9
EC	0.59	63	63	5	0.87	160	174	18
Thalamus	0.45	63	66	10	0.78	136	137	8
Putamen	0.03	−7	−18	N/A	0.68	80	81	8

Note:—NA indicates not applicable; EC external capsule.

[a] Coefficient of determination (R^2) demonstrating the goodness of exponential fit for the FA and MK nonlinear monoexponential regression curves.

[b] Percentage change in FA and MK absolute values from birth to 2 years of age.

[c] Percentage change in FA and MK absolute values from birth to 4 years 7 months of age.

[d] Approximate age in months at which 90% of developmental plateau is reached since birth for both FA and MK datasets (ie, FA_{max} and MK_{max}).

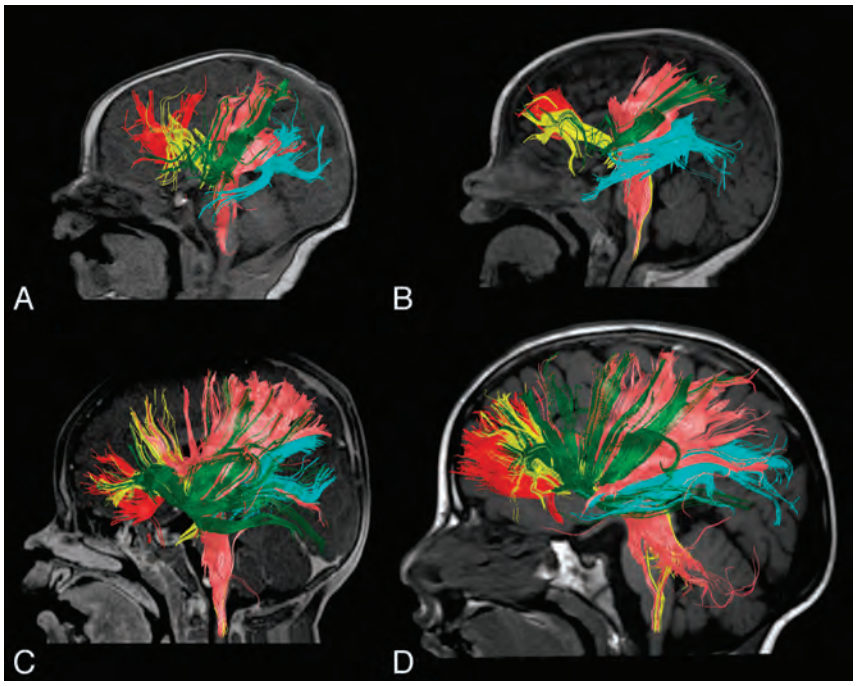

FIG 6. DKI tractography at various stages of development, including birth (*A*), 6 months (*B*), 11 months (*C*), and 2 years 1 month (*D*). Fiber tracking is displayed for the genu (red), splenium (cyan), anterior IC (yellow), posterior IC (pink), and external capsule (dark green).

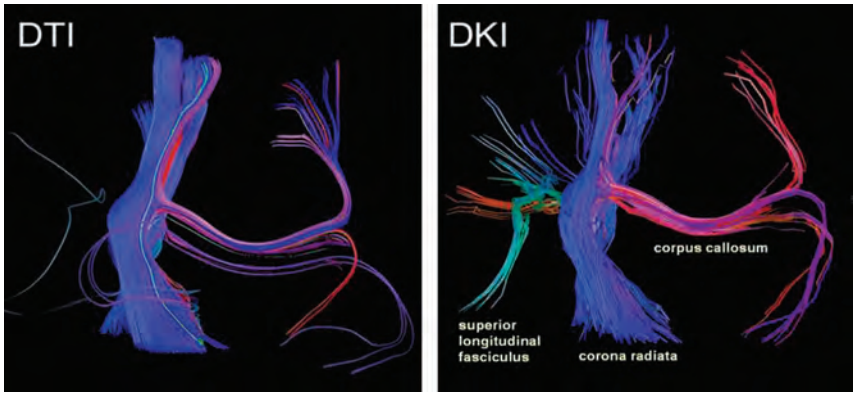

FIG 7. DTI and DKI tractographies performed on a normal brain are provided as an example to illustrate the difference in sensitivity for the detection of tiny crossing fibers between DTI and DKI fiber-tracking techniques.

This investigation was partly limited due to its retrospective nature and lack of longitudinal information, particularly pertaining to the neurologic development of the included subjects. In addition, VOI drawing by 3 independent investigators may have introduced some degree of interobserver variability in our study results, though no definite discrepancy was identified in their drawing techniques. Finally, VOI drawing on FA maps may have been influenced by subjective selection of structures defined by variable FA contrast at different ages.

Future DKI studies should be performed to further expand our understanding of non-Gaussian diffusivity in the developing brain. Previous research has shown that DTI can detect age-related microstructural changes in the brain beyond 5 years of age. In a study by Lebel et al, subtle gradual changes in FA were observed within most WM and GM locations up to early adulthood. Therefore, the use of DKI parameters to study normal developmental changes in the brain of subjects older than 5 years is another subject worth pursuing. In addition, we aim to use DKI for the evaluation of other GM regions in our future investigations. DKI also remains a promising technique for studying the developing brain in pathologic states.[32] It has already been shown to yield valuable information about the microstructural integrity of the brain in children with epilepsy[33] and in adolescents with attention deficit/hyperactivity disorder.[34] Indeed, future DKI studies may explore the sensitivity of kurtosis metrics to pathologies that alter the microstructural complexity in the developing brain.

CONCLUSIONS

This human study replicates findings made in previous rodent studies, reflecting the additional information that DKI provides for detecting microstructural changes in the developing human brain. Similar to DTI, DKI can also detect anisotropic WM changes due to myelination, predominantly during the first 2 years of life. In addition, DKI can identify other isotropic WM changes that occur beyond the first 2 years. Finally, DKI may also provide greater characterization of GM maturation. In summary, DKI offers sensitive and comprehensive measures for the quantitative evaluation of age-related microstructural changes in both WM and GM and thereby may be a valuable technique for studying the developing brain.

Disclosures: Els Fieremans—*UNRELATED: Patents (planned, pending or issued):* Siemens Medical owns a royalty-free nonexclusive license for diffusional kurtosis imaging with the pending patent held by New York University. I am one of the inventors.* *Money paid to the institution.

REFERENCES

1. Brody BA, Kinney HC, Kloman AS, et al. **Sequence of central nervous system myelination in infancy. I. An autopsy study of myelination.** *J Neuropathol Exp Neurol* 1987;46:283–301
2. Barkovich AJ, Kjos BO, Jackson DE, et al. **Normal maturation of the neonatal and infant brain: MR imaging at 1.5 T.** *Radiology* 1988; 166(1 pt 1):173–80
3. Dobbing J, Sands J. **Quantitative growth and development of human brain.** *Arch Dis Child* 1973;48:757–67
4. Kinney HC, Brody BA, Kloman AS, et al. **Sequence of central nervous system myelination in human infancy. II. Patterns of myelination in autopsied brains.** *J Neuropathol Exp Neurol* 1988;47:217–34
5. Lebel C, Walker L, Leemans A, et al. **Microstructural maturation of the human brain from childhood to adulthood.** *Neuroimage* 2008; 40:1044–55

6. Deipolyi AR, Mukherjee P, Gill K, et al. **Comparing microstructural and macrostructural development of the cerebral cortex in premature newborns: diffusion tensor imaging versus cortical gyration.** *Neuroimage* 2005;27:579–86
7. Takeda K, Nomura Y, Sakuma H, et al. **MR assessment of normal brain development in neonates and infants: comparative study of T1- and diffusion-weighted images.** *J Comput Assist Tomogr* 1997; 21:1–7
8. Basser PJ, Jones DK. **Diffusion-tensor MRI: theory, experimental design and data analysis: a technical review.** *NMR Biomed* 2002; 15:456–67
9. Mukherjee P, Miller JH, Shimony JS, et al. **Diffusion-tensor MR imaging of gray and white matter development during normal human brain maturation.** *AJNR Am J Neuroradiol* 2002;23;1445–56
10. Cheung MM, Hui ES, Chan KC, et al. **Does diffusion kurtosis imaging lead to better neural tissue characterization? A rodent brain maturation study.** *Neuroimage* 2009;45:386–92
11. Yoshida S, Oishi K, Faria AV, et al. **Diffusion tensor imaging of normal brain development.** *Pediatr Radiol* 2013;43:15–27
12. Song SK, Sun SW, Ramsbottom MJ, et al. **Dysmyelination revealed through MRI as increased radial (but unchanged axial) diffusion of water.** *Neuroimage* 2002;17:1429–36
13. Basser PJ. **Inferring microstructural features and the physiological state of tissues from diffusion-weighted images.** *NMR Biomed* 1995;8:333–44
14. Hüppi PS, Dubois J. **Diffusion tensor imaging of brain development.** *Semin Fetal Neonatal Med* 2006;11:489–97
15. Jones DK, Knosche TR, Turner R. **White matter integrity, fiber count, and other fallacies: the do's and don'ts of diffusion MRI.** *Neuroimage* 2013;73:239–54
16. Schimrigk SK, Bellenberg B, Schluter M. **Diffusion tensor imaging-based fractional anisotropy quantification in the corticospinal tract of patients with amyotrophic lateral sclerosis using a probabilistic mixture model.** *AJNR Am J Neuroradiol* 2007;28:724–30
17. Beaulieu C. **The basis of anisotropic water diffusion in the nervous system—a technical review.** *NMR Biomed* 2002;15:435–55
18. Veraart J, Poot DH, Van Hecke W, et al. **More accurate estimation of diffusion tensor parameters using diffusion kurtosis imaging.** *Magn Reson Med* 2011;65:138–45
19. Jensen JH, Helpern JA. **MRI quantification of non-Gaussian water diffusion by kurtosis analysis.** *NMR Biomed* 2010;23:698–710
20. Lu H, Jensen JH, Ramani A, et al. **Three-dimensional characterization of non-Gaussian water diffusion in humans using diffusion kurtosis imaging.** *NMR Biomed* 2006;19:236–47
21. Tournier JD, Yeh CH, Calamante F, et al. **Resolving crossing fibers using constrained spherical deconvolution: validation using diffusion-weighted imaging phantom data.** *Neuroimage* 2008;42:617–25
22. Perrin M, Poupon C, Cointepas Y, et al. **Fiber tracking in Q-ball fields using regularized particle trajectories.** *Inf Process Med Imaging* 2005;19:52–63
23. Jensen JH, Helpern JA, Ramani A, et al. **Diffusional kurtosis imaging: the quantification of non-Gaussian water diffusion by means of magnetic resonance imaging.** *Magn Reson Med* 2005; 53:1432–40
24. De Santis S, Gabrielli A, Palombo M, et al. **Non-Gaussian diffusion imaging: a brief practical review.** *Magn Reson Imaging* 2011; 29:1410–16
25. Tabesh A, Jensen JH, Ardekani BA, et al. **Estimation of tensors and tensor-derived measures in diffusional kurtosis imaging.** *Magn Reson Med* 2011;65:823–36
26. Lazar M, Jensen JH, Xuan L, et al. **Estimation of the orientation distribution function from diffusional kurtosis imaging.** *Magn Reson Med* 2008;60:774–81
27. Mori S, Crain BJ, Chacko VP, et al. **Three-dimensional tracking of axonal projections in the brain by magnetic resonance imaging.** *Ann Neurol* 1999;45:265–69
28. Provenzale JM, Isaacson J, Chen S. **Progression of corpus callosum diffusion-tensor imaging values during a period of signal changes consistent with myelination.** *AJR Am J Roentgenol* 2012;198: 1403–08
29. Sampaio RC and Truwit CL. **Myelination of the developing human brain.** In: Nelson CA, Luciana M, eds. *Handbook of Developmental Cognitive Neuroscience.* Cambridge, Massachusetts: MIT Press; 2001:35–44
30. Müller K, Homberg V, Lenard HG. **Magnetic stimulation of motor cortex and nerve roots in children: maturation of cortico-motoneuronal projections.** *Electroencephalogr Clin Neurophysiol* 1991;81: 63–70
31. Nezu A, Kimura S, Uehara S, et al. **Magnetic stimulation of motor cortex in children: maturity of corticospinal pathway and problem of clinical application.** *Brain Dev* 1997;19:176–80
32. Hui ES, Cheung MM, Qi L, et al. **Toward better MR characterization of neural tissues using directional diffusion kurtosis analysis.** *Neuroimage* 2008;42:122–34
33. Gao Y, Zhang Y, Wong CS, et al. **Diffusion abnormalities in temporal lobes of children with temporal lobe epilepsy: a preliminary diffusional kurtosis imaging study and comparison with diffusion tensor imaging.** *NMR Biomed* 2012;25:1369–77
34. Helpern JA, Adisetiyo V, Falangola MF, et al. **Preliminary evidence of altered gray and white matter microstructural development in the frontal lobe of adolescents with attention-deficit hyperactivity disorder: a diffusional kurtosis imaging study.** *J Magn Reson Imaging* 2011;33:17–23

Diffusion Imaging for Tumor Grading of Supratentorial Brain Tumors in the First Year of Life

S.F. Kralik, A. Taha, A.P. Kamer, J.S. Cardinal, T.A. Seltman, and C.Y. Ho

ABSTRACT

BACKGROUND AND PURPOSE: Supratentorial tumors in the first year of life are typically large and heterogeneous at presentation, making differentiation of these CNS neoplasms on pre-operative imaging difficult. We hypothesize that the ADC value can reliably differentiate high- versus low-grade supratentorial tumors in this patient population.

MATERIALS AND METHODS: A blinded review of ADC maps was performed on 19 patients with histologically proved supratentorial brain tumors diagnosed within the first year of life. Minimum ADC values obtained by region of interest from 2 neuroradiologists were averaged and compared with World Health Organization tumor grade. ADC values for the entire tumor were also obtained by use of a semi-automated histogram method and compared with World Health Organization tumor grade. Data were analyzed by use of Spearman ρ and Student t test, with a value of $P < .05$ considered statistically significant.

RESULTS: For the manual ADC values, a significant negative correlation was found between the mean minimum ADC and tumor grade ($P = .0016$). A significant difference was found between the mean minimum ADC of the low-grade (1.14×10^{-3} mm^2/s $\pm$ 0.30) and high-grade tumors (0.64×10^{-3} mm^2/s $\pm$ 0.28) ($P = .0018$). Likewise, the semi-automated method demonstrated a significant negative correlation between the lowest 5th ($P = .0002$) and 10th ($P = .0009$) percentile individual tumor ADC values and tumor grade, a significant difference between the mean 5th and 10th percentile ADC values of the low-grade and high-grade groups ($P = .0028$), and a significant positive correlation with values obtained by manual region-of-interest placement ($P < .000001$).

CONCLUSIONS: ADC maps can differentiate high- versus low-grade neoplasms for supratentorial tumors presenting in the first year of life, given the significant negative correlation between ADC values and tumor grade.

ABBREVIATION: WHO = World Health Organization

Supratentorial brain tumors in the first year of life are challenging from both a clinical and radiologic perspective. Clinical presentation is often delayed because of nonlocalizing symptoms and because the calvaria may accommodate increasing size of a mass and intracranial pressure at this age.[1] Consequently, these tumors are often large on presentation, resulting in greater operative risks. A wide range of low-grade and high-grade pathologies may present within the first year of life. On radiologic examination, these tumors are typically large, heterogeneous, and may not demonstrate characteristic imaging features to indicate a specific diagnosis. Imaging techniques that establish a more specific preoperative diagnosis would aid in surgical planning for gross or near total resection versus identification of locations for biopsy.

Diffusion imaging allows the evaluation of the diffusion of water in tissues. Quantitative analysis of the average diffusion rate in each voxel can be performed by use of the calculated ADC. There is a correlation between reduced diffusion of water and increasing tumor cellularity and therefore tumor grade.[2] ADC values have been previously shown to reliably differentiate pediatric cerebellar tumors.[3] We hypothesize that the ADC value can reliably differentiate high-grade versus low-grade supratentorial tumors in children presenting at an age of less than 1 year.

MATERIALS AND METHODS

After institutional review board approval was given, a retrospective radiology data base search from April 2003 to October 2011

Received July 16, 2013; accepted after revision August 28.

From Indiana University School of Medicine, Department of Radiology and Imaging Sciences, Indianapolis, Indiana.

Paper previously presented in part at: Annual Meeting of the Radiological Society of North America, November 24–30, 2012; Chicago, Illinois.

Please address correspondence to Chang Y. Ho, MD, 705 Riley Hospital Dr, MRI Department, Indianapolis, IN 46202; e-mail: cyho@iupui.edu

http://dx.doi.org/10.3174/ajnr.A3757

was performed on patients with age ≤1 year who had brain MR imaging with a supratentorial mass confirmed by pathology. Postoperative pathologic diagnosis of the tumor type and World Health Organization (WHO) grade was recorded, and a blinded, retrospective review of the preoperative presentation brain MR imaging studies was performed. In cases that precede the most recent 2007 update for WHO tumor classification of the central nervous system, the pathologic report was analyzed for potential changes of WHO grading.

MR imaging was performed on 1.5T Signa LX (GE Healthcare, Milwaukee, Wisconsin), and 1.5T and 3T Avanto and Verio (Siemens, Erlangen, Germany) MR units with axial T2-weighted, fast spin-echo, sagittal and axial T1-weighted, axial fluid-attenuated inversion recovery, and postcontrast axial, coronal, and sagittal T1-weighted sequences. DWI was performed with multisection single-shot spin-echo echo-planar imaging with 5-mm section thickness before administration of contrast material, with b-values of 0 and 1000 s/mm^2 applied in the x, y, and z directions. Processing of ADC maps was performed automatically on the MR units. Tumor characteristics including maximum dimension (cm), T2-weighted signal appearance (heterogeneity and presence of cystic areas), presence of precontrast T1 shortening or susceptibility in the tumor, T1-weighted postcontrast appearance of the noncystic areas, and tumor location were recorded for each tumor by one neuroradiologist (S.F.K.).

Manual Analysis of the Minimum ADC Tumor Value

A retrospective review and analysis of the brain MR imaging DWI/ADC was independently performed by 2 board-certified neuroradiologists (C.Y.H., S.F.K.) who were blinded to the final pathology. At least 3 regions of interest with size ranging from 1–10 mm^2 were placed in the mass at the PACS workstation (Fuji Synapse 3.2.1; Fujifilm, Tokyo, Japan) by use of a manual/free-form region-of-interest tool, and the value was automatically calculated and expressed in 10^{-3} mm^2/s. Sites of region of interest placement were chosen by visual inspection and targeted the darkest signal intensity regions on the ADC map, with the goal of including the lowest ADC portions of the tumor. The entire set of pulse sequences was available during ADC value placement to avoid placing a region of interest on an area of presumed blood products on the basis of intrinsic T1-weighted shortening, T2-weighted shortening, or susceptibility effects in the $b = 0$ images. Mean ADC values were recorded for each region of interest. The mean ADC values of the 6 ROIs for both neuroradiologists were then averaged and used as the final average minimum value for the tumor. Additionally, mean ADC values from the normal contralateral thalamus and centrum semiovale were obtained in each patient by one neuroradiologist (S.F.K.) to use as an internal reference for comparison. The average minimum ADC value for each tumor and the ratio of the average minimum ADC to the ADC value of the contralateral thalamus ($ADC_{tumor}/ADC_{thalamus}$) or contralateral centrum semiovale (ADC_{tumor}/ADC_{wm}) were compared with its respective final tumor pathology WHO grade by use of Spearman ρ correlation. The unpaired 2-tailed Student t test was used to compare for significant differences between the average minimum ADC value and the ADC ratios of the high-grade (WHO grade III and IV) and low-grade tumors (WHO grade I and II). A receiver operating characteristic curve was used to analyze threshold calculations.

Semi-Automated Tumor ADC Value Analysis

Semi-automated ADC value calculation was performed by use of an in-house script for Matlab (R2011b; MathWorks, Natick, Massachusetts) after a freehand region of interest outlining the entire tumor selected on each axial ADC image for each of the included subjects was performed by a trained medical student (T.A.S.). The ADC images were compared with additional MR imaging from the same study (precontrast and postcontrast T1, T2 sequences) to determine the extent of tumor for selection. Cystic regions of tumor were included, whereas areas of hemorrhage were excluded from the regions of interest. The results were then validated by a board-certified neuroradiologist (A.P.K.). All DICOM ADC voxel values within each of these regions of interest were collected for each individual patient and were then exported to comma-separated value files for import to Excel 2010 (Microsoft, Redwood City, California), with 1 value for each voxel within the tumor, expressed in units 10^{-3} mm^2/s. Individual histograms were generated for the ADC data from each tumor. ADC bin widths of 0.05 ($\times 10^{-3}$ mm^2/s) were chosen on the basis of the trade-off between detail and noise within the histograms (Fig 1). Normalized summation histograms were generated, 1 for each of the low-grade tumors (WHO grade I and II) and for each of the high-grade tumors (WHO grade III and IV). To create the summation histograms, the ADC histogram data for each individual tumor was normalized by dividing the bin frequencies by the total number of voxels within the tumor, so that each tumor contributed to the tumor group histogram equally, regardless of tumor size. The data in the summation histograms were then normalized by dividing the bin frequencies by the number of tumors in each group so that the group histograms were comparable, eliminating differences that were based on number of tumors in the group. Statistical metrics calculated for the raw ADC data for each tumor included mean, standard deviation, skew, kurtosis, peak height, peak location, and multiple percentiles (5th, 10th, 25th, 50th, 75th, 90th, and 95th). Means and standard deviations were calculated for each statistical metric, grouped by WHO classification. Additionally, scatterplots were generated for each statistical metric grouped by WHO classification. Probability values were calculated for each statistical metric by use of the unpaired, 2-tailed Student t test to evaluate for statistically significant differences between low-grade (WHO I and II) and high-grade (WHO III and IV) results. Also, Spearman ρ correlation was performed between the semi-automated histogram data and the manually obtained average minimum ADC values.

RESULTS

Supratentorial Tumor Characteristics

Twenty-two patients were identified; however, 3 patients were excluded. Excluded patients included 1 patient with a complex vascular malformation, 1 patient with an immature teratoma for which no WHO grading was possible, and 1 patient who was excluded because of lack of DWI sequence and ADC map. There

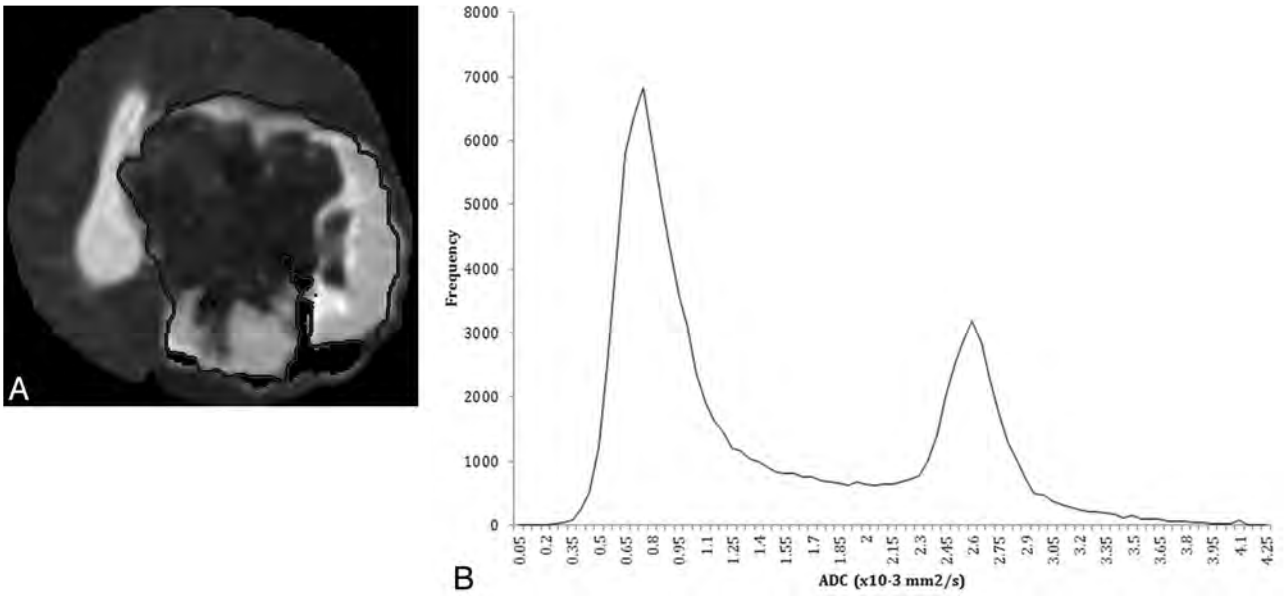

FIG 1. A 4-month-old girl with poorly differentiated carcinoma of the left cerebral hemisphere. *A*, Representative axial image from ADC map demonstrates manual tracing with general exclusion of large areas of blood products represented by susceptibility artifacts. *B*, Histogram of all included ADC values of the tumor from the semi-automated method.

Table 1: Tumor pathology with corresponding WHO grade and ADC values from manual ROI measurement

Tumor Type	WHO Grade	Average Minimum ADC × 10^{-3} mm^2/s	ADC Ratio Thalamus	ADC Ratio White Matter
Desmoplastic infantile ganglioglioma	I	1.63	1.68	1.50
Desmoplastic infantile ganglioglioma	I	0.88	1.05	0.79
Desmoplastic infantile ganglioglioma	I	0.97	1.08	0.80
Desmoplastic infantile ganglioglioma	I	1.14	0.87	0.76
Choroid plexus papilloma	I	1.01	1.05	1.10
Choroid plexus papilloma	I	0.92	1.16	0.79
Choroid plexus papilloma	I	1.31	1.53	1.23
Pilocytic astrocytoma	I	0.78	0.96	0.75
Astrocytoma, focal	II	1.71	1.50	1.35
Pilomyxoid astrocytoma	II	1.03	1.06	0.71
Astrocytoma, diffuse	II	1.12	1.27	0.98
Anaplastic ependymoma	III	0.69	0.82	0.59
Anaplastic ependymoma with tanycytic features	III	0.54	0.57	0.47
Choroid plexus carcinoma	III	1.27	0.93	0.90
Atypical teratoid/rhabdoid tumor	IV	0.67	0.53	0.41
Atypical teratoid/rhabdoid tumor	IV	0.40	0.55	0.42
Poorly differentiated carcinoma	IV	0.56	0.45	0.32
Poorly differentiated carcinoma	IV	0.40	0.51	0.35
Glioblastoma	IV	0.58	0.62	0.41
P value, *t* test between low- and high-grade groups		.0018	<.0001	.00042

Note:—All 3 parameters were significant between the difference of the means of the low-grade and high-grade groups. Of note, the choroid plexus carcinoma in our study is an outlier in the high-grade group.

were 9 boys and 10 girls, with a mean age of 4.8 months (range, 1–12 months). Tumor pathologies are listed in Table 1.

T2-weighted images demonstrated a partially cystic mass in 10 cases, whereas the remainder had no significant cystic spaces. Contrast-enhanced T1-weighted images demonstrated 1 nonenhancing tumor (a desmoplastic infantile ganglioglioma), whereas the remainder demonstrated either homogeneous enhancement ($n = 11$) or heterogeneous enhancement ($n = 7$) of the noncystic areas. Tumor size ranged from 1.3–9.4 cm (mean, 5.7 cm). Interestingly, areas of susceptibility artifact on $b = 0$ images and T1 shortening suspected to represent blood products were seen in 6 of the 8 high-grade tumors but in none of the low-grade tumors, though 1 WHO grade I choroid plexus papilloma presented with intraventricular hemorrhage but not intratumoral hemorrhage. Most of the tumors ($n = 15$) had an asymmetric supratentorial location, whereas only 4 tumors were essentially midline tumors (3 astrocytomas, 1 choroid plexus papilloma) (Figs 2 and 3).

Manual Analysis of the Average Minimum ADC Tumor Value Versus Tumor Grade

A significant negative correlation was found between the average minimum ADC value and the WHO grade (Spearman $\rho = -0.639$, $P = .0016$) (Fig 4). There was a significant difference

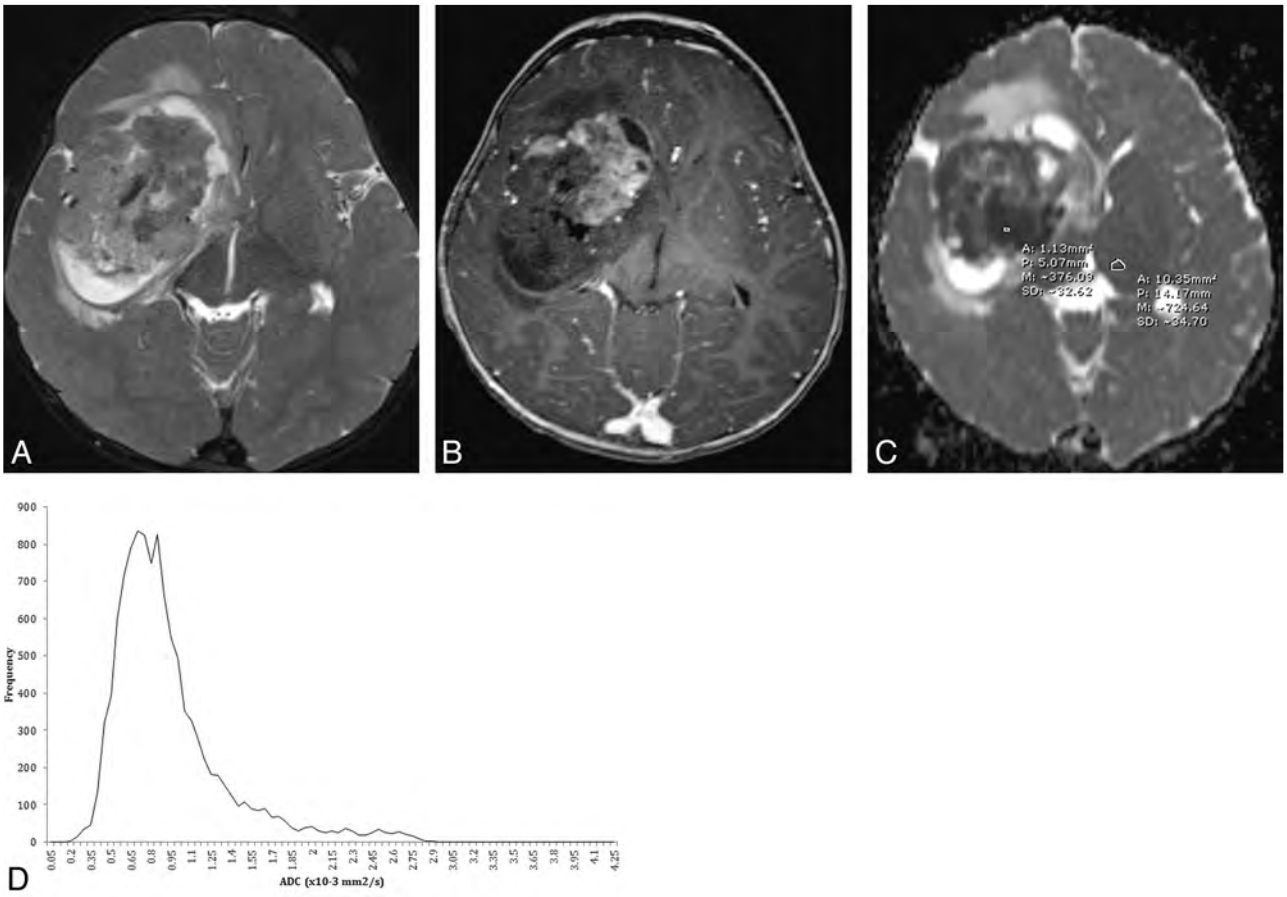

FIG 2. An 11-month-old boy with atypical teratoid/rhabdoid tumor. *A,* Axial T2-weighted image demonstrates a heterogeneous mass in the right frontal temporal lobe with peripheral cystic change, little peritumoral white matter T2 prolongation, and *B,* heterogeneous enhancement on postcontrast axial 3D T1-weighted image. *C,* Representative ADC manual region of interest measurement with a small region of interest within the lowest signal portion of the tumor and larger region of interest measuring the contralateral normal thalamus. *D,* Semi-automated histogram for the ADC values of the entire tumor.

between the average minimum ADC values of the low-grade group (1.14×10^{-3} mm^2/s $\pm$ 0.30) and high-grade group (0.64×10^{-3} mm^2/s $\pm$ 0.28) ($P = .0018$). Receiver operating characteristic analysis for threshold values (Fig 5) resulted in a 0.9 area under the curve, with 0.687–0.991 95% CI and significance of <.0001. At the furthest distance from the 50% diagonal, represented by the Youden index (0.875), the proposed threshold between low-grade versus high-grade tumors in this patient population is $\leq 0.698 \times 10^{-3}$ mm^2/s ADC (87.5% sensitivity: 57.3–99.7, 95% CI, 99.1% specificity: 71.5–100, 95% CI).

Manual Analysis of ADC Ratios Versus Tumor Grade

A significant negative correlation was found between ADC_{tumor}/$ADC_{thalamus}$ ratio and the WHO grade (Spearman $\rho = -0.76$, $P = .0001$). There was a significant difference of the ADC_{tumor}/$ADC_{thalamus}$ mean values in the low-grade group (1.201 $\pm$ 0.26) and high-grade group (0.623 $\pm$ 0.17) ($P = .000034$).

A significant negative correlation was also found between individual ADC_{tumor}/ADC_{wm} ratio and the individual WHO grade (Spearman $\rho = -0.74$, $P = .00025$). There was a significant difference of the ADC_{tumor}/ADC_{wm} mean values between the low-grade group (0.978 $\pm$ 0.28) and high-grade group (0.484 $\pm$ 0.19) ($P = .00042$) (Table 1).

Semi-Automated ADC Analysis

A significant negative correlation was found between the lowest 5th percentile ADC value and the WHO grade (Spearman $\rho = -0.663$, $P = .0002$) as well as between the lowest 10th percentile ADC value and WHO grade (Spearman $\rho = -0.666$, $P = .0009$). There was a significant difference between the lowest 5th percentile ADC values in the low-grade group (1.13×10^{-3} mm^2/s $\pm$ 0.15) and the high-grade group (0.78×10^{-3} mm^2/s $\pm$ 0.27) ($P = .0020$). Similarly, there was a significant difference between the lowest 10th percentile ADC values in the low-grade group (1.18×10^{-3} mm^2/s $\pm$ 0.15) and the high-grade group (0.86×10^{-3} mm^2/s $\pm$ 0.26) ($P = .0028$). The 95th to 50th percentile metric, a measure of spread in the upper half of ADC values, had the highest significance ($P = .004$) between the low (0.82×10^{-3} mm^2/s $\pm$ 0.43) and high-grade (1.43×10^{-3} mm^2/s $\pm$ 0.36) tumors. Histogram representations of ADC values for low- and high-grade tumors are demonstrated in Fig 6. Conversely, no significant negative correlation was found between the average of all the individual tumor ADC histogram values and the WHO grade (Spearman $\rho = -0.349$; $P = .142$) nor a statistical difference of the average ADC histogram values between the low-grade group (1.72×10^{-3} mm^2/s $\pm$ 0.38) and the high-grade group (1.46×10^{-3} mm^2/s $\pm$ 0.34) ($P = .138$). Other metrics such as standard deviation, skew,

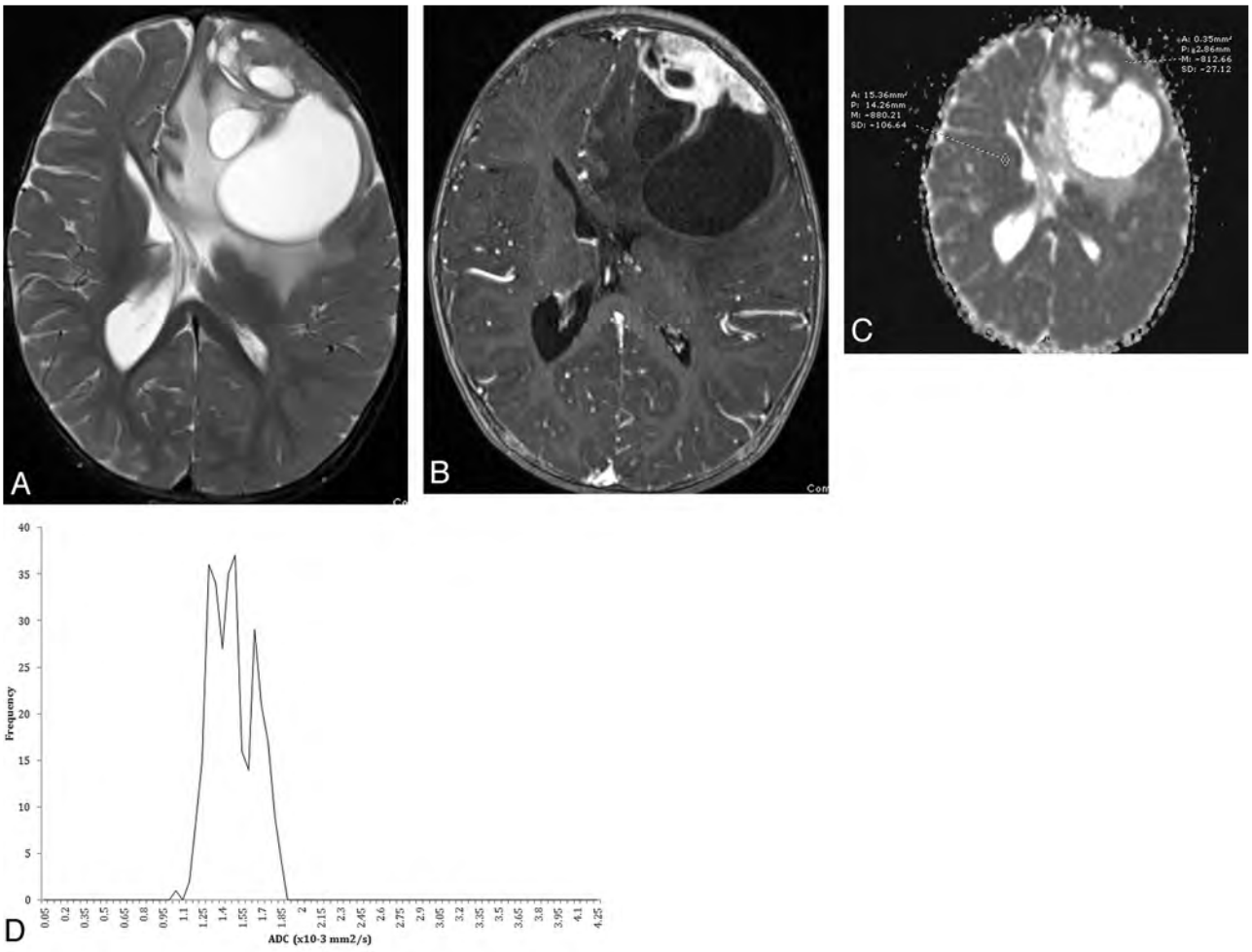

FIG 3. A 12-month-old child with desmoplastic infantile ganglioglioma. *A,* Axial T2-weighted image demonstrates a heterogeneous mass in the left frontal lobe with cystic change, adjacent T2 prolongation, midline shift, and contralateral ventricular entrapment. *B,* Axial 3D T1-weighted image demonstrates a peripheral enhancing solid component along the dural margin. *C,* ADC map with representative manual region of interest evaluation within the solid components of the tumor and contralateral white matter. *D,* Semi-automated histogram for the ADC values of the entire tumor.

kurtosis, and peak height were not significant, whereas peak location and 25th and 50th percentile bins demonstrated mild significance (Table 2).

When comparing the average minimum ADC value obtained from the manual method versus the lowest 5th and 10th percentile ADC values from the semi-automated method, there was a statistically significant correlation between the values (Spearman $\rho = 0.95$; $P < .000001$) and (Spearman $\rho = 0.92$, $P < .000001$), respectively.

DISCUSSION

In our selection of patients, we chose to limit the age of the patients with supratentorial tumors to 1 year of life on the basis of the higher incidence of supratentorial tumors in this age group and to encompass congenital tumors.[1,4] In our patient population, a diagnosis on the basis of location could be highly suspected for some pathologies, such as a clearly intraventricularly located choroid plexus tumor or an optic pathway astrocytoma; however, many of the tumors that we encountered demonstrated a challenging diagnosis with a common imaging appearance of a large, cystic, and solid enhancing mass that is asymmetric to one hemisphere. Additionally, the large size of the mass may result in difficulty determining intraventricular origin. In a series of neonatal brain tumors, Buetow et al[4] described lesions that occupied more than one-third of the intracranial volume in 75% of the cases. Comi et al[5] analyzed neuroradiologic findings in 40 children younger than 3 years of age with intracranial ependymomas: mean tumor diameter at diagnosis was approximately 4.2 cm. Similarly, we encountered a mean tumor diameter of 5.7 cm. When faced with a large, solid, and cystic enhancing supratentorial mass in a pediatric patient in the first year of life, assessment of the tumor ADC characteristics provides additional information in determining tumor grade.

T1- and T2-weighted without and with contrast MR imaging sequences (hereafter termed "conventional MR imaging") have been shown to be insufficient for differentiation and grading of brain tumors in part because peritumoral edema, enhancement, necrosis, or mass effect may be seen with both high-grade or low-grade tumors, and the enhancing portions of tumors may not always reflect the most malignant part of the tumor.[6,7] Tumoral enhancement may be caused by disruption of the blood-brain barrier or from tumoral vascular proliferation. These 2 are independent of each other, and consequently the enhancement pat-

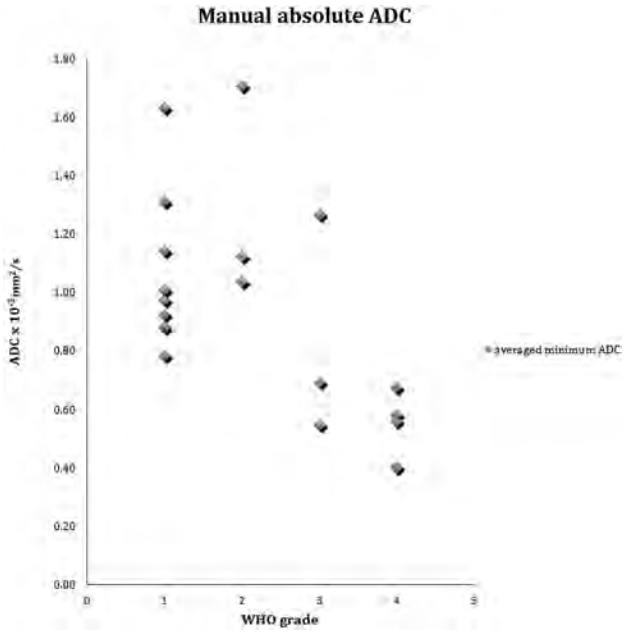

FIG 4. Scatterplot of the average absolute minimum ADC for all tumors by WHO grading.

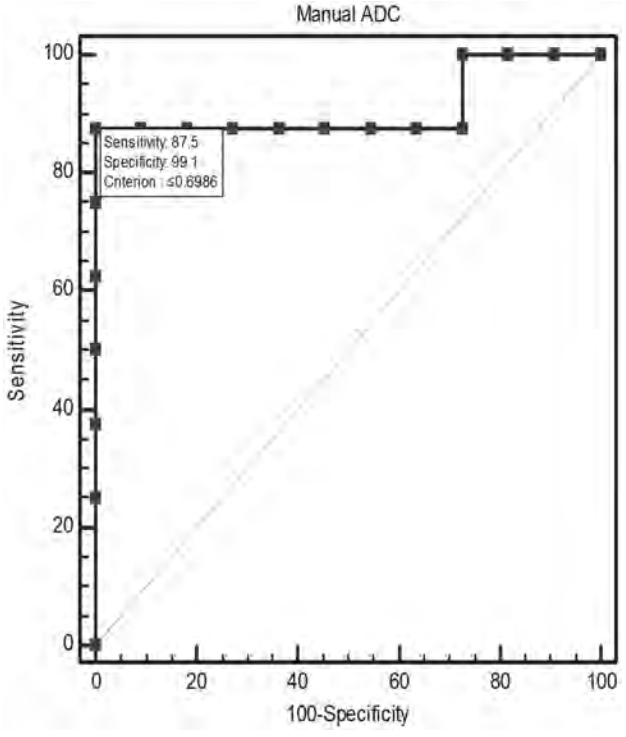

FIG 5. Receiver operating characteristic curve for manual absolute ADC demonstrates a significant area above the 50% diagonal. Threshold according to the Youden index is $\leq 0.698 \times 10^{-3}$ mm^2/s for WHO grade III and IV tumors versus grade I and II tumors.

tern of a tumor is not always reliable for differentiating high- and low-grade tumors.[6,7] Consequently, diffusion and perfusion techniques that improve specificity of tumor diagnosis and grading remain valuable.

Diffusion imaging has been shown to demonstrate particular utility in neuroimaging for a wide range of processes. Diffusion imaging can detect areas of acute ischemia that leads to limitation in molecular movement caused by cytotoxic edema. A similar application of diffusion imaging has been applied for evaluation of brain tumors that may alter the molecular motion of water from structural alterations caused by the destruction of neuronal architecture, tumor cellularity causing reduction of the interstitial space, and vasogenic edema, which may increase the extracellular space. Although studies of adult and pediatric tumors have demonstrated that increasing tumor cellularity often leads to increasing signal intensity on DWI and hypointensity on ADC maps,[8-11] one study evaluating oligodendrogliomas did not demonstrate such a relationship.[12] Multiple factors in addition to cellular density probably contribute to differences in ADC values; nonetheless, these differences in ADC values can provide information to differentiate pediatric tumors.

Diffusion imaging with ADC maps has demonstrated utility in pediatric patients with cerebellar tumors.[3] In the analysis by Rumboldt et al,[3] ADC maps could reliably differentiate the common pediatric cerebellar tumors of ependymoma, medulloblastoma, and pilocytic astrocytoma. However, subsequent studies demonstrate overlap of ADC values of these posterior fossa tumors, particularly ependymomas, indicating that diffusion imaging is a valuable but imperfect tool for cerebellar tumor differentiation.[13,14] The pathology of the supratentorial tumors commonly encountered in the first year of life includes a wide spectrum of low- and high-grade tumor types unlike cerebellar tumors. Furthermore, there is potential for tumors for which it may be difficult to determine a specific pathologic diagnosis, as was the case in 2 of our WHO grade IV tumors. Whereas high-grade diagnoses such as primitive neuroectodermal tumor, atypical teratoid/rhabdoid tumor, and choroid plexus carcinoma were considered, the final pathologic diagnosis was "poorly differentiated carcinoma, WHO grade IV." The combination of a wide range of pathologies and potential difficulty in determining a specific pathologic diagnosis illustrates the potential difficulty with specific tumor diagnosis. Pediatric cerebellar tumors may have additional supportive conventional MR imaging appearance such as the classically described cyst and solid enhancing nodule pattern of a pilocytic astrocytoma or extension through the foramen Luschka of an ependymoma. Although desmoplastic infantile gangliogliomas have been typically described with a peripheral, dural-based enhancing nodule and cyst generally, supratentorial tumors in the first year of life can present with large, heterogeneous, enhancing masses that have very similar imaging findings, whether low- or high-grade.

Recognizing these potential obstacles, our goal was to determine if ADC values demonstrate utility for differentiating low-grade and high-grade supratentorial tumors in pediatric patients presenting in the first year of life. To our knowledge, this is the first study assessing ADC values of supratentorial brain tumors in pediatric patients presenting in the first year of life. In this study, we were able to demonstrate that careful analysis of the ADC maps of supratentorial brain tumors in children younger than 1 year of age results in statistically significant differentiation of high- and low-grade tumors. We chose to use the lowest ADC value in the manual region of interest placement because of the importance of tumor differentiation, which primarily involves identifying areas of highest cellularity that result in lower ADC

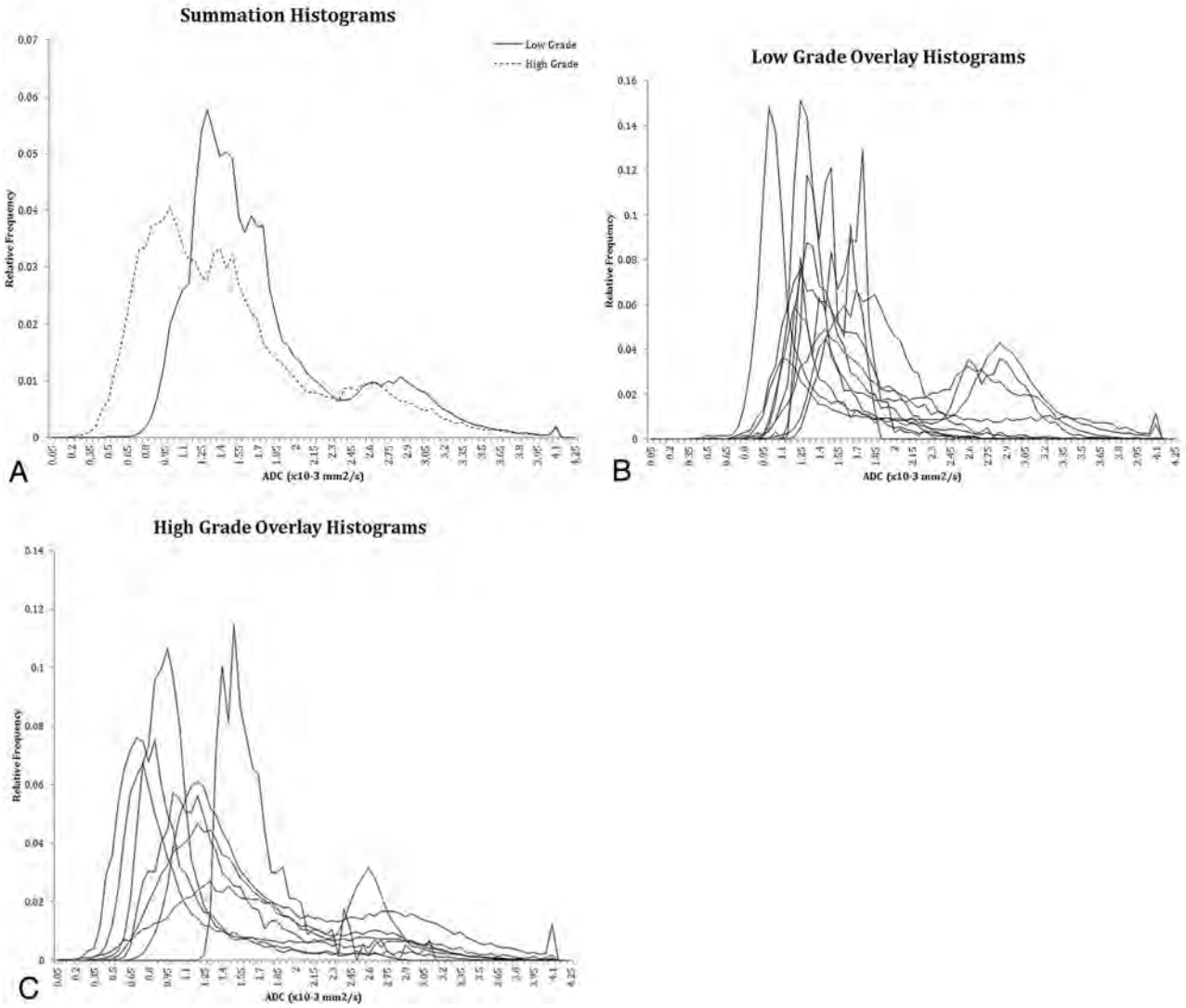

FIG 6. *A,* Summation semi-automated histograms of ADC values of all low-grade tumors compared with high-grade tumors. *B,* Overlay histograms of all low-grade tumors. *C,* Overlay histograms of all high-grade tumors.

values. We developed a semi-automated method that uses a computer algorithm to collect ADC values within a defined tumor region as a potentially more unbiased method and a method to validate the manual region of interest placement. The semi-automated method demonstrates statistically significant differences in individual tumor grades for the lowest 5th and 10th percentile ADC values obtained from each individual tumor versus a lack of a statistically significant difference between the average tumor ADC value and the tumor grade. This, in addition to the lack of significance in other parameters such as standard deviation, skew, and kurtosis, mathematically corroborates the heterogeneous nature of these tumors and the wide range of ADC values possible. Although choosing to include cystic areas does skew the average ADC value higher, including the whole of the tumor decreases selection bias while still incorporating the lowest ADC values as a metric. Furthermore, some tumors with heterogeneous cysts may be difficult to easily partition from the solid portions of the tumor. This inclusion of cystic structures probably led to significance in the 95th to 50th percentile metric, indicating that low-grade tumors tend to be more homogeneous, with less spread in the upper ranges of ADC values, whereas high-grade tumors are more heterogeneous in this ADC range. Finally, the manual method of identifying the lowest ADC value in the tumor was validated as a method when compared with the semi-automated lowest 5th and 10th percentile ADC values. This indicates that the more simple manual approach, applicable to all radiologists with reading stations allowing region of interest measurements, is not only sufficient but demonstrates more significance because of lower *P* values of the manual metrics compared with the semi-automated metrics for grading analysis of these tumors.

We analyzed both the average minimum ADC value as well as a ratio of the average minimum tumor ADC value to the ADC value of the contralateral normal thalamus and to the contralateral normal centrum semiovale. Because the ADC values of normally developing brain decrease with increasing age, especially in the white matter with normal myelin maturation, use of the average minimum ADC value may be preferred over ADC ratios despite the statistical significance obtained for the ADC ratios in this study.[15-17] However, ADC ratios were performed because our data were acquired from different MR units, and a potential in-

Table 2: Semi-automated metrics including mean and standard deviations for low- and high-grade tumors

	Low-Grade		High-Grade		
	Mean ($\times 10^{-3}$ mm^2/s)	Standard Deviation ($\times 10^{-3}$ mm^2/s)	Mean ($\times 10^{-3}$ mm^2/s)	Standard Deviation ($\times 10^{-3}$ mm^2/s)	*P* Value (*t* test)
Average	1.717	0.377	1.459	0.341	.138
Standard deviation	0.458	0.247	0.616	0.189	.135
Skew	0.803	0.753	1.372	0.704	.111
Kurtosis	1.129	2.515	1.980	2.754	.501
Peak location	1.518	0.493	1.075	0.275	.023[a]
Peak height, normalized	0.088	0.041	0.069	0.029	.258
5th Percentile	1.13	0.151	0.778	0.267	.007[a]
10th Percentile	1.18	0.151	0.858	0.260	.008[a]
25th Percentile	1.32	0.180	1.016	0.278	.018[a]
50th Percentile	1.68	0.453	1.270	0.349	.037[a]
75th Percentile	2.01	0.598	1.792	0.564	.411
90th Percentile	2.32	0.681	2.363	0.591	.903
95th Percentile	2.50	0.705	2.696	0.541	.518
95th to 5th Percentile	1.377	0.704	1.918	0.560	.080
50th to 5th Percentile	0.555	0.425	0.491	0.273	.695
95th to 50th Percentile	0.821	0.434	1.426	0.362	.004[a]

[a] Significant *P* value.

tervendor variance in absolute ADC values has been previously reported.[18]

Limitations of this study include the potential for selection bias of the ADC region of interest placement by observation of the other conventional MR images and the total number of patients. We chose not to blind the placement of the region of interest to the remainder of the anatomic sequences to prevent placing a region of interest on suspected blood products as well as to simulate region of interest placement that may occur in clinical practice. The semi-automated method validates the manual placement of the ADC, though this also has the potential for selection bias on the basis of the decision of placement of the borders of the tumor. Our study is the largest, to our knowledge, within the current literature to assess diffusion imaging for intracranial tumors within the first year of life. However, because these tumors are rare, the number of total patients in this study limits our ability to determine whether a specific pathology could be determined with ADC values within the low- or high-grade groups, as well as separating low- and high-grade tumors of similar pathology. An example of this is the 4 choroid plexus tumors in our study. The average ADC value of the 1 choroid plexus carcinoma was within the range of the 3 choroid plexus papillomas in our study group. Although this may be an outlier, only a single small study within the literature that used MR spectroscopy suggested a potential differentiation method of elevated myo-inositol levels in choroid plexus papillomas versus carcinomas.[19] In the differentiation of specific tumor pathology within the high-grade or low-grade groups, we suspect that even with a larger number of patients, differentiation of tumor pathology may not be possible with ADC values, similar to the inability of diffusion imaging to differentiate medulloblastoma from atypical teratoid/rhabdoid tumor (both WHO grade IV tumors).[20] Similarly, WHO grading may not always predict biologic behavior and ultimately outcome[21,22]; however, this does not detract from the utility of ADC values in the characterization and diagnosis of these supratentorial tumors and provides a foundation for the radiologist to establish a differential diagnosis.

CONCLUSIONS

Diffusion imaging with ADC maps provides valuable diagnostic information when brain tumors are evaluated. Manually obtaining the minimum ADC value within the tumor with region of interest measurements can be simple and reliable. Despite the considerable heterogeneity of supratentorial tumors presenting in the first year of life, there is a trend between decreasing tumoral ADC value with higher WHO grade, and the lowest tumoral ADC values can reliably differentiate low- and high-grade tumors, leading to improved diagnosis and facilitating preoperative planning.

REFERENCES

1. Sala F, Colarusso E, Mazza C, et al. **Brain tumors in children under 3 years of age: recent experience (1987–1997) in 39 patients.** *Pediatr Neurosurg* 1999;31:16–26
2. Sugahara T, Korogi Y, Kochi M, et al. **Usefulness of diffusion-weighted MRI with echo-planar technique in the evaluation of cellularity of gliomas.** *J Magn Reson Imaging* 1999;9:53–60
3. Rumboldt Z, Camacho DL, Lake D, et al. **Apparent diffusion coefficients for differentiation of cerebellar tumors in children.** *AJNR Am J Neuroradiol* 2006;27:1362–69
4. Buetow PC, Smirniotopoulos JG, Done S. **Congenital brain tumors: a review of 45 cases.** *AJR Am J Roentgenol* 1990;155:587–93
5. Comi AM, Backstrom JW, Burger PC, et al. **Clinical and neuroradiologic findings in infants with intracranial ependymomas.** *Pediatr Neurol* 1998;18:23–29
6. Knopp EA, Cha S, Johnson G, et al. **Glial neoplasms: dynamic contrast enhanced T2* weighted MR imaging.** *Radiology* 1999;211:791–98
7. Law M, Yang S, Wang H, **Glioma grading: sensitivity, specificity, and predictive values of perfusion MR imaging and proton MR spectroscopic imaging compared with conventional MR imaging.** *AJNR Am J Neuroradiol* 2003;24:1989–98
8. Gauvain KM, McKinstry RC, Mukherjee P, et al. **Evaluating pediatric brain tumor cellularity with diffusion-tensor imaging.** *AJR Am J Roentgenol* 2001;177:449–54
9. Gupta RK, Cloughesy TF, Sinha U, et al. **Relationships between choline magnetic resonance spectroscopy, apparent diffusion coefficient and quantitative histopathology in human glioma.** *J Neurooncol* 2000;50:215–26
10. Guo AC, Cummings TJ, Dash RC, et al. **Lymphomas and high-grade**

astrocytomas: comparison of water diffusibility and histologic characteristics. *Radiology* 2002;224:177–83
11. Yamashita Y, Kumabe T, Higano S, et al. **Minimum apparent diffusion coefficient is significantly correlated with cellularity in medulloblastoma.** *Neurol Res* 2009;31:940–46
12. Jenkinson MD, du Plessis DG, Smith TS, et al. **Cellularity and apparent diffusion coefficient in oligodendroglial tumours characterized by genotype.** *J Neurooncol* 2010;96:385–92
13. Gimi B, Cederberg K, Derinkuyu B, et al. **Utility of apparent diffusion coefficient ratios in distinguishing common pediatric cerebellar tumors.** *Acad Radiol* 2012;19:794–800
14. Jaremko JL, Jans LB, Coleman LT, et al. **Value and limitations of diffusion-weighted imaging in grading and diagnosis of pediatric posterior fossa tumors.** *AJNR Am J Neuroradiol.* 2010;31:1613–16
15. Morriss MC, Zimmerman RA, Bilaniuk LT, et al. **Changes in brain water diffusion during childhood.** *Neuroradiology* 1999;41:929–34
16. Sener RN. **Diffusion MRI apparent diffusion coefficient (ADC) values in the normal brain and a classification of brain disorders based on ADC values.** *Comput Med Imaging Graph* 2001;25:299–326
17. Lovblad KO, Schneider J, Ruoss K, et al. **Isotropic apparent diffusion coefficient mapping of postnatal cerebral development.** *Neuroradiology* 2003;45:400–03
18. Sasaki M, Yamada K, Watanabe Y, et al. **Variability in absolute apparent diffusion coefficient values across different platforms may be substantial: a multivendor, multi-institutional comparison study.** *Radiology* 2008;249:624–30
19. Krieger MD, Panigrahy A, McComb JG, et al. **Differentiation of choroid plexus tumors by advanced magnetic resonance spectroscopy.** *Neurosurg Focus* 2005;18:E4
20. Koral K, Gargan L, Bowers DC, et al. **Imaging characteristics of atypical teratoid-rhabdoid tumor in children compared to medulloblastoma.** *AJR Am J Roentgenol* 2008;190:809–14.
21. Gravendeel LA, Kouwenhoven MC, Gevaert O, et al. **Intrinsic gene expression profiles of gliomas are a better predictor of survival than histology.** *Cancer Res* 2009;69:9065–72
22. Zamecnik J, Snuderl M, Eckschlager T, et al. **Pediatric intracranial ependymomas: prognostic relevance of histological, immunohistochemical, and flow cytometric factors.** *Mod Pathol* 2003;16:980–91

ASNR 52ND ANNUAL MEETING & THE FOUNDATION OF THE ASNR SYMPOSIUM 2014

MAY 17-22 | **Montreal** ■ Palais des congrés de Montreal

ASNR 2014 PROGRAM CHAIR/PRESIDENT-ELECT - Gordon K. Sze, MD, FACR

THE FOUNDATION OF THE ASNR

The Foundation of the ASNR Symposium 2014: Inflammatory and Infectious Diseases of the Brain

SYMPOSIUM 2014:

- The Role of Inflammation and Infections in Stroke, Seizures, White Matter Diseases, etc.
- Advanced Imaging Techniques in the Evaluation of Inflammatory CNS Diseases
- Infectious Agents for Human Good: Oncolytic Viruses, Viral Vector Gene Therapy and Advanced Imaging

ADDITIONAL NEW EDUCATIONAL COURSE PROGRAM IN 2014 (concurrent program with the Symposium 2014): Featuring Head & Neck, Spine, and Brain Inflammatory and Infectious Diseases

EDUCATIONAL COURSE 2014: with world class speakers including

- Yoshimi Anzai, MD, MPH, Sally Candy, BSc, HED, MBCHB, FCRad, (Diag SA), Hugh D. Curtin, MD, FACR, Lawrence E. Ginsberg, MD, Patricia A. Hudgins, MD, FACR, Luiz Celso Hygino Da Cruz Jr., MD, Michele H. Johnson, MD, Kelly K. Koeller, MD, FACR, Laurie A. Loevner, MD, Michelle A. Michel, MD, Kristine M. Mosier, DMD, PhD, Thomas P. Naidich, MD, FACR, Anne G. Osborn, MD, M. Judith Donovan Post, MD, FACR, Donald R. Resnick, MD, Caroline D. Robson, MD, ChB, Jeffrey S. Ross, MD, James G. Smirniotopoulos, MD, Peter M. Som, MD, FACR, FRSM, E. Turgut Tali, MD, Patrick A. Turski, MD, FACR, Johan W. van Goethem, MD, Richard H. Wiggins, III, MD, David M. Yousem, MD, MBA and Robert D. Zimmerman, MD, FACR

JUST ADDED... ASNR Introduces Study Groups and Workshops, please visit the ASNR website for more information

- The study groups target areas of critical importance to the field of neuroradiology and are composed of neuroradiologists, neuroscientists, and investigators from associated disciplines, who are united in their interest in higher level, sophisticated investigations of these target areas.
- The workshops are intended to provide a hands-on experience that allows participants to translate knowledge learned at the ASNR meeting into direct experience that will enable them to perform these studies when they return to their practices.

ANNUAL MEETING:

- One-day **MINI SYMPOSIUM** on **TUMORS** - Organized by Girish M. Fatterpekar, MD, MBBS, DNB, Whitney B. Pope, MD, PhD and Gordon K. Sze, MD, FACR
- One-day **MINI SYMPOSIUM** on **STROKE** - Organized by Pina C. Sanelli, MD, MPH and Max Wintermark, MD
- **Nobel Prize Laureate, Stanley Prusiner, MD, Keynote Speaker, on Prions and Alzheimer's Disease, Parkinson's Disease, and Other Neurodegenerative Disorders**
- **More "Hands-On" Experience Applicable to Your Practices**
- **Young Professionals Programming**
- **Expanded Self-Assessment Module (SAM) Session Programming Throughout the Week**

PROGRAMMING DEVELOPED IN COOPERATION WITH THE...

- American Society of Functional Neuroradiology (ASFNR) David J. Mikulis, MD
- American Society of Head and Neck Radiology (ASHNR) Yoshimi Anzai, MD, MPH
- American Society of Pediatric Neuroradiology (ASPNR) Richard L. Robertson, MD
- American Society of Spine Radiology (ASSR) Meng Law, MD, MBBS, FRACR
- Society of NeuroInterventional Surgery (SNIS) Peter A. Rasmussen, MD

ASNR MONTREAL 2014

ASFNR ASHNR ASPNR ASSR SNIS

TO REQUEST PROGRAMMING AND REGISTRATION MATERIALS FOR THE ASNR 52ND ANNUAL MEETING, CONTACT:

ASNR 52ND ANNUAL MEETING
c/o American Society of Neuroradiology
800 Enterprise Drive, Suite 205
Oak Brook, Illinois 60523-4216

Phone: 630-574-0220
Fax: 630-574-0661
Email: meetings@asnr.org
Website: www.asnr.org/2014

Scan Now
to visit our website

DOTAREM® (gadoterate meglumine) injection, for intravenous use
Initial U.S. Approval: 2013

BRIEF SUMMARY OF PRESCRIBING INFORMATION
CONSULT PACKAGE INSERT FOR FULL PRESCRIBING INFORMATION

WARNING: NEPHROGENIC SYSTEMIC FIBROSIS (NSF)

Gadolinium-based contrast agents (GBCAs) increase the risk for NSF among patients with impaired elimination of the drugs. Avoid use of GBCAs in these patients unless the diagnostic information is essential and not available with non-contrasted MRI or other modalities. NSF may result in fatal or debilitating fibrosis affecting the skin, muscle and internal organs.

- **The risk for NSF appears highest among patients with:**
  - **Chronic, severe kidney disease (GFR < 30 mL/min/1.73m^2), or**
  - **Acute kidney injury.**
- **Screen patients for acute kidney injury and other conditions that may reduce renal function. For patients at risk for chronically reduced renal function (e.g. age > 60 years, hypertension, diabetes), estimate the glomerular filtration rate (GFR) through laboratory testing (5.1).**
- **For patients at highest risk for NSF, do not exceed the recommended DOTAREM dose and allow a sufficient period of time for elimination of the drug from the body prior to any re-administration *[see Warnings and Precautions (5.1)]*.**

1 INDICATIONS AND USAGE

DOTAREM is a gadolinium-based contrast agent indicated for intravenous use with magnetic resonance imaging (MRI) in brain (intracranial), spine and associated tissues in adult and pediatric patients (2 years of age and older) to detect and visualize areas with disruption of the blood brain barrier (BBB) and/or abnormal vascularity. (1)

4 CONTRAINDICATIONS

History of clinically important hypersensitivity reactions to DOTAREM. (4)

5 WARNINGS AND PRECAUTIONS

5.1 Nephrogenic Systemic Fibrosis

Gadolinium-based contrast agents (GBCAs) increase the risk for nephrogenic systemic fibrosis (NSF) among patients with impaired elimination of the drugs. Avoid use of GBCAs among these patients unless the diagnostic information is essential and not available with non-contrast MRI or other modalities. The GBCA-associated NSF risk appears highest for patients with chronic, severe kidney disease (GFR < 30 mL/min/1.73m^2) as well as patients with acute kidney injury. The risk appears lower for patients with chronic, moderate kidney disease (GFR 30 - 59 mL/min/1.73m^2) and little, if any, for patients with chronic, mild kidney disease (GFR 60 - 89 mL/min/1.73m^2). NSF may result in fatal or debilitating fibrosis affecting the skin, muscle and internal organs. Report any diagnosis of NSF following DOTAREM administration to Guerbet LLC (1-877-729-6679) or FDA (1-800-FDA-1088 or www.fda.gov/medwatch).

Screen patients for acute kidney injury and other conditions that may reduce renal function. Features of acute kidney injury consist of rapid (over hours to days) and usually reversible decrease in kidney function, commonly in the setting of surgery, severe infection, injury or drug-induced kidney toxicity. Serum creatinine levels and estimated GFR may not reliably assess renal function in the setting of acute kidney injury. For patients at risk for chronically reduced renal function (e.g., age > 60 years, diabetes mellitus or chronic hypertension), estimate the GFR through laboratory testing.

Among the factors that may increase the risk for NSF are repeated or higher than recommended doses of a GBCA and the degree of renal impairment at the time of exposure. Record the specific GBCA and the dose administered to a patient. For patients at highest risk for NSF, do not exceed the recommended DOTAREM dose and allow a sufficient period of time for elimination of the drug prior to re-administration. For patients receiving hemodialysis, physicians may consider the prompt initiation of hemodialysis following the administration of a GBCA in order to enhance the contrast agent's elimination. The usefulness of hemodialysis in the prevention of NSF is unknown *[see Dosage and Administration (2) and Clinical Pharmacology (12)]*.

5.2 Hypersensitivity Reactions

Anaphylactic and anaphylactoid reactions have been reported with DOTAREM, involving cardiovascular, respiratory, and/or cutaneous manifestations. Some patients experienced circulatory collapse and died. In most cases, initial symptoms occurred within minutes of DOTAREM administration and resolved with prompt emergency treatment *[see Adverse Reactions (6)]*.

- Before DOTAREM administration, assess all patients for any history of a reaction to contrast media, bronchial asthma and/or allergic disorders. These patients may have an increased risk for a hypersensitivity reaction to DOTAREM.
- Administer DOTAREM only in situations where trained personnel and therapies are promptly available for the treatment of hypersensitivity reactions, including personnel trained in resuscitation.
- During and following DOTAREM administration, observe patients for signs and symptoms of hypersensitivity reactions.

5.3 Acute Kidney Injury

In patients with chronically reduced renal function, acute kidney injury requiring dialysis has occurred with the use of GBCAs. The risk of acute kidney injury may increase with increasing dose of the contrast agent; administer the lowest dose necessary for adequate imaging. Screen all patients for renal impairment by obtaining a history and/or laboratory tests. Consider follow-up renal function assessments for patients with a history of renal dysfunction.

5.4 Extravasation and Injection Site Reactions

Ensure catheter and venous patency before the injection of DOTAREM. Extravasation into tissues during DOTAREM administration may result in tissue irritation *[see Nonclinical Toxicology (13.2)]*.

6 ADVERSE REACTIONS

GBCAs have been associated with a risk for NSF *[see Warnings and Precautions (5.1)]*. NSF has not been reported in patients with a clear history of exposure to DOTAREM alone. For hypersensitivity reactions and acute kidney injury see Warnings and Precautions *(5.2) and (5.3)*.

6.1 Clinical Studies Experience

Because clinical trials are conducted under widely varying conditions, adverse reaction rates observed in the clinical trials of a drug cannot be directly compared to rates in the clinical trials of another drug and may not reflect the rates observed in clinical practice.

The data described below reflect DOTAREM exposure in 2813 patients, representing 2672 adults and 141 pediatric patients. Overall, 55% of the patients were men. In clinical trials where ethnicity was recorded the ethnic distribution was 74% Caucasian, 12% Asian, 4% Black, and 10% others. The average age was 53 years (range from 0.1 to 97 years).

Overall, 3.9% of patients reported at least one adverse reaction, primarily occurring immediately or several days following DOTAREM administration. Most adverse reactions were mild or moderate in severity and transient in nature.

Table 1 lists adverse reactions that occurred in ≥ 0.2% patients who received DOTAREM.

Table 1: Adverse Reactions in Clinical Trials

Reaction	Rate (%) n = 2813
Nausea	0.6%
Headache	0.5%
Injection Site Pain	0.4%
Injection Site Coldness	0.2%
Burning Sensation	0.2%

Adverse reactions that occurred with a frequency < 0.2% in patients who received DOTAREM include: feeling cold, rash, somnolence, fatigue, dizziness, vomiting, pruritus, paresthesia, dysgeusia, pain in extremity, anxiety, hypertension, palpitations, oropharyngeal discomfort, serum creatinine increased and injection site reactions, including site inflammation, extravasation, pruritus, and warmth.

Adverse Reactions in Pediatric Patients

During clinical trials, 141 pediatric patients (7 aged < 24 months, 33 aged 2 - 5 years, 58 aged 6 - 11 years and 43 aged 12 -17) received DOTAREM. Overall, 6 pediatric patients (4.3%) reported at least one adverse reaction following DOTAREM administration. The most frequently reported adverse reaction was headache (1.5%). Most adverse events were mild in severity and transient in nature, and all patients recovered without treatment.

6.2 Postmarketing Experience

The following additional adverse reactions have been identified during postmarketing use of DOTAREM. Because these reactions are reported voluntarily from a population of uncertain size, it is not always possible to reliably estimate their frequency or establish a causal relationship to drug exposure.

- bradycardia, tachycardia, arrhythmia
- hypersensitivity / anaphylactoid reactions including cardiac arrest, respiratory arrest, cyanosis, pharyngeal edema, laryngospasm, bronchospasm, angioedema, conjunctivitis, ocular hyperemia, eyelid edema, lacrimation increased, hyperhidrosis, urticaria
- coma, convulsion, syncope, presyncope, parosmia, tremor
- muscle contracture, muscle weakness
- diarrhea, salivary hypersecretion
- malaise, fever
- NSF, in patients whose reports were confounded by the receipt of other GBCAs or in situations where receipt of other GBCAs could not be ruled out. No unconfounded cases of NSF have been reported with DOTAREM.
- superficial phlebitis

7 DRUG INTERACTIONS

DOTAREM does not interfere with serum and plasma calcium measurements determined by colorimetric assays. Specific drug interaction studies with DOTAREM have not been conducted.

8 USE IN SPECIFIC POPULATIONS

8.1 Pregnancy

Pregnancy Category C

There are no adequate and well-controlled studies with DOTAREM conducted in pregnant women. Limited published human data on exposure to other GBCAs during pregnancy did not show adverse effects in exposed neonates. No effects on embryo fetal development were observed in rats or rabbits at doses up to 10 mmol/kg/day in rats or 3 mmol/kg/day in rabbits. The doses in rats and rabbits were respectively 16 and 10 times the recommended human dose based on body surface area. DOTAREM should be used during pregnancy only if the potential benefit justifies the potential risk to the fetus.

While it is unknown if DOTAREM crosses the human placenta, other GBCAs do cross the placenta in humans and result in fetal exposure.

Reproductive and developmental toxicity studies were conducted with gadoterate meglumine in rats and rabbits. Gadoterate meglumine was administered intravenously in doses of 0, 2, 4 and 10 mmol/kg/day (or 3.2, 6.5 and 16.2 times the recommended human dose based on body surface area) to female rats for 14 days before mating throughout the mating period and until gestation day (GD) 17. Pregnant rabbits were intravenously administered gadoterate meglumine at the dose levels of 0, 1, 3 and 7 mmol/kg/day (or 3.3, 10 and 23 times the human doses based on body surface area) from GD6 to GD19. No effects on embryo fetal development were observed in rats or rabbits at doses up to 10 mmol/kg/day in rats or 3 mmol/kg/day in rabbits. Maternal toxicity was observed in rats at 10 mmol/kg/day (or 16 times the human dose based on body surface area) and in rabbits at 7 mmol/kg/day (23 times the human dose based on body surface area).

8.3 Nursing Mothers

It is not known whether DOTAREM is excreted in human milk. Limited case reports on use of GBCAs in nursing mothers indicate that 0.01 to 0.04% of the maternal gadolinium dose is excreted in human breast milk. Because many drugs are excreted in human milk, exercise caution when DOTAREM is administered to a nursing woman. Nonclinical data show that gadoterate meglumine is excreted into breast milk in very small amounts (< 0.1% of the dose intravenously administered) and absorption via the gastrointestinal tract is poor.

8.4 Pediatric Use

The safety and efficacy of DOTAREM at a single dose of 0.1 mmol/kg have been established in pediatric patients from 2 to 17 years of age. No dosage adjustment according to age is necessary in this population *[See Dosage and Administration (2.1) and Clinical Studies (14)]*. The safety and efficacy of DOTAREM have not been established in pediatric patients below 2 years of age. GFR does not reach adult levels until 1 year of age *[see Warnings and Precautions (5.1)]*.

8.5 Geriatric Use

In clinical studies of DOTAREM, 900 patients were 65 years of age and over, and 312 patients were 75 years of age and over. No overall differences in safety or efficacy were observed between these subjects and younger subjects. In general, use of DOTAREM in elderly patients should be cautious, reflecting the greater frequency of impaired renal function and concomitant disease or other drug therapy. No age-related dosage adjustment is necessary.

8.6 Renal Impairment

No DOTAREM dosage adjustment is recommended for patients with renal impairment. Gadoterate meglumine can be removed from the body by hemodialysis *[see Warnings and Precautions (5.1) and Clinical Pharmacology (12.3)]*.

10 OVERDOSAGE

DOTAREM administered to healthy volunteers and to patients at cumulative doses up to 0.3 mmol/kg was tolerated in a manner similar to lower doses. Adverse reactions to overdosage with DOTAREM have not been reported. Gadoterate meglumine can be removed from the body by hemodialysis *[See Clinical Pharmacology (12.3)]*.

13 NONCLINICAL TOXICOLOGY

13.1 Carcinogenesis, Mutagenesis, Impairment of Fertility

Long-term animal studies have not been performed to evaluate the carcinogenic potential of gadoterate meglumine.

Gadoterate meglumine did not demonstrate mutagenic potential in *in vitro* bacterial reverse mutation assays (Ames test) using Salmonella typhimurium, in an *in vitro* chromosome aberration assay in Chinese hamster ovary cells, in an *in vitro* gene mutation assay in Chinese hamster lung cells, nor in an *in vivo* mouse micronucleus assay.

No impairment of male or female fertility and reproductive performance was observed in rats after intravenous administration of gadoterate meglumine at the maximum tested dose of 10 mmol/kg/day (16 times the maximum human dose based on surface area), given during more than 9 weeks in males and more than 4 weeks in females. Sperm counts and sperm motility were not adversely affected by treatment with the drug.

13.2 Animal Toxicology and/or Pharmacology

Local intolerance reactions, including moderate irritation associated with infiltration of inflammatory cells were observed after perivenous injection in rabbits suggesting the possibility of local irritation if the contrast medium leaks around the veins in a clinical setting *[see Warnings and Precautions (5.4)]*.

17 PATIENT COUNSELING INFORMATION

17.1 Nephrogenic Systemic Fibrosis

Instruct patients to inform their healthcare provider if they:

- have a history of kidney disease, or
- have recently received a GBCA.

GBCAs increase the risk for NSF among patients with impaired elimination of the drugs. To counsel patients at risk for NSF:

- Describe the clinical manifestations of NSF.
- Describe procedures to screen for the detection of renal impairment.

Instruct the patients to contact their physician if they develop signs or symptoms of NSF following DOTAREM administration, such as burning, itching, swelling, scaling, hardening and tightening of the skin; red or dark patches on the skin; stiffness in joints with trouble moving, bending or straightening the arms, hands, legs or feet; pain in the hip bones or ribs; or muscle weakness.

17.2 Common Adverse Reactions

Inform patients that they may experience:

- Reactions along the venous injection site, such as mild and transient burning or pain or feeling of warmth or coldness at the injection site.
- Side effects of headache, nausea, abnormal taste and feeling hot.

17.3 General Precautions

Instruct patients receiving DOTAREM to inform their physician if they:

- Are pregnant or breastfeeding.
- Have a history of allergic reaction to contrast media, bronchial asthma or allergy.
- Are taking any medications.

Rx Only

Guerbet LLC
120 W 7th Street. Suite 108
Bloomington, IN 47404

Pre-filled syringes manufactured by Catalent, Belgium for Guerbet
Vials manufactured by Recipharm, France for Guerbet

GU06131043
Revised 06/2013

DOTAREM®
(gadoterate meglumine) Injection

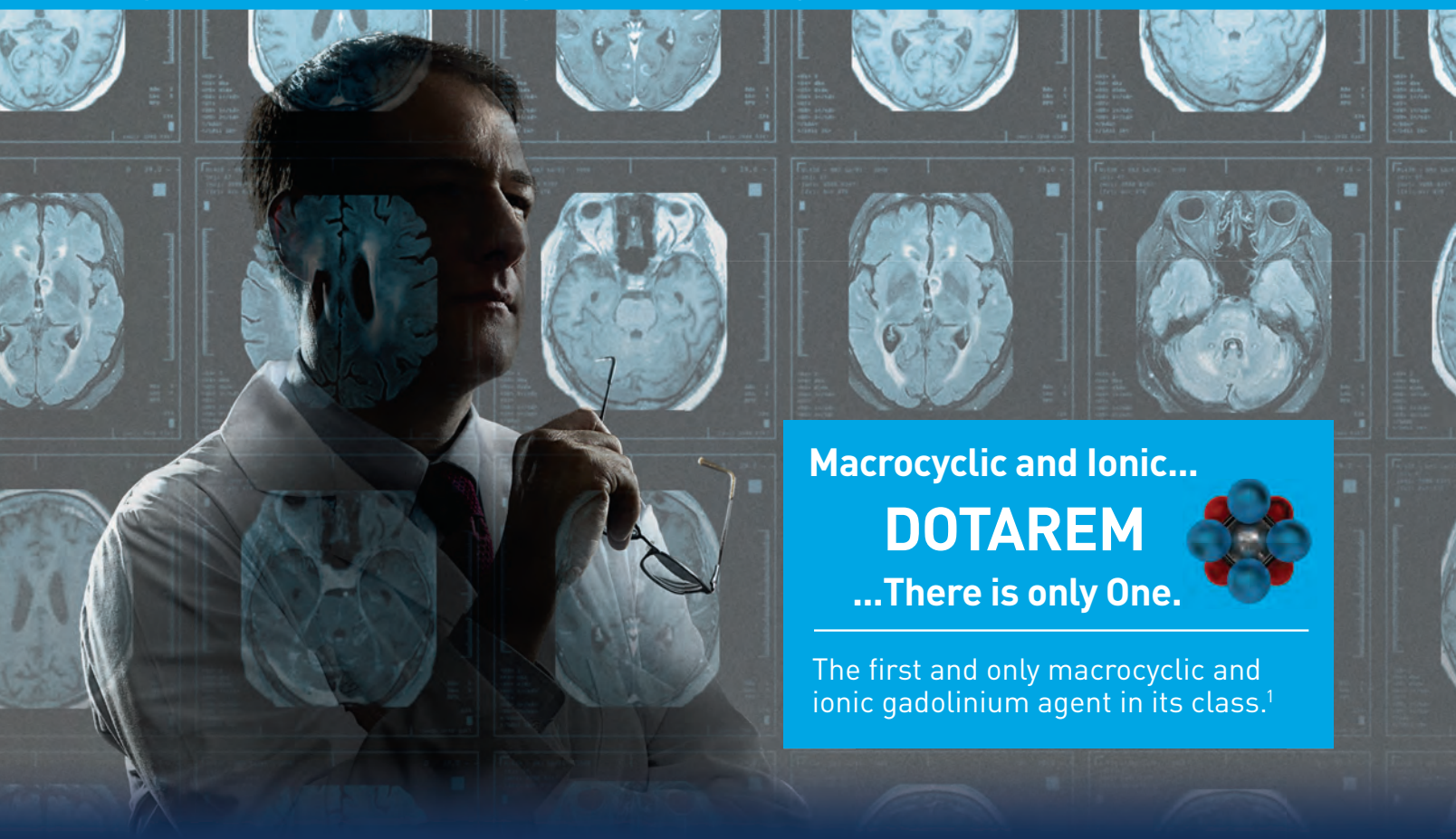

Macrocyclic and Ionic...

DOTAREM

...There is only One.

The first and only macrocyclic and ionic gadolinium agent in its class.[1]

Global clinical experience with over **43 million doses** administered outside the US.[2]

INDICATION[1]

DOTAREM is a gadolinium-based contrast agent indicated for intravenous use with magnetic resonance imaging (MRI) in brain (intracranial), spine and associated tissues in adult and pediatric patients (2 years of age and older) to detect and visualize areas with disruption of the blood brain barrier (BBB) and/or abnormal vascularity.

IMPORTANT SAFETY INFORMATION[1]

WARNING: NEPHROGENIC SYSTEMIC FIBROSIS (NSF)

Gadolinium-based contrast agents (GBCAs) increase the risk for NSF among patients with impaired elimination of the drugs. Avoid use of GBCAs in these patients unless the diagnostic information is essential and not available with non-contrasted MRI or other modalities. NSF may result in fatal or debilitating fibrosis affecting the skin, muscle and internal organs.

- **The risk for NSF appears highest among patients with:**
  - **Chronic, severe kidney disease (GFR < 30 mL/min/1.73m^2), or**
  - **Acute kidney injury.**
- **Screen patients for acute kidney injury and other conditions that may reduce renal function. For patients at risk for chronically reduced renal function (for example, age > 60 years, hypertension or diabetes), estimate the glomerular filtration rate (GFR) through laboratory testing [*see Warnings and Precautions*].**
- **For patients at highest risk for NSF, do not exceed the recommended DOTAREM dose and allow a sufficient period of time for elimination of the drug from the body prior to any re-administration [*see Warnings and Precautions*].**

Contraindicated in patients with a history of clinically important hypersensitivity reactions to DOTAREM.

The possibility of serious or life-threatening anaphylactoid/anaphylactic reactions with cardiovascular, respiratory or cutaneous manifestations, ranging from mild to severe, including death, should be considered. Monitor patients closely for need of emergency cardiorespiratory support.

In patients with chronically reduced renal function, acute kidney injury requiring dialysis has occurred with the use of GBCAs. The risk of acute kidney injury may increase with increasing dose of the contrast agent; administer the lowest dose necessary for adequate imaging. Screen all patients for renal impairment by obtaining a history and/or laboratory tests. Consider follow-up renal function assessments for patients with a history of renal dysfunction.

Ensure catheter and venous patency before the injection of DOTAREM. Extravasation into tissues during DOTAREM administration may result in tissue irritation.

The most common adverse reactions associated with DOTAREM in clinical studies were nausea, headache, injection site pain, injection site coldness, and burning sensation.

For more information about DOTAREM, including Boxed WARNING, please see the Full Prescribing Information.

Please see adjacent Brief Summary of Prescribing Information.

DOTAREM is a registered trademark of Guerbet and is available by prescription only.

GU02141011

References: 1. Dotarem [package insert]. Bloomington, IN: Guerbet LLC; 2013. **2.** Data on file, Guerbet LLC.

www.guerbet-us.com

Guerbet
Contrast for Life